Multiparametric evaluation of magnetic nanoparticles for theranostic applications in breast and pancreatic cancer.

Submitted by

Kieran Crosbie-Staunton, BA (Mod), MPhil

Being a dissertation submitted for the degree of

Doctor of Philosophy

Department of Clinical Medicine

Trinity College, the University of Dublin

2016

DECLARATION

I declare that this thesis has not been submitted as an exercise for a degree at this or any other university and it is entirely my own work, except where duly acknowledged in the text.

I have read and I understand the plagiarism provisions in the General Regulations of the University Calendar for the current year, found at: http://www.tcd.ie/calendar. I have completed the Online Tutorial on avoiding plagiarism 'Ready, Steady, Write', located at http://tcd-ie.libguides.com/plagiarism/ready-steady-write.

I agree to deposit this thesis in the University's open access institutional repository or allow the library to do so on my behalf, subject to Irish Copyright Legislation and Trinity College Library conditions of use and acknowledgement.

Kieran Crosbie-Staunton

ACKNOWLEDGEMENTS

This work was part funded by the European Commission FP7 projects of Multifun (No. 262943) and NAMDIATREAM (No. 140338), and Science Foundation Ireland (Project: 203287, Award: 13216).

Thank you to Prof Yuri Volkov for providing me the opportunity to undertake such an exciting European project, and for reviewing this thesis. To my second supervisor Dr Adriele Prina-Mello, thank you very much for your invaluable guidance over the past few years and for the many suggestions during writing of this thesis, and for my ongoing addiction to nespresso!!

I would also like to thank all my friends and colleagues who supported me throughout this PhD, especially to Dr Bashir Mohamed, Dr Omar Mahfoud, Dr Stephen Samuel, Dr Caroline Moore, Dr Ayoks Ajetunmobi, Dr Alexandra Tuzova, Dr Ciarán Maguire, Dr Claire Tully, Cristina Multari, Fionn Cleary, Gareth Clarke, Prof James Murray, Laura Kickham, Lisa Mathejczyk, Melad Aswisi, Dr Sarah Brophy, and Dr Susan Heavey. I hope someday we can all meet and reminisce about the highly educational times we've had in the reading room. Christmas trees will never be the same again!

Thank you to all members of Multifun, especially Dr Oliviero Gobbo, Dr Maria del Puerto Morales, Dr Gorka Salas, Dr Marzia Marciello, Dr Macarena Calero, Dr Michele Chiappi, Dr Pierre Couleaud, Dr Susanne Kossatz, Dr Maha Sadir, Yurena Luengo, Ana Lázaro Carrillo and other friends I made throughout my travels, Dr Carlos Alvarez, Dr Bea Salinas, Dr Cristina Blanco and Dr Amalia Ruiz Estrada. The past few years have been filled with excitement, unforgettable experiences and cherished memories; you have all shown me such kindness during this time and for that I'm deeply grateful.

A special thanks goes to Prof Seamas Donnelly, Dr Ciaran O Reilly and Mohammad Doroudian, not only for the financial support in the last 6 months of the PhD project but for your friendship and many words of encouragement.

Words cannot express how thankful I am to my family for their support over the past few years, especially to my wife, Dr Tatsiana Rakovich, for being there at every moment to offer scientific guidance and moral support during the difficult times. To my son Alexei, you will grow up knowing that these few years have shaped me into the father that will always stand by your side in support and will never sit idly by in the face of those who wish to put you down. Through perseverance you will succeed and will progress higher than you can imagine. To my mother Valerie, father William, sister Sabina, brother-in law Paddy, nephews Ben, Adam and Jack, mother-in-law Dr Diana Savateeva, father-in-law Prof Yury Rakovich, and sister-in-law Dr Alexsandra Rakovich, I am truly grateful for all the sacrifices that you've made on my behalf and for all the anguish you've had to endure over the past few years, I swear I won't do another PhD! Thank you for everything.

This thesis is dedicated to my Grandfather John B. Crosbie (1927 – 2013)

ABSTRACT

Magnetic iron oxide nanoparticles (MNP) are superparamagnetic below 30 nm in size, have high surface to volume ratio in the nanometre size range, display no remnant magnetism in the absence of a magnetic field yet have high coercivity at high magnetisation and have high magnetic susceptibility. These beneficial properties favour the use of MNP in applications such as magnetic resonance imaging where they can be used as contrast agents, and in therapeutic applications such as magnetic-hyperthermia. In addition, the ability to coat the MNP with a range of surface modifying molecules provides further potential to functionalise the surface with targeting moieties and therapeutic agents such as chemotherapeutic drugs. Detecting cancers at an early stage not only increases the potential for complete removal of the diseased tissue, such as the lumpectomy of breast cancers, but also increases survival rate in diseases such as pancreatic cancer, where symptomatic presentation occurs mostly at the late stage of disease progression. Current therapies involving chemotherapeutic drugs, radiotherapy regimens and surgical intervention are highly invasive and generate undesirable side effects. The advent of nanomedicines has opened up a new avenue for potential detection and therapeutic applications. Through precise targeting of MNP via the incorporation of a surface bound targeting molecule specific for the diseased tissue, and the controlled release of chemotherapy drug at the site of the tumour, the systemic exposure to the chemotherapy drug can be dramatically reduced or completely eliminated, thereby preventing the associated side effects. In addition, the systemic dose delivered can be substantially lowered while maintaining the therapeutic dose delivered to the tumour bed. Furthermore, through exploiting the magnetic properties of the MNP, their *in vivo* biodistribution can be determined via imaging applications such as magnetic resonance imaging and *in situ* hyperthermia can be conducted in order to kill the cancer cells via thermal ablation. Therefore MNP could provide both a diagnostic and therapeutic modality for the detection and treatment of cancers at an early stage.

In this study, a three-tiered safe-by-design characterisation approach was employed to facilitate the selection of a theranostic MNP. Characterisation steps included physicochemical characterisation (PCC), *in vitro* cytotoxicity, determination of *in vitro* anticancer efficacy, and *in vivo* biodistribution of seven MNP as part of the European Commission FP-7 project of Multifun. MNP synthesized by co-precipitation in water or by thermal decomposition were characterised by nanoparticle tracking analysis (NTA) and compared with characterisation conducted by Multifun partners in IMDEA, Madrid, Spain, using transmission electron microscopy (TEM) and dynamic light scattering (DLS). MNP High content screening analysis (HCSA) in four breast cancer cell lines (MCF-7, MDA-MB-231, BT-474 and SK-BR-3) and a normal-like breast-derived cell line (MCF-10A) was conducted to identify non-cytotoxic formulations. Lysosomal uptake was determined using LysoTracker® stained cells and bright field overlay to confirm localization of MNP following 24h exposure, which was confirmed as active uptake into lysosomes via clathrin-mediated endocytosis and micropinocytosis by partners in IMDEA, Madrid, Spain. Two biocompatible MNP were identified, OD15 and MF66. *In vivo* biodistribution and biocompatibility testing of MF66 MNP using a 7T magnetic resonance imaging device found that reliable detection of the MNP in the mouse was possible with imaging conducted at 4h post-injection. MNP uptake into mouse liver, spleen, lung, kidney, heart and brain was analysed by pEPR and blood circulation half-life was determined in a rat model. Furthermore, three linkers to facilitate functionalization onto OD15 and MF66

MNP were screened by HCSA for the ability to release an active drug compound (doxorubicin hydrochloride) and induce an anticancer effect. In addition, OD15 and MF66 were functionalized with the Nucant (N6L) pseudopeptide which, despite being cytotoxic in free form, enabled enhanced uptake of nanoparticles into cells. Multifunctionalised formulations including the N6L targeting moiety and gemcitabine hydrochloride chemotherapy drug were shown to have higher uptake into cells compared to non-targeted formulations and anticancer efficacy of both non-targeted and targeted formulations was similar to drug alone. Further *in vitro* evaluation demonstrated mitochondrial toxicity following exposure to drug-functionalised MNP which was associated with an increase in cell death by apoptotic or necrotic pathways. Evaluation of genotoxic potential by the OECD guideline (test 487) cytokinesis block micronucleus assay demonstrated that the MNP formulations did not induce chromosomal aberration compared to colchicine, a known micronucleus inducing compound.

Therefore, this study enabled the identification and elimination of cytotoxic MNP formulations and facilitated the selection of the most suitable lead drug-functionalised MNP through systematic selection following a three-tiered safe-by-design approach.

TABLE OF CONTENTS

LIST OF FIGURES

LIST OF TABLES

LIST OF SUPPLEMENTAL FIGURES

ABBREVIATIONS

7-AAD	7-aminoactinomycin D
%	Percentage
µL	Microliter
µm	Micrometer
µM	Micromolar
AIF	Apoptosis Inducible Factor
ALDH	Aldehyde Dehydrogenase
AnnV	Annexin V
Apaf-1	Apoptotic Protease Activating Factor 1
BCT	Breast Conserving Therapy
CBMN	Cytokinesis Block Micronucleus Assay
CdSe QD	Cadmium Selenide Quantum Dot
CSC	Cancer Stem Cells
CT	Computerised Tomography
CTRL(-)	Negative Control
CTRL(+)	Positive Control
CytoB	Cytochalasin B
DAPI	4',6-diamidino-2-phenylindole
DI water	Deionised water
DLS	Dynamic Light Scattering
DMEM	Dulbecco Modified Eagles Medium
DMSA	meso-2,3-dimercaptosuccinic acid
DMSO	Dimethyl sulfoxide
Doxo	Doxorubicin
DPBS	Dulbecco's Phosphate Buffered Saline
EE	Early Endosome
EGF(R)	Epidermal Growth Factor (Receptor)
EPR	Enhanced Permeability and Retention
ER	Endoplasmic Reticulum
FBS	Foetal Bovine Serum
Fe_3O_4	Magnetite
γ-Fe_2O_3	Maghemite
FDA	Federal Drug Administration
FITC	Fluorescein Isothiocyanate
FP7	Framework Programme 7
g	gram
GTP	Guanosine Triphosphate
HCl	Hydrochloric Acid

HCSA	High Content Screening Analysis
HER2	Human Epidermal Growth Factor Receptor 2
HIF	Hypoxia Inducible Factor
HR	Homologous Recombination
kg	kilogram
L	Litre
LDH	Lactate Dehydrogenase
LE	Late Endosome
LRR	Locoregional Recurrence Rate
M	Molar
mg	milligram
mL	Millilitre
MN	Micronuclei
MNP	Superparamagnetic Iron Oxide Nanoparticle
MRI	Magnetic Resonance Imaging
MRM	Modified Radical Mastectomy
mtDNA	Mitochondrial Deoxyribonucleic Acid
MTOC	Microtubule Organising Centre
MTT	3-(4,5-dimethylthiazole-2-yl)-2,5-diphenyltetrazolium bromide
Multifun	Multifunctional Nanotechnology for Selective Detection and Treatment of Cancer
mV	Milivolt
N6L	Nucant pseudopeptide
NADH	Nicotinamide Adenine Dinucleotide
nm	Nanometer
nM	Nanomolar
NTA	Nanoparticle Tracking Analysis
OECD	Organisation for Economic Cooperation and Development
PanIN	Pancreatic Intra-epithelial Neoplasia
PARPi	poly (adenosine diphosphate [ADP]) ribose polymerase inhibitors
PCC	Physicochemical Characterisation
PDAC	Pancreatic Ductal Adenocarcinoma
PEG	Polyethylene glycol
PEI	Polyethylenimine
pEPR	Particle Electron Paramagnetic Resonance
PFA	Paraformaldehyde
PI	Propidium Iodide
PI3K	Phosphatidylinositol 3-Kinase
PPM	Parts Per Million
PR	Progesterone Receptor
Q	Quadrant

RES	Reticulocyte Endothelial System
ROS	Reactive Oxygen Species
RPMI	Rosewell Park Memorial Institute
RT	Room Temperature
SAR	Specific Absorption Rate
SEM	Scanning Electron Microscopy
SInt	Signal Intensity
siRNA	Small Interfering Ribonucleic Acid
SMAC/DIABLO	Secondary Mitochondra Activator of Caspase
TEM	Transmission Electron Microscopy
TR	Texas Red
TRITC	Tetramethylrhodamine
WP	Work Packages

COMMUNICATIONS

Peer reviewed publications

- OL Gobbo, F Wetterling, P Vaes, S Teughels, F Markos, D. Edge, CM Shortt, **K Crosbie-Staunton** et al. Biodistribution and Pharmacokinetic studies of SPION using particle Electron Paramagnetic Resonance, MRI and ICP-MS. Nanomedicine 06/2015; 10(11):1751-1760. DOI:10.2217/NNM.15.22
- Susanne Kossatz, Julia Grandke, Pierre Couleaud, Alfonso Latorre, Antonio Aires, **Kieran Crosbie-Staunton** et al. Efficient treatment of breast cancer xenografts with Multifunctionalized iron oxide nanoparticles combining magnetic hyperthermia and anticancer drug delivery. Breast Cancer Research 05/2015; 17(66). DOI: 10.1186/s13058-015-0576-1
- Macarena Calero, Michele Chiappi, Ana Lazaro-Carrillo, María José Rodríguez, Francisco Javier Chichón, **Kieran Crosbie-Staunton** et al. Characterization of interaction of magnetic nanoparticles with breast cancer cells. J Nanobiotechnology. 2015; 13(1): 16. DOI: 10.1186/s12951-015-0073-9
- Schütz CA, Davide Staedler, **Crosbie-Staunton K** et al. Differential stress reaction of human colon cells to oleic-acid-stabilized and unstabilized ultrasmall iron oxide nanoparticles. Int J Nanomedicine. 2014; 9(1): 3481 – 3498. DOI: 10.2147/IJN.S65082
- Tatsiana Y Rakovich, Omar K Mahfoud, Bashir M Mohamed, Adriele Prina-Mello, **Kieran Crosbie-Staunton** et al. Highly Sensitive Single Domain Antibody-Quantum Dot Conjugates for Detection of HER2 Biomarker in Lung and Breast Cancer Cells. ACS Nano. 2014; 8(6). DOI: 10.1021/nn500212h.
- Patrick Hole, Katherine Sillence, Claire Hannell, Ciaran Manus Maguire, Matthias Roesslein, Guillaume Suarez, Sonja Capracotta, Zuzana Magdolenova, Limor Horev-Azaria, Agnieszka Dybowska, Laura Cooke, Andrea Haase, Servane Contal, Stein Manø, Antje Vennemann, Jeans-Jacques Sauvain, **Kieran Crosbie Staunton** et al. Interlaboratory comparison of size measurements on nanoparticles using nanoparticle tracking analysis (NTA). J. Nanopart.Res.2013;15. DOI: 10.1007/s11051-013-2101-8
- Oliviero Gobbo, Friedrich Wetterling, **Kieran Crosbie-Staunton**, et al. Pharmacokinetics and biodistribution of superparamagnetic nanoparticles using pEPR in the mouse: an *in vivo*, *in vitro* and ex vivo validation. Proc. Intl. Soc. Mag. Reson. Med. 2013; 21. DOI: 10.13140/2.1.1183.9681
- Navin Kumar Verma, **Kieran Crosbie-Staunton** et al. Magnetic core-shell nanoparticles for drug delivery by nebulization. J Nanobiotechnology. 2013; 11(1): 1. DOI: 10.1186/1477-3155-11-1
- Adriele Prina-Mello, **Kieran Crosbie-Staunton** et al. Multiparametric Toxicity Evaluation of SPIONs by High Content Screening Technique: Identification of Biocompatible Multifunctional Nanoparticles for Nanomedicine. IEEE Trans. Magn. 2013 49(1). DOI: 10.1109/TMAG.2012.2225024
- Bashir M Mohamed, Navin K Verma, Anthony M Davies, Aoife McGowan, **Kieran Crosbie-Staunton** et al. Citrullination of proteins: a common post-translational modification pathway induced by different nanoparticles *in vitro* and *in vivo*. Nanomedicine. 2012; 7(8). DOI: 10.2217/nnm.11.177

Oral Presentations

- **Kieran Crosbie-Staunton**, Gorka Salas, Oliviero Gobbo, Marzia Marciello, Pierre Couleaud, Bashir M Mohamed, Tatsiana Rakovich, Rodolfo Miranda, Maria del Puerto Morales, Adriele Prina-Mello, Yuri Volkov. "Screening of Multifunctional Magnetic Iron Oxide Nanoparticles for Theranostic Applications", 08-04-2015, BioNanoMed 2015, Graz, Austria.
- **K. Crosbie-Staunton**, G. Salas, O. Gobbo, M. Marciello, P. Couleaud, B. M Mohamed, T. Rakovich, R. Miranda, M. del Puerto Morales, A. Prina-Mello, Y. Volkov. "Screening of Multifunctional Magnetic Iron Oxide Nanoparticles for Theranostic Applications", 07-11-2014, IMM 17th Annual Meeting, Ireland.
- **Kieran Crosbie-Staunton**, Adriele Prina-Mello, Oliviero L. Gobbo, Gorka Salas, Maria del Puerto Morales, Yuri Volkov. "*In vitro* and *in vivo* nanotoxicology and biocompatibility testing of coated iron oxide nanoparticles in the selection and development of a multifaceted cancer imaging tool and theranostic drug delivery platform", 29-05-2013, E-MRS Strasbourg, Spring 2013, France.
- **K. Crosbie-Staunton**, A. Prina-Mello, O.L. Gobbo, G. Salas, M. del Puerto Morales, Y. Volkov. "Nanotoxicology screening of coated iron oxide nanoparticles: for the selection of lead candidate for theranostic applications", 03-03-2013, Namdiatream Winter School, Villars-sur-Ollon, Switzerland.

Poster Presentations

- **K. Crosbie-Staunton**, *et al*. "Screening of Multifunctional Magnetic Iron Oxide Nanoparticles for Theranostic Applications", 07-11-2014, IMM 17th Annual Meeting, Ireland.
- **K. Crosbie-Staunton** *et al.* "Multifun Project: Multifunctional Nanotechnology for Selective Detection and Treatment of Breast and Pancreatic Cancer." 18-06-2013, EuroNanoForum 2013, Co. Dublin, Ireland.
- **K. Crosbie-Staunton** *et al.* Biocompatibility Screening of Magnetic Nanoparticles for Theranostic Application. 17-09-2012, Nanoweek Conference, TCD (CRANN), Co. Dublin, Ireland.
- **K. Crosbie-Staunton** *et al.* High Content Screening as an in vitro pre-screening tool for Multifunctional nanoparticle selection. 19-09-2011, Postgraduate Research Day 2011, TCD, Co. Dublin, Ireland.
- **K. Crosbie-Staunton** *et al.* Development of a Nanodrug Delivery Platform with Surface Modified Magnetite and Gold Nanoparticles. 21-06-2011, 7th NanoBio-Europe, Co. Cork, Ireland.
- **K. Crosbie-Staunton** *et al.* Biocompatibility Analysis of Functionalized Gold and Surface Modified Magnetite Nanoparticles. 31-01-2011, Nanoweek 2011, Carton House, Co. Kildare, Ireland.

Chapter 1
Introduction

Chapter 1: Introduction

1.1 Nanotechnology: a brief history

Nanotechnology is the manipulation of matter on the nanoscale (10^{-9} meter) encompassing the fields of science, engineering and technology. From the historical perspective, nanotechnology has been harnessed for thousands of years in the production of stained glass and for medicinal purposes using liquid gold. Gold and silver nanoparticles added to molten glass provided a means to fine tune optical properties and produce an array of colours. A famous example of this is the "Lycurgus cup", a 4th century Roman glass cage cup with red-green colouration. These colloidal dispersions, whether added by intent or by accident, are one of the first examples of nanoparticle use existing to this day. It is proposed that the basis for modern-day nanoparticle research was established during the 19th century, with the research of Michael Faraday on dispersions of colloidal gold [1]. It was not until 1959 that nanotechnology was brought into the spotlight following a radical lecture by Richard Feynman who proposed that "there is plenty of room at the bottom", and is heralded as the inspiration for modern day nanotechnology. He considered the ramifications of being able to manipulate at the atomic scale, and the possibility of developing increasingly smaller devices that would be capable of building even smaller devices. Feynman's lecture however went largely unnoticed at the time and it wasn't until Kim Eric Drexler published his PhD thesis "*Nanosystems: Molecular Machinery, Manufacturing and Computation*" that nanotechnology, as we know it, was born [2]. Since then, nanotechnology has progressed rapidly, facilitated largely by the immense technological advancements made over the past two decades.

1.1.1 Nanomaterials

The term nanomaterials refers to an extensive and highly varied population of nanosized objects (chemicals and materials) that have been systematically researched over the past few decades. Nanomaterials can fall into three major categories, whether they are naturally occurring, incidentally produced, or engineered for a specific purpose. Naturally occurring nanosized materials include viruses, antibodies, lipids, proteins and other small molecules such as glucose and water (Figure 1). It is accepted that a material can be referred to as a nanomaterial if it satisfies a set of pre-defined physical conditions as outlined by the European Commission [3]:

A natural, incidental or manufactured material containing particles, in an unbound state or as an aggregate or as an agglomerate and where, for 50 % or more of the particles in the number size distribution, one or more external dimensions is in the size range 1 nm - 100 nm.

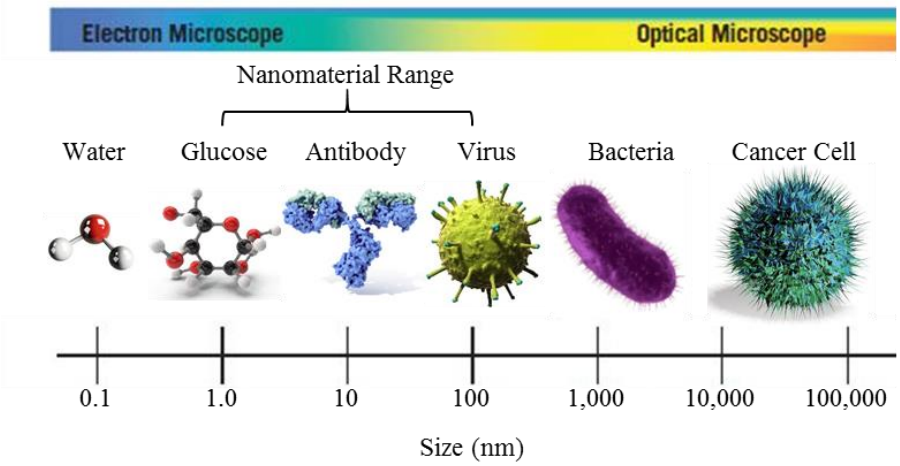

Figure 1: Nanomaterials size range in relation to biological examples.

Nanomaterials range between 1 and 100 nm in size, similar in size to glucose, antibodies and viruses. Adapted from: http://www.particlesciences.com/services/micro-nano-technology/

It is estimated that approximately 11 million tonnes of nanomaterials are produced per year, with a market value of €20 billion. Applications of nanomaterials are diverse, with research providing new and unique uses of a vast array of material; for example gold nanoparticles have been used in the purification of air, when embedded in a porous manganese oxide as a room temperature catalyst [4]; as probes in the application of transmission electron microscopy owing to their dense structure and in fuel cell applications [5]. In comparison, silver in its nanosized forms have been extensively used for their anti-bacterial properties [6]. Carbon black nanomaterials have been utilised for their black pigment and also for their conductive properties in vehicle tyres [7]. It has been shown to facilitate heat dissipation from the thread and belt area of tyres therefore extending tyre life. It has also been used as toner and printer ink, as a food colouring (E153), in electronics on account of its high conductivity, and in food packaging due to its retention in plastics [8]. Silica based nanomaterials have also been used as an additive in tyres, as a strengthening agent in concrete, in lithium ion batteries, in solar panels, in food and in cosmetics [9-13]. Superparamagnetic iron oxide nanoparticles (MNP) are used in a wide range of applications including data storage [14], toners and inks [15], tattoos [16], water purification and waste water management systems [17, 18], but most importantly they have shown huge promise in medical applications as diagnostic and therapeutic compounds [19-24]. Due to their small size, MNP have a large surface-to-volume ratio and along with their suitability to act as scaffolds for the functionalization of a wide range of therapeutic compounds, a high concentration of drug delivery to the site of a tumour is possible. Their superparamagnetism opens up an array of possibilities such as the *in vivo* visualisation of MNP by magnetic resonance imaging, in cellular labelling, and biosensing applications [25, 26]. They have been utilised in molecular biology as an efficient means of transfection through exploiting their superparamagnetic properties in a technique called magnetofection [27]. In this application, nucleic acids, transfection reagents or viruses are electrostatically attached onto the surface of the nanomaterials and the nanoparticles are concentrated onto cells by the influence of a magnetic field, thereby increasing cellular uptake through natural biological processes such as endocytosis and pinocytosis. The application of MNP in this manner

is unique in transfection as the membrane architecture and structure remain intact, unlike other physical transfection reagents, which damage and create holes in the cell membrane. An alternative approach, and one that does not require the use of a magnetic field, is the surface modification of nanomaterials with targeting ligands. Such targeting can increase the concentration and deposition of nanomaterials within the tumour bed by exploiting the surface presentation of markers on tumour cells, which are otherwise not expressed in normal, healthy tissue. MNP have the potential to be tailored on a per-case basis through functionalization with tumour-targeting ligands such as monoclonal antibodies, peptides or small molecules and therapeutic agents to improve diagnostic rigor and therapeutic effect [28-32]. Such properties make MNP suitable candidates for theranostic applications and their role as MRI contrast agents [33], in drug/gene delivery platforms [34-36] and hyperthermia [37, 38] are being intensively researched. The capability to visualise MNP using techniques such as MRI and the ease with which they are functionalized with drugs heralded them as the most widely used and important nanoparticle type developed to date. While nanomaterials have been employed in a vast array of applications, it is their use in medicine that will be explored in greater detail in the subsequent sections.

1.1.2 Superparamagnetic iron oxide nanoparticles

The family of MNP display outstanding properties on account of their small size, and high surface-to-volume ratios, which differentiate them from larger particles and their bulk material. The major advantage of MNP is largely owing to their superparamagnetic properties: high coercivity at high magnetisation, low to zero coercivity when the field is removed, low curie temperature and very high magnetic susceptibility which favours their use in a broad range of applications (Figure 2) [39, 40]. These properties make superparamagnetic nanoparticles attractive for the purpose of drug delivery and hyperthermia, as magnetisation within the nanoparticle exposed tumour is lost as soon as the magnetic field is removed due to thermally induced spin flipping. This is beneficial as remnant magnetisation could induce MNP agglomeration and embolization of capillary vessels [41].

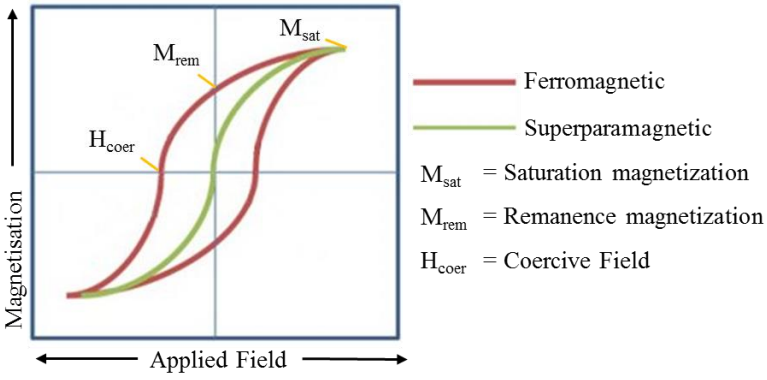

Figure 2: Hysteresis loops (magnetisation versus applied magnetic field) of nanoparticles.

Characteristic hysteresis loops of ferromagnetic and superparamagnetic MNP. Adapted from [40].

The most prevalent iron oxide nanomaterials are magnetite (Fe_3O_4) and its oxidised form maghemite (γ-Fe_2O_3), and are preferentially used in medical research on account of their biocompatibility and

superparamagnetism [42]. Iron is ordinarily present in the human body and the liberation of free iron by the biodegradation of the MNP could be utilised in subsequent metabolic processes, thereby preventing prolonged risk from exposure [43]. While both magnetite and maghemite are ferromagnetic at room temperature (retain their magnetisation in the absence of a field), it is known that below a critical size of 30 nm, the permanent magnetism is lost and they become superparamagnetic [44, 45]. Superparamagnetism occurs when the nanomaterials contain a single magnetic domain, in which all magnetic moments are aligned with one another and they point in the same direction when in the presence of an external magnetic field. The sum of all the individual magnetic moments results in a single giant magnetic moment, which align along the applied field, leading to a net magnetisation. The length of time it takes for the magnetic moment to flip, from parallel to anti-parallel orientations, is referred to as the Néel relaxation time. The emergence of zero magnetism in these superparamagnetic MNP, in the absence of an applied field, is due to the long transition time between these two orientations, which exceed that of the Néel relaxation time.

It is well known that size governs the magnetic properties [46], and it is therefore important to have a reliable synthesis method to ensure that the nanomaterials produced maintain a core size of less than 30 nm. There exist many methods to synthesise iron oxide nanomaterials such as co-precipitation, thermal decomposition, microemulsion, hydrothermal synthesis, sonochemical synthesis, sol-gel synthesis, thermolysis of precursors, and more recently green chemical synthesis methods involving the bacterium *Actinobacter sp.* [47]. These methods have been explored for their ability to produce nanomaterials that are of uniform size and have suitable physicochemical properties for their required application [48]. Thermal decomposition generates a narrow size distribution and homogeneity in structural characteristics, however the production of MNP by this method is both time-consuming and expensive, and chemical remnants from synthesis could pose a risk during the development phase in *in vitro* cytotoxicity experiments and tolerance *in vivo* if adequate washes are not carried out. While co-precipitation results in a wider size distribution and non-uniformity in population shape characteristics, it does produce nanomaterials that are water soluble and as a result it is often the synthesis method of choice [39].

1.2 Multifun: a European Commission FP7 project

The European Commission has provided considerable funding for scientific research, and through the seventh framework programme (FP7) (2007 – 2013) the expenditure was €55.8 billion [49]. Funding for nanomedicine projects has accounted for €400 million of this, and has directly supported 85 projects within the discipline of nanoscience, nanotechnology, materials and new technology [50]. Nanomedicine is the application of nanotechnology in a healthcare setting and is based on the advances in physics, chemistry, biology, engineering and medicine. The nanomedicine field aims to drive the development of next generation nanomaterials to enable early detection and improve diagnosis, treatment and follow-up of many diseases [51]. According to the EU Community Research and Development Information Service [52], the application of nanotechnology in medicine raises high expectations for better, more efficient and affordable healthcare, utilising nanotechnology for targeted drug delivery, diagnostics and regenerative medicine.

One such project with an aim to develop and validate a set of complementary and minimally invasive technologies for the early detection and elimination of breast and pancreatic cancer was the Multifun project (Multifunctional Nanotechnology for Selective Detection and Treatment of Cancer) (www.Multifun-project.eu.). The project was initiated in June 2011, and involved the collaborative effort of thirteen university groups and three industrial partners spanning multiple European countries (Figure 3). Multifun sought to develop a MNP that could be used as a diagnostic tool in applications such as magnetic resonance imaging (MRI), as a therapeutic agent through exploiting the heating capacity of the MNP in an alternating magnetic field, and to target tumour cells and the tumour stem cell population with anticancer drugs as presented in Figure 4. Comprehensive project design ensured the successful development and delivery of a validated and functional theranostic (as the two-in-one application of diagnostic and treatment) nanoparticle. The following sections introduce the background to the Multifun project and the motivation for the work conducted and presented in this thesis within the *in vitro* and *in vivo* screening for the selection of the most suitable Multifun-engineered MNP formulation for breast and pancreatic cancer theranostics.

Figure 3: Multifun FP7 partner locations

Trans-European city involvement in the successful completion of the Multifun FP7 project. Project partners from Dublin (Trinity College Dublin); Cork (University College Cork); Bangor, Wales (Liquids Research LTD); Manchester, England (University of Manchester); London, England (Queen Mary University of London, and Kings College London); Leuven, Belgium (Pepric NV); Jena, Germany (Universitätsklinikum Jena); Prague, Czech Republic (Fyzikalni Ustav); Paris, France (Universite Paris XII - Val De Marne(CRRET)); Toulouse, France (Institute National Des Sciences Appliques De Toulouse); Madrid and Barcelona, Spain (ATOS-project coordinator, CNIO, CSIC, IMDEA and Pharmamar S.A.U). Image adapted from www.wikipedia.org ("blank map of Europe").

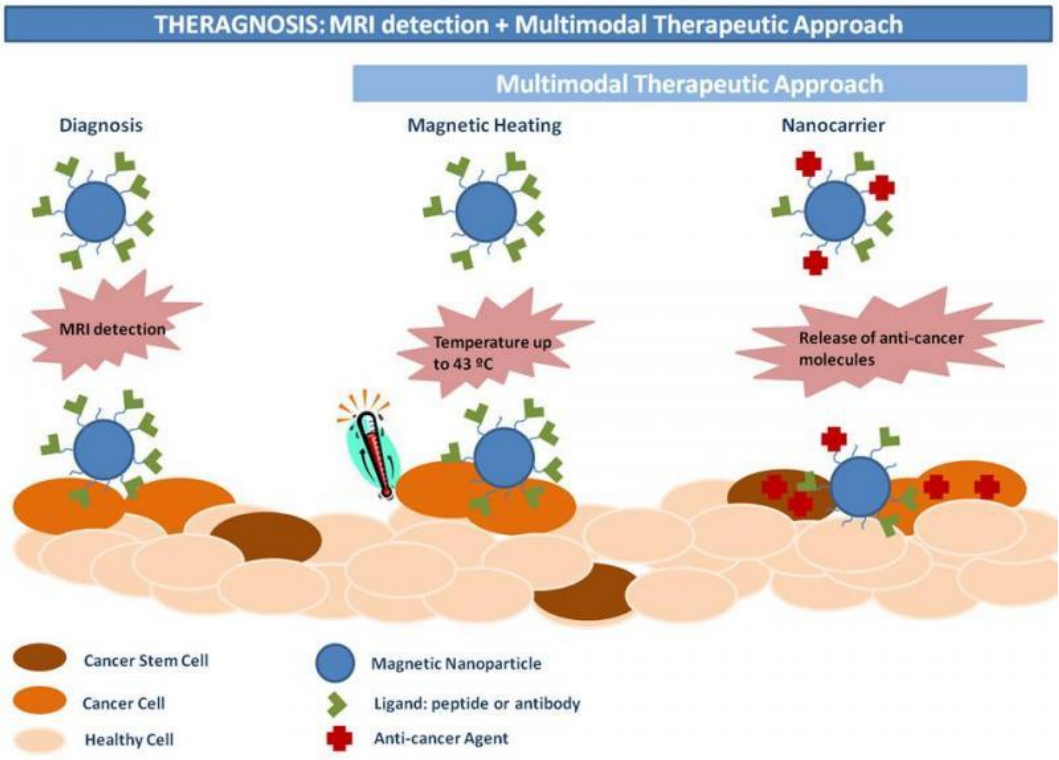

Figure 4: Multifun FP7 project rationale

Overview of the three applications investigated within the Multifun project, including detection of cancer cells using targeted nanoparticles by magnetic resonance imaging, magnetic hyperthermia for tumour ablation and targeted drug delivery using anticancer agents. Image obtained from www.Multifun-project.eu.

1.2.1 Currently approved nanomedicines.

The use of nanomaterials in medicine is already a reality, and a handful of approved nanomedicines are used in the clinic for the purpose of theranostics. These nanomedicines are largely liposomal based, either in non-PEGylated form (DaunoXome®, Myocet® and Onco TCS®) or in PEGylated form (Doxil®), while other nanoparticle types include albumin based Abraxane® and the PEG-L-asparaginase based Oncaspar® [53]. These nanomedicines have been developed and approved for the treatment of specific cancers, however, Doxil® is currently employed to treat multiple cancers including those of the breast and ovary, multiple myeloma and Kaposi's sarcoma. Doxil® was the first such nanomedicine to receive the approval by the federal drug administration. When doxorubicin was encapsulated it was shown to extend the effective half-life of the drug therefore maximising the drug accumulation in the tumour [54], where delivery to the tumour was passive. This mode of non-specific targeting is an effective means to deliver nanomaterials, and exploits the Enhanced Permeability and Retention (EPR) effect, detailed in Figure 5 [55]. The EPR effect occurs as a consequence of abnormal tumour vascularisation in the absence of adequate lymphatic drainage from the tumour site which is otherwise observed in normal tissue [56], and was described by Matsumura et al. in 1986, when the accumulation and retention of dye-complexed serum albumin at the tumour site in a mouse model was observed [57]. Additional growth characteristics of tumours can limit

the effectiveness of targeting by the EPR effect whereby tumour cells grow at a higher rate in the areas nearest to the vasculature and can form a sheath around blood vessels [58]. This growth characteristic of some tumours can limit the penetration of nanomaterials and drugs into the tumour bed, and it may be necessary to target the vasculature-associated tumour cells and induce apoptosis or necrosis within these perivascular regions prior to treatment with nanomedicines and drugs [59]. The reduced lymphatic drainage within a tumour and the subsequent increase in interstitial pressure causes the tumour vasculature to become constricted, thereby limiting the blood flow and ultimately the amount of extravasation that can occur deep in the tissue. The proliferation of tumour cells occurs at such a rate that the blood supply to certain regions of the tumour can be affected. These hypoxic niches are exacerbated by the rapid growth of the tumour and are a dynamic environment in which cancer stem cells (CSCs) can thrive. CSCs are pluripotent cells that display properties that are associated with normal stem cells. They can self-renew, differentiate, resist apoptosis, and have sufficient motility whereby they can form new tumours distant to the primary site [60, 61]. The lack of oxygen within the tumour hampers the targeting of CSCs in this niche and has been demonstrated that hypoxia impairs the effectiveness of treatment such as radiotherapy and chemotherapy [62]. Many factors confer resistance in these cells on account of tumour cell extrinsic conditions such as hypoxia and include a low rate of growth, lack of long-lived reactive oxygen species, and cell cycle arrest [62]. In hypoxic conditions, the hypoxia-inducible factor (HIF) family of proteins are more highly expressed. HIFs are key regulators for the hypoxic response and influence angiogenesis, metabolic adaption, erythropoiesis, cell growth and differentiation [63]. These downstream effects of HIF activity and continued tumour growth lead to constant oxygen fluctuations in the tumour, and has been linked to lower patient survival [64]. Continued survival of the CSCs ensures that a continuous supply of cells are available for tumour growth. On account of this, the targeting of the CSCs has become a major focus in cancer research and nanomaterials have demonstrated their effectiveness at targeting the CSC population. Markers for CSCs in breast and pancreatic cancers include BCRP/ABCG2, ALDH1, CD24, and CD44 among others [65]. Nanomaterials could provide a means to target the deep, high-pressure regions of tumours and the CSC as long as they are of a suitable size and concentration to deliver their therapeutic payload. It is proposed that nanomaterials between 10 and 200 nm in diameter are capable of penetrating deep into tumours and be homogenously distributed [66]. It has been shown that pre-treatment with anti-angiogenic drugs supresses tumour angiogenesis and tumour growth, and has been suggested that treatment may in fact improve blood flow in the tumour through normalisation of the tumour vasculature [67]. Another method to increase the leakiness of the tumour vasculature is nanomaterial-based hyperthermia [68], a localised heating effect which preferentially ablates cancer cells. It has also been shown that 12h after radiation treatment, the cells in the vicinity of the tumour vasculature are damaged and nanomaterials delivery is increased up to 2.2 fold [69]. These approaches have the potential to increase access of the MNP to the hypoxic niche of the tumour thereby enabling delivery of their therapeutic payload. Current research is focused on targeting the CSC population through exploiting the expression of CSC markers using a variety of nanomaterial. One study utilising a similar basic MNP as presented in this thesis functionalised their MNP with an antibody against the breast cancer resistance protein otherwise known as ABCG2. This is a plasma membrane protein of the ATP-binding cassette transporter superfamily and is expressed in the placenta, blood brain barrier, intestines, liver, in stem-cells, and the kidney [70]. It has been implicated in

multi-drug resistance through the export of chemotherapeutic agents such as mitoxantrone, topotecan, and methotrexate [71]. Expression is up-regulated by hypoxia and involves HIF-1α and confers a survival advantage as ABCG2 $^{-/-}$ cells died when exposed to porphyrins [72]. Yang et al. utilised an anti-ABCG2 monoclonal antibody functionalised to DMSA coated paclitaxel MNP *in vitro* and *in vivo* in multiple myeloma cells. They demonstrated that in combination the MNP functionalised with paclitaxel were more effective with co-functionalisation with the ABCG2 targeting antibody [73]. They further demonstrated that the combination of drug loaded MNP had a marked effect on CSC growth in vitro and in vivo with inhibition correlating with caspase 9/8/3 expression [74]. They hypothesised that targeting and effective elimination of CSC was possibly due to the blocking of paclitaxel efflux from the CSC, thus extending the time for release of drug from the MNP [73], and that death of CSC was mainly due to the activation of apoptotic pathways [74]. Another CSC marker currently being studied is the family of aldehyde dehydrogenases (ALDH). CSCs expressing ALDH have been shown to become enriched following chemotherapy treatment, with high expression and activity of ALDH1 being associated with poor prognosis in breast cancer [75]. ALDH1 has been shown as a universal CSC marker in breast [76] and pancreatic cancers [77], and while no studies exist that specifically focus on MNP targeting the ALDH family members, it is an extremely important marker that is closely linked to the ABC proteins in the development of drug resistance in cancer [78]. Other noteworthy targets include CD44 and CD24. It has been demonstrated that the DMSA coated MNP presented in this thesis have the capability of specifically targeting CD44 positive breast and pancreatic cancer cells which was confirmed via down-regulation of CD44 using siRNA [79]. In addition, the MNP were loaded with gemcitabine chemotherapeutic drug which were capable of selective and rapid release, and the efficacy was greater than drug alone and non-targeted nanoparticles [79]. CD44 is frequently expressed in a large number of cancers and correlates with decreased patient survival [80]. In breast cancers the $CD44^{+}/CD24^{-/low}$ phenotype is a marker for breast CSCs [81], and is an attractive marker for the identification and targeting of CSC by MNP.

Harnessing a number of these approaches such as hyperthermia and targeted drug delivery should enable a greater degree of MNP-tumour uptake and homogenous deposition of nanomaterials into the tumour bed. The design of targeted nanomedicines capable of hyperthermia and specific tumour binding via a functionalised ligand was therefore the main aim of the Multifun project, and the following section will focus on the key contribution of the work presented in this thesis as part of the Multifun project in the selection of suitable lead MNP formulations following a safe-by-design approach.

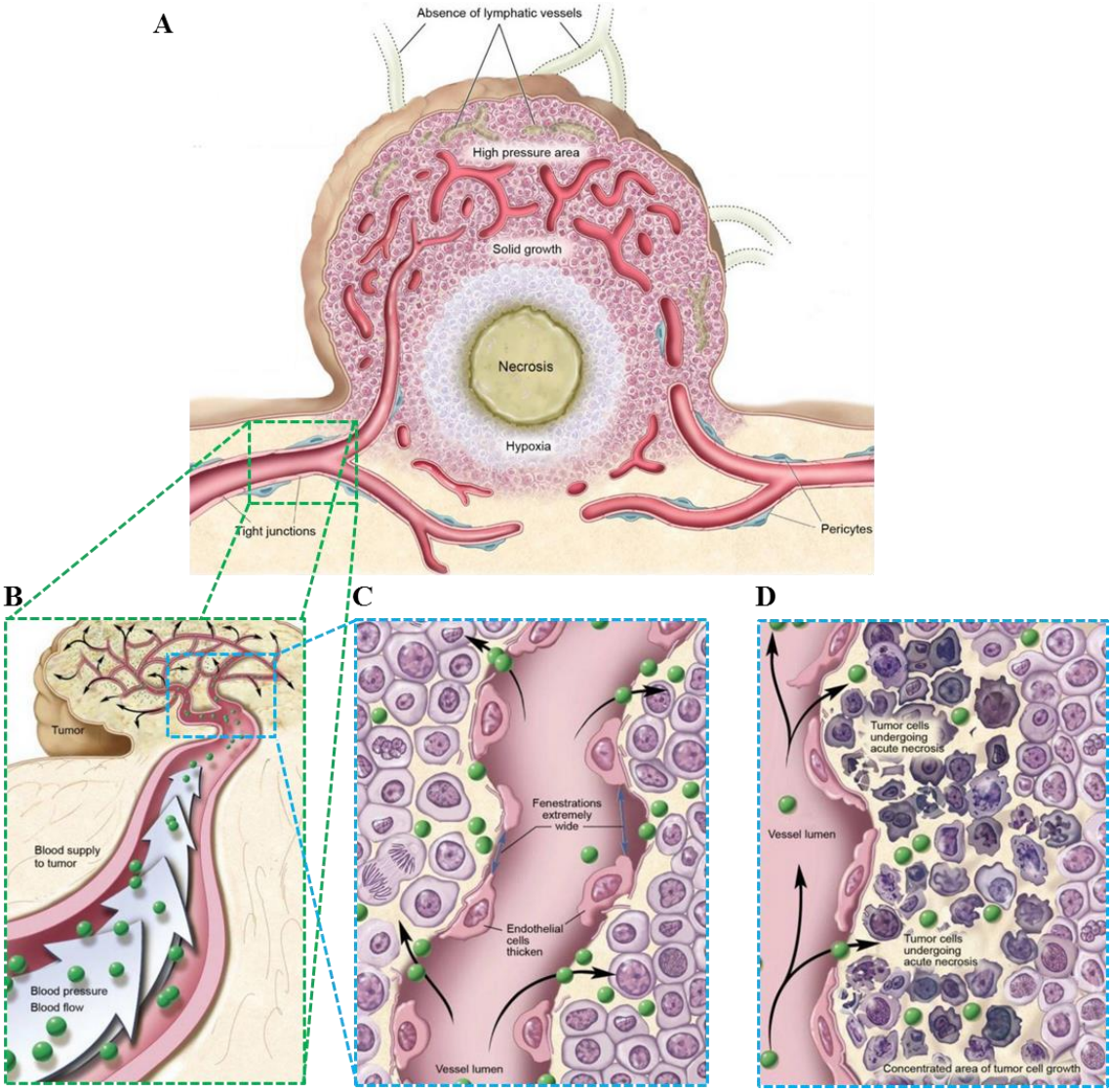

Figure 5: Tumour microenvironment and the EPR effect.

A) Tumour tissue is heterogeneous, with a central necrotic zone distal to the vasculature, hypoxic zone and proximal hyper-vascularised region with high pressure inside the tumour due to a lack of lymphatic drainage. **B)** Delivery of nanomaterials (green spheres) to the tumour. **C)** Nanomaterials are taken up at the tumour site due to leaky vasculature because of large fenestrations between endothelial cells. **D)** Deposition of nanomaterials within the tumour and the application of an alternating magnetic field results in localised hyperthermia and cancer cell ablation. (Adapted from [82]).

1.2.2 Development of next generation MNP: a safe-by-design approach

The currently approved nanomedicines lack a targeting moiety on their surface and rely on the EPR effect for tumour localisation. The aim of the Multifun project was to design a biocompatible nano-enabled carrier for therapeutic applications. In order to achieve this aim, a series of systematic tests were conducted (Figure 6), based on a three-tiered characterisation approach [83]. In Tier 1, the physicochemical characteristics (PCC) of a range of coated MNP was accessed. In Tier 2, basic MNP formulations were evaluated *in vitro* by high content screening analysis (HCSA) employing a multiparametric testing approach to select biocompatible formulations. Tier 2 methodologies further enabled the screening of drug-functionalised MNP to select the most efficient anticancer formulations. In Tier 3, basic MNP formulations capable of industrial scale-up were tested *in vivo* to determine toxicity in a small animal model, pharmacokinetics and organ distribution. MRI was carried out in small and large animal models.

The Multifun project was divided into specific work packages (WP) which were closely linked to ensure coherent and efficient output as detailed in Figure 7. Fundamental to the progress of the project were the activities within WP3 and WP4, as presented in this thesis, which involved the implementation of the safe-by-design approach. WP1 synthesised the basic MNP while WP2 functionalised the basic MNP with chemotherapeutic drugs and a targeting peptide. WP3 (TCD WP leader) was central to the decision making process using the safe-by-design approach and through collaboration with WP4 (TCD main contributing partner), lead formulations were identified which were safely introduced into small and large animal models. Nanomaterials were subsequently made in bulk and provided to WP5 for *in vivo* testing using magnetic hyperthermia. Coordination of all WPs with WP6 was essential for the development of an induction-coil instrument capable of magnetic heating. Therefore, through adopting a tiered safe-by-design approach it facilitated the selection of MNP candidates to bring forward to the next stage towards the development of a nano-enabled drug carrier for therapeutic applications. The following sections introduce the types of cancer chosen to demonstrate the effectiveness of the anticancer nanoparticles produced. Subsequently, a breakdown of each tiered characterisation step as presented in Figure 6, is provided, and based on current knowledge from the literature.

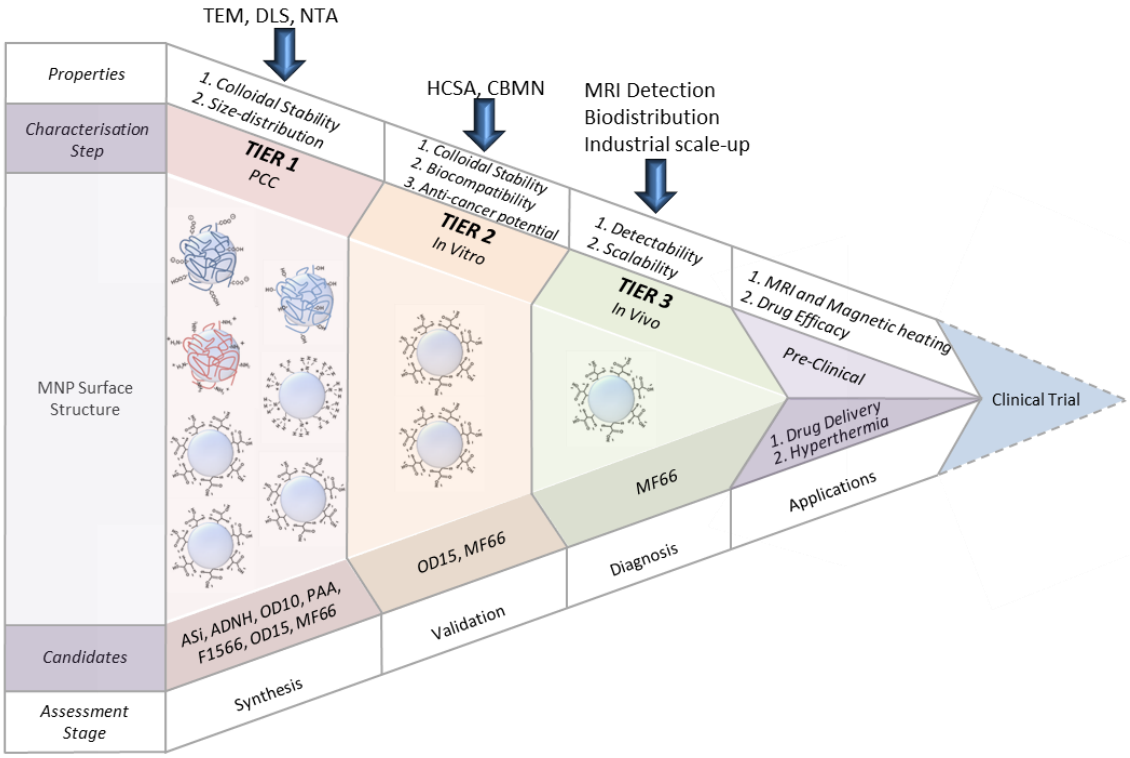

Figure 6: Schematic of the tiered safe-by-design approach.

A three-tier decision making process was employed in order to select the most suitable lead for future clinical use. **TIER 1:** Physicochemical Characterisation (PCC) was conducted to aid decision making based on magnetic MNP core size, shape and colloidal stability when dispersed in water and culture medium by transmission electron microscopy (TEM), dynamic light scattering (DLS) and nanoparticle tracking analysis (NTA). **TIER 2:** *In vitro* MNP multiparametric cytotoxicity evaluation by high content screening analysis (HCSA) identified suitable basic formulations that demonstrated stability in biological media and did not induce acute cytotoxicity. Further analysis of drug-functionalised MNP by the same approach identified MNP anticancer potential compared to efficacy of free chemotherapy drug. Lastly, nanomaterials were tested to determine genotoxic potential through the cytokinesis block micronucleus assay (CBMN). **TIER 3:** Suitable MNP underwent scale-up production; the selection was based on the capability to produce industrial quantities while maintaining strict physicochemical specifications and the absence of acute toxicity in a small animal model. Visualisation of MNP biodistribution was conducted by magnetic resonance imaging (MRI).

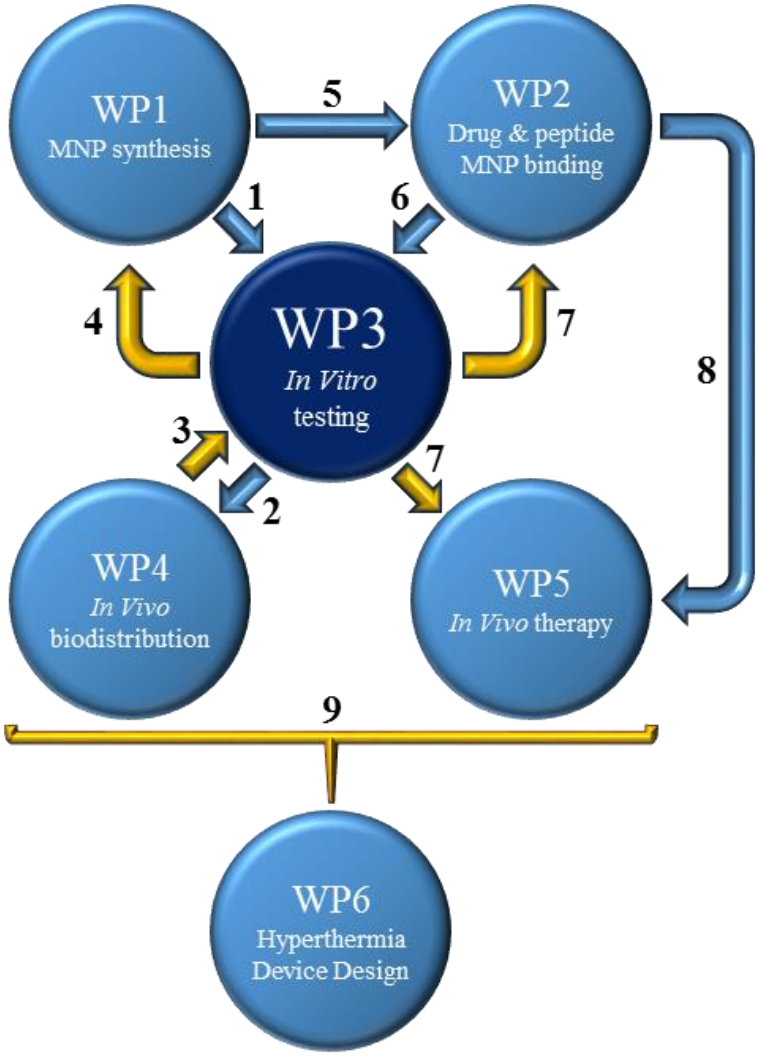

Figure 7: Multifun FP7 workflow

Overview of workflow implemented to streamline selection of MNP formulations; from basic coated formulations (WP1 to WP3 to WP4) to the testing of mono-functionalised and multi-functionalised MNP for anticancer capabilities (WP2 to WP3 to WP5). Sequence of nanomaterials movement (blue arrow) between work packages and decision on suitable nanomaterials (gold arrow) are indicated numerically.

1.3 Breast and pancreatic cancers

1.3.1 Breast cancer

According to the national cancer registry of Ireland (www.ncri.ie), breast cancer was the second most prevalent cancer diagnosed in Ireland. Between 2008 and 2010, 22% of all invasive cancers diagnosed in females were of the breast. In males, the incidence of breast cancer ranked 16th at 0.2% for the same period. Mortality rates in females were 16.4% in 2010, making it the second most common cause of cancer related death. Cancer of the breast can arise from within the ducts, lobules and in the tissue and can be invasive, non-invasive, recurrent, and metastatic. Of the three regions of the breast that can harbour a tumour there are multiple types such as: ductal carcinoma in situ, invasive ductal carcinoma, tubular, medullary, mucinous, papillary, and cribriform carcinoma of the breast, invasive lobular carcinoma, inflammatory breast cancer, and lobular carcinoma in situ. Individuals can spontaneously develop breast cancer or some may harbour hereditary mutations that predispose them to the disease during their lifetime. Whether breast cancer onset is spontaneous or hereditary, the molecular profile of the tumours broadly fit within four major subtypes of breast cancer which have been determined by gene expression profiling.

1.3.1.1 Breast cancer subtypes

The breast is a complex tissue and many different subtypes of breast cancer exist, it is broadly accepted that there are four major subgroups of breast cancer which all differ in gene expression, Luminal A, Luminal B, HER2, and triple-negative/basal-like [84]. Each of the subtypes is segregated according to their molecular profile and the association with the luminal or basal layers of the breast. The segregation of tumours into these subtypes is of prognostic and predictive value and facilitates the selection of the most appropriate treatment for the patient taking into account the tumour stage, tumour grade, hormone receptor status, and HER2 status. It is of paramount importance that patients receive the necessary and proportionate treatment for the presenting cancer which is dependent on a multitude of factors, and to ensure that overtreatment is kept to a minimum [85].

The luminal breast cancers, aptly named due to the expression of luminal epithelial markers such as keratin 8 and 18 [86, 87], have a high expression of hormone receptors with luminal A having higher expression than luminal B. Both subtypes can include ER+/PR+, ER+/PR–, ER–/PR+ status and are either HER2– (Luminal A) or may have HER2 enrichment (Luminal B). Ki67 is a prognostic marker in early breast cancers and is associated with a worse prognosis [88], but has yet to demonstrate sufficient reproducibility for routine clinical practice [89, 90]. Luminal A tumours tend to have low expression of Ki67, while luminal B tumours can have high Ki67 in the absence of HER2 expression [91]. Luminal breast cancers account for up to 70% of all invasive tumours where luminal A tumours are of low grade, proliferate slowly, and have the best prognostic outlook while Luminal B cancers grow faster, have genomic instability, harbour TP53 mutations and do not have the same positive outlook [92]. Luminal B cancers are, at the molecular level, more distinct from luminal A with a higher degree of alteration in gene expression, copy number, mutation and DNA methylation compared to Luminal A [86] and have some overlap in gene expression to basal-like cancers such as the expression of the proliferation marker *MKI67*, surviving gene *BIRC5* and cyclin B1 gene [86]. Therefore it is more correct to suggest that Luminal B tumours represent

a unique subtype of breast cancer and are not simply a more aggressive or advanced form of Luminal A [86]. There is a marked difference in response to chemotherapy with Luminal B tumours responding to treatment compared to Luminal A tumours that generally show no benefit, as evidenced by the low response rate for Luminal A tumours after neoadjuvant chemotherapy [92], and recently it was reported at the 2015 San Antonio Breast Cancer Symposium by Prof. Torsten Nielsen that there was no difference in 10-year invasive disease-free survival rates in a cohort of premenopausal patients with Luminal A tumours who received chemotherapy treatment compared to those that did not. In addition to this, Luminal B tumours, while being ER+, do not respond to hormone treatment as readily as Luminal A, and are believed to rely less on the estrogen pathway. The targeting of alternative pathways (EGFR/PI3K/Akt/mTOR) in these tumours has shown some advancement in progression-free survival [93, 94]. Therefore, while the treatment of Luminal A tumours is mostly limited to endocrine therapy, the Luminal B tumours benefit with the inclusion of chemotherapy, yet there still exists a need to identify patients with Luminal B tumours that would benefit from chemotherapy treatment. A recent study focused on epigenetic alteration via DNA methylation using a panel of 3 CpG markers (cg17108819, cg13577076 and cg09260089) to stratify a cohort of samples into two categories of luminal B tumours with one subgroup of luminal B demonstrating a methylator phenotype which clustered with Luminal B/HER2 tumours while the second demonstrated less methylated events and clustered with Luminal A tumours [91]. Degree of methylation was indicative of clinical outcome with the luminal B/HER2 tumours displaying a CpG island methylation signature that are associated with unfavourable clinical parameters and reduced survival [91]. These results suggest that the Luminal B/HER2+ patient cohort may benefit with the inclusion of chemotherapy as well as anti-HER2 therapy, while those Luminal B tumours that clustered with the Luminal A tumours may not gain any benefit with chemotherapy.

HER2/ERBB2 is a transmembrane tyrosine kinase receptor that can initiate a variety of signalling pathways such as mitogen-activated protein kinase, phosphoinositide 3-kinase, protein kinase C, phospholipase C and signal transducer and activator of transcription. Through each of these signal transduction pathways, HER2 functions to control cell proliferation and oppose apoptosis. Therefore, dysfunction of HER2 can result in uncontrolled cell growth which is otherwise tightly controlled. Activation of HER2 through binding its extracellular ligand leads to dimerization with itself or with three other family members (HER1, HER3, and HER4). The heterodimer HER2-HER3 is the most potent for downstream signals, especially the PI3K/Akt pathway which is the master regulator of proliferation and survival [95]. In addition, dimerization of HER2 promotes rapid degradation of $p27^{Kip1}$, a cell-cycle inhibitor, which therefore promotes cell growth [95]. Breast cancers that do not express or express low levels of ER and associated genes and are enriched with the oncogene HER2 account for approximately 15 – 30% of invasive breast tumours [96, 97]. These cancers are characterised by high expression of HER2 and other genes in the amplicon and are associated with high recurrence rates with poor prognosis [98]. In a study of 704 node-negative breast cancers, it was shown that HER2 overexpression conferred a 9.5 fold increase in recurrence compared to those cancers where expression was at normal levels [99], with the identification that a fold increase of 3 or greater negatively impacted on disease-free survival [100]. HER2 is shown to be expressed in DCIS with no nodal involvement, and has been related to an invasive-component as tumours develop [101, 102]. In a more recent publication it was shown that while HER2

positivity was a prognostic factor for invasive breast cancers, the prognostic significance in DCIS was less clear [85]. In this study a cohort of 458 patients were screened and an extensive long-term follow-up was conducted, and they concluded that HER2 positivity in patients with DCIS conferred a lower risk of late invasive breast cancer recurrence following 10 years from primary DCIS treatment [85]. Therefore it is important that further studies are conducted and include long-term assessment in order to determine whether patients would benefit from adjuvant therapy after surgical excision or whether they can be safely omitted from needless therapy [103].

The triple-negative and basal-like breast cancers lack expression of ER and PR, and do not overexpress HER2. The basal-like breast cancers also express genes that are usually found in the basal/myoepithelial cells of the normal breast [104], such as cytokeratin 5, 6, 14, and 17; and epidermal growth factor receptor (EGFR) [87, 105], and over 70% of basal-like breast cancers have been shown to harbour dysfunctional BRCA1 [106]. They tend to be high grade, highly aggressive tumours that have very poor prognosis and due to the lack of expression of hormone receptors and HER2, it precludes their treatment with hormone and anti-HER2 therapy. The triple-negative breast cancers account for approximately 10 – 17% of all invasive breast carcinomas while basal-like breast cancers account for approximately 15% [107]. While most triple-negative breast cancers have a basal-like phenotype and most basal-like tumours have a triple-negative phenotype, both subtypes are not synonymous. There are cases where triple-negative breast cancers were devoid of basal gene expression [108, 109] and cases where basal-like cancers express ER, PR and HER2 [110, 111]. BRCA1 tumours are regarded as being similar to the basal-like subgroup, whereby they are negative for ER, PR and HER2. These tumours are generally p53 positive and have a high frequency of p53 mutation [112]. They tend to be c-Myc amplified and over-express EGFR and Cyclin E [113-116]. They also express cytokeratins 5, 6, 14, and 17, p-cadherin, EGFR, laminin, osteonectin and vimentin; which is a feature shared with basal-like tumours [117-119]. In addition to this, they are often high grade with early onset, with lymph node negativity, high mitotic index and pushing margins which display high lymphocytic infiltrate [120-122]. These tumours do not express $p27^{Kip1}$ [123], or Cyclin D [116]. BRCA1 tumours can occur sporadically via the silencing of BRCA1, or can occur due to inherited mutation. A number of studies have also demonstrated a reduction of BRCA1 gene and protein expression in basal-like sporadic tumours [124], which was on account of allelic imbalance through loss of heterozygosity [125], and a result of hypermethylation of the BRCA1 promoter of which 30 CpG islands are implicated in its silencing [126]. Hypermethylation of the BRCA1 promoter has been reported in sporadic basal-like breast cancers in 10 – 31% of cases [124, 127-132], which provides an explanation for the observed reduction in BRCA1 mRNA and protein expression), and due to high expression of the inhibitor of DNA binding 4 protein which was shown to have a 9.1 fold increase in basal-like tumours compared to grade matched controls [133, 134], and is known to act as a negative BRCA1 transcriptional regulator [135]. In addition, BRCA1 loss has been shown to result in downregulation of ER [136], and it has previously been demonstrated by the author of this thesis, within the publication of Gorski *et al*., that reduction in BRCA1 expression results in a luminal cell line expressing markers of basal-like cancers [87], with reconstitution of BRCA1 expression in an ER– and BRCA1 mutant cell line conferring a more luminal phenotype with an observed reduction in basal-like markers [87]. This may suggest that basal-like cancers are driven by BRCA1 dysfunction and as such, a considerable number of basal-like cancers may lack a

competent homologous recombination (HR) DNA repair mechanism [107]. It has been demonstrated that tumours harbouring a defective HR repair pathway are especially sensitive towards Poly-(ADP-Ribose) Polymerase Inhibitors (PARPi) and platinum-based chemotherapy drugs [137]. PARPi selectively target BRCA1 deficient tumour cells and function by inhibiting single strand break repair, and are thought to trap PARP at the DNA break site thus forming a cytotoxic PARP-DNA complex [138]. Clinical trials are ongoing and have shown encouraging results for the treatment of basal-like breast cancers where surgery, radiotherapy and chemotherapy were previously the only viable treatment option available to patients.

1.3.1.2 Current treatment options

Breast cancer is a heterogeneous disease and as such there exist a multitude of treatment options which are dependent on tumour subtype and classification, and are selected to provide the greatest eradication potential of the tumour while limiting damage to the neighbouring healthy tissue. With early-stage breast cancer, the estimation of risk and benefit of chemotherapy use is of great importance. Three genomic assays are commercially available for risk assessment and determination of recurrence: Oncotype DX (Genomic Health Inc., Redwood City, California, USA), MammaPrint (Agendia, Irvine, California, USA), and the Prosigna assay (NanoString Technologies Inc., Seattle, Washington, USA).

The Oncotype DX assay estimates the likelihood of disease recurrence (within 10 years) in patients with early-stage hormone positive only breast cancer, with node negativity. The assay uses a panel of 21 genes within a tumour to determine a recurrence score. Typically hormone therapy such as tamoxifen (a selective estrogen-receptor modulator) or aromatase inhibitors (class of drug used to block estrogen production or action of estrogen on receptors in postmenopausal woman) are utilised on patients that present with such tumours. Oncotype DX has demonstrated that it can be utilised to determine whether the patients would benefit with the inclusion of a chemotherapy regime, and was capable of predicting the magnitude of chemotherapy benefit [139].

Similarly the MammaPrint assay is a diagnostic test to determine the risk of metastasis within breast tumours. It is a microarray based platform that utilises a 70 breast cancer gene signature and is FDA approved for the testing of lymph node negative breast cancer patients of all ages in the United States of America while in the European Union it is utilised in patients that have up to three positive nodes and also in patients that are both ER+ and ER–. The assay has been tested in the MINDACT (Microarray In Node negative and 1-3 positive lymph node Disease may Avoid ChemoTherapy) clinical trial (a multi-centre, randomised, phase III, controlled clinical trial) for the ability to identify patients that were unlikely to benefit from adjuvant chemotherapy with early stage breast cancer. It was determined that women with high risk breast cancer should be treated with a combination of anthracycline chemotherapy and hormone therapy while those classified as low risk were recommended to receive hormone therapy alone [140].

In contrast to both Oncotype DX and MammaPrint which are capable of determining recurrence and effectiveness of chemotherapy in early-stage hormone positive breast cancer patients, the Prosigna Assay (formerly known as PAM50), is a PCR-based test using a list of 50 genes (the PAM50 gene signature) which is capable of classifying all breast cancers into the four intrinsic subtypes of breast cancer and can provide a risk category based on both the Prosigna risk of recurrence score and nodal status for post-menopausal women with hormone receptor-positive, early stage breast cancer. The assay utilises RNA

extracted from FFPE breast tumour tissue samples from patients with node-negative (Stage I or II) or node-positive (Stage II) hormone receptor-positive breast cancer [141, 142]. The gene expression profiles of the PAM50 test were retrained on the nCounter Dx Analysis System, which at present is the only CE-marked and FDA approved genomic assay on the market [142].

Through the implementation of such assays it is possible for clinicians to determine the best treatment regime for each patient, taking into account tumour subtype, classification, risk of recurrence and nodal status to either include chemotherapy as part of the therapy or to safely omit its use. These tests are unfortunately limited to early stage hormone positive breast cancers and might only weakly offer assistance in decision making for hormone negative tumours such as the HER2 and triple-negative/basal-like subtypes.

Tumours that have confirmed HER2 amplification in protein expression or increased gene copy number can be treated with a range of targeted biological therapies and chemotherapy drugs. Tumours can be treated with trastuzumab (Herceptin), a monoclonal antibody that can be utilised in early stage and late stage disease; pertuzumab (Perjeta), a monoclonal antibody that can be given in combination with trastuzumab and chemotherapy (such as anthracycline and taxane drugs) as a neoadjuvant and adjuvant treatment; lapatinib (tykerb), a kinase inhibitor which is used to treat advanced breast cancer and is a secondary line of treatment utilised when trastuzumab no longer works. In fact it has been demonstrated that a combination of lapatinib and trastuzumab is effective in the regression of BT-474 cell-derived xenographs in mice with complete remission after 10 days of treatment, with no relapse after 8 months in the treated animals [143]. However, the ALTTO clinical trial (Breast International Group BIG 2-06/EGF106708 and North Central Cancer Treatment Group [Alliance] N063D) has recently determined that adjuvant treatment of 8381 patients with metastatic HER2+ breast cancer demonstrated no significant improvement in disease free survival with the inclusion of lapatinib alongside trastuzumab over trastuzumab alone, and concluded that continued use of trastuzumab alone remains as the standard of care for these patients [144].

While there exists the potential to treat hormone positive and HER2 amplified breast cancers with hormone and anti-HER2 therapies the inclusion of chemotherapy and radiotherapy for locally advanced and metastatic disease remains an option for patients with these subtypes. In contrast and only until recently the options available for patients with triple-negative breast cancers included surgery, radiotherapy and chemotherapy, whereby the inclusion of chemotherapy was at earlier stages compared to other subtypes [145]. Treatment of early stage disease may include surgical interventions such as breast-conserving therapy (BCT) and modified radical mastectomy (MRM) [146]. A large study consisting of 768 patients with stage I – stage II triple-negative breast cancers found that locoregional recurrence rates (LRR) differed between individuals that received BCT, MRM, and MRM + radiotherapy, and five year LRR-free survival was 94%, 85% and 87% respectively [147]. Another trial with 681 randomised patients with stage I – stage II triple-negative breast cancer were retrospectively studied, with all patients receiving chemotherapy after MRM +/– radiotherapy [148]. Of the patients in this study, 315 received chemotherapy alone while 366 received radiotherapy following chemotherapy. Median follow up of 86.5 months was conducted with a 5-year recurrence-free survival of 74.6% and 88.3% for adjuvant chemotherapy alone versus adjuvant chemotherapy plus radiation respectively. Five year overall survival was also higher in patients that received adjuvant chemotherapy plus radiation (90.4%) compared to those that received adjuvant

chemotherapy alone (78.7%) [148]. The decision to include adjuvant chemotherapy in triple-negative breast cancer is dependent on the tumour stage and node involvement with Anders et al. proposing the use of Adjuvant anthracycline/taxane-based chemotherapy for all tumours with lymph node involvement and for lymph node negative tumours with a tumour size in excess of 1 cm [145]. The basal-like breast cancers account for approximately 75% of all triple-negative breast cancers [149], and like other triple-negative cancers, they demonstrate sensitivity to anthracycline and taxane chemotherapy. However, while the cancers respond well to chemotherapy early on, early complete response does not correlate to an overall survival advantage and relapse within 3 – 5 years is higher than hormone positive breast cancer subtypes [149, 150]. The current knowledge of chemosensitivity has been obtained from the neoadjuvant therapy setting, where a greater pathological complete response has been obtained compared to other breast cancer subtypes, but has also demonstrated that metastatic relapse occurs at a higher rate for the triple-negative breast cancers [151]. In comparison, adjuvant treatment of triple-negative breast cancers is similar to the other subtypes and can employ standalone drugs and drug combinations such as Doxorubicin or Epirubicin (anthracyclines); Doxorubicin and Cyclophosphamide (AC); Paclitaxel and Docetaxel; Doxorubicin, Cyclophosphamide and Paclitaxel; Cyclophosphamide, methotrexate and 5-fluorouracil (CMF); and antimetabolites such as Gemcitabine or Capecitabine [149]. Until recently the treatment of triple-negative/basal-like breast cancers was limited to radiotherapy and chemotherapy for neoadjuvant and adjuvant therapy, and surgery. Recently it has been demonstrated that triple-negative breast cancers of the basal-like subtype are sensitive towards treatment with PARPi where there is a defect in DNA repair, such as HR in BRCA1-sporadic and hereditary cancers. Clinical trials using PARPi (olaparib) and DNA damaging agents have shown promising results [152], and may present an additional treatment option for the triple-negative/basal-like breast cancers. Combination of PARPi with platinum based drugs has demonstrated greater efficacy in multiple clinical trials using a variety of PARPi currently in late phase clinical trials such as caparib (AGO14699; Clovis, Boulder, CO, USA), niraparib (MK4827; Tesaro, Waltham, MA, USA), talazoparib (BMN-673; Medivation, San Francisco, CA, USA) and veliparib (ABT-888; Abbvie, North Chicago, IL, USA) [153]. Drug resistance to both PARPi and platinum based chemotherapy drugs has been reported and understanding of the mechanisms conveying resistance in each case must be addressed. Multiple mechanisms exists which include but are not limited to the reactivation of BRCA function as a consequence of secondary mutation [154-156], compensatory mutation in additional genes (synthetic viability), such as the loss of 53BP1 [157-159], upregulation of drug efflux pumps such as Abcref-1a and Abcref-1b genes which encode the P-glycoprotein efflux pump, which are upregulated in BRCA1 mutated tumour models treated with Olaparib [160], and upregulation of a miRNA, miR-622, in BRCA1-mutant tumours which suppresses the non-homologous end joining DNA repair pathway and restores the HR-deficiency [161].

1.3.2 Pancreatic cancer

Pancreatic cancer is ranked 9th in females and 11th in males and accounts for a much lower incidence rate than breast cancers with an average of 500 people diagnosed in Ireland each year. However, according to the Irish cancer registry, the 5 year net survival rate is as low as 8.7%. A steady increase in the net survival rate has been observed since 1994 yet considerable advancements are drastically required to improve the outlook. With a median mortality age of 74, it is the older population that are most affected and account for 41.8% of individuals diagnosed with the disease.

Most pancreatic cancers are asymptomatic at the early stages of disease progression and those that present with symptoms are of late stage, and have much worse prognosis. Unfortunately this means that advanced stage tumours are most often diagnosed, with stage II signifying possible lymph node metastasis, stage III with spread to the blood vessels and possibly lymph nodes, and stage IV with metastasis of any size spread to multiple organs. The majority of pancreatic cancers diagnosed are stage IV, and have low survival rates with >50% dying within three months of diagnosis (Figure 11).) Cancers of the pancreas do not have to grow very large prior to invasion which is in part due to the proximity of the pancreas to large blood vessels (celiac artery and superior mesenteric artery. The current lack in progress in the development of effective early diagnosis and treatment options, evidenced by the statistical data on the survival rate of pancreatic cancer patients, highlights the pressing need to develop new diagnostic and therapeutic approaches for asymptomatic pancreatic cancer, and for minimally invasive tumour resection methods.

1.3.2.1 Pancreatic cancer types

Both the exocrine (99% of pancreas by weight) and endocrine (1% by weight) cells of the pancreas can form cancers, with exocrine cancers being the most prominent. Not all tumours of the pancreas are cancerous while some are “pre-cancerous” and prevalent to a different extent in both sexes (Figure 10).

The exocrine portion is composed of a series of ducts which branch from areas dense with acinar cells, within which the digestive enzymes are synthesised and released. Approximately 95% of all pancreatic cancers are classified as exocrine tumours and a vast majority of these (approximately 90%) are pancreatic ductal adenocarcinomas (PDAC) of which the pancreatic intra-epithelial neoplasia (PanIN) are the most extensively studied. Other neoplasms in these cells include serous cystadenoma (common benign pancreatic neoplasm [162]), mucinous cystic neoplasms (commonly affect females with a 20:1 ratio [163]), solid pseudo-papillary neoplasia (extremely rare and of low malignant potential [164]), and intraductal papillary mucinous neoplasms (accounting for only 1% of all pancreatic cancers [165]).

The endocrine segment of the pancreas is composed of small bundles of cells called Islets of Langerhans. This area is highly vascularised and allows for rapid systemic transport of the two main endocrine hormones: glucagon (α cells) and insulin (β cells). Endocrine cancers include Gastrinomas (produce gastrin), Insulinomas (produce insulin), Somatostatinomas (produce somatostatin), VIPomas (produce VIP), Glucagonomas (produce glucagon), whereby two thirds of these tumours are malignant and produce no hormone or symptoms. Those that produce hormones are referred to as functioning carcinomas and can release large quantities of insulin, glucagon and gastrin into the bloodstream, leading to symptoms such as low blood sugar which inadvertently aid in the early detection of the cancer.

PanIN is the most extensively studied pancreatic cancer and is a precursor lesion for PDAC. These microscopic lesions are non-invasive epithelial proliferations that reside in the ducts of the pancreas and are too small to detect. They can progress to PDAC if left untreated with PDAC developing as glands with the capacity to infiltrate tissues. PDAC have a tendency to localise and invade nerves and spread along the perineural region and associate with a dense desmoplastic stroma [166]. These solid tumours invade both the lymphatic space and veins from which they can metastasise to multiple organs such as the liver, lungs, kidney, brain and spleen [166]. To date a total of 119 somatic mutations have been identified by whole genome sequencing analysis in pancreatic cancer patients, and result in at least 12 signalling pathways being altered in 67 – 100% of tumours [167]. The most commonly altered oncogenes and tumour suppressor genes in pancreatic cancers include KRAS, $p16^{INK4a}$, P53, and SMAD4 [168, 169].

KRAS is a proto-oncogene that encodes a 21kDa membrane bound GTPase, which is a component in many signal transduction pathways. Point mutations in codon G12, G13 and Q61 are responsible for an activating mutation of KRAS and are found in high rates in pancreatic cancers (approximately 98%) [170, 171], and are the earliest event in pancreatic carcinogenesis [172]. Constitutive activation of KRAS leads to persistent stimulation of downstream signalling pathways that drive proliferation, metabolic-alteration, increased anti-apoptotic capacity, development of the tumour microenvironment, evasion of the immune system, and metastasis [171, 173]. It has been demonstrated that the development of PanIN is possible with the targeting of mutant KRAS to the murine pancreas which over time develop into PDAC [173, 174]. Continuous activation of KRAS is a requirement for the development and maintenance of PanIN, PDAC and associated metastatic lesions [175, 176]. In addition Collins *et al.* demonstrated that cancer cells harbouring mutant KRAS can remain dormant for some time, and reactivation of oncogenic KRAS can result in rapid progression of the disease [176]. Therefore KRAS was considered a very promising target for the treatment of PDAC. However the heterogeneity of PDAC demonstrated that a subset of PDAC cells could resist KRAS inactivation [177], and therefore only a subset of patients would benefit from inhibition of KRAS. In addition to this, all inhibitors developed to target oncogenic KRAS have failed [171]. A shift in focus has occurred whereby the downstream effectors of oncogenic KRAS are being studied in order to develop a viable treatment [171]. The phosphatidylinositol 3-kinase (PI3K)/Pdk1/Akt pathway is one such pathway downstream of KRAS that has been implicated in the development of PanIN and PDAC, with inhibitors of this pathway demonstrating modest effects in $Kras^{G12D}$-driven PDAC [178].

The tumour suppressor protein, $p16^{INK4a}$, plays an important role in the regulation of the cell cycle via the inhibition of cyclin dependent kinases such as CDK4/6 which therefore prevents the phosphorylation and activation of retinoblastoma and maintenance of the G1/S checkpoint. The loss of $p16^{INK4a}$ occurs in approximately 95% of PDAC cases and can occur via homozygous deletion, intragenic mutation with loss of the second allele or via promotor hypermethylation [172]. KRAS mutational activation and $p16^{INK4a}$ loss closely correlate with the rapid progression of PanIN lesions to highly invasive or metastatic PDAC [179-181]. Epigenetic promoter hypermethylation of $p16^{INK4a}$, induced by mutated KRAS, has been shown to be an important step in malignant transformation [182]. Cells in PanIN lesions contain both active KRAS and $p16^{INK4a}$ which can result in the onset of senescence in these cells, and it has been suggested that senescence is therefore a defining feature of premalignant tumours and may be a valuable diagnostic and prognostic marker in cancer [183].

TP53 is a proto-oncogene and encodes a 43.7 kDa tumour suppressor protein, p53, which is involved in conserving cell stability by preventing genomic instability, plays a role in apoptosis, and inhibition of angiogenesis [184, 185]. It is mutated in approximately 50 – 75% of PDAC cases which is a result of intragenic mutations combined with second allele loss [168, 186]. These mutations inactivate the intrinsic anti-proliferative properties but have been known to promote metastasis via "gain-of-function" activity [187]. Gain-of-function activity can occur whereby a point mutation in p53 can result in the stable expression of the variant protein, while wild-type p53 is rapidly turned over via the activation of E3 ubiquitin ligases [187]. PDAC harbouring mutated p53 in which KRAS is also mutated has been shown to induce more metastases compared to mice with a p53 null allele [187, 188]. Weissmuller *et al.* demonstrated that metastatic potential in p53 mutant PDAC tumours is driven by platelet-derived growth receptor factor β (PDGFRβ), which may be a useful prognostic marker and therapeutic target [187]. It was reported in 2012 that the targeting of mutant p53 had failed and was deemed not to be druggable [189], however publications that demonstrate the reactivation of wild-type p53 and the capacity to induce tumour regression and eradication do exist [190, 191]. In a more recent publication, it was demonstrated that treatment of a PDAC cell line with gemcitabine chemotherapy led to the activation of mutant p53 and subsequently an increase in chemoresistance [192]. The authors discovered that treatment of these PDAC cells with p53-reactivating small molecules (CP-31398 and RITA) alongside gemcitabine led to reduced proliferation rate and initiation of apoptosis [192]. Work is currently ongoing to develop small molecules and compounds that have the capacity to restore wild-type functionality to mutant p53, thus inducing cell cycle arrest and apoptosis in these cells. In addition to CP-31398, a small molecule called SCH529074 has been shown to bind to the DNA binding domain of p53 and has the capacity to reactivate mutant-p53 and activate wild-type p53. It acts by restoring DNA binding activity to mutant p53 and re-establishing the growth-suppressive function of p53 via inhibition of MDM2-mediated ubiquitination of wild-type p53 [193]. Considerable ground has been made in the development of mutant-p53 targeting compounds with some undergoing clinical trials. Not only would these be valuable molecules to use in the treatment of pancreatic cancer, but could provide substantial benefit for treatment of a variety of cancers on account of approximately 50% of all cancers harbouring mutant p53.

SMAD4 is a key signal transducer of the TGFβ signalling pathway and a transcription factor which is activated via the SMAD pathway of which it is a family member. SMAD4 is only found expressed in the skin, colon, pancreas, uterus, and epithelial cells and is often mutated in cancers. In pancreatic cancer, SMAD4 is mutated in approximately 55% of cases by homozygous deletion of both alleles or by the intragenic mutation of one allele with loss of the second allele [194, 195]. Expression of SMAD4 has been demonstrated to confer a survival advantage over mutant SMAD4 carriers [196], with a recent meta-analysis concluding that loss of SMAD4 expression was associated with a shorter overall survival and may provide additional information for the optimisation of therapeutic approaches. The authors highlight that there is a distinct lack of large-scale studies currently published and as a result, the prognostic value of SMAD4 has yet to be elucidated [197].

1.3.2.2 Current treatment options

A patient with pancreatic cancer may present with painless jaundice, the development of diabetes mellitus, or malabsorption [198]. The onset of abdominal and back pain may occur and is a consequence of a blocked bile duct, and is indicative of pancreatitis which requires a diagnostic work-up to determine the cause [199]. Clinical methods used to diagnose pancreatic cancers and molecular subtype include magnetic resonance imaging, ultrasound, and biopsy. Due to the position of the pancreas, ultrasound is often carried out with the use of an endoscope, and presents as a beneficial method to identify pancreatic lesions [200]. If a tissue mass is identified in the pancreas, a biopsy can be obtained using ultrasound-guided fine-needle aspiration [201, 202], core needle biopsy, or by surgery [203, 204]. Additional diagnostic tools include computerised tomography (CT) which is considered a high resolution method to diagnose cancers of the pancreas with a sensitivity ranging from 89% to 97% [205]. Legmann *et al.* reported that CT could detect 100% of the tumours they investigated which were greater than 15 mm in size [206], with identification of only 67% of tumours less than 15 mm in size. A study from 2004 claimed CT could only identify 77% of tumours less than 2 cm in size [207]. Therefore the use of more sensitive testing such as contrast-enhanced multidetector CT imaging would enable better visualisation of adenocarcinoma in relation to their proximity to the major veins and arteries [208, 209].

The current treatment options depend largely on the molecular subtype and stage of the disease with options such as neoadjuvant therapy (prior to surgery), adjuvant therapy (post-surgery) and surgical intervention. In pancreatic cancers, the position of the tumour dictates the approach taken. If the tumour is located in the neck of the pancreas or in close proximity to (abutment) or concentric around an artery (encasement), they may be considered unresectable. Surgery is considered the only potential curative treatment for resectable pancreatic cancer, but only 15 – 20% of patients present with a resectable disease, with survival rate between 12 – 20% at 5 years following resection [210]. Those patients that present with an unresectable tumour will undergo radiation and/or chemotherapy to reduce tumour size in the hope of shrinking the tumour away from the vasculature [211]. Surgical resection is indicated mostly for venous invasion whereas involvement with arterial vessels is mostly contraindicated [211].

Similar to breast cancer, neoadjuvant and/or adjuvant therapy may be prescribed for the treatment of pancreatic cancer depending on cancer stage, position and subtype. Radiotherapy alongside or in isolation to chemotherapy may be provided to aid in tumour shrinkage as a neoadjuvant approach, and it may be prescribed as an adjuvant therapy to ensure any remaining cancer cells are eradicated. The development of effective early stage diagnosis and treatment for pancreatic cancers requires considerable improvement, which is evident from the overall survival statistics (Figures 4 & 6). Pancreatic cancers at all stages have a poor prognosis with less than 20% surviving 5 years post treatment (Figure 11), by virtue of their position to major organs, vital function, high vascularisation with important arteries and veins, and late onset of signs and symptoms makes the treatment of pancreatic cancers a challenge. *Chemotherapy treatment is mostly conducted using single-agent therapy, which is recognised as a weak link due to both intrinsic and acquired drug resistance* [212]. One of the most widely used chemotherapeutic drugs for pancreatic cancer treatment is gemcitabine, which was approved in 1997 and tested as a first-line drug in patients with locally-advanced or metastatic adenocarcinoma [213]. As demonstrated by Burris et al., gemcitabine was shown to provide greater improvement in survival rate compared to 5-fluorouracil

(another drug commonly used in pancreatic cancer treatment) with 22% survival for gemcitabine treated patients and 2% in 5-fluorouracil treated patients at one year [213]. Unfortunately, rapid resistance to gemcitabine treatment translates into poor prognosis, and is a common feature in the treatment of pancreatic cancers. At first the tumour is highly vulnerable yet becomes rapidly resistant, with groups currently focused on identifying the genetic and epigenetic alterations that convey resistance [214].

Common to both breast and pancreatic cancers is the use of doxorubicin and gemcitabine in the treatment of metastatic disease. Doxorubicin is a bacteria-derived anthracycline antibiotic that was identified in the 1950s with the initial discovery of daunorubicin [215]. Following modification to the Streptomyces peucetius strain from which daunorubicin was made, a new compound was formed and subsequently named doxorubicin [215]. Gemcitabine, a nucleoside analog, was first synthesised by Eli Lilly during the 1980s [216] with an intention to be used as an antiviral drug, and later discovered to kill leukemia cells *in vitro* [216]. Both doxorubicin and gemcitabine have been used in the treatment of pancreatic cancer with doxorubicin recently being used in combination therapy to successfully treat pancreatic cancer [217]. However, like all chemotherapeutic drugs, a number of major drawbacks exist with both doxorubicin and gemcitabine. Common side effects reported with the administration and treatment of doxorubicin include cardiotoxicity [218], infusion-related reactions [219], hand-foot syndrome [220, 221], and secondary oral neoplasms [222]. Common and less frequent side effects with gemcitabine administration include schedule-dependent toxicity [223], short-lived myelosuppression [224], pulmonary toxicity and respiratory failure [225-227], haemolytic uremic syndrome [228, 229], and infrequent reports of cardiotoxicity [230]. Due to these side effects, it is common for patients to experience discomfort and pain during treatment.

Pancreatic cancer remains one of the most painful malignancies, and the management of pain is in fact one of the criteria of response to the chosen treatment in some clinical trials [213, 231]. Pancreatic cancer cells and neuronal cells may share certain similarities in their growth factor receptors, surface adhesion molecules and have an affinity to neuronal tissues [232]. This similarity and interaction may explain the migration of pancreatic cells along the dorsal root ganglia which is facilitated by the release of neurotrophic factors and chemokines from nerve cells [233-235]. The onset of pain has been linked to the necrotic damage of the nerve endings due to factors released by the pancreatic cancer cells (calcitonin gene-related peptide and tyrosine hydroxylase) [236, 237]. For patients with locally advanced or metastatic disease the primary reason for the implementation of a chemotherapeutic regime may be for pain control as survival advantage is quite small. Gemcitabine, 5-fluorouracil and a combination of four chemotherapeutic drugs (folinic acid, 5-fluorouracil, irinotecan and oxaliplatin) called FOLFIRINOX have all shown benefit in reducing associated pain and are considered for palliative care and in the management of metastatic pancreatic cancers [213, 231].

1.3.3 Clinical potential of nanoparticles

There is a considerable opportunity to develop new nanoparticle formulations for the diagnosis and treatment of both breast and pancreatic cancers. As detailed in the previous sections there is a substantial benefit with the early detection of breast and pancreatic cancers which is associated with greater response to treatment and increased overall survival. The invasiveness of obtaining a biopsy, of surgery and side effects of chemotherapy should be addressed to help reduce the associated discomfort. *Nanomedicine*

provides a unique opportunity to develop a range of products that, following single bolus injection, could potentially travel to the site of a tumour by targeted delivery and release a therapeutic payload. A targeted superparamagnetic MNP without a payload could be used for the identification of a tumour mass by MRI, therefore acting as a diagnostic tool for the detection of early stage cancer where a chemotherapy drug is not indicated. In addition, the MNP could be used as a targeted therapeutic agent to deliver compounds that are subtype-specific to tumour cells, with the potential to reduce tumour mass in locally advanced disease, the ablation of the stem cell population and also target distant metastases. In addition, the capability of targeted drug delivery using nanoparticles would dramatically limit systemic drug exposure and the associated adverse side effects. Combining both diagnostic and therapeutic modalities onto a targeted MNP would provide a theranostic MNP capable of clinical detection and immediate *in-situ* tumour targeting. Such a theranostic nanoparticle currently remains a goal for the nanomedicine field with considerable advances being made over the past few years as evidenced by the increase in approved nanomedicines.

As introduced in section 1.2.1 there are many approved nanomedicines on the market and include DaunoXome® (daunorubicin), Myocet® (doxorubicin), Onco TCS® (vincristine), Doxil® (doxorubicin), Oncaspar® (l-asparaginase), DepoCyt® (cytarabine), Marqibo® (vincristine), Mepact® (muramyl dipeptide), Zinostatin stimalamer® (SMANCS), Genexol-PM® (paclitaxel), Abraxane® (paclitaxel), NanoTherm® (MNP), Kadcyla® (emtansine/trastuzumab), and Adcetris® (brentuximab vedotin) [53, 238]. A number of nanotherapeutics are currently in Phase III clinical trial such as LipoPlatin® (cisplatin), MM-398 (irinotecan), ThermoDox® (doxorubicin), Tecemotide (lipopeptide), NKTR-102 (irinotecan), paclitaxel poliglumex (paclitaxel), Paclical® (paclitaxel), and Livatag® (doxorubicin) [238]. Nanotherapeutics currently approved or in clinical trials for the treatment of breast cancer include Caelyx®, Lipo-Dox®, Myocet®, NKTR-102, Genexol-PM®, Abraxane® and Kadcyla® while MM-398 and Abraxane® are being used to treat pancreatic cancers. The majority of these nanomaterials have been developed for the sole purpose of being therapeutic agents with approximately 60% of all Phase III and 80% of Phase I/II candidates fitting into this category [239]. The second most important category of nanoparticles under development are those which function in imaging and diagnostics with iron oxide nanoparticles being the first such nanoparticles approved in 1996 [239]. Theranostic nanoparticles, like magnetic iron oxides, are classified as such due to the combination of both an imaging modality, payload delivery capability and thermal capability to achieve diagnosis and treatment with a single system. Unlike the clinically accepted second generation nanomaterials listed above, the MNP developed in Multifun and presented in this thesis were third generation and included a targeting moiety.

In the next section the background to the stepwise decision making process that was employed in this thesis following a three tiered safe-by-design approach will be addressed.

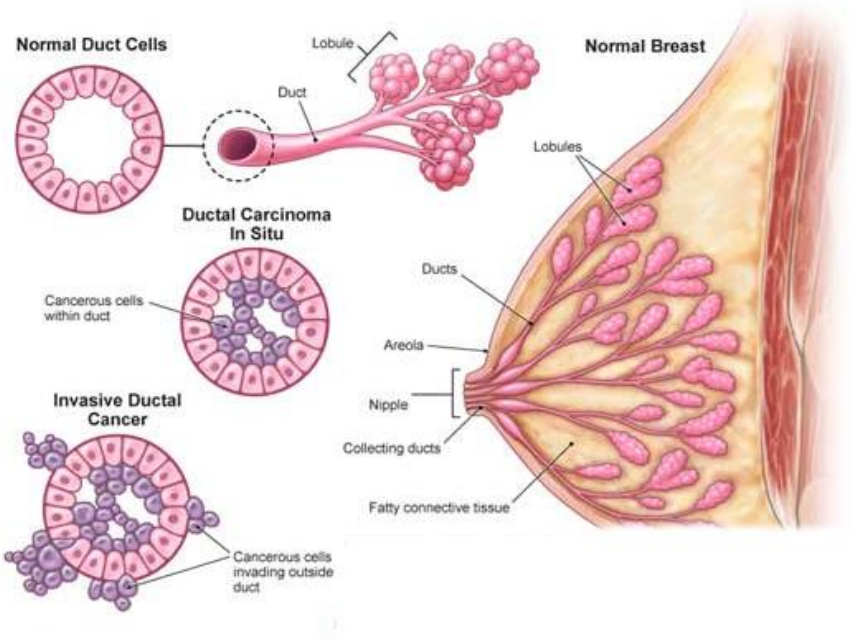

Figure 8: Types of breast cancer.

Overview of breast cancer types from normal to invasive ductal cancer. Image adapted from medicalexhibits.com.

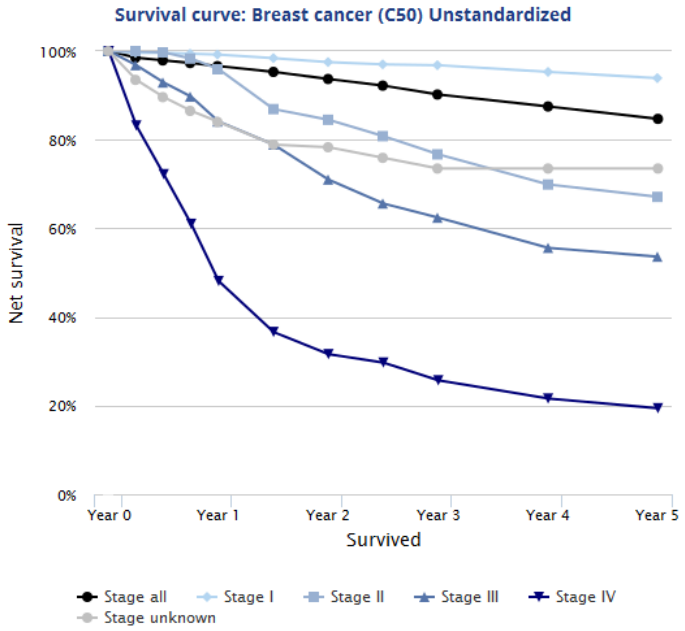

Figure 9: Five year survival rate of breast cancer based on cancer stage.

Overview of survival rate of females with different cancer stages over a five year period. Graph obtained from www.ncri.ie, representing data collected 2008 – 2012.

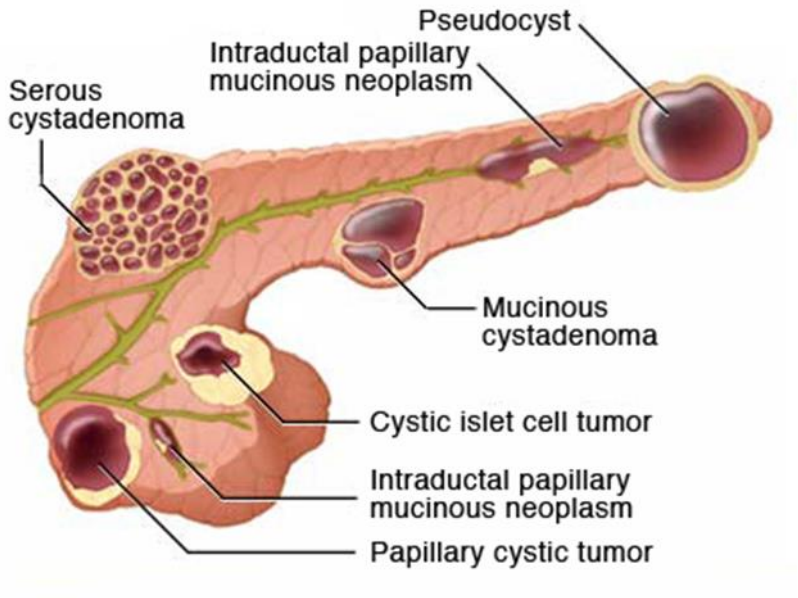

Figure 10: Types of pancreatic cysts.

Overview of the regions and types of exocrine and endocrine cysts that can present in the pancreas. Image obtained from http://www.drugs.com/mcd/pancreatic-cysts#Image_Definition

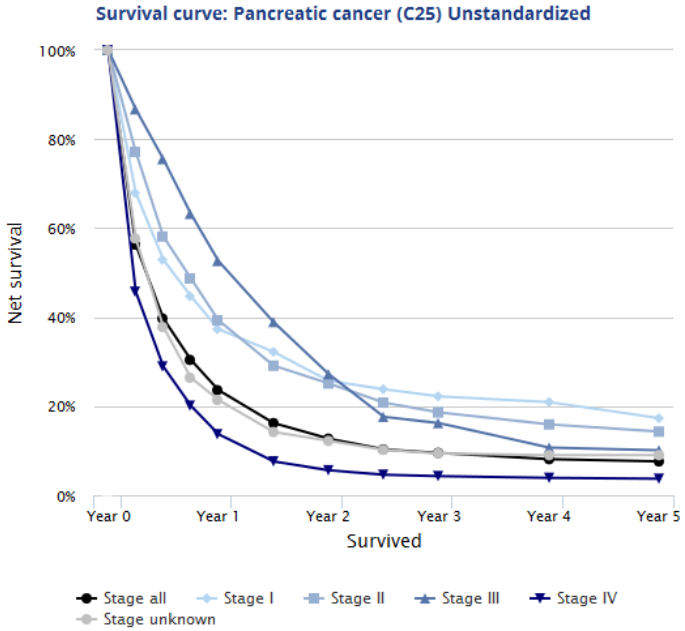

Figure 11: Five year survival rate of pancreatic cancer based on cancer stage.

Overview of survival rate of both males and females with different cancer stages over a five year period. Graph obtained from www.ncri.ie, representing data collected 2008 – 2012.

1.4 MNP characterisation: safe-by-design

Engineered nanomaterials for use in theranostics will ultimately come into contact with protein-rich physiological fluids. Therefore, the importance of understanding the physicochemical properties of engineered MNP should not be overlooked. Knowing how the properties of MNP are affected by dispersion in physiological medium is decisive for the success of the MNP in its specific application [240]. Consequently, the development of a nanomedicine requires the use of a range of characterisation steps to select suitable MNP. The characterisation of physicochemical parameters pre- and post-incubation with biological medium followed by *in vitro* evaluation of MNP biocompatibility and efficacy of drug-loaded MNP formulations, and finally the *in vivo* evaluation of biodistribution, would provide substantial information on MNP properties and their potential to generate unwanted biological side effects. The following sections provide the background to each stage of the three tiered approach presented in Figure 6.

1.4.1 Physicochemical characterisation of MNP

1.4.1.1 Size

Slight changes in physiochemical properties have significant implications on the behaviour of MNP in the biological environment such as the mechanism of uptake [241]. Particle size plays a decisive role in nanoparticle properties and therefore particle sizing is an essential task in nanoparticle characterisation. The size of the core material can dictate the applications for which they are suitable, for example, nanometre sized particles can be used for targeted drug delivery and are small enough to enter cells to carry out their intended function, whereas particles in the micron range have shown great promise in protein and cell separation applications. The degree of reactivity of MNP is size dependent and is related to their surface area, with smaller nanomaterials (greater surface area) having higher dissolution reactivity compared to their larger analogues. Enhancement in MNP reactivity can be particularly high at sizes less than or equal to 10 nm [242]. It has been demonstrated that iron oxides of 4 nm have a surface area normalised reactivity that is 20 times higher than 6 nm nanoparticles of the same composition [243]. Nanoparticle size can be altered through the association with a range of biopolymers such as proteins, which are organised on the nanoparticle surface as the "protein corona", with possible implications for biological impacts [244]. Opsonisation by serum proteins, resulting in the formation of a hard and soft protein corona, occurs rapidly following intravenous injection [245-247]. This interaction can result in changes of the MNP hydrodynamic diameters and has also been reported to increase MNP stability [248]. Ehrenberg *et al* [249] demonstrated protein adsorption on the surface of polystyrene nanomaterials incubated with a range of serum samples. They concluded that the protein adsorption capacity of nanoparticles is an excellent predictor of cellular association, with nanoparticles of larger hydrodynamic size having increased uptake [249]. While opsonisation may facilitate cellular uptake, it increases the physical size of the MNP, which increases the likelihood of being retained in the liver and spleen by the reticulocyte endothelial system (RES) [250, 251]. Therefore, it is important for new nanomaterials or batches from existing formulations to be characterised following gold standard procedures and techniques. Methods to monitor MNP characteristics such as core size, shape and hydrodynamic diameter include the gold standard approaches of Transmission Electron

Microscopy (TEM) to obtain quantitative measurements of nanoparticle core size, population size distribution, and morphology; and Dynamic Light Scattering (DLS) to measure the hydrodynamic diameter of nanoparticle dispersions. A refined technique for the measurement of hydrodynamic diameter has been commercialised and is called nanoparticle tracking analysis (NTA). The determination of hydrodynamic diameter of nanoparticles in NTA is similar to DLS whereby both techniques use nanoparticle dispersions, and both rely on the scattering of laser light diffracted by the nanoparticles to measure size. Unlike DLS, NTA determines the size of the nanoparticle dispersion based on the movement of individual nanoparticles in a sample. The Brownian motion of each nanoparticle is recorded and the size is calculated based on the degree of motion and density of the solution to provide a detailed, particle-by-particle sample size [252]. NTA is a reliable platform for the study of a broad range of nanomaterials and in many applications, from quantification of exosomes [253-255], platelet-derived extracellular vesicles [256], virus particles [257], polystyrene nanospheres [258], silver nanoparticles [259], gold nanoparticles [260], and iron oxides [261, 262]. Thus, over the past twelve years, NTA has become a gold standard technique and can provide a substantial advancement in knowledge and compliment already established technologies such as DLS.

1.4.1.2 Surface coating

A key component to ensure long circulation time with increased presentation at a tumour site or organ of interest is the avoidance of the RES system and the organs responsible for nanoparticle clearance, namely the liver, spleen and kidney [48, 250, 251]. While MNP size has been shown to be a major predictor for nanoparticle clearance from the blood [263], the presence of hydrophobic residues on the nanoparticle surface have also been shown to reduce circulation time on account of increased protein opsonisation [264]. Coating the nanoparticles with hydrophilic polymers, or with biodegradable co-polymers that contain hydrophilic components such as PEG will resist opsonisation through steric repulsion [265]. Surface molecules are commonly used to coat the inorganic core of the MNP, generally as a means to increase the biocompatibility of the formulation, maintain stability, and provide accessible functional groups for attachment of additional therapeutic and targeting moieties. Examples of common hydrophilic and biocompatible coatings include dextran and dimercaptosuccinic acid (DMSA). Historically, DMSA (FDA approved small organic molecule) has been used as a treatment against acute heavy metal poisoning and is highly effective at removing lead [266], and mercury [267] from multiple areas of the body. DMSA, when used as a nanoparticle coating, imparted greater stability to MNP, which was maintained across a broad pH range (pH 1 – 14) [268]. The DMSA coating plays an important role in sample monodispersibility and has been shown to increase cellular association and uptake by up to three fold compared to uncoated nanomaterials, and it is thought to be facilitated through non-specific binding of the outer cell membrane [269, 270]. Nanomaterials coated with DMSA have also demonstrated little to no cytotoxicity or genotoxicity *in vitro* [271, 272] and *in vivo* [273]. *In vitro* cytotoxicity has been observed at concentrations greater than 100 µg/mL [271], which far exceed the concentrations used with clinically implemented MNP, such as Ferumoxtran-10, which is typically delivered at 3.4 mg Fe/kg (44.16 µg/mL) [274]. Concentrations in excess of 100 µg/mL have been tested using DMSA coated MNP and no adverse effects up to 500 µg/mL were observed in hepatic cells [275]. *In vivo* analysis confirmed biotransformation in the liver and spleen but following three months post exposure, animal survival was not compromised [275]. A study by Mou et

al., demonstrated that DMSA coated MNP had the capacity to reduce intracellular reactive oxygen species levels in cardiomyocytes [276]. Therefore, the cardiotoxicity side effect observed with extended cancer treatment with the chemotherapy doxorubicin could benefit with the use of DMSA coated MNP to deliver the agent to tumour cells.

1.4.1.3 Surface charge

Surface charge is an important characteristic of engineered nanomaterials, and determines cellular uptake and biodistribution. It is accepted that positively charged nanoparticles have a higher rate of cell uptake on account of the attraction with the negatively charged plasma membrane at non-specific sites, when compared to neutral and negatively charged nanoparticles [277-279]. The increase in cellular association generally confers that positively charged nanomaterials are more toxic compared to negative variants of the same size and composition [280, 281]. Thus neutral and negative nanomaterials have been shown to limit the extent of protein opsonisation, have an increased circulation time, and have a lower rate of nonspecific cellular uptake [241]. A study has shown that thiolated nanoparticles were preferentially localised in the tumour mass of breast-tumour bearing nude mice compared to non-thiolated nanoparticles [282]. This finding suggests that a negative surface coating consisting of DMSA, which contains two thiol groups and two carboxylic acid groups, could be used to design a nanoparticle capable of preferential tumour localisation with limited protein opsonisation and increased circulation time. Thus, surface functionality and surface charge of nanomaterials are the critical parameters in the development of a nanomaterials for theranostics.

1.4.2 MNP-cell interaction in biological environment

The cells of the body present further molecular barriers for nanomaterial uptake and include the plasma membrane, endocytic vesicles, lysosomes, peroxisomes, cytoskeletal structures, enzymes, and the nuclear membrane. In tumours, additional barriers such as intra-tumoural pressure, and the dense interstitial matrix exist. Nanoparticle uptake can occur by energy independent (passive) and dependent (active) mechanisms, and can be harnessed and exploited for targeted drug delivery and in understanding the mechanisms involved in potential toxicity. The plasma membrane consists of an amphipathic bilayer across which nutrients and waste products must be capable of passing. It is a selective barrier that tightly controls the access and egress of chemicals and molecules, concentrating nutrients it gathers from the environment and removing waste products that it produces. The mammalian plasma membrane consists of phospholipids (phosphatidylcholine, phosphatidylethanolamine, phosphatidylserine, sphingomyelin and phosphatidylinositol to a lesser extent), cholesterol and glycolipids which are present in varying quantities which can alter the fluidity and permeability of the membrane [283]. Cholesterol, consisting of a rigid steroid ring structure, decreases the permeability of the membrane and immobilises the hydrocarbon head groups of surrounding phospholipids. The different types of lipids that form the plasma membrane are randomly distributed, however order in the form of lipid rafts occurs transiently with the interaction of sphingolipids together with cholesterol to form dense microdomains that have a greater thickness than the surrounding membrane on account of their longer fatty acid tails [283]. These microdomains are formed in both the trans-Golgi network and the plasma membrane and are shuttled from the trans-Golgi network via transport vesicles to the apical plasma membrane and exist as caveolae as either flask-like invaginations or in planar form. Evidence exists to suggest that lipid raft organisation is mediated by the cytoskeleton and several proteins, cytoskeletal components and binding partners localise to lipid rafts and function to control the movement of membrane proteins in response to extracellular signals [284]. They are the site for a large number of glycosylphophatidylinositol anchored proteins that are involved in signal transduction such as Ras signalling and hedgehog signalling [285]. Owing to the complex structure and organisation of the plasma membrane, the passage of chemicals and molecules through the bilayer can occur passively or via active mechanisms.

1.4.2.1 Passive uptake

Passive uptake involves the movement of biomolecules and other substances across the plasma membrane without the requirement of energy. The four methods of passive uptake into cells are diffusion, facilitated diffusion, filtration and osmosis. Diffusion involves the movement of particles from an area of high concentration to an area of low concentration. Diffusion rate is dependent on the hydrophobicity of the molecule with hydrophobic molecule diffusion occurring at a higher rate than hydrophilic molecules. Water, oxygen and carbon dioxide rapidly diffuse across the lipid bilayer while charged molecules cannot. In these instances diffusion can occur if facilitated by highly selective membrane-spanning transport proteins. Binding of large molecules to the transport proteins alters their confirmation and enables movement of the molecule to either the inside or outside face of the membrane. Filtration is the movement of solutes across the plasma membrane due to hydrostatic pressure differences, such as those found in the vasculature. Filtration is a primary function of the kidney cells in which the glomerular capsule contains a

filtration barrier composed of endothelial cells and podocytes through which water, ions and small molecules can pass. The last method of passive uptake involves osmosis, the movement of water molecules across the plasma membrane down the water potential gradient, and is dependent on the surrounding environment (hypertonic, hypotonic and isotonic) for movement of water.

Passive uptake has been shown to occur for nanoparticles < 4.7 nm in size [286, 287]. Since nanomaterials are of a similar size to biological molecules, they can equally invade cells, taking advantage of passive uptake as well as active uptake mechanisms. The interaction of nanomaterial with the lipid bilayer is dependent on size, surface composition and charge [288, 289]; with cationic nanomaterial of 20 nm shown to adhere strongly to the cell membrane via nonspecific electrostatic interactions which resulted in membrane poration [290]. Larger nanomaterials have been shown to penetrate the lipid bilayer which can occur by inducing defects in membrane structure. Uptake in this manner can result in membrane rupture and a marked increase in cytotoxicity. Such defects can include the formation of nanosized holes and thinning of the membrane [291], and has been demonstrated to facilitate the uptake of large (600 nm) silica nanoparticles into red blood cells [292]. While passive uptake is the main method of entry for small molecules and ions, larger molecules such as MNP are preferentially taken into cells via active uptake.

1.4.2.2 Active uptake

Nanomaterials that contact the plasma membrane enter through an energy-dependent mechanism. The method of uptake depends on the size of the presenting nanomaterial and the type of cell being exposed, but includes either clathrin mediated, caveolin mediated, micropinocytosis, clathrin & caveolin-independent mechanisms or phagocytosis. Active uptake requires energy in the form of adenosine triphosphate [293], and involves multiple cellular proteins to orchestrate the formation of the membrane pits such as clathrin and caveolin, projections from the cell membrane and into the cell, formed by polymerisation of actin filaments, and the vesicle scission by the guanosine triphosphate driven (GTP) dynamin protein. Of vital importance to the endocytic pathway is the involvement and maturation of endosomes and formation of lysosomes. Endosomes consist of three distinct types: early endosomes, late endosomes and recycling endosomes [294]. The process of endocytosis forms intracellular coated vesicles which encapsulate extracellular solutes, fluid, macromolecules, and components of the plasma membrane [295]; when these endocytic vesicles become uncoated they fuse with early endosomes from where they are sorted prior to degradation in lysosomes. The early endosomes have slightly acidic lumens due to the action of V-ATPase [296], and can facilitate the release of targeting ligands from the endosome and recycling of their receptor back to the plasma membrane. The internal pH continues to drop during maturation of the endosomes from early endosomes (pH 6.0 – 6.5) to late endosomes and lysosomes (pH 4.5 – 5.5) [297, 298], and can be exploited in the delivery of nanomaterial with pH sensitive compounds such as dyes, linkers, and coatings. Lysosomes are highly specialised vesicles in cells that are responsible for the disposal of unwanted materials from the cytoplasm and from external materials taken up by endocytosis. The lysosomal enzymes (of which more than 50 are known) are translated by ribosomes of the rough endoplasmic reticulum. From here they are modified and transported to the cis-Golgi apparatus where a mannose 6-phosphate tag is added. The enzymes move to the trans-Golgi network where they specifically bind to mannose 6-phosphate receptors which ensures that they are sorted correctly from other products in

the trans-Golgi network. Vesicles containing the enzymes bud from the trans-Golgi body and fuse with late endosomes which themselves can grow into mature lysosomes [283]. The interplay between endosomes and lysosomes is vital for the sustained enzymatic function of lysosomes. The lysosomes depend on the influx of enzymes and other components from endosomes to maintain their acidity and intactness [299]. The most prominent uptake mechanisms are discussed next and although there exist a number of studies that report on the uptake of nanomaterial into cells, there is very little known about the route of internalisation of MNP [300]. A recent publication using superparamagnetic iron oxide nanoparticles demonstrated via siRNA knockdown of key proteins necessary for active uptake that caveolin mediated endocytosis was the main mode of uptake of MNP in HeLa cells [300]. Cengelli et al. demonstrated that ultrasmall superparamagnetic iron oxide nanoparticles (9 – 10 nm diameter) in both 2D and 3D human melanoma cell cultures were taken up by clathrin-mediated endocytosis with localisation to lysosomes [301]. In another study, it was demonstrated that MNP with a silica shell of 50 nm size were internalised into cells via clathrin mediated endocytosis [302]. Another recent publication highlighted that although uptake studies have been performed with superparamagnetic iron oxide nanoparticles, little is known about what physicochemical characteristics provide the most optimal uptake into non-phagocytic cells [303].

Clathrin-mediated transport is the most highly studied mechanism of endocytosis and exocytosis and is the main method of nanoparticle internalisation with mean size of 200 nm [279, 289]. The importance of the clathrin coated pits lies in the crucial role in the movement of nutrients, recycling of receptors and lipids from the cell membrane and the movement of substances from the Golgi network to the cell surface. The formation of the clathrin coated pit begins with the assembly of individual units called triskelion composed of three clathrin heavy chains and three light chains. As the clathrin coated pit forms, the legs of the triskelion structure interdigitate and form a cage around the membrane invagination [304]. The actin cytoskeleton facilitates the elongation of the opening to the clathrin coated pit to enable complete endocytosis, while dynamin has been shown to act as a mechanochemical structure through the hydrolysis of GTP to create a twisting motion around the membrane invagination, increasing longitudinal tension and supercoiling of the dynamin structure, the tension on the membrane increases until membrane fission occurs and the vesicle is liberated from the plasma membrane [305]. Dissociation of the clathrin triskelion structure is a necessary step before the contents of the vesicle can be shuttled between the different phases of the endocytic pathway. The heat shock cognate 70 protein was found to be instrumental alongside the cofactor auxilin to facilitate clathrin disassembly [306, 307].

Caveolin is a family of integral membrane proteins consisting of a hairpin loop structure that is inserted into the membrane, does not span the bilayer, and has both C-terminus and N-terminus localised on the cytoplasmic face. Caveolin 1, 2 and 3 are expressed in different cell types, with caveolin-1 and 2 predominantly expressed in endothelial, fibrous and adipose tissue, while caveolin-3 is restricted to smooth and striated muscle. Their localisation in the membrane coincides with lipid rafts and they constitute a subdomain of the glycolipid raft structure. Uptake via this mechanism can therefore be referred to as caveolin and lipid raft mediated endocytosis. The caveolin proteins form invaginations in the plasma membrane called caveolae which are approximately 50 – 100 nm in diameter [308]. Nanoparticles or clusters greater than 200 nm in size are preferentially taken up by caveolae-mediated internalisation, albeit at a slower rate compared to clathrin-mediated uptake [279]. The observation that nanoparticles >200 nm

are preferentially taken up by this mechanism may be related to the activity of the recruitment proteins for both processes, and also related to the internalisation kinetics which favours the uptake of larger nanomaterials by the caveolae-mediated mechanism, potentially due to a maximum allowable size that can be accommodated inside the clathrin pits [279]. Another feature of caveolae is the evasion of the lysosomal degradative pathway, and while they do interact with the early endosomes, they never fuse and the contents of caveolae are never exposed to the lysosome and is the entry method of choice by viruses [309].

Macropinocytosis, unlike the clathrin-mediated uptake mechanism, is a non-specific form of endocytosis that facilitates the uptake of solutes from extracellular fluid [310]. The vesicles that are formed range between 0.5 – 5 μm in size and are initiated by the ruffling of the plasma membrane which eventually fuse to form the macropinosome [311]. The fate of the macropinosome is through the endocytic pathway and eventual fusion with lysosome vesicles [312]. The dynamics of the maturation process has been difficult to elucidate due to the absence of significant membrane markers like those found in the clathrin and caveolin mediated processes, with the most distinguishing feature of macropinosomes being their large size in the cytoplasm [313]. Uptake of nanoparticles by this mechanism, on account of vacuole size, can accommodate large nanoparticle aggregates in excess of 200 nm, as we have demonstrated using MNP coated with DMSA [314]. It provides an additional mechanism for nanomaterials uptake and one which can be harnessed for the delivery of larger nanodrug payloads.

The ability of MNP to interact with the plasma membrane of cells, to induce uptake by endocytosis or passive uptake by interacting with the plasma membrane indicates that it is possible that MNP could escape from endosomes and lysosomes. Such an event could cause considerable intracellular damage to the Golgi apparatus, endoplasmic reticulum (ER) and mitochondria. A thorough study has recently been published (June 2016) and demonstrates that bare (uncoated) MNP induced the formation of autophagosomes in MCF7 cells to a greater degree than PLGA coated MNP following 24h exposure [315]. Zhang et al. demonstrated that upon uptake of bare MNP into lysosomes, the lysosomal membrane was disrupted and subsequently diffused into the intracellular space while PLGA coated MNP did not cause such pronounced lysosomal damage. In addition, the bare MNP caused a reduction in mitochondrial membrane potential while coated MNP did not and reactive oxygen species (ROS) were induced following exposure to bare MNP only. Not only did bare MNP affect the integrity of lysosomes and mitochondria, they were also shown to disrupt the structure of the ER and Golgi. *In vivo* analysis in the same study demonstrated that mice exposed for 30 days to the bare MNP induced autophagosome accumulation in the kidney and spleen while PLGA MNP significantly reduced the toxicity in these organs [315]. There is a growing body of evidence that demonstrates that oxide nanomaterials can induce ROS production, mitochondrial damage, ER stress and autophagy which precedes apoptosis [316-320]. Autophagy was shown to correlate with ROS production alongside mitochondrial damage in A549 lung fibroblast cells exposed to bare MNP [319], and to induce ER stress in a murine peritoneal macrophage cell line 24h post exposure to phospholipid coated MNP [320]. Therefore the uptake, internalisation, release/degradation of MNP in the cell can have a profound effect on lysosomal, ER, Golgi and mitochondrial integrity.

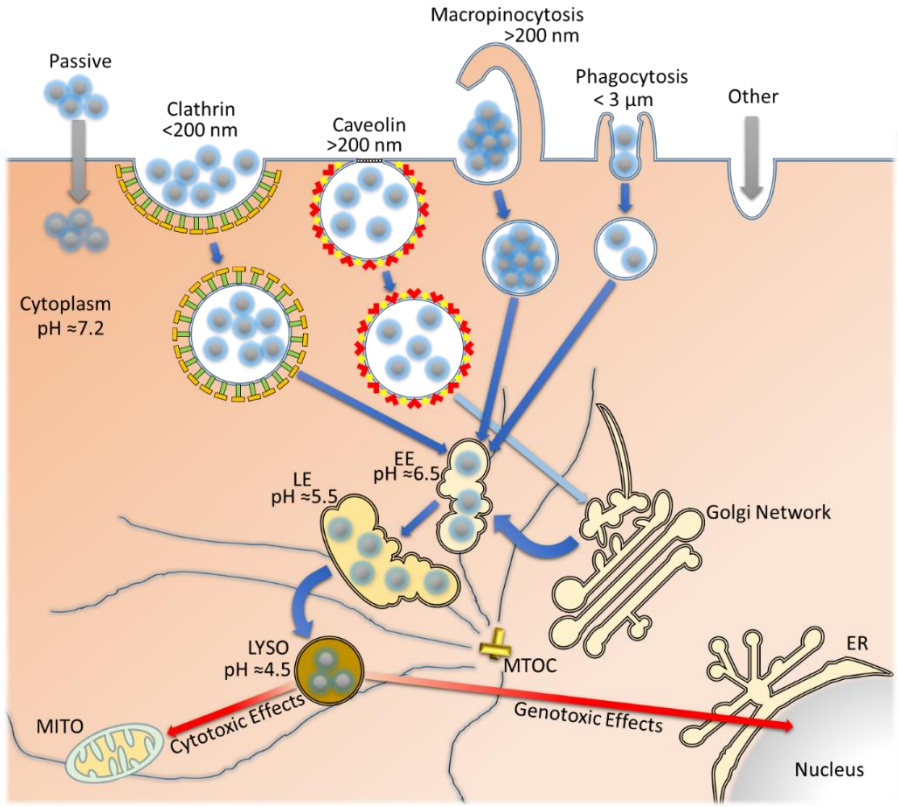

Figure 12: Modes of nanoparticle uptake.

An overview of nanoparticle uptake into the eukaryotic cell. Passive diffusion across the plasma membrane, clathrin mediated endocytosis, caveolin mediated uptake, micropinocytosis, phagocytosis, and other uptake mechanisms facilitate nanoparticle uptake. Nanoparticles enter the early endosomes (EE) which move along microtubules nucleating from the microtubule organising centre (MTOC) and mature into late endosomes (LE), and finally into lysosomes (LYSO). pH dependent release of nanoparticle functionalities in the lysosome can diffuse into the cytoplasm and enter key subcellular organelles such as mitochondria (MITO) and induce cytotoxicity and to the nucleus where genotoxic events can occur.

1.4.3 MNP degradation and *in vitro* cytotoxicity

An essential checkpoint that must be carried out prior to the use of nanomaterials *in vivo*, is the screening of each formulation to determine biocompatibility and capacity to induce acute toxicity following intracellular degradation and resulting appearance of the constitutive parts of the MNP. According to the three-tiered approach (Figure 6), the testing of nanomaterials constitutes Tier 2, whereby *in vitro* assays are employed to screen the engineered nanomaterials for biocompatibility or anticancer efficacy. Nanomaterials can enter the body and induce a wide range of effects, which are dependent on the mode of entry and whether nanomaterials reside outside or inside the cell. Many nanomaterials may not induce toxic effects when localised to the extracellular environment, but may induce toxicity upon entry into the acidic environment of the lysosome. The physicochemical characteristics and stability in solution can impede the measurements of toxicity, with interference of the dyes used to measure cellular viability, metabolic activity and intracellular events. Considerable attention has been turned towards the development of assays that provide a rapid means to screen a broad range of nanomaterials efficiently with an emphasis on developing

ways to limit or remove the capacity for interference. Two broad approaches can be taken to determine nanomaterials toxicity *in vitro*, firstly the utilisation of viability tests that rely on a colour change to provide a measure of cellular viability, such as those used to determine the suitability of drugs in the pharmaceutical setting; or secondly, the use of fluorescent viability tests against specific cellular markers or organelles. Both approaches suffer from interference to some degree, with conflicting reports as to the extent of nanoparticle-induced toxicity, using the same nanomaterials. The most common techniques are discussed, with a focus on high throughput fluorescent assays that provide multiple parameter readout compared to the single output obtained using colorimetric assays.

Testing of nanomaterials has been typically conducted using assays originally developed to determine the toxicity of chemicals and drugs [321]. However, it has been demonstrated that nanomaterial interference can occur with assays employing dyes such as those found in the lactate dehydrogenase (LDH), 3-(4,5-dimethylthiazol-2-yl)-2,5-diphenyltetrazolium bromide (MTT) and WST-1 assays [322, 323]. Nanomaterials have been shown to interact with chemical compounds and macromolecules such as proteins in these assays. In a recent study [324], silver nanoparticles coated with PVP caused considerable interference with the LDH assay by up to 50%, while a second formulation coated with citrate at the same concentration caused a 70% interference compared to the control group. Separately, it was shown that silver nanoparticles either bare or capped with citrate interfered with the LDH assay [325]. Oh et al. effectively demonstrated that careful assay development and removal of nanomaterials prior to assessment could minimise interference and ensure correct cytotoxic evaluation using these common colorimetric tests [325].

Fluorescent compounds provide an alternative to the single readout colorimetric tests, whereby they absorb light at specified wavelengths and can provide a multi-coloured readout for a wide range of parameters. In an unbound state they can label subcellular organelles and vesicles, irreversibly bind DNA and provide a measure of DNA content, nuclear shape and size. They may also indicate changes in intravesicle pH, having the ability to indirectly measure increases or decreases in pH through emitted light intensity. When coupled to nanomaterials, the ability to study uptake kinetics, track progression in the cell and measure stability is also possible. Additionally, it is possible to use subcellular organelle dyes to provide evidence of the uptake of nanomaterials, onset of cell death through depolarisation of mitochondrial membrane potential, and cell loss by measuring the total number of nuclei in the sample. While fluorescence based toxicity testing can provide a broad range of possible outputs, it remains vital to adequately screen the nanomaterials tested to ensure interference with fluorescent signal does not occur. As described above in the publication of Oh et al., adequate washing of cells prior to testing may aid in the reduction in assay interference. The distance between the nanomaterials and fluorescent molecule has been shown to be an important factor in fluorescent quenching with a range of possible relaxation pathways accounting for the reduction in fluorescence intensity [326]. Radiative decay, non-radiative decay, energy transfer between fluorescent dye and nanoparticle core, dye-dye coupling and nanomaterials surface interactions can all contribute to the reduction in fluorescent intensity [326]. The quenching of fluorescence by MNP can also be quite advantageous, such as in the production of smart nanoparticles. A study by Josephson et al. utilised MNP in MRI and were able to identify nanoparticle biodistribution by both contrast and fluorescence using near-infrared fluorescence spectroscopy, whereby fluorescence was restored once linker cleavage liberated the dyes from the nanoparticle [327].

1.4.3.1 High throughput multi-parametric analysis

The move towards an automated microscopy platform utilising a fluorescent based assay can dramatically reduce extracellular nanoparticle interference through direct visualisation of subcellular organelles. High-throughput assays such as HCSA provide the flexibility required in image analysis to enable subcellular data mining without the interference that MNP may otherwise induce in a colorimetric test. HCSA is a convergence between high resolution fluorescence-based imaging and cell-based assays. It provides advanced image analysis capabilities through the use of specialised software and data output is provided on a cell-by-cell basis. It is a powerful technique for the simultaneous detection of many biological pathways that has the capacity to screen thousands of compounds when used in a fully automated robotic platform. With the surge in nanoparticle development it is important to have an established and unified screening and analysis platform that can process newly developed nanomaterials and increase the selection of safer formulations at an efficient rate [328].

The researchers from our centre have demonstrated the suitability of the HCSA technique in monitoring the cytotoxic effect of a number of nanomaterials in a range of cell types such as cadmium telluride quantum dots and gold nanoparticles in murine neuroblastoma cells and HepG2 human hepatocellular carcinoma cells [328], amorphous silicon dioxide nanoparticles in human monocytic leukemia cell line THP-1 and human alveolar epithelial cell line A549 [329], nonfunctionalised quantum dots with human blood monocyte-derived primary macrophages and phagocytic, epithelial, and endothelial cell lines [330], carbon nanotubes in macrophage-like THP-1 cells [331], nebulised MNP [332] and most recently gold nanoboxes in A549 cells [333].

The intracellular degradation and liberation of the constitutive parts of the MNP can result in the excessive formation of ROS. ROS are highly reactive molecules and are present in the cell as by-products of metabolism. Under normal physiological conditions the low level of ROS present in the cell is due to the superoxide dismutase family of enzymes catalysing the dismutation of superoxide into hydrogen peroxide and water [334]. An increase in ROS can occur due to oxidative stress which can result in damage to DNA, RNA, lipids and proteins [334]. Degradation of MNP and release of Fe^{2+} can directly increase formation of ROS through the fenton reaction whereby hydrogen peroxide can oxidise Fe^{2+} to produce the hydroxide ion (OH-) and the highly reactive hydroxyl radicle (OH˙) [332, 334-336].

With a broad range of fluorescent dyes to choose from, the initial screening of nanomaterials should aim to provide an adequate readout to identify acute cytotoxicity and understanding of the mechanism of nanoparticle interaction with the biological sample. Cytotoxicity can occur via the direct impact on the integrity of the plasma membrane. It was previously noted that silica nanoparticles of 600 nm could interact with the surface of red blood cells and induce cell uptake through membrane ruffling [292]. Uptake in this manner caused haemolysis shortly following membrane interaction. In addition to plasma membrane damage, it is possible that uptake of nanomaterials can cause considerable cytotoxicity following degradation into their constitutive parts, which can release ions and result in the generation of reactive oxygen species as introduced above.

With this in mind, the most appropriate parameters to test as an initial screen of newly designed nanomaterials are those that provide a measure of total cell count (nuclear Hoechst 33342 dye), nanoparticle uptake into lysosomes (Lysotracker®), membrane permeability (YO-PRO®-1 iodide) and mitochondrial

membrane potential (Mitotracker®). Hoechst 33342 is designed to rapidly and selectively bind to the minor groove of dsDNA and preferentially to adenine-thymine (A-T) rich regions; cell membrane permeability dye (YO-PRO®-1 iodide) is a membrane impermeable dye that binds to DNA when cell membrane integrity is compromised. It has been demonstrated that YO-PRO®-1 iodide can pass through specific cell membrane channels, therefore cytoplasmic staining may be observed, and it is nuclear staining that signifies cytotoxicity. LysoTracker® dye is a weak base and can freely move into the cell, the dye is protonated and fluoresces upon entering acidic organelles where it is retained. Finally, the MitoTracker® cyanine dye contains a cationic charge and is capable of crossing the strong proton gradient of the mitochondrial membrane and is retained well following aldehyde fixation.

HCSA has become an approved approach for toxicity testing due to the high informational output and multi-parameter capabilities, and is becoming established as a gold standard method to screen a wide range of nanoparticles [328-333].

1.4.4 Assessment of genotoxicity

A genotoxin is an agent (chemical or radiation substance) that can directly or indirectly damage DNA and cause mutations and potentially result in cancer. The screening of nanoparticles to identify whether they possess genotoxic potential has received backing by the organisation for economic cooperation and development (OECD) with the aim to make it safer for consumers (www.oecd.org). The OECD has established guidelines to test chemical substances to determine the safety and biosafety of each. The test guidelines are an internationally recognised and agreed method used by governments, industrial sector and laboratories, and include the establishment of good laboratory practice guidelines to ensure high quality and reliable test data is obtained. Screening of nanomaterials for toxicity has been addressed by the OECD through implementation of over 110 different chemical tests. The OECD has recently completed a seven year experimental testing programme into the toxicity screening of 11 commercially available nanomaterials to be used from the chemical to the food industry. This programme facilitated over 780 studies into the evaluation of nanomaterial properties and it was concluded that the chemical-based guidelines outlined by OECD are, for the most part, suitable for testing nanomaterials [337]. Specifically, the guideline Test 487 (CBMN assay) has been adopted for the genotoxicity testing of nanomaterials and has been demonstrated as a superior method compared to alternative OECD genotoxicity tests [338].

1.4.4.1 Cytokinesis block micronucleus assay

The cytokinesis-block micronucleus assay is a powerful test to determine whether a nanoparticle formulation is genotoxic, and if capable of inducing genotoxicity, the test can identify whether the nanoparticle formulation is clastogenic or aneugenic. A clastogen is defined as an agent that induces breakages in chromosomes, leading to large sections of chromosomes being rearranged, added or deleted. An aneugen is defined as an agent that causes aneuploidy in a daughter cell. The most famous example being colchicine, an ancient mitotic spindle poison drug that was used to treat rheumatism and swelling in 1500 BC [339], and is currently used to treat gout [340], atrial fibrillation [341], and pericarditis [342], but can cause considerably potent adverse effects. Toxicity with colchicine can occur in as little as 2 hours post exposure with the onset of multi-system trauma and organ failure occurring between 24 hours and 72 hours.

Hypovolemic shock followed by cardiogenic shock due to extensive damage to the vasculature can cause death. To date no therapeutic methods exist to eliminate colchicine, while supportive care has shown promise in promoting patient survival [343]. The utilisation of colchicine in *in vitro* tests requires the identification of an appropriate concentration that does not result in substantial cell loss as outlined by the OECD in test no 487 [344]. The inhibition of cytokinesis (formation of a cleavage furrow and actin/myosin II contractile ring driven separation of two daughter cells), is facilitated by the chemical cytochalasin-B (Cyto-B) [345]. Cyto-B is a fungal metabolite which inhibits the polymerisation of actin through the inhibition of monomer addition to the barbed end of the nascent actin filament [346]. It was specifically shown by Carter et al. to inhibit the complete separation of bi-nuclear cells into daughter cells [347]. The mode of action of Cyto-B confers its level of toxicity, and accordingly the cells to be tested must be pre-screened with Cyto-B to identify a concentration that results in no greater than 55% cell loss [344]. The timing of Cyto-B exposure is an important aspect to capture the majority of cells in a bi-nucleate state, and must be conducted to ensure that cells undergoing their first division are inhibited from separation [345]. Typically cells are exposed to Cyto-B for 24 – 29 hours [345]. While fluorescent HCSA-specific assays exist for determining micronucleus formation, they are severely limited due to the toxicity of colchicine and Cyto-B compounds, with considerable cell loss hampering acquisition of an appropriate number of bi-nuclear cells (unpublished observation). The most appropriate test involves the cytology method of cytospin to concentrate cells onto microscope slides [348], and the staining of the nuclear material using a commercial Wright-Giemsa stain variant, to visualise nuclear containing cytosolic compartments [345]. The possible fates of cytokinesis blocked cells exposed to a genotoxic agent is outlined in Figure 13.

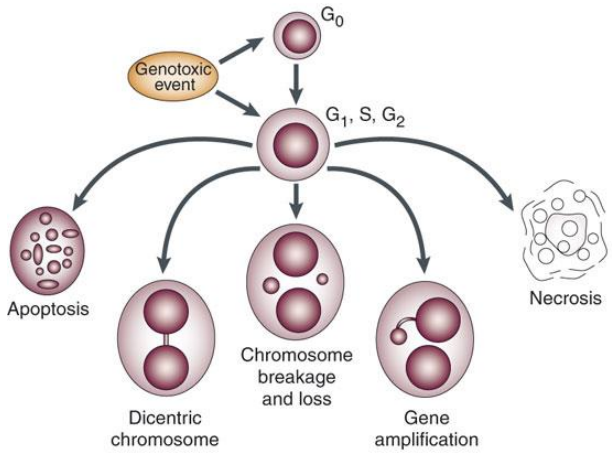

Figure 13: Various fates of cultured cytokinesis-blocked cells following genotoxic insult.

An overview of the five possible fates of cells exposed to a genotoxic agent. Apoptosis, generation of dicentric chromosomes, gene amplification, necrosis and breakage of chromosomes to form micronuclei. Image from reference [345].

1.4.5 Nanodrug design for targeted drug delivery

Conventional chemotherapy regimens have been aptly referred to as "shotgun" approaches in the treatment of cancer. Whilst cancer cells are the preferred targets of conventional chemotherapies, they also indiscriminately target healthy and rapidly dividing cells such as those found in the nails, hair follicles, blood, mouth and intestinal tract. The side effects experienced by patients undergoing chemotherapy treatment are different from patient to patient, with the most common being extreme fatigue, widespread hair loss, mouth ulcers, diarrhoea, nausea and vomiting. Side effects can range from mild to severe, with anaphylaxis at the extreme end of the spectrum. Unfortunately, these unwanted effects are common in chemotherapy treatment regimens and cardiac damage can occur due to the high and prolonged systemic doses that are administered (reviewed in [349]). Cardiac toxicity refers to the onset of arrhythmias, myocardial ischemia, coronary artery disease, hypertension and myocardial dysfunction following the treatment with chemotherapeutic agents. Two such agents, doxorubicin and gemcitabine, have been shown to affect heart function. Doxorubicin, an anthracycline cancer therapy drug, can cause left ventricular dysfunction and heart failure through the formation of reactive oxygen species, inhibition of DNA repair and impaired protein synthesis [350]. Gemcitabine on the other hand is an antimetabolic cancer therapy medication that can cause arrhythmias and ischemia due to coronary vasospasm and reduced blood flow and supraventricular tachycardia [351]. The broad ranging side effects presenting with the use of conventional cancer therapy drugs has been the main driver in the discovery for alternative methods.

Nanomaterial-drug conjugates, or nanocarriers, offer the means by which cancers can be directly and selectively targeted. They have several advantages over conventional drugs whereby they can protect the conjugated drug from degradation and increase the drug half-life, increase bioavailability and ensure that the nanocarrier can reach their intended target, and interact specifically with cancer cells therefore avoiding indiscriminate drug release and lessen or eradicate the observed side effects common with conventional treatments [352]. Nanocarriers are appropriately referred to as "smart drugs", due to their small size, large surface to volume ratio and drug carrying capacity, capability to bind to hydrophobic and hydrophilic compounds and their suitability for multiple delivery methods [353]. Current nanoparticle based therapies in clinical use exploit the EPR effect, a consequence of "leaky" and defective vasculature architecture and low lymphatic drainage, but many regions of the tumour are less vascularised and heterogeneous in nature and therefore chemotherapeutic drugs may not effectively reach all regions of the tumour [55]. In this case, having the capacity to exploit an additional therapeutic modality would provide an advantage over conventional methods. Incorporating a targeting moiety on the surface of the MNP has the advantage of selectively binding tumour cells and increasing the delivery of the chemotherapeutic drug. Through targeting only the tumour, the common side effects associated with chemotherapy treatment would be dramatically reduced.

Multiple strategies for drug delivery are being investigated which include active targeting to tumour cells, active targeting to angiogenic cell surface markers of endothelial cells, magnetic-field assisted delivery and triggered drug delivery. With the additional functionalisation comes a further layer of complexity whereby the nanoparticles must remain colloidally stable but must also have a high drug-loading capacity. Steric hindrance, availability of sufficient functional groups and employing spacer molecules play a role in the amount of drug incorporated. Functionalization strategies for MNP include

electrostatic and covalent attachment of the molecule of interest to the surface of the MNP. Electrostatic attachment involves the interaction of an oppositely charged moiety to the surface of the MNP, attractive force or bond strength depends on the charge of both the moiety to be attached and the nanoparticle surface, and can easily be disrupted in the presence of a high salt solution. In such an environment, drug release occurs as a passive process [354]. Taking this limitation into account, the covalent functionalisation of drugs and targeting moieties onto the surface of the nanomaterials seems to be the best approach. Covalent attachment is a type of chemical bond whereby electron pairs are shared between atoms, one such covalent bond is the disulphide bond involving electron pair sharing between two sulphur atoms, formed by the oxidation of sulfhydryl (-SH) groups. These bonds are strong, but less so than carbon to carbon and carbon to hydrogen bonds and therefore present a "weak link" in many molecules, thus enabling specific bond cleavage by reduction [355]. The implementation of covalent strategies to facilitate functionalization of the MNP enables specific drug release depending on the covalent bond formed. In the case of a disulphite bond, breakage of the bond in a reducing environment such as the lysosome would provide a situation whereby drug release can occur only following cellular uptake. Further to this, considerable challenges exist in the delivery of drug to all regions of the tumour as discussed previously in relation to the tumour vasculature. This is indeed one of the major obstacles in the treatment of cancer that exist today and one that requires considerable attention if systemic MNP-drug delivery is to be successful in the clinic. Geospatial localisation of MNP and payload dissemination are key factors in the development of a suitable MNP formulation and at present MNP delivered intravenously have a tendency to become sequestered in the liver and spleen and subsequently a low percentage of injected MNP enters the tumour. There is a clear divide with regards to the most appropriate method to validate the suitability of MNP *in vivo*. Intravenous injection of MNP that can adequately evade the reticuloendothelial system have been shown to cover irregularly shaped tumours more precisely than the punctate localisation offered with directly injected nanomaterial [356]. A clear advantage of direct injection of MNP is delivery of high concentrations of MNP and payload in the tumour, however it is not an accurate technique for the treatment of small, irregularly shaped tumours [357]. Huang et al. demonstrated that 0.19% of their intravenously injected MNP localised to subcutaneous tumour cells which was sufficient for tumour ablation following hyperthermia treatment [357]. They suggest that complete tumour coverage is not required in order for the tumour to be targeted by the MNP, in their case this was in relation to thermal ablation whereby convection currents would facilitate MNP movement during treatment to all areas of the tumour. Another study by Sugahara et al. demonstrated the efficacy of the iRGD tumour-homing peptide [358]. This peptide employed a three-step process to firstly target the tumour vasculature, secondly to penetrate into tissue and cells via neuropilin-1 expression and thirdly to enhance the activity of the abraxane anti-tumour drug. They did not utilise MNP nanoparticles in this study but nevertheless, they demonstrated an 11-fold increase in drug delivery in the abraxane resistant BT-474 breast cancer cell line, which significantly inhibited tumour growth *in vivo* [358]. Over the last few years considerable advances have been made in the development of nanomaterials that are targeted to specific tumours and a multitude of liposomal and polymeric nanoparticles with the capacity to target specific tumours are currently in clinical development [359, 360]. The bioactive compounds attached to these nanoparticles include small interfering RNA (CALAA-01, Atu027) [361], chemotherapeutic drugs such as oxaliplatin (MBP-426), doxorubicin (MCC-465, C225-ILS-DOX) and docetaxel (BIND-014

Accurins™), and the p53 gene (SGT53). Active targeting is facilitated through functionalising targeting moieties onto the nanomaterials surface such as monoclonal antibodies [362-364], small molecules [365-367], DNA or RNA based aptamers [368, 369], and peptides [370-372], as detailed in the following paragraphs.

Monoclonal antibodies: These have been the preferred class of targeting molecule for many years. It has been effectively demonstrated that conjugation of the her2/neu (Herceptin) antibody on the surface of superparamagnetic MNP could preferentially bind to HER2 expressing cells *in vitro* and *in vivo* [362, 363]. More recently the ability to specifically identify HER2 expressing lung and breast cancer cells using single domain antibody-nanoparticle conjugates has been demonstrated [364]. Current research favours the use of single-domain antibody fragments due to low immunogenicity and a higher functionalisation ability because of their small size compared to full size antibodies [373].

Small molecules: Small molecules are typically ≤ 500 Da in size and include growth factors, carbohydrates, and receptor ligands [365]. The most extensively studied small molecule is folic acid, which binds to the folate receptor. Overexpression of the folate receptor has been reported in many types of human cancers and in the case of breast cancer, it is a strong predictor of poor outcome [374]. In a study by Meier et al. using ultrasmall MNP functionalised with folic acid [366], a range of breast cancer cell lines were employed and exposed to the nanomaterials for 24 hours. Folic acid facilitated the binding and uptake of the nanoparticles into the cells. A recent study, using a novel recombinant protein based nanoparticle demonstrated folic acid mediated uptake to be greater than six times that of non-targeting nanoparticles [367]. While small molecules are an attractive option for targeted drug delivery due to their relatively low cost to produce, ease of conjugation and stability, their affinity with cell surface receptors is weak [375].

Aptamers: These are small, single stranded RNA or DNA sequences that are designed to bind, with high affinity, to specific protein or other cellular targets [376, 377]. Essentially they can be considered a chemical equivalent of antibodies. Because of their size (typically 15 – 60 bases in length), aptamer immunogenicity does not occur [378], which is a major advantage for their use compared to antibody-based approaches. In addition, they are highly specific and can discriminate targets based on slight structural differences [379, 380]. The most relevant application under development is in targeting angiogenesis. One anti-angiogenic aptamer product (Pegaptanib®) has been FDA approved for use in macular degeneration and targets the vascular endothelial growth factor [368]. There are currently two aptamers in development for application in oncology (AS1411 and NOX-A12). In pre-clinical testing the aptamer AS1411 was shown to bind the nuclear matrix protein nucleolin on the surface of cancer cells and inhibit proliferation. It has also been employed to utilise nucleolin targeting for the delivery of siRNA in the treatment of malignant melanoma [381-384]. In fact, AS1411 was the first nucleolin-targeting agent (and the first anticancer aptamer) to reach human clinical trials [369]. In a recent publication, Malick et al., the group that discovered and developed AS1411 as an anticancer agent, demonstrated that AS1411 conjugated to gold nanoparticles had preferential uptake via nucleolin binding into breast cancer cells (MCF-7 and MDA-MB-231) compared to non-

malignant cell lines (MCF-10A), and were shown to exhibit greater stability in complex compared to free forms and induce greater *in vitro* and *in vivo* therapeutic effects when in combination [369].

Peptide-based approaches: The use of peptide-based targeting moieties provide the same affinity, specificity, stability and small size as observed with the monoclonal antibodies and aptamers described previously. They also exhibit relatively low immunogenicity, making them an attractive targeting molecule. Peptide ligands are as short as three amino acids in length such as the NGR peptide [370], which has shown promise in targeting upregulated CD13 on the tumour vasculature [370]. A particular peptide of interest, HB-19, which was constructed in 1996 was shown to have anti-HIV capabilities [371]. Synthesis was facilitated using a template assembled synthetic peptide construct as detailed by Mutter et al. [385]. This helical peptide was Lysine rich, and provided a template from which the tripeptide (Lys$\Psi(CH_2$-NH)-Pro-Arg) could be anchored. The reduction of the peptide bond between Lysine and Proline, denoted as $\Psi(CH_2$-NH), was carried out to promote stability and resistance to proteases [371]. In 1999 the anti-HIV effect of HB-19 was delineated. It was discovered that HB-19 prevented HIV particle attachment to target cells through competitive binding of cell surface-expressed nucleolin [386, 387], and was suggested as a potential anti-HIV drug thereafter [388]. *In vivo* studies provided evidence for its rapid uptake (5 minutes) in the spleen, liver, bone and kidneys following administration and preferential uptake and stability in lymphoid organs, the site of HIV propagation [389]. This early work was promising and it was later discovered that HB-19 could markedly suppress the *in vivo* growth of human breast tumour xenografts [390], significantly limit the potential for metastasis through restoring contact inhibition [391], and have profound inhibitory effects on the highly malignant rhabdoid tumour of the kidney [392]. It was in 2011 that a related hexavalent Nucant (nucleolin antagonist) pseudopeptide (N6L) was described (Figure 14) [372]. This related peptide had a greater affinity for nucleolin compared to HB-19 and other variations tested [372], and was independently shown to bind a second cell surface protein nucleophosmin [393], providing an additional marker through which it could potentially exhibit its anti-tumour effects. In addition, N6L had anti-angiogenic capabilities *in vivo* at low concentrations (0.4 nM, 0.8 nM and 2 nM), and induced apoptotic cell death following 16 h exposure at higher concentrations (10 µM, 20 µM and 40 µM) [393]. Binding nucleolin results in clustering of the receptors in lipid raft microdomains, which are then endocytosed [372, 394]. This mechanism could be exploited for targeted drug delivery by functionalising N6L onto the surface of MNP for combination therapy. The value of N6L as a clinically-implemented anticancer agent is close to becoming a reality. As of February 2015, N6L (referred to as IPP-204106) completed a Phase I/IIa clinical trial in solid tumours in France and Belgium (NCT01711398). Phase II of testing will focus on the treatment of pancreatic cancers using the optimum concentration of N6L identified in the previous phase (9 mg/kg). In pre-clinical testing it was reported that at a dose of 1 mg/kg in combination with the anticancer drug gemcitabine resulted in a massive reduction in tumour volume in a mouse pancreatic cancer model [395]. To date, the results of this first stage of testing have not been released to the scientific community.

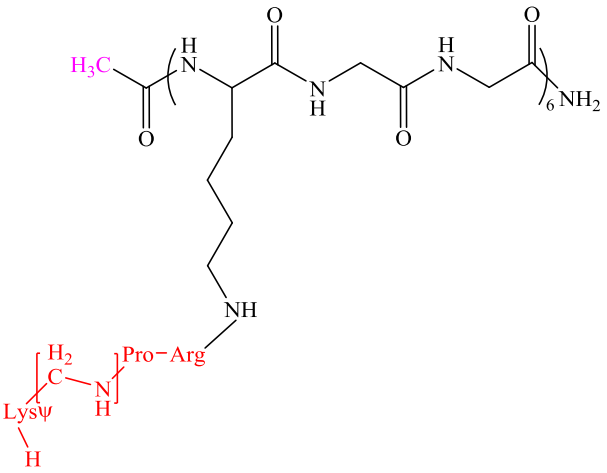

Figure 14: Structure of Nucant.

Structure of Nucant (N6L), whereby all lysine residues in the KΨPR unit (red) are in the L configuration. N6L displays a lysine-rich template (black) which is a 310 helical matrix composed respectively of 6 repeats of LysΨ-Pro-Arg. The C-terminal sequence (pink) was elongated with Cys-Aib-Gly to generate N6L-Cys to enable binding to the iron oxide via a disulfide bridge.

Efficient targeting of MNP to the site of a tumour is of major importance, with a considerable number of barriers in place that MNP must overcome before payload delivery. Firstly MNP must evade the RES; secondly they must extravasate the vascular endothelium which can be enhanced by local hyperthermia [396]; thirdly, the MNP must pass the tumour microenvironment encompassing the extracellular matrix (when highly developed it can limit diffusion of the payload [397]). This was addressed by Kuhn et al. who functionalised MNP with collagenase therefore enabling mobility through the matrix [398]. Fourthly, MNP penetration in the tumour is influenced by high intratumoral pressure which is a consequence of defective vasculature and lack of proper lymphatic drainage [399]; and fifthly, MNP need to effectively cross the plasma membrane and release their functionalised drugs. Only when all of these conditions are met will the MNP be capable of payload dissemination. Coupled with techniques such as magnetic heating it is possible to target the tumours from within using a two pronged approach with delivery of a chemotherapeutic agent where necessary and the thermal ablation of tumour cells by hyperthermia.

The study of MNP cytotoxicity and drug-functionalised MNP anticancer effect, as presented in this thesis, utilised a 2D cell model system to facilitate automated in vitro multiparametric analysis using high content screening. 2D cell culture is a rapid, easily accessible and well documented method of screening a large quantity of compounds utilising a high content screening approach. All cells in the assay are of an equal size, nuclear size is largely the same and ensures that scanning and analysis by high content screening is streamlined. Limitations to 2D cell culture include the inability to study the effect treatment has on cells in their natural environment which consist of a multitude of different cells and therefore have a decreased compatibility with *in vivo* systems. An advancement to this approach would have been the implementation of a 2D co-culture model system and a 3D cell culture model. Co-culture using an *in vitro* endothelial-fibroblast organotypic model would have allowed for the examination and elucidation of angiogenesis via the construction of a 3D vascular network [400]. Co-culture for the study of angiogenesis was described in 1999 [401] and later by Donovan et al. who demonstrated that co-culture could develop

capillaries *in vitro* using the matrigel assay [402]. Vascularised connective tissue was developed by Sorrell et al., without the need of matrigel, in which they utilised human umbilical vein endothelial cells and human dermal microvascular endothelial cells grown on a monolayer of human fibroblast cells, and was stable for up to 5 weeks [403]. 3D cell culture models have gained considerable attention due to the physiologically relevant information and comparative data for in vivo tests [404]. Cells that are grown in 3D cultures are distinctly different (morphologically and physiologically) than their 2D counterparts [405], and more closely predict the results obtained *in vivo*. However challenges exist with 3D models which precluded their use in this project, mainly the inability to implement an automated scanning protocol with the GE healthcare InCell 1000 instrument utilised in the screening of all MNP formulations. This is due to topographical inconsistencies with 3D models and the labour-intensive need to capture slices of each sample and construct a 3D rendered image in order to gather the necessary information. Such challenges should not hinder future work with the use of more modern microscopes that include automated and rapid high content screening microscopes such as the InCell 6000.

1.4.6 MNP in vivo biodistribution and magnetic heating

1.4.6.1 Magnetic resonance imaging

MRI image contrast is remarkably superior to CT and other imaging techniques [406]. Image contrast in both these techniques is a function of tissue density but unlike CT scans, MRI relies on tissue relaxation properties which contribute to the image quality. Two types of relaxation properties exist in MRI, with T1 relaxation and T2 relaxation. T1 relaxation time generates contrast by measuring the time taken for individual excited protons to return to their unexcited state (Figure 15). In comparison, T2 weighted images measure the time taken for two different excited protons to become dephased (desynchronised spins). The image generated is due to either T1 or T2 relaxation and intensity is a function of the hydrogen content in each tissue type. The two approaches are therefore dependent on the excitation of protons, however, the magnetic moment of electrons are approximately 700 times that of a proton. In the clinic, contrast agents such as the iron oxides discussed here and gadolinium nanoparticles are employed to enhance the signal that is obtained. They are capable of providing sufficient contrast compared to the surrounding tissue in order for pathological and healthy tissue to be differentiated. This capability to enhance contrast lies in their unpaired electrons (4 in magnetite and 7 in gadolinium) which contribute dramatically to the relaxation rate of the protons in the tissue. At sufficiently high enough concentrations, the superparamagnetic iron oxide contrast agents provide superior T2/T2* imaging capabilities, in excess of that provided by gadolinium due to their large magnetic moment as previously discussed.

It was their use as contrast agents that brought the first iron oxide nanomaterials into the clinic, with a range of approved compounds for intravenous delivery over the past few years. Examples include Endorem® (Dextran coated MNP, 80 – 150 nm), Resovist® (Carboxydextran-coated ultra-small MNP, 20 nm), Sinerem® (Dextran-coated ultra-small MNP 15 – 30 nm), Feruglose (pegylated starch-coated ultra-small MNP 20 nm), and iron oxide-based agents for gastrointestinal contrast which are given orally such as Ferumoxsil® (silicon-coated MNP, 300 nm) and Abdoscan® (sulphonated styrene-divinylbenzene-coated MNP, >300nm) [25, 407]. It would appear that most of these approved iron oxide-based contrast

agents are no longer utilised in the clinic, either due to discontinuation by the manufacturer or due to concerns over toxicity. This leaves a large gap in the market for the production of clinically viable contrast agents, and the potential for providing novel nanoparticles for molecular imaging, targeted drug delivery and thermal therapy [408].

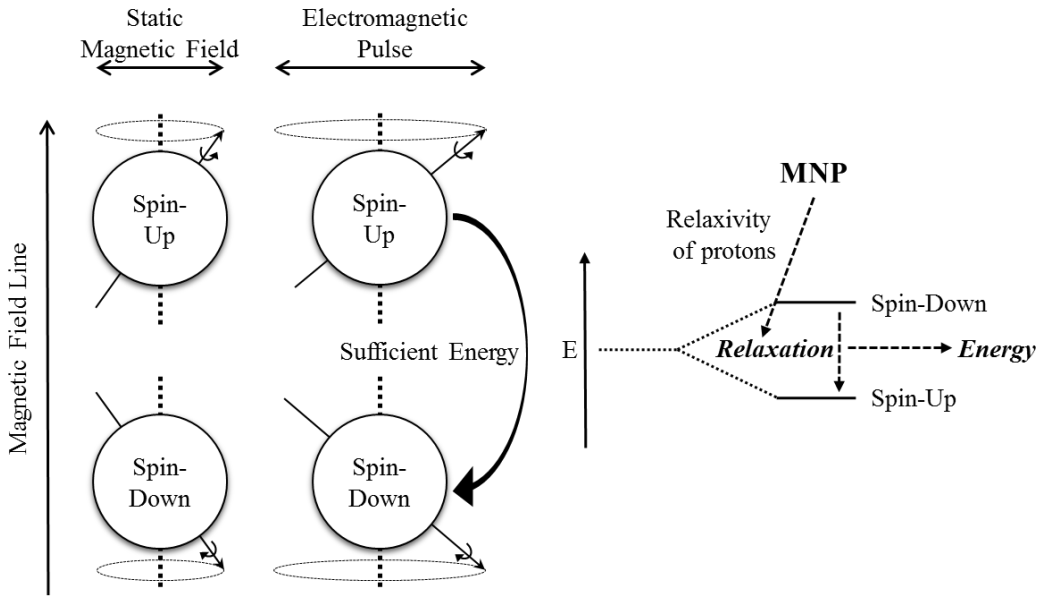

Figure 15: Magnetic resonance imaging: proton spin state and energy liberation

Schematic of the quantum changes that occur in magnetic resonance imaging. Protons exposed to a static magnetic field have either a Spin-Up or Spin-Down configuration. They will orient along the magnetic field line and have a magnetic dipole moment that will align along the same axis (dotted vertical line), angular momentum prevents perfect axial alignment and the protons will process about the axis. An electromagnetic pulse applied will flatten out the procession of the protons, as they align with the new wave. If sufficient energy (E) is provided the protons will transition from the spin-up to the spin-down orientation, a higher energy state. Relaxation to the lower spin-up energy state releases energy of varying intensities which generate the MRI image. Iron oxide nanomaterials function to facilitate proton relaxation by accepting energy from the excited protons via unpaired electrons.

1.4.6.2 Magnetic hyperthermia

Magnetic hyperthermia is the heating of an area containing magnetic material under the influence of an alternating magnetic field. Superparamagnetic MNP are well suited for hyperthermia, owing to their high saturation magnetisation in an AMF and lack of residual magnetization following removal of the magnetic field. The application of magnetic hyperthermia was first demonstrated by Gilchrist et al. in 1957 using iron oxide particles with a size range of 10 nm – 1 µm, to heat lymph nodes using a 1.2 – 2.0 MHz magnetic field [409], in a manner so as to "pasteurize the nodes" [409]. The basis for the development of this technology exploits the temperature-sensitivity of many cancer cells. It has been shown that sustaining a temperature above 43°C is sufficient for clinical hyperthermia and that sustaining temperature for more than one hour would cause cancer cell death [410]. Hyperthermia has the benefit of increasing the localised

blood flow which, if carried out as an adjuvant with drug delivery, could improve delivery of therapeutic agents [411]. Delivery of nanomaterials to the tumour by direct injection, as shown in the original study by Gilchrist et al., remains the most reliable method to study nanomaterials and hyperthermia. By this method, the quantity of nanomaterials in the tumour is known and while distribution is not homogenous, it is possible to quantify the temperature dose delivered according to the CEM43T90 (cumulative equivalent minutes of T90 above 43 degrees °C) whereby 90% of the tumour area has reached the therapeutic dose of 43 °C for a defined time period. In addition, the quantity of available nanomaterials for repeated therapy has been shown to remain largely in the tumour, with a small percentage detected in the scavenging centres of the liver and spleen [412]. Utilising hyperthermia as an adjuvant therapy is one of the key points for its development, and it has also provided a means to trigger drug release [413-417], which was more pronounced when in a low pH environment, and dependent on both the drug linker and nanoparticle coating employed [418].

1.5 Aims of this study

There is a need to develop a nanoparticle based theranostic product that can be used for the early detection and treatment of breast and pancreatic cancer. Advancements are being made but fundamental research is needed towards streamlining the testing of nanomaterials and the selection of suitable lead formulations.

The work presented in this thesis summarises the progress made towards the selection of suitable nanoparticles as theranostic leads and was in line with the aim to address the assessment and selection of future nanodrugs for cancer theranostics. The aim of this project was fourfold:

Firstly to investigate a range of MNP, focusing on their dynamics in culture medium and interaction with adherent cells, to assess their capacity to induce cytotoxicity following short-term exposure.

Secondly, the validation of the most suitable surface linker for MNP drug functionalisation, demonstration of anticancer potential using doxorubicin functionalised MNP, testing of the N6L pseudopeptide for anticancer capabilities, identification of N6L-mediated MNP uptake into cell lines and primary cells, and efficacy testing of gemcitabine functionalised MNP with and without the N6L targeting ligand.

Thirdly, to investigate MNP intracellular effect on mitochondrial membrane potential and the determination of nanomaterial-induced cell death through apoptosis and/or necrosis and to identify genotoxic capacity using the lead formulations and their individual components through the induction of micronuclei.

Fourthly, to further understand the *in vivo* interaction and detectability of MNP in a small animal model using a 7T magnetic resonance imaging device.

Chapter 2
Materials and Methods

Chapter 2: Materials and methods

2.1 Experimental design

MNP were supplied by the Multifun partners involved in WP1 (as presented in section 2.2.1), along with information on the core nanomaterials size, shape, charge and hydrodynamic diameter. In-house characterisation by NTA was the first test applied to the basic MNP entering the lab to verify the supplied DLS data. Changes in the hydrodynamic size following incubation in serum containing cell culture medium was tested by NTA to gain an understanding of nanomaterials stability, and the degree of biological interaction affecting the particle size and stability. Human breast cell lines were then exposed to the supplied MNP to identify formulations that induced acute cytotoxicity using high throughput techniques such as high content screening analysis and flow cytometry. Following this, a range of qualitative studies were carried out by WP3 to study MNP interaction with cells, and to identify rate of cellular uptake, method of uptake and intracellular localisation. It was vital to understand how the MNP interacted with cells to develop a formulation with specific drug release capabilities. Prior to functionalising the MNP, the lead formulation was tested *in vivo* to ensure adequate contrast was provided by MRI and to screen the biodistribution, and biopersistence over a five-week period. The biocompatible nanomaterials were functionalised with doxorubicin chemotherapy drug, and a study was done to identify the best functionalisation route between covalent and electrostatic strategies. Further studies identified the best linker for drug functionalisation to facilitate triggered drug release. Building on these studies, formulations with the linker of choice were functionalised with gemcitabine chemotherapy drug, and were further functionalised with the N6L targeting peptide. The targeting peptide was shown to increase MNP uptake into cells by the Perls' Prussian blue and multiparameter assays. Uptake and release of chemotherapy drug resulted in cell death, and the intracellular effect on mitochondria and specific cell death pathway activation were determined. Finally, the genotoxic potential of the lead formulations and their individual components was determined. The following sections outline the material used in this project and their source, and provide stepwise protocols for each assay, focused initially on the *in vitro* qualitative assays and the quantitative assays and finally the *in vivo* assays employed.

2.2 Source of material

2.2.1 Nanomaterials

Seven MNP formulations differing in their core size and surface coating were produced within WP1 by the involved partners, namely IMDEA, ICMM, CSIC (Madrid, Spain); Nanotex® (Zaragoza, Spain); and Liquids Research Limited (Bangor, Wales) as presented in Figure 3. Five surface coatings (aminopropylsilane, aminodextran, dimercaptosuccinic acid, polyacrylic-acid and dextran) were used to functionalise the core nanomaterials, either at the stage of MNP formation or in a second step reaction. The MNP were named according to the surface material used. ASi MNP contained aminopropylsilane, ADNH MNP was aminodextran, PAA MNP was polyacrylic-acid, F1566 MNP was dextran and OD10, OD15 and MF66 MNP were dimercaptosuccinic acid coated. The basic MNP formulations were functionalized with

a targeting pseudo-peptide (N6L) and chemotherapy drugs (doxorubicin hydrochloride and gemcitabine) by Dr. Pierre Couleaud at IMDEA. NUCANT 6L was supplied by Professor José Courty from CCRET (Paris, France). Cadmium Selenide Quantum Dots (CdSe QD) were synthesised and provided by Dr Valerie Gerard and Dr Joseph McCarthy, Department of Chemistry, Trinity College Dublin, Ireland.

2.2.2 General materials and consumables

Dulbecco's modified Eagle–high glucose medium (DMEM), DMEM with nutrient mixture F12 (DMEM-F12), McCoy's 5A, Rosewell Park Memorial Institute medium (RPMI), Foetal Bovine Serum (FBS), horse serum, penicillin-streptomycin, recombinant human insulin, hydrocortisone, epidermal growth factor (EGF), sodium pyruvate, HEPES, cholera toxin, 0.1 μm filtered DNase/RNase free water, dulbecco's phosphate buffered saline, tacrine hydrochloride, valinomycin, dimethyl sulfoxide (DMSO), doxorubicin hydrochloride, gemcitabine hydrochloride, ethanol, methanol, Helmanex™, colchicine HPLC grade, and Eppendorf® epT.I.P.S. Biopur® tips were from Sigma Aldrich, Dublin, Ireland. TrypLE™ Select solution was from Bio-Sciences Ltd., Dublin, Ireland. Microscope slides and 8 well BD falcon culture slides were from BD Biosciences, Belgium. MycoAlert® PLUS test kit was from Lonza, Switzerland. All NUNC plasticware was from Thermo Scientific™, New York, USA.

2.2.3 Fluorescent dye kits

2.2.3.1 High content screening analysis kits

The HCSA kit selected for the cytotoxicity testing was sourced from Thermo Scientific (formerly Cellomics®) and was a multiplex kit containing Hoechst 33342, cell membrane permeability dye (YO-PRO®-1 iodide), Lysosomal (LysoTracker® Red) and Mitochondrial (MitoTracker® Orange) probes.

2.2.3.2 Flow cytometry kits

Two test kits were used, one to evaluate the impact of MNP exposure on cell cycle progression and the second to determine the mechanism of cell death following exposure to basic MNP and functionalised MNP formulations. The CycleTEST™ PLUS DNA test kit (BD Biosciences, Belgium) contained the fluorescent dye propidium iodide. The second kit (FITC Annexin V Apoptosis Detection Kit with 7-AAD), was obtained from Biolegend, San Diego, California and contained both 7-aminoactinomycin D (7-AAD) and FITC conjugated Annexin V.

2.2.4 Colorimetric kits

2.2.4.1 Perls' Prussian blue

Reagents required for Perls' Prussian blue staining and mounting of microscope slides include methanol, hydrochloric acid, potassium ferrocyanide, neutral red and DPX mountant and were all purchased from Sigma Aldrich Ireland.

2.2.4.2 Kwik Diff™ kit for CBMN assay

Colorimetric reagents used for the cytokinesis block micronucleus assay include a methanol fixative, eosin stain solution and methylene blue solution, purchased from Thermo Scientifc™ as Shandon™ Kwik-Diff™ staining kit. Cytochalasin B was sourced from Sigma Aldrich Ireland

2.3 Nanoparticle characterisation

2.3.1 Characterisation of MNP by NTA

Both TEM and DLS were carried out by Dr Gorka Salas (IMDEA, Spain) as described earlier [419]. Results were provided in order to aid in the selection of the MNP, and on the basis of comparison with the findings presented in this thesis to select the most suitable lead formulations.

The measurement of nanoparticle hydrodynamic size was carried out by NTA using the Malvern NS500 microfluidic device equipped with a 50 mW 532 nm laser (Malvern Instruments Ltd., Amesbury, UK). The device records and tracks the Brownian motion of nanoparticles in solution in 2 dimensions. The determination of average distance travelled by each particle in the x and y direction allows the particle diffusion coefficient (*Dt*) to be determined. As the temperature (*T*) and solvent viscosity (η) is known at the time of recording, based on temperature control settings and manual setting of viscosity, the sphere-equivalent hydrodynamic diameter of the nanoparticles can be identified using the Stokes-Einstein equation:

$$Dt = TK\frac{TK_{\mathrm{B}}}{3\pi\eta d}$$

Brownian motion occurs in 3D, while NTA observes motion only in 2D. Therefore the determination of *Dt* as shown in the equation above, is possible by measuring the mean squared displacement in the x and y axis according to the equation below:

$$\frac{\overline{(x,y)}^2}{4} = Dt = TK\frac{TK_{\mathrm{B}}}{3\pi\eta d}$$

2.3.1.1 NTA set-up

The fluidic system and sample stage were primed with 0.1 µm filtered DNase/RNase free water. The system was routinely checked prior to introducing a nanoparticle sample for the presence of any contaminating nanomaterials. Contamination was removed either physically (Kimtek wipes used to clean optical stage), chemically by introducing a 5% solution of Hellmanex™, an optical cleaning solution, into the device for five minutes or by both methods to ensure a clear field of view devoid of unwanted nanomaterials is attained. An automated and pre-defined flush cycle allowed for all traces of contamination and Hellmanex® solution to be removed from the system.

The stage was set to the scatter position and a diluted calibration sample was loaded by an automated sample loading protocol. Calibration was conducted prior to loading samples of unknown size to ensure size was accurately determined Figure 16. The optimal concentration range for samples lies between 10^7 to 10^{10} particles per mL, and will provide statistically sound and reproducible data (> 200 recorded tracks). Samples below or above this optimal concentration range were diluted accordingly and re-introduced into the device to ensure the optimal concentration was achieved. A unique name was assigned for each sample and an acquisition script was generated.

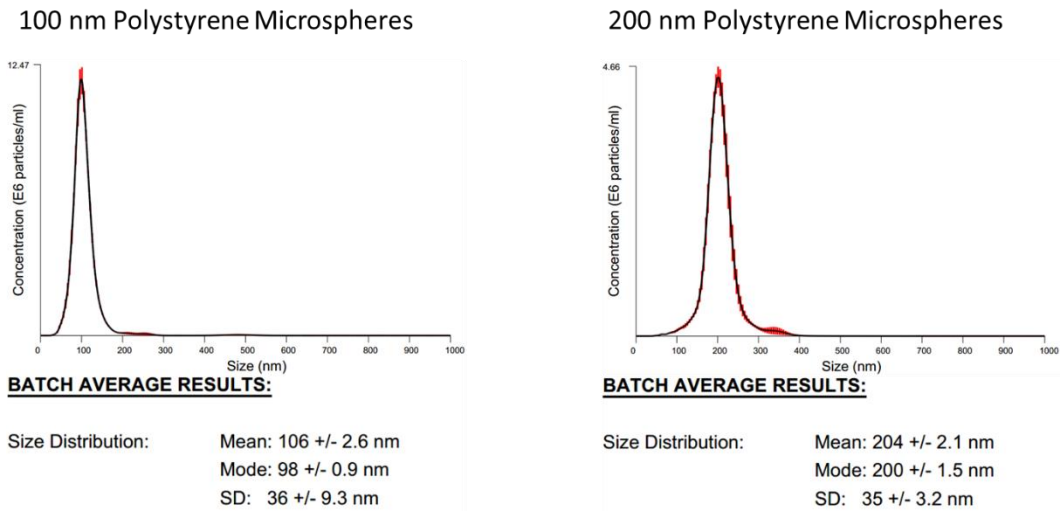

Figure 16: Nanoparticle tracking analysis calibration.

Calibration of the NTA was carried out routinely prior to use and confirmed accurate size determination. Calibration standards of 100 nm and 200 nm polystyrene microspheres, supplied by Malvern (Malvern Instruments Ltd., Amesbury, UK), were used to certify instrumentation alignment prior to each session.

2.3.1.2 Nanoparticle acquisition

Prior to running the acquisition script to record the nanoparticle motion, correct focusing of the device was required. The sample was visualised in a 100 µm by 80 µm window and approximately 10 µm in depth. Depending largely on the nanoparticle size and refractive index, the manual focusing for each sample was required. Focusing was carried out to obtain spot diffraction patterns that were well defined and devoid of diffraction rings, where possible. Once correct focusing was attained, the camera intensity was set so as to maximise the number of nanoparticles visible within the optical field of view, without causing interference from increased background intensity. For each nanoparticle formulation to be tested, six independent 90 second videos were acquired. For each video, the automated script was set to advance the nanoparticle solution prior to recording, so that the optical field of view would contain a new batch of previously un-recorded nanoparticles, thus providing a robust hydrodynamic size determination for the whole sample. Following acquisition, the device was set to allow correct nanoparticle identification.

2.3.1.3 Nanoparticle hydrodynamic size determination

The detection threshold was adjusted (increased or decreased) from the pre-set value of 10, depending on whether more stringent (>10) or less stringent (<10) detection was required. The selected threshold was set to maximise the number of nanoparticles identified without compromising the integrity of the data that may occur from the selection of background artefacts and by the erroneous identification of multiple nanoparticles within diffraction rings of a single nanoparticle. Following the selection of the appropriate threshold, an automated script was run and the positioning and motion of individual nanoparticles was tracked. The analysis of each sample was conducted in batch mode, so that a mean hydrodynamic size could be obtained. The software used for the analysis in this thesis was the NTA2.3 Build 0025.

2.3.1.4 Nanoparticle sample preparation: retrieval from serum containing medium

Nanoparticles dispersed in complete medium containing 10% FBS are not suitable for NTA, without prior sample clean-up to remove excess and unbound serum proteins. The MNP presented in this thesis were removed from solution by magnetic separation. The samples were washed three times and re-suspended in 1mL aliquots of 0.1 µm filtered sterile water prior to NTA assessment.

2.4 Cell culture methods

2.4.1 Cell lines

A diverse range of cell lines were selected for testing in this study (Table 1). All cell lines were selected by the Multifun consortium based on their diverse molecular profile, subtype and disease type. All cell lines were purchased from ATCC (Manassas, Virginia, USA), and maintained by consortium members from the University of Manchester and Queen Mary University of London. Cell lines were distributed from these two sources to all members of the consortium. Breast-derived cell lines provided by the University of Manchester include: MCF-7, BT-474, SK-BR-3, MDA-MB-231, and MCF-10A. Pancreatic-derived cancer cells provided by the Queen Mary University of London include BxPC3 and PANC-1. The A549 lung carcinoma cell line, and NIH-3T3 mouse fibroblast cell line were directly sourced from ATCC.

Breast cancer cell lines and a normal-like breast cell line were used as a model to screen the range of basic MNP to select biocompatible formulations. Two pancreatic cancer cell lines were used to validate the results obtained with respect to drug functionalised MNP. Both a lung epithelial cell line (A549) and a mouse fibroblast cell line (NIH-3T3) were included as a requirement of the Multifun project. The A549 cell line was selected by the Multifun consortium to carry out a risk assessment of the developed MNP and their respective components. Risk assessment was to be carried out by high content screening focusing on mitochondrial mass and potential over an exposure period of 36h. The A549 was retained in this study for testing mitochondrial toxicity to determine if the engineered nanomaterials could affect cells unlike those used during the MNP development phase. The NIH-3T3 cell line is recognised by the OECD as being extremely suitable for the testing of nanomaterials. In the same way as the A549 cell line, the NIH-3T3 cell line was selected initially by the Multifun consortium to carry out a risk assessment of the MNP and their components. In addition to this, and on account of the OECD sanctioning this cell line for nanoparticle

toxicity testing, it was retained for both mitochondrial toxicity testing and genotoxic evaluation following the OECD micronucleus test (No. 487). The NIH-3T3 cells have been used in earlier toxicological studies and therefore provide a good basis for comparison [420, 421]. Both cell lines were utilised so as to establish a benchmark from which the results of the Multifun project could be disseminated to the wider scientific community. Following from this, it would be appropriate to conduct a series of OECD toxicity tests using normal cell lines such as liver, kidney, and spleen which would reflect the organs first exposed to injected nanoparticles, and lung cell lines for determining toxicity of MNP exposure via inhalation.

Table 1: Origin and molecular profiles of cell lines.

Selection of the most suitable cell lines was based on cancer status, tumour type and subtype. Met AC = metastatic adenocarcinoma; IDC = invasive ductal carcinoma; AC = adenocarcinoma; F = fibrocytic disease; DC = ductal carcinoma; N/A = not applicable.

Cell Line	Status	Origin	Disease Type	Subtype	Doubling Time (Approximate)
MCF-7	Cancerous	Breast	Met AC	Luminal	29h
BT-474	Cancerous	Breast	IDC	Luminal	29h
MDA-MB-231	Cancerous	Breast	Met AC	Basal	24h
SK-BR-3	Cancerous	Breast	AC	Luminal	65h
MCF-10A	Normal	Breast	F	Basal	20h
BxPC3	Cancerous	Pancreas	AC	N/A	48h
PANC-1	Cancerous	Pancreas	DC	N/A	52h
A549	Cancerous	Lung	AC	Basal	22h
NIH-3T3	Normal	Mouse Embryo	N/A	N/A	20h

2.4.2 Maintaining cell lines

All cell lines were grown at 37˚C in a humidified atmosphere containing 5% CO_2. They were maintained as monolayers in T175cm^2 flasks (NUNC), in growth medium specific for each cell line, indicated below. Cells were tested using the MycoAlert® PLUS test kit for the presence of mycoplasma (Lonza, Switzerland). Cells were observed daily to monitor any morphological changes. Experiments were prepared using sub-confluent cells in the exponential phase of growth.

MCF-7

A luminal epithelial breast cell line isolated from the pleural effusion of a 69 year old female Caucasian with metastatic adenocarcinoma. Cells were cultured in DMEM high glucose (4.5g/L) medium with L-glutamine and supplemented with 50µg/ml penicillin-streptomycin, 1mM sodium pyruvate and 10% FBS.

BT-474

A luminal invasive ductal carcinoma cell line isolated from a 60 year old female Caucasian. Cells were cultured in RPMI 1640 with L-glutamine and supplemented with 50µg/ml penicillin-streptomycin, 1mM sodium pyruvate and 10% FBS.

MDA-MB-231

A basal B breast cell line from the pleural effusion of a 51 year old female Caucasian with metastatic adenocarcinoma. Cells were cultured in DMEM high glucose (4.5g/L) medium with L-glutamine and supplemented with 50μg/ml penicillin-streptomycin, 1mM sodium pyruvate and 10% FBS.

SK-BR-3

A luminal breast cell line from the pleural effusion of a 43 year old female Caucasian with metastatic adenocarcinoma. Cells were cultured in McCoy's 5A modified medium supplemented with 50μg/ml penicillin-streptomycin and 10% FBS.

MCF-10A

A basal B primary epithelial breast cell line attained by reduction mammoplasty from a 36 year old female Caucasian with fibrocystic disease. Cells were cultured in DMEM/F12 containing L-glutamine and 15mM HEPES and supplemented with 0.5μg/ml hydrocortizone, 10 μg insulin, 100 μg/ml epidermal growth factor, 0.1 μg/ml cholera toxin, and 5% horse serum.

BxPC3

A primary epithelial pancreatic cell line derived from a 61 year old female with adenocarcinoma of the body of the pancreas. Cells were cultured in RPMI 1640 with L-glutamine and supplemented with 50μg/ml penicillin-streptomycin, 1mM sodium pyruvate and 10% FBS.

PANC-1

A primary epithelial pancreatic cell line derived from a 56 year old female with metastatic adenocarcinoma in the head of the pancreas which invaded the duodenal wall. Cells were cultured in DMEM high glucose (4.5g/L) medium with L-glutamine and supplemented with 50μg/ml penicillin-streptomycin, 1mM sodium pyruvate and 10% FBS.

A549

An epithelial lung cell line derived from a 58 year old male with alveolar carcinoma. Cells were cultured in F12/K with L-glutamine and supplemented with 50μg/ml penicillin-streptomycin, 1mM sodium pyruvate and 10% FBS.

NIH-3T3

A BALB/c mouse embryonic fibroblast cell line which was isolated and initiated in 1962. Cells were cultured in DMEM high glucose (4.5g/L) medium with L-glutamine and supplemented with 50μg/ml penicillin-streptomycin, 1mM sodium pyruvate and 10% FBS.

2.4.3 Passage of cell lines

All cells were cultured until approximately 80% confluent at which point they were passaged. Cells were not allowed to form a complete monolayer or dense colonies. Growth medium was removed from the cells and the monolayer washed once with PBS. A 1X solution of TrypLE™, a non-animal alternative to porcine trypsin, was added to cells (1.5 mL/75 cm^2 surface area) and detachment was induced by incubating the cells at 37 ˚C for approximately 5 minutes. To the detached cells, complete medium was added (4 mL/75cm^2) and a single cell suspension was achieved by gentle pipetting the medium up and down several times. The cell pellet was collected by centrifugation at 800g for 5 minutes, and cells were reseeded at a ratio of 1:4 to 1:10 depending upon the length of time needed before cells were used for experiments. A maximum passage number of 20 was used for all cell lines.

2.4.4 Cell counting using a haemocytometer

Cell concentration was determined by counting their number within a defined area of known volume. At least $1x10^6$ cells/mL were required for accurate counting. A haemocytometer was prepared by cleaning all surfaces with 70% ethanol, and a clean coverslip was placed onto the slide and was left undisturbed until Newton's rings were observed on the coverslip. A single-cell suspension was prepared and 10 µL of a 1:1 cell suspension to trypan blue was immediately introduced to the haemocytometer. Cells were counted in all four corners and the total number of cells obtained was divided by 2, to obtain the average per 16 squares and to account for the 1:2 dilution in trypan blue. The average cell count was multiplied by 10^4/mL to obtain the total cell count.

2.4.5 Cryopreservation of cell lines

Cells were cultivated in T75 flasks until they reached 80% confluence. They were detached from the plate using TrypLE and centrifuged at 800g for 5 minutes. The cell pellet was re-suspended in 6 mL of Cellbanker® 2 freezing medium (AMS Biotechnology, Abingdon, UK). Aliquots of 1mL, containing approximately $1x10^6$ cells, were dispensed into cryotubes (NUNC) and cells were immediately transferred to the -80˚C freezer. For long term storage, cells were transferred to a liquid nitrogen container. Frozen cell stocks were rapidly thawed by partially submerging cryotubes in a 37 °C water bath to re-establish cell lines. Once the suspension was thawed, cells were transferred to 9 mL of pre-warmed complete medium and pelleted by centrifuging at 800g for 5 minutes. The pellet was re-suspended in 15 mL of medium and plated into a T75 flask.

2.5 High throughput *in vitro* assays

Two main techniques have been employed in this work to study nanomaterials interaction with biological samples: (1) high content screening analysis, and (2) flow cytometry. High content image acquisition provides high quality images for qualitative analysis and high content analysis and flow cytometry provide quantitative data. An important consideration for adequate toxicity testing is the range of nanomaterials concentration selected. It has been shown that MNP have an acceptable safety profile below 100 µg/mL [422]. Above 100 µg/mL, cytotoxicity was induced in multiple cell lines [423]. Indeed, we have previously

shown that cytotoxicity is not induced at concentrations below 100 µg/mL using high quality nebulised MNP [332]. Therefore one concentration above and a series of concentrations below 100 µg/mL should provide a reasonable range by which to test the nanomaterials cytotoxic potential.

The following sections detail the methodology behind the generation of qualitative and quantitative data, firstly by high content screening analysis followed by flow cytometry.

2.5.1 Interaction of MNP and fluorescent dyes

The interaction between the MNP and fluorescent dyes used in HCSA were evaluated using a fluorescent spectrophotometer (Fluoroskan Ascent™ FL, Thermo Scientific™, USA). The stock MNP were diluted in serum-free and phenol-red-free medium to a concentration of 200 µg/mL in the presence of each fluorescent dye and incubated in the dark at 37 °C for 30 minutes prior to recording fluorescent intensity. The plates were scanned in the Fluoroskan spectrophotometer at the wavelengths appropriate for each dye (Table 2).

2.5.2 Multi-parametric high content screening analysis

The InCell 1000 high content screening system (GE Healthcare, UK) (Figure 17) is a fully automated multi-parameter imaging device using a range of microplates for both living and fixed cell analysis. Equipped with a xenon lamp, the InCell 1000 provides a flat field illumination from UV to infrared wavelengths and can accommodate the visualisation of a broad range of fluorophores, limited only by the excitation, emission and dichroic filters selected. The dichroic filter cube employed (61002bs) was specific for 4',6-diamidino-2-phenylindole (DAPI), fluorescein isothiocyanate (FITC) and texas red (TR) fluorophores, the excitation and emission wavelengths of which are shared with the fluorophores used in this study.

Cells were seeded in-96 well plates in a dropwise manner to facilitate uniform cell coverage at a density of 5 x 10^3 cells/well in a 100 µL volume. All seeded plates were returned to the humidified incubator for 24 h prior to MNP exposure. Basic MNP were tested using incremental doses (10, 25, 50, 100, 200 µg/mL) and delivered at 100 µL/well. Cells exposed to the functionalised MNP were exposed according to the desired concentration of drug required, and was dependent on the amount of drug functionalised on the MNP surface (method conducted and published by WP2 [424]).

Cells exposed to 1 µM CdSe quantum dots served as the positive (toxicity inducing) control (CTRL+) and untreated controls (CTRL-) were included in order to quantify possible cytotoxic response induced by each MNP. Data was acquired from three independent experiments using triplicate samples for each condition. Following exposure, cells were stained using the Cellomics® Cytotoxicity 2 HCSA reagent HitKit™ (Thermo Fisher Scientific, USA). HCSA was carried out using the InCell 1000 system (GE Healthcare, UK). Cytotoxicity was determined through multiparametric analysis using the InCell Investigator software (Version 1.6), as extensively published by the group (section 1.4.3.1).

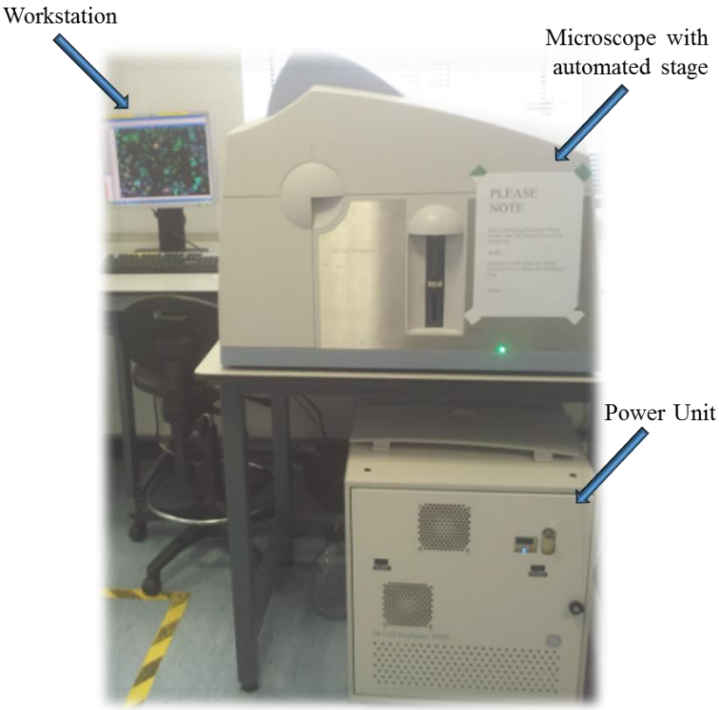

Figure 17: InCell 1000 system.

Image shows the various components of the HCSA InCell 1000 system, consisting of a workstation, microscope with an automated stage and a power unit.

2.5.2.1 Cell staining protocol

Cells seeded in 96-well plates were limited to the 60 inner wells with all border wells filled with DPBS to avoid the edge well effect. Following treatment of cells with MNP, medium was removed and cells were washed once with DPBS. Cells were stained according to the manufacturers recommended procedure whereby cells were washed twice with pre-warmed DBPS and complete medium containing lysosomal or mitochondrial dye (3.5 µL/mL) and cell membrane permeability dye (0.35 µL/mL) was added to each well and plates returned to the incubator for 30 minutes. A 3.7% solution of paraformaldehyde was prepared using DPBS and warmed to 37 °C for 30 minutes. Following incubation with dyes, cells were washed once with PBS and incubated at room temperature (RT) with 3.7% PFA solution for 20 minutes in the dark. Fixed cells were washed twice with PBS, stained with Hoechst 33342 (0.5 µL/mL) for 10 minutes after which they were washed a final time with PBS. Prior to sealing the plate, 200 µL of PBS was added to each well. Plates were kept at 4 °C and protected from light prior to image acquisition and analysis by HCSA.

2.5.2.2 Image acquisition and analysis

HCSA is a powerful platform for the acquisition of images. Simultaneous acquisition of up to three different fluorophores and bright field imaging provides a useful tool for multiple assessments such as the determination of MNP uptake. In addition, the use of post image analysis software such as the InCell Investigator 1.6 from GE Healthcare can provide substantial quantitative data for each fluorophore employed, and do so on a cell by cell basis. The following sections will detail the protocol for acquiring the qualitative data, followed by the generation of quantitative data.

2.5.2.2.1 Qualitative image acquisition protocol

Defining a protocol for the acquisition of qualitative images was dependent on the number of fluorophores to be measured, objective used, and the filters required. In this project, the protocol design included the definition of three fluorescent channels, bright field channel and merged pseudo-coloured image. Prior to the automated image acquisition, each plate was focused using the hardware autofocus feature, and image contrast was set for each channel using untreated cells as a baseline. Images were acquired from six defined fields per well using a 10x/0.45 Plan Apo dry objective. The HCSA acquisition protocol was set-up according to the peak excitation and emission parameters of each dye and the excitation and emission available on the device detailed in Table 2 and Table 3. Fluorescence spectra of each dye is provided in Appendix 4.

Table 2: Peak excitation and emission wavelengths of fluorescent dyes

Fluorescent probe	Peak Abs (nm)	Peak Em (nm)
Hoechst 33342	350	461
YO-PRO®-1	491	509
Lysotracker® Red	577	590
Mitotracker® Orange	554	576

Table 3: HCSA-optimised fluorophore excitation, emission and filter cube setup.

Fluorophore	Wavelength Designation	Excitation	Emission	Filter Cube
Hoechst 33342	Wave 1: Nucleus	360/40	460/40	D-F-TR
YO-PRO®-1	Wave 2: Cell	480/40	535/50	D-F-TR
Lysotracker® Red	Wave 3: Organelle	565/50	620/60	D-F-TR
Mitotracker® Orange	Wave 3: Organelle	535/50	600/50	D-F-TR

2.5.2.2.2 Quantitative image analysis protocol

Analysis of images stacks was conducted in batch analysis mode using the InCell Investigator V1.6 software by GE Healthcare (Buckinghamshire, United Kingdom) to generate quantitative data from all acquired images. Defining the multi-target analysis protocol required the classification of each wavelength used as outlined in Table 3 above. Segmentation of each parameter was defined (Figure 18). Nuclei were segmented using top-hat segmentation, enabling the accurate selection of closely positioned nuclei. Minimum nuclear size was determined through selection of the smallest nuclei using the arrow tool, which estimates the size based on local background intensity, and returns the measured object's area in square microns. Cell segmentation used the region growing method by which the boundaries of the cell were well defined. For this parameter, data was generated based on the intensity of dye which overlaid with the nuclear segmentation, and provided the positive readout for cytotoxicity. The segmentation of organelles defining the lysosomal or mitochondrial staining was by the multiscale top-hat method, whereby the detection of inclusions was confined to the cytoplasm. Data generated by the defined multi-target analysis included cell count, cell intensity, nuclear localised cell staining (average intensity of pixels within the nuclear region in

the cells channel) and organelle intensity. Results were exported as tab-delimited text providing an accessible means to organise data through Microsoft Excel. Graphing of data and statistical analysis was completed using GraphPad Prism 5.

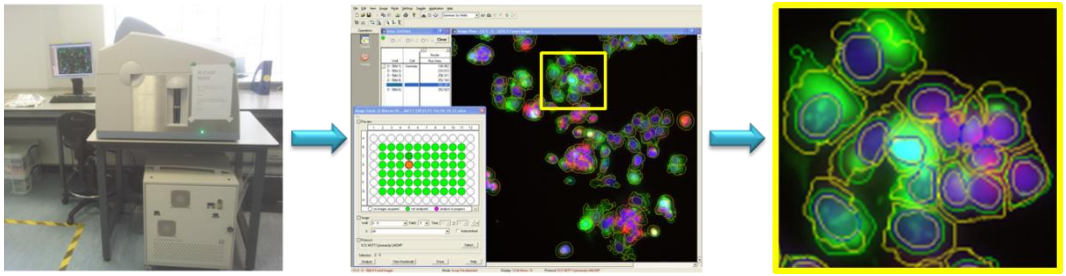

Figure 18: Data acquisition, parameter segmentation and analysis.

Images acquired by the InCell1000 system were segmented to enable identification and selection of nuclei shown in blue, cell membrane permeability dye shown in green and lysosomal organelles shown in red.

2.5.2.3 Cytotoxicity HitKit™ data interpretation

The cytotoxicity HitKit™ included four fluorescent dyes as detailed in Table 2. Hoechst 33342 enabled the quantification of total cells in each well whereby the reduction in the total number of cells compared to negative (untreated) control indicated cytotoxicity.

The membrane permeability dye (YO-PRO®-1) was used to determine whether the treatment with MNP could damage the integrity of the cell membrane and induce apoptosis. As the dye can leak into the cytoplasm in healthy cells, the presence of the dye within the nucleus was selected as a positive indicator for cytotoxicity.

The lysosomal dye (Lysotracker®) stained acidic organelles, with an intensity directly correlated to the internal pH, and to the total number of lysosomes present in the cell. An increase in this parameter compared to untreated control levels was a good indicator for MNP uptake and localisation within the lysosome. A decrease in intensity below untreated control levels was indicative of lysosome damage.

The mitochondrial dye (Mitotracker®) stained healthy mitochondria with an intact membrane potential. A decrease in the fluorescence intensity was directly correlated with mitochondrial membrane damage and a loss of membrane potential, and constituted an early marker for the onset of apoptosis.

2.5.3 Flow cytometry

Flow cytometry is a laser-based technology that analyses cells suspended in a stream of fluid. Cells fluorescently stained with specific markers are detected based on their excitation and emission spectra and quantitative data can be obtained regarding the marker employed. It is a complementary high-throughput cell-screening technique and when used alongside HCSA it can provide additional information on cell cycle status and the method of cell death following exposure to nanomaterials. Flow cytometry has the ability to screen thousands of cells in seconds and some common fluorescent dyes employed in flow cytometry for cell cycle and apoptosis/necrosis screening include propidium iodide (PI), 7-aminoactinomycin D (7AAD) and Annexin V. PI is a DNA intercalating fluorescent dye that is excited at 488 nm using an argon-ion

laser. It is used to measure the total DNA content in the cell population to determine changes in the cell cycle. Unlike Hoechst 33342, PI intercalates with DNA with little or no sequence preference. As PI also binds to RNA, the treatment of samples with RNase A is vital. The second flow cytometry assay that can be used to determine apoptosis and necrosis onset is the FITC Annexin V Apoptosis Detection Kit with 7-AAD contained both 7-AAD and FITC conjugated Annexin V. 7-AAD intercalates dsDNA with high affinity to Guanine-Cytosine (G-C) rich regions. FITC conjugated Annexin V enables identification of exposed phosphatidyl-serine on the inner cell membrane when membrane integrity is compromised.

Flow cytometry provided quantitative data and facilitated the identification of changes to the cell cycle of MNP exposed cells and the mechanism of cell death upon exposure to the basic and functionalised MNP. The BD Accuri C6 flow cytometer equipped with a 488 nm laser (Becton Dickinson, Belgium) was used to carry out this work. Details of the fluorophores used are in Table 4, and fluorescence spectra for each fluorophore are in Appendix 4.

Table 4: Peak excitation and emission wavelengths of suitable flow cytometry dyes

Fluorescent probe	Peak Abs (nm)	Peak Em (nm)
Propidium Iodide	536	617
7-AAD	546	647
Annexin V-FITC	490	525

2.5.3.1 Cell cycle determination

Cell cycle testing was carried out according to the manufacturer's instructions using the CycleTEST™ PLUS DNA Reagent kit (Becton Dickinson, Belgium). Cell pellets were washed using buffer solution (DMSO in sucrose-sodium citrate), re-suspended in 125 µL of trypsin in spermine tetrahydrochloride detergent buffer and incubated for 10 minutes at RT. 100 µL of RNase A and trypsin inhibitor in spermine buffer was added for 10 minutes and 100 µL of ice cold propidium iodide in spermine buffer was added in the dark and left at 4°C for a further 10 minutes. 10,000 fluorescent events were recorded for each sample. Untreated samples (negative controls) were gated to select G_0/G_1, S and G_2/M phases and all treated samples were compared within the defined gated regions.

2.5.3.2 Apoptosis assay using 7-AAD and annexin 5

Cells were washed twice using cold cell staining buffer, and re-suspended in Annexin V binding buffer at a concentration of 2.5 x 10^6 cells/mL. Centrifugation at each step was done at 800g for 5 minutes. A 100 µL volume of cell suspension was added to a 5 mL test tube into which 5 µL of FITC Annexin V and 5 µL of 7-AAD viability staining solution were added. Cells were vortexed briefly and left to incubate for 15 minutes at RT in the dark. A 400 µL volume of Annexin V binding buffer was added to each tube and the suspension analysed by flow cytometry with a maximum 10,000 events recorded.

2.6 Generation of heatmaps

Heatmaps can be generated using many bioinformatics computer programes, the software used in this work was Spotfire® (Build version: 7.0.0.53) by TIBCO® (Boston, MA, USA) to enable easy visualisation of the multiparametric quantitative data. Each individual experiment was normalised to the matched untreated control with the average of the n=3 independent experiments being used to generate the heatmaps. The heatmap colour scheme is provided in Figure 19. Variation in parameters is presented using up to six colours. For both cell count and membrane permeability, a shift in colour from green towards red indicates a cytotoxic response. For lysosomal mass/pH staining, an extra level is added to the heatmaps (0.85 - yellow) due to the dual readout potential of this dye. A decrease in lysosomal staining can indicate either lysosomal membrane damage, increase in intra-vesicle pH or decrease in lysosomal mass. An increase in the staining intensity of lysosomes, as presented in this study, can indicate cytotoxicity and/or an increase in MNP uptake which is possibly due to an increase in the number of lysosomes (lysosomal mass increase) or acidification of the lysosomal vesicles.

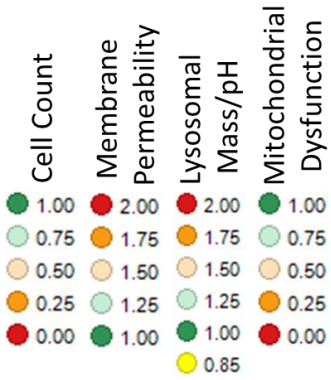

Figure 19: Heatmap colour gradient.

The selected gradients were used in the construction of heatmaps. Untreated control samples (CTRL(-)) in all heatmaps are normalised to 1.00 and coloured green, variation from 1.00 in 25% increments is presented as a change in colour as indicated above.

2.7 *In vitro* uptake analysis

The uptake and localisation of MNP was determined by lysotracker staining (section 2.5.2.1), Perls' Prussian blue staining, and high resolution transmission electron microscopy. TEM was conducted by Dr Michele Chiappi (CSIC, CNB, Spain) according to his published protocol [314].

2.7.1 Perls' Prussian blue assay

Cells were grown on 8 well BD Falcon™ culture slides at a concentration of $1x10^5$ cells/well for 24h. Exposure of cells to MNP formulations using a concentration of 100 µg/mL was conducted for 24h. Cells were washed twice with DPBS and fixed for 5 minutes with cold methanol. The chamber was removed and slides allowed to air dry. Equal parts of 4% hydrochloric acid and 4% potassium ferrocyanide were prepared immediately prior to use and slides were immersed in this solution for 15 minutes. Following incubation,

the slides were rinsed three times using distilled water and counterstained with 0.5% neutral red for 2 minutes. Slides were rinsed a further two times with distilled water and allowed to air dry. Three drops of DEPX mounting medium was applied to slides and a coverslip was mounted. Slides were left to dry for 24h prior to image acquisition.

2.8 *In vitro* genotoxicity analysis

To determine whether MNP induce DNA damage, the formation of micronuclei and analysis of DNA fragmentation was carried out. The cytokinesis block micronucleus assay, an established OECD guideline test for screening drugs (test 487), was employed to determine whether the developed MNP could induce the formation of micronuclei.

2.8.1 Cytokinesis block micronucleus assay

The cytokinesis blocking agent, cytochalasin B, was tested to select a concentration that was least cytotoxic while remaining within the recommended range of 1 – 6 µg/mL. Cells were plated in 24-well plates at a concentration of $4x10^4$ cells/well and left undisturbed for 24h. Cells were exposed to MNP for 24h after which the medium was removed and cells washed twice with DPBS. Pre-warmed medium containing 1 µg/mL cytochalasin B was added and cells were left undisturbed for a further 24h. Visualisation at 20x using a light microscope facilitated the identification of bi-nuclear cells and when the majority of cells were bi-nuclear, the experiment was stopped. Cells were washed twice with DPBS, and a cell suspension was prepared using TrypLE Select, as described previously. Cells were centrifuged at 800g for 5 minutes and cell pellets re-suspended in 200 µL of DPBS. Cytospins were prepared by spinning 70 µL of sample onto slides at 800g for 5 minutes using a Shandon cytospin 3 centrifuge (Thermo Scientific, Ireland) (Figure 20). Slides were removed from the cassettes and air dried for strictly 10 minutes and then fixed for 15 minutes in methanol. All slides were stained individually for 14 seconds in Eosin staining solution and 4 seconds in methylene blue staining solution. Removal of residual dye by blotting the edge of the slides onto tissue paper was done between stains. Rinsing of slides following methylene blue staining was done for 10 seconds using distilled water. Slides were allowed to air dry for 30 minutes and coverslips were applied using DPX medium. Imaging was completed 24h post mounting using the Nikon E800W microscope with 20x objective. Images were acquired using the micropublisher 3.3RTV colour camera (photometrics, UK).

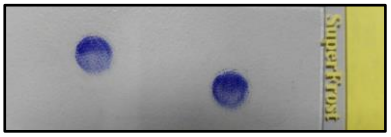

Figure 20: Cells cytospun onto glass microscope slide and stained by Kwik Diff™ kit.

Cytospinning cells onto the surface of a glass microscope slide provides flexibility in adjusting cell density for optimal visualisation by microscopy.

2.9 *In vivo* biodistribution: magnetic resonance imaging

2.9.1 Ethical conduct

The protocols employed for the *in vivo* study were approved by the Animal Research Ethics Committee, Trinity College Dublin and the Department of Health and Children (Ireland), in accordance with European Community Directive (86/609). The *in vivo* work was carried out with the licence holder, Dr Oliviero Gobbo (Trinity Institute of Neuroscience, Trinity College Dublin). The use of animals was strictly limited to the testing of MNP approved by WP3. Pathogen free BALB/c mice (23 ± 2g) were sourced from Harlan Laboratories, UK and male Wistar rats (283 ± 27g) were supplied by TCD BioResources unit. Animals were housed in a thermo-regulated environment with a 12h light/dark cycle. Food and water were available ad libitum.

2.9.2 Experimental procedure

2.9.2.1 Magnetic resonance imaging

BALB/c mice were anesthetized using 5% isoflurane and maintained with 1.5% isoflurane, respiration rate and temperature were continuously monitored during the imaging period in a 7T MRI Bruker system (Bruker, Germany). To acquire reference scans, all mice were imaged before and after MNP administration (100 µl of 3.3 mg Fe/ml MNP or saline control). T2-weighted images were acquired and MNP organ accumulation was observed 4h post injection.

2.9.2.2 Particle electron paramagnetic resonance

The particle Electron Paramagnetic Resonance (pEPR) technique was developed and conducted by Pepric NV (Leuven Belgium) using their particle spectrometer instrument as part of Multifun WP4. This instrument selectively detects and enables quantification of MNP in biological samples by measuring the MNP electron spin resonance in an applied magnetic field. A 10 millitesla magnetic field enables the alignment of the MNP magnetic moments while a low radio frequency (300 MHz) induces resonant tilting of the magnetic spin. This allows for total MNP quantification via the detection of induced radio frequency signal proportional to the number of MNP present as detailed in Gobbo et al. [425].

2.9.2.2.1 MNP quantification in organ biopsies

Following MRI, animals were euthanized using 100 mg/kg sodium pentobarbital i.p., and organs were harvested. Liver, spleen, lung, heart, kidney and brain were sectioned, weighed, transferred to 150 µl PCR tubes, and analysed by pEPR without further sample preparation.

2.9.2.2.2 MNP pharmacokinetic evaluation in whole rat blood

The evaluation of MNP blood circulation time was conducted by Dr Oliviero Gobbo (Trinity Institute of Neuroscience, Trinity College Dublin) using Wistar rats. Cannulation of the left femoral artery using heparinised polyurethane tubing allowed for blood sampling (200 µL) at defined time points of 3, 10, 20, 30, 60, 90 and 120 minutes following tail vein injection of 1 mL of 3.3 mg/mL MF66 MNP. Blood was replaced at each time point with an equal volume of isotonic solution. Samples were analysed by pEPR and blood half-life calculated as detailed in Gobbo et al. [425].

2.10 Statistical analysis

Data is representative of at least three experimental replicates and are expressed as the means ± SEM. Data acquired by high content screening was outputted as tab-delimited text which, when transferred to Microsoft Excel, provided a basis for data sorting and averaging of each experimental triplicate. The averaged values from three individual experiments were compared for statistical significance using Graphpad Prism 5 software. Where two distinct data sets were compared (eg.: untreated control versus valinomycin) the two-tail unpaired student's t-test was used. For comparison of variance within a matched dataset where a concentration gradient was being analysed the statistical significance was determined using 1 way ANOVA with Tukey post-test. In all cases $P < 0.05$ was significant and indicated: <0.05 = *; <0.01 = ** and <0.001 = ***.

2.11 Thesis contribution

Name	WP	University	Figures
Gorka Salas	1	IMDEA	Figure 21 & 22
Macarena Calero	3	IMDEA	Figure 32 Figure 34A (slide preparation)
Michele Chiappi	3	IMDEA	Figure 33 & 35
Oliviero Gobbo	4	TCD	Figure 36 & 37
Pierre Couleaud/ Alfonso Latorre	2	IMDEA	Figure 41 & 42
Sara Trabulo	3	QMUL	Figures 59 – 62
Kieran Crosbie-Staunton	3 & 4	TCD	Figure 21: figure design Figure 22: graphing of data Figures 23 – 31: own data Figure 34A: microscopy and figure design Figure 34B: analysis & graphing of data Figure 36 A&B: contribution to work Figure 37: graphing of data Figures 38 – 40, 43 – 58, 63 – 87: own data

Results

Chapter 3: Selection of biocompatible MNP formulations.

Chapter 4: Multifunctional MNP for targeted cancer treatment.

Chapter 5: Subcellular mechanisms of MNP-induced anticancer effects.

Chapter 3: Selection of biocompatible MNP formulations.

3.1 Introduction

Advances in nanotechnology have facilitated the manufacture of engineered nanomaterials for use in a broad range of applications. In the field of nanomedicine, one goal is to produce nanomaterials that will enable rapid and accurate diagnosis, while effectively treating the patient without the associated side effects. Nanomaterials present a multifaceted platform by which non-invasive diagnosis and in-situ treatment can potentially be carried out. There are endless possibilities for the use of MNP in medical applications with nanoparticles below 30 nm in core size displaying superparamagnetic properties that can be exploited for use as hyperthermia agents in MRI. There are a number of MNP used as MRI contrast agents in the clinic such as Endorem (120 – 180 nm), and Resovist (60 nm). However, these products are limited in their use and only serve to detect focal liver lesions such as metastases, primary liver cancer, cysts and various benign tumours, adenomas and hyperplasia. Current advancements have enabled surface modification of nanoparticles to facilitate the attachment of a broad range of drugs and targeting compounds for use as an additional mode of treatment. However, the gains made in the field of nanomedicine present unique challenges. The rate of production of nanomaterials has now exceeded the rate at which they are being tested to effectively establish safety standards and understanding of the effects of exposure on personnel, the public and environment in a timely manner. During the development of a nanoparticle based theranostic product, it is essential that repeated batch to batch testing is conducted to ensure the toxicity status of the nanoparticle does not change.

To date, no consensus within the nanomedicine field or within governmental bodies tasked with the regulation of nanomaterials has been reached on the most appropriate method for testing nanomaterials. There exist reports providing evidence that the most widely accepted assays to determine cytotoxicity suffer from interference by the nanoparticles being tested. Therefore it is vital that a reliable testing method for the evaluation of potential toxicity is established. In 2009, Kroll et al. presented a detailed review of nanoparticle interference using a number of common assays [321]. Interference was shown to occur in the MTT, LDH, neutral red, caspase, ROS production and cytokine assays. These findings have been further validated in a more recent study by Guadagnini et al. where it was demonstrated that MNP interfered with the nuclear red assay through the increase of optical density readings due to the potential liberation of nanoparticles previously localised inside cells prior to testing. In addition, the testing of MNP toxicity using the MTT assay was shown to result in an increase in the optical density readings, and therefore skewing results to appear non-cytotoxic at cytotoxic concentrations. Interference was also observed in WST-1 assays whereby MNP present in supernatants led to the underestimation of their cytotoxicity. Unlike the work and findings presented by Kroll et al., Guadagnini et al. demonstrated that extensive washes and removal of residual MNP in solution prior to assessment resulted in more accurate cytotoxicity data measurements [323].

The aim of this part of the study was to investigate the effect of a range of MNP on breast-derived cell lines and to further understand their interaction *in vitro* and *in vivo* towards the selection of a biocompatible formulation.

To achieve this aim, the specific objectives were:

1. Investigation of the physicochemical properties of MNP by TEM and DLS.
2. Detection of MNP hydrodynamic diameter changes following incubation in complete medium by NTA.
3. Determine cytotoxic potential of MNP using validated HCSA assay.
4. Localisation, quantification and mechanism of MNP uptake.
5. Examination of MNP biodistribution using a small animal model by MRI.

3.2 Results

3.2.1 Comparative analysis of basic nanomaterials by TEM, DLS and NTA.

The qualitative assessment and quantitative analysis of all MNP was an essential step in the selection of suitable formulations to bring forward in the study and was dependent on the size range and sample uniformity of the produced MNP. To conduct this analysis the gold standard approaches of TEM, DLS and NTA were selected. TEM and DLS analysis was carried out by Dr Gorka Salas (IMDEA, Nanosciencia, Madrid) to identify core nanoparticle features such as global sample size and shape within the nanoparticle population and hydrodynamic diameter measurement of each MNP formulation in aqueous solution.

TEM images of MNP samples are shown in Figure 21 and demonstrate a uniform size distribution in five of the seven MNP samples. PAA and F1566 samples displayed unequal and unsatisfactory size profiles. The DMSA coated OD10, OD15 and MF66 MNP show the greatest uniformity, with the MNP produced by thermal decomposition (OD10 and OD15) having a highly uniform cuboid structure while the MNP (MF66), produced by co-precipitation in water, lacked the uniformity of spherical shape.

The DLS hydrodynamic size profile shown in Figure 22 represents MNP dispersed in water. Of the seven MNP tested, five had a mean hydrodynamic size less than 60 nm (ASi, OD10, PAA, F1566, OD15), one sample was below 85 nm (MF66) while the ADNH MNP sample had the largest hydrodynamic size of 142 nm. Data is presented in Table 5.

Nanoparticles dispersed in water generally have their hydrodynamic diameter determined by DLS as presented above. We have confirmed the DLS measurements through the use of a newly accepted gold standard approach called NTA [252]. This technique provided quantitative hydrodynamic size data of the MNP in aqueous solution on a particle by particle basis. In addition, the analysis of MNP following incubation in serum containing medium was conducted. NTA results are provided in Figure 23, with complete PCC mean size data provided in Table 5.

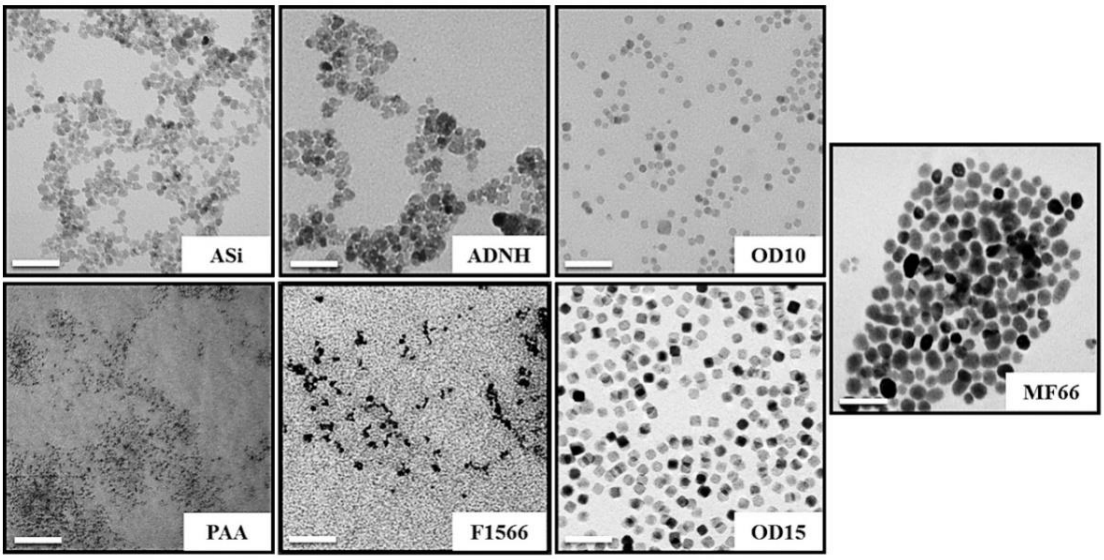

Figure 21: TEM analysis of nanoparticle core size and surface.

Uniformity in size and shape was evident for ASi, ADNH, OD10, OD15 and MF66 MNP. Scale bar = 50 nm. TEM imaging was carried out by Dr Gorka Salas, IMDEA Nanociencia, Madrid.

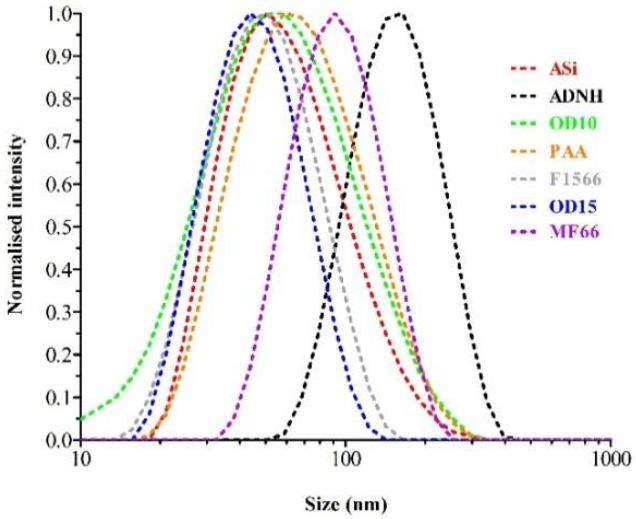

Figure 22: Nanoparticle hydrodynamic size characterisation by DLS.

Hydrodynamic diameter was evaluated by dynamic light scattering and intensity vs. size is represented. The values of Dhyd expressed as Z-average size are presented in Table 5. DLS was conducted by Dr Gorka Salas and data was graphed by author.

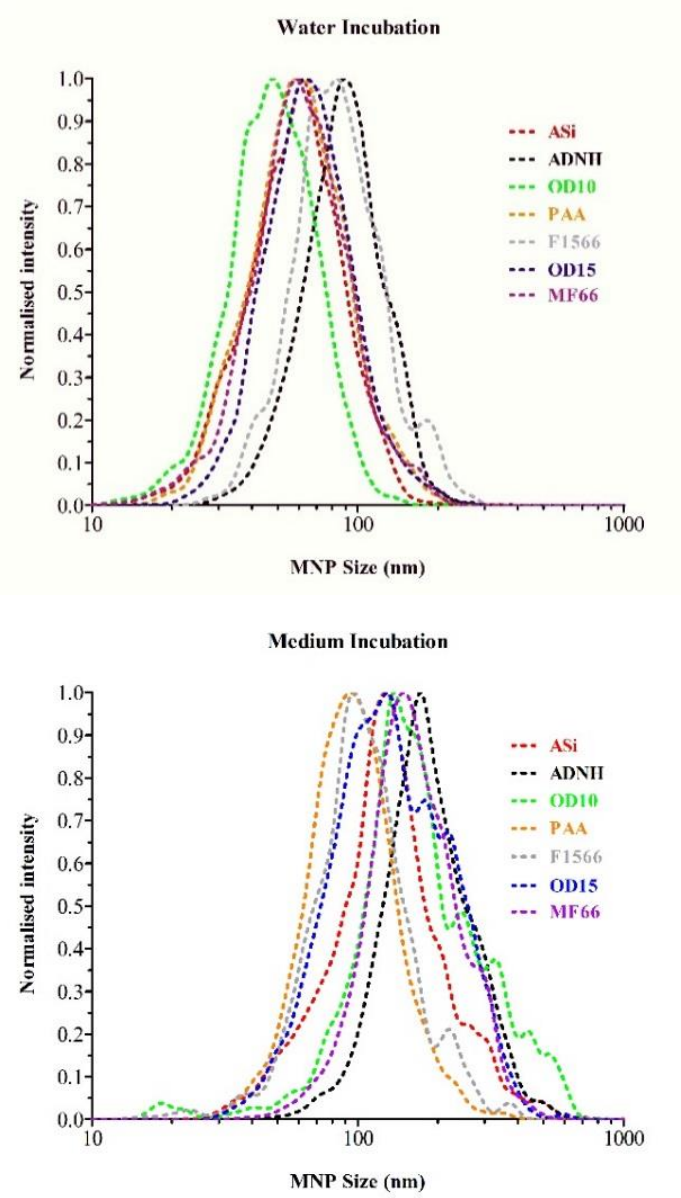

Figure 23: Effect of FBS on the hydrodynamic diameter of basic MNP.

MNP incubated with 0.1 µm filtered water (top graph) or complete medium (bottom graph) containing 10% FBS were analysed by NTA to evaluate changes to hydrodynamic diameter.

Five of the seven MNP tested in DI water were less than 100 nm, with ADNH and F1566 having sizes of 105 nm and 108 nm respectively (Table 5). Following incubation in FBS containing medium, a two- to four-fold increase in hydrodynamic size was observed for five of the seven MNP. The hydrodynamic sizes of each MNP increased by: ASi (117 nm), ADNH (123 nm), OD10 (200 nm), PAA (46 nm), F1566 (27 nm), OD15 (105 nm) and MF66 (123 nm)

Table 5: Analysis of nanomaterials characterisation determined by TEM, DLS and NTA.

Physicochemical characterisation of MNP was carried out on: (1) MNP core size determination by TEM confirmed MNP sizes between 5 nm and 14 nm with low polydispersity index (PDI). (2) Mean hydrodynamic size was determined by DLS and confirmed by NTA. DI water incubation and post-incubation with DMEM serum containing cell culture medium (DI Water & Post-Med) with MNP enabled comprehensive understanding of changes to hydrodynamic diameter following 24h exposure.

	Synthesis method	pH	TEM nm/(PDI) (PDI=σ/d_{TEM})	DLS Z-average nm/(PDI)	NTA DI Water (nm/SD)	NTA Post-Med (nm/SD)	Core/ stabilizers	Zeta Potential pH 7 (mV)
ASi	Co-precipitation + acid treatment + coated with APS	7	8.5 (0.23)	59 (0.25)	74 ± 33	191 ± 106	γ-Fe_2O_3/ ASi	+35
ADNH	Co-precipitation in the presence of aminodextran	7	6,5 (0.26)	142 (0.20)	105 ± 35	228 ± 89	γ-Fe_2O_3/ Aminodextran	+35
OD10	Thermal decomposition in organic media	7	10 (0.15)	47 (0.20)	59 ± 22	259 ± 135	Fe_3O_4/ DMSA	-40
PAA	Co-precipitation in the presence of PAA	7	5 (0.20)	59 (0.25)	80 ± 37	126 ± 70	γ-Fe_2O_3/ PAA	-44
F1566	Co-precipitation in the presence of dextran	6.8	8.5 (0.29)	44 (0.20)	108 ± 46	135 ± 60	γ-Fe_2O_3/ Dextran	-6.5
OD15	Thermal decomposition in organic media	7.4	14.0 (0.09)	42 (0.14)	84 ± 37	189 ± 88	Fe_3O_4/ DMSA	-40
MF66	Co-precipitation + recrystallization, + coated with oleic acid & DMSA	7.3	11.6 (0.16)	85 (0.12)	79 ± 34	202 ± 78	γ-Fe_2O_3/ DMSA	-38

3.2.2 Cellomics® cytotoxicity 2 HitKit™.

Colorimetric assay interference by MNP is a well-documented issue that prohibits the use of standard assays to evaluate MNP cytotoxicity and there exists a need for an alternative approach [321-323]. Fluorometric multiplexed assays are an attractive alternative to the single output offered by colorimetric assays, however, fluorescent quenching can occur in the presence of MNP. Therefore we sought to identify any fluorescence quenching that may occur with the iron oxide MNP employed in this study.

The dye kit used was commercially sourced and certified to contain optimised dye reagents. Possible interference of fluorescent signal between MNP and key dye reagents (Hoechst 33342, membrane permeability dye (YO-PRO®-1 Iodide), LysoTracker® and MitoTracker® in the commercial kit was investigated (Figure 24). The experiment was conducted in the presence of dye reagent in serum free medium and at the concentration of nanoparticles indicated. No interference with fluorescent intensity compared to a medium containing dye control was observed.

We next sought to determine whether the dye reagents would provide a positive result when known cytotoxic agents were used on all cell lines. Both tacrine and valinomycin were employed to address this question and results are provided in Figure 25. The use of tacrine and valinomycin as positive controls to test the commercial dyes was carried out in the MCF-7, BT-474, MDA-MB-231, SK-BR-3 and MCF-10A cell lines. It was determined by the manufacturer of the dye kit that a concentration of 120 µM valinomycin and 100 µM tacrine should be employed to validate the activity of the membrane permeability dye (permeability increases in the presence of 120 µM valinomycin) and lysosomal Mass/pH dye (increases in the presence of 100 µM tacrine).

Cells were exposed to valinomycin (120 µM) and to tacrine (100 µM) for 24 h. Cell count was measured for each cell line and for both valinomycin and tacrine there was a pronounced reduction in cell count. MCF-10A cells were least affected by valinomycin with no observed reduction in cell count. However, in all cell lines there was an increase in the cell membrane permeability parameter, compared to untreated controls following treatment with valinomycin. In addition, there was a marked increase in the lysosomal Mass/pH parameter upon treatment with tacrine (Figure 25).

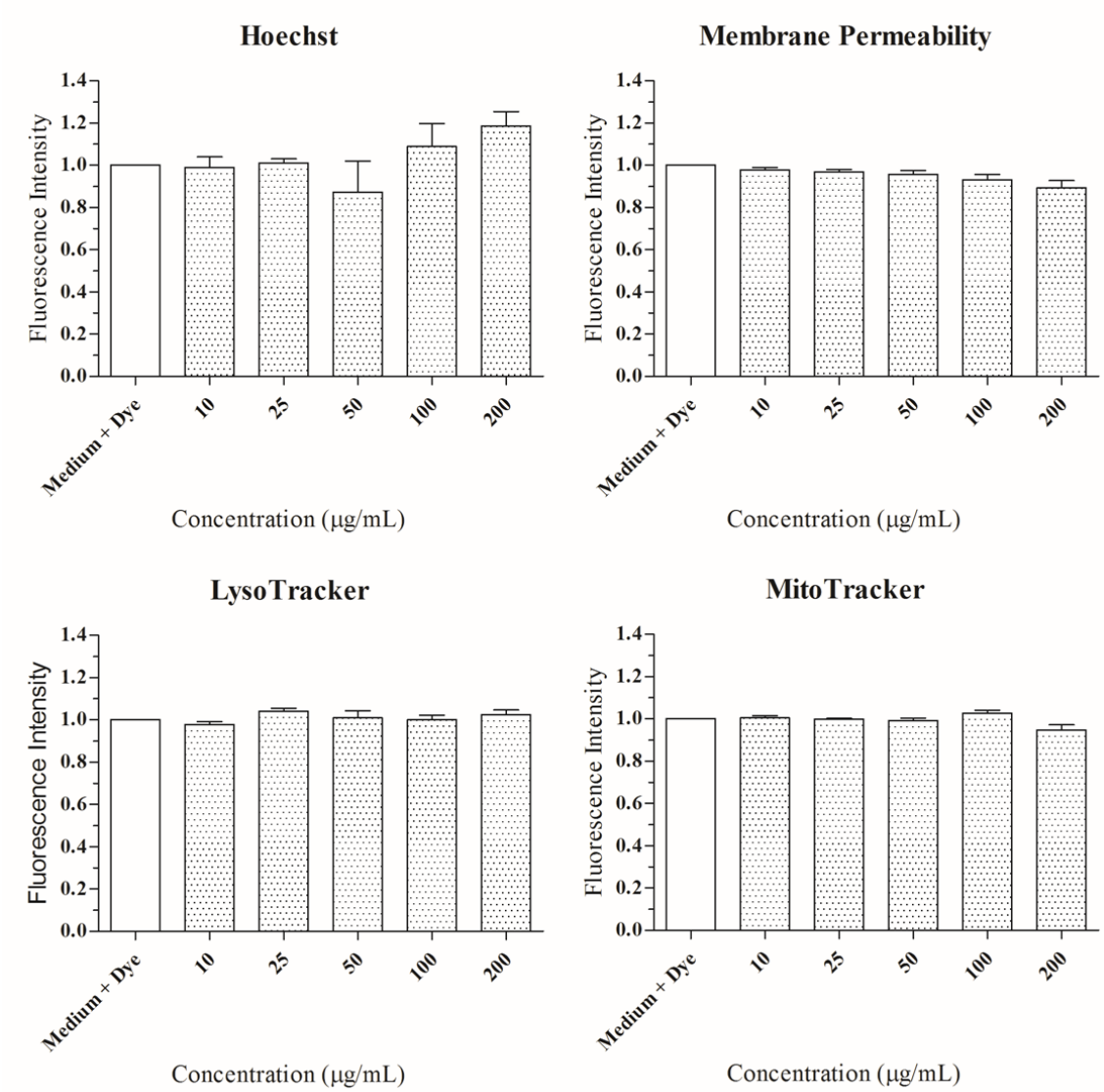

Figure 24: Investigating MNP – dye interference using fluorescent spectrometry.

Nanoparticles were diluted in serum-free medium and fluorescence intensity measured at 30 minutes using a fluorescent spectrophotometer (Fluoroskan Ascent™ FL, Thermo Scientific™, USA). Hoechst, cell permeability dye, LysoTracker®, and MitoTracker® were recorded. No reduction in fluorescent intensity was recorded for any dye throughout the concentration range tested.

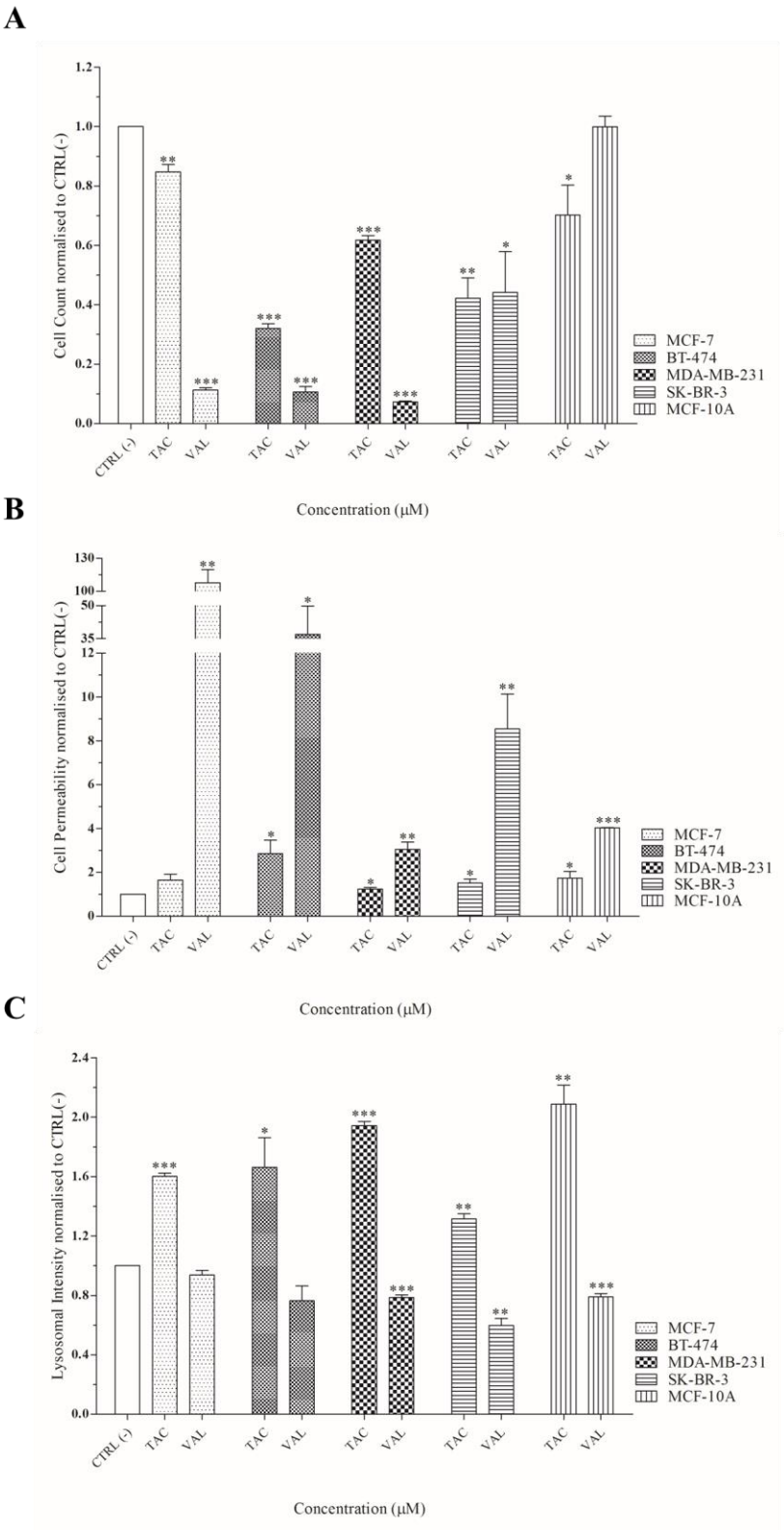

Figure 25: Evaluation of cytotoxicity-indicator dyes using tacrine and valinomycin positive controls.

Breast-derived cell lines treated with 100 µM tacrine (TAC) or 120 µM valinomycin (VAL) for 24 h (A) Cell count; (B) Cell permeability; and (C) Lysosomal intensity were measured. Statistical significance was determined using the unpaired two-tailed t-test for each column compared to untreated control (CTRL(-)). p value: *** = <0.001, **=<0.01, *=<0.05.

3.2.3 Effect of MNP exposure on viability of cell lines

High content screening analysis is a powerful microscopy and software based automated platform for the acquisition and analysis of multiplex experiments. Following on from the previous experiments where the HCSA dye kit functionality was established, we next investigated the cytotoxic potential of the manufactured MNP using four breast cancer cell lines and a normal-like cell line. Heatmap representation of results is provided (Figure 26) and corresponding graphs with statistical analysis can be found in Appendix 1. Cell lines were exposed for 24h to the initial batch of five MNP (ASi, ADNH, OD10, PAA and F1566) (Figure 26). The BT-474 cell line was the most sensitive following exposure to each MNP with a marked reduction in cell count recorded for all but one MNP (PAA). The membrane permeability parameter was increased with all MNP and the lysosomal mass/pH decrease was observed for PAA and F1566. The MDA-MB-231 cell line closely resembled the BT-474 cell line with reduction at the highest dose of 200 µg/mL for all but one MNP (ASi). An increase in membrane permeability parameter was observed with ADNH and F1566 exposure only. The three remaining cell lines (MCF-7, SK-BR-3 and MCF-10A) displayed no statistically significant reduction in cell count. Membrane permeability in both the MCF-7 and SK-BR-3 cell lines showed an increase upon exposure to ASi, ADNH, OD10 and F1566 MNP, however statistical significance was only present in the SK-BR-3 cell line for both ASi and ADNH. Lysosomal intensity was increased in the MCF-7 cell for the highest concentration of ADNH only, in the BT-474 cell line for ASi, ADNH, OD10, and PAA, in the MDA-MB-231 for all MNP tested, in the SK-BR-3 cell line for PAA only and in the MCF10A cell line for ASi MNP only. No significant reduction in lysosomal intensity was observed in any cell lines.

Following the above cytotoxicity testing, two further MNP were synthesised. Both OD15 and MF66 MNP were tested in the five breast-derived cell lines (Figure 27 and Appendix 1). Cell-line exposure to OD15 did not result in any reduction in cell count. No significant increase in cell permeability was observed in any cell line but a marginal increase in lysosomal intensity was observed in all carcinoma cell lines. In contrast, the MF66 MNP caused statistically significant cell count reduction in the MCF-7 cell line (200 µg/mL only), MDA-MB-231 (50 µg/mL to 200 µg/mL), and MCF-10A (200 µg/mL only). Cell permeability was increased in only the MDA-MB-231 (100 – 200 µg/mL). As with OD15, MF66 caused an increase in the lysosomal intensity parameter in all carcinoma cell lines. Representative images are provided in Figure 28.

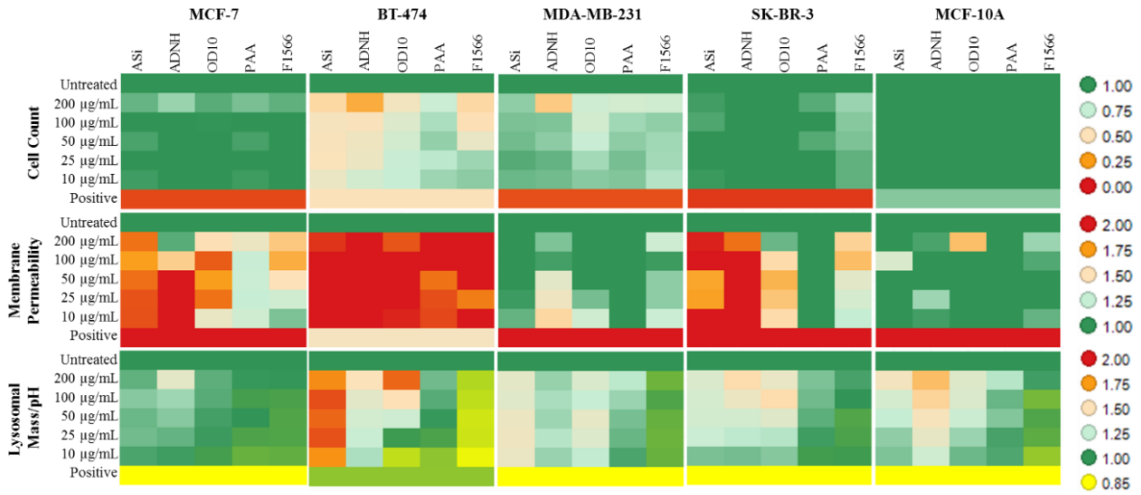

Figure 26: Multiparametric analysis in breast-derived cell lines exposed to basic MNP.

Three parameters were used to determine cytotoxic potential of each MNP in four breast cancer cell lines and a normal-like breast-derived cell line: cell count, cell membrane permeability and lysosomal mass/pH. Colorimetric gradient ranges are provided, and are unique for each parameter. Cytotoxicity with MNP exposure was identified by reduction in cell count, increase in membrane permeability and decrease in lysosomal Mass/pH. MNP uptake into cells was measured by the increase in lysosomal Mass/pH parameter. Values were normalized to untreated control and each unit represents the mean value of at least three experimental replicates. Positive control = 1µM CdSe QD.

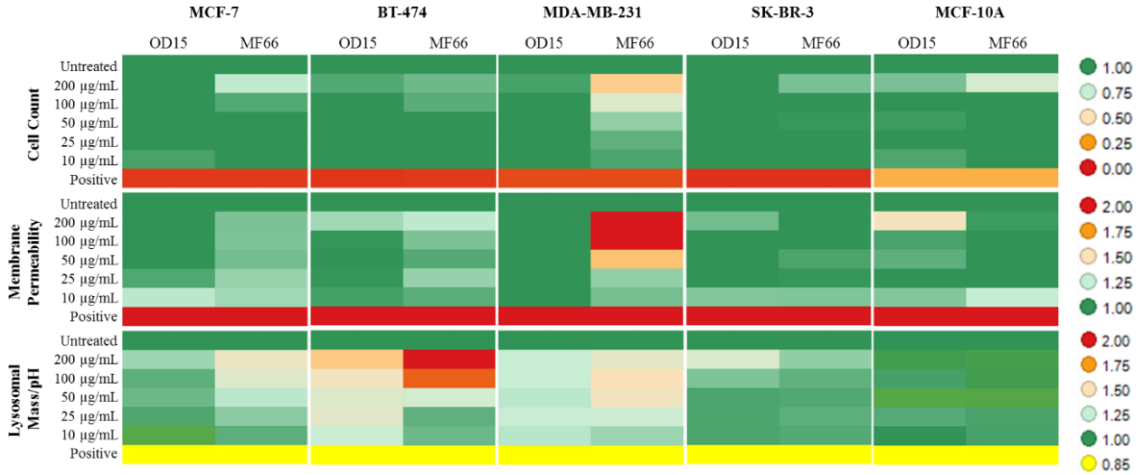

Figure 27: Multiparametric analysis in breast-derived cell lines exposed to OD15 and MF66.

Three parameters were used to determine cytotoxic potential of each MNP in four breast cancer cell lines and a normal-like breast-derived cell line: cell count reduction, cell membrane permeability and lysosomal mass/pH. Colorimetric gradient ranges are provided, and are unique for each parameter. OD15 MNP did not induce acute cytotoxicity in the majority of cell lines tested, MF66 MNP was determined to be suitable at concentrations below 100 µg/mL. Values were normalized to untreated control and each unit represents the mean value of at least three experimental replicates. Positive control = 1µM CdSe QD.

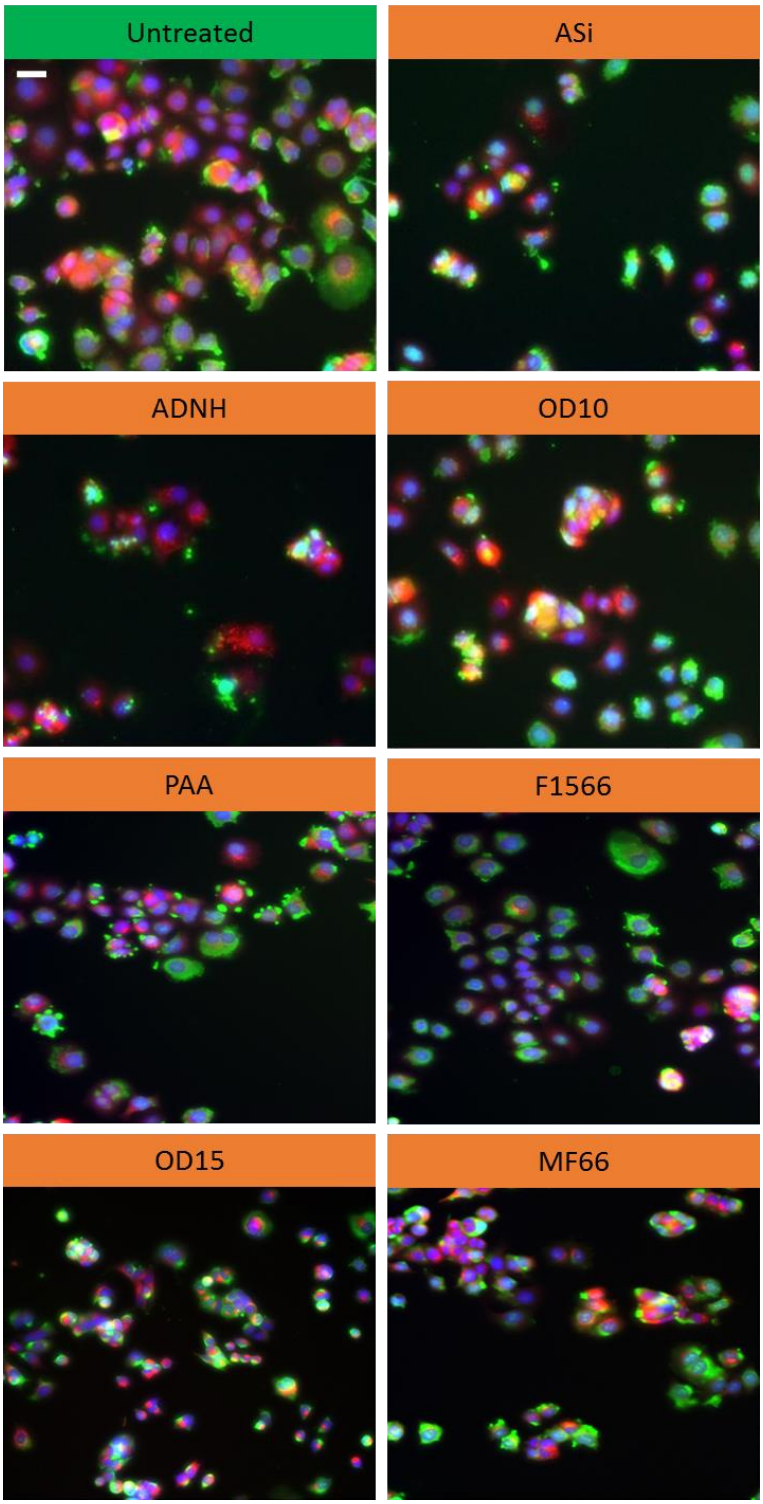

Figure 28: MCF-7 cell line exposed to basic MNP formulations.

Representative images of the MCF-7 cell line exposed to basic MNP for 24h. Cells were stained with Hoechst 33342 (Blue), YO-PRO®-1 iodide: cell membrane permeability (Green) and Lysotracker® (Red). Images acquired by HCSA at 10x magnification. Scale bar (white line, top left of "Untreated" panel) = 50 µm, applicable to all images.

3.2.4 Evaluation of MF66 MNP effect on cell cycle by flow cytometry

OD15 MNP did not induce any measurable acute cytotoxic effect following exposure in the breast-derived cell lines detailed previously. However, MF66 MNP did induce an acute cytotoxic effect which was especially pronounced at the highest concentration of 200 µg/mL. The MF66 MNP was available in industrial quantities from the Multifun WP2 partner Liquids Research (Bangor, Wales). To further test the suitability of this MNP we carried out flow cytometry on MNP exposed cells to determine if incubation at 72h could have a negative influence on normal cell cycle progression (Figure 29). The results show that a slight reduction in the G0/G1 phase at the highest concentration of MF66 was observed in the MCF-7 cell line (arrow) with a slight increase in the S and G2/M phases (arrowhead). No changes were recorded in the MDA-MB-231 and MCF-10A cell lines across the concentration range.

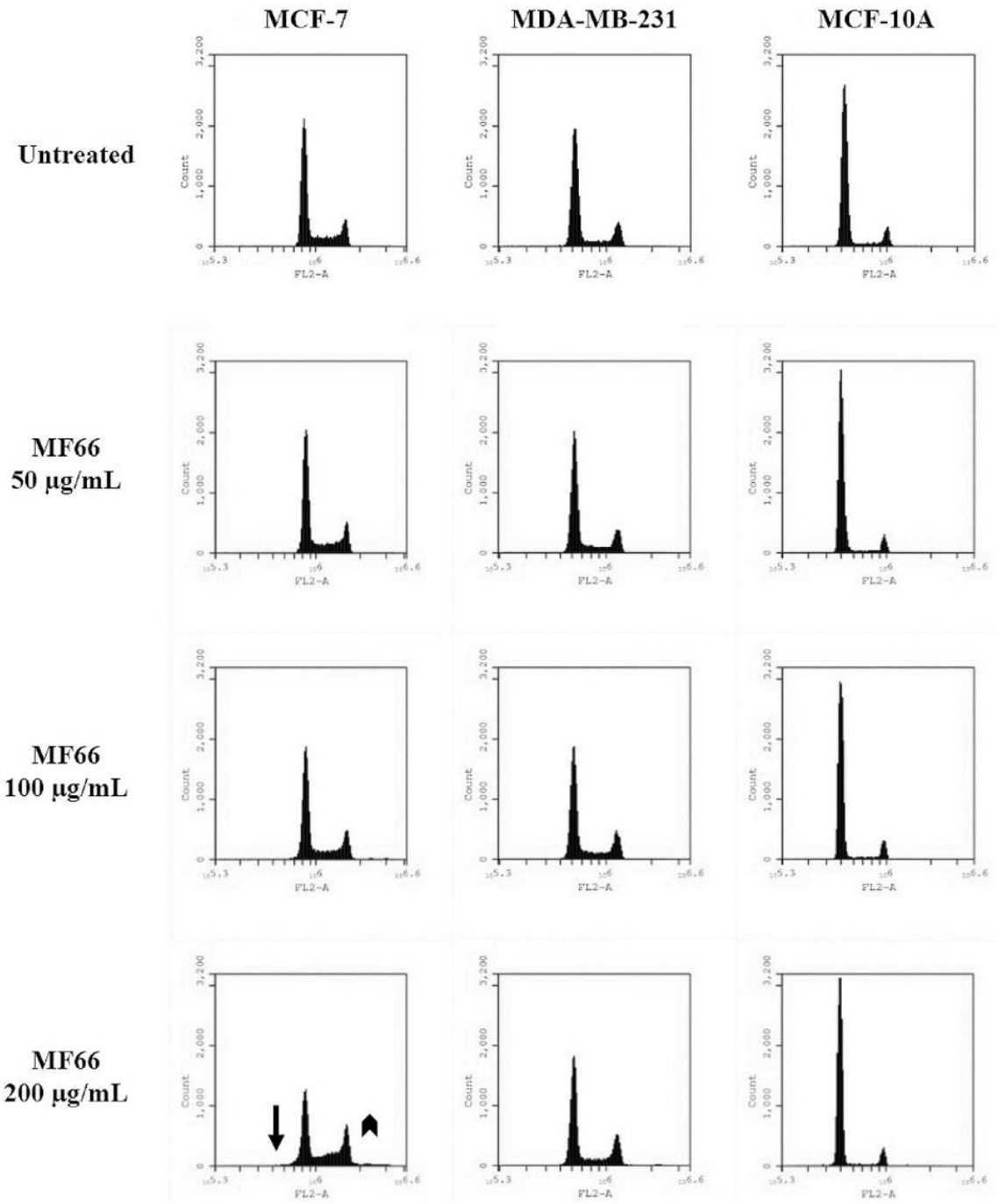

Figure 29: Cell cycle analysis in cell lines exposed to MF66 MNP.

Cell cycle changes were investigated following exposure of MCF-7, MDA-MB-231 and MCF-10A cell lines to MF66 MNP for 72h. Three concentrations of MF66 were selected: 50, 100 and 200 µg/mL and compared to untreated control (Top Row). A minimum of 10,000 events were recorded per concentration.

3.2.5 Localisation of basic MNP to lysosomal vesicles.

Following the results of the HCSA cytotoxicity experiments, we sought to further clarify the data obtained for the lysosomal parameter. While both an increase and a decrease in lysosomal intensity can signify cytotoxicity, the introduction of a physical entity such as the MNP can result in an increase in lysosomal mass through the mechanism of uptake. Therefore, the MCF-7 cell line was exposed to MNP at 100 µg/mL for 24h. Cells were stained with Lysotracker® and both fluorescent and bright field images were acquired. The result demonstrates the uptake of MNP (Figure 30 & Figure 31, white arrows), whereby the dense MNP containing regions overlay precisely with that of lysotracker® stained vesicles. From this experiment, it was possible to rank the degree of uptake for each MNP. MNP with the highest uptake include OD15, MF66, OD10 and ASi, while MNP with low or no uptake registered included PAA, ADNH and F1566 MNP treated cells. In addition, considerable colloidal instability was identified for the ADNH MNP with aggregation of MNP visible over the surface of all cells.

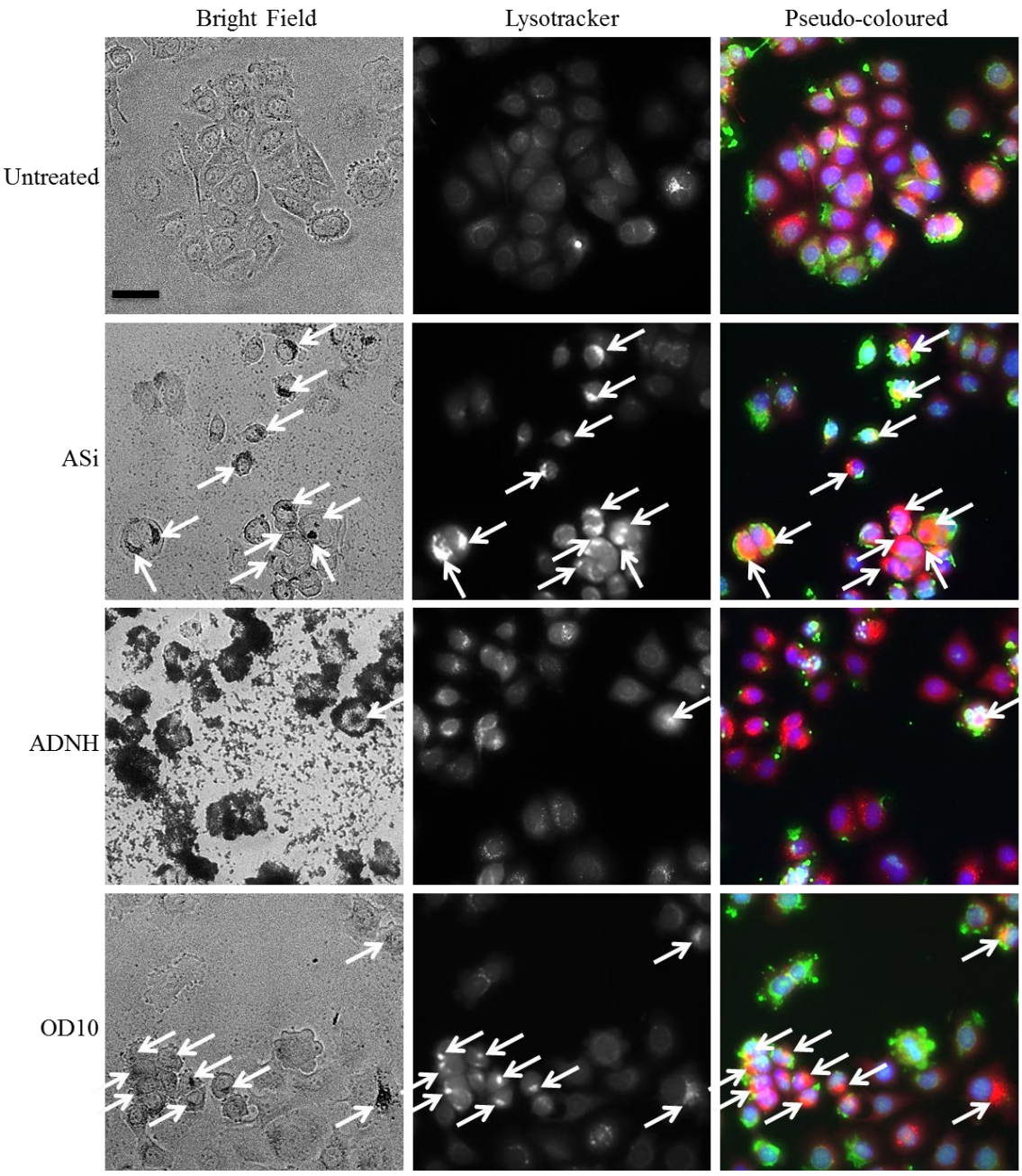

Figure 30: MNP uptake into lysosomes visualized using the InCell 1000 system.

MCF-7 cell line exposed to 100 µg/mL of the indicated MNP for 24h were assessed for lysosomal localization. Cells were stained with LysoTracker® Red, Hoechst 33342 (blue) and cell permeability dye (green) and both bright field and fluorescent imaging was carried out by HCSA with pseudo-images generated automatically following image acquisition. White arrows indicate location of MNP and matching lysosomal compartments. Scale bar (black line, top left "Untreated" panel) = 50 µm, applicable to all images.

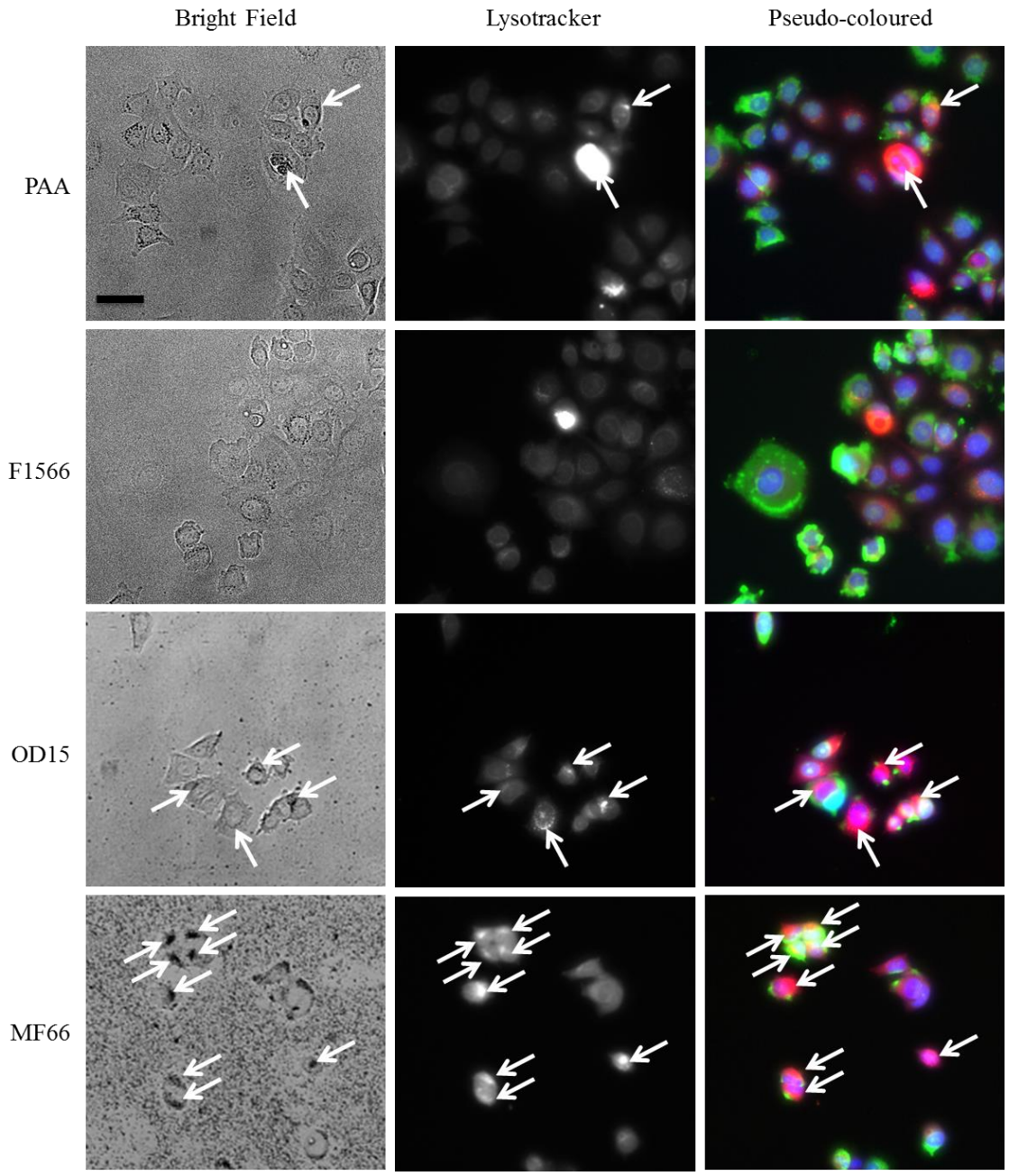

Figure 31: MNP uptake into lysosomes visualized using the InCell 1000 system.

MCF-7 cell line exposed to 100 µg/mL of the indicated MNP for 24h were assessed for lysosomal localization. Cells were stained with LysoTracker® Red, Hoechst 33342 (blue) and cell permeability dye (green) and both bright field and fluorescent imaging was carried out by HCSA with pseudo-images generated automatically following image acquisition. White arrows indicate location of MNP and matching lysosomal compartments. Scale bar (black line, top left "Untreated" panel) = 50 µm, applicable to all images.

3.2.6 Evaluation of DMSA MNP uptake mechanism and localisation.

MNP co-localisation with Lysotracker® stained regions has been demonstrated in the previous section. MNP uptake into cells occurs during the 24h period of exposure and it remained necessary to identify whether the uptake of MNP was an active or passive process, and to verify whether MNP taken up by cells did indeed localise to the lysosomes. The following work has been carried out in collaboration with Professor José L. Carrascosa, Dr Michele Chiappi and Dr Macarena Calero, and fully detailed in our manuscript [314].

MCF-7 cells exposed to DMSA coated MNP (OD15) were analysed by a range of techniques namely by Perls' Prussian blue, epi-fluorescent microscopy, and TEM to identify the mode of uptake, rate of uptake, degree of uptake, and finally the identification of the range of sub-cellular compartments in which MNP reside. The mode of uptake of MNP was shown by Dr Macarena Calero to be energy dependent (Figure 32A). Cells which were incubated with MNP and kept at 4 °C for 3h had MNP localised on the external surface of the outer membrane compared to cells stored at 37 °C for 3h where MNP were localised inside the cytoplasm. Cells stored at 37 °C for 3h were stained with lysotracker and the dense MNP clusters were shown to localise to the lysosomal compartment (Figure 32B), which confirmed the results presented in Figure 30 & Figure 31. TEM analysis conducted by Dr Michele Chiappi identified that after a very short time-period (0.5h), MNP clusters were identified within the cytoplasm of cells (Figure 33). The MNP were located inside membrane bound vesicles and no MNP clusters were identified free inside the cytoplasm. Over time (1h – 24h) the number of MNP-vesicles increased as did the quantity of MNP within vesicles. In addition, they were found to accumulate closer to the nucleus (24h insert image), and morphological changes in the vesicles were noted, with an evolution from translucent membranes to a multivesicular membrane (0.5h –vs– 6h). The degree of MNP uptake was quantified (Figure 34 A&B), and represented as the ratio of inorganic iron content versus the total cell area. Of the cells quantified an average of 12.44% of total cell area was occupied by MNP. Further evaluation of MNP uptake by TEM identified different mechanisms of endocytosis, depending on the size of MNP aggregates. Small MNP aggregates (< 200 nm) were seen near to the cell membrane adjacent to clathrin-coated patches (Figure 35 A1), and in the cytoplasm, near to the membrane, within clathrin-coated vesicles (Figure 35 A3&A4). In contrast, large MNP aggregates (>200 nm) were seen near the periphery of the cell and were engulfed by membrane extensions. This indicated that large MNP aggregates were being taken-up by macropinocytosis (Figure 35 B1&B2). In addition the MNP were shown to be localised within a variety of different vesicles dependent on time of exposure, from early endosomes (Figure 35 C1), to denser MNP containing vesicles with multivesicular bodies and intraluminal vesicles (Figure 35 C2), to late endosomes (Figure 35 C3) and finally localised to lysosomes (Figure 35 C4).

A

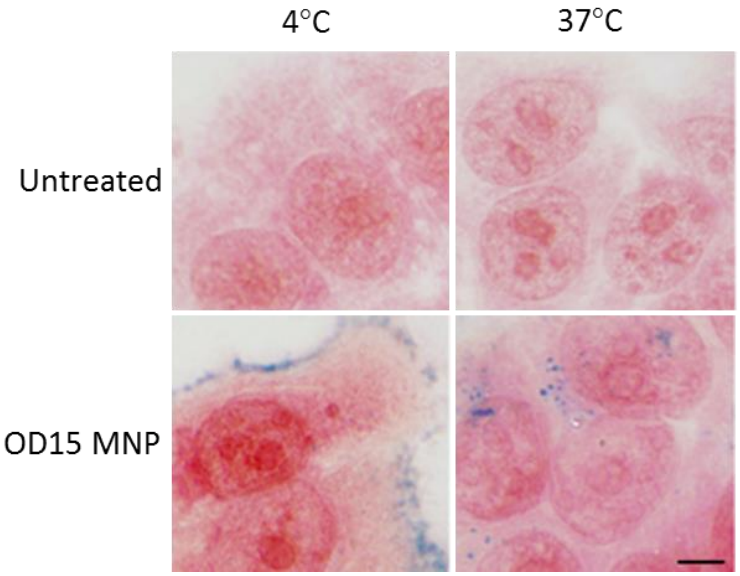

B

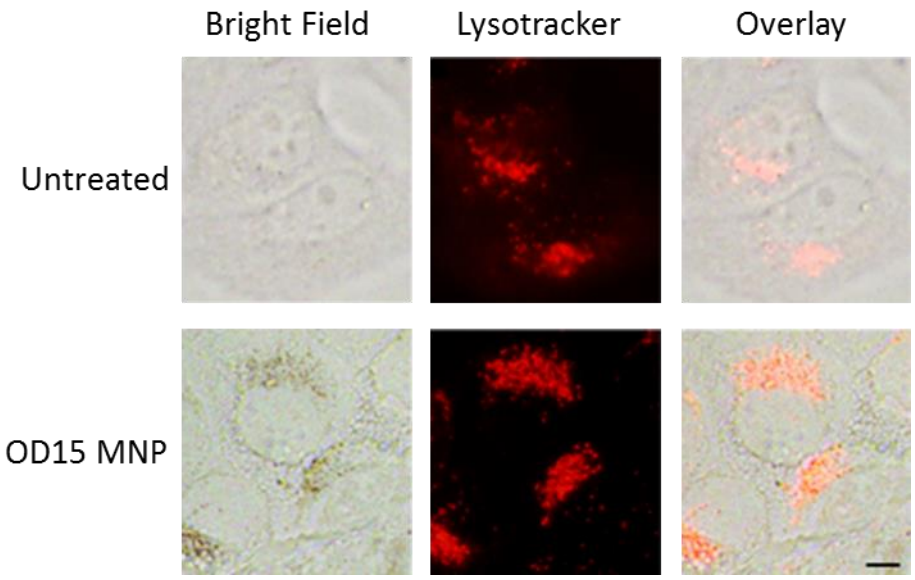

Figure 32: Mechanism of internalisation and accumulation of OD15 MNP.

MCF-7 cell line exposed to OD15 MNP for **(A)** 3h at 4°C or 37°C, demonstrating a temperature dependent MNP uptake by Perls' Prussian blue staining. Scale bar = 10 µm and (**B)** 24h to determine subcellular localisation through the overlay of MNP observed through bright field and lysosomal association using lysotracker red. Images courtesy of Macarena Calero, extracted from [314]. Scale bar = 20 µm.

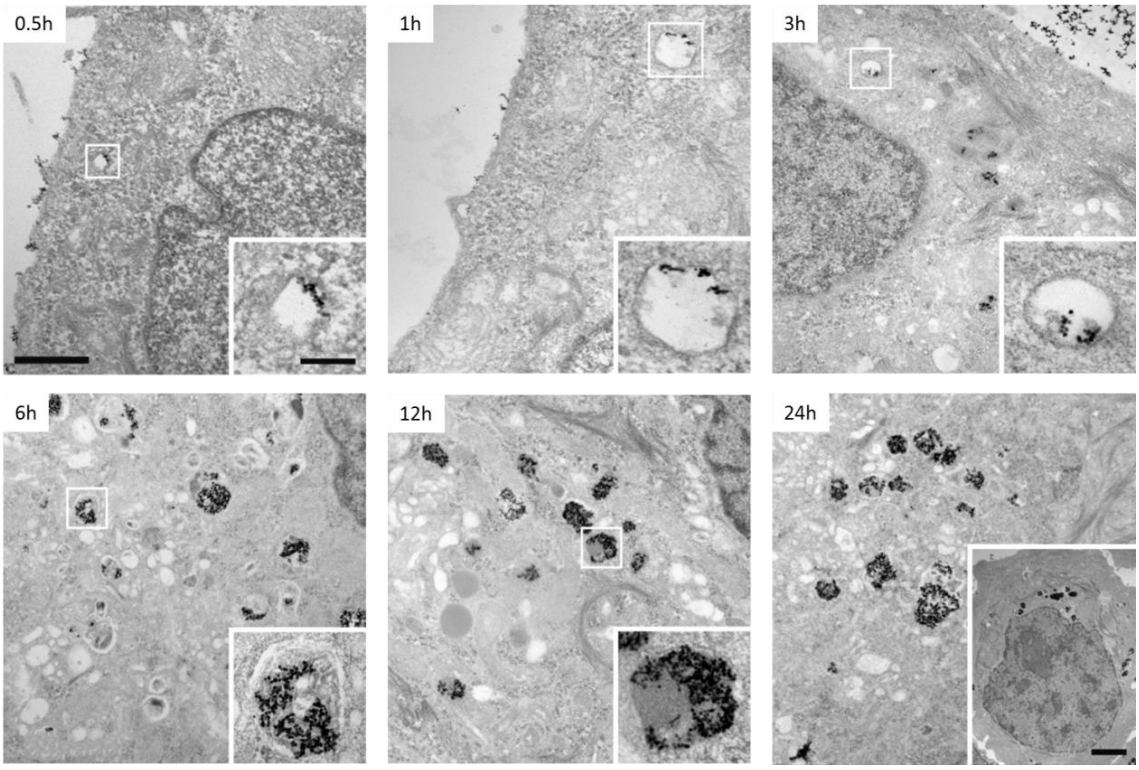

Figure 33: Investigation of MNP uptake kinetics by electron microscopy.

Thin sections of MCF-7 cells were imaged by electron microscopy following exposure to DMSA coated MNP for 0.5h, 1h, 3h, 6h, 12h, and 24h. Images courtesy of Dr Chiappi, extracted from [314]. Scale bar = 1 mm for 0.5h – 12h image, 200 µm for inserts 0.5h – 12h and 2µm for 24h insert, showing the overall cell shape and morphology.

A

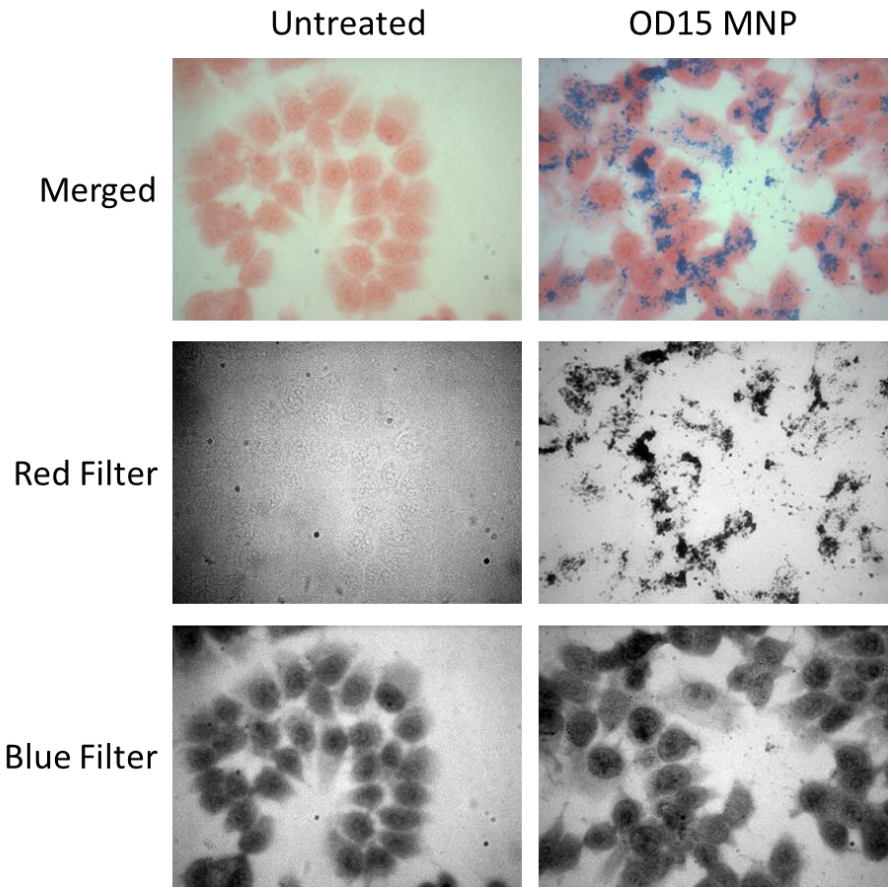

B

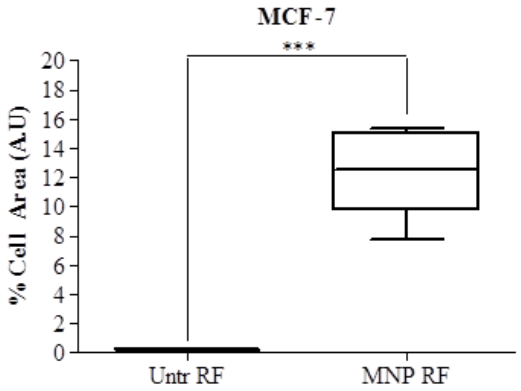

Figure 34: Quantification of MNP association and uptake in MCF-7 cell line.

MCF-7 cells were exposed to OD15 MNP for 24h. Slides were prepared and stained by the Perls' Prussian blue assay. Images were acquired using a Nikon epifluorescent microscope with colour camera. Coloured filters were applied to aid visualisation of MNP only (red filter; RF) and cells (blue filter). Quantitative analysis demonstrated degree of MNP association compared to untreated sample. Microscope slides were provided by Macarena Calero, and were imaged and analysed by the author of this thesis [314].

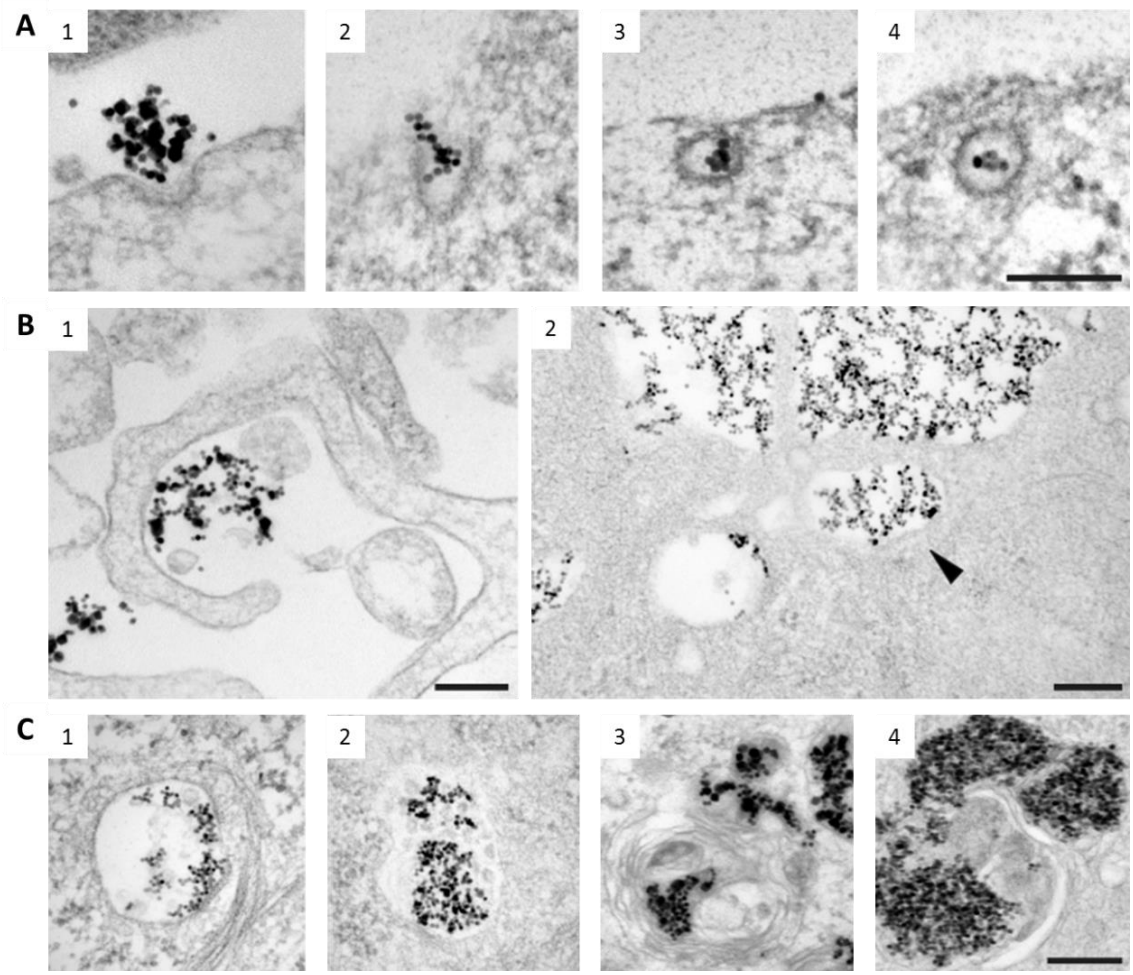

Figure 35: Evaluation of MNP interaction and uptake into MCF-7 cells by TEM.

Thin sections of MCF-7 cells were imaged by electron microscopy following exposure to DMSA coated MNP. Clathrin mediated endocytosis was observed (A) where MNP aggregates were <200 nm in diameter. (B) Macropinocytosis was observed where MNP aggregates were > 200 nm in diameter and (C) Different types of endosomes were observed to contain MNP aggregates: 1) Early endosome, 2) Multivesicular body containing intraluminal vesicles, 3) late endosome (multilamellar morphology) and 4) late endosome and lysosomes (multivesicular and electron-dense areas). Images courtesy of Dr Chiappi, extracted from [314]. Scale bar = 200 nm.

3.2.7 *In vivo* detection and biodistribution of MNP in small animal model

The results presented support the selection of both OD15 and MF66 MNP for further investigation. The OD15 were the most suitable MNP from these initial studies, but was not available in large quantities and therefore not tested *in vivo*. MF66 MNP is a commercially produced MNP (Liquids Research, Bangor, Wales) and was used as a reference nanoparticle to determine adequate detection and biodistribution by MRI. Both MNP will be retained for all further *in-vitro* tests, with direct comparison made between the suitability of each formulation.

An *in vivo* study using MF66 was carried out in collaboration with Dr Oliviero Gobbo (TCD) using a 7T Bruker MRI. MF66 (330 µg/100 µL) was delivered by a single tail vein injection which did not negatively impact on the health of the treated animals. A final concentration of MNP injected was estimated at 206.25 µg/mL based on the reported total blood volume in the BALB/c mice [426-428]. While a 200 µg/mL concentration of MF66 was shown to induce an acute cytotoxic response in the *in vitro* experiments, the animals did not display any adverse reaction, suggesting MF66 is tolerable to the animal at this concentration. Injected MNP were detected by MRI (Figure 36 A) and provide sufficient contrast compared to pre-MNP control. Biodistribution was determined at 4h with uptake into the liver observed via conventional MRI contrast (Figure 36 (A1)) and pseudo-coloured imaging (Figure 36(A2)). Organs were harvested from BALB/c mice and total MNP iron content was determined by the pEPR iron assay (Figure 36(B)). A high MNP concentration was recorded in liver, spleen and lung, with a low amount of iron detected in the heart and brain. The concentration of MNP remained constant in the liver and spleen over 96 h, with a decrease observed in the lung and heart. MNP concentrations increased in the kidney over the same period with a maximum observed at 48 h.

Due to the limitation in blood sampling volume in the BALB/c mouse model the larger Wistar rat was employed to facilitate blood sampling at multiple time points. This model was used to determine MNP blood circulation time with 200 µl blood samples taken at 3, 10, 20, 30, 60, 90 and 120 minutes and analysed by pEPR. The blood circulation half-life of the MNP was determined to be 32 ± 6 minutes.

Animal behaviour and body weight was monitored and while the MF66 MNP was retained in the liver to modify the SInt at the 5 week time point (data not shown), there was no change in normal animal behaviour. Weight gain was consistent for both exposed and control groups up to 5 weeks post administration with an increase of 3 g (Figure 37), demonstrating that the appetite of the MNP injected mice did not differ from saline injected mice.

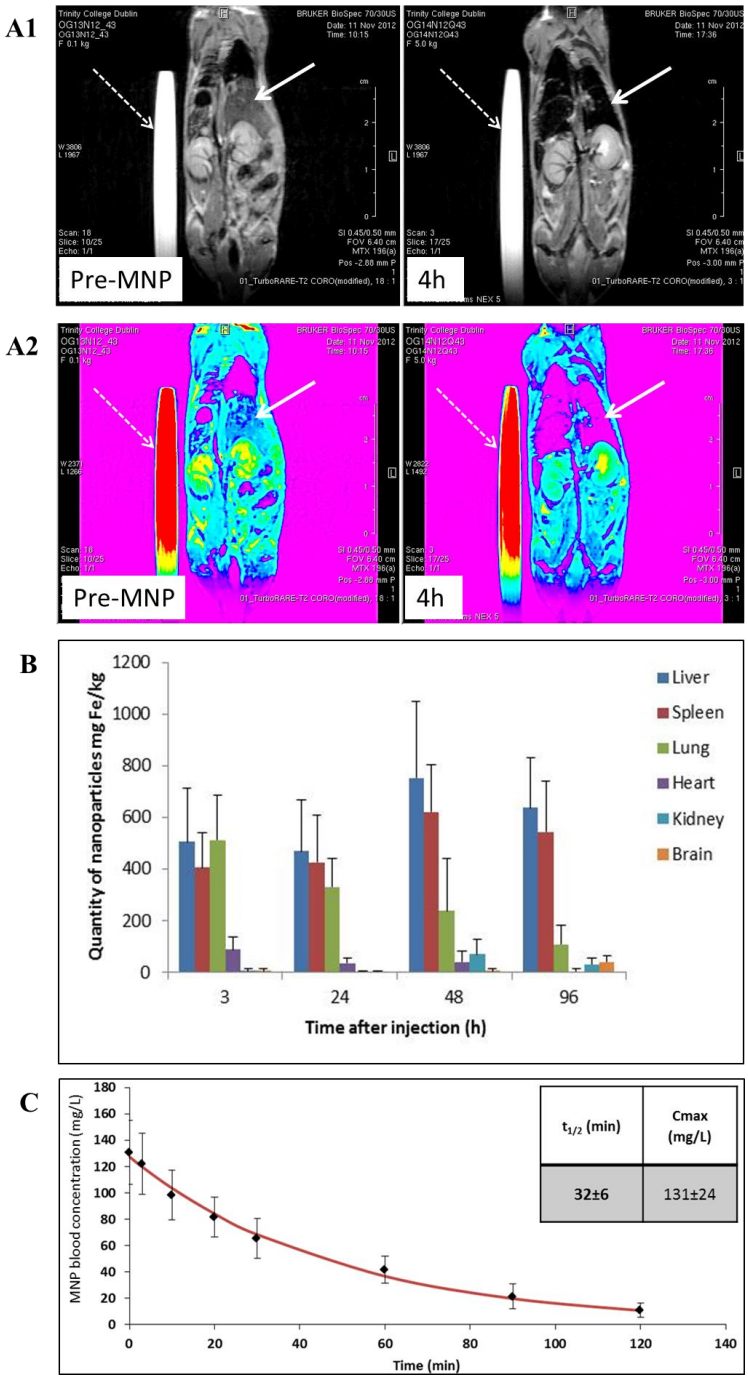

Figure 36: MNP biodistribution by MRI.

MF66 MNP biodistribution was monitored at 4h post injection using a 7T MRI scanner. (A) Qualitative assessment of the T2 weighted images (A1), and pseudo-coloured images (A2), revealed MNP localisation to the liver (solid white arrow). A tube of water (broken white arrow) was placed beside the mouse to provide a reference signal for each scan. (B) MNP organ accumulation at 3h, 24h, 48h and 96h post injection was determined by pEPR, uptake in liver and spleen was highest at 48h. (C) Blood circulation half-life of MNP in Wistar rats was determined by pEPR. Images courtesy of Dr Oliviero Gobbo, TCD.

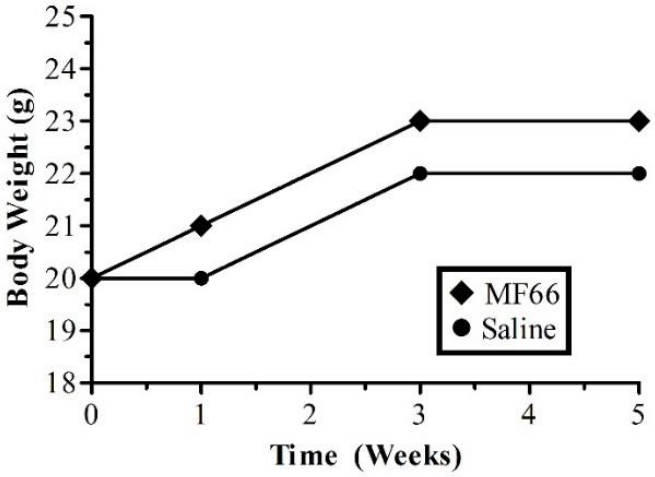

Figure 37: Mouse body weight analysis.

Mice were weighed at time zero, one week, three week and five week post injection with MF66 or saline control. Body weight was recorded and compared to saline injected mice to identify changes in appetite.

3.3 Discussion

The purpose of this part of the study was to identify a suitable MNP formulation to bring forward as a basis on which chemotherapeutic drugs and targeting moieties could be functionalised, according to the three-tiered approach outlined in Figure 6. The goals included the validation of HCSA as a suitable method for nanoparticle-cytotoxicity analysis and subsequently screen a range of characterised MNP to enable the identification of biocompatible formulations using multiparametric assessment. Furthermore, MNP uptake and localisation was determined using diverse techniques to further evaluate the ability of the basic MNP to enter cells and determine if uptake was dependent on the physicochemical characteristics of each formulation.

Characterisation of stock nanomaterials is important to monitor consistency between batches. Physicochemical characterisation of the basic MNP in this study was carried out by three techniques in order to assess the quality of each nanoparticle sample. TEM analysis of the basic nanoparticles (Figure 21) showed the nanoparticle size and shape to be uniform within five of the seven MNP tested (ASi, ADNH, OD10, OD15 and MF66). Whilst high resolution TEM can provide qualitative assessment of the MNP core, due to the nature of the testing method it cannot measure the hydrodynamic diameter of the MNP. DLS and NTA provided information on the hydrodynamic diameter and colloidal dispersion of each MNP formulation (Figure 22 & Figure 23). DLS and NTA results were closely comparable, with NTA recording a larger hydrodynamic size for F1566 (44 nm DLS and 108 nm NTA) and OD15 (42 nm DLS and 84 nm NTA) (Table 5). For these MNP the results of NTA were more accurate due to the generation of a concise sample-size due to the direct visualisation of individual nanoparticles dispersed in water and the acquisition of videos from fresh nanoparticle populations for each recording. Utilizing the NTA technique in this study, we determined the size distribution of all synthesized MNP, and most importantly we investigated the stability of the MNP in complete culture medium. Following the incubation with complete DMEM medium, NTA analysis recorded an increase in hydrodynamic size for all MNP. It is known that the adsorption of proteins on MNP can increase hydrodynamic size [245] and we observed that the extent of MNP hydrodynamic size increase varied between samples, with the biggest increase of 200 nm observed for OD10 and 123 nm for both ADNH and MF66 (Table 5). ASi and OD15 MNP size increases reached 120 nm and 105 nm respectively, and both PAA and F1566 hydrodynamic sizes were raised marginally by 46 nm and 27 nm, respectively. Investigation of the zeta potential to determine whether the extent of protein adsorption on the surface of the MNP was charge dependent did not provide any additional information. It can be concluded from the physicochemical characterisation steps taken, that direct visualisation of MNP core structure and the determination of hydrodynamic size in water and complex medium provided a greater understanding of each nanomaterial.

Before starting the cytotoxicity screening of MNP, it was necessary to verify that the test being undertaken was not interfered with by the nanoparticles. It has been shown that nanomaterials can interfere with standard cytotoxicity assays [322, 323]. Therefore the presence of fluorescent quenching was investigated as a means of assessing the potential interference that basic MNP formulations could have on the dyes in the commercial staining kit (Figure 24). MNP incubated with Hoechst 33342, cell membrane permeability dye (YO-PRO®-1 iodide), Lysosomal (LysoTracker® Red) and Mitochondrial (MitoTracker® Orange) probes for 30 minutes were examined in a fluorimeter to determine if fluorescent

intensity was quenched compared to a medium containing fluorescent dye control. The results show that no statistically significant reduction in fluorescent dye intensity was recorded. It is known that the use of colorimetric methods for MNP cytotoxicity testing can result in false positive results as a consequence of interference with iron from the MNP. It has been demonstrated here that even in the presence of high concentrations of MNP, quenching of the fluorescent signal does not occur. Thus, the use of fluorescent dyes as probes to measure cellular events following exposure to the engineered MNP is reliable and is not affected by the engineered MNP in this study. The method used to test fluorescent interference did not account for the fact that prior to staining of cells for evaluation of cytotoxicity, cells are washed several times with PBS, thus removing excess MNP, and therefore reducing the ability of the MNP to cause interference in the cytotoxicity assays.

To evaluate the suitability of the HCSA technique and the commercial dye kit, the intensity of the dyes intended for cell permeability detection and lysosomal staining were measured following exposure to two validated control compounds (Figure 25). Firstly, it has been shown that treatment with valinomycin causes damage to mitochondria, uncoupling of oxidative phosphorylation and damage to cell membranes [429] and was therefore used as a positive control for the membrane permeability dye, which rapidly and irreversibly enters nuclei upon loss of membrane integrity. The results here demonstrate that valinomycin is highly cytotoxic with significant reduction in cell count, and causes pronounced increase in the signal intensity of the cell permeability parameter. Secondly, tacrine was shown to induce apoptosis through lysosomal membrane permeabilisation and subsequent mitochondrial damage [430]. In addition, a concentration dependent increase in Lysotracker® dye intensity was observed by the manufacturer at a concentration of 100 µM. Tacrine was subsequently selected and used at this concentration to demonstrate that lysosomal staining was specific and determine whether the variation in fluorescent signal strength could be detected by the InCell 1000. For the purpose of this study, a concentration of 100 µM was used to study lysosomal mass/pH changes. The results demonstrate that in all cell lines tacrine resulted in a statistically significant ($p > 0.01$) increase in the lysosomal staining. Verification using valinomycin and tacrine established that changes in cell permeability dye and Lysotracker® fluorescent intensity were detected and recorded by the InCell 1000 system. Through both methodologies, the assessment of MNP fluorescent dye interference and confirmation of dye sensitivity and detection by HCSA provided a strong basis for accurate and high throughput MNP cytotoxicity testing.

Following the evaluation of MNP by PCC and the validation of the HCSA technique, the cytotoxicity testing of each formulation was explored by multiparametric analysis. The results show that cell line sensitivity was present in two out of five cell lines tested. The BT-474 and MDA-MB-231 cell lines displayed dose-dependent cytotoxic response to five out of seven MNP formulations. The BT-474 had the highest response with pronounced cell count reduction and increased cell membrane permeability recorded for ASi, ADNH, OD10, PAA and F1566 (Figure 26 & Figure 27). Similar effects were recorded for these MNP in the MDA-MB-231 cell line. As one of the results of this study we found that MCF-7 cell line proved to be the most robust model with little to no decrease in cell count in response to any MNP across the tested concentration range. However, increased cell permeability, indicating the onset of apoptosis [431] was noted in the MCF-7 cell line for ASi, ADNH, OD10 and F1566. The results and observations from biocompatibility testing identified many of the MNP as not suitable for further bio-

application due to their cytotoxic response. However, both the OD15 and MF66 MNP formulations did not induce any measureable cytotoxicity at concentrations up to 100 µg/mL at 24h and were therefore brought forward in the *in vitro* study with functional moieties and also *in vivo* for evaluation of the maximum tolerated dose and the ability to detect by MRI. The scaling up of MNP production and the development of a clinical product is a vital step in the translation from *in vitro* studies to *in vivo* and ultimately the clinical setting. The MF66 MNP was the most suitable for *in vivo* analysis due to the capability for industrial volume scale-up with 1 litre per day production possible while maintaining the physicochemical characteristics and quality as assessed and reported in Table 5. However, due to the observed cytotoxicity of MF66 at the highest concentration of 200 µg/mL further testing of MF66 was performed with an emphasis on cell proliferation through the analysis of cell cycle progression to determine the suitability of MF66 for *in vivo* testing (Figure 29). Three cell lines were selected, two robust cell lines (MCF-7 and MCF-10A) and a more sensitive cell line (MDA-MB-231) as identified in this study, and the cell cycle was monitored following 72h exposure to MF66 (50, 100 and 200 µg/mL). These new results obtained for MF66 highlighted a dose dependent cytotoxic response at the highest concentration of 200 µg/mL. Cell cycle analysis identified slight reduction in the G0/G1 fraction of cells in the MCF-7 cell line at the highest MF66 concentration, suggesting that cells were arrested in G2/M resulting in G0/G1 fraction decrease. The MCF-10A and MDA-MB-231 cell lines did not exhibit an increase in the duration of the cell cycle phases following 72h exposure. No changes in cell cycle profiles were observed in any cell line at concentrations below 200 µg/mL, suggesting that MF66 was suitable when used at concentrations below this.

It is accepted that nanoparticle surface charge does not dictate the degree of protein adsorption but dictates the type of proteins that adsorb strongly on the nanoparticle surface to form the hard and soft protein corona [246, 247]. The absorption of serum proteins onto the MNP surface has been reported to increase MNP stability in biological solution with adsorption and desorption occurring dynamically, as described by Saptarshi *et al* [248]. Even though OD15 and MF66 MNP were the only MNP selected for retention in the study, all MNP were dispersed in complete medium to observe changes to colloidal stability and record possible uptake through bright field visualisation. The most obvious aggregation occurred with the ADNH MNP sample following 24h incubation in complete medium (Figure 30, bright field), suggesting that the presence of serum proteins in this sample may have resulted in the formation of inter-particle bridges, in turn leading to destabilization of the MNP in solution and strong adsorption to the outer cell membrane. Nevertheless, a causative link was identified between the increase in hydrodynamic diameter described previously and MNP uptake into lysosomes (Figure 30 & Figure 31). With increasing hydrodynamic diameter there was an increase in the amount of MNP uptake into cells and ultimately into lysosomes. Qualitative assessment of MNP uptake demonstrated that OD10 (200 nm increase), MF66 (123 nm increase), ASi (120 nm increase) and OD15 (105 nm increase) had the greatest uptake into lysosomes while PAA (46 nm increase) and F1566 (27 nm increase) had little to no observed uptake. These findings suggest that the amount of protein adsorbed onto the surface of the MNP was directly associated with their ability to interact with cells thus presenting a greater opportunity to enter cells through the endocytic pathway. The protein adsorption capacity of nanoparticles has been previously shown as an excellent predictor of cellular association [249]. It has also been well documented that positively charged MNP are internalised into cells to a greater degree compared to neutral and negatively charged MNP [277-279], which is confirmed here

with uptake of positively charged ASi MNP occurring to a higher degree compared to negatively charged formulations.

This approach, while identifying MNP-cell interaction, also highlighted ADNH as unsuitable due to the pronounced instability and aggregation in complete culture medium, confirming data obtained by DLS, NTA and HCSA. If ADNH were delivered to an *in vivo* model system, it could lead to cardiovascular compromise due to interaction with serum proteins causing an increase in vascular thrombus formation as a consequence of increased platelet aggregation [432]. Taken together with the PCC assessment and cytotoxicity analysis, it has been possible to identify unsuitable MNP at an early stage and enabled the selection of both OD15 and MF66 MNP for further evaluation.

MNP interaction with cells and uptake was further investigated to determine the energy requirements of uptake, uptake kinetics, quantification of uptake and the method by which MNP entered cells. Through HCSA we have shown that intracellular regions containing aggregates of MNP overlay precisely with fluorescently stained lysosomal vesicles (Figure 30 & Figure 31). This observation was made at a set time point of 24h and it was not possible to determine the rate at which MNP were taken into cells, nor was it possible to identify the mechanism of MNP uptake. As part of WP3, temperature dependent experiments were conducted whereby MCF-7 cells were exposed to OD15 MNP for 3h (Figure 32). Incubation at 4 °C and at 37 °C sought to identify whether uptake was energy dependent. MNP were taken up into cells following incubation at 37 °C only, indicating that an active energy-dependent transport was necessary for MNP internalisation. As none of the Multifun engineered MNP were spherical, a study by Gratton et al. provided an explanation for the uptake observed in this work, where they suggested that nanomaterials with non-spherical shape are taken up with greater efficiency [433]. The rate of uptake was determined by TEM, with MNP present inside cells even after very short incubation times (0.5h) (Figure 33). Interestingly, and in agreement with the active uptake study, it was evident that no free MNP were present in the cytoplasm. Instead, all MNP were confined to membrane bound vesicles, which contained increasingly greater amounts of MNP over time and localised closer to the nucleus. Maturation of MNP containing vesicles from translucent to multivesicular morphology was noted at later time-points. The formation of dense vesicles at 12h suggested that the MNP were localised inside lysosomes, which are visible due to their amorphous electron dense core [434]. Quantification of the degree of uptake observed in the MCF-7 cell line exposed to OD15 MNP provided evidence that high cell loading efficiency can be attained at 24h exposure. Yet, while it was shown that MNP entered cells through an energy dependent mechanism in as little as 0.5h and ultimately localised to lysosomal compartments, it was unknown exactly how the MNP entered cells. TEM analysis investigating the mechanism of uptake identified that uptake was dependent on the size of MNP clusters (Figure 35), with macropinocytosis facilitating uptake with larger MNP cluster sizes (> 200 nm), and clathrin-mediated endocytosis occurring with small MNP clusters (< 200 nm). This finding was in agreement with the literature as macropinocytosis has been previously shown as the preferential mechanism for uptake of larger nanoparticles [435].

MNP have been screened and suitable formulations selected, the degree of uptake, mode of uptake and rate of uptake was determined by Dr Chiappi. The next logical step was to investigate whether the engineered MNP could be detected by MRI, as a fundamental requirement for use as a diagnostic tool and to identify the bio-distribution and tolerability of the engineered MNP in the BALB/c mouse. The MF66

MNP was the only formulation available in large quantities at the time of experimentation and the *in vivo* analysis was carried out using this formulation. Following tail vein injection there was rapid accumulation in the liver, observed by MRI at 4h (Figure 36 A), and from 3h by pEPR in liver, spleen, lung, heart and kidney (Figure 36 B). Clearance from the liver was not evident 5 weeks post injection (data not shown). MNP blood clearance with a half-life of 32±6 minutes as determined in the Wistar rats and the observed uptake of MNP in liver and spleen in BALB/c mice could be due to the uptake of MF66 into specialised Kupffer cells in the liver and into macrophages in the spleen. These cells function in the clearance of pathogens, apoptotic cells and immune complexes from circulation and have been shown to be necessary for nanoparticle clearance [436, 437]. In addition, a recent study using human subjects injected with ferumoxytol (Feraheme®), an FDA approved superparamagnetic MNP, found that complete liver clearance was achieved 11 months post-delivery with no adverse effect [438].

3.4 Conclusion

The characterisation of the basic-MNP formulations in accordance with the safe-by-design approach presented in Figure 6, facilitated the selection of OD15 and MF66 MNP as lead formulations. Both OD15 and MF66 did not induce acute cytotoxic responses in all cell lines below 100 µg/mL, despite active uptake into cells occurring 30 minutes following exposure. Limitations were identified in the production phase when transitioning from *in vitro* to *in vivo* tests, with MF66 as the only MNP capable of being produced in high enough quantities to test in the animal models at that time. It was demonstrated that detection of MF66 by MRI was possible and MNP was localised to liver, spleen, lung, heart, and kidney as determined by pEPR on tissue biopsies. In addition, blood circulation half-life was determined to be 32±6 minutes in the Wistar rat. MF66 and OD15 were the two basic MNP of choice for subsequent functionalisation with targeting moieties such as N6L and the chemotherapeutic agents, doxorubicin and gemcitabine, which will be presented in the next chapter of results.

Chapter 4: Multifunctional MNP for targeted cancer treatment

4.1 Introduction

Cancer is a heterogeneous disease and treatment options are currently limited to surgery, radiation and chemotherapy. All of these methods carry a high risk of damage to healthy tissues or the incomplete eradication of the disease. Doxorubicin and gemcitabine chemotherapy drugs have been used as MNP functional moieties due to their use in treating both breast and pancreatic cancers. While treatment options for both diseases are available, breast cancer remains the second most diagnosed cancer in women in Ireland and is the highest in the UK. Pancreatic cancer accounts for a much lower incidence rate with 500 people on average being diagnosed in Ireland each year, however, the net 5 year survival, according to the Irish cancer registry, is only 8.7%. Survival over 10 years, according to cancer research UK, is as little as 1.1%.

With this in mind, the aims of this part of the thesis included the demonstration of anticancer potential using doxorubicin functionalised MNP, the validation of the most suitable linker for drug functionalization, determination of N6L pseudopeptide-induced anticancer effect, demonstration of N6L-mediated MNP uptake into cell lines and primary cells, and anticancer efficacy of gemcitabine functionalised MNP with and without the N6L targeting ligand.

To achieve these aims, the specific objectives were:

1. Comparative analysis of electrostatically and covalently functionalised doxorubicin MNP for specific drug release.
2. Identification of a suitable linker on the MNP surface for drug functionalization and release.
3. Investigation of the anticancer potential of N6L pseudo-peptide functionalised to OD15 and MF66 MNP.
4. Examination of N6L-mediated MNP uptake in breast and pancreatic cell lines.
5. Examination of multi-functionalised MNP-induced anticancer effect using N6L and gemcitabine MNP conjugates.

4.2 Results

4.2.1 Doxorubicin hydrochloride dose response

HCSA was performed to determine the anticancer potential of MF66 MNP functionalized with doxorubicin drug as detailed in Table 6 below.

Table 6: Details of nanomaterials containing functionalized doxorubicin drug.

Nanomaterials were supplied by Dr Pierre Couleaud as suspensions at pH 6.5. Core particle size was determined by TEM, and hydrodynamic size by DLS. All nanoparticles were negatively charged ranging between – 39.2 mV to 42.4 mV. Concentrations supplied were consistently 2.4 mg Fe/mL with the indicated concentration of doxorubicin drug attached.

Name	pH	Particle size TEM (nm)	Hydrodynamic size (DLS; Intensity) (nm)	Surface charge at pH 6 (mV)	Concentration (mg Fe/ml)	Biomolecule Loaded
MF66_Doxo (Electrostatic)	6.5	11.7	115.8 ± 0.8	-39.2 ± 1.1	2.4	26 µmol Doxo / g Fe
MF66_Doxo (Covalent)	6.5	11.7	143.1 ± 1.3	-42.4 ± 3.0	2.4	26 µmol Doxo / g Fe

The effective concentration of free doxorubicin at which a response could be obtained was investigated and efficacy was compared to doxorubicin functionalised MNP. The activity of free doxorubicin in the MCF-7, MDA-MB-231 and MCF-10A cell lines at 24h and at 72h was investigated by HCSA. The concentration range selected included five concentrations above the known IC50 of doxorubicin in the MCF-7 cell line (100 nM [439]), up to 2600 nM. The results are presented in Figure 38 with graphs provided in Appendix 2. There was a significant decrease in cell count for all cell lines at 24h with a further decrease at the 72h timepoint. Cell count decrease was matched with an increase in membrane permeability, with statistical significance at concentrations higher than 650 nM in the MCF-7 and MCF-10A cell line, and concentrations exceeding 200 nM in the MDA-MB-231 cell line. Reduction in lysosomal intensity following exposure to doxorubicin indicated lysosomal membrane damage, and was confirmed by the increase of the membrane permeability parameter.

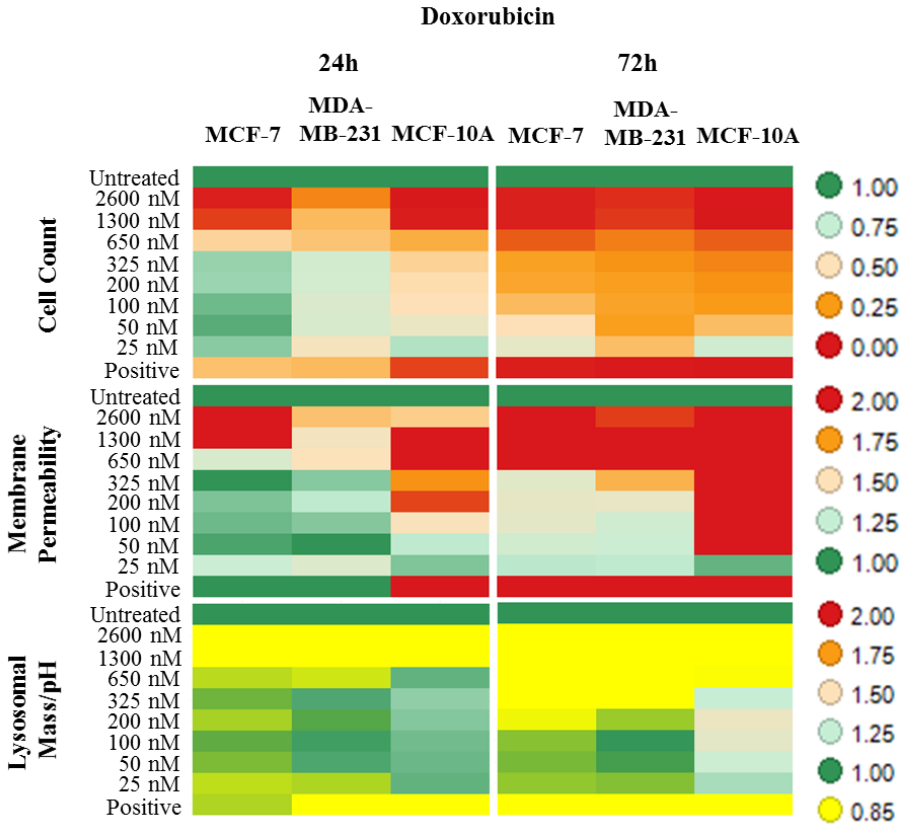

Figure 38: Dose and time dependent toxicity of doxorubicin hydrochloride in cell lines.

Breast cancer and normal-like cell lines were exposed to doxorubicin chemotherapeutic agent for 24h and 72h at a wide range of concentrations, ranging between 25 nM and 2600 nM. Multiparametric analysis was used to determine the effect free drug had on each parameter. Doxorubicin caused substantial cell death, increased membrane permeability and lysosomal mass/pH decrease, and was most pronounced at 72h post exposure. Positive control = 1µM CdSe QD.

4.2.2 Electrostatic vs covalent drug functionalisation approaches

Doxorubicin functionalized MF66 (electrostatic and covalent formulations) as detailed in Table 6 were tested at 24h and 72h. Doses delivered were higher than the reported IC50 of 100 nM for MCF-7 ([439]) and were between 130 nM and 2600 nM, similar to those of free drug. The corresponding iron oxide content delivered to obtain the required drug dose is provided in Figure 39 (lower panel). For the electrostatic functionalized MNP (Figure 39), there was significant reduction in cell count at the highest concentration in the MCF-7 and MCF-10A cell lines at 24h. In comparison, at 72h there was significant cell count reduction above 260 nM in the MCF-7 and MCF-10A cell lines and at all concentrations in the MDA-MB-231 cell lines. In comparison, the covalent functionalised MNP (Figure 40) caused a significant reduction in cell count only in the MCF-10A cell line at 24h, while at 72h all concentrations in the MDA-MB-231, above 1300 nM in the MCF-7 and the 2600 nM concentration in the MCF-10A cell lines showed a significant reduction in cell count.

Cell membrane permeability increased in the MCF-7 cell line following exposure only to the covalent functionalised MNP (Figure 40). In the MDA-MB-231 and MCF-10A cell line, membrane permeability increase was observed for both electrostatic and covalent formulations, with significant increases above 260 nM for the electrostatic formulation compared to 1300 nM and above for the covalent formulation.

Doxorubicin alone has the capacity to damage lysosomes which was observed in the previous experiment (Figure 38). However, both Figure 39 and Figure 40 demonstrate quite strikingly that when functionalised to the MNP, doxorubicin delivered to the cells did not result in lysosomal damage. This result is in clear contrast to the lysosomal damage observed with free doxorubicin exposure (Figure 38). Instead, and especially with the covalent MNP formulations, there was a significant increase in the lysosomal intensity observed at all time-points in all cell lines.

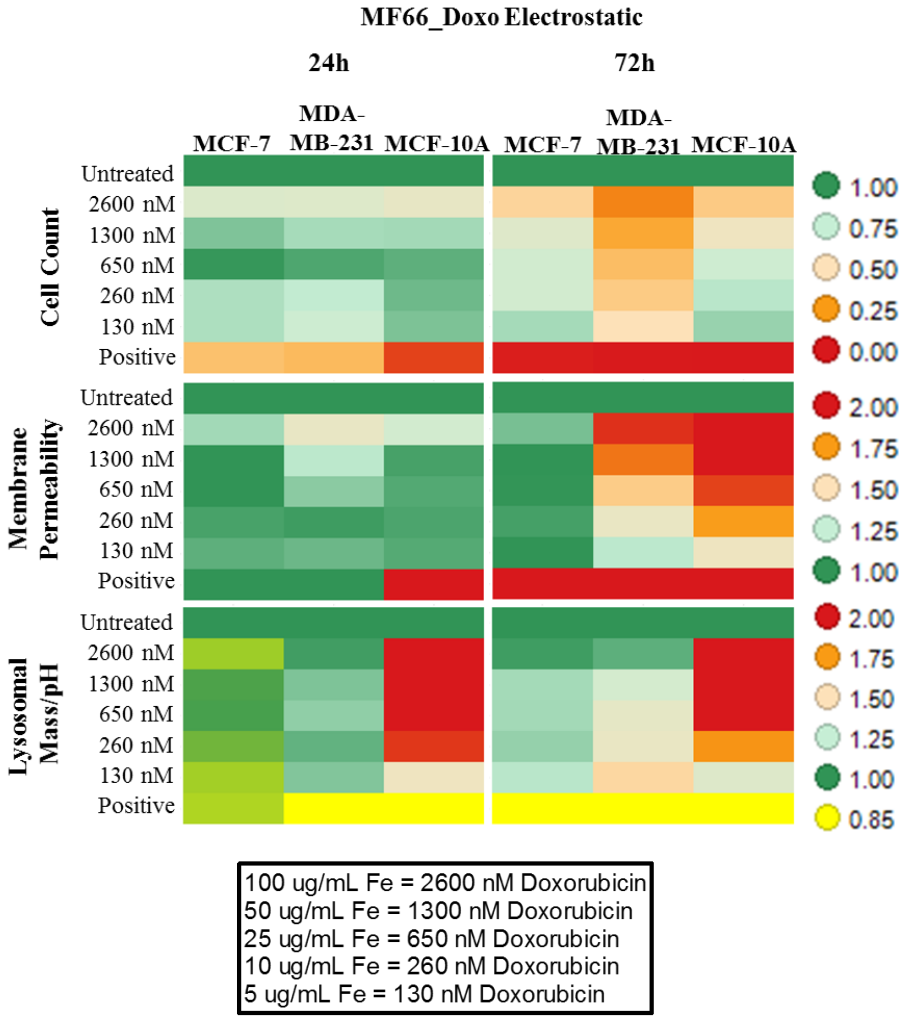

Figure 39: Effect of electrostatically functionalized doxorubicin MF66 MNP.

Cell lines were exposed to MF66 MNP with electrostatically-functionalised doxorubicin for 24h and 72h using a range of concentrations (25 nM and 2600 nM). Multiparametric analysis was used to determine the effect the electrostatic functionalization approach had on each cell line**.** MDA-MB-231 cell line was most affected by this formulation with significant cell count reduction observed. Membrane permeability in the MCF-10A cell line was increased following 72h exposure, with an increase observed in the lysosomal mass/pH parameter. Positive control = 1µM CdSe QD.

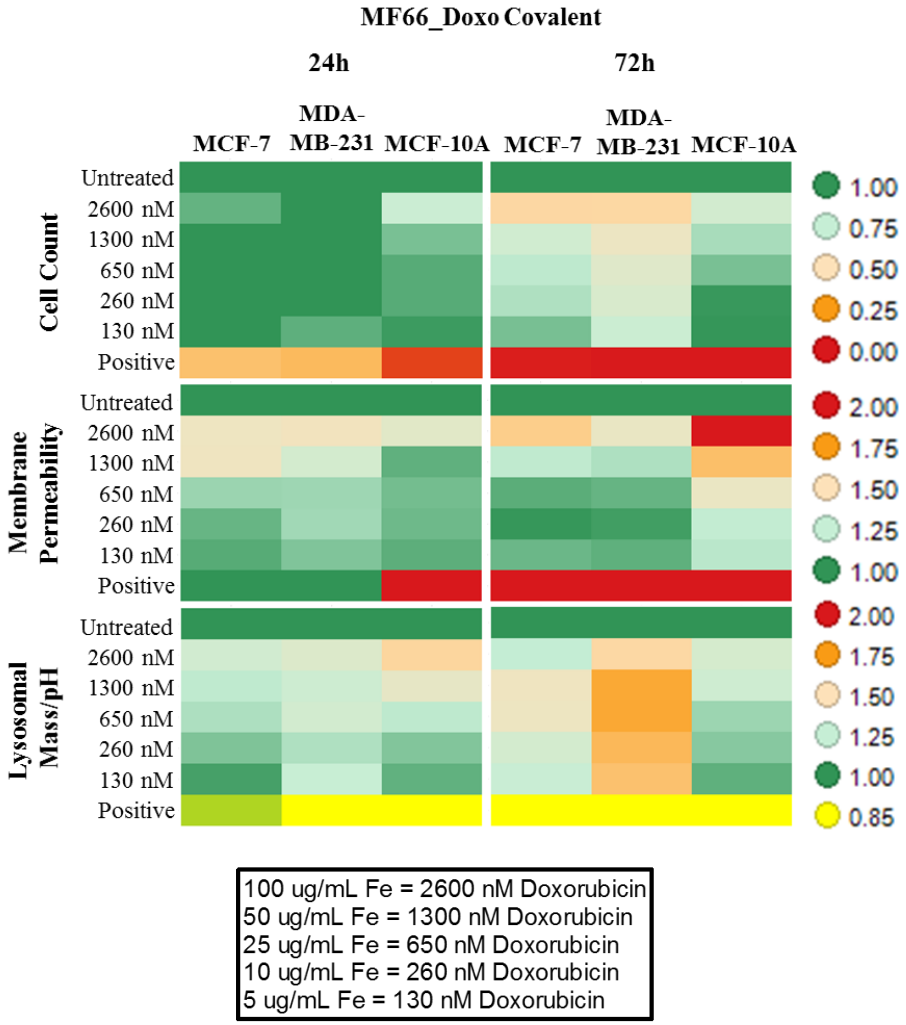

Figure 40: Effect of covalently functionalized doxorubicin MF66 MNP.

Cell lines were exposed to MF66 MNP with covalently-functionalised doxorubicin for 24h and 72h using a range of concentrations (25 nM and 2600 nM). Multiparametric analysis was used to determine the effect the covalent functionalization approach had on each cell line**.** The MDA-MB-231 cell line was most affected following 72h exposure and a decrease in cell count was observed. An increase in membrane permeability was observed in all cell lines, which was most pronounced in the MCF-10A cell line. Lysosomal mass/pH changes were most pronounced in the MDA-MB-231 cell line. Positive control = 1µM CdSe QD.

4.2.3 MF66 and OD15 functionalized with N-, O- and I- linked doxorubicin.

Following the screening of MF66 electrostatic and covalent doxorubicin functionalized MNP, the WP2 partners involved in the functionalisation of MNP sought to identify the most effective method to covalently functionalize doxorubicin on MF66 and OD15 MNP. Extensive HCSA-based testing was conducted on MNP functionalised with doxorubicin with the use of three distinct linkers, enabling specific release of doxorubicin (Figure 41). The linkers include O-linked and N-linked which are doxorubicin bound and contain a disulfide linker (PySS) that is cleavable in a reducing environment. The linker for O_doxorubicin contains an oxygen atom (carbamate group) while N_doxorubicin contains a nitrogen atom (urea group). An I-linked formulation contained a dual-cleavable linker that has a disulfide bond and an imine moiety that is cleaved in acidic pH. All linkers, when cleaved, release unmodified doxorobucin drug (Figure 42). The functionalised MNP are detailed in Table 7. All nanomaterials had a net negative surface charge between -42.2 and -49.7 mV, with hydrodynamic sizes of between 59.4 nm to 112.0 nm for the functionalized MNP. The concentration of doxorubicin loaded onto MNP is indicated in Table 7.

Two breast-derived cell lines (MCF-7 and MCF-10A) and two pancreatic cancer cell lines (BxPC3 and PANC-1) were tested to determine anticancer efficacy. Comparison was made between functionalized MNP, the basic MNP formulations and free chemotherapeutic drug to ensure any measured cytotoxicity was on account of the functionalized drug release and not the core nanoparticle.

Table 7: Details of nanomaterials containing functionalized doxorubicin drug.

Nanomaterials were supplied as suspensions at pH7.4 in water by Dr Pierre Couleaud, IMDEA, Madrid, Spain from WP2. Core particle size was determined by TEM, and hydrodynamic size by DLS. All nanoparticles were negatively charged. The concentration of doxorubicin in µmol per g of Fe was supplied and the total MNP used to achieve the highest drug dose is provided for both breast (2600 nM maximum) and pancreatic (2000 nM maximum) cell lines.

Name	pH	Particle size TEM (nm)	Hydrodynamic size (DLS; Intensity) (nm)	Surface charge at pH7 (mV)	Doxo Loaded (µmol/g Fe)	MNP conc. @2600 nM (µg/mL)	MNP conc. @2000 nM (µg/mL)
OD15	7.4	15.0	59.4	-49.7	N/A	N/A	N/A
OD15-N-Dox	7.4	15.0	76.7	-48.2	21	123.8	95.2
OD15-O-Dox	7.4	15.0	93.9	-47.9	22	118.2	90.9
OD15-I-Dox	7.4	15.0	75.3	-46.4	30	86.7	66.7
MF66	7.4	11.7	70.6	-42.2	N/A	N/A	N/A
MF66-N-Dox	7.4	11.7	104.1	-46.6	13	200.0	153.8
MF66-O-Dox	7.4	11.7	112.0	-46.2	20	130.0	100
MF66-I-Dox	7.4	11.7	92.9	-47.2	12	216.7	166.7

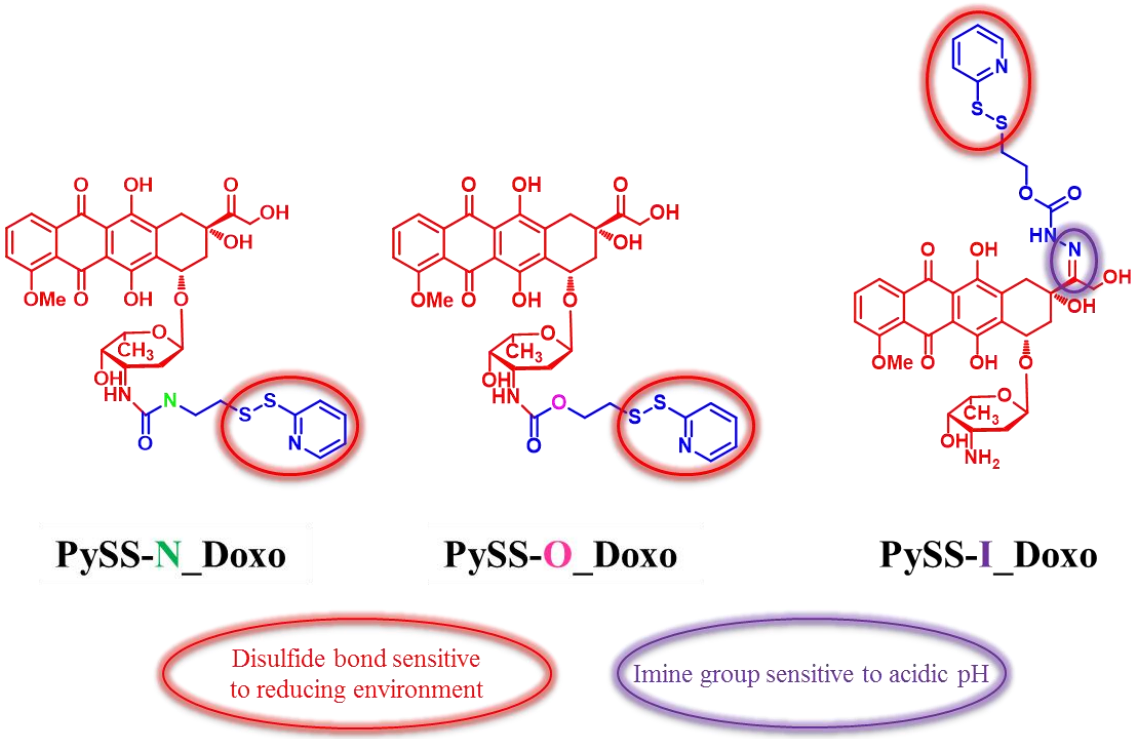

Figure 41: Chemical structure of N_, O_ and I_Doxorubicin with alternative linker molecules.

Linker molecules contained a disulfide group or both a disulfide group and imine group. N_Doxo linker contained a urea structural group (N-C(=O)-N) whereas O_Doxo linker contained a carbamate structural group (O-C(=O)-N) and I_Doxo employed the same linker as O_Doxo, but was bound to the drug at an alternative site and through an imine group. Both N_Doxo and O_Doxo liberate the drug when in a reducing environment while I_Doxo required both a reducing environment and low pH (below pH 5.5). Image courtesy of Dr Pierre Couleaud and Dr Alfonso Latorre, IMDEA, Madrid, Spain.

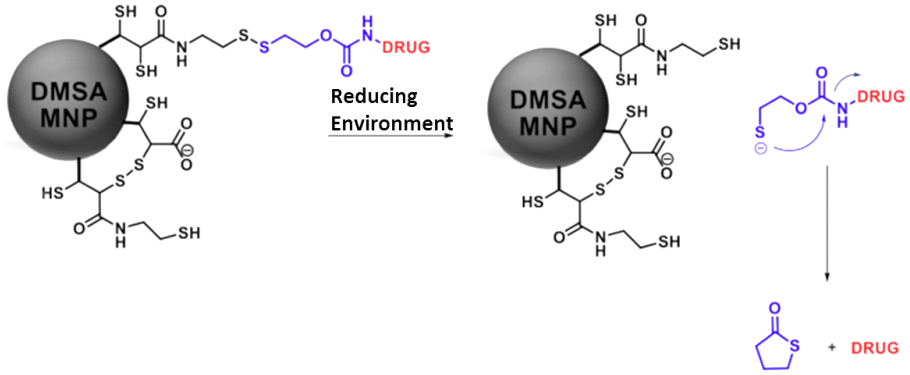

Figure 42: Mechanism of drug release from MNP.

Release of drug from MNP in reducing environment yields an unmodified drug, and the free linker molecule. Image courtesy of Dr Pierre Couleaud and Dr Alfonso Latorre, IMDEA, Madrid, Spain.

The concentration of doxorubicin delivered to the breast-derived cell lines was 2600, 1300, 650, 260, and 130 nM and to the pancreatic cancer cell lines was 2000, 1000, 500, 250 and 125 nM.

The results are presented as heatmaps: MCF-7 cell line in Figure 43; MCF-10A cell line in Figure 44, BxPC3 cell line in Figure 45, and PANC-1 cell line in Figure 46. All graphs are provided in Appendix 2. Testing with free doxorubicin drug yielded a similar response in all four cell lines; with significant cell count reduction at all concentrations at the 72h time point. As previously shown, doxorubicin exposure caused an increase in cell permeability at high concentrations in the breast-derived cell lines, a trend seen here also for the pancreatic cell lines. The PANC-1 cell was least affected but a significant increase in cell permeability was observed at the highest concentration of doxorubicin (2000 nM). The lysosomal intensity was reduced, as previously observed, in the breast-derived cell lines while the pancreatic cell lines showed no reduction in the lysosomal intensity.

OD15 MNP exposure caused no reduction in cell count in the MCF-7, MCF-10A and PANC-1 cell lines at 72h, while a significant reduction was observed in the BxPC3 cell line at the highest concentration (200 µg/mL). No increase in cell membrane permeability was observed in the MCF-7, MCF-10A and BxPC3 cell lines, while a slight increase was present at the highest concentration in the PANC-1 cell line. Lysosomal intensity was not increased in the MCF-7, MCF-10A and PANC-1 cell lines while a significant increase was observed in the BxPC3 cell line at both 24h and 72h time points.

OD15_N_Doxorubicin exposure at 72h resulted in a significant reduction in cell count for the MCF-7 cell line and a reduction in the BxPC3 cell line. Both MCF-10A and PANC-1 exposed cell lines had no cell count reduction. Cell membrane permeability was increased in BxPC3 and PANC-1 only at 72h while lysosomal intensity was significantly increased in the BxPC-3 cell line.

OD15_O_Doxorubicin exposure at 72h caused a significant reduction in cell count at the highest concentration in the MCF-7, BxPC3 and PANC-1 cell lines, with the BxPC3 having the greatest reduction. Cell permeability was increased in both the BxPC3 and PANC-1 cell lines only, with PANC-1 having an increase at all concentrations while the increase in the BxPC3 cell line was only at the highest concentration. Lysosomal intensity increase was observed only in the pancreatic cancer cell lines, with increases observed at concentrations greater than 1000 nM. The OD15_O_Doxorubicin induced no effect on the MCF-10A cell line with any measured parameter.

OD15_I_Doxorubicin exposure at 72h resulted in cell count reduction in all cell lines, with significant decreases observed in the MCF-7 cell line at concentrations above 650 nM, in the MCF-10A cell line at all concentrations, in the BxPC3 cell line more than 500 nM and in the PANC-1 cell line at concentrations exceeding 250 nM. Cell membrane permeability was increased in all cell lines, in the MCF-7 cell line at concentrations above 1300 nM, in the MCF-10A cell line at 2600 nM, in the BxPC3 cell line above 1000 nM and in the PANC-1 cell line at concentrations exceeding 500nM. Lysosomal intensity was increased in all cell lines, in the MCF-7 cell line at concentrations between 260nM and 1300 nM, in the MCF-10A cell line at 2600 nM, and in the BxPC3 and PANC-1 cell lines at concentrations beyond 1000 nM.

MF66 MNP exposure caused no reduction in cell count in the MCF-7 cell line at 72h, while a significant reduction was observed in the MCF-10A, BxPC3 and PANC-1 cell lines at the highest concentration (200 µg/mL). No increase in cell membrane permeability was observed in the MCF-7 cell

line, while slight decrease was present at all concentrations in the MCF-10A cell line. Significant increases were observed in the BxPC3 (above 200 µg/mL) and PANC-1 (exceeding 100 µg/mL) cell lines. Lysosomal intensity was increased in the MCF-7 cell line between 10 – 50 µg/mL, in the MCF-10A cell line greater than 50 µg/mL and in the BxPC3 cell line above 200 µg/mL. A reduction in the lysosomal intensity was observed in the PANC-1 cell line at 200 µg/mL.

MF66_N_Doxorubicin exposure at 72h caused a reduction in cell count in all cell lines, at varying concentrations. In the MCF-7 cell line at concentrations greater than 1300 nM, in the MCF-10A cell line at 260 nM and above 1300 nM, in the BxPC3 cell line beyond 1000 nM and in the PANC-1 cell line at concentrations surpassing 500 nM. Cell membrane permeability was increased in the MCF-7 cell line at 2600 nM, and in the PANC-1 cell line at all concentrations. A marginal decrease in cell permeability was observed in the MCF-10A cell line at 260 and 650 nM and no change was observed in the BxPC3 cell line. Lysosomal intensity was increased in all cell lines apart from PANC-1, an increase was observed in the MCF-7 cell line at concentrations between 130 nM and 1300 nM, in the MCF-10A cell line at concentrations above 260 nM, and in the BxPC3 cell line at concentrations exceeding 500nM.

MF66_O_Doxorubicin exposure at 72h caused a reduction in cell count in the MCF-10A, BxPC3 and PANC1 only. Cell count reduction was observed in the MCF-10 cell line at 2600 nM, in the BxPC3 cell line at concentrations beyond 500 nM, and in the PANC-1 cell line greater than 250 nM. Cell membrane permeability was increased in the BxPC3 cell line and in the PANC-1 cell line at concentrations above 1000 nM and 250 nM respectively. Lysosomal intensity was increased in all cell lines apart from the PANC-1 cell line, an increase was observed in the MCF-7 cell line at 650 nM only, in the MCF-10A cell line at concentrations above 1300 nM, and in the BxPC3 cell line at concentrations exceeding 500 nM. Minimal yet significant decrease in lysosomal intensity was observed in the PANC-1 at concentrations greater than 1000 nM.

MF66_I_Doxorubicin exposure at 72h caused a reduction in cell count in all cell lines. Cell count reduction was observed in the MCF-7 and MCF-10A cell lines at concentrations above 650 nM, and at all concentrations in the BxPC3 and PANC-1 cell lines. Cell membrane permeability was increased in the BxPC3 cell line and in the PANC-1 cell line at concentrations higher than 500 nM and 250 nM respectively. Lysosomal intensity was increased in all cell lines apart from PANC-1, an increase was observed in the MCF-7 cell line between 130 – 650 nM, in the MCF-10A cell line at concentrations exceeding 650 nM, and in the BxPC3 cell line at concentrations beyond 250 nM.

Representative pseudo-coloured merged images of all four cell lines tested and stained for multiparametric analysis are provided in Figure 47 (MCF-7), Figure 48 (MCF-10A), Figure 49 (BxPC3), and Figure 50 (PANC-1).

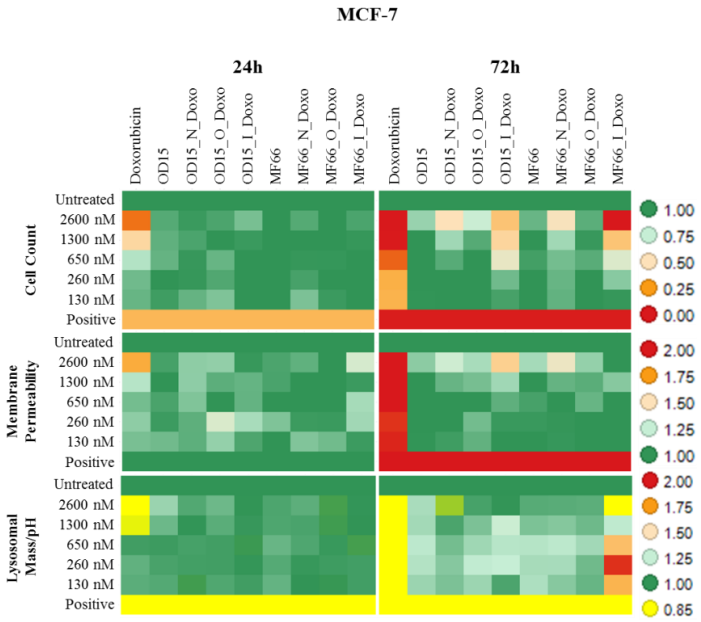

Figure 43: Effect of covalently functionalized doxorubicin MNP on MCF-7 cell line.

The MCF-7 cell line was exposed to doxorubicin functionalized OD15 and MF66 MNP for 24h and 72h at a range of concentrations (130 nM to 2600 nM). Exposure to the OD15_I_Doxo and MF66_I_Doxo MNP formulations resulted in the greatest cell count reduction. Positive control = 1µM CdSe QD.

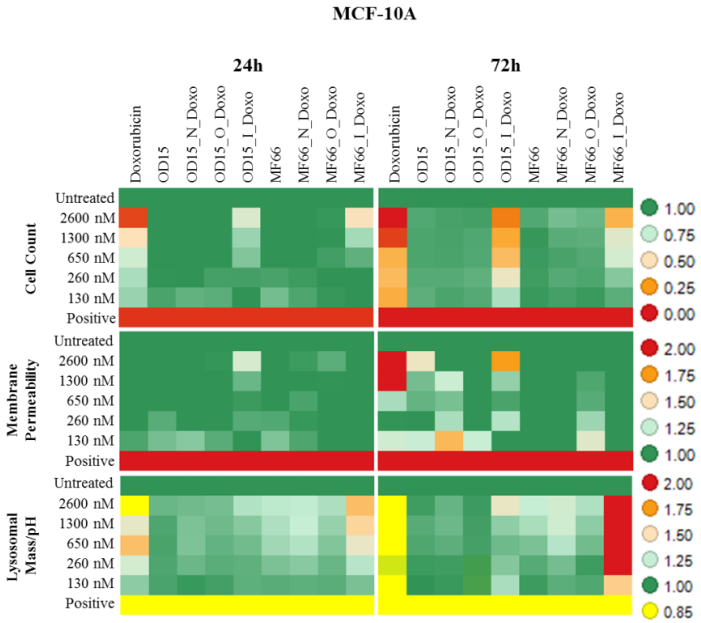

Figure 44: Effect of covalently functionalized doxorubicin MNP on MCF-10A cell line.

The MCF-10A cell line was exposed to doxorubicin functionalized OD15 and MF66 MNP for 24h and 72h at a range of concentrations (130 nM to 2600 nM). Exposure to the OD15_I_Doxo and MF66_I_Doxo MNP formulations resulted in the greatest cell count reduction. Positive control = 1µM CdSe QD.

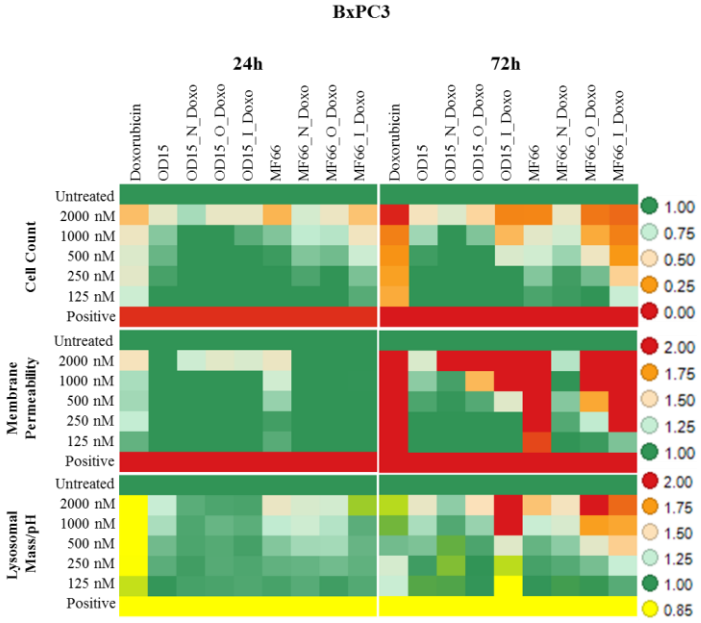

Figure 45: Effect of covalently functionalized doxorubicin MNP on BxPC3 cell line.

The BxPC3 cell line was exposed to doxorubicin functionalized OD15 and MF66 MNP for 24h and 72h at a range of concentrations (125 nM to 2000 nM). Exposure to OD15_O_Doxo and MF66_O_Doxo MNP formulations resulted in cell count reduction and membrane permeability increase, while OD15_I_Doxo and MF66_I_Doxo caused the greatest reduction in cell count and increase in membrane permeability. Positive control = 1µM CdSe QD.

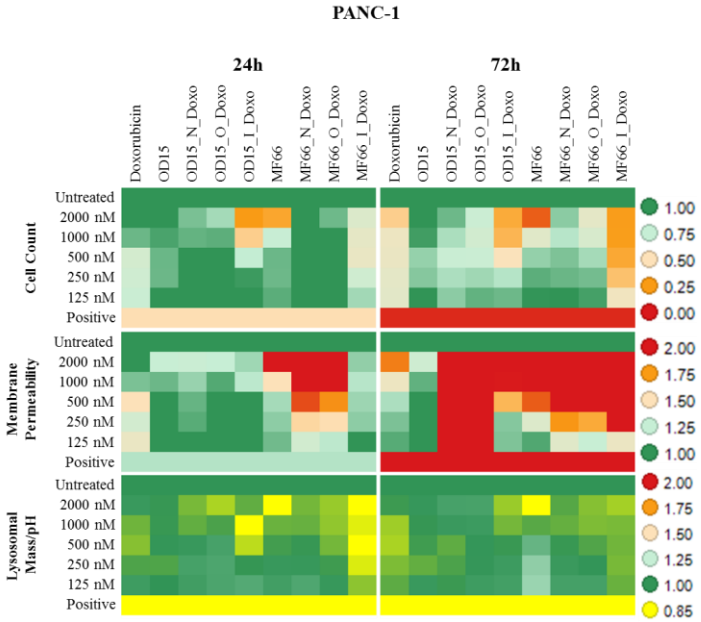

Figure 46: Effect of covalently functionalized doxorubicin MNP on PANC-1 cell line.

The PANC-1 cell line was exposed to doxorubicin functionalized OD15 and MF66 MNP for 24h and 72h at a range of concentrations (125 nM to 2000 nM). Exposure to the OD15_I_Doxo and MF66_I_Doxo MNP formulations resulted in the greatest cell count reduction. Membrane permeability increase and reduction in Lysosomal mass/pH was observed following exposure to most formulations. Positive control = 1µM CdSe QD.

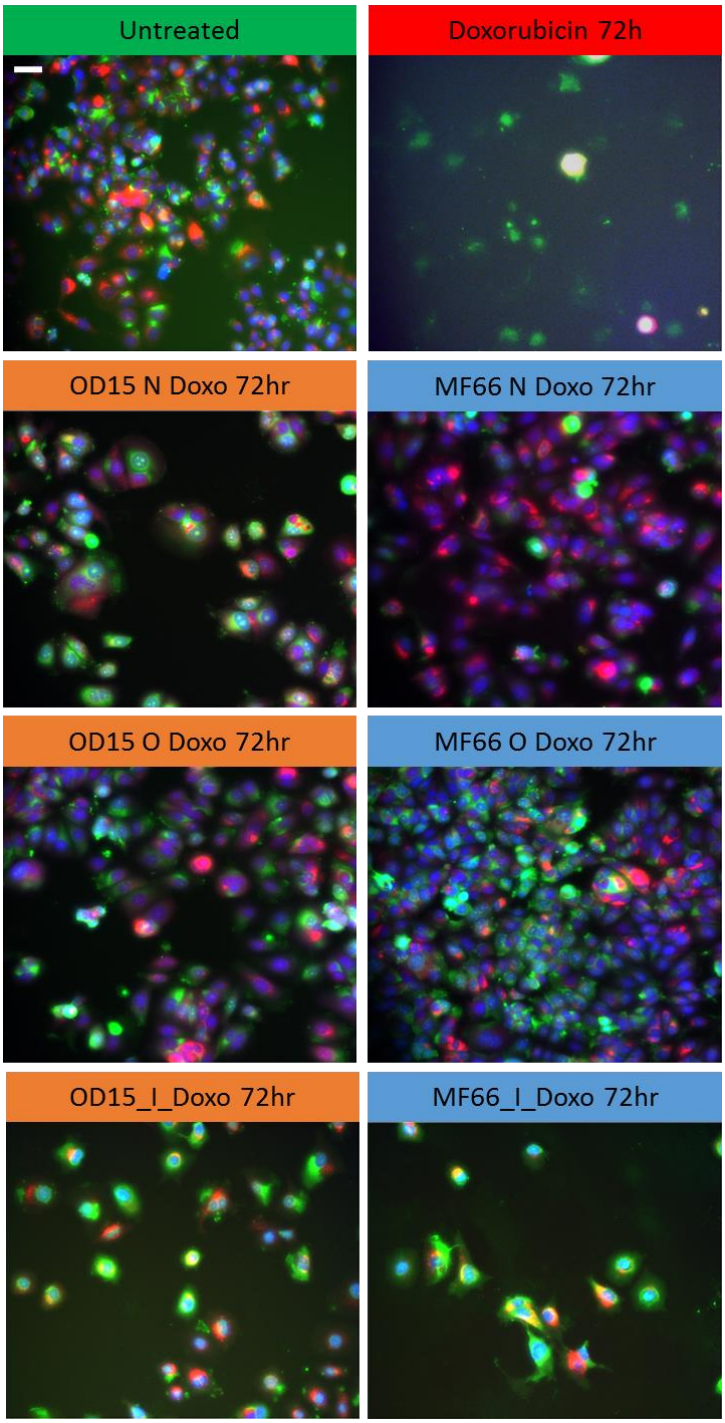

Figure 47: MCF-7 cell line exposed to doxorubicin and MNP formulations.

Representative images of the MCF-7 cell line exposed to doxorubicin functionalised MNP for 24h. Cells were stained with Hoechst 33342 (Blue), YO-PRO®-1 iodide: cell membrane permeability (Green) and Lysotracker® (Red). Doxorubicin (top right panel) caused substantial cell death compared to untreated control. OD15_N_Doxo and MF66_N_Doxo effectively reduced cell count. OD15_I_Doxo and MF66_I_Doxo were the most effective MNP formulation with the highest cell count reduction observed. Scale bar (white line, top left of "Untreated" panel) = 50 µm, applicable to all images.

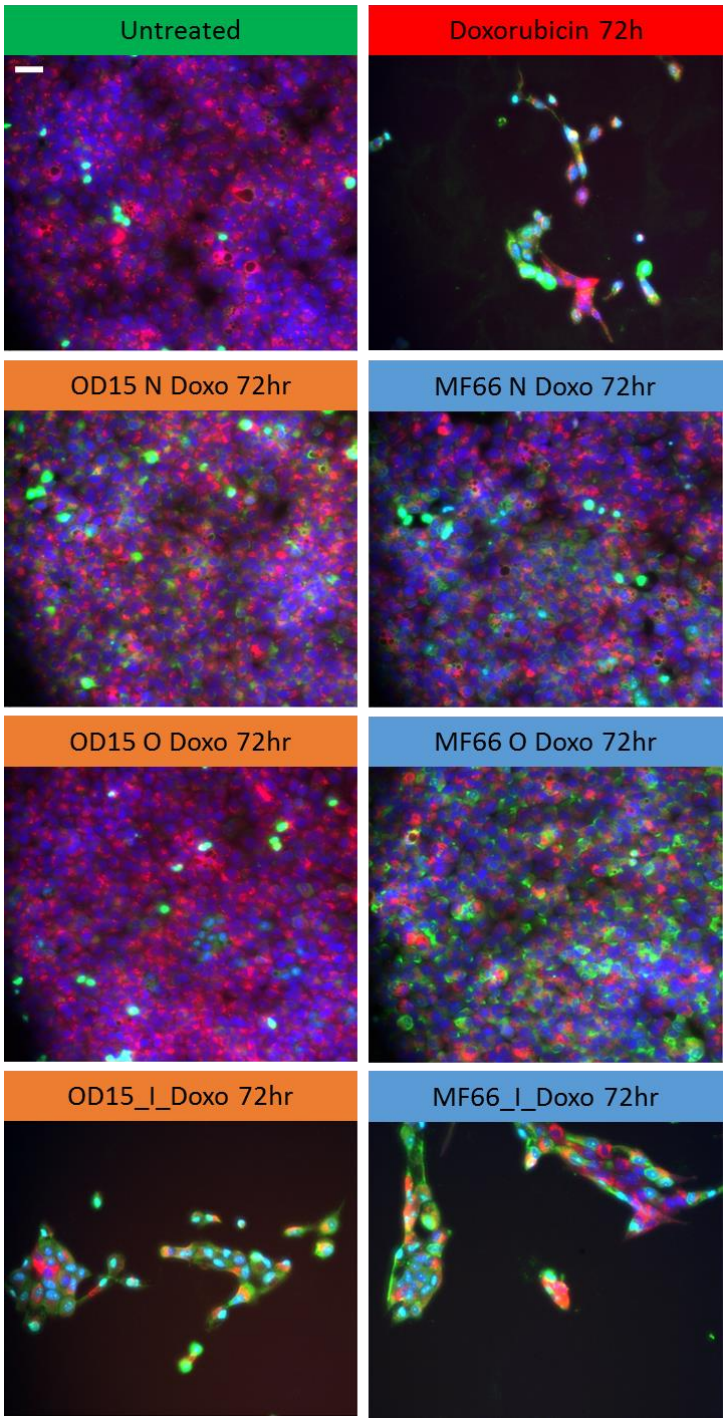

Figure 48: MCF-10A cell line exposed to doxorubicin and MNP formulations.

Representative images of the MCF-10A cell line exposed to doxorubicin functionalised MNP for 24h. Cells were stained with Hoechst 33342 (Blue), YO-PRO®-1 iodide: cell membrane permeability (Green) and Lysotracker® (Red). Doxorubicin (top right panel) caused substantial cell death compared to untreated control. OD15_I_Doxo and MF66_I_Doxo were the only two MNP formulations that caused significant cell death, compared to untreated control. Scale bar (white line, top left of "Untreated" panel) = 50 µm, applicable to all images.

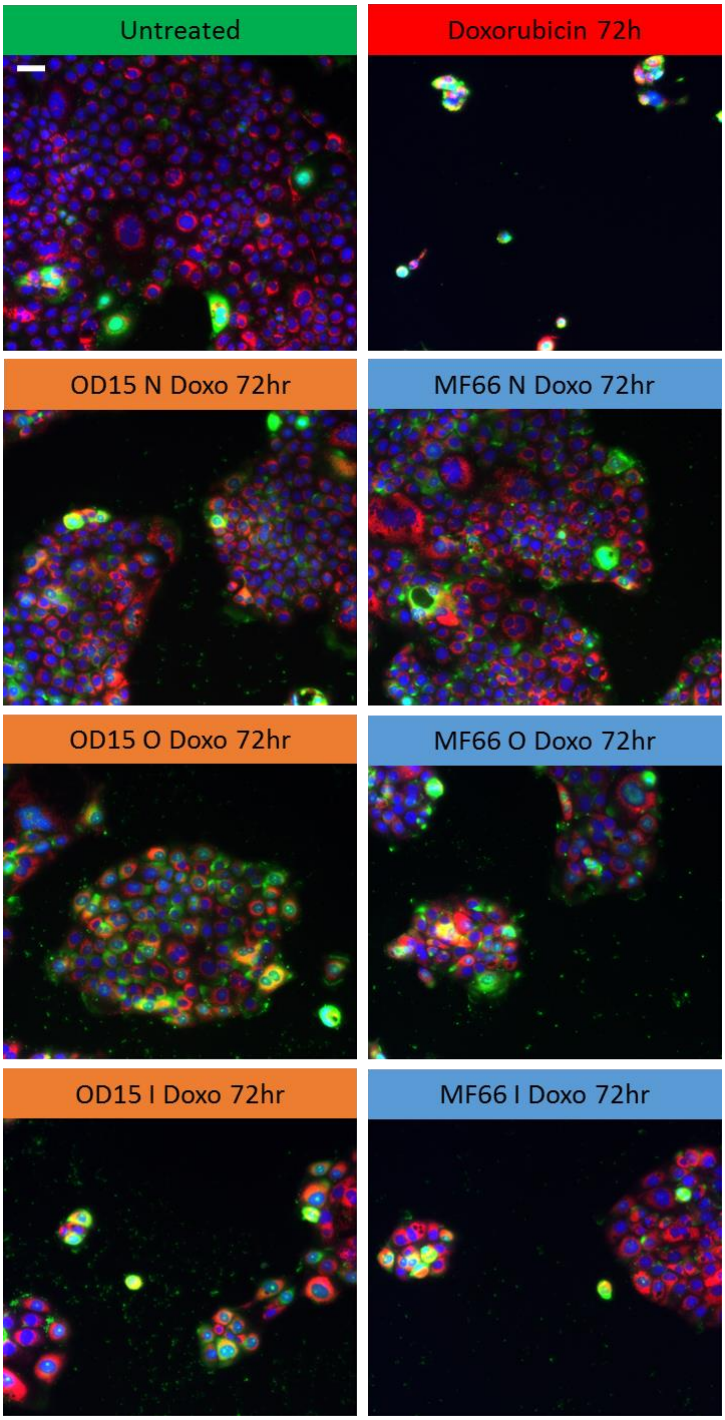

Figure 49: BxPC3 cell line exposed to doxorubicin and MNP formulations.

Representative images of the BxPC3 cell line exposed to doxorubicin functionalised MNP for 24h. Cells were stained with Hoechst 33342 (Blue), YO-PRO®-1 iodide: cell membrane permeability (Green) and Lysotracker® (Red). Doxorubicin (top right panel) caused substantial cell death compared to untreated control. OD15_I_Doxo and MF66_I_Doxo exposure provided the greatest anticancer effect following 72h exposure compared to N_Doxo and O_Doxo formulations. Scale bar (white line, top left of "Untreated" panel) = 50 µm, applicable to all images.

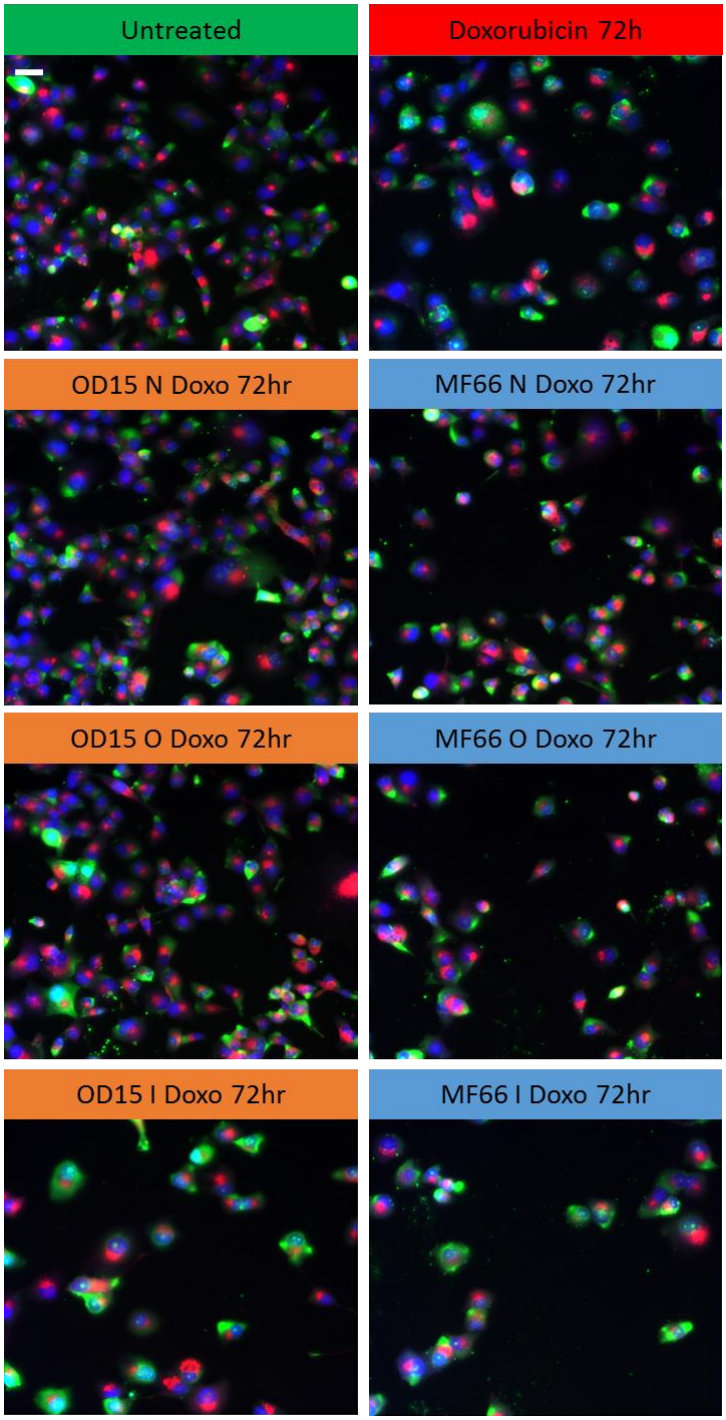

Figure 50: PANC-1 cell line exposed to doxorubicin and MNP formulations.

Representative images of the PANC-1 cell line exposed to doxorubicin functionalised MNP for 24h. Cells were stained with Hoechst 33342 (Blue), YO-PRO®-1 iodide: cell membrane permeability (Green) and Lysotracker® (Red). Doxorubicin (top right panel) caused substantial cell death compared to untreated control. OD15_I_Doxo and MF66_I_Doxo exposure provided the greatest anticancer effect following 72h exposure compared to N_Doxo and O_Doxo formulations. Scale bar (white line, top left of "Untreated" panel) = 50 µm, applicable to all images.

4.2.4 Anticancer effectiveness of N6L and N6L-MNP

HCSA was conducted using all five breast-derived cell lines to investigate the cytotoxic potential of free N6L, the effect of a new batch of OD15 and MF66, and the cytotoxic potential of the N6L functionalized MNP. The experiments sought to determine whether cytotoxicity can be induced in all cell lines with N6L exposure. The concentration of N6L present within 200 µg Fe/mL of delivered MNP is provided in Table 8. The results are presented as heatmaps for each cell line: MCF-7 in Figure 51; BT-474 in Figure 52, MDA-MB-231 in Figure 53, SK-BR-3 in Figure 54, and MCF-10A in Figure 55. All graphs are provided in Appendix 2.

Table 8: Quantity of N6L immobilized on MNP.

Delivery of 200 µg Fe/mL of all MNP and quantity of N6L present in delivered MNP load.

Name	pH	Particle size TEM (nm)	Hydrodynamic size (DLS; Intensity) (nm)	Surface charge at pH7 (mV)	N6L Quantity Delivered @ 200 µg Fe/mL (µM)
OD15	7.5	15.0	80.6	-46.0	N/A
OD15-N6L	7.5	15.0	95.8	-40.0	0.48
MF66	7.4	11.7	70.6	-42.2	N/A
MF66-N6L	7.3	11.7	104.2	-36.7	0.96

A range of N6L concentrations, from 5 µM to 80 µM was used. Cell count was reduced in the MCF-7 cell line at all concentrations, the MDA-MB-231 cell line was reduced at concentrations higher than 10 µM and in both the SK-BR-3 and MCF-10A cell lines reduction in cell count was observed at concentrations exceeding 20 µM. Cell membrane permeability was increased in the MDA-MB-231 cell line at 80 µM, in the SK-BR-3 cell line at all concentrations and in the MCF-10A cell line at concentrations over 40 µM.

OD15 MNP had no effect on the cell count of MCF-7, BT-474 and SK-BR-3 exposed cells, minor but statistically significant reduction in the MDA-MB-231 was observed at 25 µg/mL and above, and concentrations higher than 25 µg/mL in the MCF-10A cell line caused a reduction in cell count. Cell membrane permeability was increased in all cell lines apart from the BT-474 cell line, with the MCF-7 cell line having an increase at 10, 25 and 100 µg/mL, the MDA-MB-231 cell line at concentrations above 100 µg/mL, the SK-BR-3 with a minor increase at all concentrations and in the MCF-10A cell line at concentrations exceeding 50 µg/mL. Lysosomal intensity was increased in all cell lines apart from the MCF-10A's. MCF-7 cell line had an increase at concentrations above 100 µg/mL, the BT-474 and MDA-MB-231 cell lines at all concentrations, and the SK-BR-3 cell line at concentrations greater than 25 µg/mL. The MCF-10A cell line had a decrease in the lysosomal intensity at concentrations beyond 100 µg/mL.

OD15_N6L MNP exposure partially reduced cell count in the MDA-MB-231 cell line at concentrations greater than 25 µg/mL and in the SK-BR-3 cell line at 200 µg/mL. The most significant reduction in cell count was observed in the MCF-10A cell line at all concentrations. Cell membrane permeability was increased at 10 and 25 µg/mL in the MCF-7 cell line, at 200 µg/mL in the MDA-MB-231, at concentrations above 100 µg/mL in the SK-BR-3 and concentrations exceeding 50 µg/mL in the MCF-10A. The BT-474 cell line had slight reduction in cell membrane permeability at both 50 and 100

µg/mL concentrations. Lysosomal intensity was increased in all cell lines at all concentrations apart from the MCF-10A, where a reduction in intensity was observed at concentrations over 50 µg/mL.

MF66 MNP exposure caused a reduction in cell count in the MCF-7, MDA-MB-231 and MCF-10A cell lines at concentrations exceeding 50 µg/mL, and in the SK-BR-3 cell line at 200 µg/mL only. Cell membrane permeability was increased in the MCF-7 and MDA-MB-231 cell lines above 100 µg/mL and in the MCF-10A cell line at concentrations higher than 50 µg/mL. No change was observed in the cell membrane permeability of BT-474 and SK-BR-3 cell lines. The lysosomal intensity was increased in all cell lines, for the MCF-7, BT-474, MDA-MB-231 and MCF-10A this increase was significant at all concentrations while in the SK-BR-3 cell line an increase was observed with concentrations between 10 and 100 µg/mL.

MF66_N6L MNP exposure reduced cell count in the MCF-7 and BT-474 cell lines beyond 25 µg/mL, in the MDA-MB-231 cell line at concentrations greater than 50 µg/mL and at all concentrations in the MCF-10A cell line. Cell membrane permeability was increased in the MCF-7 cell line at concentrations exceeding 100 µg/mL, in the MDA-MB-231 cell line above 25 µg/mL and in the MCF-10A cell line at concentrations surpassing 50 µg/mL. No change was observed in the BT-474 and SK-BR-3 cell lines. Lysosomal intensity was increased in all cell lines at all concentrations.

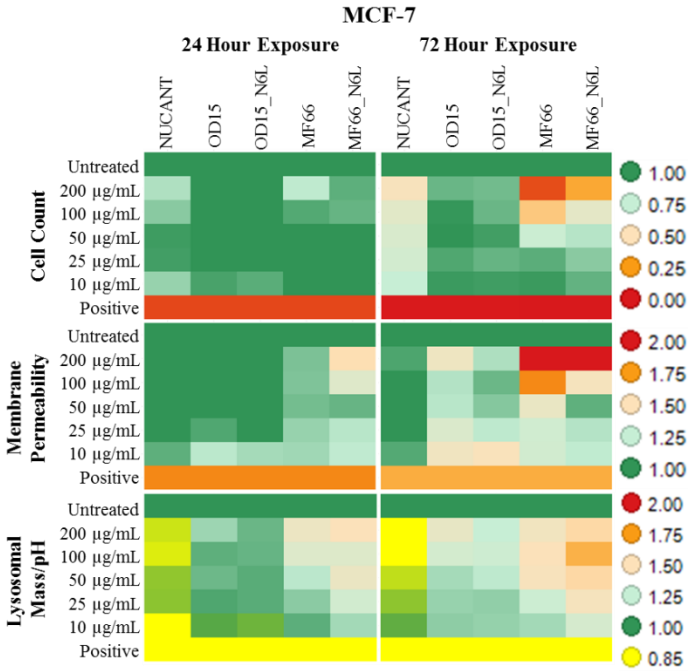

Figure 51: MCF-7 cell line exposed to N6L and N6L functionalized OD15 and MF66.

MCF-7 cells were exposed to free N6L, OD15 MNP, OD15_N6L, MF66 or MF66_N6L for 24h and 72h. Concentration of free N6L delivered: 5 µM, 10 µM, 20 µM, 40 µM and 80 µM. Concentration of delivered OD15/MF66 and N6L functionalized samples is provided. Positive control = 1µM CdSe QD.

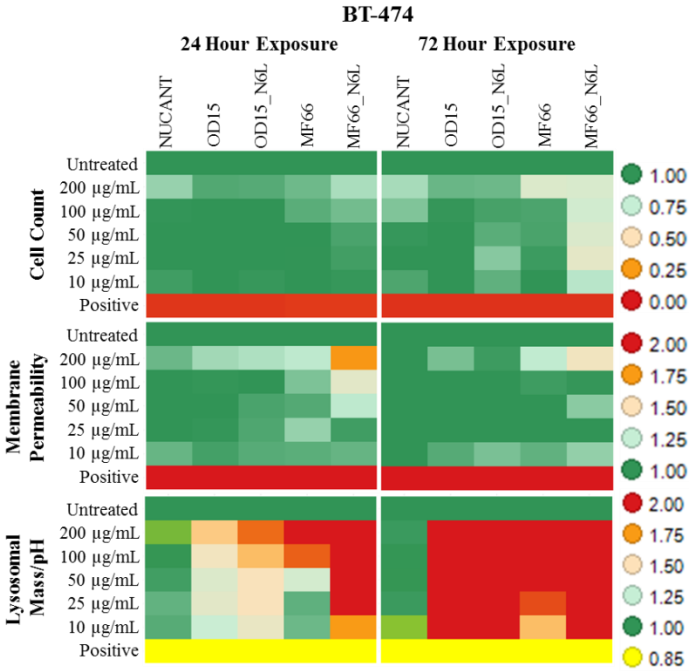

Figure 52: BT-474 cell line exposed to N6L and N6L functionalized OD15 and MF66.

BT-474 cells were exposed to free N6L, OD15 MNP, OD15_N6L, MF66 or MF66_N6L for 24h and 72h. Concentration of free N6L delivered: 5 µM, 10 µM, 20 µM, 40 µM and 80 µM. Concentration of delivered OD15/MF66 and N6L functionalized samples is provided. Positive control = 1µM CdSe QD.

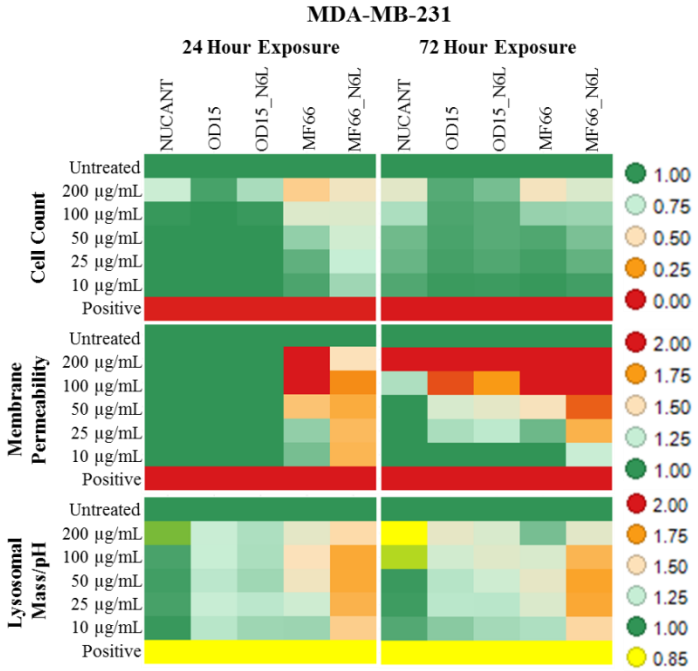

Figure 53: MDA-MB-231 cell line exposed to N6L and N6L functionalized OD15 and MF66.

MDA-MB-231 cells were exposed to free N6L, OD15 MNP, OD15_N6L, MF66 or MF66_N6L for 24h and 72h. Concentration of free N6L delivered: 5 µM, 10 µM, 20 µM, 40 µM and 80 µM. Concentration of delivered OD15/MF66 and N6L functionalized samples is provided. Positive control = 1µM CdSe QD.

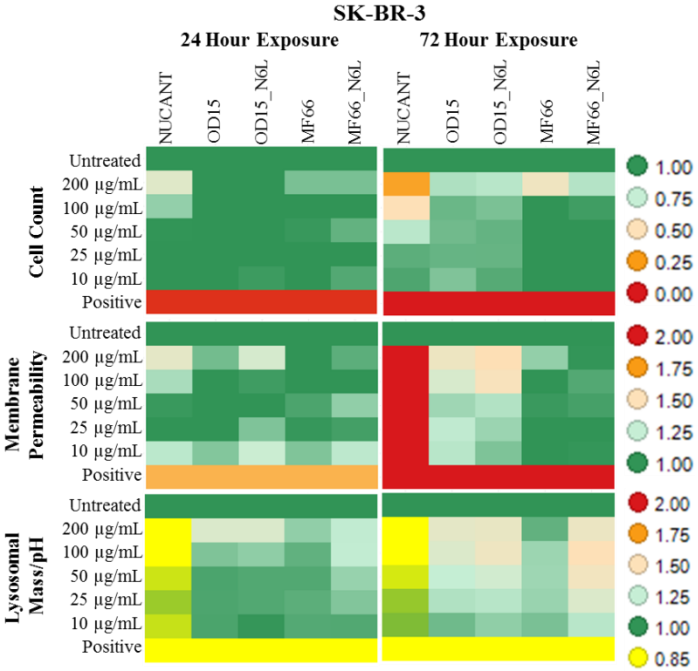

Figure 54: SK-BR-3 cell line exposed to N6L and N6L functionalized OD15 and MF66.

SK-BR-3 cells were exposed to free N6L, OD15 MNP, OD15_N6L, MF66 or MF66_N6L for 24h and 72h. Concentration of free N6L delivered: 5 µM, 10 µM, 20 µM, 40 µM and 80 µM. Concentration of delivered OD15/MF66 and N6L functionalized samples is provided. Positive control = 1µM CdSe QD.

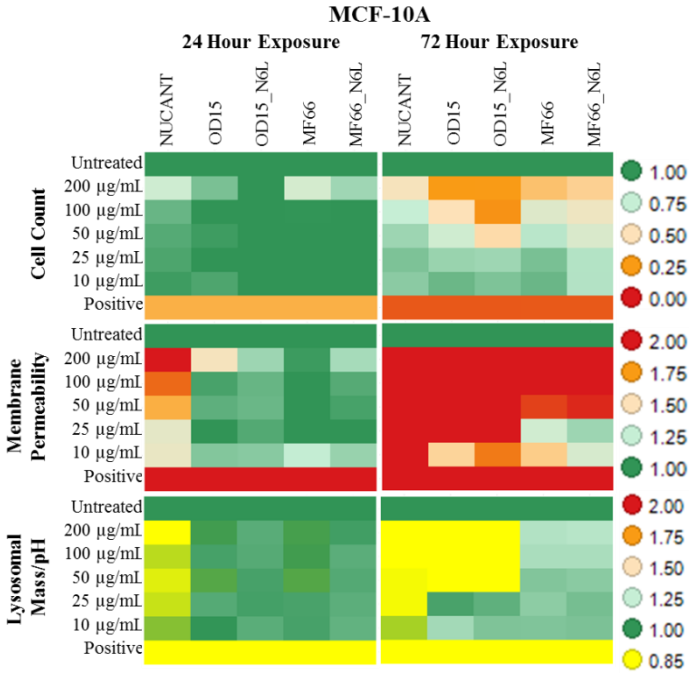

Figure 55: MCF-10A cell line exposed to N6L and N6L functionalized OD15 and MF66.

MCF-10A cells were exposed to free N6L, OD15 MNP, OD15_N6L, MF66 or MF66_N6L for 24h and 72h. Concentration of free N6L delivered: 5 µM, 10 µM, 20 µM, 40 µM and 80 µM. Concentration of delivered OD15/MF66 and N6L functionalized samples is provided. Positive control = 1µM CdSe QD.

4.2.5 N6L-MNP enhanced targeting and cellular uptake

The cytotoxicity testing in section 4.2.4 did not conclusively demonstrate that N6L had the capability to induce an anticancer effect when conjugated to the MNP. This was due in-part to the maximum delivered load being considerably less than the effective dose of free N6L pseudo-peptide. However, the mechanism of N6L binding to the surface of cells has been well documented [372, 393, 440, 441] and we have demonstrated previously that MNP are taken up by cells and this correlates with the lysosomal intensity parameter from HCSA. Here, the ability of N6L to mediate the uptake of MNP compared to MNP devoid of N6L was investigated and the degree of uptake comparing N6L-covalent and N6L-electrostatic functionalization strategies was evaluated. Since the 100 µg/mL concentration of MF66_N6L caused the greatest increase in lysosomal intensity for most cell lines, the same concentration was used to study the uptake of MNP in the following section. The details of the MNP used are provided in Table 9.

Table 9: Quantity of N6L immobilized on MNP.

Delivery of 100 µg Fe/mL of all MNP and quantity of N6L present in delivered MNP load.

Name	pH	Particle size TEM (nm)	Hydrodynamic size (DLS; Intensity) (nm)	Surface charge at pH7 (mV)	N6L Quantity Delivered @ 100 µg Fe/mL (µM)
MF66	6.8	11.7	80.0	-44.3	N/A
MF66-N6L Covalent	8	11.7	96.4	-37.8	0.4
MF66_N6L Electrostatic	6.5	11.7	153.3	-29.9	0.3

4.2.5.1 N6L mediated uptake of MNP into breast-derived cell lines

The Perls' Prussian blue assay is a sensitive assay for the detection of ferric iron and has a reported detection limit for intracellular MNP of approximately 1 µg/ml (1 ppm) [442]. The Perls' Prussian blue assay stained any ferric iron present an intense blue/black colour. Untreated cells of the MCF-7, MDA-MB-231 and MCF-10A cell lines were stained red only. All cell lines exposed to MF66 MNP were positive for uptake with the presence of blue staining within the cytosol. No staining was identified in the nuclear region and a consistent staining pattern around the outer nuclear membrane was observed. Comparison between the covalent and electrostatic N6L functionalization on the MF66 MNP demonstrated that the covalent formulation had a higher uptake in the MCF-7 (Figure 56) and MDA-MB-231 (Figure 57) cell lines. Staining was observed within the cytosol and for both formulations the degree of uptake exceed that of MNP alone. No nuclear staining was observed. The MDA-MB-231 cell line had extensive uptake of the covalent MF66_N6L formulation, with almost all cells having a cytoplasmic region stain positive for the presence of ferric iron. The MCF-10A (Figure 58) cell line differed from the breast cancer cell lines in that the degree of uptake comparing between the covalent and electrostatic N6L formulations did not differ, however, increased uptake was observed compared to MNP alone for both N6L formulations.

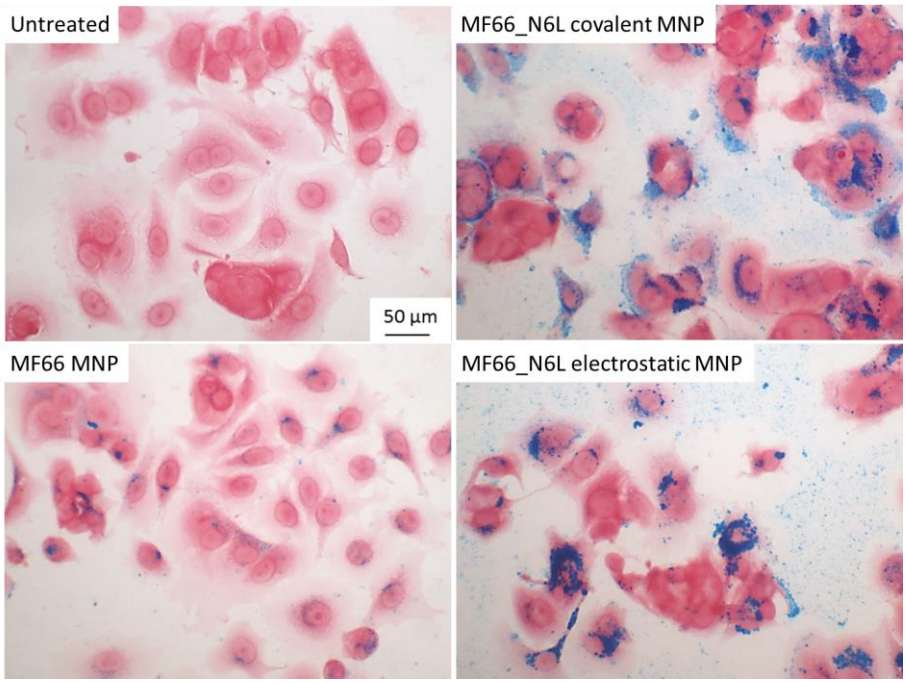

Figure 56: MCF-7 cell line exposed to N6L functionalized MF66.

Perls' Prussian blue staining demonstrating MF66_N6L uptake into MCF-7 cell line. Cells were exposed to 100 µg/mL of the indicated MNP for 24h, washed x3 with DPBS and stained by Perls' Prussian blue assay. Cell uptake was most pronounced for the covalently-functionalised MNP. Scale bar = 50 µm.

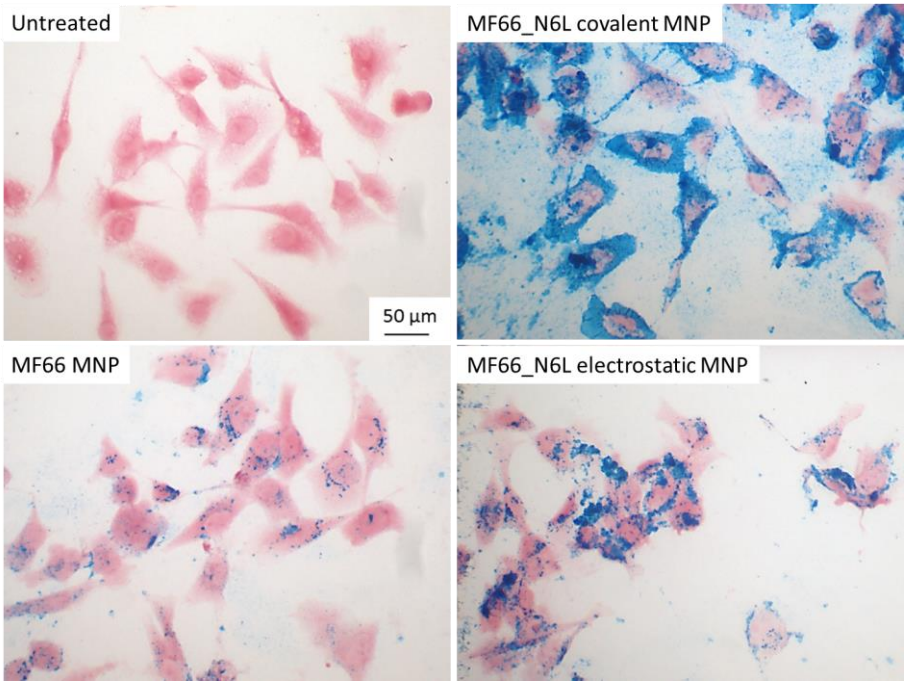

Figure 57: MDA-MB-231 cell line exposed to N6L functionalized MF66.

Perls' Prussian blue staining demonstrating MF66_N6L uptake into MDA-MB-231 cell line. Cells were exposed to 100 µg/mL of the indicated MNP for 24h, washed x3 with DPBS and stained by Perls' Prussian blue assay. Cell uptake was most pronounced for the covalently-functionalised MNP. Scale bar = 50 µm.

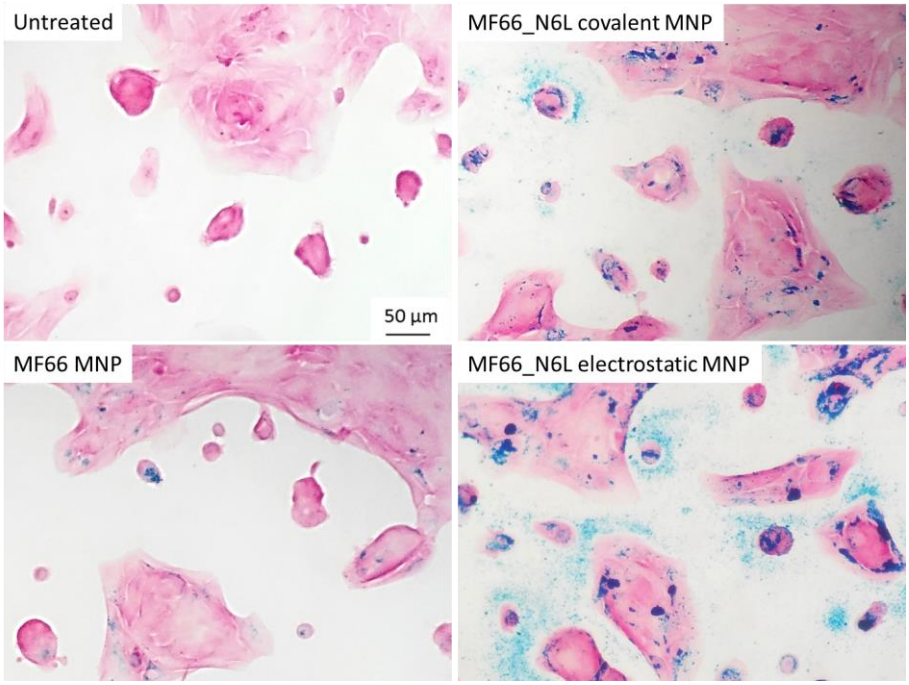

Figure 58: MCF-10A cell line exposed to N6L functionalized MF66.

Perls' Prussian blue staining demonstrating MF66_N6L uptake into MCF-10A cell line. Cells were exposed to 100 µg/mL of the indicated MNP for 24h, washed x3 with DPBS and stained by Perls' Prussian blue assay. Cell uptake was similar for both the covalently-functionalised and electrostatically-functionalised MNP. Scale bar = 50 µm.

4.2.5.2 N6L mediated uptake of MNP into established and primary pancreatic cells.

N6L-mediated MNP uptake into pancreatic cell lines and primary cells was carried out by Dr Sara Trabulo, Queen Mary University of London, England, as part of Multifun WP3 activities. Untreated cells of the BxPC3 and PANC-1 cell lines and the primary pancreatic cancer cells were stained red only. All cell lines exposed to MF66 MNP were positive for uptake with the presence of blue/black staining within the cytosol. Similar to the breast-derived cell lines, there was no staining in the nuclear region and a consistent staining pattern around the outer nuclear membrane was observed. Comparison between the covalent and electrostatic N6L functionalization on the MF66 MNP demonstrated that the uptake of covalent formulations in the BxPC3 (Figure 59), PANC-1 (Figure 60), 185 primary cells (Figure 61) and 354 primary cells (Figure 62) exceed that of the electrostatic formulations. Staining was observed within the cytosol and for both N6L-MNP formulations the degree of uptake was more than MNP alone. No nuclear localisation was observed in either the established cell lines or primary cells. Similar to the breast cancer cell lines, the pancreatic cells had a higher degree of uptake with the covalent MF66_N6L formulation compared to electrostatic MF66_N6L.

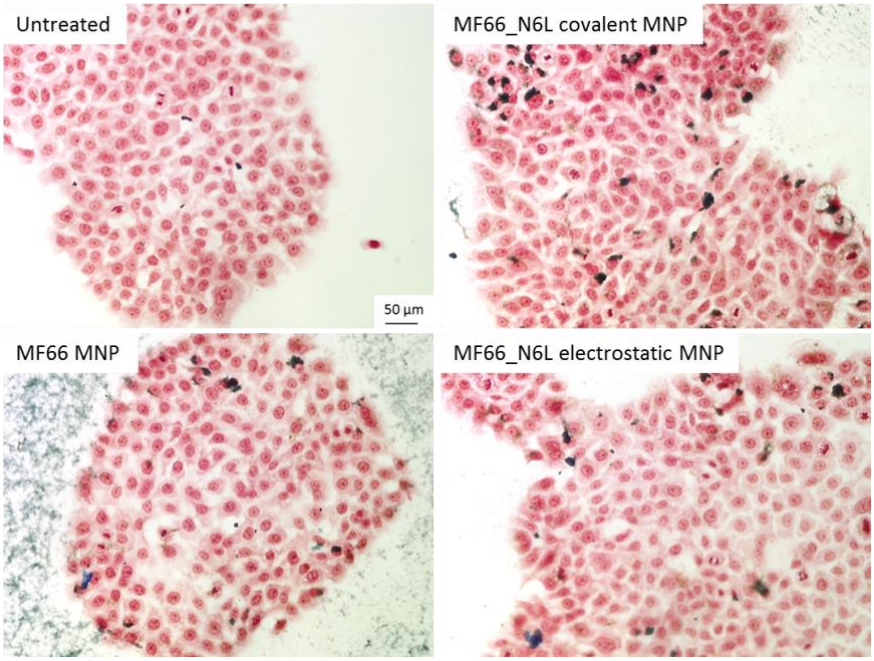

Figure 59: BxPC3 cell line exposed to N6L functionalized MF66.

Perls' Prussian blue staining demonstrating MF66_N6L uptake into BxPC3 cell line. Cells were exposed to 100 µg/mL of the indicated MNP for 24h, washed x3 with DPBS and stained by Perls' Prussian blue assay. Images courtesy of Dr Sara Trabulo, Queen Mary University of London, England. Cell uptake was most pronounced for the covalently-functionalised MNP. Scale bar = 50 µm.

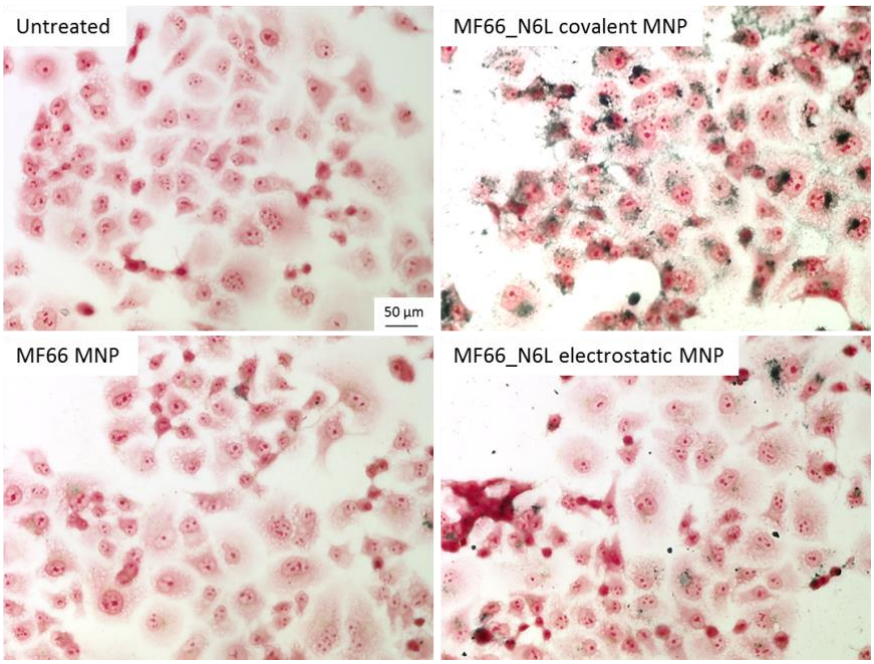

Figure 60: PANC-1 cell line exposed to N6L functionalized MF66.

Perls' Prussian blue staining demonstrating MF66_N6L uptake into PANC-1 cell line. Cells were exposed to 100 µg/mL of the indicated MNP for 24h, washed x3 with DPBS and stained by Perls' Prussian blue assay. Images courtesy of Dr Sara Trabulo, Queen Mary University of London, England. Cell uptake was most pronounced for the covalently-functionalised MNP. Scale bar = 50 µm.

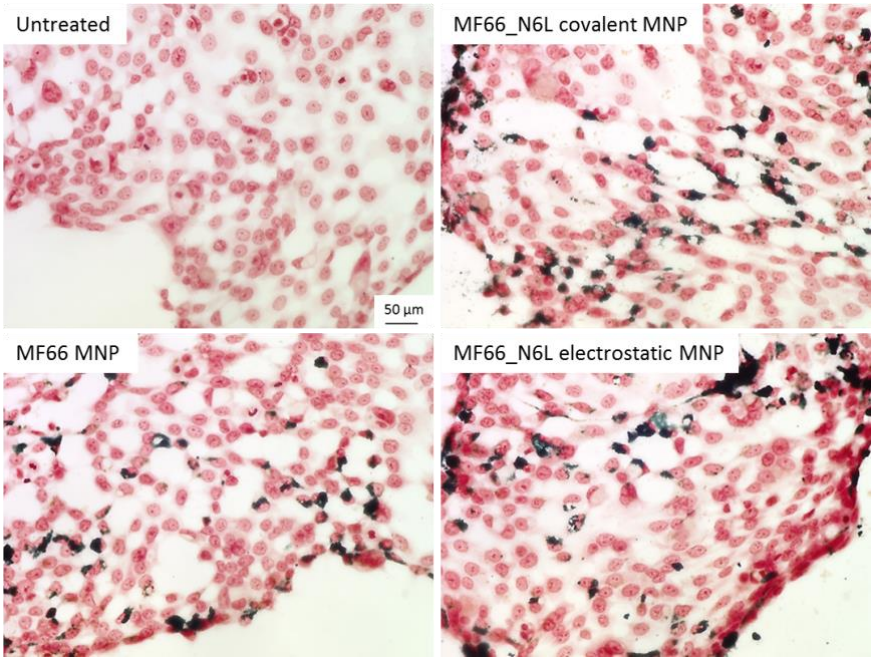

Figure 61: 185 primary pancreatic cancer cells exposed to N6L functionalized MF66.

Perls' Prussian blue staining demonstrating MF66_N6L uptake into 185 primary pancreatic cancer cells. Cells were exposed to 100 µg/mL of the indicated MNP for 24h, washed x3 with DPBS and stained by Perls' Prussian blue assay. Images courtesy of Dr Sara Trabulo, Queen Mary University of London, England. Cell uptake was most pronounced for the covalently-functionalised MNP. Scale bar = 50 µm.

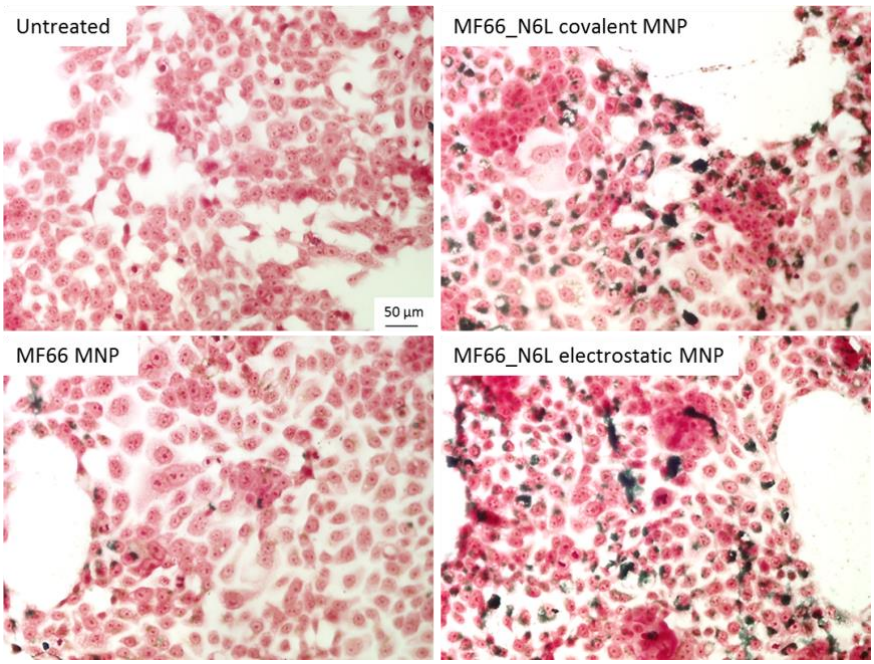

Figure 62: 354 primary pancreatic cancer cells exposed to N6L functionalized MF66.

Perls' Prussian blue staining demonstrating MF66_N6L uptake into 354 primary pancreatic cancer cells. Cells were exposed to 100 µg/mL of the indicated MNP for 24h, washed x3 with DPBS and stained by Perls' Prussian blue assay. Images courtesy of Dr Sara Trabulo, Queen Mary University of London, England. Cell uptake was most pronounced for the covalently-functionalised MNP. Scale bar = 50 µm.

4.2.6 Anticancer potential of gemcitabine and N6L multi-functionalised MNP

The treatment of both late stage breast and pancreatic cancers involves a diverse range of chemotherapeutic drugs either as stand-alone treatment options or, most commonly, a combination with one or more drugs. Therefore we have studied the cytotoxic potential of the gemcitabine drug (Gemzar), routinely used in both breast and pancreatic cancer treatment, and employed the nanomaterials platform developed to determine the efficacy of MNP compared to free drug treatments. The MNP supplied for testing are detailed in Table 10, with results displayed as heatmaps for each cell line: MCF-7 (Figure 63), MCF-10A (Figure 64), BxPC3 (Figure 65) and PANC-1 (Figure 66). All graphs with statistical significance are available in Appendix 2. The linker used to attach the gemcitabine to the MNP was the same as presented for imino-Doxorubicin nanoparticles, and for N6L the linker contained a disulfide group for release in a reducing environment.

Table 10: Details of MNP containing covalently functionalised gemcitabine drug +/- N6L.
Nanomaterials were supplied as suspensions in water at the indicated pH. Core particle size was determined by TEM, and hydrodynamic size by DLS. All nanoparticles were negatively charged ranging between –23.4 mV to 49.7 mV. Concentrations supplied were consistently 2.4 mg Fe/mL with the indicated concentration of gemcitabine drug attached. Total MNP concentration to deliver specified drug load is provided and the concentration of N6L present on MNP is provided.

Name	pH	TEM (nm)	Hydrodynamic size (DLS; Intensity) (nm)	Surface charge at pH7 (mV)	Gem/N6L loaded (µmol/g Fe)	MNP conc. @1600/800 nM (µg/mL)	N6L conc. @ MNP conc. (µM)
OD15	7.4	15.0	59.4	-49.7	N/A	N/A	N/A
OD15_Gem	7.4	15.0	73.9	-48.9	35/0	45.71/22.85	N/A
OD15_ N6L_Gem	8.1	15.0	203.6	-26.8	35/4	45.71/22.85	0.18/0.09
MF66	7.4	11.7	70.6	-42.2	N/A	N/A	N/A
MF66_Gem	7.4	11.7	114.1	-23.4	19/0	84.2/42.1	N/A
MF66_ N6L_Gem	8.1	11.7	220.0	-34.8	19/3	84.2/42.1	0.34/0.17

The concentration of Gemcitabine delivered to the breast-derived cell lines was 1600, 800, 400, 200, and 100 nM concentrations and the pancreatic cancer cell lines were exposed to 800, 400, 200, 100 and 50 nM. The clinical dose of gemcitabine for treatment of breast cancer is higher (1250 mg/m2) than the dose used for pancreatic cancer treatment (1000 mg/m2) [443], therefore in the following experiments, the dose used for the multi-functionalised MNP evaluation in the pancreatic cancer cell lines did not exceed that used in the breast-derived cell lines.

Gemcitabine exposure reduced cell count in all cell lines at all concentrations tested at the 72h timepoint. Cell membrane permeability was increased in all cell lines at all concentrations and lysosomal intensity was decreased at all concentrations in the MCF-7, MCF-10A and PANC-1 cell line. Lysosomal intensity increase was observed in the BXPC3 cell lines with all concentrations.

OD15 MNP exposure at 72h caused a slight decrease with all concentrations in the MCF-10A cell line of approximately 5%. An increase in cell count was recorded in the MCF-7 cell line at the 50 µg/mL concentration only, while a decrease was observed in the BxPC3 cell line at 200 µg/mL. Cell

membrane permeability was decreased at 50 µg/mL in the MCF-7 cell line, and in the PANC-1 cell line a decrease was observed with the 10 and 25 µg/mL concentrations while an increase was recorded at 200 µg/mL. Lysosomal intensity was increased in the MCF-7 and BxPC3 cell lines at 50 µg/mL concentration only.

OD15_Gem MNP exposure at 72h caused a reduction in cell count in all cell lines. The MCF-7 and MCF-10A had significant cell count reduction at all concentrations. An increase was observed in the BxPC3 cell line at 100 nM while there was a decrease at 800 nM. A decrease in the PANC-1 cell line was observed for concentrations above 400 nM. Cell membrane permeability was increased with all concentrations in the MCF-10A cell line at 72h only. Lysosomal intensity increased in the MCF-10A cell line at 24h but at 72h there was a decrease observed at all concentrations. The BxPC3 cell line displayed a marginal increase in lysosomal intensity at the 72h time point with the 800 nM concentration.

OD15_N6L_Gem MNP exposure at 72h caused a reduction in cell count in all cell lines at all concentrations. Cell membrane permeability was increased in all cell lines at concentrations exceeding 800 nM in the MCF-7 and MCF-10A cell lines, at concentrations above 100 nM in the BxPC3 cell line and at the 800 nM concentration in the PANC-1 cell line. Lysosomal intensity was increased in all cell lines, at all concentrations in the MCF-7 cell line, at 100, 200 and over 800 nM in the MCF-10A cell line, at concentrations greater than 100 nM in the BxPC3 and at the 100 nM concentration in the PANC-1 cell line. The increase observed in the MCF-10A cell line at 72h was less than that observed at 24h, where all concentrations caused an increase in lysosomal intensity to be recorded.

MF66 MNP exposure at 72h resulted in a decrease in cell count at the highest concentration of 200 µg/mL in the MCF-10A, BxPC3 and PANC-1 cell lines. Cell permeability was decreased at all concentration in the MCF-10A, increased at the 200 µg/mL concentration in the BxPC3 and increased at concentrations above 100 µg/mL in the PANC-1 cell line. Lysosomal intensity was increased between 10 and 50 µg/mL in the MCF-7, at concentrations higher than 50 µg/mL in the MCF-10A and at 200 µg/mL in the BxPC3 cell line. There was a decrease in lysosomal intensity recorded at the 200 µg/mL concentration in the PANC-1 cell line.

MF66_Gem MNP exposure at 72h caused a reduction in cell count in all cell lines except for the PANC-1 cell line. Cell count reduction was recorded in the MCF-7 and MCF-10A at all concentrations and in the BxPC3 at 800 nM. Cell membrane permeability was increased in the MCF-7 and MCF-10A cell lines at all concentrations with no increase observed in the pancreatic cancer cell lines. Lysosomal intensity was not affected in the MCF-7 cell line at the 72h time point. There was an increase in intensity observed in the MCF-10A cell line at concentrations above 800 nM at the 72h time point, while at the 24h time point all concentrations caused an increase in lysosomal intensity by approximately 40% compared to untreated control. An increase was also observed in the BxPC3 cell line at concentrations exceeding 400 nM (approximately 25% increase compared to untreated control), and in the PANC-1 cell line at the 200 nM concentration only.

MF66_N6L_Gem MNP exposure at 72h caused a decrease in cell count in all cell lines, with the MCF-7 and MCF-10A displaying a decrease at all concentrations, and the BxPC3 and PANC-1 cell lines at concentrations above 400 nM. Cell membrane permeability was increased in all cell lines, with an increase observed with all concentrations in the MCF-7 and MCF-10A cell lines. An increase was

observed in both the BxPC3 and PANC-1 at the highest concentration of 800 nM. Lysosomal intensity was increased in all cell lines. In the MCF-7 cell line a significant increase was observed at concentrations exceeding 200 nM, in the MCF-10A at concentrations over 400 nM, in the BxPC3 cell line at concentrations greater than 400 nM (approximately 60% increase compared to untreated control) and in the PANC-1 cell line at 800 nM.

Representative pseudo-coloured merged images of all four cell lines tested and stained for multiparametric analysis are provided in Figure 67 (MCF-7), Figure 68 (MCF-10A), Figure 69 (BxPC3), and Figure 70 (PANC-1).

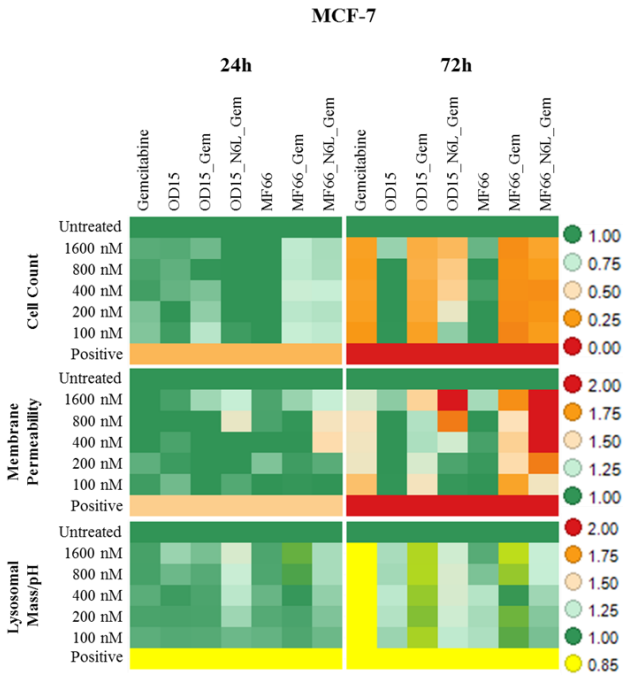

Figure 63: MCF-7 cell line exposed to Gem and N6L-Gem functionalized OD15 and MF66.
MCF-7 cells were exposed to gemcitabine and the indicated MNP formulations for 24h and 72h. Concentration of basic MNP: 200, 100, 50, 25, 10 µg/mL. Gemcitabine concentration is provided on heatmap. N6L-mediated MNP uptake observed by increase in lysosomal mass/pH parameter. Positive control = 1µM CdSe QD.

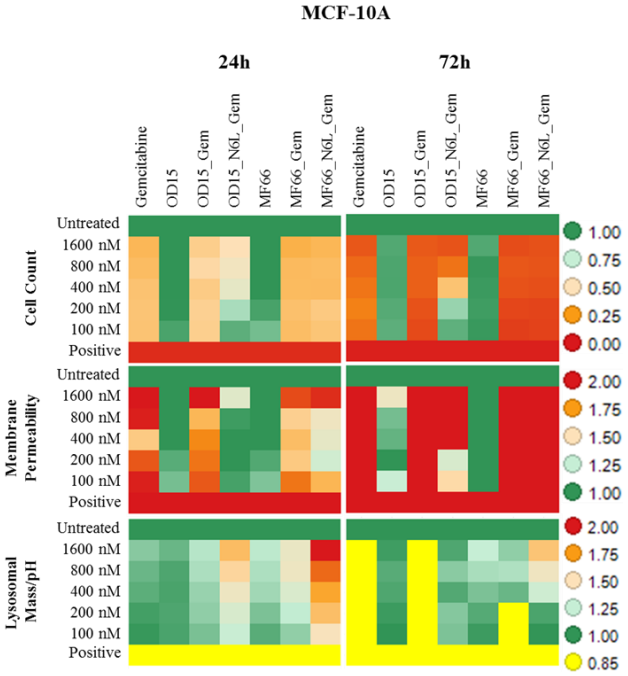

Figure 64: MCF-10A cell line exposed to Gem and N6L-Gem functionalized OD15 and MF66.
MCF-10A cells were exposed to gemcitabine and the indicated MNP formulations for 24h and 72h. Concentration of basic MNP: 200, 100, 50, 25, 10 µg/mL. Gemcitabine concentration is provided on heatmap. N6L-mediated MNP uptake observed by increase in lysosomal mass/pH parameter. Positive control = 1µM CdSe QD.

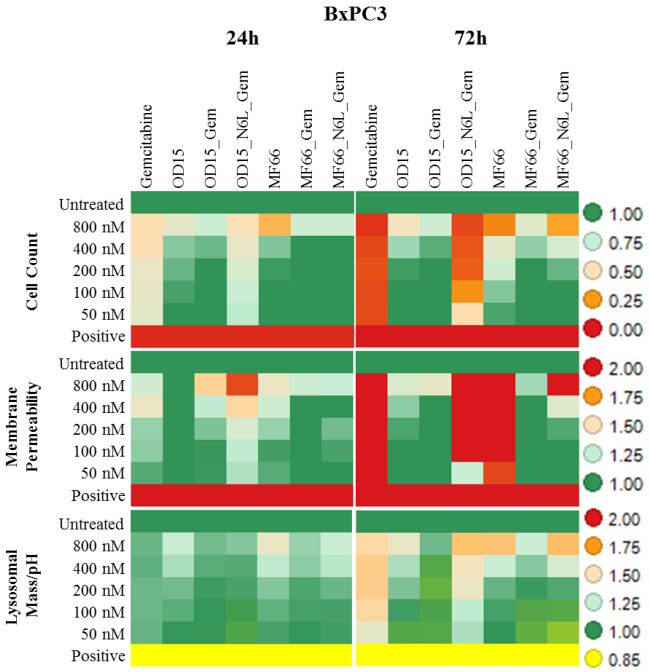

Figure 65: BxPC3 cell line exposed to Gem and N6L-Gem functionalized OD15 and MF66.

BxPC3 cells were exposed to free Gemcitabine (Gem), OD15 MNP, OD15_Gem, OD15_N6L_Gem, MF66, MF66_Gem or MF66_N6L_Gem for 24h and 72h. Concentration of basic MNP: 200, 100, 50, 25, 10 µg/mL. Concentration of delivered Gemcitabine concentration is provided on heatmap. N6L-mediated MNP uptake observed by increase in lysosomal mass/pH parameter. Positive control = 1µM CdSe QD.

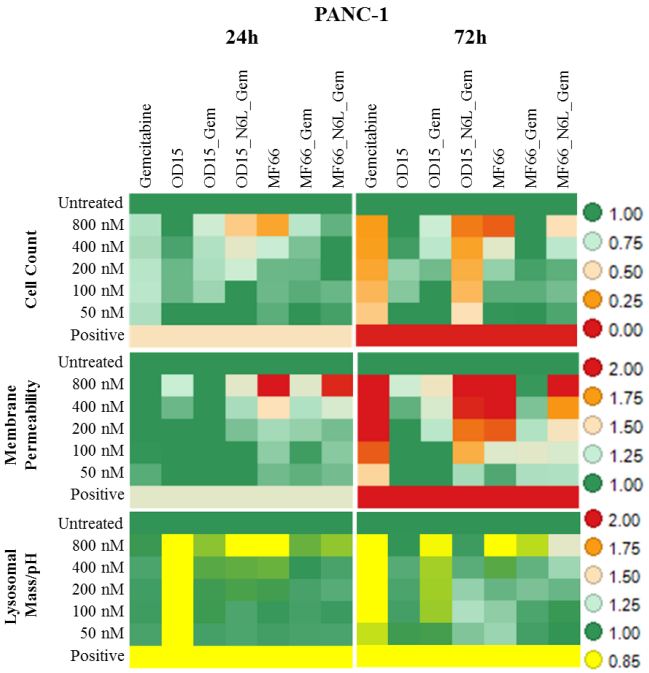

Figure 66: PANC-1 cell line exposed to Gem and N6L-Gem functionalized OD15 and MF66.

PANC-1 cells were exposed to free Gemcitabine (Gem), OD15 MNP, OD15_Gem, OD15_N6L_Gem, MF66, MF66_Gem or MF66_N6L_Gem for 24h and 72h. Concentration of basic MNP: 200, 100, 50, 25, 10 µg/mL. Concentration of delivered Gemcitabine concentration is provided on heatmap. N6L-mediated MNP uptake observed by increase in lysosomal mass/pH parameter. Positive control = 1µM CdSe QD.

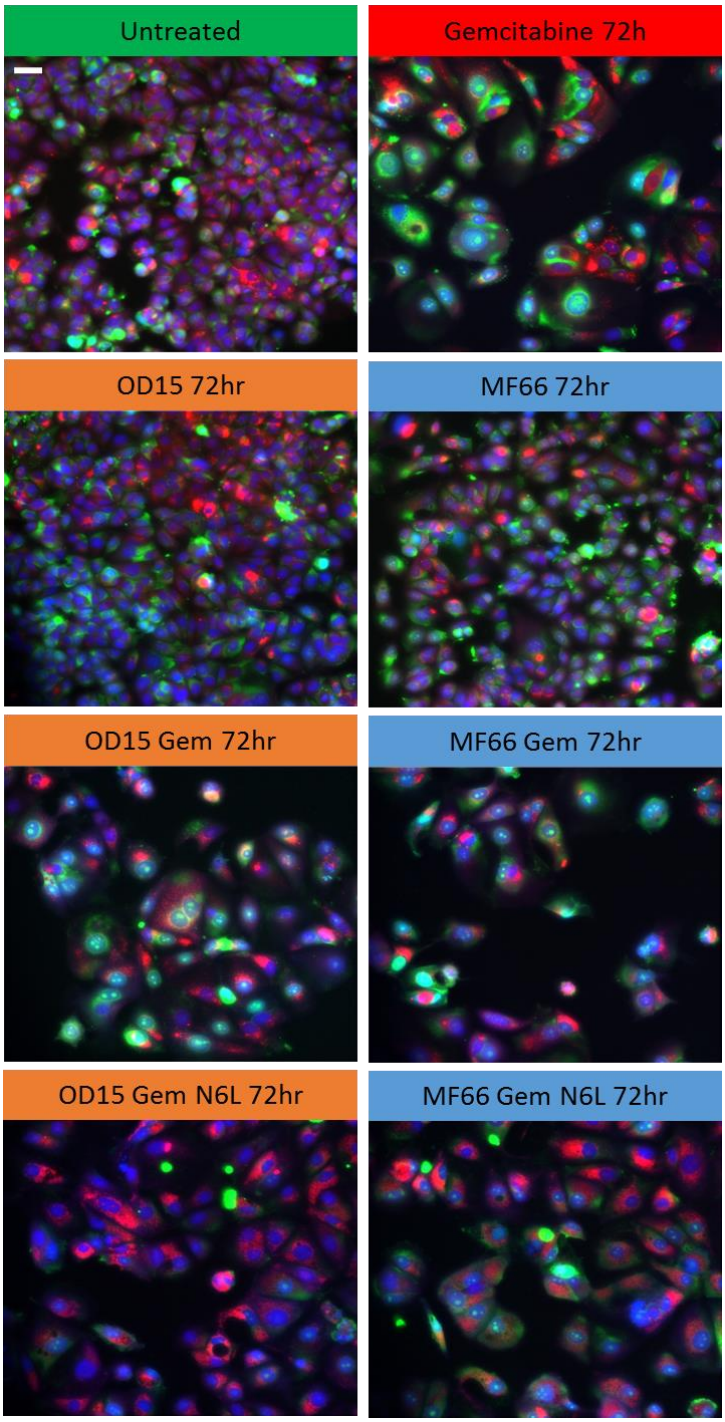

Figure 67: MCF-7 cell line exposed to gemcitabine and MNP formulations.

Representative images of the MCF-7 cell line exposed to gemcitabine functionalised MNP for 24h. Cells were stained with Hoechst 33342 (Blue), YO-PRO®-1 iodide: cell membrane permeability (Green) and Lysotracker® (Red). Gemcitabine (top right panel), OD15_Gem, OD15_N6L_Gem, MF66_Gem and MF66_N6L_Gem caused substantial cell death compared to untreated control. Scale bar (white line, top left of "Untreated" panel) = 50 µm, applicable to all images.

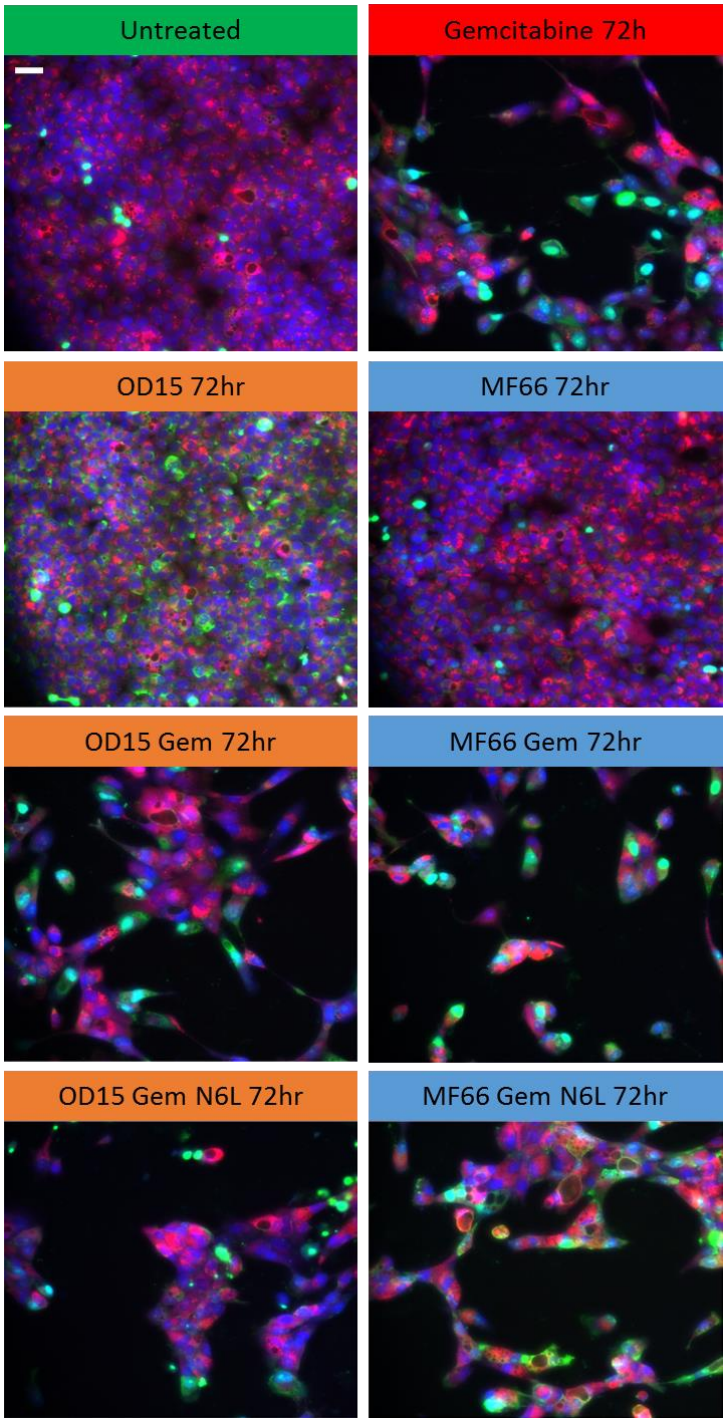

Figure 68: MCF-10A cell line exposed to gemcitabine and MNP formulations.

Representative images of the MCF-10A cell line exposed to gemcitabine functionalised MNP for 24h. Cells were stained with Hoechst 33342 (Blue), YO-PRO®-1 iodide: cell membrane permeability (Green) and Lysotracker® (Red). Gemcitabine (top right panel), OD15_Gem, OD15_N6L_Gem, MF66_Gem and MF66_N6L_Gem caused substantial cell death compared to untreated control. Scale bar (white line, top left of "Untreated" panel) = 50 µm, applicable to all images.

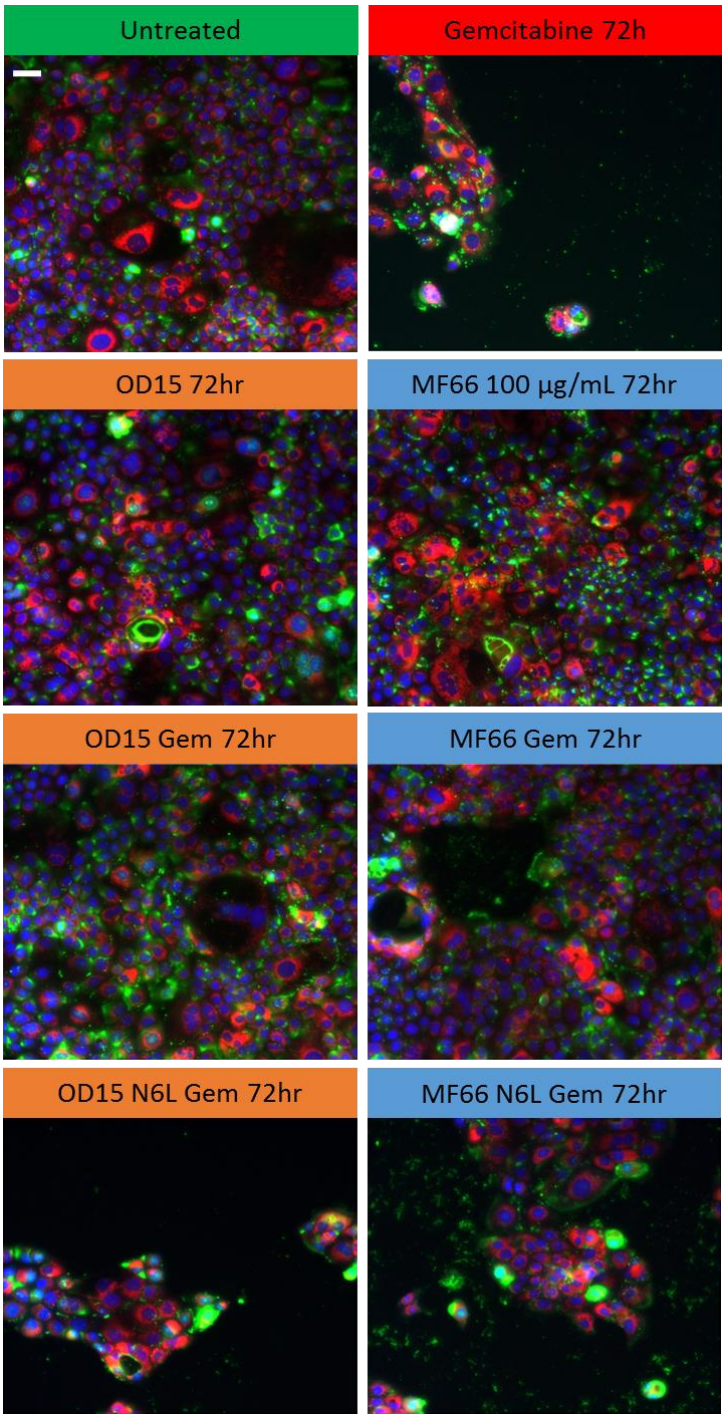

Figure 69: BxPC3 cell line exposed to gemcitabine and MNP formulations.

Representative images of the BxPC3 cell line exposed to gemcitabine functionalised MNP for 24h. Cells were stained with Hoechst 33342 (Blue), YO-PRO®-1 iodide: cell membrane permeability (Green) and Lysotracker® (Red). Gemcitabine (top right panel) caused substantial cell death compared to untreated control. OD15_Gem, OD15_N6L_Gem, MF66_Gem and MF66_N6L_Gem caused cell death at the highest concentration (800 nM). MNP formulations containing N6L displayed the greatest anticancer effect. Scale bar (white line, top left of "Untreated" panel) = 50 µm, applicable to all images.

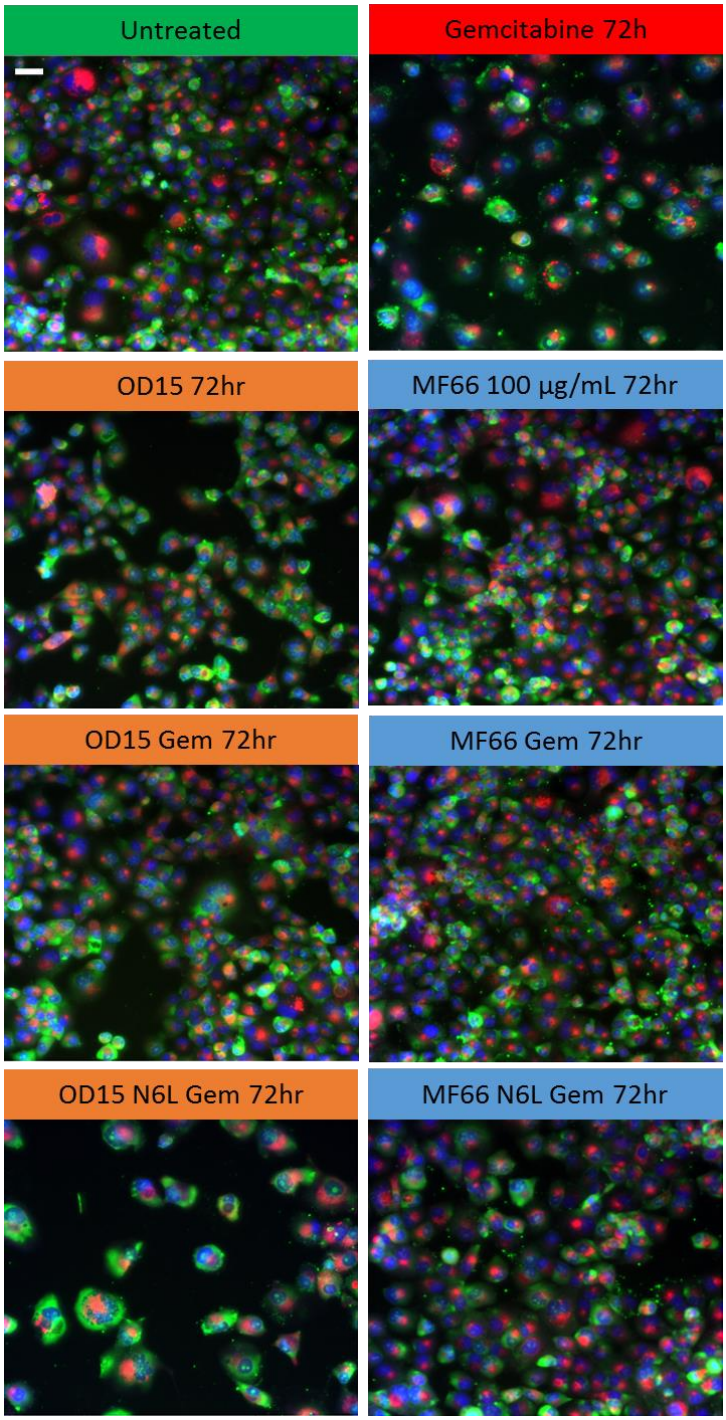

Figure 70: PANC-1 cell line exposed to gemcitabine and MNP formulations.

Representative images of the PANC-1 cell line exposed to gemcitabine functionalised MNP for 24h. Cells were stained with Hoechst 33342 (Blue), YO-PRO®-1 iodide: cell membrane permeability (Green) and Lysotracker® (Red). Gemcitabine (top right panel) caused substantial cell death compared to untreated control. OD15_Gem MNP exposure caused slight cell count reduction, OD15_N6L_Gem and MF66_N6L_Gem exposure caused substantial cell death following 72h exposure. Scale bar (white line, top left of "Untreated" panel) = 50 µm, applicable to all images.

4.3 Discussion

In this part of the study, the comparison of doxorubicin electrostatically and covalently functionalized MNP was carried out. In addition, the cytotoxicity testing of the N6L pseudo-peptide followed by the capability of N6L to increase the uptake of MNP into model cell lines and primary pancreatic cells was tested. Finally, multi-functional MNP containing the N6L targeting peptide and gemcitabine chemotherapy drug were tested.

MNP electrostatically and covalently functionalised with doxorubicin drug were examined by HCSA, to measure their anticancer efficacy, compared to free doxorubicin drug control. Both functionalisation approaches produced MNP that were stable in aqueous solution and had the potential to deliver an anticancer agent whose effect could be measured. TEM analysis presented in the previous chapter has shown that the MNP are present inside the cells within 0.5h following exposure, but this does not infer that all MNP dispersed in the medium will ultimately enter all cells, and especially enter to such a degree as to induce an anticancer response, which is both time dependent and concentration dependent. Whilst it has been shown that the MNP are present within multivesicular lysosomal vesicles 12h post exposure (Figure 33, chapter 3), the time between drug release from the MNP and initiation of a measurable effect from the action of the drug must be identified. To address this, the effect of doxorubicin drug was firstly tested on three of the cell lines used in this study to identify the effective concentration range and measure the degree of response at two time points (Figure 38). MCF-7, MDA-MB-231 and MCF-10A cell lines were tested at 24h and 72h and exposed to eight concentrations of doxorubicin (25 nM to 2600 nM). Cell count was considerably reduced at the 72h time point at all concentrations greater than 25 nM. This was accompanied by an increase in membrane permeability. The doxorubicin drug caused a reduction in lysosomal mass/pH in all cell lines at approximately 200 nM and above. A possible explanation for these observations can be tied to the currently known mode of action for doxorubicin. Doxorubicin passively diffuses through the cell and nuclear membranes, where it can intercalate with DNA. The cells exposed to the drug were unsynchronised, and with doubling times of 20h, 24h and 29h for the MCF10A, MDA-MB-231 and MCF-7 respectively, the results obtained were as expected, whereby the MCF-10A cell line displays the highest effect compared to the slower growing MCF-7 cell line. The exact mechanism of action for doxorubicin is heavily debated, even though it has been in the clinic for over four decades. Studies have shown that doxorubicin could stimulate the *de novo* synthesis of ceramide which results in the activation and cleavage of CREB3L1 which migrates to the nucleus and acts as a transcriptional activator for cell cycle repressors [444], and is capable of binding to both AT and CG rich regions of DNA [445]. Therefore the results observed for free doxorubicin could be due to a number of complementary mechanisms.

Firstly, direct binding of doxorubicin to DNA can present as a physical transcriptional block, preventing the unwinding of DNA at the replication fork due to DNA conformational changes [446].

Secondly, doxorubicin has been shown extensively to interact with and inhibit the function of topoisomerase II enzyme, thus preventing the unwinding of DNA through the inability to relax the stress of supercoiled DNA (Reviewed in [447]).

Thirdly, doxorubicin and other anthracycline drugs have been shown to induce protein:DNA crosslinking, with the topoisomerase II enzyme shown to covalently bind DNA in the presence of anthracycline drugs, such as doxorubicin [448].

Fourthly, doxorubicin has been extensively shown to induce ROS production and mitochondrial ROS generation [449], which could be the reason for the observed lipid peroxidation by doxorubicin [450].

Fifthly, doxorubicin treatment has been shown to induce the production of the tumour suppressor gene p53, which accounts for cells undergoing apoptosis following doxorubicin exposure [451, 452].

Our results demonstrate that doxorubicin exposure effectively reduces cell count compared to untreated control, and causes an increase in cell membrane permeability and decrease in lysosomal mass/pH which could be due to doxorubicin-mediated lipid peroxidation. Due to experimental time constraints the induction of ROS by free doxorubicin and doxorubicin-functionalised MNP was not investigated, however, future work would benefit with the analysis of ROS either directly via the production of reactive molecules such as hydrogen peroxide and nitric oxide or indirectly by measuring oxidative stress via the induction of antioxidants (glutathione peroxidase, catalase, and superoxide dismutase) [453].

Drug resistance is a major factor in the failure of chemotherapy, and with an increasing prevalence of multi-drug resistant tumours, it has become a real challenge to effectively treat such cancers. Combination therapies have been suggested as the best approach in treating cancers that develop resistance [454], but resistance can also be avoided through the evasion of elements of the resistance mechanism such as the membrane transporters. It has been shown that doxorubicin conjugated to a solid nanoparticle delivery system has the capacity to evade the P-glycoprotein membrane transporter-mediated drug export when released from the nanoparticle surface inside lysosomes [455]. This further demonstrates the usefulness of a nanoparticle based delivery mechanism over conventional methods.

Electrostatically functionalized MNP induced greater cell count reduction and membrane permeability increase compared to the covalently functionalized MNP in this study. Cell count was considerably reduced 80% compared to 50% for covalently functionalized MNP. However, it cannot be guaranteed that the electrostatically functionalized MNP release their drug payload in a controlled manner, thus presenting a situation whereby free chemotherapeutic drug is interacting with cells alongside the basic MNP formulation. An explanation for the pronounced anticancer effect observed for the electrostatic formulation could be attributed to the high salt medium environment causing premature release of the conjugated drug. As demonstrated by Kossatz et al. using the electrostatic MF66_N6L_Doxorubicin MNP, the incubation of these MNP with PBS or complete medium caused rapid release of up to 30% of doxorubicin within minutes of dispersion, with maximal release recorded at 80 h of 78% and 64% respectively [354]. For this reason, the covalent functionalization strategy was considered the most appropriate route for functionalization as the electrostatic route, if delivered systemically, could rapidly lose its functionalized drug through desorption. While the electrostatic MNP formulations would not be suitable for systemic drug delivery, they were retained for the purpose of hyperthermia treatment where MNP are delivered by direct injection into a tumour xenograft model and heated by placing into an alternating magnetic field, as described in our joint publication with Kossatz et al. [354].

HCSA was used to validate a range of doxorubicin covalently functionalized MNP. Covalent attachment of doxorubicin to the OD15 and MF66 nanoparticles was facilitated by means of a linker molecule directly bound to the drug and attached via a disulphide bridge to the DMSA thiol group on the MNP surface (Figure 41), conducted by Dr Pierre Couleaud (IMDEA, Madrid, Spain). The efficacy of each formulation containing distinct linker molecules was examined by HCSA and compared to free doxorubicin

drug treatment. The results demonstrate that the specific linker through which the chemotherapeutic drug is attached to the MNP can influence the response *in vitro*, even though in a reducing environment (N_ and O_Doxorubicin) as demonstrated by Latorre et al. [424], and in low pH (I_Doxorubicin), the drug is designed to be released unmodified as presented in Figure 42.

Testing was carried out in the first instance using the basic MNP at the extended exposure time of 72h. No reduction in cell count occurred with any concentration of OD15 and MF66 delivered (between 10 and 200 µg/mL) in the MCF-7 and MCF-10A cell lines, with reduction observed at the highest concentration (200 µg/mL) for OD15 and MF66 in the BxPC3 cell line and for MF66 in the PANC1 cell line. Fortunately, drug loading efficiency ensured that the OD15 MNP concentration did not exceed 100 µg/mL while capable of delivering cytotoxic doses of Doxorubicin chemotherapy. The MF66 MNP had lower doxorubicin functionalised and the MNP concentration required to deliver the required dose of doxorubicin was approximately 200 µg/mL in the breast-derived cell lines (no cytotoxicity observed at this concentration) and less than 166.7 µg/mL in the pancreatic cell lines (cytotoxicity observed only at 200 µg/mL). No statistically significant reduction in cell count was observed in the pancreatic cell lines at 100 µg/mL for either OD15 or MF66, therefore any reduction in cell count within the drug functionalised samples, was on account of the doxorubicin drug.

The drug functionalised MNP provided mixed efficacy results, with some demonstrating an effect in some cell lines and not in others. In the MCF-7 cell line (Figure 43), cell count reduction occurred with exposure to OD15_N_Doxorubicin and MF66_N_Doxorubicin which was not observed in the MCF-10A cell line (Figure 44). Interestingly, both OD15_O_Doxorubicin and MF66_O_Doxorubicin had no effect on either cell line at the 72h time point. In contrast, both N_Doxorubicin and O_Doxorubicin MNP effectively reduced cell count in the BxPC3 cell line (Figure 45), with a reduction observed in the PANC-1 cell line for OD15_O_Doxorubicin and with MF66_N and O_Doxorubicin MNP (Figure 46). The observation made in the breast-derived cell lines regarding efficacy of N_Doxorubicin and O_Doxorubicin MNP was unexpected. The O_Doxorubicin formulation, by the nature of the carbamate linker, should release the drug more efficiently than the N_Doxorubicin linker, as the carbamate moiety is weaker than the urea moiety on account of the higher electronegativity of the oxygen atom. The pancreatic cell lines were most affected by the O_Doxorubucin formulations, with a greater overall cell count reduction at 72h compared to the N_Doxorubicin formulations. In contrast to the N_ and O_Doxorubicin formulations, the Imino_Doxorubicin linked MNP were the best functionalization method identified and provided reproducible data in all cell lines. Cell count reduction following I_Doxorubicin exposure was comparable to that of free drug control and enabled the estimation of efficacy from each nanoparticle formulation. At the highest concentration of OD15_I_Doxorubicin tested (1600 nM breast and 800 nM pancreatic) the response was equivalent to approximately 325 nM (MCF-7), between 650 nM – 1300 nM (MCF-10A), 1000 nM (BxPC3) and >2000 nM (PANC-1) of free drug. Furthermore, the MF66_I_Doxorubicin at the highest concentration was more efficient than free drug in the MCF-7 cell line and was comparable to 2600 nM of free drug. MF66_I_Doxorubicin in the MCF10A cell line was not as effective yet was comparable to 650 nM of free drug at the highest concentration delivered. In the pancreatic cell lines, cell count reduction was equivalent to 1000 – 2000 nM of free drug in BxPC3, and in the PANC-1 the highest concentration of MF66_I_Doxorubicin was more cytotoxic than the highest concentration of free

doxorubicin. It is clear that the implementation of a dual-cleavable linker results in higher anticancer efficacy and over the time course of the experiment, the cellular response to the functionalised MNP was similar to or exceeded that of free drug. The implementation of the dual-cleavable linker containing a disulfide and carbamate moiety, as detailed in [424] should only be cleaved when the MNP enters the cell, and specifically when MNP are localised to the highly acidic and reducing environment of the lysosomes. With each step of the endocytic maturation process, there is a gradual decrease in the intravesicular pH. Early endosomes have a pH of between 6.0 and 6.5, while late endosomes and lysosomes have a pH of 4.5 to 5.5. The carbamate linker is stable above pH 5.5, therefore release occurs at the later stage of the endocytic process. The Imino_Doxorubicin MNP produced the most consistent and best result compared to the N_Doxorubicin and O_Doxorubicin and suggests that the position at which the drug is attached to the linker and subsequently to the nanomaterial surface is of great importance. The Imino_Doxorubicin linker molecule contains a carbamate moiety in the same position as O_Doxorubicin but both structures have a different point of attachment to the doxorubicin drug. While O_Doxorubicin and N_Doxorubicin linkers are functionalised to doxorubicin at the same position, the results presented in this thesis suggest that the functionalisation of the linker at an alternative site via an imine group as demonstrated with the Imino_Doxorubicin yields more consistent results. Conformational differences between the drug-loaded MNP on account of the different point of drug attachment may facilitate the efficient release of drug in the case of Imino_Doxorubicin formulations.

Currently, the approved nanomedicines available in the clinic are all passively targeted to the tumour site, with a handful of targeted nanomedicines currently in clinical trials [360]. Passive targeting is an effective means to deliver nanomaterials to the tumour, taking advantage of the EPR effect [55, 456]. However, limitations exist with passive targeting due to the variability in tumour vascularisation and the porosity of tumour vessels [457, 458], therefore the ability to target a nanoparticle formulation specifically and directly to the cancer cell would enable high drug load delivery and limit the chances of developing multiple drug resistance [459]. The targeting ligand used in this work was the pseudopeptide N6L that acts both as an anticancer drug and as a targeting agent, which is currently in clinical trial (NCT01711398).

The cytotoxic capability of N6L was tested using a range of concentrations (10 to 80 µM). Previous studies have shown N6L to be sufficiently cytotoxic at 20 µM following 72h exposure [393], and the results presented here further demonstrate that N6L results in a decrease in cell count following 72h exposure. N6L efficacy to induce an anticancer effect was observed at the early time point of 24h, at which the highest concentration of 80 µM induced cytotoxicity in all cell lines. Furthermore, following 72h exposure it was shown that two cell lines, MCF-7 (Figure 51) and MCF-10A (Figure 55) displayed a reduction in cell count at all concentrations and cell count reduction in the SK-BR-3 cell line (Figure 54) was observed at concentrations above 20 µM. Interestingly, N6L had a consistent effect on lysosomal vesicles. A dramatic decrease in lysosomal mass/pH was observed in all cell lines with the exception of the BT-474s (Figure 52), matching the response of the positive control, and indicating that following N6L uptake it effects the integrity of the lysosomal compartment or indeed, the internal pH of the lysosome could be increased towards a more alkaline state causing the dye intensity to reduce. Nevertheless, it is clear that N6L has a profound effect on the internal lysosomal environment and could therefore induce apoptosis and/or necrosis through lysosomal disruption and release of lysosomal hydrolases or more

specifically, the cathepsins as a secondary effect of uptake. This is a concentration dependent event, which is less pronounced at the lowest concentration of 10 µM.

The results demonstrate that N6L is capable of inducing a cytotoxic response in the cell line models, and therefore we sought to determine whether MNP functionalized with N6L could induce a similar response. The initial cytotoxicity screening assessment of MNP presented in chapter 3 identified a maximal dose of 200 µg/mL for OD15, and below 100 µg/mL for MF66 MNP. This limited the amount of N6L that could be delivered to cells. Due to the molecular size of N6L, the amount functionalised was considerably less than drug functionalised formulations. At the maximum concentration of 200 µg/mL for OD15 and MF66 MNP, the quantity of N6L functionalised was 0.48 µM and 0.96 µM respectively (Table 8), which was considerably less than the 20 µM concentration needed to induce a cytotoxic response. Nevertheless, the results highlight that in the presence of N6L, there is a propensity for an increase in the lysosomal mass/pH parameter, indicative perhaps of an increase in cellular uptake. Due to the method by which N6L enters cells, through binding the nucleolin receptor, which is localised on lipid rafts [394], the uptake of N6L MNP may be through lipid-raft mediated endocytosis or alternative endocytic routes such as clatherin mediated endocytosis and micropinocytosis as previously described. Another explanation for the observed increase in cellular uptake with N6L functionalised MNP may be attributed to the differences in nanoparticle surface charge. The nanoparticle formulations had an overall net negative charge, but N6L functionalised MNP were less negative than their basic MNP counterparts. OD15 MNP were -46.0 mV but following functionalisation (OD15_N6L) surface charge was -40.0 mV; basic MF66 MNP were -42.2 mV and following functionalisation (MF66_N6L) a surface charge of -36.7 mV was recorded. An increase in the lysosomal parameter was observed with the N6L functionalised MNP and while it may be mostly attributed to uptake via the recognised binding of nucleolin, passive uptake mediated by a less-negative surface charge may play a contributory role in MNP uptake. It has been extensively demonstrated that MNP with a positive surface charge are taken up more readily into cells compared to neutral/negatively charged nanoparticles [277-281]. This suggests that N6L, while not at concentrations high enough to induce cytotoxicity, could in fact enable or drive the uptake of MNP into cells that express high levels of nucleolin and passively via cell-surface interaction (section 4.2.4). The data obtained suggest that the presence of N6L functionalised MNP does in fact result in an increase in cytotoxicity compared to the basic MNP formulations.

An increase in cellular uptake by N6L functionalised MNP was confirmed by Perls' Prussian blue staining, which enabled the identification of iron inside cells. Breast and pancreatic cell lines and primary pancreatic stem cells were exposed to non-targeted basic MF66 MNP, covalently attached N6L_MNP and electrostatically attached N6L_MNP. Kossatz et al. [354], further confirm the results obtained using the electrostatic N6L_MNP. As presented in this thesis and discussed above, there was a distinct increase in uptake with MNP containing the N6L moiety, which may be attributed in part to the surface charge (basic MNP -44.3 mV, covalent MNP_N6L -37.8 mV and electrostatic MNP_N6L -29.9 mV). Covalently functionalised MNP displayed greater uptake compared to their electrostatic counterparts even though the electrostatic MNP_N6L had a surface charge of -29.9 mV. This observation is possibly due to the electrostatic MNP losing the surface bound moieties over time in a high salt environment as demonstrated

by Kossatz et al. [354], which would ultimately change the surface charge back to that of the more negative basic MNP formulation.

Gemcitabine, an antimetabolite chemotherapeutic drug, is used extensively to treat cancers of the breast and pancreas. OD15 and MF66 formulations were mono-functionalized with gemcitabine and multi-functionalized with gemcitabine and N6L. The results demonstrate that the gemcitabine MNP are highly cytotoxic, more-so than the doxorubicin formulations previously tested. Gemcitabine is an analogue of deoxycytidine and during DNA synthesis it can be incorporated into the nascent DNA strand, thus halting DNA polymerase activity [460]. As a single agent, gemcitabine can effectively reduce cell viability in both breast cancer and normal-like cell lines and pancreatic cancer cell lines, as shown in this thesis. Gemcitabine has been utilised as a single agent in the clinic with considerable success in treating metastatic breast and pancreatic cancers [213, 461, 462]. Combination therapy has shown a limited increase in overall survival rate in pancreatic cancers and a real need exists to address this lack of a viable treatment [463]. The results obtained in this work demonstrate that multi-functionalised formulations of N6L and gemcitabine in combination resulted in considerable cell count reduction and where reduction was not as pronounced as the mono-functionalised MNP, the cell membrane permeability parameter was increased considerably more, indicating that a greater proportion of cells were undergoing cell death. Most strikingly from these results, we have demonstrated that N6L functionalised MNP have much higher lysosomal intensity and as previously determined, this is directly correlated to cellular uptake. In addition, the cytotoxic trend (reduction in cell count and increased cell membrane permeability) observed in the MCF-7, MCF-10A, BxPC3 and PANC-1 cell lines upon exposure to OD15_N6L_Gemcitabine for 72h suggests that the N6L on the MNP facilitates the dose dependent delivery of the gemcitabine payload. Unlike OD15_Gemcitabine which appears largely ineffective (pancreatic cell lines) or largely the same across all concentrations (breast cell lines), the OD15_N6L_Gemcitabine demonstrates a controlled drug release profile and through multiparametric testing it was possible to confirm increased cellular uptake compared to mono-functionalised MNP through the lysosomal intensity parameter. While the functionalised MF66 MNP formulations had similar results and efficacy, the functionalised OD15 MNP were more consistent and demonstrated a higher anticancer capacity across all cell lines tested. The results obtained in this chapter can be summarised in Figure 71 below.

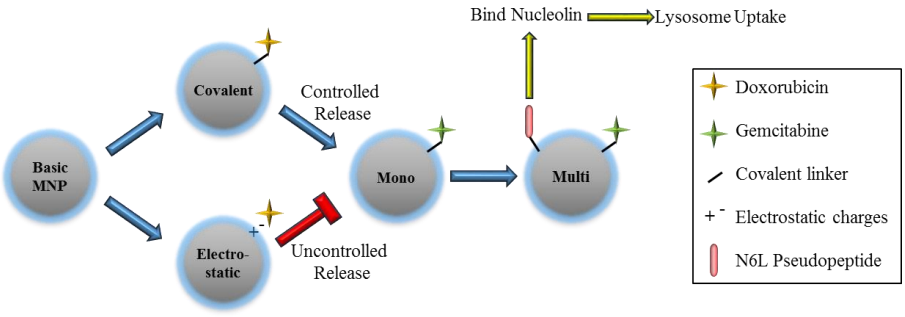

Figure 71: Stepwise selection of nanomaterials

Overview of workflow within WP3, testing of basic MNP to select suitable formulations. Selection of suitable functionalisation method using MNP functionalised with covalently or electrostatically bound doxorubicin. MNP functionalised with gemcitabine (Mono) to validate drug release. Multifunctionalised (Multi) MNP containing N6L and gemcitabine drug to determine efficacy with targeting capability.

4.4 Conclusion

This part of the study was focused on the evaluation of therapeutic compounds functionalised to the OD15 and MF66 MNP and their anticancer efficacy in breast and pancreatic cell lines. The effectiveness of chemotherapy alone served as a baseline to which the efficiency of the drug-functionalised MNP could be compared. Chemotherapy drugs alone caused considerable reduction in cell count at 72h which was accompanied by an increase in the permeability of cell membranes and a decrease in the integrity of lysosome membranes. The anticancer efficacy of drug-functionalised MNP was demonstrated using MF66 MNP formulations electrostatically and covalently functionalised with doxorubicin drug. Covalent functionalisation provided greater control over drug release and evaluation of three linkers containing either a carbamate group, a urea group or both a carbamate group and an imine group identified the latter dual-cleavable linker to provide substantially better anticancer effect. Furthermore, N6L is a known anticancer agent which has been confirmed to induce cell death when cells are exposed to N6L alone. Bound to MNP, this efficacy is considerably reduced. It has been demonstrated for the first time that the HCSA multiparametric assay could be used to identify MNP uptake as N6L was shown to increase uptake of MNP into cells, which was subsequently confirmed by the Perl's Prussian blue assay.

Functionalisation of both N6L and gemcitabine drug further enhanced cell uptake and provided substantial benefit over gemcitabine-functionalised MNP formulations alone in the pancreatic cell lines. N6L is a known nucleolin binding peptide as detailed in section 1.4.5 and as discussed in section 4.3, the increase in uptake efficiency and anticancer effect may be attributed to nucleolin-mediated uptake via N6L binding or may be related to the surface charge of the multi-functionalised MNP compared to mono-functionalised MNP. A shift in the surface charge as demonstrated when N6L is functionalised may in part drive the uptake of multi-functionalised MNP via increased interaction with the negatively charged cell membrane and thus result in greater anticancer efficiency. In addition, the concentration of gemcitabine on mono-functionalised and multi-functionalised MNP was the same, therefore the presence of N6L may in fact order the gemcitabine on the surface of the MNP due to steric hindrance thus making the gemcitabine more "bio-available". In the case of MNP devoid of N6L it is possible that the drug complex shields the disulphide group on the linker molecule, therefore limiting the release of drug. Another potential explanation for the increased anticancer efficiency of the multi-functional MNP is that upon entry into the cell both gemcitabine and N6L are released and via two distinct modes of action they may synergistically function to kill the cancer cells.

The subcellular mechanisms of MNP-induced anticancer effects will be investigated in the following chapter, focusing on the dual cleavable imino doxorubicin and N6L functionalised gemcitabine MNP formulations, and their individual components such as basic MNP, doxorubicin alone, gemcitabine alone, and N6L alone.

Chapter 5: Subcellular mechanisms of MNP-induced anticancer effects

5.1 Introduction

Mitochondria are often referred to as the powerhouses of the cell and until recently, they were viewed as isolated bodies. Their structure is complex and contain four specialised compartments to accommodate the vast array of functions [464]. The outer membrane contains a network of proteins called porins that control passage of small molecules through the membrane, and the protein translocase is also present and is necessary for enabling larger proteins containing the correct N-terminal signalling sequence through the membrane and into the intermembrane space [464]. It is within the intermembrane space that high levels of the caspase activator protein cytochrome c is found and when the outer membrane of mitochondria is damaged, a series of events occur that seal the fate of the cell towards cell death. Membrane damage causes instant loss in mitochondrial membrane potential, cessation of ATP synthesis and initiation of redox crisis as well as release of cytochrome c, Smac/Diablo and apoptosis initiation factor which can freely diffuse into the cytosol and initiate numerous cell death pathways [465, 466]. The inner membrane houses proteins that function in redox reactions, and also contain transport proteins and ATP synthase [464]. The final specialised compartment is the matrix, where 2/3 of the total protein is located [464]. ATP is generated within the matrix through the reduction of ADP by the proton motive force from the intermembrane space through ATP synthase and into the matrix [467]. The Citric acid cycle/Krebs cycle also occurs in the matrix and is the main mechanism by which guanosine triphosphate and nicotinamide adenine dinucleotide (NADH) are produced via a series of enzymatic reactions [467]. NADH is a vital co-enzyme in the electron transport chain which drives the creation of an electrochemical gradient and the proton motive force to facilitate ATP production. The genetic material, mitochondrial DNA (mtDNA), also resides in the matrix and it is here that many mitochondrial-derived polypeptides are synthesised [464].

It is clear, given the diverse and vital role of mitochondria, that their dysfunction can have serious implications on cellular fate and have major repercussions on the whole body. Many disorders have been identified as mitochondrial-derived which are caused by mutations in the mtDNA or nuclear gene. These disorders may present at any age and include Kearns-Sayre syndrome [468], chronic progressive external ophthalmoplegia [469], Leigh syndrome [470], and cardiomyopathy [471]. The electron transport chain is a major site for the leakage of electrons to oxygen, resulting in ROS formation and oxidative stress. This is most often observed following exposure to MNP due to imbalance of biochemical homeostasis in cells and direct free radicle formation through the fenton reaction of hydrogen peroxide oxidation of Fe^{2+} into the hydroxide and the highly reactive hydroxyl radicle [332].

Under normal physiological conditions the mitochondria contain antioxidants such as superoxide dismutase, catalase, and glutathione peroxidase to protect itself from oxidative stress [467]. Nevertheless, the continuous exposure to ROS can result in considerable mtDNA damage, and it has been determined that a 10 – 20 fold higher susceptibility to DNA damage exist in mtDNA compared to nuclear DNA [472, 473], and is attributed to the mtDNA lacking nucleosomes and therefore being more prone to DNA damage compared to nuclear DNA [474, 475]. While mitochondria possess most repair pathways found in the nucleus, the repair of mtDNA damage is believed to occur predominantly through the base excision repair mechanism [476, 477]. Each mitochondria can contain between 5 – 10 copies of mtDNA [478], with each

cell containing a few thousand mitochondria. The presence of mutations in the mtDNA in a proportion of these mitochondria is referred to as heteroplasmy, in which a cell contains mitochondria harbouring mtDNA containing a mutation and wild type mtDNA. It is believed that through clonal expansion the persistence of mutated mtDNA can occur if the mutation confers a growth and survival advantage [479]. Such persistence can result in cells becoming homoplasmic mutant. It is possible that homoplasmic mutant cells could account for the main population in tumours during tumour development if they conferred a growth advantage [479]. In fact, a high frequency of mtDNA mutation exist in many cancers such as breast [480], pancreatic [481, 482], and lung [483, 484]. Mitochondrial involvement in the progression of cancer has received much attention in the last few years with dysfunction of these "powerhouses" being proposed as a key contributor towards cancer progression [485-487]. This is largely due to their integral role in the intrinsic apoptotic pathway and their role in anabolic metabolism which make them key organelles for a prospective cancer to manipulate, firstly to prevent recognition and release of pro-apoptotic signals and harnessing of the electron transport chain to provide the energy necessary for rapid cell growth. From this perspective, it would be beneficial if mitochondria residing within cancer cells could be targeted during cancer therapy (Reviewed in [478]). An alternative viewpoint, in light of the far reaching implications of mitochondrial dysfunction, is the alteration of wild type mitochondria in healthy cells as a result of the prescribed treatment, and the increased predisposition for the onset of cancer.

With this in mind, it is important to consider the effect that engineered nanomaterials may have on mitochondrial integrity and capacity to induce apoptosis in cancer. Drug functionalised MNP can cause considerable cell death as presented previously in this thesis. The onset of this cytotoxicity has been attributed to the release of drug from the MNP, on account of their intended inhibitory effect as detailed in section 1.3.3. The implications of engineered MNP exposure and their individual components on the integrity of mitochondria is an important consideration to better understand the risk posed. Therefore the effect of the functionalised MNP and their individual components on mitochondrial membrane potential and on cell death over a 36h period was evaluated.

There exists a multitude of cell assessment assays employed for the validation of engineered MNP. The uptake of MNP into the cell and localisation to the acidic environment of the lysosome can result in the degradation of the coating and release/leaching of iron ions [488]. Iron homeostasis is effectively controlled by the hepcidin protein which is central to the process [489]. Hepcidin is a hormone synthesised in the liver and secreted into circulation in response to the increase of iron. The increase of Fe^{2+} and Fe^{3+} ions in the cell can alter cell homeostasis and the expression of intracellular iron homeostasis genes [488]. The excessive intracellular release of iron can result in iron overload, which hepcidin cannot adequately reduce [490]. Excess iron in the cell can cause oxidative stress which can manifest as DNA damage, mitochondrial damage, endoplasmic reticulum stress, cell cycle alteration, protein denaturation, lipid damage, inflammatory processes, and cytotoxicity [315, 491-494]. It is important to note that while cytotoxicity may not be registered, it is possible that subtle deleterious effects can occur to the DNA which could lead to carcinogenesis [494]. It has also been demonstrated that oxidative stress can be transient without causing any cytotoxic effects [495]. Oxidative stress is associated with the production of oxidizing species or a decrease in the effectiveness of antioxidants such as gluthathione [496]. Central to oxidative damage is the formation of highly reactive free radicals that are generated by the reaction of free iron ions

(Fe^{2+} and Fe^{3+}) with oxygen to produce ROS. ROS caused extensive lipid peroxidation and membrane permeabilisation of the mitochondrial membrane and intense mtDNA damage as observed using mitochondrial extracts from Wistar rats [497], and can disrupt other organelles such as lysosomes, nuclei and trigger cell signalling pathways leading to the death of the cell [498]. The primary polyunsaturated fats targeted by free radicals are arachidonic acid and its precursor, linoleic acid, which are present in phospholipids (phosphatidylethanolamine, phosphatidylcholine, and phosphatidylinositides) [499]. The leaching of free iron ions from the MNP can freely move into the nucleus and mitochondria, within which the fenton reaction can occur, liberating ROS. The interaction of MNP or indeed free iron ions may lead to mitochondrial membrane potential changes and ultimately to the uncoupling of oxidative phosphorylation [500]. As detailed previously, the disruption of the mitochondrial membrane can lead to irreversible damage with the dissipation of the membrane potential and the release of cytochrome c, apoptosis inducible factor (AIF), secondary mitochondrial activator of caspase (Smac/DIABLO) and nitric oxide [465, 466, 501]. Cytochrome c resides within the intermembrane space loosely bound to the inner membrane via attachment to cardiolipin. Upon damage to mitochondria, cytochrome c is released into the cytosol where it can bind to the apoptotic protease activating factor-1 (Apaf-1). The release of cytochrome c and binding to Apaf-1, the apoptosome, initiates apoptosis via the activation of caspase 9, thus initiating the caspase cascade and apoptosis ensues [502]. AIF is involved in the activation of a caspase-independent pathway for apoptosis and can freely diffuse into the nucleus where it binds DNA and initiates caspase-independent chromatin condensation [503] [504]. The release of cytochrome c leads to interaction with the inositol triphosphate receptor on the endoplasmic reticulum which results in the release of calcium which in turn results in substantial release of cytochrome c [505]. The rising calcium concentration results in an influx of Ca^{2+} into mitochondria and modulates nucleases that control apoptosis [506]. Smac/DIABLO is released from mitochondria upon DNA damage, cytotoxic drug exposure and UV- or γ-irradiation and binds to inhibitor of apoptosis proteins (XIAP and cIAP) thus enabling caspase activation. In addition to the above, nitric oxide is also instrumental in promoting the apoptotic pathway in response to a diverse number of pro-apoptotic stimuli. Nitric oxide has been shown to favour production of H_2O_2, $ONOO^-$ and $O_2^{\bullet-}$ [507], and can result in irreversible damage to mitochondrial ATP synthase and aconitase, while promoting cytochrome c release and apoptosis. Inducible Nitric oxide can activate p53 which in turn can activate pro-apoptotic proteins such as p21Waf1/Cip1 and Bax [508]. Therefore a myriad of proteins and chemicals released and/or activated upon damage to mitochondria and other organelles can be monitored as part of the cell assessment following exposure to MNP. Dissipation of the mitochondrial membrane potential is a penultimate event prior to phosphatidyl serine exposure on the external plasma membrane face and subsequent cell death. This event can be measured with the use of fluorescent dyes that localise to the matrix space in intact mitochondria and are released into the cytosol upon loss of the mitochondrial membrane potential (TMRM, TMRE, Rhod123 and JC-1) or in the case of MitoTracker orange used in this project, it is not released from the mitochondria if mitochondrial membrane potential is lost post staining or post fixation [509]. The MitoTracker orange dye only accumulates in mitochondria with an intact membrane potential, therefore cells that have a disrupted mitochondrial membrane at the time of staining will not retain the dye. Additional assessment, as presented in this thesis, includes the analysis of

apoptosis/necrosis initiation using flow cytometry and difference in cell count, indicating cell death and detachment from assay plate, post incubation with MNP by multiparametric analysis.

DNA is found in both the mitochondria and the nucleus and as the chemotherapy drugs functionalised on the MNP function by intercalating with or integrating into DNA, therefore the MNP genotoxic capacity was evaluated by the OECD guideline micronucleus test. The NIH-3T3 mouse fibroblast cell line was selected for the micronucleus testing to compliment the small animal studies conducted throughout the Multifun project, and according to the OECD, it is a good cell-line model to identify carcinogenic compounds [510].

The aim of this part of the study was to identify whether the developed MNP in their basic and functionalised forms could induce damage to mitochondria, whether this damage could be associated with cell death, and whether the MNP cause genetic alteration to nuclear DNA.

To achieve these aims, the specific objectives were:

1. High content screening of A549, NIH-3T3, MCF-7 and MCF-10A cell lines for changes in mitochondrial membrane potential following 12h, 24h and 36h exposure to a range of MNP concentrations.
2. Assessment of cell death following 36h exposure to MNP.
3. Identification of optimum cytochalasin B concentration.
4. Identification of a suitable micronucleus-inducing positive control.
5. Investigation of MNP-induced genotoxicity through micronucleus formation.

5.2 Results

5.2.1 Mitochondrial dysfunction analysis

5.2.1.1 Reduction in mitochondrial dye intensity by valinomycin.

The mitochondrial membrane potential of cell lines exposed to valinomycin for 12h, 24h and 36h at 120 µM were significantly reduced at every time point except in the MCF-10A cell line where a reduction in mitochondrial potential was observed at 24h and 36h (Figure 72), and representative images in Figure 73 (A549 and NIH-3T3) and Figure 74 (MCF-7 and MCF-10A). Valinomycin was therefore used as a positive control to indicate mitochondrial damage in subsequent tests.

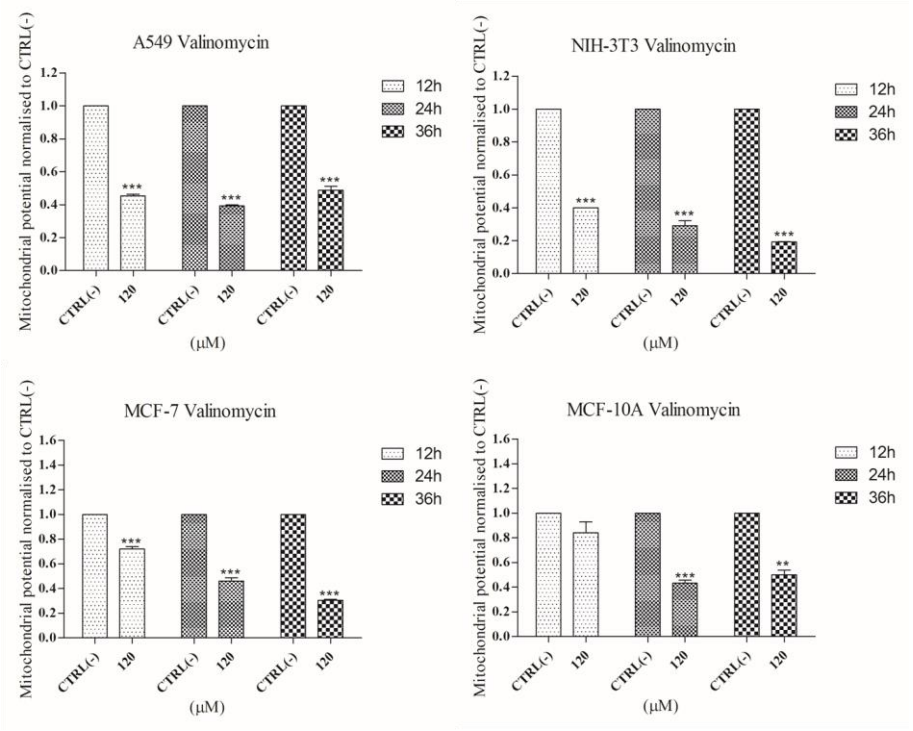

Figure 72: Cell lines exposed to valinomycin and effect on mitochondria membrane potential.

A549, NIH-3T3, MCF-7 and MCF-10A cell lines were exposed to 120 µM valinomycin for 12h, 24h and 36h. Cells were stained using the mitochondria membrane potential indicator from the Cytotoxicity II HitKit™ and analysed using the InCell 1000 HCSA device. Variation in staining intensity was measured and compared to untreated control (CTRL(-)). Statistical significance was determined using the unpaired two-tailed t-test for each valinomycin-exposed sample compared to untreated control. p value: *** = <0.001, **=<0.01, *=<0.05.

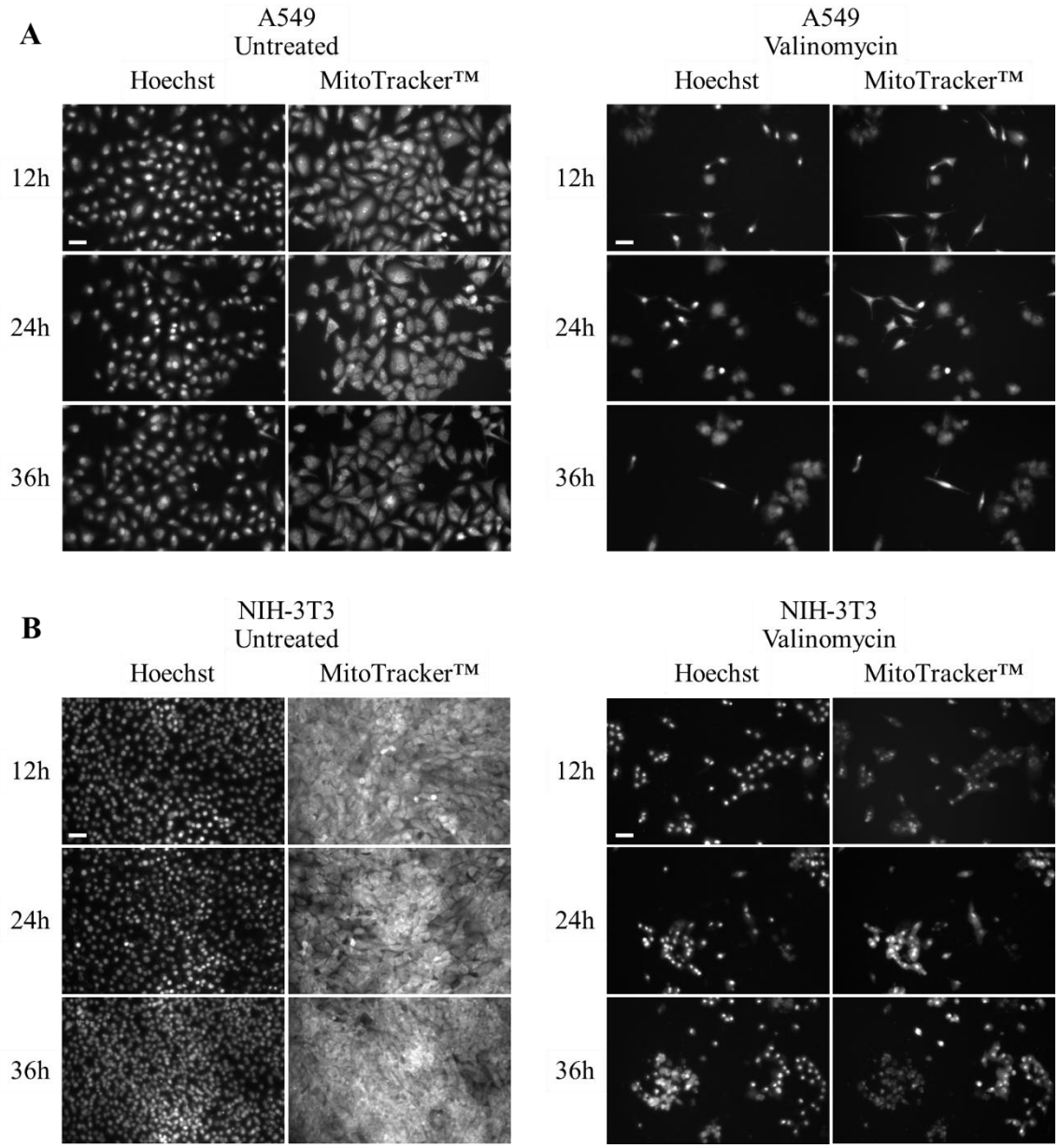

Figure 73: Loss of mitochondrial membrane potential in A549 and NIH-3T3 cell lines.

(A) A549 and (B) NIH-3T3 cell lines exposed to valinomycin (120 µM) display a reduction in the mitochondrial staining intensity using MitoTracker® at 12h, 24h and 36h time points, compared to untreated controls. Scale bar (white line, top left panel) = 50 µm, applicable to all images.

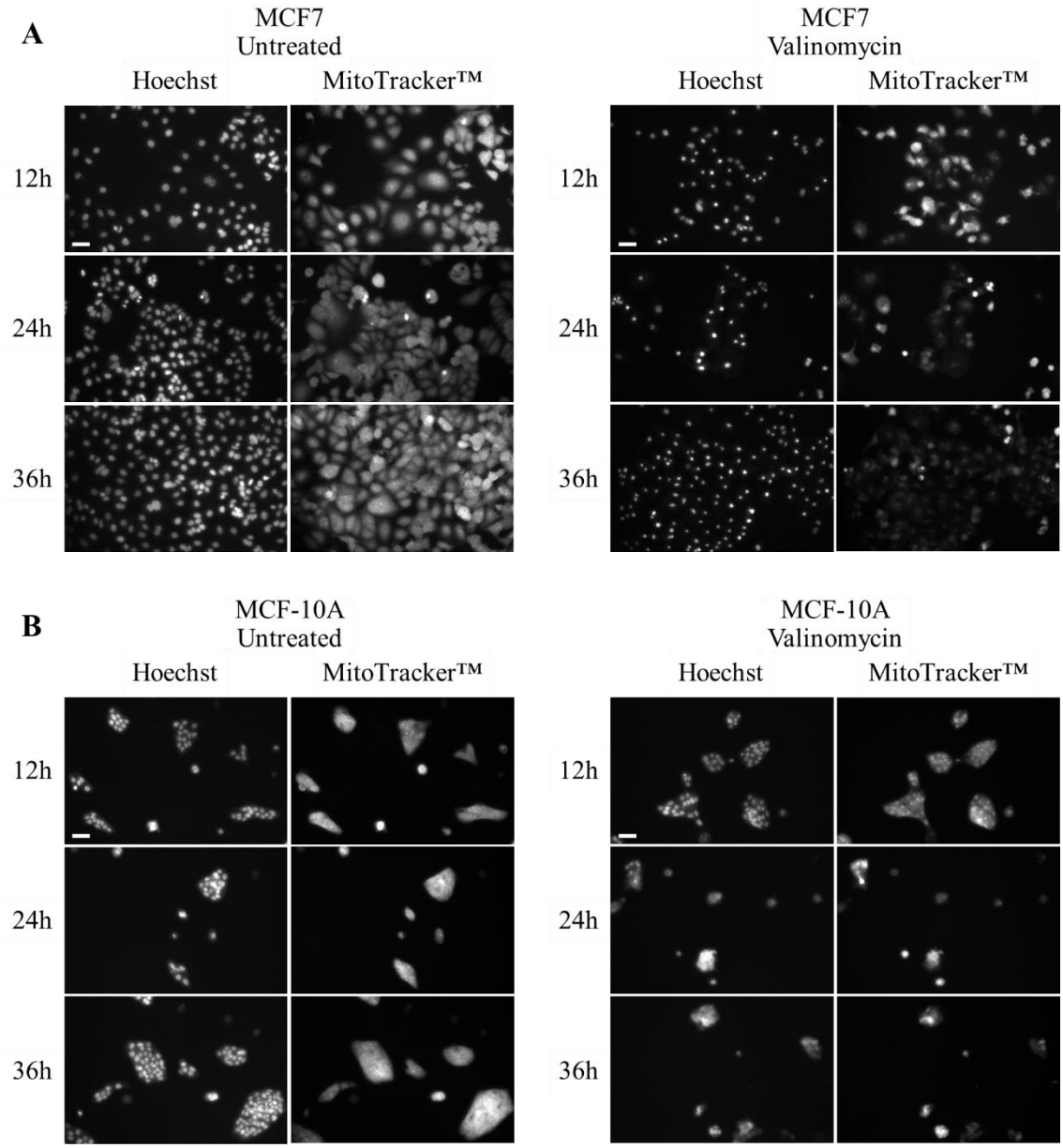

Figure 74: Loss of mitochondrial membrane potential in MCF-7 and MCF-10A cell lines.

(A) MCF-7 and (B) MCF-10A cell lines exposed to valinomycin (120 µM) display a time-dependent reduction in the mitochondrial staining intensity using MitoTracker® at 12h, 24h and 36h time points, compared to untreated controls. Scale bar (white line, top left panel) = 50 µm, applicable to all images.

5.2.1.2 MNP induced mitochondrial damage

The details of the MNP used to test for mitochondrial damage are provided in Table 11 below. The concentrations of doxorubicin or gemcitabine drug used were selected based on the effective dose identified in the breast-derived cell lines as previously determined in the cytotoxicity tests. Data is presented as heatmaps for the A549 (Figure 75), NIH-3T3 (Figure 76), MCF-7 (Figure 78) and MCF-10A (Figure 79) and representative HCSA images are provided in Figure 77 (A549 and NIH-3T3) and Figure 80 (MCF-7 and MCF-10A). All graphs with statistical significance indicated are in Appendix 3.

Table 11: Details of MNP containing covalently functionalised chemotherapy drug +/- N6L.

Nanomaterials were supplied as suspensions in water at the indicated pH. Core particle size was determined by TEM. MNP were supplied at 2.4 mg Fe/mL with the indicated amount of doxorubicin and gemcitabine/N6L functionalised. Total MNP concentration necessary to deliver specified drug load and the concentration of N6L is provided.

Name	pH	TEM (nm)	Doxorubicin Loaded (µmol/g Fe)	Gem/N6L loaded (µmol/g Fe)	MNP conc. @1300 nM Doxo @400 nM Gem (µg/mL)	N6L conc. @ MNP conc. (nM)
OD15	6.9	15.0	N/A	N/A	N/A	N/A
OD15_I_Doxo	7.9	15.0	23	N/A	56.5	N/A
OD15_ N6L_Gem	7.9	15.0	N/A	14/4	28.6	110
MF66	6.9	11.7	N/A	N/A	N/A	N/A
MF66_I_Doxo	7.9	11.7	22	N/A	59.1	N/A
MF66_ N6L_Gem	7.9	11.7	N/A	12/4	33.3	130

Doxorubicin exposure caused a decrease in cell count in all cell lines, with statistically significant reduction observed with all concentrations at 36h. Mitochondrial intensity was reduced in all cell lines at concentrations above 260 nM in the A549, all concentrations in the NIH-3T3 cell line, and concentrations exceeding 650 nM in the MCF-7 and MCF-10A cell lines.

Gemcitabine exposure caused a decrease in cell count in all cell lines, with significant reduction observed with all concentrations at 36h. Mitochondrial intensity was reduced at the 400 nM concentration in the A549, at concentrations above 50 nM in the NIH-3T3 cell line and at all concentrations in the MCF-10A cell line. No change in mitochondrial intensity was observed in the MCF-7 cell line.

N6L exposure caused a reduction in cell count of approximately 10% and 20% in the MCF-7 and MCF-10A cell lines respectively at the 130 nM concentration. Both observations were made following 36h exposure. No reduction in mitochondrial intensity was observed in any cell line and at any time point or concentration.

OD15 MNP exposure caused reduction in cell count in the NIH-3T3 and MCF-7 cell lines. At the highest concentration (60 µg/mL) cell count was reduced by approximately 60% in the NIH-3T3 and 30% in the MCF-7 cell line. Mitochondrial intensity was decreased in both NIH-3T3 and MCF-7 cell lines by approximately 40% and 20% respectively.

OD15_I_Doxorubicin MNP caused reduction in cell count in all cell lines. At the 36h time point, cell count was reduced in the A549 cell line at concentrations greater than 260 nM, in the MCF-7 and MCF-10A cell line at 1300 nM and at all concentrations in the NIH-3T3 cell line. Mitochondrial intensity was reduced at concentrations higher than 130 nM in the NIH-3T3 cell line, and at the highest concentration of 1300 nM in the MCF-7 and MCF-10A cell lines. No reduction was observed in the A549 cell line.

OD15_N6L_Gemcitabine MNP caused reduction in cell count in all cell lines. At the 36h time point, cell count was reduced at concentrations above 50 nM in the A549, NIH-3T3 and MCF-7 cell lines and at all concentrations in the MCF-10A cell line. Mitochondrial intensity was reduced at concentrations higher than 100 nM in the NIH-3T3, at the 400 nM concentration in the MCF-7 cell line and at both the 50 and 400 nM concentrations in the MCF-10A cell line.

MF66 MNP caused a reduction in cell count in the NIH-3T3 cell line above 30 µg/mL and in the MCF-7 cell line at 60 µg/mL. Mitochondrial intensity was reduced only in the NIH-3T3 cell line at concentrations exceeding 30 µg/mL.

MF66_I_Doxorubicin MNP caused cell count reduction in all cell lines, with all concentrations effectively reducing cell count in the A549, NIH-3T3 and MCF-10A cell lines, with the highest concentration of 1300 nM reducing cell count in the MCF-7 cell line. Mitochondrial intensity was reduced at concentrations over 130 nM in the NIH-3T3 cell line, and at 1300 nM in the MCF-7 and MCF-10A cell line.

MF66_N6L_Gemcitabine MNP caused cell count reduction in all cell lines, with all concentrations in the A549, above 100 nM in the NIH-3T3 and at 400 nM in both the MCF-7 and MCF-10A cell lines. Mitochondrial intensity was reduced in the MCF-7 cell line at 400 nM but was significantly increased at all other concentrations. No reduction in mitochondrial intensity was observed in any of the other cell lines.

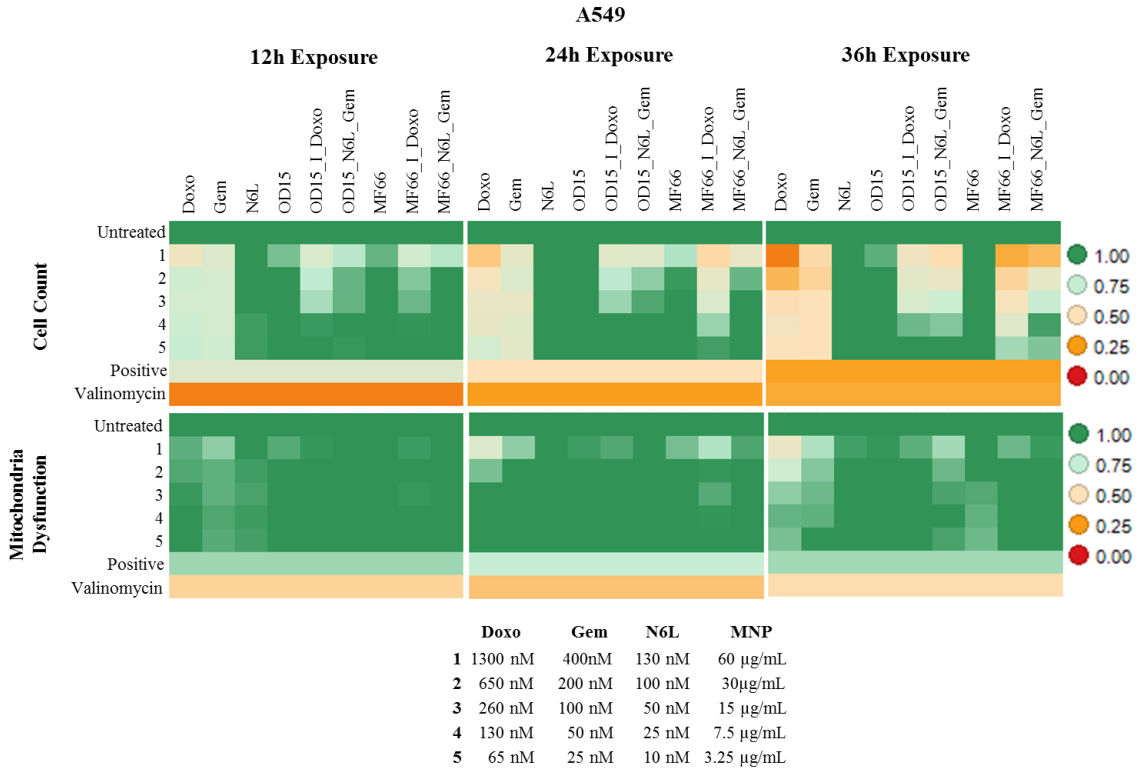

	Doxo	Gem	N6L	MNP
1	1300 nM	400nM	130 nM	60 µg/mL
2	650 nM	200 nM	100 nM	30µg/mL
3	260 nM	100 nM	50 nM	15 µg/mL
4	130 nM	50 nM	25 nM	7.5 µg/mL
5	65 nM	25 nM	10 nM	3.25 µg/mL

Figure 75: A549 cell line exposed to free drug and MNP formulations.

A549 cells were exposed to either free Doxorubicin (Doxo), free Gemcitabine (Gem), free N6L, OD15 MNP, OD15_I_Doxo, OD15_N6L_Gem, MF66, MF66_I_Doxo or MF66_N6L_Gem. Reduction in cell count and onset of mitochondrial dysfunction were recorded by high content screening at 12h, 24h and 36h time points. Free drug and drug conjugated MNP reduced cell count and mitochondrial membrane potential was reduced for free doxorubicin drug, OD15, OD15_I_Doxo, OD15_N6L_Gem, MF66_I_Doxo, and MF66_N6L_Gem. Concentration of delivered Doxorubicin, Gemcitabine N6L and MNP samples is provided.

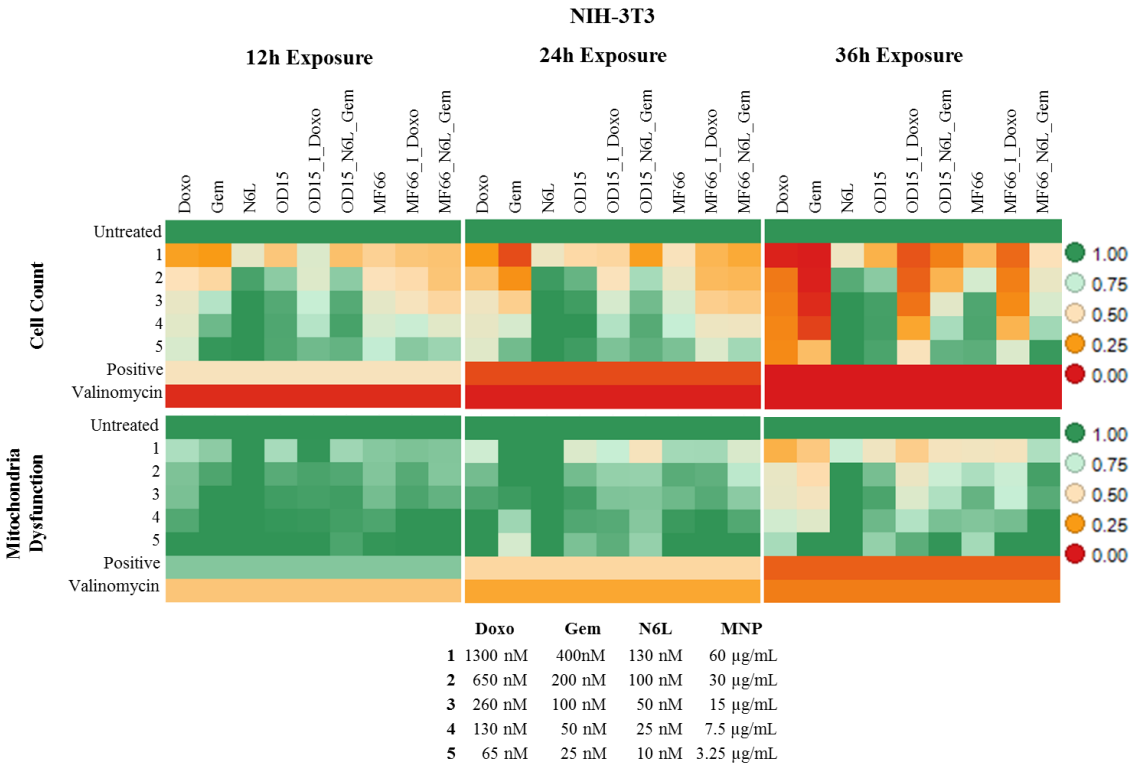

Figure 76: NIH-3T3 cell line exposed to free drug and MNP formulations.

NIH-3T3 cells were exposed to either free Doxorubicin (Doxo), free Gemcitabine (Gem), free N6L, OD15 MNP, OD15_I_Doxo, OD15_N6L_Gem, MF66, MF66_I_Doxo or MF66_N6L_Gem. Reduction in cell count and onset of mitochondrial dysfunction were recorded by high content screening at 12h, 24h and 36h timepoints. Free drug and drug conjugated MNP reduced cell count and mitochondrial membrane potential was reduced for free doxorubicin drug, OD15, OD15_I_Doxo, OD15_N6L_Gem, MF66_I_Doxo, and MF66_N6L_Gem. Concentration of delivered Doxorubicin, Gemcitabine N6L and MNP samples is provided.

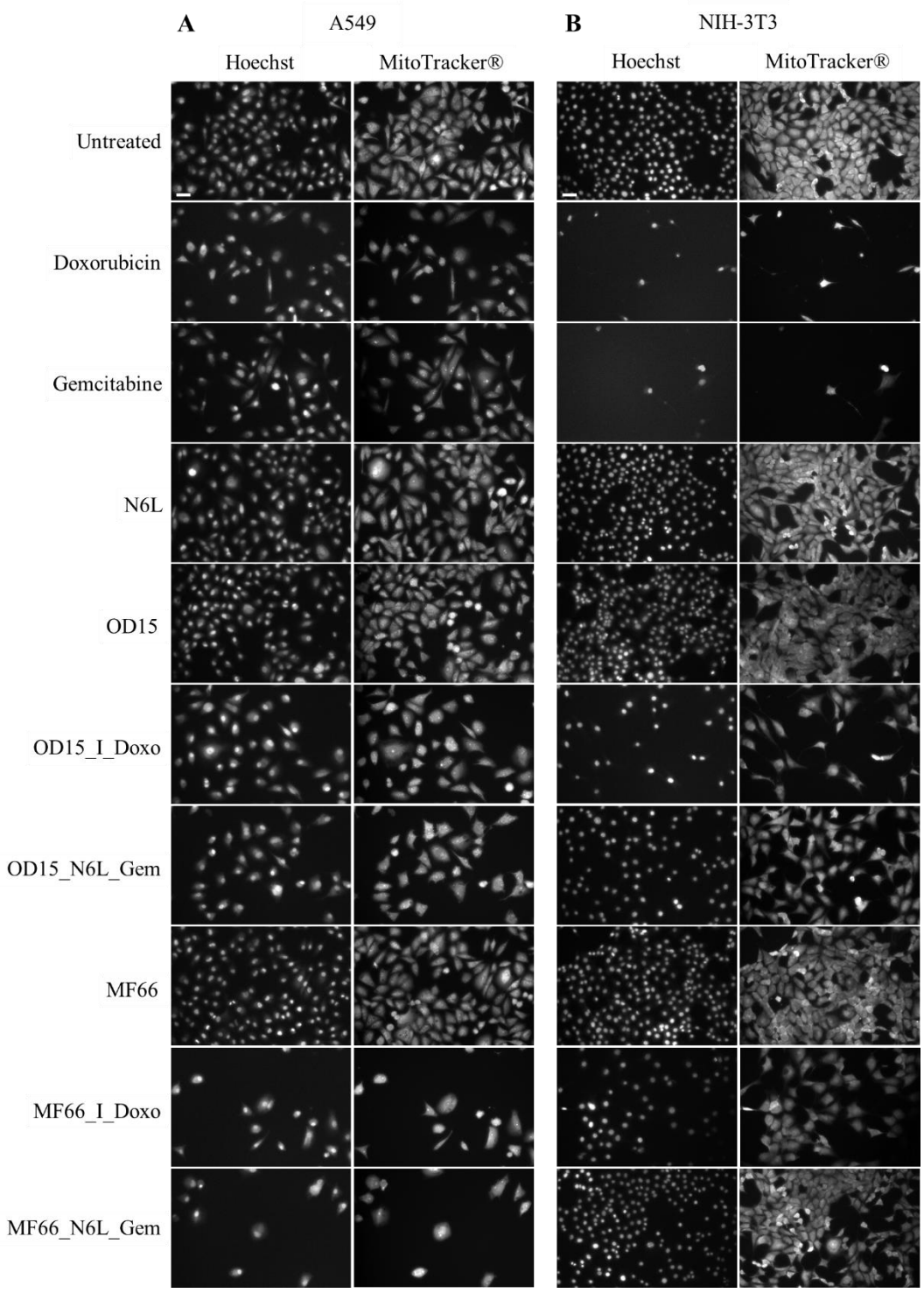

Figure 77: Analysis of mitochondrial toxicity in A549 and NIH-3T3 cell lines.

Representative images from (A) A549 and (B) NIH-3T3 cell lines exposed to the indicated drugs at the highest concentration and MNP formulations for 36h. Reduction in mitochondrial staining, indicating mitochondrial toxicity, was observed following exposure to doxorubicin and gemcitabine in both cell lines, and following exposure to OD15, OD15_I_Doxo, OD15_N6L_Gem, MF66 and MF66_I_Doxo in the NIH-3T3 cell line. Scale bar (white line, top left panel) = 50 µm, applicable to all images.

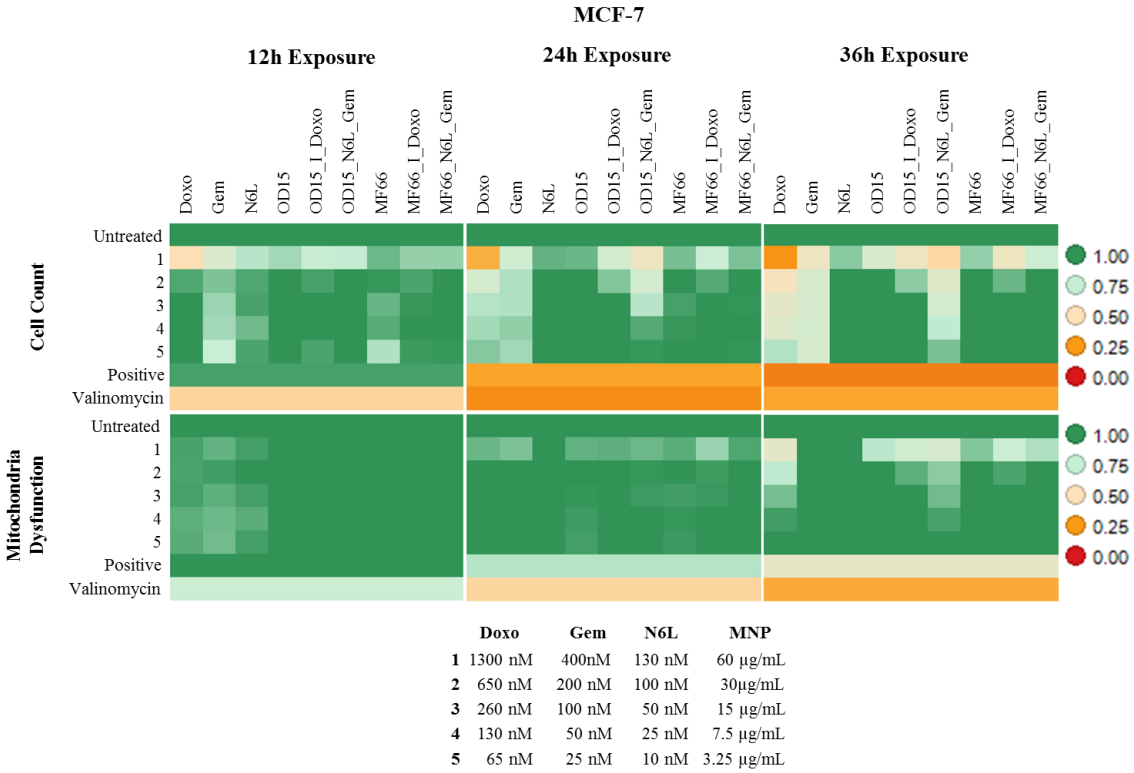

Figure 78: MCF-7 cell line exposed to free drug and MNP formulations.

MCF-7 cells were exposed to either free Doxorubicin (Doxo), free Gemcitabine (Gem), free N6L, OD15 MNP, OD15_I_Doxo, OD15_N6L_Gem, MF66, MF66_I_Doxo or MF66_N6L_Gem. Reduction in cell count and onset of mitochondrial dysfunction were recorded by high content screening at 12h, 24h and 36h timepoints. Free drug and drug conjugated MNP reduced cell count and mitochondrial membrane potential was reduced for free doxorubicin drug, OD15, OD15_I_Doxo, OD15_N6L_Gem, MF66_I_Doxo, and MF66_N6L_Gem. Concentration of delivered Doxorubicin, Gemcitabine N6L and MNP samples is provided.

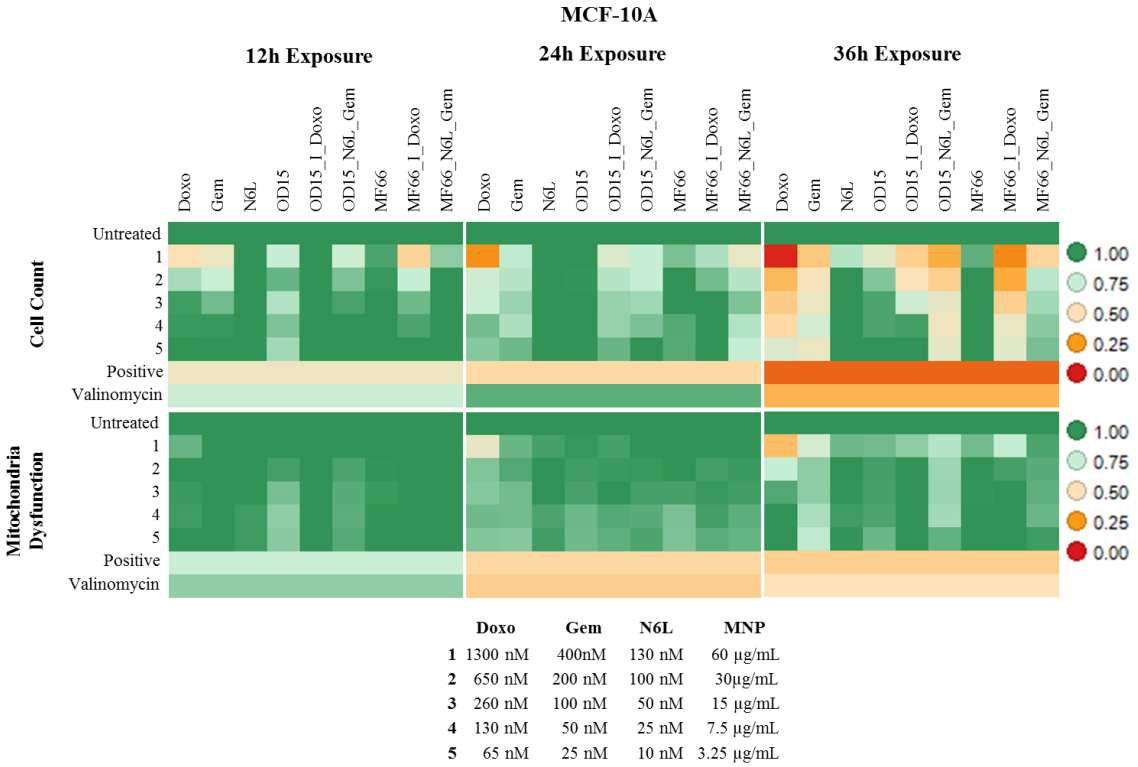

	Doxo	Gem	N6L	MNP
1	1300 nM	400nM	130 nM	60 µg/mL
2	650 nM	200 nM	100 nM	30µg/mL
3	260 nM	100 nM	50 nM	15 µg/mL
4	130 nM	50 nM	25 nM	7.5 µg/mL
5	65 nM	25 nM	10 nM	3.25 µg/mL

Figure 79: MCF-10A cell line exposed to free drug and MNP formulations.

MCF-10A cells were exposed to either free Doxorubicin (Doxo), free Gemcitabine (Gem), free N6L, OD15 MNP, OD15_I_Doxo, OD15_N6L_Gem, MF66, MF66_I_Doxo or MF66_N6L_Gem. Reduction in cell count and onset of mitochondrial dysfunction were recorded by high content screening at 12h, 24h and 36h timepoints. Free drug and drug conjugated MNP reduced cell count and mitochondrial membrane potential was reduced for free drug, OD15_I_Doxo, OD15_N6L_Gem, and MF66_I_Doxo. Concentration of basic MNP: 60, 30, 25, 12.5, 6.25 µg/mL. Concentration of delivered Doxorubicin, Gemcitabine and N6L in free and functionalized samples is provided.

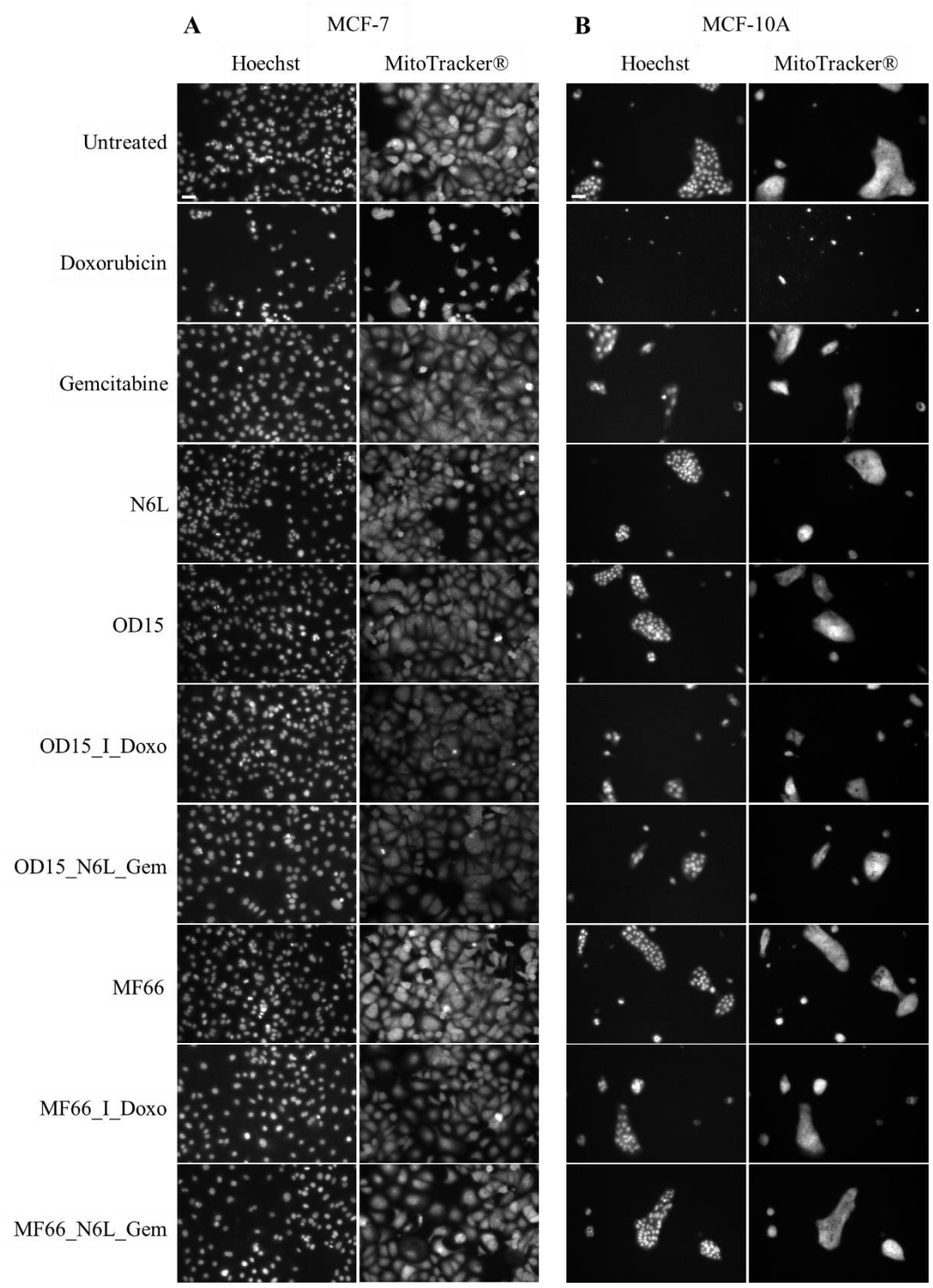

Figure 80: Analysis of mitochondrial toxicity in MCF-7 and MCF-10A cell lines.

Representative images from (A) MCF-7 and (B) MCF-10A cell lines exposed to the indicated drugs at the highest concentration and MNP formulations for 36h. Reduction in mitochondrial staining, indicating mitochondrial toxicity, was observed following exposure to doxorubicin, OD15, OD15_I_Doxo, OD15_N6L_Gem, MF66_I_Doxo, and MF66_N6L_Gem in the MCF-7 cell line and following exposure to doxorubicin, gemcitabine, OD15_I_Doxo, OD15_N6L_Gem, and MF66_I_Doxo in the MCF-10A cell line. Scale bar (white line, top left panel) = 50 µm, applicable to all images.

5.2.2 Analysis of MNP-induced cell death

MCF-7 cells were exposed to the mono-functionalised and multi-functionalised MNP formulations as well as the components of the nanoparticles. This included doxorubicin and gemcitabine chemotherapy drugs, N6L pseudo-peptide, OD15 MNP and MF66 MNP alone (Figure 81). Valinomycin was shown to reduce mitochondrial membrane potential (section 5.2.1.1) and was included as a positive control for mitochondrial dysfunction and cell death.

Baseline testing with untreated/unstained cells (A1), untreated/stained cells (A2) and valinomycin treated and stained cells (A3) provided a reference for correctly gating the populations. The results show that untreated/stained cells have a low percentage of late apoptotic cells present in quadrant 2 (Q2) (8.1%), with the majority of cells (90.2%) as a healthy population in quadrant 3 (Q3). Treatment with valinomycin caused a substantial shift in the cell population with an increase in late apoptotic/necrotic cells (Q2) to 54.6% while dead cells account for 11.4% of the cell population (Q1). Healthy cells were still present and accounted for 33.8% of the total cells sampled. The majority of cells exposed to N6L (B1) were healthy (76%) while a proportion were found to be at the late stage of apoptosis/necrosis (21.9%). Doxorubicin exposed cells (B2) were mostly present as a dead population (58.5%) and late apoptotic/necrotic population (40.2%), with low percentage of healthy cells (1.3%). Gemcitabine exposed cells (B3) had a 23.1% late apoptotic/necrotic population and a 74.4% healthy population. Cells exposed to OD15 MNP (C1) had a late apoptotic/necrotic population of 15.9% and healthy population of 81.7%. MF66 MNP exposure (D1) was similar to OD15 MNP with a late apoptotic/necrotic population of 17.1% and healthy population of 80.9%. When functionalised with doxorubicin there was a dramatic increase in the dead cell population to 73.2% for OD15_I_Doxo (C2) and late apoptotic/necrotic population of 20.6%. A greater proportion of cells were present in the dead cell quadrant (78.8%) following exposure to MF66_I_Doxo (D2) with a lower proportion undergoing late apoptosis/necrosis (16.4%). Functionalisation with both Gemcitabine and N6L preferentially increased the cell population undergoing late apoptosis/necrosis with 36% for OD15_N_Gem (C3) and 32.5% for MF66_N_Gem (D3), with the healthy cell population accounting for 58.7% and 63.8% respectively, approximately 15% lower than with Gemcitabine alone.

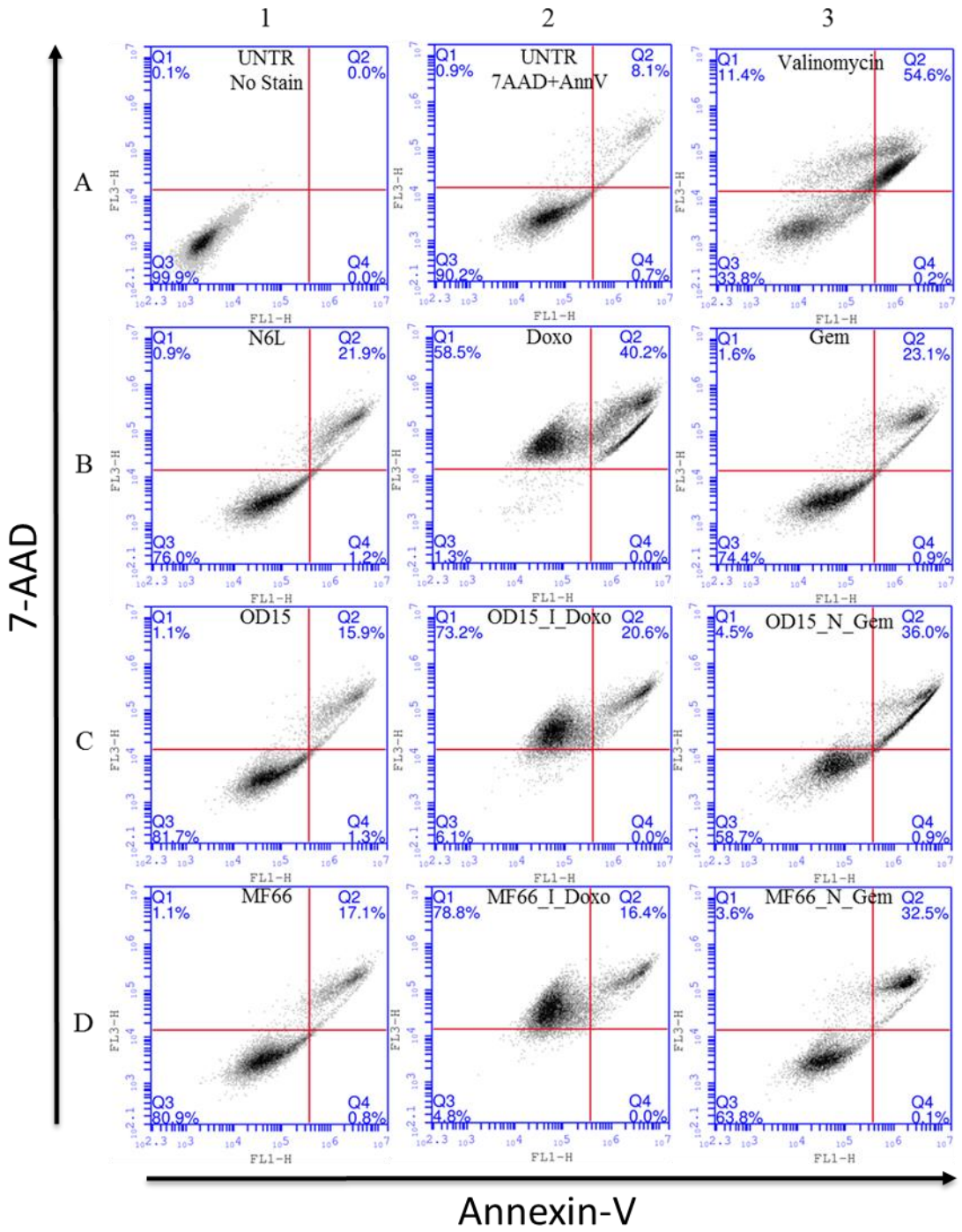

Figure 81: Cell death induced by free drug and functionalised MNP formulations.

MCF-7 cells were stained with Annexin V (AnnV) (FL1, x-axis) and 7AAD (FL3, y-axis) following exposure to chemotherapeutic drugs and functionalised MNP for 36h. Dead cells were identified in Quadrant 1 (Q1), early apoptotic cells were identified in Q4, late apoptotic/necrotic cells were identified in Q2 and healthy cells were identified in Q3. Cells were untreated and unstained (A1), untreated and stained with Annexin V and 7AAD (A2). Cells were exposed to 120 µM Valinomycin (A3), 130 nM N6L (B1), 1300 nM Doxorubicin (B2), 400 nM Gemcitabine (B3), 30 µg/mL OD15 (C1), 1300 nM OD15_I_Doxorubicin (C2), 400 nM OD15_N6L_Gemctiabine (C3), 30 µg/mL MF66 (D1), 1300 nM MF66_I_Doxorubicin (D2), and 400 nM MF66_N6L_Gemctiabine (D3). UNTR = Untreated, Doxo = doxorubicin, Gem = gemcitabine, N = N6L.

5.2.3 Cytokinesis block micronucleus assay

The study of micronucleus formation requires that the process of cytokinesis is inhibited and as a result, bi-nuclear cells are formed. The treatment with Cyto-B, an inhibitor of actin polymerisation and cytokinesis, can lead to substantial cytotoxicity if the concentration used is too high. The first step in carrying out the CBMN assay was the screening of Cyto-B concentrations to identify a suitable range. According to the OECD, a 55% reduction in cell count is acceptable, conditional on the final number of bi-nuclear cells available for analysis.

To determine the Cyto-B concentration suitable for use in the CBMN assay, six concentrations from 1 µg/mL to 6 µg/mL were used. The NIH-3T3 cell line was exposed for 44h, a time point set as standard by OECD guidelines. A 45% reduction in cell count was observed at the 1 µg/mL concentration, with 2 µg/mL and higher concentrations having greater than 70% reduction in cell count (Figure 82). Subsequently cells were grown on 24 well plates at a seeding density of 40,000 cells per well and were exposed to Cyto-B at 1 µg/mL concentration for 24h. Figure 83 demonstrates the sufficient formation of bi-nuclear cells in the presence of Cyto-B exposed cells compared to a control sample not exposed to Cyto-B.

Following the optimisation of Cyto-B concentration, a positive control was identified. The OECD specify a range of controls that can be used including six clastogenic compounds (Benzo(a)pyrene, Cyclophosphamide, Cytosine arabinoside, Methyl methanesulphonate, Mitomycin C, 4-Nitroquinoline-N-Oxide) and two aneugenic compounds (Colchicine and Vinblastine). Of these compounds, only colchicine was found to induce micronucleus formation in the NIH-3T3 cell line (Figure 84). Three concentrations (0.5, 1 and 2 µg/mL) of colchicine were selected and all three led to the formation of micronuclei.

Figure 85 shows representative images from NIH-3T3 cells treated with Doxorubicin, N6L and Gemcitabine, Figure 86 of OD15, OD15_I_Doxorubicin, OD15_N6L_Gem treated cells, and Figure 87 shows MF66, MF66_I_Doxorubicin, MF66_N6L_Gem exposed cells. No micronuclei were identified following exposure of cells to the MNP and drugs; however exposure to gemcitabine, doxorubicin and doxorubicin-functionalised MNP demonstrated the effect of the chemotherapeutic drugs on nuclear division, with the formation of mono-nuclear cells containing substantially larger nuclei (Figure 85).

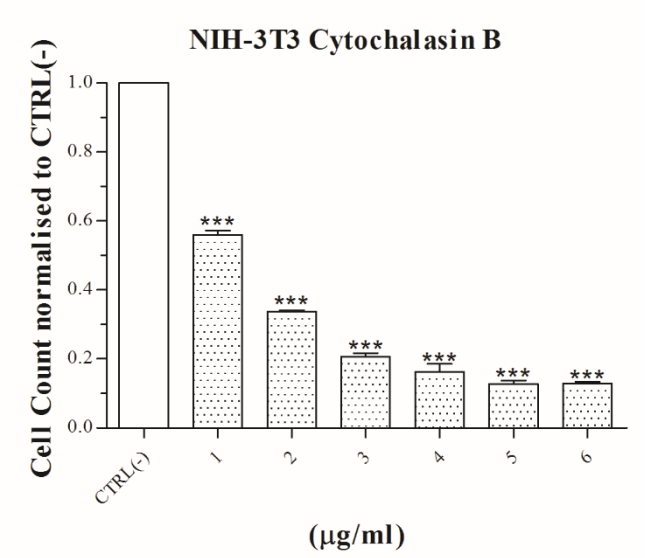

Figure 82: NIH-3T3 cell line cytotoxicity testing following exposure to Cyto-B.

Cytotoxicity testing with Cyto-B using the recommended concentration range of 1 – 6 µg/mL for 44h. Cell counts were normalised to untreated control (CTRL(-)) and data acquired from n=3 experiments. High content screening analysis was used to carry out the experiment. Statistical significance was determined using the one way ANOVA with Tukey post-test for each column compared to untreated control (CTRL(-)). p value: *** = <0.001, **=<0.01, *=<0.05.

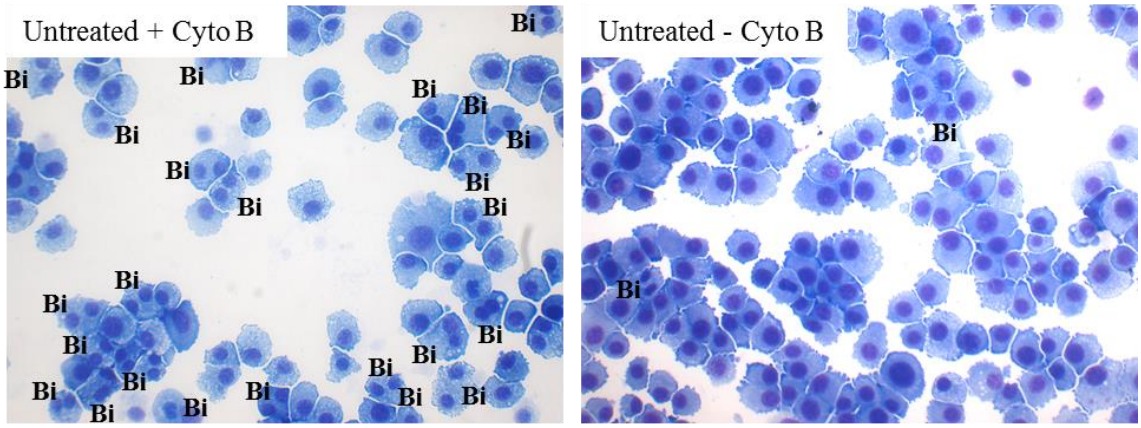

Figure 83: NIH-3T3 cell line binuclear morphology +/- Cyto-B exposure.

Cells were grown in medium with (+) or without (-) 1µg/mL Cyto-B for 24h. Cells were stained with the Kwik Diff™ staining kit. Images were acquired at 20X magnification with cells exposed to Cyto-B (left Image) having a greater degree of binuclear cells (Bi) compared to cells grown in the absence of Cyto-B (right Image).

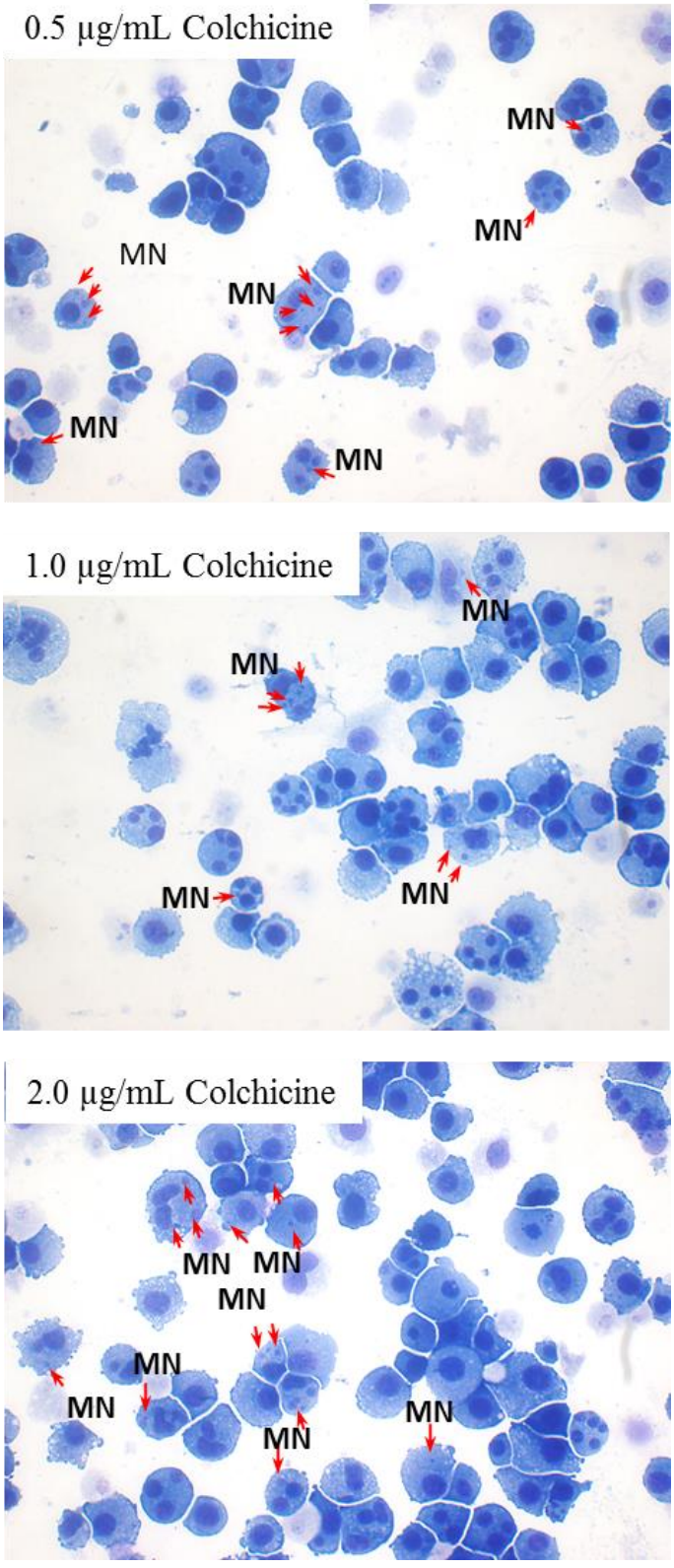

Figure 84: NIH-3T3 cell line: positive micronucleus formation with colchicine.

Colchicine (an *aneugen* that inhibits tubulin polymerisation) was used to induce micronuclei in the NIH-3T3 cell line. Three concentrations were tested (0.5, 1.0 and 2.0 µg/mL) to ensure positive micronucleus formation. Micronuclei (MN) are indicated by a red arrow.

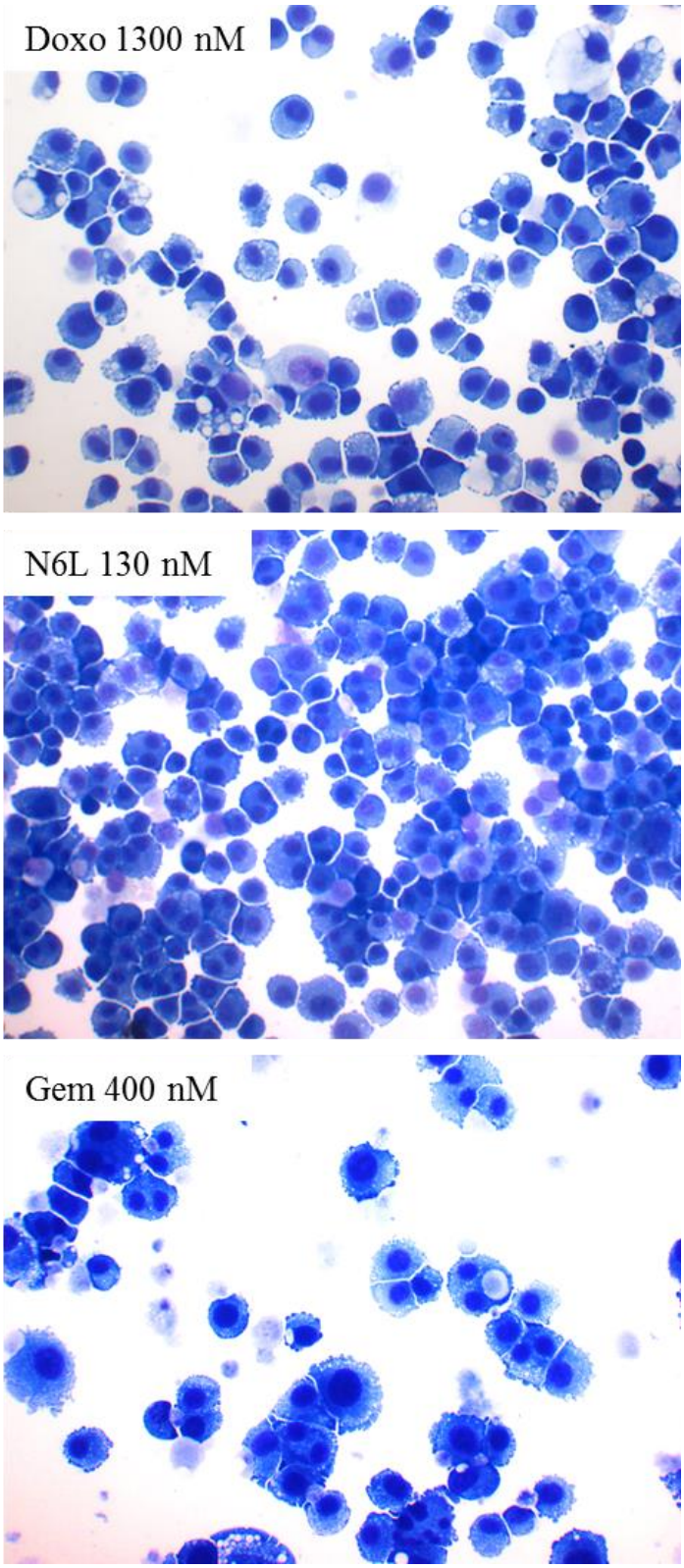

Figure 85: NIH-3T3 cell line: Investigation of micronucleus formation with N6L and chemotherapy.

NIH-3T3 cells exposed to doxorubicin, N6L and gemcitabine at the specified concentrations. Micronuclei were not induced following 24h exposure. Binuclear cell formation was not observed in doxorubicin exposed samples. Images were acquired using a 20x objective.

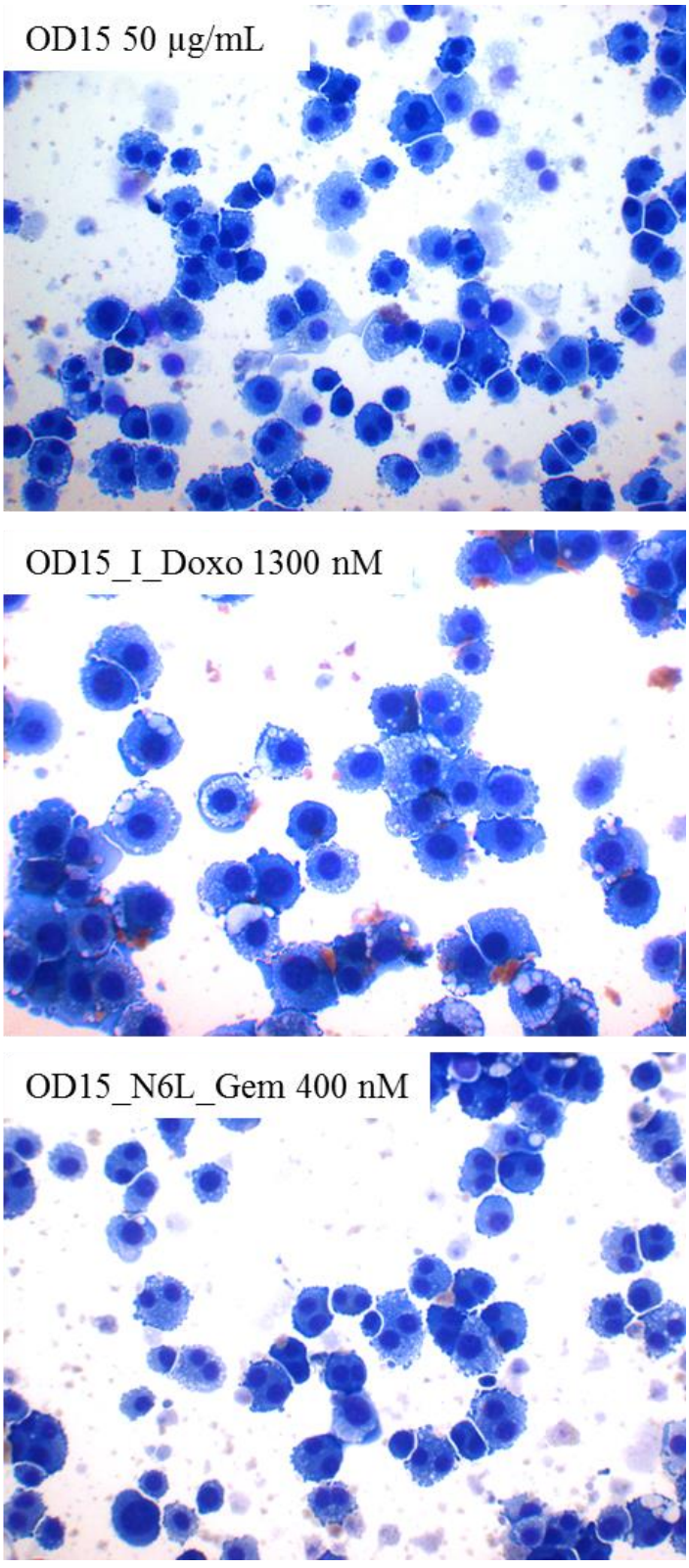

Figure 86: NIH-3T3 cell line: Investigation of micronucleus formation with OD15 MNP.

NIH-3T3 cells exposed to OD15, OD15_I_Doxo and OD15_N6L_Gem at the indicated concentrations. Micronuclei were not induced following 24h exposure. Images were acquired using a 20x objective.

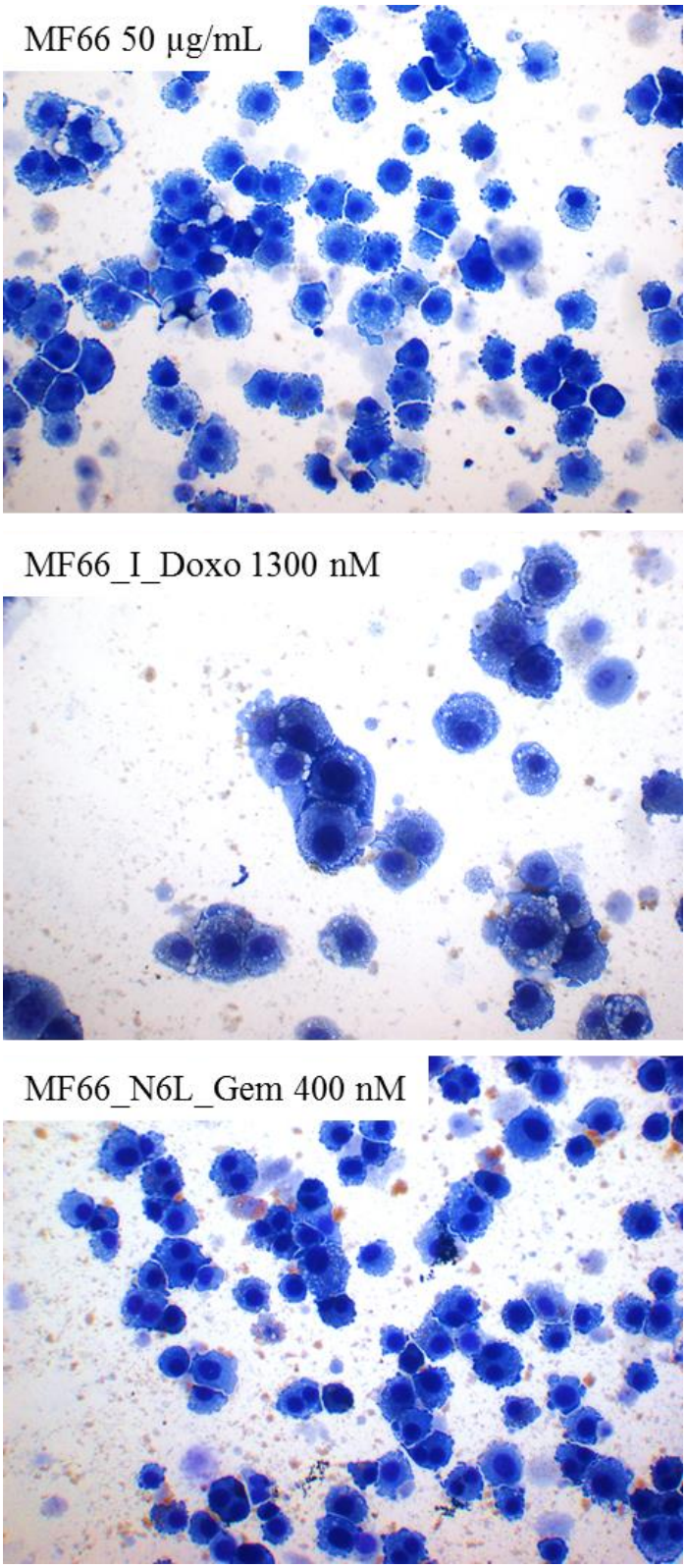

Figure 87: NIH-3T3 cell line: Investigation of micronucleus formation with MF66 MNP.

NIH-3T3 cells exposed to MF66, MF66_I_Doxo and MF66_N6L_Gem at the indicated concentrations. Micronuclei were not induced following 24h exposure. Images were acquired using a 20x objective.

5.3 Discussion

The rapid development of the nanomedicine field has resulted in a broad range of nanomaterials being produced but considerable work is needed to fully understand the health risk posed by exposure. Early evaluation of drugs with regards to their potential to cause mitochondrial damage is becoming a key requirement in drug development, since many drugs have failed to receive accreditation, and already marketed medicines have been withdrawn because of mitochondrial toxicity affecting liver function [511]. The pivotal role played by mitochondria in almost all cells of the body re-enforces the need to ensure that any product intended for human use is screened for their potential to elicit mitochondrial damage.

It has been documented that chemotherapy exposure can result in damage to mitochondria and the systemic delivery of doxorubicin has been reported to cause considerable cardiotoxicity [218], which has been associated with the production of oxygen radicles through the reduction and subsequent auto-oxidation of doxorubicin [512]. Gemcitabine was shown to directly affect mtDNA replication and deplete the nucleotide pool within the mitochondria [513], such depletion and imbalance has previously been shown to be mutagenic to the mtDNA [514], and it has been postulated that mitochondrial genomic instability produced by gemcitabine may persist and cause considerable health issues as observed for the fialuridine drug [513]. Fialuridine is a nucleoside analog similar to gemcitabine and is directly responsible for the death of five participants in a clinical trial in 1992, due to extensive mitochondrial disruption which resulted in hepatic failure, lactic acidosis, pancreatitis, neuropathy and myopathy [515]. Therefore the observation of gemcitabine-induced toxicity in the clinic may be due, in part, to mitochondrial dysfunction.

It was unknown whether the novel engineered multi-functionalised MNP made within the Multifun project could affect the integrity of mitochondria. WP3 partners from IMDEA, Madrid, Spain have shown that basic OD15 MNP do not increase the production of reactive oxygen species in the MCF-7 cell line at 72h exposure [314], indicating that the MNP does not contribute to the fenton reaction as described in section 5.1. However, in this thesis, the permeability of cell membranes of drug-exposed cells was increased considerably and lysosome staining was reduced, indicative of lysosomal membrane damage. Therefore, for the purpose of this part of the thesis it was decided to investigate the effect the MNP had on both mitochondria and nuclear integrity.

The sensitivity of the NIH-3T3 cell line has been demonstrated in other studies. An inter-laboratory study was carried out in 2012 involving Japanese and European institutions using the NIH-3T3 cell line and they found it to be sensitive to chemical compounds [516], this was further supported by the OECD who suggested using the NIH-3T3 cell line for the identification of genotoxic and non-genotoxic carcinogens, due to its suitability and responsiveness to chemical agents [510]. In addition to this, fibroblasts are key elements of cancers, and play a definite role in cancer progression [517]. They form the structural framework on which cancer cells develop and are the main stromal component of breast and pancreatic cancers [518, 519]. Their involvement in the progression of cancer is multifaceted in that they are activated by cancer cells as the tumour develops and reciprocally they aid in the development of cancer cells [520]. There is substantial cross-talk between the cancer cells and the surrounding microenvironment which promotes tumour growth and development [521]. The surrounding fibroblast cells promote extracellular matrix remodelling, cell migration, neoangiogenesis, invasion, drug resistance and evasion from the immune system [521, 522]. The close interplay between activated fibroblasts and the tumour

underlines the necessity to include such cells as models in the development of a theranostic product. There is a substantial need for the assessment of these cells in co-culture alongside cancer cells or as 3D tri-cultures where the cross-talk between fibroblasts, macrophages and cancer cells can be evaluated before and after treatment with functionalised MNP. Future work should include a co-/tri-culture study of fibroblast cell lines as well as a detailed assessment *in vivo* [523].

In the present work, valinomycin was employed as a positive control as it causes the highly specific transport and accumulation of K^+ ions in the mitochondria, and results in mitochondrial vesicle swelling and dissipation of the mitochondrial electrochemical gradient [524, 525]. In agreement with the reported effect of doxorubicin on mitochondria [512], we have observed mitochondrial damage in all cell lines following 36h exposure at and above 650 nM, with the A549 cell line showing significant reduction at all concentrations above 260 nM. The NIH-3T3 cell line was profoundly affected, with all concentrations causing mitochondrial damage. One fascinating observation made between the doxorubicin and the doxorubicin-functionalised MNP-treated cells was the similar mitochondrial toxicity observed in each of the non-cancerous cell lines (NIH-3T3, and MCF-10A), which indicated that the drug was released from the MNP within the 36h experimental time-frame to such a degree that resulted in mitochondrial damage similar to free drug exposed samples.

In comparison, the gemcitabine and gemcitabine-functionalised MNP-treated cells showed a considerably different pattern in mitochondrial toxicity. Free drug caused significant mitochondrial toxicity but the drug functionalised MNP caused considerably less. The NIH-3T3 cell line displayed mitochondrial toxicity at concentrations exceeding 50 nM for gemcitabine alone. Only the OD15_N_Gem formulation caused mitochondrial toxicity at concentrations above 100 nM. The same was observed in the MCF-10A cell line whereby gemcitabine alone caused mitochondrial toxicity at all concentrations, but was only observed in the OD15_N_Gem formulation at the highest concentration of 400 nM. The MF66_N_Gem formulation did not cause any mitochondrial toxicity in the NIH-3T3 or MCF-10A cell lines. This observation could be dependent on the anti-cancer efficacy of both OD15_N_Gem and MF66_N_Gem formulations. The OD15_N_Gem formulations are significantly more effective in the NIH-3T3 and MCF-10A cell lines compared to MF66_N_Gem. For instance, OD15_N_Gem in the NIH-3T3 cell line effectively reduces cell number at concentrations above 50 nM while MF66_N_Gem does so at concentrations exceeding 100 nM. Even more striking are the results in the MCF-10A cell line whereby OD15_N_Gem has a profound effect at all concentrations in line with results of free drug exposure, compared to MF66_N_Gem which reduces cell number only at the highest concentration. These results suggest that a reduction in mitochondrial membrane potential is observed only when cell loss is pronounced in these cell lines. While mitochondrial membrane potential of both non-cancer cell lines were profoundly affected by the gemcitabine drug, the A549 and MCF-7 cancer cell lines were not. The A549 cell line displayed mitochondrial toxicity at the highest concentration of free gemcitabine only, while the mitochondria in the MCF-7 cell line were unaffected by free gemcitabine. This observation was surprising as both of these cell lines display a reduction in cell number at all gemcitabine concentrations (approximately 50% cell loss in the A549 and 40% cell loss in the MCF-7 cell line). In comparison the NIH-3T3 and MCF-10A cell lines displayed approximately 99% loss and 60% loss respectively at the highest concentration of gemcitabine, clearly demonstrating that there may indeed be a link between cell

death and the registering of a reduction in mitochondrial membrane potential in the assay. Another possibility is that A549 and MCF-7 cells that were affected, and had damaged mitochondria, were lost during the assay on account of this damage, leaving behind healthy, unaffected cells. In comparison, it is possible that most NIH-3T3 and MCF-10A cells were affected by the treatment with gemcitabine, and regardless of cell loss in the assay, those that remained displayed a loss in mitochondrial membrane potential, perhaps on account of an increased sensitivity to exposure as previously suggested for the NIH-3T3 [516], and reported here for MCF-10A cell line exposed to gemcitabine (Figure 64) as compared to the MCF-7 cell line (Figure 63).

Cell loss may account for the otherwise normal mitochondrial membrane integrity recorded in the MCF-7 cell line following free gemcitabine exposure. To further support this assumption, we identified that cells exposed to gemcitabine-functionalised MNP, while not as effective as the free drug, did display a reduction in mitochondrial membrane potential. It is possible that mitochondrial toxicity was captured as an early event prior to cell loss. It is important to note that both OD15 and MF66 basic MNP did not cause reduction in mitochondrial membrane potential in the MCF-10A and A549 cell lines. Reduction in mitochondrial membrane potential was observed only for the highest concentration of OD15 in the MCF-7 cell line and for both OD15 and MF66 in the most sensitive NIH-3T3 cell line.

A reduction in mitochondrial membrane potential is recognised as an early event prior to the onset of apoptosis, and is indeed the case for cells exposed to doxorubicin [526]. It is a non-reversible event, and once mitochondria loose membrane potential through either membrane damage or opening of the permeability membrane pore, cells are destined to die [527]. Considerable debate surrounds the actual function of mitochondria in apoptosis from the perspective of it being an initiator and/or an amplifier in the extrinsic and intrinsic signalling cascade (Reviewed in [528]). It has been reported that sensing of perturbations in homeostatic balance can be facilitated by the nucleus, endoplasmic reticulum, Golgi apparatus, plasma membrane, cytoskeleton, cytosol, lysosomes and mitochondria [529], all of which can initiate cell death. In this thesis, the basic and drug-functionalised MNP were investigated for their potential to kill cells, using high content screening analysis, whereby a reduction in total cell count provided a positive measure for cytotoxicity. However, we have yet to demonstrate the mechanism of death, and to identify whether death actually occurs in a population of cells exposed to the engineered nanomaterials as opposed to the onset of stress-induced premature senescence. It was therefore imperative to screen the nanomaterials to identify the response pathway activated upon MNP exposure. Cell senescence is referred to as a stable and long-term loss of proliferative capacity, despite the continued survival of the cell [530]. This phenomenon can occur by a variety of mechanisms, for example: when telomere erosion reaches a critical point the cell will activate the DNA damage response and the communication with the cell cycle machinery results in proliferation arrest and the increased potential for the onset of senescence [530], or through telomere-independent mechanisms such as stress-induced senescence whereby cells exposed to sub-cytotoxic concentrations of external agents cease to multiply [531]. The gold standard approach to test the onset of senescence is through the use of the X-gal (5-bromo-4-chloro-3-indolyl-β-D-galactopyranoside) assay. It has long been recognised that β-galactosidase is upregulated and expressed in cells upon senescence, and is biochemically detectable at pH 6 using X-gal [532]. While it may have been interesting to monitor senescence in the MNP exposed cells in this study, the first approach undertaken to

determine cell fate following exposure to MNP and each functional constituent demonstrated that cells did in fact die by apoptosis/necrosis 36h post exposure. These findings negated the need in this study to determine if cells were becoming senescent. However, it would be interesting to monitor if using lower concentrations of MNP at longer exposure times could lead to the onset of senescence in future studies. Through flow cytometry and the use of an apoptotic/necrotic assay it was determined that all drugs and drug-functionalised MNP used in this study cause cell death following 36h exposure (Figure 81). Flow cytometry provided a reliable method to determine the degree of cell death, and to generate a complete picture any de-adhered cells were collected from the culture medium by centrifugation prior to cell staining and flow cytometry quantification. N6L was shown to induce cell death with 21.9% population of cells present within the late apoptotic/necrotic zone, this result is in agreement with that found in the literature [393]. The percentage of apoptotic/necrotic cell death compared to the healthy cell population was consistent between doxorubicin and doxorubicin-functionalised MNP (Figure 81, B2, C2, and D2). Unlike the valinomycin positive control (Figure 81, A3), a high percentage of cells within Q1 following doxorubicin exposure was recorded. Two recently published studies using the 7-AAD and Annexin V test have referred to the cell population in Q1 as the "dead" cell population [533, 534], another recent study refer to Q1 as the necrotic or dead cell population [535], and another considers Q1 to contain damaged cells [536]. In fact, a considerable number of studies fail to provide reasoning for the identity of cell populations located within Q1. However, a study by Sawai et al. has provided a reasoning behind the observed positivity in Q1 using the related nuclear dye, propidium iodide [537]. In this study, they observed cells over a five hour period transition through an Annexin V+/PI– state (early apoptosis), to Annexin V+/PI+ state (late apoptosis or necrosis) and between 4-5 hours they observed a population appearing within Q1. They considered this Q1 population as necrotic and postulated that PI+ staining in the absence of Annexin V staining may be due to the loss of necrotic plasma membranes during the staining procedure [537]. Prior to treating cells with the necrosis inhibitor, necrostatin-1, they were unsure whether Q1 cells were a primary necrotic population or post-apoptotic secondary necrotic population. The use of necrostatin-1 enabled them to discern between these two possibilities. They also indicated that cells present in Q4 are not necessarily confined to being early apoptotic cells, but could also contain early necrotic cells, with Annexin V+/PI– staining observed in the early necrotic cells in their study [537]. Therefore, even though we refer to cells in Q1 as "dead" cells in the present study, they may indeed include primary necrotic and/or post-apoptotic secondary necrotic cells. Nevertheless, doxorubicin is the only chemotherapy drug to induce such a response, compared to gemcitabine which only increases the late apoptotic or necrotic cell population in Q2 (Figure 81, B3, C3, and D3). One interesting observation, which complements the results obtained for the mitochondrial membrane potential test in the MCF-7 cell line with gemcitabine exposure, is that free gemcitabine drug treatment results in 23.1% late apoptotic or necrotic cells while drug-functionalised MNP have even greater late apoptotic or necrotic cell populations of 36% and 32.5% (OD15_N_Gem and MF66_N_Gem respectively). Even though drug-functionalised MF66 MNP at the highest concentration of 400 nM cause a reduction in cell viability in the MCF-7 cell line of approximately 30%, as determined by HCSA, compared to approximately 40% for gemcitabine, they were shown here to contain more late apoptotic or necrotic cells compared to gemcitabine-exposed cells. This corresponds to the results obtained for mitochondrial membrane potential whereby MF66_N_Gem in the MCF-7 cell line had the most

significant ($p<0.001$ = ***) reduction in mitochondrial membrane potential. In agreement, the OD15_N_Gem MNP caused a greater reduction in cell count than gemcitabine alone in the MCF-7 cell line (approximately 50% reduction in cell count), contained the greatest number of late apoptotic or necrotic cells (36%) and displayed reduction in mitochondrial membrane potential ($p<0.01$ = **). Therefore by combining the two high throughput methods of HCSA and flow cytometry, it was possible to obtain a thorough insight into MNP cytotoxicity, mitochondrial dysfunction and method of cell death.

Further analysis of the functionalised MNP and their individual components was carried out to determine if they were genotoxic and could lead to the formation of micronuclei in a population of actively proliferating cells. A limited number of studies are published to date that report on MNP-induced micronucleus formation, and of those published, there is little consensus on their genotoxicity. MNP have been reported as non-genotoxic due to their failure to affect cells using common genotoxic assays (ames assay, micronucleus assay and comet assay) [538], while another study reported on the presence of a genotoxic effect [539], both studies used MNP with an average size of 8nm. In this thesis the NIH-3T3 cell line, the most sensitive cell line as seen in the mitochondrial membrane potential tests, was exposed to all functionalised MNP and their individual components. Colchicine was the first chemical shown to induce micronuclei [540], and out of all the chemicals tested in this present study (data not shown), it was the only one to reproducibly form micronuclei in the NIH-3T3 cell line. Unlike colchicine, all the functionalised MNP and their individual components did not result in the formation of micronuclei (Figure 85, Figure 86, and Figure 87). However the test did provide further evidence for efficient doxorubicin drug release from the functionalised MNP. It is well documented that doxorubicin induces S and G2/M cell cycle arrest [541]. The results presented in Figure 85, Figure 86, and Figure 87 show the majority of cells in a mono-nuclear state while only one bi-nuclear cell was identified following OD15_I_Doxo and Cyto-B exposure (Figure 86). Cyto-B does not prevent a cell forming two nuclei during mitosis but inhibits daughter cell formation. The vast majority of cells contained a single large nucleus following exposure to free doxorubicin drug and MNP functionalised with doxorubicin. This result suggests that the majority of cells arrested at the S and/or G2/M phase when DNA content is double that of a non-dividing cell. Due to the inability of these cells to complete mitosis attributable to the mode of action of doxorubicin, it was not possible to visualise micronuclei as nuclear division is required for micronucleus formation.

5.4 Conclusion

The novel engineered multifunctional MNP developed within Multifun were tested to determine whether they directly or indirectly resulted in mitochondrial damage. Uptake into cells was confirmed in the previous chapter, in addition to confirmation of chemotherapy drug efficacy via functionalised MNP delivery. In this chapter it has been shown that the observed anticancer effect occurs due to the release of the chemotherapy drug, an observation which was made possible by flow cytometry through the evaluation of apoptotic or necrotic cell death induced by MNP alone and chemotherapy alone. It was confirmed that OD15_I_Doxo, MF66_I_Doxo and OD15_N6L_Gem caused mitochondrial toxicity at 36h in three cell lines tested. However, MF66_N6L_Gem induced mitochondrial toxicity only in the MCF-7 cell line. Therefore in relation to the targeted formulations that have been tested in this work the OD15_N6L_Gem MNP displayed the most promising anticancer effect compared to the MF66_N6L_Gem formulation. It is

possible that OD15_N6L_Gem MNP is taken up more readily into the cell on account of a surface charge of -26.8 mV compared to -34.8 mV for MF66_N6L_Gem MNP and therefore exhibit a greater effect. Delivery of payload should theoretically be the same as the same linker and targeting molecule were employed for both. However, a distinct difference in cell morphology was observed upon exposure to either functionalised OD15 MNP (Figure 86) or functionalised MF66 MNP (Figure 87). OD15_N6L_Gem MNP exposed cells displayed signs of endosome/lysosomal damage with the presence of cytoplasmic vacuoles, which was also a feature with cells exposed to OD15_I_Doxo. In comparison the MF66_N6L_Gem did not appear to form such intracellular vacuoles while some were identified with MF66_I_Doxo. It is possible that upon uptake into cells the OD15_N6L_Gem MNP causes considerable lysosomal damage via a number of complementary routes. Firstly the release of gemcitabine may result in direct lysosome damage via the activation of acid sphingomyelinase which in turn leads to the lysosomal accumulation of ceramide and the activation of cathepsin D, all of which can facilitate cell death via damage to the mitochondrial membrane (ceramide [542]) and activation of pro-apoptotic proteins (cathepsin D [543]). Secondly, the core OD15 MNP could contribute to the effectiveness of the drug-induced toxicity through the production of reactive oxygen species via the fenton reaction. In addition, cellular stress to lysosomes, mitochondria, Golgi body and endoplasmic reticulum could all lead to the formation of autophagosomes [315], which may account for the large vacuoles visualised in Figure 86. Therefore the MNP core may in fact be contributing to the potency of the chemotherapeutic agent and as such would indicate distinct advantage over conventional drug delivery methodologies.

While mitochondrial damage was identified at 36h, chromosomal aberration was not detected during this time frame. Genotoxicity is expected to occur with exposure to chemotherapeutic agents via direct interaction with genomic and mitochondrial DNA, however these events were not observed using the OECD approved cytokinesis block micronucleus assay.

Chapter 6
General Discussion and Future Work

Chapter 6: General discussion and future work

6.1 Discussion

The extraordinary developments in the field of nanomedicine over the past decade have generated an immense wealth of knowledge. In this short timeframe nanomedicine research has significantly pushed the boundaries of material science and ignited immense enthusiasm across the academic community, giving hope to many future patients who may not have to endure the currently available therapies. It is thought that nanomedicine, with the vast array of nanomaterials available, can provide limitless potential in the fight against life threatening diseases. It is exciting to think what lies ahead if the depth and breadth of today's knowledge pales into insignificance compared to what has yet to be discovered. The fundamental research currently being carried out is expanding scientific appreciation for the complexity and intricate dynamics of nanomaterials at the molecular level in cells. Nanomaterials possess unique physical and chemical characteristics compared to the same compounds in the micrometre size range. The rapid expansion in the production of nanomaterials has surpassed the rate at which each formulation can be adequately screened to evaluate the risk posed by their exposure. Considerable effort and attention has turned to the development of rapid and reliable assays for screening nanomaterials, with regulatory bodies striving to develop a uniform approach for nanoparticle cytotoxicity and genotoxicity testing to facilitate accurate cross-study comparisons.

The European Commission has provided substantial funding towards the development of biomedical tools based on nanomaterials suitable for disease diagnosis and treatment. The Multifun FP-7 project set out to design, develop, validate and apply novel iron oxide nanoparticles for the targeted delivery of drugs with the capability of localised magnetic heating. Instrumental in the validation process within the Multifun project was WP3. The goal of this thesis, which reflects a major part of the work completed within WP3, was to develop and test a series of methods for screening a range of iron oxide nanoparticles, where to identify the lead formulations with set physicochemical characteristics such as uniform shape, narrow size distribution, stability in biological medium and to measure the onset of acute cytotoxicity upon exposure to chosen cell lines. Increasing the level of MNP complexity through surface modification and decoration with chemotherapeutic drugs and peptide molecules, an additional requirement was the identification of formulations that could elicit an anticancer response, and to determine efficacy of MNP drug delivery compared to free drug controls. Finally, Multifun WP3 partners investigated the MNP effects on mitochondria and genomic DNA and investigated the mechanism of cell death, for the lead formulations and their individual components.

The data presented in chapter 3 (section 3.2 Results) demonstrate that the MNP synthesised by Multifun partners with a core size greater than 10 nm have greater uniformity in shape (OD10, OD15 and MF66) compared to the other formulations, with OD10 and OD15 MNP having highly ordered shapes. This is probably due to the choice of synthesis with both OD10 and OD15 synthesised via thermal decomposition, which is regarded as one of the best methods to produce MNP of narrow size distribution and homogeneity in structural characteristics [39]. Prior to screening the MNP to identify the most suitable biocompatible formulation, the selection and validation of suitable assays was required. The assay method for testing the capacity of the MNP to induce acute cytotoxicity was an important consideration as it has

been extensively reported that nanomaterials can cause interference with the most common colorimetric based assays [321-323]. Therefore a high-throughput assay using fluorescent dyes was optimised and implemented. Interference with fluorescent dyes by nanomaterials was tested at a high concentration to determine whether interference would occur. The experimental approach involved the use of MNP which were dispersed in phenol-free and serum-free medium containing fluorescent dyes. No reduction in fluorescent intensity was observed when compared against an untreated fluorescent control, indicating that even at high concentrations, the fluorescent intensity of the dyes is not affected, as shown in Figure 24. The assay employed in this thesis did not involve staining of cells in the presence of such high MNP concentrations. Cell staining was carried out following the washing of the cell monolayer and MNP removal to further ensure that interference would not occur. To determine the suitability of the multiparameter fluorescent kit we exposed cells to known cytotoxic agents. Controls such as valinomycin have been used since it is known to damage cell membranes and mitochondria [429], while tacrine is known to damage lysosome vesicles [430]. The results demonstrated that the fluorescent dyes could be used in HCSA to accurately identify changes in cell count, cell membrane permeability, lysosomal mass/pH, and mitochondrial integrity, as shown in Figure 25 and Figure 72. Only when these tests were complete was it possible to start the cytotoxicity testing of the MNP.

The cytotoxicity experiments demonstrated that the OD15 MNP, containing a magnetite core, was the least cytotoxic compound compared to all other MNP tested, as shown in Figure 27. The MF66 MNP, containing a maghemite core, demonstrated dose dependent toxicity in three cell lines, at the highest concentration of 200 µg/mL. Below this concentration the MF66 MNP did not induce cytotoxicity in four of the five cell lines tested and did not negatively affect normal cell proliferation and was retained in the study. The hydrodynamic diameter of MNP dispersed in cell culture medium containing 10% FBS were shown to increase in all formulations. This increase appeared to correlate with the degree of cellular uptake (Table 5, Figure 30 & Figure 31) and it was shown that the increase in hydrodynamic diameter was not a positive indicator for increased MNP instability in complete medium, with ADNH and MF66 MNP having the same increase in hydrodynamic diameter of 123 nm, with only ADNH MNP being highly unstable in solution (Figure 30). The surface charge of all MNP did not provide any additional information to explain the observed instability of the ADNH formulation. Both ASi and ADNH had an overall positive zeta potential with ASi being considerably more stable in solution. In fact it is known that positively charged MNP enter cells more readily than negatively charged MNP [277, 544, 545], and the results demonstrate this (Figure 30 & Figure 31). However, this does not infer that negatively charged nanomaterials do not enter cells as uptake of negatively charged MNP into lysosomes was observed (Figure 30 & Figure 31) and via the TEM-uptake study conducted by Dr Michele Chiappi, IMDEA, Madrid, Spain (Figure 33). An important pre-requisite for developing an MNP with intracellular drug delivery capabilities is knowing how rapidly uptake occurs, the method of uptake and where the nanomaterials reside, in order to design the nanomaterials to allow for triggered drug release. We have shown that OD15 MNP was taken up into cells within the first 30 minutes of exposure, with a maximal uptake observed at 24h. Uptake was via the active process of clathrin-mediated endocytosis and macropinocytosis, and was dependent on the size of the nanoparticle clusters on the surface of the cell [314]. The *in vivo* experimentation indicated that the MF66 MNP could be detected by MRI and that soon after injection there was contrast observed within the liver,

which remained unchanged five weeks post exposure. Most importantly, this experiment demonstrated suitability of the MNP *in vivo*, with no observed adverse effects between the exposed and placebo injected animals (Figure 36).

The cytotoxicity assay was further employed to determine the suitability of electrostatic and covalent drug functionalisation regimes as presented in chapter 4 (4.2 Results). Both formulations sufficiently led to the reduction in cell count but in order to design nanomaterials with controlled drug release capability, the covalent functionalisation was selected on account that a chemical bond is harder to break than an electrostatic interaction and would provide a more controlled method for drug release when exposed to a reducing environment (e.g., temperature, pH or mechanical) capable of cleaving the drug from the MNP surface. It has been demonstrated that electrostatic MNP can release the attached drug within minutes of being dispersed in cell culture medium [354]. The next consideration was the identification and selection of a linker molecule that could be used to attach the drug to the surface of the nanomaterials but upon release would liberate an unmodified and fully functional drug. Three pH sensitive linkers were investigated, one containing a carbamate group, a second containing a urea group and the third containing an imine group. All linkers contained a disulfide group but the linker containing the imine group had the additional capability of cleaving at both the disulfide moiety (reducing environment) to release the drug but also at the imine moiety (acidic pH) to liberate an unmodified drug. The added cleavage point in this linker may be one of the explanations behind the observed increase in cytotoxicity. This linker was adapted for the remainder of the study and was used for the attachment of gemcitabine onto the surface of the MNP while the O-linker was used for attachment of the N6L targeting peptide. Targeting of the nanomaterials using the N6L anticancer peptide was shown to increase the amount of MNP interacting with breast and pancreatic cells. From the outcome of the cytotoxicity assay, confirmation of MNP uptake via an increase in the lysosomal staining parameter compared to cells exposed to non-targeting formulations was possible. When both gemcitabine drug and N6L were functionalised onto the MNP the combined cytotoxic effect was greater than that observed in cells exposed to gemcitabine-MNP alone, and was most pronounced in the pancreatic cell lines.

The evaluation of possible consequences caused by the accidental exposure to drug functionalised nanomaterials which can occur through direct skin contact, inhalation or ingestion can have serious health effects [546-549] was also carried out. Therefore, the focus was on identifying whether the engineered nanomaterials, functionalised with doxorubicin, gemcitabine and N6L could cause mitochondrial damage in the A549 lung cancer cell line, NIH-3T3 mouse fibroblast cell line, MCF-7 breast cancer cell line and MCF-10A breast-derived normal-like cell line. All MNP functionalised with doxorubicin caused mitochondrial damage in the majority of cell lines tested. In comparison, gemcitabine functionalised MNP did not cause the same degree of mitochondrial damage with OD15_N_Gem causing more mitochondrial toxicity compared to MF66_N_Gem. While mitochondrial damage can be considered a significant marker for increased risk in healthy individuals, the results obtained can also be considered favourable since uptake into tumour cells would allow for mitochondrial damage, which would directly starve the cell of energy and activate the irreversible cell death pathway [527]. The functionalised MNP tested in this thesis caused mitochondrial damage and was due to the functionalised chemotherapy agent. The reduction in cell count observed throughout this thesis was a result of apoptotic or necrotic cell death (Figure 81), which is also

attributed to the release of the functionalised chemotherapy agent. Since both doxorubicin and gemcitabine interact with DNA, we carried out genotoxicity testing using the OECD micronucleus guideline test to determine whether the nanomaterials had the capacity to cause substantial chromosomal alteration. While micronuclei were induced using colchicine, the MNP did not induce micronuclei formation over the course of the experiment, which translates into the absence of genotoxicity.

6.2 Conclusion

This study has demonstrated that the basic MNP (OD15 and MF66) do not induce acute cytotoxicity in a range of breast and pancreatic cell lines. The stepwise approach taken in this study enabled the *in vivo* testing of a single formulation to demonstrate sensitivity of MRI for MNP detection and to further investigate aspects of biocompatibility within the chosen small animal models. Implementation of the safe-by-design three tiered approach described in this study (Figure 6) ensured that within the Multifun project, a reduced dependence on the use of animals for the screening of all engineered formulations was achieved without compromising the depth of the acquired information. In addition, the functionalisation of the biocompatible MNP with chemotherapeutic agents was shown to be highly effective at killing breast and pancreatic cell lines. Furthermore, it has been demonstrated for the first time that the HCSA-employed assay could be used as a positive indicator for MNP uptake, with an increase observed with cells exposed to N6L-functionalised MNP. It was shown that the MNP drug-functionalised anticancer effect could occur as a direct consequence of the chemotherapeutic drug interaction with cells dying via apoptotic or necrotic cell death pathways, and it was also identified that cytotoxicity could occur through mitochondrial damage. Finally, while genotoxicity is expected via the chemotherapy drug interaction with genomic and mitochondrial DNA, it was established that the engineered nanomaterials did not result in the formation of micronuclei, indicating the absence of genotoxicity.

The findings of this thesis suggest that the stepwise approach employing a range of complementary techniques can be used for short term *in vitro* cytotoxicity and anticancer efficacy assessment, and long term *in vivo* biodistribution monitoring. Through implementation of the safe-by-design approach, four MNP formulations have been identified, which are capable of inducing anticancer effects (OD15_I_Doxo, MF66_I_Doxo, OD15_N_Gem, and MF66_N_Gem).

6.3 Future work

While the current work has presented a method to screen a broad range of nanomaterials to determine cytotoxic and genotoxic potential, it is in no way an exhaustive approach. More work is necessary to bring the manufactured materials by Multifun into the next technological readiness level. It would be beneficial to study the effect of long term MNP exposure in cells and monitor the onset of toxicity, which can be initiated through the degradation of MNP within intracellular organelles and the liberation of excess iron and/or components of the MNP coating agent. Iron-driven oxidation of proteins and lipids can be easily repaired, but the sustained exposure to iron within the cell can lead to subtle alteration of the mitochondrial DNA, via interaction between free iron and reactive oxygen species [491]. Therefore it is important to monitor any changes to mitochondrial DNA over longer periods, in excess of 72h as preliminarily conducted in this study, to determine whether engineered nanomaterials can induce mitochondrial toxicity

with long-term exposure. ROS production was analysed by WP3 partners and found not to be amplified following OD15 MNP exposure, using a fluorescent based approach. It would be of interest to analyse the activity of mitochondrial superoxide dismutase activation in response to ROS production, as it may provide a more sensitive assay to determine ROS production.

Two major considerations with the exposure of cells to MNP, and which have not been investigated in this thesis, are the changes that may occur in transcription and translation. It would be interesting to carry out gene expression analysis pre- and post- MNP exposure. Disease specific arrays for a wide range of cancers are available on the market, and would enable to determine whether basic and functionalised MNP exposure could facilitate the activation of pro-apoptotic pathways and would allow for comprehensive analysis of a broad range of gene alterations. Cancers evolve and acquire the ability to survive according to the six hallmarks of cancer [550] (sustaining proliferative signalling, evading growth suppressors, activating invasion and metastasis, enabling replicative immortality, inducing angiogenesis, and resisting cell death), therefore it would be extremely interesting to screen whether the engineered MNP could affect the many processes that support cancer survival such as the inhibition of aerobic glycolysis, inhibition of the proliferative signal, activation of growth suppressors, labelling of cancer cells for recognition by the immune system, inhibition of telomerase, repression of tumour-promoting inflammation, repression of invasion and metastasis, inhibition of tumour-driven angiogenesis, promotion of genomic instability and increased mutation in tumour cells and the ability to promote cell death. These can potentially be achieved through functionalisation of specific inhibitors and drugs on the surface of the MNP.

It would be interesting to carry out MNP risk assessment using complex *in vitro* 3D tissue models, to evaluate the effect of exposure on a range of associated cells and the impact on tissue pathology in relation to the other cancer types such as lung cancer. Novel *in vitro* 3D primary human lung cell models have been available for many years by Epithelix Sàrl, with MucilAir™ as their flagship product for healthy 3D tissue models. Their sister company Oncothesis, established in 2014, provides OncoCilAir™ as their flagship product, which incorporates lung adenocarcinoma cells within normal human lung fibroblasts. The sustained survival of these novel model systems would enable long term MNP exposure testing, with the ability to conduct repeat exposure experiments over many months.

MNP in this study have shown limited blood circulation time, with rapid liver accumulation observed with maximum signal intensity three hours post injection (data not shown). The reticulocyte endothelial system is very efficient at removing circulating particulates with nanoparticle uptake observed in Kupffer cells [436, 437]. Therefore it would be beneficial to design nanomaterials that contain hydrophilic polymers that can resist opsonisation and removal from the circulation. Work has been initiated by Dr Morales of WP1 to design a long circulating OD15 MNP formulation containing different lengths of PEG polymer as a surface coat. It would be interesting to continue the development of this formulation and demonstrate longer circulation time and increased tumour bioavailability.

HCSA has been instrumental in this project, it has provided a means to rapidly screen a variety of nanomaterials in multiple cell lines and the assay employed has proven useful in detecting changes in key cellular organelles. It would be important to further develop assays that could be used to observe real-time changes in cellular homeostasis and would be interesting to observe and document the onset and

progression of cardiac cell damage following exposure to doxoroubicin functionalised MNP, and to establish whether DMSA coated MNP provide a protective effect compared to other coated formulations.

With regard to the current study, it would be beneficial to carry out comprehensive animal testing with exposure to sub-cytotoxic doses and cytotoxic doses of basic and functionalised MNP. Since the chemotherapy agents employed are known to affect genomic DNA and mtDNA, it would be interesting to carry out behavioural studies and determine whether adverse neurological events occur, such as reduced or increased neurotransmitter levels and neuronal cell death via mitochondrial damage following exposure to the functionalised MNP. It would also be interesting to study post-exposure liver function and kidney function by NMR spectroscopy, specifically recording changes in key metabolites such as lactate, alanine, sugars, and amino acids etc, owing to the fact that localisation to the liver was observed in this study and that the excretion of iron metabolites from the liver may be detected in the urine.

Based on the findings of this thesis, the selected MNP have been successfully used in *in vivo* hyperthermia experiments by colleagues at the University of Jena, as part of WP5 of the Multifun project. Mouse models with subcutaneous tumours were intratumorally injected with MF66 MNP functionalised with N6L, Doxo, or N6L_Doxo and subjected to a series of hyperthermia treatments up to 28 days post injection. Reduction in tumour volume was observed in all animals injected with MNP and subjected to the hyperthermia regimen [354].

Building on the success of the Multifun project, the European Commission has recently funded a continuation project (NoCanTher) which launched at the kick-off meeting on 01/04/2016, and is focused on the upscaling of the lead formulations identified in this thesis for early clinical phase testing.

Chapter 7

References

Chapter 7: References

1. Faraday, M., *The Bakerian Lecture: Experimental Relations of Gold (and Other Metals) to Light.* Philosophical Transactions of the Royal Society of London, 1857. **147**: p. 145-181.
2. Drexler, K.E., *Nanosystems : molecular machinery, manufacturing, and computation*. 1992: Wiley.
3. Commission, E., *Commission Recommendation of 18 October 2011 on the definition of nanomaterial Text with EEA relevance.* Official Journal of the European Union, 2011. **L275**: p. 38-40.
4. Sinha, A.K., et al., *Mesostructured manganese oxide/gold nanoparticle composites for extensive air purification.* Angew Chem Int Ed Engl, 2007. **46**(16): p. 2891-4.
5. Dykman, L.A. and N.G. Khlebtsov, *Gold nanoparticles in biology and medicine: recent advances and prospects.* Acta Naturae, 2011. **3**(2): p. 34-55.
6. Kim, J.S., et al., *Antimicrobial effects of silver nanoparticles.* Nanomedicine, 2007. **3**(1): p. 95-101.
7. Evans, K., *New roles for conductive rubbers and plastics.* Materials & Design, 1984. **5**(1): p. 43-45.
8. Bott, J., A. Stormer, and R. Franz, *Migration of nanoparticles from plastic packaging materials containing carbon black into foodstuffs.* Food Addit Contam Part A Chem Anal Control Expo Risk Assess, 2014. **31**(10): p. 1769-82.
9. Potapov, V.V., et al., *Enhancement of concrete durability by introducing SiO2 nanoparticles.* Glass Physics and Chemistry, 2013. **39**(4): p. 425-430.
10. Tesfaye, A.T., et al., *Porous Silicon Nanotube Arrays as Anode Material for Li-Ion Batteries.* ACS Appl Mater Interfaces, 2015. **7**(37): p. 20495-8.
11. Liu, K., et al., *Improved photovoltaic performance of silicon nanowire/organic hybrid solar cells by incorporating silver nanoparticles.* Nanoscale Res Lett, 2013. **8**(1): p. 88.
12. Yang, Y.X., et al., *Evaluation of the toxicity of food additive silica nanoparticles on gastrointestinal cells.* J Appl Toxicol, 2014. **34**(4): p. 424-35.
13. Lohani, A., et al., *Nanotechnology-Based Cosmeceuticals.* ISRN Dermatology, 2014. **2014**: p. 14.
14. Sun, S., et al., *Monodisperse FePt nanoparticles and ferromagnetic FePt nanocrystal superlattices.* Science, 2000. **287**(5460): p. 1989-92.
15. Ataeefard, M., E. Ghasemi, and M. Ebadi, *Effect of micro- and nanomagnetite on printing toner properties.* ScientificWorldJournal, 2014. **2014**: p. 706367.
16. Huzaira, M. and R.R. Anderson, *Magnetite tattoos.* Lasers Surg Med, 2002. **31**(2): p. 121-8.
17. Mayo, J.T., et al., *The effect of nanocrystalline magnetite size on arsenic removal.* Science and Technology of Advanced Materials, 2007. **8**(1-2): p. 71.
18. Jiang, W., et al., *Spherical polystyrene-supported nano-Fe3O4 of high capacity and low-field separation for arsenate removal from water.* J Hazard Mater, 2012. **243**: p. 319-25.
19. Hahn, P.F., et al., *Clinical application of superparamagnetic iron oxide to MR imaging of tissue perfusion in vascular liver tumors.* Radiology, 1990. **174**(2): p. 361-6.
20. Stark, D.D., et al., *Superparamagnetic iron oxide: clinical application as a contrast agent for MR imaging of the liver.* Radiology, 1988. **168**(2): p. 297-301.

21. Santra, S., et al., *Gadolinium-encapsulating iron oxide nanoprobe as activatable NMR/MRI contrast agent.* ACS Nano, 2012. **6**(8): p. 7281-94.
22. Kossatz, S., et al., *High Therapeutic Efficiency of Magnetic Hyperthermia in Xenograft Models Achieved with Moderate Temperature Dosages in the Tumor Area.* Pharm Res, 2014.
23. Unterweger, H., et al., *Development and characterization of magnetic iron oxide nanoparticles with a cisplatin-bearing polymer coating for targeted drug delivery.* Int J Nanomedicine, 2014. **9**: p. 3659-76.
24. Momtazi, L., et al., *Synthesis, characterization, and cellular uptake of magnetic nanocarriers for cancer drug delivery.* J Colloid Interface Sci, 2014. **433C**: p. 76-85.
25. Li, L., et al., *Superparamagnetic iron oxide nanoparticles as MRI contrast agents for non-invasive stem cell labeling and tracking.* Theranostics, 2013. **3**(8): p. 595-615.
26. Kaushik, A., et al., *Iron oxide nanoparticles-chitosan composite based glucose biosensor.* Biosens Bioelectron, 2008. **24**(4): p. 676-83.
27. Scherer, F., et al., *Magnetofection: enhancing and targeting gene delivery by magnetic force in vitro and in vivo.* Gene Ther, 2002. **9**(2): p. 102-9.
28. Gultepe, E., et al., *Monitoring of magnetic targeting to tumor vasculature through MRI and biodistribution.* Nanomedicine (Lond), 2010. **5**(8): p. 1173-82.
29. Mejias, R., et al., *Dimercaptosuccinic acid-coated magnetite nanoparticles for magnetically guided in vivo delivery of interferon gamma for cancer immunotherapy.* Biomaterials, 2011. **32**(11): p. 2938-52.
30. Roca, A.G., et al., *Effect of nanoparticle and aggregate size on the relaxometric properties of MR contrast agents based on high quality magnetite nanoparticles.* J Phys Chem B, 2009. **113**(19): p. 7033-9.
31. Tartaj, P., et al., *The iron oxides strike back: from biomedical applications to energy storage devices and photoelectrochemical water splitting.* Adv Mater, 2011. **23**(44): p. 5243-9.
32. Corr, S.A., et al., *Magnetic-fluorescent nanocomposites for biomedical multitasking.* Chem Commun (Camb), 2006(43): p. 4474-6.
33. Peng, X.H., et al., *Targeted magnetic iron oxide nanoparticles for tumor imaging and therapy.* Int J Nanomedicine, 2008. **3**(3): p. 311-21.
34. Gupta, A.K. and M. Gupta, *Synthesis and surface engineering of iron oxide nanoparticles for biomedical applications.* Biomaterials, 2005. **26**(18): p. 3995-4021.
35. De Jong, W.H. and P.J. Borm, *Drug delivery and nanoparticles:applications and hazards.* Int J Nanomedicine, 2008. **3**(2): p. 133-49.
36. Veiseh, O., et al., *Inhibition of tumor-cell invasion with chlorotoxin-bound superparamagnetic nanoparticles.* Small, 2009. **5**(2): p. 256-64.
37. Sadeghi-Aliabadi, H., et al., *Preparation and Cytotoxic Evaluation of Magnetite (Fe3O4) Nanoparticles on Breast Cancer Cells and its Combinatory Effects with Doxorubicin used in Hyperthermia.* Avicenna J Med Biotechnol, 2013. **5**(2): p. 96-103.
38. Hirsch, L.R., et al., *Nanoshell-mediated near-infrared thermal therapy of tumors under magnetic resonance guidance.* Proc Natl Acad Sci U S A, 2003. **100**(23): p. 13549-54.

39. Wu, W., Q. He, and C. Jiang, *Magnetic iron oxide nanoparticles: synthesis and surface functionalization strategies.* Nanoscale Res Lett, 2008. **3**(11): p. 397-415.
40. Kolhatkar, A.G., et al., *Tuning the magnetic properties of nanoparticles.* Int J Mol Sci, 2013. **14**(8): p. 15977-6009.
41. Arruebo, M., et al., *Magnetic nanoparticles for drug delivery.* Nano Today, 2007. **2**(3): p. 22-32.
42. Wahajuddin and S. Arora, *Superparamagnetic iron oxide nanoparticles: magnetic nanoplatforms as drug carriers.* Int J Nanomedicine, 2012. **7**: p. 3445-71.
43. Thorek, D.L., et al., *Superparamagnetic iron oxide nanoparticle probes for molecular imaging.* Ann Biomed Eng, 2006. **34**(1): p. 23-38.
44. Mahmoudi, M., et al., *Assessing the in vitro and in vivo toxicity of superparamagnetic iron oxide nanoparticles.* Chem Rev, 2012. **112**(4): p. 2323-38.
45. Baumgartner, J., et al., *Formation of magnetite nanoparticles at low temperature: from superparamagnetic to stable single domain particles.* PLoS One, 2013. **8**(3): p. e57070.
46. Dunlop, D.J. and O.z. O\zdemir, *Rock magnetism : fundamentals and frontiers*. 1997, Cambridge: Cambridge University Press.
47. Bharde, A.A., et al., *Bacteria-mediated precursor-dependent biosynthesis of superparamagnetic iron oxide and iron sulfide nanoparticles.* Langmuir, 2008. **24**(11): p. 5787-94.
48. Laurent, S., et al., *Magnetic iron oxide nanoparticles: synthesis, stabilization, vectorization, physicochemical characterizations, and biological applications.* Chem Rev, 2008. **108**(6): p. 2064-110.
49. Commission, E., *https://ec.europa.eu/research/fp7/index_en.cfm?pg=budget*. Accessed 20/10/2015.
50. Gobbo, O.L., et al., *Magnetic Nanoparticles in Cancer Theranostics.* Theranostics, 2015. **5**(11): p. 1249-63.
51. ETPN, *http://www.etp-nanomedicine.eu/public/about-nanomedicine*. Accessed 10/09/2015.
52. CORDIS, *https://cordis.europa.eu/nanotechnology/nanomedicine.htm* Accessed 18/11/2015.
53. Dawidczyk, C.M., L.M. Russell, and P.C. Searson, *Nanomedicines for cancer therapy: state-of-the-art and limitations to pre-clinical studies that hinder future developments.* Front Chem, 2014. **2**: p. 69.
54. Lowery, A., et al., *Tumor-targeted delivery of liposome-encapsulated doxorubicin by use of a peptide that selectively binds to irradiated tumors.* J Control Release, 2011. **150**(1): p. 117-24.
55. Netti, P.A., et al., *Effect of transvascular fluid exchange on pressure-flow relationship in tumors: a proposed mechanism for tumor blood flow heterogeneity.* Microvasc Res, 1996. **52**(1): p. 27-46.
56. McDonald, D.M. and P.L. Choyke, *Imaging of angiogenesis: from microscope to clinic.* Nat Med, 2003. **9**(6): p. 713-25.
57. Matsumura, Y. and H. Maeda, *A new concept for macromolecular therapeutics in cancer chemotherapy: mechanism of tumoritropic accumulation of proteins and the antitumor agent smancs.* Cancer Res, 1986. **46**(12 Pt 1): p. 6387-92.
58. Divan, A., et al., *p53 and p21waf-1 expression correlates with apoptosis or cell survival in poorly differentiated, but not well-differentiated, retinoblastomas.* Cancer Res, 2001. **61**(7): p. 3157-63.

59. Au, J.L., S.H. Jang, and M.G. Wientjes, *Clinical aspects of drug delivery to tumors.* J Control Release, 2002. **78**(1-3): p. 81-95.
60. Ezashi, T., P. Das, and R.M. Roberts, *Low O2 tensions and the prevention of differentiation of hES cells.* Proc Natl Acad Sci U S A, 2005. **102**(13): p. 4783-8.
61. Koren, E. and Y. Fuchs, *The bad seed: Cancer stem cells in tumor development and resistance.* Drug Resistance Updates, 2016. **28**: p. 1-12.
62. Rohwer, N. and T. Cramer, *Hypoxia-mediated drug resistance: novel insights on the functional interaction of HIFs and cell death pathways.* Drug Resist Updat, 2011. **14**(3): p. 191-201.
63. Weidemann, A. and R.S. Johnson, *Biology of HIF-1alpha.* Cell Death Differ, 2008. **15**(4): p. 621-7.
64. Vaupel, P. and A. Mayer, *Hypoxia in cancer: significance and impact on clinical outcome.* Cancer Metastasis Rev, 2007. **26**(2): p. 225-39.
65. Medema, J.P., *Cancer stem cells: the challenges ahead.* Nat Cell Biol, 2013. **15**(4): p. 338-44.
66. Allen, T.M. and P.R. Cullis, *Drug delivery systems: entering the mainstream.* Science, 2004. **303**(5665): p. 1818-22.
67. Chauhan, V.P., et al., *Normalization of tumour blood vessels improves the delivery of nanomedicines in a size-dependent manner.* Nat Nanotechnol, 2012. **7**(6): p. 383-8.
68. Kong, G., R.D. Braun, and M.W. Dewhirst, *Characterization of the effect of hyperthermia on nanoparticle extravasation from tumor vasculature.* Cancer Res, 2001. **61**(7): p. 3027-32.
69. Kobayashi, H., et al., *Application of a macromolecular contrast agent for detection of alterations of tumor vessel permeability induced by radiation.* Clin Cancer Res, 2004. **10**(22): p. 7712-20.
70. Staud, F. and P. Pavek, *Breast cancer resistance protein (BCRP/ABCG2).* Int J Biochem Cell Biol, 2005. **37**(4): p. 720-5.
71. Ni, Z., et al., *Structure and function of the human breast cancer resistance protein (BCRP/ABCG2).* Curr Drug Metab, 2010. **11**(7): p. 603-17.
72. Krishnamurthy, P., et al., *The stem cell marker Bcrp/ABCG2 enhances hypoxic cell survival through interactions with heme.* J Biol Chem, 2004. **279**(23): p. 24218-25.
73. Yang, C., et al., *Anti-ABCG2 monoclonal antibody in combination with paclitaxel nanoparticles against cancer stem-like cell activity in multiple myeloma.* Nanomedicine (Lond), 2014. **9**(1): p. 45-60.
74. Yang, C., et al., *Gamma-Fe2O3 nanoparticles increase therapeutic efficacy of combination with paclitaxel and anti-ABCG2 monoclonal antibody on multiple myeloma cancer stem cells in mouse model.* J Biomed Nanotechnol, 2014. **10**(2): p. 336-44.
75. Ginestier, C., et al., *ALDH1 is a marker of normal and malignant human mammary stem cells and a predictor of poor clinical outcome.* Cell Stem Cell, 2007. **1**(5): p. 555-67.
76. Tanei, T., et al., *Association of breast cancer stem cells identified by aldehyde dehydrogenase 1 expression with resistance to sequential Paclitaxel and epirubicin-based chemotherapy for breast cancers.* Clin Cancer Res, 2009. **15**(12): p. 4234-41.
77. Rasheed, Z.A., et al., *Prognostic significance of tumorigenic cells with mesenchymal features in pancreatic adenocarcinoma.* J Natl Cancer Inst, 2010. **102**(5): p. 340-51.

78. Januchowski, R., K. Wojtowicz, and M. Zabel, *The role of aldehyde dehydrogenase (ALDH) in cancer drug resistance.* Biomed Pharmacother, 2013. **67**(7): p. 669-80.
79. Aires, A., et al., *Multifunctionalized iron oxide nanoparticles for selective drug delivery to CD44-positive cancer cells.* Nanotechnology, 2016. **27**(6): p. 065103.
80. Shipitsin, M., et al., *Molecular definition of breast tumor heterogeneity.* Cancer Cell, 2007. **11**(3): p. 259-73.
81. Li, F., et al., *Beyond tumorigenesis: cancer stem cells in metastasis.* Cell Res, 2007. **17**(1): p. 3-14.
82. Kobayashi, H., R. Watanabe, and P.L. Choyke, *Improving conventional enhanced permeability and retention (EPR) effects; what is the appropriate target?* Theranostics, 2013. **4**(1): p. 81-9.
83. Movia, D., et al., *A safe-by-design approach to the development of gold nanoboxes as carriers for internalization into cancer cells.* Biomaterials, 2014. **35**(9): p. 2543-57.
84. Sorlie, T., et al., *Repeated observation of breast tumor subtypes in independent gene expression data sets.* Proc Natl Acad Sci U S A, 2003. **100**(14): p. 8418-23.
85. Borgquist, S., et al., *The prognostic role of HER2 expression in ductal breast carcinoma in situ (DCIS); a population-based cohort study.* BMC Cancer, 2015. **15**: p. 468.
86. Creighton, C.J., *The molecular profile of luminal B breast cancer.* Biologics, 2012. **6**: p. 289-97.
87. Gorski, J.J., et al., *BRCA1 transcriptionally regulates genes associated with the basal-like phenotype in breast cancer.* Breast Cancer Res Treat, 2010. **122**(3): p. 721-31.
88. de Azambuja, E., et al., *Ki-67 as prognostic marker in early breast cancer: a meta-analysis of published studies involving 12,155 patients.* Br J Cancer, 2007. **96**(10): p. 1504-13.
89. Papathomas, T.G., et al., *An International Ki67 Reproducibility Study in Adrenal Cortical Carcinoma.* Am J Surg Pathol, 2016. **40**(4): p. 569-76.
90. Polley, M.Y., et al., *An international Ki67 reproducibility study.* J Natl Cancer Inst, 2013. **105**(24): p. 1897-906.
91. Bediaga, N.G., et al., *Luminal B breast cancer subtype displays a dicotomic epigenetic pattern.* Springerplus, 2016. **5**: p. 623.
92. Kittaneh, M., A.J. Montero, and S. Gluck, *Molecular profiling for breast cancer: a comprehensive review.* Biomark Cancer, 2013. **5**: p. 61-70.
93. Osborne, C.K., et al., *Gefitinib or placebo in combination with tamoxifen in patients with hormone receptor-positive metastatic breast cancer: a randomized phase II study.* Clin Cancer Res, 2011. **17**(5): p. 1147-59.
94. Baselga, J., et al., *Everolimus in postmenopausal hormone-receptor-positive advanced breast cancer.* N Engl J Med, 2012. **366**(6): p. 520-9.
95. Iqbal, N. and N. Iqbal, *Human Epidermal Growth Factor Receptor 2 (HER2) in Cancers: Overexpression and Therapeutic Implications.* Mol Biol Int, 2014. **2014**: p. 852748.
96. Mitri, Z., T. Constantine, and R. O'Regan, *The HER2 Receptor in Breast Cancer: Pathophysiology, Clinical Use, and New Advances in Therapy.* Chemother Res Pract, 2012. **2012**: p. 743193.
97. Moasser, M.M. and I.E. Krop, *The Evolving Landscape of HER2 Targeting in Breast Cancer.* JAMA Oncol, 2015. **1**(8): p. 1154-61.

98. Tan, M. and D. Yu, *Molecular mechanisms of erbB2-mediated breast cancer chemoresistance.* Adv Exp Med Biol, 2007. **608**: p. 119-29.
99. Press, M.F., et al., *Her-2/neu expression in node-negative breast cancer: direct tissue quantitation by computerized image analysis and association of overexpression with increased risk of recurrent disease.* Cancer Res, 1993. **53**(20): p. 4960-70.
100. Seshadri, R., et al., *Clinical significance of HER-2/neu oncogene amplification in primary breast cancer. The South Australian Breast Cancer Study Group.* J Clin Oncol, 1993. **11**(10): p. 1936-42.
101. Liao, N., et al., *HER2-positive status is an independent predictor for coexisting invasion of ductal carcinoma in situ of the breast presenting extensive DCIS component.* Pathol Res Pract, 2011. **207**(1): p. 1-7.
102. Roses, R.E., et al., *HER-2/neu overexpression as a predictor for the transition from in situ to invasive breast cancer.* Cancer Epidemiol Biomarkers Prev, 2009. **18**(5): p. 1386-9.
103. Independent, U.K.P.o.B.C.S., *The benefits and harms of breast cancer screening: an independent review.* Lancet, 2012. **380**(9855): p. 1778-86.
104. Foulkes, W.D., I.E. Smith, and J.S. Reis-Filho, *Triple-negative breast cancer.* N Engl J Med, 2010. **363**(20): p. 1938-48.
105. Nielsen, T.O., et al., *Immunohistochemical and clinical characterization of the basal-like subtype of invasive breast carcinoma.* Clin Cancer Res, 2004. **10**(16): p. 5367-74.
106. Waddell, N., et al., *Subtypes of familial breast tumours revealed by expression and copy number profiling.* Breast Cancer Res Treat, 2010. **123**(3): p. 661-77.
107. Badve, S., et al., *Basal-like and triple-negative breast cancers: a critical review with an emphasis on the implications for pathologists and oncologists.* Mod Pathol, 2011. **24**(2): p. 157-67.
108. Bertucci, F., et al., *How basal are triple-negative breast cancers?* Int J Cancer, 2008. **123**(1): p. 236-40.
109. Weigelt, B., et al., *Breast cancer molecular profiling with single sample predictors: a retrospective analysis.* Lancet Oncol, 2010. **11**(4): p. 339-49.
110. Weigelt, B., F.L. Baehner, and J.S. Reis-Filho, *The contribution of gene expression profiling to breast cancer classification, prognostication and prediction: a retrospective of the last decade.* J Pathol, 2010. **220**(2): p. 263-80.
111. Rakha, E.A., et al., *Are triple-negative tumours and basal-like breast cancer synonymous?* Breast Cancer Res, 2007. **9**(6): p. 404; author reply 405.
112. Manie, E., et al., *High frequency of TP53 mutation in BRCA1 and sporadic basal-like carcinomas but not in BRCA1 luminal breast tumors.* Cancer Res, 2009. **69**(2): p. 663-71.
113. Grushko, T.A., et al., *MYC is amplified in BRCA1-associated breast cancers.* Clin Cancer Res, 2004. **10**(2): p. 499-507.
114. Arnes, J.B., et al., *Expression of epidermal growth factor receptor in relation to BRCA1 status, basal-like markers and prognosis in breast cancer.* J Clin Pathol, 2009. **62**(2): p. 139-46.
115. Greenblatt, M.S., et al., *TP53 mutations in breast cancer associated with BRCA1 or BRCA2 germ-line mutations: distinctive spectrum and structural distribution.* Cancer Res, 2001. **61**(10): p. 4092-7.

116. Foulkes, W.D., et al., *The prognostic implication of the basal-like (cyclin E high/p27 low/p53+/glomeruloid-microvascular-proliferation+) phenotype of BRCA1-related breast cancer.* Cancer Res, 2004. **64**(3): p. 830-5.
117. Rakha, E. and J.S. Reis-Filho, *Basal-like breast carcinoma: from expression profiling to routine practice.* Arch Pathol Lab Med, 2009. **133**(6): p. 860-8.
118. Turner, N.C. and J.S. Reis-Filho, *Basal-like breast cancer and the BRCA1 phenotype.* Oncogene, 2006. **25**(43): p. 5846-53.
119. Rodriguez-Pinilla, S.M., et al., *Vimentin and laminin expression is associated with basal-like phenotype in both sporadic and BRCA1-associated breast carcinomas.* J Clin Pathol, 2007. **60**(9): p. 1006-12.
120. Lakhani, S.R., et al., *The pathology of familial breast cancer: predictive value of immunohistochemical markers estrogen receptor, progesterone receptor, HER-2, and p53 in patients with mutations in BRCA1 and BRCA2.* J Clin Oncol, 2002. **20**(9): p. 2310-8.
121. Foulkes, W.D., et al., *Disruption of the expected positive correlation between breast tumor size and lymph node status in BRCA1-related breast carcinoma.* Cancer, 2003. **98**(8): p. 1569-77.
122. Hedenfalk, I., et al., *Gene-expression profiles in hereditary breast cancer.* N Engl J Med, 2001. **344**(8): p. 539-48.
123. Chappuis, P.O., et al., *Germline BRCA1/2 mutations and p27(Kip1) protein levels independently predict outcome after breast cancer.* J Clin Oncol, 2000. **18**(24): p. 4045-52.
124. Wei, M., et al., *BRCA1 promoter methylation in sporadic breast cancer is associated with reduced BRCA1 copy number and chromosome 17 aneusomy.* Cancer Res, 2005. **65**(23): p. 10692-9.
125. Johnson, S.M., J.A. Shaw, and R.A. Walker, *Sporadic breast cancer in young women: prevalence of loss of heterozygosity at p53, BRCA1 and BRCA2.* Int J Cancer, 2002. **98**(2): p. 205-9.
126. Rice, J.C., et al., *Methylation of the BRCA1 promoter is associated with decreased BRCA1 mRNA levels in clinical breast cancer specimens.* Carcinogenesis, 2000. **21**(9): p. 1761-5.
127. Catteau, A., et al., *Methylation of the BRCA1 promoter region in sporadic breast and ovarian cancer: correlation with disease characteristics.* Oncogene, 1999. **18**(11): p. 1957-65.
128. Esteller, M., et al., *Promoter hypermethylation and BRCA1 inactivation in sporadic breast and ovarian tumors.* J Natl Cancer Inst, 2000. **92**(7): p. 564-9.
129. Turner, N., A. Tutt, and A. Ashworth, *Hallmarks of 'BRCAness' in sporadic cancers.* Nat Rev Cancer, 2004. **4**(10): p. 814-9.
130. Rice, J.C. and B.W. Futscher, *Transcriptional repression of BRCA1 by aberrant cytosine methylation, histone hypoacetylation and chromatin condensation of the BRCA1 promoter.* Nucleic Acids Res, 2000. **28**(17): p. 3233-9.
131. Xu, J., et al., *CpG island methylation affects accessibility of the proximal BRCA1 promoter to transcription factors.* Breast Cancer Res Treat, 2010. **120**(3): p. 593-601.
132. G. Giorgetti, E.G., F. Bianchi, L. Belvederesi, C. Loretelli, G. Piccinini, D. Gagliardini, R. Bracci, A. Santinelli, R. Cellerino. *BRCA1 epigenetic silencing in sporadic breast cancers*. in *2007 Breast Cancer Symposium* 2007.

133. Turner, N.C., et al., *BRCA1 dysfunction in sporadic basal-like breast cancer.* Oncogene, 2007. **26**(14): p. 2126-32.
134. Welcsh, P.L., et al., *BRCA1 transcriptionally regulates genes involved in breast tumorigenesis.* Proc Natl Acad Sci U S A, 2002. **99**(11): p. 7560-5.
135. Beger, C., et al., *Identification of Id4 as a regulator of BRCA1 expression by using a ribozyme-library-based inverse genomics approach.* Proc Natl Acad Sci U S A, 2001. **98**(1): p. 130-5.
136. Hosey, A.M., et al., *Molecular basis for estrogen receptor alpha deficiency in BRCA1-linked breast cancer.* J Natl Cancer Inst, 2007. **99**(22): p. 1683-94.
137. Benafif, S. and M. Hall, *An update on PARP inhibitors for the treatment of cancer.* Onco Targets Ther, 2015. **8**: p. 519-28.
138. Murai, J., et al., *Trapping of PARP1 and PARP2 by Clinical PARP Inhibitors.* Cancer Res, 2012. **72**(21): p. 5588-99.
139. Paik, S., et al., *Gene expression and benefit of chemotherapy in women with node-negative, estrogen receptor-positive breast cancer.* J Clin Oncol, 2006. **24**(23): p. 3726-34.
140. Piccart, M., et al., *Abstract CT039: Primary analysis of the EORTC 10041/ BIG 3-04 MINDACT study: a prospective, randomized study evaluating the clinical utility of the 70-gene signature (MammaPrint) combined with common clinical-pathological criteria for selection of patients for adjuvant chemotherapy in breast cancer with 0 to 3 positive nodes.* Cancer Research, 2016. **76**(14 Supplement): p. CT039-CT039.
141. Parker, J.S., et al., *Supervised risk predictor of breast cancer based on intrinsic subtypes.* J Clin Oncol, 2009. **27**(8): p. 1160-7.
142. Wallden, B., et al., *Development and verification of the PAM50-based Prosigna breast cancer gene signature assay.* BMC Med Genomics, 2015. **8**: p. 54.
143. Scaltriti, M., et al., *Lapatinib, a HER2 tyrosine kinase inhibitor, induces stabilization and accumulation of HER2 and potentiates trastuzumab-dependent cell cytotoxicity.* Oncogene, 2009. **28**(6): p. 803-14.
144. Piccart-Gebhart, M., et al., *Adjuvant Lapatinib and Trastuzumab for Early Human Epidermal Growth Factor Receptor 2-Positive Breast Cancer: Results From the Randomized Phase III Adjuvant Lapatinib and/or Trastuzumab Treatment Optimization Trial.* J Clin Oncol, 2016. **34**(10): p. 1034-42.
145. Anders, C.K., T.M. Zagar, and L.A. Carey, *The management of early-stage and metastatic triple-negative breast cancer: a review.* Hematol Oncol Clin North Am, 2013. **27**(4): p. 737-49, viii.
146. Adkins, F.C., et al., *Triple-negative breast cancer is not a contraindication for breast conservation.* Ann Surg Oncol, 2011. **18**(11): p. 3164-73.
147. Abdulkarim, B.S., et al., *Increased risk of locoregional recurrence for women with T1-2N0 triple-negative breast cancer treated with modified radical mastectomy without adjuvant radiation therapy compared with breast-conserving therapy.* J Clin Oncol, 2011. **29**(21): p. 2852-8.
148. Wang, J., et al., *Adjuvant chemotherapy and radiotherapy in triple-negative breast carcinoma: a prospective randomized controlled multi-center trial.* Radiother Oncol, 2011. **100**(2): p. 200-4.

149. O'Reilly, E.A., et al., *The fate of chemoresistance in triple negative breast cancer (TNBC).* BBA Clin, 2015. **3**: p. 257-75.
150. Hudis, C.A. and L. Gianni, *Triple-negative breast cancer: an unmet medical need.* Oncologist, 2011. **16 Suppl 1**: p. 1-11.
151. Carey, L.A., et al., *The triple negative paradox: primary tumor chemosensitivity of breast cancer subtypes.* Clin Cancer Res, 2007. **13**(8): p. 2329-34.
152. Fong, P.C., et al., *Inhibition of poly(ADP-ribose) polymerase in tumors from BRCA mutation carriers.* N Engl J Med, 2009. **361**(2): p. 123-34.
153. Brown, J.S., S.B. Kaye, and T.A. Yap, *PARP inhibitors: the race is on.* Br J Cancer, 2016. **114**(7): p. 713-5.
154. Norquist, B., et al., *Secondary somatic mutations restoring BRCA1/2 predict chemotherapy resistance in hereditary ovarian carcinomas.* J Clin Oncol, 2011. **29**(22): p. 3008-15.
155. Swisher, E.M., et al., *Secondary BRCA1 mutations in BRCA1-mutated ovarian carcinomas with platinum resistance.* Cancer Res, 2008. **68**(8): p. 2581-6.
156. Sakai, W., et al., *Secondary mutations as a mechanism of cisplatin resistance in BRCA2-mutated cancers.* Nature, 2008. **451**(7182): p. 1116-20.
157. Oplustilova, L., et al., *Evaluation of candidate biomarkers to predict cancer cell sensitivity or resistance to PARP-1 inhibitor treatment.* Cell Cycle, 2012. **11**(20): p. 3837-50.
158. Bunting, S.F., et al., *BRCA1 functions independently of homologous recombination in DNA interstrand crosslink repair.* Mol Cell, 2012. **46**(2): p. 125-35.
159. Grotsky, D.A., et al., *BRCA1 loss activates cathepsin L-mediated degradation of 53BP1 in breast cancer cells.* J Cell Biol, 2013. **200**(2): p. 187-202.
160. Rottenberg, S. and J. Jonkers, *Modeling therapy resistance in genetically engineered mouse cancer models.* Drug Resist Updat, 2008. **11**(1-2): p. 51-60.
161. Choi, Y.E., et al., *Platinum and PARP Inhibitor Resistance Due to Overexpression of MicroRNA-622 in BRCA1-Mutant Ovarian Cancer.* Cell Rep, 2016. **14**(3): p. 429-39.
162. Tseng, J.F., et al., *Serous cystadenoma of the pancreas: tumor growth rates and recommendations for treatment.* Ann Surg, 2005. **242**(3): p. 413-9; discussion 419-21.
163. Testini, M., et al., *Management of mucinous cystic neoplasms of the pancreas.* World J Gastroenterol, 2010. **16**(45): p. 5682-92.
164. Yagci, A., et al., *Diagnosis and treatment of solid pseudopapillary tumor of the pancreas: experience of one single institution from Turkey.* World J Surg Oncol, 2013. **11**: p. 308.
165. Belyaev, O., et al., *Intraductal papillary mucinous neoplasms of the pancreas.* J Clin Gastroenterol, 2008. **42**(3): p. 284-94.
166. Wolfgang, C.L., et al., *Recent progress in pancreatic cancer.* CA Cancer J Clin, 2013. **63**(5): p. 318-48.
167. Waddell, N., et al., *Whole genomes redefine the mutational landscape of pancreatic cancer.* Nature, 2015. **518**(7540): p. 495-501.
168. Polireddy, K. and Q. Chen, *Cancer of the Pancreas: Molecular Pathways and Current Advancement in Treatment.* J Cancer, 2016. **7**(11): p. 1497-514.

169. Abramson, M.A., et al., *The molecular biology of pancreatic cancer.* Gastrointest Cancer Res, 2007. **1**(4 Suppl 2): p. S7-S12.
170. Almoguera, C., et al., *Most human carcinomas of the exocrine pancreas contain mutant c-K-ras genes.* Cell, 1988. **53**(4): p. 549-54.
171. Eser, S., et al., *Oncogenic KRAS signalling in pancreatic cancer.* Br J Cancer, 2014. **111**(5): p. 817-22.
172. Chang, Z., et al., *Cooperativity of oncogenic K-ras and downregulated p16/INK4A in human pancreatic tumorigenesis.* PLoS One, 2014. **9**(7): p. e101452.
173. Pylayeva-Gupta, Y., E. Grabocka, and D. Bar-Sagi, *RAS oncogenes: weaving a tumorigenic web.* Nat Rev Cancer, 2011. **11**(11): p. 761-74.
174. Morris, J.P.t., S.C. Wang, and M. Hebrok, *KRAS, Hedgehog, Wnt and the twisted developmental biology of pancreatic ductal adenocarcinoma.* Nat Rev Cancer, 2010. **10**(10): p. 683-95.
175. Collins, M.A., et al., *Oncogenic Kras is required for both the initiation and maintenance of pancreatic cancer in mice.* J Clin Invest, 2012. **122**(2): p. 639-53.
176. Collins, M.A., et al., *Metastatic pancreatic cancer is dependent on oncogenic Kras in mice.* PLoS One, 2012. **7**(12): p. e49707.
177. Singh, A., et al., *A gene expression signature associated with "K-Ras addiction" reveals regulators of EMT and tumor cell survival.* Cancer Cell, 2009. **15**(6): p. 489-500.
178. Eser, S., et al., *Selective requirement of PI3K/PDK1 signaling for Kras oncogene-driven pancreatic cell plasticity and cancer.* Cancer Cell, 2013. **23**(3): p. 406-20.
179. Aguirre, A.J., et al., *Activated Kras and Ink4a/Arf deficiency cooperate to produce metastatic pancreatic ductal adenocarcinoma.* Genes Dev, 2003. **17**(24): p. 3112-26.
180. Bardeesy, N., et al., *Both p16(Ink4a) and the p19(Arf)-p53 pathway constrain progression of pancreatic adenocarcinoma in the mouse.* Proc Natl Acad Sci U S A, 2006. **103**(15): p. 5947-52.
181. Hingorani, S.R., et al., *Preinvasive and invasive ductal pancreatic cancer and its early detection in the mouse.* Cancer Cell, 2003. **4**(6): p. 437-50.
182. Serra, R.W., et al., *A KRAS-directed transcriptional silencing pathway that mediates the CpG island methylator phenotype.* Elife, 2014. **3**: p. e02313.
183. Collado, M., et al., *Tumour biology: senescence in premalignant tumours.* Nature, 2005. **436**(7051): p. 642.
184. Matlashewski, G., et al., *Isolation and characterization of a human p53 cDNA clone: expression of the human p53 gene.* EMBO J, 1984. **3**(13): p. 3257-62.
185. Surget, S., M.P. Khoury, and J.C. Bourdon, *Uncovering the role of p53 splice variants in human malignancy: a clinical perspective.* Onco Targets Ther, 2013. **7**: p. 57-68.
186. Redston, M.S., et al., *p53 mutations in pancreatic carcinoma and evidence of common involvement of homocopolymer tracts in DNA microdeletions.* Cancer Res, 1994. **54**(11): p. 3025-33.
187. Weissmueller, S., et al., *Mutant p53 drives pancreatic cancer metastasis through cell-autonomous PDGF receptor beta signaling.* Cell, 2014. **157**(2): p. 382-94.
188. Morton, J.P., et al., *Mutant p53 drives metastasis and overcomes growth arrest/senescence in pancreatic cancer.* Proc Natl Acad Sci U S A, 2010. **107**(1): p. 246-51.

189. Lehmann, B.D. and J.A. Pietenpol, *Targeting mutant p53 in human tumors.* J Clin Oncol, 2012. **30**(29): p. 3648-50.
190. Feldser, D.M., et al., *Stage-specific sensitivity to p53 restoration during lung cancer progression.* Nature, 2010. **468**(7323): p. 572-5.
191. Junttila, M.R., et al., *Selective activation of p53-mediated tumour suppression in high-grade tumours.* Nature, 2010. **468**(7323): p. 567-71.
192. Fiorini, C., et al., *Mutant p53 stimulates chemoresistance of pancreatic adenocarcinoma cells to gemcitabine.* Biochim Biophys Acta, 2015. **1853**(1): p. 89-100.
193. Demma, M., et al., *SCH529074, a small molecule activator of mutant p53, which binds p53 DNA binding domain (DBD), restores growth-suppressive function to mutant p53 and interrupts HDM2-mediated ubiquitination of wild type p53.* J Biol Chem, 2010. **285**(14): p. 10198-212.
194. Hahn, S.A., et al., *DPC4, a candidate tumor suppressor gene at human chromosome 18q21.1.* Science, 1996. **271**(5247): p. 350-3.
195. Hua, Z., et al., *Loss of DPC4 expression and its correlation with clinicopathological parameters in pancreatic carcinoma.* World J Gastroenterol, 2003. **9**(12): p. 2764-7.
196. Tascilar, M., et al., *The SMAD4 protein and prognosis of pancreatic ductal adenocarcinoma.* Clin Cancer Res, 2001. **7**(12): p. 4115-21.
197. Shugang, X., et al., *Prognostic Value of SMAD4 in Pancreatic Cancer: A Meta-Analysis.* Transl Oncol, 2016. **9**(1): p. 1-7.
198. DiMagno, E.P., *Pancreatic cancer: clinical presentation, pitfalls and early clues.* Ann Oncol, 1999. **10 Suppl 4**: p. 140-2.
199. Lin, A. and E.R. Feller, *Pancreatic carcinoma as a cause of unexplained pancreatitis: report of ten cases.* Ann Intern Med, 1990. **113**(2): p. 166-7.
200. Puli, S.R., et al., *How good is endoscopic ultrasound-guided fine-needle aspiration in diagnosing the correct etiology for a solid pancreatic mass?: A meta-analysis and systematic review.* Pancreas, 2013. **42**(1): p. 20-6.
201. Di Stasi, M., et al., *Ultrasound-guided fine needle biopsy of pancreatic masses: results of a multicenter study.* Am J Gastroenterol, 1998. **93**(8): p. 1329-33.
202. Rotten, D., et al., *Ultrasonographically guided fine needle aspiration cytology and core-needle biopsy in the diagnosis of breast tumors.* Eur J Obstet Gynecol Reprod Biol, 1993. **49**(3): p. 175-86.
203. Li, L., et al., *CT-guided core needle biopsy in the diagnosis of pancreatic diseases with an automated biopsy gun.* J Vasc Interv Radiol, 2008. **19**(1): p. 89-94.
204. Bruening, W., et al., *Systematic review: comparative effectiveness of core-needle and open surgical biopsy to diagnose breast lesions.* Ann Intern Med, 2010. **152**(4): p. 238-46.
205. Valls, C., et al., *Dual-phase helical CT of pancreatic adenocarcinoma: assessment of resectability before surgery.* AJR Am J Roentgenol, 2002. **178**(4): p. 821-6.
206. Legmann, P., et al., *Pancreatic tumors: comparison of dual-phase helical CT and endoscopic sonography.* AJR Am J Roentgenol, 1998. **170**(5): p. 1315-22.
207. Bronstein, Y.L., et al., *Detection of small pancreatic tumors with multiphasic helical CT.* AJR Am J Roentgenol, 2004. **182**(3): p. 619-23.

208. Catalano, C., et al., *Pancreatic carcinoma: the role of high-resolution multislice spiral CT in the diagnosis and assessment of resectability.* Eur Radiol, 2003. **13**(1): p. 149-56.
209. Karmazanovsky, G., et al., *Pancreatic head cancer: accuracy of CT in determination of resectability.* Abdom Imaging, 2005. **30**(4): p. 488-500.
210. Wong, J.C. and S. Raman, *Surgical resectability of pancreatic adenocarcinoma: CTA.* Abdom Imaging, 2010. **35**(4): p. 471-80.
211. Buchs, N.C., et al., *Vascular invasion in pancreatic cancer: Imaging modalities, preoperative diagnosis and surgical management.* World J Gastroenterol, 2010. **16**(7): p. 818-31.
212. Long, J., et al., *Overcoming drug resistance in pancreatic cancer.* Expert Opin Ther Targets, 2011. **15**(7): p. 817-28.
213. Burris, H.A., 3rd, et al., *Improvements in survival and clinical benefit with gemcitabine as first-line therapy for patients with advanced pancreas cancer: a randomized trial.* J Clin Oncol, 1997. **15**(6): p. 2403-13.
214. Kim, M.P. and G.E. Gallick, *Gemcitabine resistance in pancreatic cancer: picking the key players.* Clin Cancer Res, 2008. **14**(5): p. 1284-5.
215. Arcamone, F., *Doxorubicin : anticancer antibiotics*. 1981, New York ; London: Academic Press.
216. Sneader, W., *Drug discovery : a history*. 2005, Chichester: Wiley.
217. Kouvaraki, M.A., et al., *Fluorouracil, doxorubicin, and streptozocin in the treatment of patients with locally advanced and metastatic pancreatic endocrine carcinomas.* J Clin Oncol, 2004. **22**(23): p. 4762-71.
218. Chatterjee, K., et al., *Doxorubicin cardiomyopathy.* Cardiology, 2010. **115**(2): p. 155-62.
219. Chanan-Khan, A., et al., *Complement activation following first exposure to pegylated liposomal doxorubicin (Doxil): possible role in hypersensitivity reactions.* Ann Oncol, 2003. **14**(9): p. 1430-7.
220. Fiegl, M., et al., *Single-agent pegylated liposomal doxorubicin (PLD) in the treatment of metastatic breast cancer: results of an Austrian observational trial.* BMC Cancer, 2011. **11**: p. 373.
221. Farr, K.P. and A. Safwat, *Palmar-plantar erythrodysesthesia associated with chemotherapy and its treatment.* Case Rep Oncol, 2011. **4**(1): p. 229-35.
222. Cannon, T.L., et al., *Squamous cell carcinoma of the oral cavity in nonsmoking women: a new and unusual complication of chemotherapy for recurrent ovarian cancer?* Oncologist, 2012. **17**(12): p. 1541-6.
223. Cividalli, A., et al., *Schedule dependent toxicity and efficacy of combined gemcitabine/paclitaxel treatment in mouse adenocarcinoma.* J Cancer Res Clin Oncol, 2000. **126**(8): p. 461-7.
224. Mavroudis, D., et al., *A dose-escalation and pharmacokinetic study of gemcitabine and oxaliplatin in patients with advanced solid tumors.* Ann Oncol, 2003. **14**(2): p. 304-12.
225. Chi, D.C., et al., *Gemcitabine-induced pulmonary toxicity.* Anticancer Res, 2012. **32**(9): p. 4147-9.
226. Katsenos, S. and M. Nikolopoulou, *Gemcitabine-induced severe peripheral edema in a patient with lung cancer.* J Pharm Pract, 2012. **25**(3): p. 393-5.
227. Davidoff, S., R.D. Shah, and T. Arunabh, *Gemcitabine-induced respiratory failure associated with elevated erythrocyte sedimentation rate (ESR).* Respir Med, 2006. **100**(4): p. 760-3.

228. Walter, R.B., M. Joerger, and B.C. Pestalozzi, *Gemcitabine-associated hemolytic-uremic syndrome.* Am J Kidney Dis, 2002. **40**(4): p. E16.
229. Glezerman, I., et al., *Gemcitabine nephrotoxicity and hemolytic uremic syndrome: report of 29 cases from a single institution.* Clin Nephrol, 2009. **71**(2): p. 130-9.
230. Khan, M.F., et al., *Gemcitabine-induced cardiomyopathy: a case report and review of the literature.* J Med Case Rep, 2014. **8**: p. 220.
231. Conroy, T., et al., *FOLFIRINOX versus gemcitabine for metastatic pancreatic cancer.* N Engl J Med, 2011. **364**(19): p. 1817-25.
232. Lahoud, M.J., et al., *Road map for pain management in pancreatic cancer: A review*. World J Gastrointest Oncol, 2016. **8**(8): p. 599-606.
233. Eibl, G. and H.A. Reber, *A xenograft nude mouse model for perineural invasion and recurrence in pancreatic cancer.* Pancreas, 2005. **31**(3): p. 258-62.
234. Ceyhan, G.O., et al., *Neural invasion in pancreatic cancer: a mutual tropism between neurons and cancer cells.* Biochem Biophys Res Commun, 2008. **374**(3): p. 442-7.
235. Gil, Z., et al., *Paracrine regulation of pancreatic cancer cell invasion by peripheral nerves.* J Natl Cancer Inst, 2010. **102**(2): p. 107-18.
236. Lindsay, T.H., et al., *Pancreatic cancer pain and its correlation with changes in tumor vasculature, macrophage infiltration, neuronal innervation, body weight and disease progression.* Pain, 2005. **119**(1-3): p. 233-46.
237. Grelik, C., S. Allard, and A. Ribeiro-da-Silva, *Changes in nociceptive sensory innervation in the epidermis of the rat lower lip skin in a model of neuropathic pain.* Neurosci Lett, 2005. **389**(3): p. 140-5.
238. Marchal, S., et al., *Anticancer Drug Delivery: An Update on Clinically Applied Nanotherapeutics.* Drugs, 2015. **75**(14): p. 1601-11.
239. Schutz, C.A., et al., *Therapeutic nanoparticles in clinics and under clinical evaluation.* Nanomedicine (Lond), 2013. **8**(3): p. 449-67.
240. Calatayud, M.P., et al., *The effect of surface charge of functionalized Fe3O4 nanoparticles on protein adsorption and cell uptake.* Biomaterials, 2014. **35**(24): p. 6389-99.
241. Alexis, F., et al., *Factors affecting the clearance and biodistribution of polymeric nanoparticles.* Mol Pharm, 2008. **5**(4): p. 505-15.
242. Auffan, M., et al., *Towards a definition of inorganic nanoparticles from an environmental, health and safety perspective.* Nat Nanotechnol, 2009. **4**(10): p. 634-41.
243. Anschutz, A. and R.L. Penn, *Reduction of crystalline iron(III) oxyhydroxides using hydroquinone: Influence of phase and particle size.* Geochemical Transactions, 2005. **6**(3): p. 60.
244. Lundqvist, M., et al., *Nanoparticle size and surface properties determine the protein corona with possible implications for biological impacts.* Proc Natl Acad Sci U S A, 2008. **105**(38): p. 14265-70.
245. Sakulkhu, U., et al., *Protein corona composition of superparamagnetic iron oxide nanoparticles with various physico-chemical properties and coatings.* Sci Rep, 2014. **4**: p. 5020.

246. Aggarwal, P., et al., *Nanoparticle interaction with plasma proteins as it relates to particle biodistribution, biocompatibility and therapeutic efficacy.* Adv Drug Deliv Rev, 2009. **61**(6): p. 428-37.
247. Gessner, A., et al., *Influence of surface charge density on protein adsorption on polymeric nanoparticles: analysis by two-dimensional electrophoresis.* Eur J Pharm Biopharm, 2002. **54**(2): p. 165-70.
248. Saptarshi, S.R., A. Duschl, and A.L. Lopata, *Interaction of nanoparticles with proteins: relation to bio-reactivity of the nanoparticle.* J Nanobiotechnology, 2013. **11**: p. 26.
249. Ehrenberg, M.S., et al., *The influence of protein adsorption on nanoparticle association with cultured endothelial cells.* Biomaterials, 2009. **30**(4): p. 603-10.
250. Brigger, I., C. Dubernet, and P. Couvreur, *Nanoparticles in cancer therapy and diagnosis.* Adv Drug Deliv Rev, 2002. **54**(5): p. 631-51.
251. Müller, R.H. and K.H. Wallis, *Surface modification of i.v. injectable biodegradable nanoparticles with poloxamer polymers and poloxamine 908.* International Journal of Pharmaceutics, 1993. **89**(1): p. 25-31.
252. Hole, P., et al., *Interlaboratory comparison of size measurements on nanoparticles using nanoparticle tracking analysis (NTA).* J Nanopart Res, 2013. **15**: p. 2101.
253. Mehdiani, A., et al., *An innovative method for exosome quantification and size measurement.* J Vis Exp, 2015(95): p. 50974.
254. Sarker, S., et al., *Placenta-derived exosomes continuously increase in maternal circulation over the first trimester of pregnancy.* J Transl Med, 2014. **12**: p. 204.
255. Oosthuyzen, W., et al., *Quantification of human urinary exosomes by nanoparticle tracking analysis.* J Physiol, 2013. **591**(Pt 23): p. 5833-42.
256. Aatonen, M.T., et al., *Isolation and characterization of platelet-derived extracellular vesicles.* J Extracell Vesicles, 2014. **3**.
257. Kramberger, P., et al., *Evaluation of nanoparticle tracking analysis for total virus particle determination.* Virol J, 2012. **9**: p. 265.
258. Wright, M., *Nanoparticle tracking analysis for the multiparameter characterization and counting of nanoparticle suspensions.* Methods Mol Biol, 2012. **906**: p. 511-24.
259. Mwilu, S.K., et al., *Changes in silver nanoparticles exposed to human synthetic stomach fluid: effects of particle size and surface chemistry.* Sci Total Environ, 2013. **447**: p. 90-8.
260. James, A.E. and J.D. Driskell, *Monitoring gold nanoparticle conjugation and analysis of biomolecular binding with nanoparticle tracking analysis (NTA) and dynamic light scattering (DLS).* Analyst, 2013. **138**(4): p. 1212-8.
261. Schutz, C.A., et al., *Differential stress reaction of human colon cells to oleic-acid-stabilized and unstabilized ultrasmall iron oxide nanoparticles.* Int J Nanomedicine, 2014. **9**: p. 3481-98.
262. Graczyk, H., et al., *Physicochemical characterization of nebulized superparamagnetic iron oxide nanoparticles (SPIONs).* J Aerosol Med Pulm Drug Deliv, 2015. **28**(1): p. 43-51.

263. Longmire, M., P.L. Choyke, and H. Kobayashi, *Clearance properties of nano-sized particles and molecules as imaging agents: considerations and caveats.* Nanomedicine (Lond), 2008. **3**(5): p. 703-17.
264. Chouly, C., et al., *Development of superparamagnetic nanoparticles for MRI: effect of particle size, charge and surface nature on biodistribution.* J Microencapsul, 1996. **13**(3): p. 245-55.
265. Olivier, J.C., *Drug transport to brain with targeted nanoparticles.* NeuroRx, 2005. **2**(1): p. 108-19.
266. Jones, M.M., et al., *Effect of chelate treatments on kidney, bone and brain lead levels of lead-intoxicated mice.* Toxicology, 1994. **89**(2): p. 91-100.
267. Planas-Bohne, F., *The influence of chelating agents on the distribution and biotransformation of methylmercuric chloride in rats.* J Pharmacol Exp Ther, 1981. **217**(2): p. 500-4.
268. Chen, Z.P., et al., *Preparation and characterization of water-soluble monodisperse magnetic iron oxide nanoparticles via surface double-exchange with DMSA.* Colloids and Surfaces A: Physicochemical and Engineering Aspects, 2008. **316**(1–3): p. 210-216.
269. Pisanic, T.R., 2nd, et al., *Nanotoxicity of iron oxide nanoparticle internalization in growing neurons.* Biomaterials, 2007. **28**(16): p. 2572-81.
270. Wilhelm, C., et al., *Intracellular uptake of anionic superparamagnetic nanoparticles as a function of their surface coating.* Biomaterials, 2003. **24**(6): p. 1001-11.
271. Auffan, M., et al., *In vitro interactions between DMSA-coated maghemite nanoparticles and human fibroblasts: A physicochemical and cyto-genotoxical study.* Environ Sci Technol, 2006. **40**(14): p. 4367-73.
272. Gupta, A.K. and M. Gupta, *Cytotoxicity suppression and cellular uptake enhancement of surface modified magnetic nanoparticles.* Biomaterials, 2005. **26**(13): p. 1565-73.
273. Monge-Fuentes, V., et al., *Biodistribution and biocompatibility of DMSA-stabilized maghemite magnetic nanoparticles in nonhuman primates (Cebus spp.).* Nanomedicine (Lond), 2011. **6**(9): p. 1529-44.
274. Hudgins, P.A., et al., *Ferumoxtran-10, a superparamagnetic iron oxide as a magnetic resonance enhancement agent for imaging lymph nodes: a phase 2 dose study.* AJNR Am J Neuroradiol, 2002. **23**(4): p. 649-56.
275. Mejias, R., et al., *Long term biotransformation and toxicity of dimercaptosuccinic acid-coated magnetic nanoparticles support their use in biomedical applications.* J Control Release, 2013. **171**(2): p. 225-33.
276. Mou, Y., et al., *Effects of 2,3-dimercaptosuccinic acid modified Fe2O3 nanoparticles on microstructure and biological activity of cardiomyocytes.* RSC Advances, 2015. **5**(25): p. 19493-19501.
277. Yue, Z.G., et al., *Surface charge affects cellular uptake and intracellular trafficking of chitosan-based nanoparticles.* Biomacromolecules, 2011. **12**(7): p. 2440-6.
278. Villanueva, A., et al., *The influence of surface functionalization on the enhanced internalization of magnetic nanoparticles in cancer cells.* Nanotechnology, 2009. **20**(11): p. 115103.
279. Rejman, J., et al., *Size-dependent internalization of particles via the pathways of clathrin- and caveolae-mediated endocytosis.* Biochem J, 2004. **377**(Pt 1): p. 159-69.

280. Goodman, C.M., et al., *Toxicity of gold nanoparticles functionalized with cationic and anionic side chains.* Bioconjug Chem, 2004. **15**(4): p. 897-900.
281. Bhattacharjee, S., et al., *Role of surface charge and oxidative stress in cytotoxicity of organic monolayer-coated silicon nanoparticles towards macrophage NR8383 cells.* Part Fibre Toxicol, 2010. **7**: p. 25.
282. Kommareddy, S. and M. Amiji, *Biodistribution and pharmacokinetic analysis of long-circulating thiolated gelatin nanoparticles following systemic administration in breast cancer-bearing mice.* J Pharm Sci, 2007. **96**(2): p. 397-407.
283. Alberts, B., *Molecular biology of the cell*. 4th ed. 2002, New York: Garland Science. xxxiv, 1548 p.
284. Head, B.P., H.H. Patel, and P.A. Insel, *Interaction of membrane/lipid rafts with the cytoskeleton: impact on signaling and function: membrane/lipid rafts, mediators of cytoskeletal arrangement and cell signaling.* Biochim Biophys Acta, 2014. **1838**(2): p. 532-45.
285. Simons, K. and D. Toomre, *Lipid rafts and signal transduction.* Nat Rev Mol Cell Biol, 2000. **1**(1): p. 31-9.
286. Samuel, S.P., et al., *Multifactorial determinants that govern nanoparticle uptake by human endothelial cells under flow.* International Journal of Nanomedicine, 2012. **7**: p. 2943-2956.
287. Wang, T., et al., *Cellular uptake of nanoparticles by membrane penetration: a study combining confocal microscopy with FTIR spectroelectrochemistry.* ACS Nano, 2012. **6**(2): p. 1251-9.
288. Laurencin, M., et al., *Interactions between giant unilamellar vesicles and charged core-shell magnetic nanoparticles.* Langmuir, 2010. **26**(20): p. 16025-30.
289. Shang, L., K. Nienhaus, and G.U. Nienhaus, *Engineered nanoparticles interacting with cells: size matters.* J Nanobiotechnology, 2014. **12**: p. 5.
290. Li, S. and N. Malmstadt, *Deformation and poration of lipid bilayer membranes by cationic nanoparticles.* Soft Matter, 2013. **9**(20): p. 4969-4976.
291. Leroueil, P.R., et al., *Wide varieties of cationic nanoparticles induce defects in supported lipid bilayers.* Nano Lett, 2008. **8**(2): p. 420-4.
292. Zhao, Y., et al., *Interaction of mesoporous silica nanoparticles with human red blood cell membranes: size and surface effects.* ACS Nano, 2011. **5**(2): p. 1366-75.
293. Schmid, S.L. and L.L. Carter, *ATP is required for receptor-mediated endocytosis in intact cells.* J Cell Biol, 1990. **111**(6 Pt 1): p. 2307-18.
294. Mellman, I., *Endocytosis and molecular sorting.* Annu Rev Cell Dev Biol, 1996. **12**: p. 575-625.
295. Huotari, J. and A. Helenius, *Endosome maturation.* EMBO J, 2011. **30**(17): p. 3481-500.
296. Lafourcade, C., et al., *Regulation of the V-ATPase along the endocytic pathway occurs through reversible subunit association and membrane localization.* PLoS One, 2008. **3**(7): p. e2758.
297. Sorkin, A. and M. Von Zastrow, *Signal transduction and endocytosis: close encounters of many kinds.* Nat Rev Mol Cell Biol, 2002. **3**(8): p. 600-14.
298. Mindell, J.A., *Lysosomal acidification mechanisms.* Annu Rev Physiol, 2012. **74**: p. 69-86.
299. Bucci, C., et al., *Rab7: a key to lysosome biogenesis.* Mol Biol Cell, 2000. **11**(2): p. 467-80.
300. Bohmer, N. and A. Jordan, *Caveolin-1 and CDC42 mediated endocytosis of silica-coated iron oxide nanoparticles in HeLa cells.* Beilstein J Nanotechnol, 2015. **6**: p. 167-76.

301. Cengelli, F., F. Voinesco, and L. Juillerat-Jeanneret, *Interaction of cationic ultrasmall superparamagnetic iron oxide nanoparticles with human melanoma cells.* Nanomedicine (Lond), 2010. **5**(7): p. 1075-87.
302. Kim, J.S., et al., *Cellular uptake of magnetic nanoparticle is mediated through energy-dependent endocytosis in A549 cells.* J Vet Sci, 2006. **7**(4): p. 321-6.
303. Hanot, C.C., et al., *Effects of Iron-Oxide Nanoparticle Surface Chemistry on Uptake Kinetics and Cytotoxicity in CHO-K1 Cells.* Int J Mol Sci, 2016. **17**(1).
304. Wakeham, D.E., et al., *Clathrin self-assembly involves coordinated weak interactions favorable for cellular regulation.* EMBO J, 2003. **22**(19): p. 4980-90.
305. Roux, A., et al., *GTP-dependent twisting of dynamin implicates constriction and tension in membrane fission.* Nature, 2006. **441**(7092): p. 528-31.
306. Kirchhausen, T., *Clathrin.* Annu Rev Biochem, 2000. **69**: p. 699-727.
307. Massol, R.H., et al., *A burst of auxilin recruitment determines the onset of clathrin-coated vesicle uncoating.* Proc Natl Acad Sci U S A, 2006. **103**(27): p. 10265-70.
308. Gervasio, O.L., et al., *Caveolae respond to cell stretch and contribute to stretch-induced signaling.* J Cell Sci, 2011. **124**(Pt 21): p. 3581-90.
309. Kiss, A.L. and E. Botos, *Endocytosis via caveolae: alternative pathway with distinct cellular compartments to avoid lysosomal degradation?* J Cell Mol Med, 2009. **13**(7): p. 1228-37.
310. Racoosin, E.L. and J.A. Swanson, *M-CSF-induced macropinocytosis increases solute endocytosis but not receptor-mediated endocytosis in mouse macrophages.* J Cell Sci, 1992. **102 (Pt 4)**: p. 867-80.
311. Kruth, H.S., et al., *Macropinocytosis is the endocytic pathway that mediates macrophage foam cell formation with native low density lipoprotein.* J Biol Chem, 2005. **280**(3): p. 2352-60.
312. Cohn, Z.A. and B. Benson, *The in Vitro Differentiation of Mononuclear Phagocytes. Ii. The Influence of Serum on Granule Formation, Hydrolase Production, and Pinocytosis.* J Exp Med, 1965. **121**: p. 835-48.
313. Jones, A.T., *Macropinocytosis: searching for an endocytic identity and role in the uptake of cell penetrating peptides.* J Cell Mol Med, 2007. **11**(4): p. 670-84.
314. Calero, M., et al., *Characterization of interaction of magnetic nanoparticles with breast cancer cells.* J Nanobiotechnology, 2015. **13**: p. 16.
315. Zhang, X., et al., *Iron Oxide Nanoparticles Induce Autophagosome Accumulation through Multiple Mechanisms: Lysosome Impairment, Mitochondrial Damage, and ER Stress.* Mol Pharm, 2016. **13**(7): p. 2578-87.
316. Chen, Y., et al., *Nano neodymium oxide induces massive vacuolization and autophagic cell death in non-small cell lung cancer NCI-H460 cells.* Biochem Biophys Res Commun, 2005. **337**(1): p. 52-60.
317. Yu, L., et al., *Rare earth oxide nanocrystals induce autophagy in HeLa cells.* Small, 2009. **5**(24): p. 2784-7.
318. Zhang, Y., et al., *Nano rare-earth oxides induced size-dependent vacuolization: an independent pathway from autophagy.* Int J Nanomedicine, 2010. **5**: p. 601-9.

319. Khan, M.I., et al., *Induction of ROS, mitochondrial damage and autophagy in lung epithelial cancer cells by iron oxide nanoparticles.* Biomaterials, 2012. **33**(5): p. 1477-88.
320. Park, E.J., et al., *Magnetic iron oxide nanoparticles induce autophagy preceding apoptosis through mitochondrial damage and ER stress in RAW264.7 cells.* Toxicol In Vitro, 2014. **28**(8): p. 1402-12.
321. Kroll, A., et al., *Current in vitro methods in nanoparticle risk assessment: limitations and challenges.* Eur J Pharm Biopharm, 2009. **72**(2): p. 370-7.
322. Casey, A., et al., *Spectroscopic analysis confirms the interactions between single walled carbon nanotubes and various dyes commonly used to assess cytotoxicity.* Carbon, 2007. **45**(7): p. 1425-1432.
323. Guadagnini, R., et al., *Toxicity screenings of nanomaterials: challenges due to interference with assay processes and components of classic in vitro tests.* Nanotoxicology, 2013.
324. Liang, L., et al., *Nanoparticles' interference in the evaluation of in vitro toxicity of silver nanoparticles.* RSC Advances, 2015. **5**(82): p. 67327-67334.
325. Oh, S.J., et al., *Incompatibility of silver nanoparticles with lactate dehydrogenase leakage assay for cellular viability test is attributed to protein binding and reactive oxygen species generation.* Toxicol Lett, 2014. **225**(3): p. 422-32.
326. Reineck, P., et al., *Distance and wavelength dependent quenching of molecular fluorescence by Au@SiO2 core-shell nanoparticles.* ACS Nano, 2013. **7**(8): p. 6636-48.
327. Josephson, L., et al., *Near-infrared fluorescent nanoparticles as combined MR/optical imaging probes.* Bioconjug Chem, 2002. **13**(3): p. 554-60.
328. Jan, E., et al., *High-content screening as a universal tool for fingerprinting of cytotoxicity of nanoparticles.* ACS Nano, 2008. **2**(5): p. 928-38.
329. Mohamed, B.M., et al., *Activation of stress-related signalling pathway in human cells upon SiO2 nanoparticles exposure as an early indicator of cytotoxicity.* J Nanobiotechnology, 2011. **9**: p. 29.
330. Nabiev, I., et al., *Nonfunctionalized nanocrystals can exploit a cell's active transport machinery delivering them to specific nuclear and cytoplasmic compartments.* Nano Lett, 2007. **7**(11): p. 3452-61.
331. Movia, D., et al., *Screening the cytotoxicity of single-walled carbon nanotubes using novel 3D tissue-mimetic models.* ACS Nano, 2011. **5**(11): p. 9278-90.
332. Verma, N.K., et al., *Magnetic core-shell nanoparticles for drug delivery by nebulization.* J Nanobiotechnology, 2013. **11**: p. 1.
333. Movia, D., et al., *A safe-by-design approach to the development of gold nanoboxes as carriers for internalization into cancer cells.* Biomaterials, 2014.
334. Winterbourn, C.C., *Toxicity of iron and hydrogen peroxide: the Fenton reaction.* Toxicol Lett, 1995. **82-83**: p. 969-74.
335. Lemire, J.A., J.J. Harrison, and R.J. Turner, *Antimicrobial activity of metals: mechanisms, molecular targets and applications.* Nat Rev Microbiol, 2013. **11**(6): p. 371-84.
336. Huang, G., et al., *Superparamagnetic iron oxide nanoparticles: amplifying ROS stress to improve anticancer drug efficacy.* Theranostics, 2013. **3**(2): p. 116-26.
337. OECD, *http://www.oecd.org/chemicalsafety/news-nanomaterials-safety.htm*. Accessed 12/10/2015.

338. Kim, H.R., et al., *Appropriate in vitro methods for genotoxicity testing of silver nanoparticles.* Environ Health Toxicol, 2013. **28**: p. e2013003.
339. Graham, W. and J.B. Roberts, *Intravenous colchicine in the management of gouty arthritis.* Ann Rheum Dis, 1953. **12**(1): p. 16-9.
340. Chen, L.X. and H.R. Schumacher, *Gout: an evidence-based review.* J Clin Rheumatol, 2008. **14**(5 Suppl): p. S55-62.
341. Deftereos, S., et al., *Colchicine for prevention of atrial fibrillation recurrence after pulmonary vein isolation: mid-term efficacy and effect on quality of life.* Heart Rhythm, 2014. **11**(4): p. 620-8.
342. Alabed, S., et al., *Colchicine for pericarditis.* Cochrane Database Syst Rev, 2014. **8**: p. CD010652.
343. Lee, S.-H., et al., *Acute Colchicine Poisoning Treated with Granulocyte Colony Stimulating Factor and Transfusion.* Korean J Crit Care Med, 2015. **30**(3): p. 207-211.
344. OECD, *http://dx.doi.org/10.1787/9789264224438-en*. Accessed 14/10/2015.
345. Fenech, M., *Cytokinesis-block micronucleus cytome assay.* Nat Protoc, 2007. **2**(5): p. 1084-104.
346. MacLean-Fletcher, S. and T.D. Pollard, *Mechanism of action of cytochalasin B on actin.* Cell, 1980. **20**(2): p. 329-41.
347. Carter, S.B., *Effects of cytochalasins on mammalian cells.* Nature, 1967. **213**(5073): p. 261-4.
348. Koh, C.M., *Preparation of cells for microscopy using cytospin.* Methods Enzymol, 2013. **533**: p. 235-40.
349. Salvatorelli, E., et al., *The concomitant management of cancer therapy and cardiac therapy.* Biochim Biophys Acta, 2015.
350. Lee, B.H., et al., *Alterations in left ventricular diastolic function with doxorubicin therapy.* J Am Coll Cardiol, 1987. **9**(1): p. 184-8.
351. Tayer-Shifman, O.E., Y. Rottenberg, and M. Shuvy, *Gemcitabine-induced supraventricular tachycardia.* Tumori, 2009. **95**(4): p. 547-9.
352. Davis, M.E., Z.G. Chen, and D.M. Shin, *Nanoparticle therapeutics: an emerging treatment modality for cancer.* Nat Rev Drug Discov, 2008. **7**(9): p. 771-82.
353. Thakor, A.S. and S.S. Gambhir, *Nanooncology: the future of cancer diagnosis and therapy.* CA Cancer J Clin, 2013. **63**(6): p. 395-418.
354. Kossatz, S., et al., *Efficient treatment of breast cancer xenografts with multifunctionalized iron oxide nanoparticles combining magnetic hyperthermia and anti-cancer drug delivery.* Breast Cancer Res, 2015. **17**: p. 66.
355. Keten, S., et al., *Tunable nanomechanics of protein disulfide bonds in redox microenvironments.* J Mech Behav Biomed Mater, 2012. **5**(1): p. 32-40.
356. Dutz, S., et al., *Magnetic multicore nanoparticles for hyperthermia--influence of particle immobilization in tumour tissue on magnetic properties.* Nanotechnology, 2011. **22**(26): p. 265102.
357. Huang, H.S. and J.F. Hainfeld, *Intravenous magnetic nanoparticle cancer hyperthermia.* Int J Nanomedicine, 2013. **8**: p. 2521-32.
358. Sugahara, K.N., et al., *Tissue-penetrating delivery of compounds and nanoparticles into tumors.* Cancer Cell, 2009. **16**(6): p. 510-20.

359. van der Meel, R., et al., *Ligand-targeted particulate nanomedicines undergoing clinical evaluation: current status.* Adv Drug Deliv Rev, 2013. **65**(10): p. 1284-98.
360. Sanna, V., N. Pala, and M. Sechi, *Targeted therapy using nanotechnology: focus on cancer.* Int J Nanomedicine, 2014. **9**: p. 467-83.
361. Zuckerman, J.E., et al., *Correlating animal and human phase Ia/Ib clinical data with CALAA-01, a targeted, polymer-based nanoparticle containing siRNA.* Proc Natl Acad Sci U S A, 2014. **111**(31): p. 11449-54.
362. Shamsipour, F., et al., *Conjugation of Monoclonal Antibodies to Super Paramagnetic Iron Oxide Nanoparticles for Detection of her2/neu Antigen on Breast Cancer Cell Lines.* Avicenna J Med Biotechnol, 2009. **1**(1): p. 27-31.
363. Oghabian, M.A., et al., *Detectability of Her2 positive tumors using monoclonal antibody conjugated iron oxide nanoparticles in MRI.* J Nanosci Nanotechnol, 2011. **11**(6): p. 5340-4.
364. Rakovich, T.Y., et al., *Highly sensitive single domain antibody-quantum dot conjugates for detection of HER2 biomarker in lung and breast cancer cells.* ACS Nano, 2014. **8**(6): p. 5682-95.
365. Weissleder, R., et al., *Cell-specific targeting of nanoparticles by multivalent attachment of small molecules.* Nat Biotechnol, 2005. **23**(11): p. 1418-23.
366. Meier, R., et al., *Breast cancers: MR imaging of folate-receptor expression with the folate-specific nanoparticle P1133.* Radiology, 2010. **255**(2): p. 527-35.
367. Ren, D., F. Kratz, and S.W. Wang, *Engineered drug-protein nanoparticle complexes for folate receptor targeting.* Biochem Eng J, 2014. **89**: p. 33-41.
368. Ng, E.W., et al., *Pegaptanib, a targeted anti-VEGF aptamer for ocular vascular disease.* Nat Rev Drug Discov, 2006. **5**(2): p. 123-32.
369. Malik, M.T., et al., *AS1411-conjugated gold nanospheres and their potential for breast cancer therapy.* Oncotarget, 2015.
370. Simnick, A.J., et al., *In vivo tumor targeting by a NGR-decorated micelle of a recombinant diblock copolypeptide.* J Control Release, 2011. **155**(2): p. 144-51.
371. Callebaut, C., et al., *Inhibition of HIV infection by pseudopeptides blocking viral envelope glycoprotein-mediated membrane fusion and cell death.* Virology, 1996. **218**(1): p. 181-92.
372. Krust, B., et al., *Targeting surface nucleolin with multivalent HB-19 and related Nucant pseudopeptides results in distinct inhibitory mechanisms depending on the malignant tumor cell type.* BMC Cancer, 2011. **11**: p. 333.
373. Peer, D., et al., *Nanocarriers as an emerging platform for cancer therapy.* Nat Nanotechnol, 2007. **2**(12): p. 751-60.
374. Hartmann, L.C., et al., *Folate receptor overexpression is associated with poor outcome in breast cancer.* Int J Cancer, 2007. **121**(5): p. 938-42.
375. Friedman, A.D., S.E. Claypool, and R. Liu, *The smart targeting of nanoparticles.* Curr Pharm Des, 2013. **19**(35): p. 6315-29.
376. Ellington, A.D. and J.W. Szostak, *In vitro selection of RNA molecules that bind specific ligands.* Nature, 1990. **346**(6287): p. 818-22.

377. Tuerk, C. and L. Gold, *Systematic evolution of ligands by exponential enrichment: RNA ligands to bacteriophage T4 DNA polymerase.* Science, 1990. **249**(4968): p. 505-10.
378. Keefe, A.D., S. Pai, and A. Ellington, *Aptamers as therapeutics.* Nat Rev Drug Discov, 2010. **9**(7): p. 537-50.
379. Sassanfar, M. and J.W. Szostak, *An RNA motif that binds ATP.* Nature, 1993. **364**(6437): p. 550-3.
380. Jenison, R.D., et al., *High-resolution molecular discrimination by RNA.* Science, 1994. **263**(5152): p. 1425-9.
381. Bates, P.J., et al., *Antiproliferative activity of G-rich oligonucleotides correlates with protein binding.* J Biol Chem, 1999. **274**(37): p. 26369-77.
382. Soundararajan, S., et al., *The nucleolin targeting aptamer AS1411 destabilizes Bcl-2 messenger RNA in human breast cancer cells.* Cancer Res, 2008. **68**(7): p. 2358-65.
383. Li, L., et al., *Nucleolin-targeting liposomes guided by aptamer AS1411 for the delivery of siRNA for the treatment of malignant melanomas.* Biomaterials, 2014. **35**(12): p. 3840-50.
384. Bates, P.J., et al., *Discovery and development of the G-rich oligonucleotide AS1411 as a novel treatment for cancer.* Exp Mol Pathol, 2009. **86**(3): p. 151-64.
385. Mutter, M. *The Construction of New Proteins and Enzymes-a Prospect for the Future? Angewandte Chemie International Edition in English Volume 24, Issue 8*. Angewandte Chemie International Edition in English, 1985. **24**, 639-653.
386. Nisole, S., et al., *The anti-HIV pseudopeptide HB-19 forms a complex with the cell-surface-expressed nucleolin independent of heparan sulfate proteoglycans.* J Biol Chem, 1999. **274**(39): p. 27875-84.
387. Nisole, S., et al., *The anti-HIV pentameric pseudopeptide HB-19 binds the C-terminal end of nucleolin and prevents anchorage of virus particles in the plasma membrane of target cells.* J Biol Chem, 2002. **277**(23): p. 20877-86.
388. Nisole, S., et al., *The HB-19 pseudopeptide 5[Kpsi(CH2N)PR]-TASP inhibits attachment of T lymophocyte- and macrophage-tropic HIV to permissive cells.* AIDS Res Hum Retroviruses, 2000. **16**(3): p. 237-49.
389. Krust, B., et al., *The anti-HIV pentameric pseudopeptide HB-19 is preferentially taken up in vivo by lymphoid organs where it forms a complex with nucleolin.* Proc Natl Acad Sci U S A, 2001. **98**(24): p. 14090-5.
390. Destouches, D., et al., *Suppression of tumor growth and angiogenesis by a specific antagonist of the cell-surface expressed nucleolin.* PLoS One, 2008. **3**(6): p. e2518.
391. El Khoury, D., et al., *Targeting surface nucleolin with a multivalent pseudopeptide delays development of spontaneous melanoma in RET transgenic mice.* BMC Cancer, 2010. **10**: p. 325.
392. Krust, B., et al., *Suppression of tumorigenicity of rhabdoid tumor derived G401 cells by the multivalent HB-19 pseudopeptide that targets surface nucleolin.* Biochimie, 2011. **93**(3): p. 426-33.
393. Destouches, D., et al., *A simple approach to cancer therapy afforded by multivalent pseudopeptides that target cell-surface nucleoproteins.* Cancer Res, 2011. **71**(9): p. 3296-305.
394. Chen, X., et al., *Nucleolin-mediated cellular trafficking of DNA nanoparticle is lipid raft and microtubule dependent and can be modulated by glucocorticoid.* Mol Ther, 2011. **19**(1): p. 93-102.

395. ImmuPharma, *http://www.londonstockexchange.com/exchange/news/market-news/market-news-detail/12246039.html*. Accessed 09/10/2015.
396. Li, L., et al., *Improved intratumoral nanoparticle extravasation and penetration by mild hyperthermia.* J Control Release, 2013. **167**(2): p. 130-7.
397. Kuppen, P.J., et al., *Tumor structure and extracellular matrix as a possible barrier for therapeutic approaches using immune cells or adenoviruses in colorectal cancer.* Histochem Cell Biol, 2001. **115**(1): p. 67-72.
398. Kuhn, S.J., et al., *Proteolytic surface functionalization enhances in vitro magnetic nanoparticle mobility through extracellular matrix.* Nano Lett, 2006. **6**(2): p. 306-12.
399. Junttila, M.R. and F.J. de Sauvage, *Influence of tumour micro-environment heterogeneity on therapeutic response.* Nature, 2013. **501**(7467): p. 346-54.
400. Hetheridge, C., G. Mavria, and H. Mellor, *Uses of the in vitro endothelial-fibroblast organotypic co-culture assay in angiogenesis research.* Biochem Soc Trans, 2011. **39**(6): p. 1597-600.
401. Bishop, E.T., et al., *An in vitro model of angiogenesis: basic features.* Angiogenesis, 1999. **3**(4): p. 335-44.
402. Donovan, D., et al., *Comparison of three in vitro human 'angiogenesis' assays with capillaries formed in vivo.* Angiogenesis, 2001. **4**(2): p. 113-21.
403. Sorrell, J.M., M.A. Baber, and A.I. Caplan, *A self-assembled fibroblast-endothelial cell co-culture system that supports in vitro vasculogenesis by both human umbilical vein endothelial cells and human dermal microvascular endothelial cells.* Cells Tissues Organs, 2007. **186**(3): p. 157-68.
404. Edmondson, R., et al., *Three-dimensional cell culture systems and their applications in drug discovery and cell-based biosensors.* Assay Drug Dev Technol, 2014. **12**(4): p. 207-18.
405. Nelson, C.M. and M.J. Bissell, *Modeling dynamic reciprocity: engineering three-dimensional culture models of breast architecture, function, and neoplastic transformation.* Semin Cancer Biol, 2005. **15**(5): p. 342-52.
406. Albiin, N., *MRI of Focal Liver Lesions.* Curr Med Imaging Rev, 2012. **8**(2): p. 107-116.
407. Wang, Y.X., *Superparamagnetic iron oxide based MRI contrast agents: Current status of clinical application.* Quant Imaging Med Surg, 2011. **1**(1): p. 35-40.
408. Shenoi, M.M., et al., *Nanoparticle preconditioning for enhanced thermal therapies in cancer.* Nanomedicine (Lond), 2011. **6**(3): p. 545-63.
409. Gilchrist, R.K., et al., *Selective inductive heating of lymph nodes.* Ann Surg, 1957. **146**(4): p. 596-606.
410. Field, S.B. and C.C. Morris, *The relationship between heating time and temperature: its relevance to clinical hyperthermia.* Radiother Oncol, 1983. **1**(2): p. 179-86.
411. Song, C.W., et al., *Implications of increased tumor blood flow and oxygenation caused by mild temperature hyperthermia in tumor treatment.* Int J Hyperthermia, 2005. **21**(8): p. 761-7.
412. Kettering, M., et al., *Minimal-invasive magnetic heating of tumors does not alter intra-tumoral nanoparticle accumulation, allowing for repeated therapy sessions: an in vivo study in mice.* Nanotechnology, 2011. **22**(50): p. 505102.

413. Amstad, E. and E. Reimhult, *Nanoparticle actuated hollow drug delivery vehicles.* Nanomedicine (Lond), 2012. **7**(1): p. 145-64.
414. Edelman, E.R., et al., *Modulated release from polymeric drug delivery systems using oscillating magnetic fields: in vitro and in vivo characteristics.* Trans Am Soc Artif Intern Organs, 1984. **30**: p. 445-9.
415. Kost, J., et al., *Magnetically controlled release systems: effect of polymer composition.* J Biomed Mater Res, 1985. **19**(8): p. 935-40.
416. Kost, J., J. Wolfrum, and R. Langer, *Magnetically enhanced insulin release in diabetic rats.* J Biomed Mater Res, 1987. **21**(12): p. 1367-73.
417. Su, W., et al., *PEG/RGD-modified magnetic polymeric liposomes for controlled drug release and tumor cell targeting.* Int J Pharm, 2012. **426**(1-2): p. 170-81.
418. Zhang, J. and R.D. Misra, *Magnetic drug-targeting carrier encapsulated with thermosensitive smart polymer: core-shell nanoparticle carrier and drug release response.* Acta Biomater, 2007. **3**(6): p. 838-50.
419. Salas, G., S. Veintemillas-Verdaguer, and P. Morales Mdel, *Relationship between physico-chemical properties of magnetic fluids and their heating capacity.* Int J Hyperthermia, 2013. **29**(8): p. 768-76.
420. Yamamoto, A., et al., *Cytotoxicity evaluation of ceramic particles of different sizes and shapes.* J Biomed Mater Res A, 2004. **68**(2): p. 244-56.
421. Takeuchi, T., M. Nakajima, and K. Morimoto, *A human cell system for detecting asbestos cytogenotoxicity in vitro.* Mutat Res, 1999. **438**(1): p. 63-70.
422. Karlsson, H.L., et al., *Copper oxide nanoparticles are highly toxic: a comparison between metal oxide nanoparticles and carbon nanotubes.* Chem Res Toxicol, 2008. **21**(9): p. 1726-32.
423. Ankamwar, B., et al., *Biocompatibility of Fe(3)O(4) nanoparticles evaluated by in vitro cytotoxicity assays using normal, glia and breast cancer cells.* Nanotechnology, 2010. **21**(7): p. 75102.
424. Latorre, A., et al., *Multifunctionalization of magnetic nanoparticles for controlled drug release: a general approach.* Eur J Med Chem, 2014. **82**: p. 355-62.
425. Gobbo, O.L., et al., *Biodistribution and pharmacokinetic studies of SPION using particle electron paramagnetic resonance, MRI and ICP-MS.* Nanomedicine (Lond), 2015. **10**(11): p. 1751-60.
426. Vacha, J., *Blood volume in inbred strain BALB/c, CBA/J and C57BL/10 mice determined by means of 59Fe-labelled red cells and 59Fe bound to transferrin.* Physiol Bohemoslov, 1975. **24**(5): p. 413-9.
427. Sluiter, W., et al., *Determination of blood volume in the mouse with 51chromium-labelled erythrocytes.* J Immunol Methods, 1984. **73**(1): p. 221-5.
428. Diehl, K.H., et al., *A good practice guide to the administration of substances and removal of blood, including routes and volumes.* J Appl Toxicol, 2001. **21**(1): p. 15-23.
429. Lofrumento, D.D., et al., *Valinomycin induced energy-dependent mitochondrial swelling, cytochrome c release, cytosolic NADH/cytochrome c oxidation and apoptosis.* Apoptosis, 2011. **16**(10): p. 1004-13.

430. Gao, C., et al., *Tacrine induces apoptosis through lysosome- and mitochondria-dependent pathway in HepG2 cells.* Toxicol In Vitro, 2014. **28**(4): p. 667-74.
431. Idziorek, T., et al., *YOPRO-1 permits cytofluorometric analysis of programmed cell death (apoptosis) without interfering with cell viability.* J Immunol Methods, 1995. **185**(2): p. 249-58.
432. Radomski, A., et al., *Nanoparticle-induced platelet aggregation and vascular thrombosis.* Br J Pharmacol, 2005. **146**(6): p. 882-93.
433. Gratton, S.E., et al., *The effect of particle design on cellular internalization pathways.* Proc Natl Acad Sci U S A, 2008. **105**(33): p. 11613-8.
434. Bright, N.A., et al., *Dense core lysosomes can fuse with late endosomes and are re-formed from the resultant hybrid organelles.* J Cell Sci, 1997. **110 (Pt 17)**: p. 2027-40.
435. Kuhn, D.A., et al., *Different endocytotic uptake mechanisms for nanoparticles in epithelial cells and macrophages.* Beilstein J Nanotechnol, 2014. **5**: p. 1625-36.
436. Helmy, K.Y., et al., *CRIg: a macrophage complement receptor required for phagocytosis of circulating pathogens.* Cell, 2006. **124**(5): p. 915-27.
437. Sadauskas, E., et al., *Kupffer cells are central in the removal of nanoparticles from the organism.* Part Fibre Toxicol, 2007. **4**: p. 10.
438. Storey, P., et al., *MRI assessment of hepatic iron clearance rates after USPIO administration in healthy adults.* Invest Radiol, 2012. **47**(12): p. 717-24.
439. Fornari, F.A., et al., *Interference by doxorubicin with DNA unwinding in MCF-7 breast tumor cells.* Mol Pharmacol, 1994. **45**(4): p. 649-56.
440. Birmpas, C., et al., *Nucleolin mediates the antiangiogenesis effect of the pseudopeptide N6L.* BMC Cell Biol, 2012. **13**: p. 32.
441. Destouches, D., et al., *Multivalent pseudopeptides targeting cell surface nucleoproteins inhibit cancer cell invasion through tissue inhibitor of metalloproteinases 3 (TIMP-3) release.* J Biol Chem, 2012. **287**(52): p. 43685-93.
442. Dadashzadeh, E.R., et al., *Rapid spectrophotometric technique for quantifying iron in cells labeled with superparamagnetic iron oxide nanoparticles: potential translation to the clinic.* Contrast Media Mol Imaging, 2013. **8**(1): p. 50-6.
443. GlobalRPh, *http://www.globalrph.com/gemcitabine.htm*. Accessed 03/11/2015.
444. Denard, B., C. Lee, and J. Ye, *Doxorubicin blocks proliferation of cancer cells through proteolytic activation of CREB3L1.* Elife, 2012. **1**: p. e00090.
445. Perez-Arnaiz, C., et al., *New insights into the mechanism of the DNA/doxorubicin interaction.* J Phys Chem B, 2014. **118**(5): p. 1288-95.
446. Agudelo, D., et al., *Intercalation of antitumor drug doxorubicin and its analogue by DNA duplex: structural features and biological implications.* Int J Biol Macromol, 2014. **66**: p. 144-50.
447. Nitiss, J.L., *Targeting DNA topoisomerase II in cancer chemotherapy.* Nat Rev Cancer, 2009. **9**(5): p. 338-50.
448. Covey, J.M., et al., *Topoisomerase II-mediated DNA damage produced by 4'-(9-acridinylamino)methanesulfon-m-anisidide and related acridines in L1210 cells and isolated nuclei: relation to cytotoxicity.* Cancer Res, 1988. **48**(4): p. 860-5.

449. Wang, Z., et al., *Mitochondria-derived reactive oxygen species play an important role in Doxorubicin-induced platelet apoptosis.* Int J Mol Sci, 2015. **16**(5): p. 11087-100.
450. Hrelia, S., et al., *Doxorubicin induces early lipid peroxidation associated with changes in glucose transport in cultured cardiomyocytes.* Biochim Biophys Acta, 2002. **1567**(1-2): p. 150-6.
451. Lowe, S.W., et al., *p53 status and the efficacy of cancer therapy in vivo.* Science, 1994. **266**(5186): p. 807-10.
452. Wang, S., et al., *Doxorubicin induces apoptosis in normal and tumor cells via distinctly different mechanisms. intermediacy of H(2)O(2)- and p53-dependent pathways.* J Biol Chem, 2004. **279**(24): p. 25535-43.
453. Weydert, C.J. and J.J. Cullen, *Measurement of superoxide dismutase, catalase and glutathione peroxidase in cultured cells and tissue.* Nat Protoc, 2010. **5**(1): p. 51-66.
454. Housman, G., et al., *Drug resistance in cancer: an overview.* Cancers (Basel), 2014. **6**(3): p. 1769-92.
455. Arora, H.C., et al., *Nanocarriers enhance Doxorubicin uptake in drug-resistant ovarian cancer cells.* Cancer Res, 2012. **72**(3): p. 769-78.
456. Taurin, S., H. Nehoff, and K. Greish, *Anticancer nanomedicine and tumor vascular permeability; Where is the missing link?* J Control Release, 2012. **164**(3): p. 265-75.
457. Hobbs, S.K., et al., *Regulation of transport pathways in tumor vessels: role of tumor type and microenvironment.* Proc Natl Acad Sci U S A, 1998. **95**(8): p. 4607-12.
458. Bae, Y.H., *Drug targeting and tumor heterogeneity.* J Control Release, 2009. **133**(1): p. 2-3.
459. Shen, Y.A., et al., *Bypassing the EPR effect with a nanomedicine harboring a sustained-release function allows better tumor control.* Int J Nanomedicine, 2015. **10**: p. 2485-502.
460. Plunkett, W., et al., *Gemcitabine: metabolism, mechanisms of action, and self-potentiation.* Semin Oncol, 1995. **22**(4 Suppl 11): p. 3-10.
461. Spielmann, M., et al., *Single-agent gemcitabine is active in previously treated metastatic breast cancer.* Oncology, 2001. **60**(4): p. 303-7.
462. Burris, H. and A.M. Storniolo, *Assessing clinical benefit in the treatment of pancreas cancer: gemcitabine compared to 5-fluorouracil.* Eur J Cancer, 1997. **33 Suppl 1**: p. S18-22.
463. Ciliberto, D., et al., *Role of gemcitabine-based combination therapy in the management of advanced pancreatic cancer: a meta-analysis of randomised trials.* Eur J Cancer, 2013. **49**(3): p. 593-603.
464. Alberts, B., *Molecular biology of the cell*. 4th ed / Bruce Alberts ... [et al.] ed. 2002, New York: Garland Science.
465. Chipuk, J.E., L. Bouchier-Hayes, and D.R. Green, *Mitochondrial outer membrane permeabilization during apoptosis: the innocent bystander scenario.* Cell Death Differ, 2006. **13**(8): p. 1396-402.
466. Galluzzi, L., et al., *Mitochondrial gateways to cancer.* Mol Aspects Med, 2010. **31**(1): p. 1-20.
467. Voet, D., J.G. Voet, and C.W. Pratt, *Fundamentals of biochemistry : life at the molecular level*. 2nd ed. ed. 2005, New York ; Chichester: Wiley.
468. Larsson, N.G., et al., *Progressive increase of the mutated mitochondrial DNA fraction in Kearns-Sayre syndrome.* Pediatr Res, 1990. **28**(2): p. 131-6.

469. Smits, B.W., et al., *Disease impact in chronic progressive external ophthalmoplegia: more than meets the eye.* Neuromuscul Disord, 2011. **21**(4): p. 272-8.

470. Ruhoy, I.S. and R.P. Saneto, *The genetics of Leigh syndrome and its implications for clinical practice and risk management.* Appl Clin Genet, 2014. **7**: p. 221-34.

471. Meyers, D.E., H.I. Basha, and M.K. Koenig, *Mitochondrial cardiomyopathy: pathophysiology, diagnosis, and management.* Tex Heart Inst J, 2013. **40**(4): p. 385-94.

472. Lightowlers, R.N., et al., *Mammalian mitochondrial genetics: heredity, heteroplasmy and disease.* Trends Genet, 1997. **13**(11): p. 450-5.

473. Tatarenkov, A. and J.C. Avise, *Rapid concerted evolution in animal mitochondrial DNA.* Proc Biol Sci, 2007. **274**(1619): p. 1795-8.

474. Yakes, F.M. and B. Van Houten, *Mitochondrial DNA damage is more extensive and persists longer than nuclear DNA damage in human cells following oxidative stress.* Proc Natl Acad Sci U S A, 1997. **94**(2): p. 514-9.

475. Prakash, A. and S. Doublie, *Base Excision Repair in the Mitochondria.* J Cell Biochem, 2015. **116**(8): p. 1490-9.

476. LeDoux, S.P., et al., *Repair of mitochondrial DNA after various types of DNA damage in Chinese hamster ovary cells.* Carcinogenesis, 1992. **13**(11): p. 1967-73.

477. Alexeyev, M., et al., *The maintenance of mitochondrial DNA integrity--critical analysis and update.* Cold Spring Harb Perspect Biol, 2013. **5**(5): p. a012641.

478. van Gisbergen, M.W., et al., *How do changes in the mtDNA and mitochondrial dysfunction influence cancer and cancer therapy? Challenges, opportunities and models.* Mutat Res Rev Mutat Res, 2015. **764**: p. 16-30.

479. Lu, J., L.K. Sharma, and Y. Bai, *Implications of mitochondrial DNA mutations and mitochondrial dysfunction in tumorigenesis.* Cell Res, 2009. **19**(7): p. 802-15.

480. Fendt, L., et al., *Accumulation of mutations over the entire mitochondrial genome of breast cancer cells obtained by tissue microdissection.* Breast Cancer Res Treat, 2011. **128**(2): p. 327-36.

481. Kassauei, K., et al., *Mitochondrial DNA mutations in pancreatic cancer.* Int J Gastrointest Cancer, 2006. **37**(2-3): p. 57-64.

482. Navaglia, F., et al., *Mitochondrial DNA D-loop in pancreatic cancer: somatic mutations are epiphenomena while the germline 16519 T variant worsens metabolism and outcome.* Am J Clin Pathol, 2006. **126**(4): p. 593-601.

483. Fliss, M.S., et al., *Facile detection of mitochondrial DNA mutations in tumors and bodily fluids.* Science, 2000. **287**(5460): p. 2017-9.

484. Hosgood, H.D., 3rd, et al., *Mitochondrial DNA copy number and lung cancer risk in a prospective cohort study.* Carcinogenesis, 2010. **31**(5): p. 847-9.

485. Kulawiec, M., et al., *Tumorigenic transformation of human breast epithelial cells induced by mitochondrial DNA depletion.* Cancer Biol Ther, 2008. **7**(11): p. 1732-43.

486. Parrella, P., et al., *Detection of mitochondrial DNA mutations in primary breast cancer and fine-needle aspirates.* Cancer Res, 2001. **61**(20): p. 7623-6.

487. Lam, E.T., et al., *Mitochondrial DNA sequence variation and risk of pancreatic cancer.* Cancer Res, 2012. **72**(3): p. 686-95.

488. Liu, Y. and J. Wang, *Effects of DMSA-coated Fe3O4 nanoparticles on the transcription of genes related to iron and osmosis homeostasis.* Toxicol Sci, 2013. **131**(2): p. 521-36.

489. Buratti, P., et al., *Recent Advances in Iron Metabolism: Relevance for Health, Exercise, and Performance.* Med Sci Sports Exerc, 2015. **47**(8): p. 1596-604.

490. Lee, H.J., et al., *Effect of excess iron on oxidative stress and gluconeogenesis through hepcidin during mitochondrial dysfunction.* J Nutr Biochem, 2015. **26**(12): p. 1414-23.

491. Gao, X., et al., *Mitochondrial DNA damage in iron overload.* J Biol Chem, 2009. **284**(8): p. 4767-75.

492. Hayashi, T., et al., *Damage to the endoplasmic reticulum and activation of apoptotic machinery by oxidative stress in ischemic neurons.* J Cereb Blood Flow Metab, 2005. **25**(1): p. 41-53.

493. Dissanayake, N.M., K.M. Current, and S.O. Obare, *Mutagenic Effects of Iron Oxide Nanoparticles on Biological Cells.* Int J Mol Sci, 2015. **16**(10): p. 23482-516.

494. Singh, N., et al., *Potential toxicity of superparamagnetic iron oxide nanoparticles (SPION).* Nano Rev, 2010. **1**.

495. Stroh, A., et al., *Iron oxide particles for molecular magnetic resonance imaging cause transient oxidative stress in rat macrophages.* Free Radic Biol Med, 2004. **36**(8): p. 976-84.

496. Schafer, F.Q. and G.R. Buettner, *Redox environment of the cell as viewed through the redox state of the glutathione disulfide/glutathione couple.* Free Radic Biol Med, 2001. **30**(11): p. 1191-212.

497. Almeida, A.M., et al., *Mitochondrial DNA damage associated with lipid peroxidation of the mitochondrial membrane induced by Fe2+-citrate.* An Acad Bras Cienc, 2006. **78**(3): p. 505-14.

498. Boya, P. and G. Kroemer, *Lysosomal membrane permeabilization in cell death.* Oncogene, 2008. **27**(50): p. 6434-51.

499. Porter, N.A., *A perspective on free radical autoxidation: the physical organic chemistry of polyunsaturated fatty acid and sterol peroxidation.* J Org Chem, 2013. **78**(8): p. 3511-24.

500. Vatassery, G.T., et al., *Iron uncouples oxidative phosphorylation in brain mitochondria isolated from vitamin E-deficient rats.* Biochim Biophys Acta, 2004. **1688**(3): p. 265-73.

501. Circu, M.L. and T.Y. Aw, *Reactive oxygen species, cellular redox systems, and apoptosis.* Free Radic Biol Med, 2010. **48**(6): p. 749-62.

502. Baliga, B. and S. Kumar, *Apaf-1/cytochrome c apoptosome: an essential initiator of caspase activation or just a sideshow?* Cell Death Differ, 2003. **10**(1): p. 16-8.

503. Cande, C., et al., *Apoptosis-inducing factor (AIF): a novel caspase-independent death effector released from mitochondria.* Biochimie, 2002. **84**(2-3): p. 215-22.

504. Cande, C., et al., *Apoptosis-inducing factor (AIF): key to the conserved caspase-independent pathways of cell death?* J Cell Sci, 2002. **115**(Pt 24): p. 4727-34.

505. Boehning, D., et al., *Cytochrome c binds to inositol (1,4,5) trisphosphate receptors, amplifying calcium-dependent apoptosis.* Nat Cell Biol, 2003. **5**(12): p. 1051-61.

506. Ermak, G. and K.J. Davies, *Calcium and oxidative stress: from cell signaling to cell death.* Mol Immunol, 2002. **38**(10): p. 713-21.

507. Boveris, A. and E. Cadenas, *Mitochondrial production of hydrogen peroxide regulation by nitric oxide and the role of ubisemiquinone.* IUBMB Life, 2000. **50**(4-5): p. 245-50.
508. Brune, B., *Nitric oxide: NO apoptosis or turning it ON?* Cell Death Differ, 2003. **10**(8): p. 864-9.
509. Kholmukhamedov, A., J.M. Schwartz, and J.J. Lemasters, *Isolated mitochondria infusion mitigates ischemia-reperfusion injury of the liver in rats: mitotracker probes and mitochondrial membrane potential.* Shock, 2013. **39**(6): p. 543.
510. Vasseur, P. and C. Lasne, *OECD Detailed Review Paper (DRP) number 31 on "Cell Transformation Assays for Detection of Chemical Carcinogens": main results and conclusions.* Mutat Res, 2012. **744**(1): p. 8-11.
511. Tolosa, L., et al., *High-content screening of drug-induced mitochondrial impairment in hepatic cells: effects of statins.* Archives of Toxicology, 2015. **89**(10): p. 1847-1860.
512. Nohl, H., L. Gille, and K. Staniek, *The exogenous NADH dehydrogenase of heart mitochondria is the key enzyme responsible for selective cardiotoxicity of anthracyclines.* Z Naturforsch C, 1998. **53**(3-4): p. 279-85.
513. Fowler, J.D., et al., *Kinetic investigation of the inhibitory effect of gemcitabine on DNA polymerization catalyzed by human mitochondrial DNA polymerase.* J Biol Chem, 2008. **283**(22): p. 15339-48.
514. Song, S., L.J. Wheeler, and C.K. Mathews, *Deoxyribonucleotide pool imbalance stimulates deletions in HeLa cell mitochondrial DNA.* J Biol Chem, 2003. **278**(45): p. 43893-6.
515. McKenzie, R., et al., *Hepatic failure and lactic acidosis due to fialuridine (FIAU), an investigational nucleoside analogue for chronic hepatitis B.* N Engl J Med, 1995. **333**(17): p. 1099-105.
516. Tanaka, N., et al., *Prevalidation study of the BALB/c 3T3 cell transformation assay for assessment of carcinogenic potential of chemicals.* Mutat Res, 2012. **744**(1): p. 20-9.
517. Cirri, P. and P. Chiarugi, *Cancer associated fibroblasts: the dark side of the coin.* Am J Cancer Res, 2011. **1**(4): p. 482-97.
518. Kalluri, R. and M. Zeisberg, *Fibroblasts in cancer.* Nat Rev Cancer, 2006. **6**(5): p. 392-401.
519. Pietras, K. and A. Ostman, *Hallmarks of cancer: interactions with the tumor stroma.* Exp Cell Res, 2010. **316**(8): p. 1324-31.
520. De Wever, O. and M. Mareel, *Role of tissue stroma in cancer cell invasion.* J Pathol, 2003. **200**(4): p. 429-47.
521. Bussard, K.M., et al., *Tumor-associated stromal cells as key contributors to the tumor microenvironment.* Breast Cancer Res, 2016. **18**(1): p. 84.
522. Hanahan, D. and L.M. Coussens, *Accessories to the crime: functions of cells recruited to the tumor microenvironment.* Cancer Cell, 2012. **21**(3): p. 309-22.
523. Olsen, C.J., et al., *Human mammary fibroblasts stimulate invasion of breast cancer cells in a three-dimensional culture and increase stroma development in mouse xenografts.* BMC Cancer, 2010. **10**: p. 444.
524. Varma, S., D. Sabo, and S.B. Rempe, *K+/Na+ selectivity in K channels and valinomycin: over-coordination versus cavity-size constraints.* J Mol Biol, 2008. **376**(1): p. 13-22.

525. Klein, B., et al., *Perturbation of intracellular K(+) homeostasis with valinomycin promotes cell death by mitochondrial swelling and autophagic processes.* Apoptosis, 2011. **16**(11): p. 1101-17.
526. Green, P.S. and C. Leeuwenburgh, *Mitochondrial dysfunction is an early indicator of doxorubicin-induced apoptosis.* Biochim Biophys Acta, 2002. **1588**(1): p. 94-101.
527. Ferri, K.F. and G. Kroemer, *Organelle-specific initiation of cell death pathways.* Nat Cell Biol, 2001. **3**(11): p. E255-63.
528. Ly, J.D., D.R. Grubb, and A. Lawen, *The mitochondrial membrane potential (deltapsi(m)) in apoptosis; an update.* Apoptosis, 2003. **8**(2): p. 115-28.
529. Galluzzi, L., J.M. Bravo-San Pedro, and G. Kroemer, *Organelle-specific initiation of cell death.* Nat Cell Biol, 2014. **16**(8): p. 728-36.
530. Kuilman, T., et al., *The essence of senescence.* Genes Dev, 2010. **24**(22): p. 2463-79.
531. Dierick, J.F., et al., *Stress-induced premature senescence and replicative senescence are different phenotypes, proteomic evidence.* Biochem Pharmacol, 2002. **64**(5-6): p. 1011-7.
532. Dimri, G.P., et al., *A biomarker that identifies senescent human cells in culture and in aging skin in vivo.* Proc Natl Acad Sci U S A, 1995. **92**(20): p. 9363-7.
533. Kuroda, K., et al., *Antimicrobial peptide FF/CAP18 induces apoptotic cell death in HCT116 colon cancer cells via changes in the metabolic profile.* Int J Oncol, 2015. **46**(4): p. 1516-26.
534. Sakkas, A., et al., *Safety and efficacy of suicide gene therapy with adenosine deaminase 5-fluorocytosine silmutaneously in in vitro cultures of melanoma and retinal cell lines.* J Cancer, 2014. **5**(5): p. 368-81.
535. Al-Sheddi, E.S., et al., *Novel all trans-retinoic Acid derivatives: cytotoxicity, inhibition of cell cycle progression and induction of apoptosis in human cancer cell lines.* Molecules, 2015. **20**(5): p. 8181-97.
536. Yuan, X., et al., *G0/G1 arrest and apoptosis induced by SARS-CoV 3b protein in transfected cells.* Virol J, 2005. **2**: p. 66.
537. Sawai, H. and N. Domae, *Discrimination between primary necrosis and apoptosis by necrostatin-1 in Annexin V-positive/propidium iodide-negative cells.* Biochem Biophys Res Commun, 2011. **411**(3): p. 569-73.
538. Sadiq, R., et al., *In vitro toxicological assessment of iron oxide, aluminium oxide and copper nanoparticles in prokaryotic and eukaryotic cell types.* Drug Chem Toxicol, 2015. **38**(2): p. 152-61.
539. Gomaa, I.O., et al., *Evaluation of in vitro mutagenicity and genotoxicity of magnetite nanoparticles.* Drug Discov Ther, 2013. **7**(3): p. 116-23.
540. Klein, G. and E. Klein, *The viability and the average desoxypentosenucleic acid content of micronuclei-containing cells produced by colchicine treatment in the Ehrlich ascites tumor.* Cancer Res, 1952. **12**(7): p. 484-9.
541. Park, E.J., et al., *Doxorubicin induces cytotoxicity through upregulation of pERK-dependent ATF3.* PLoS One, 2012. **7**(9): p. e44990.
542. Dumitru, C.A., et al., *Lysosomal ceramide mediates gemcitabine-induced death of glioma cells.* J Mol Med (Berl), 2009. **87**(11): p. 1123-32.
543. Aits, S. and M. Jaattela, *Lysosomal cell death at a glance.* J Cell Sci, 2013. **126**(Pt 9): p. 1905-12.

544. Frohlich, E., *The role of surface charge in cellular uptake and cytotoxicity of medical nanoparticles.* Int J Nanomedicine, 2012. **7**: p. 5577-91.

545. Chen, L., et al., *The role of surface charge on the uptake and biocompatibility of hydroxyapatite nanoparticles with osteoblast cells.* Nanotechnology, 2011. **22**(10): p. 105708.

546. Smita, S., et al., *Nanoparticles in the environment: assessment using the causal diagram approach.* Environ Health, 2012. **11 Suppl 1**: p. S13.

547. Vaseashta, A., *Life Cycle Analysis of Nanoparticles: Reducing Risk and Liability*. 2015: DEStech Publications, Incorporated.

548. Seaton, A., et al., *Nanoparticles, human health hazard and regulation.* J R Soc Interface, 2010. **7 Suppl 1**: p. S119-29.

549. Journeay, W.S. and R.H. Goldman, *Occupational handling of nickel nanoparticles: a case report.* Am J Ind Med, 2014. **57**(9): p. 1073-6.

550. Hanahan, D. and R.A. Weinberg, *Hallmarks of cancer: the next generation.* Cell, 2011. **144**(5): p. 646-74.

References

Chapter 8

Appendices and Supplemental Information

Chapter 8: Appendices and supplemental material

Appendix 1: Chapter 3 graphs

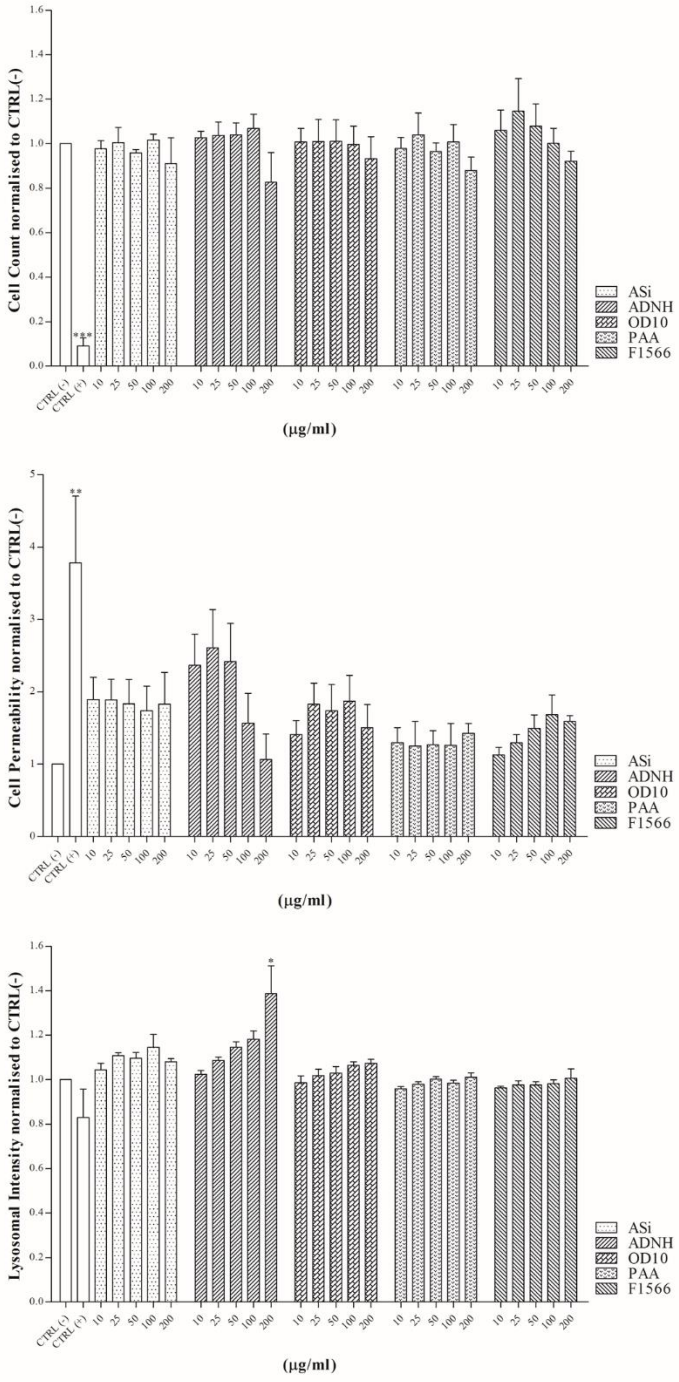

Figure S1: MCF-7 cell line exposed to basic MNP to determine cytotoxic potential.

MCF7 breast-derived cell line exposed to ASi, ADNH, OD10, PAA, F1566 MNP for 24 h. Cells were stained using the Cytotoxicity II HitKit™ and analysed using the InCell 1000 HCSA device. Variation in cell count, cell membrane permeability and lysosomal intensity were measured compared to untreated control (CTRL(-)) and 1µM CdSe positive control (CTRL(+)). Statistical significance was determined using the one way ANOVA with Tukey post-test for each column compared to untreated control (CTRL(-)). p value: *** = <0.001, **=<0.01, *=<0.05.

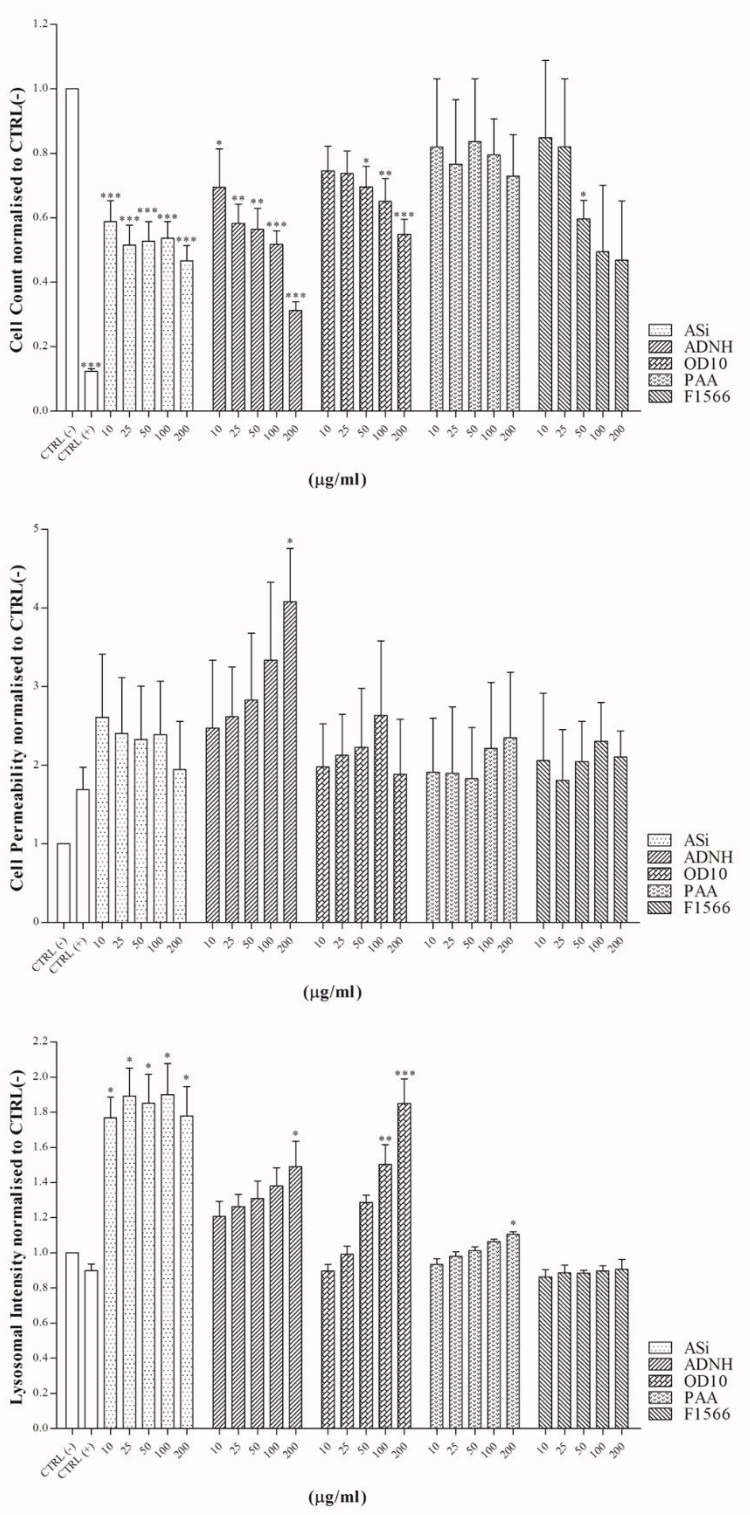

Figure S2: BT-474 cell line exposed to basic MNP to determine cytotoxic potential.

BT-474 breast-derived cell line was exposed to ASi, ADNH, OD10, PAA, F1566 MNP for 24 h. Cells were stained using the Cytotoxicity II HitKit™ and analysed using the InCell 1000 HCSA device. Variation in cell count, cell membrane permeability and lysosomal intensity were measured compared to untreated control (CTRL(-)) and 1µM CdSe positive control (CTRL(+)). Statistical significance was determined using the one way ANOVA with Tukey post-test for each column compared to untreated control (CTRL(-)). p value: *** = <0.001, **=<0.01, *=<0.05.

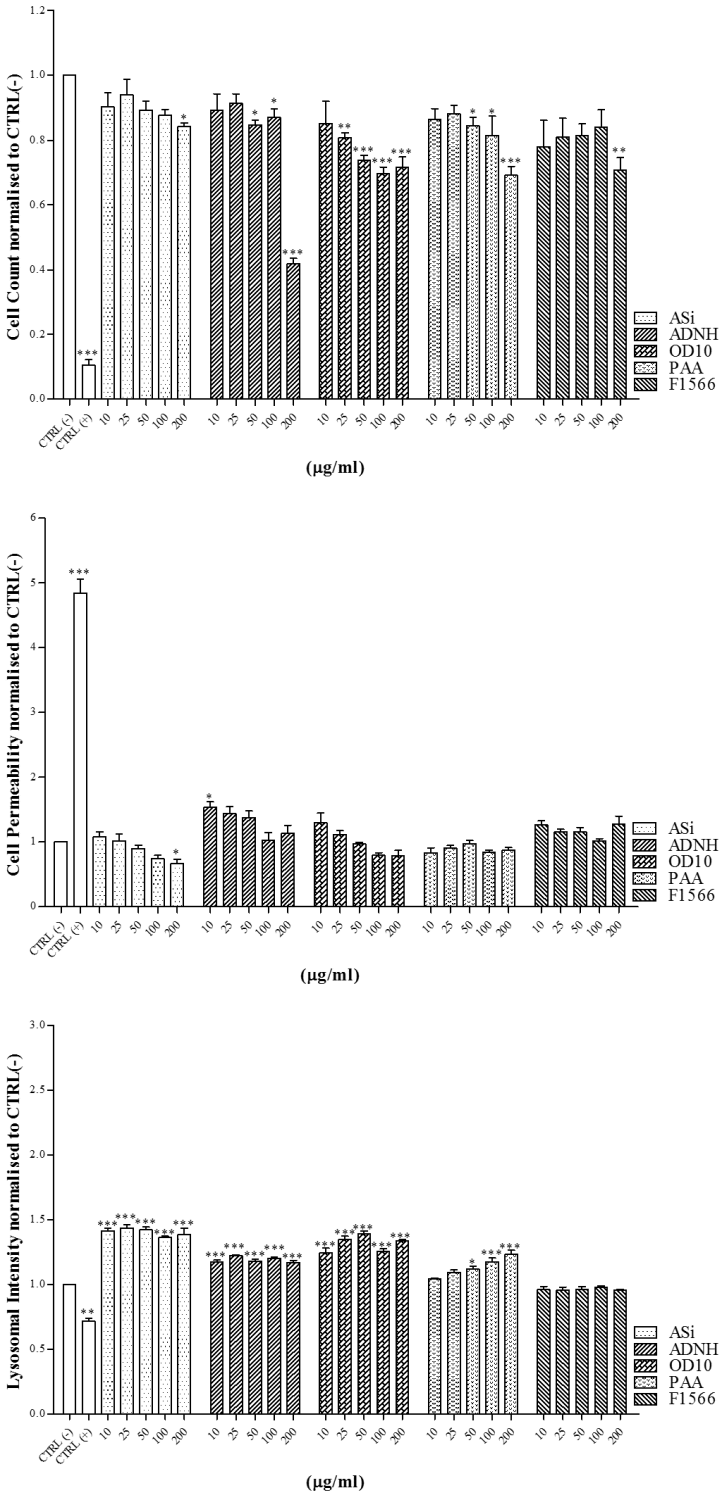

Figure S3: MDA-MB-231 cell line exposed to basic MNP to determine cytotoxic potential.

MDA-MB-231 breast-derived cell line was exposed to ASi, ADNH, OD10, PAA, F1566 MNP for 24 h. Cells were stained using the Cytotoxicity II HitKit™ and analysed using the InCell 1000 HCSA device. Variation in cell count, cell membrane permeability and lysosomal intensity were measured compared to untreated control (CTRL(-)) and 1µM CdSe positive control (CTRL(+)). Statistical significance was determined using the one way ANOVA with Tukey post-test for each column compared to untreated control (CTRL(-)). p value: *** = <0.001, **=<0.01, *=<0.05.

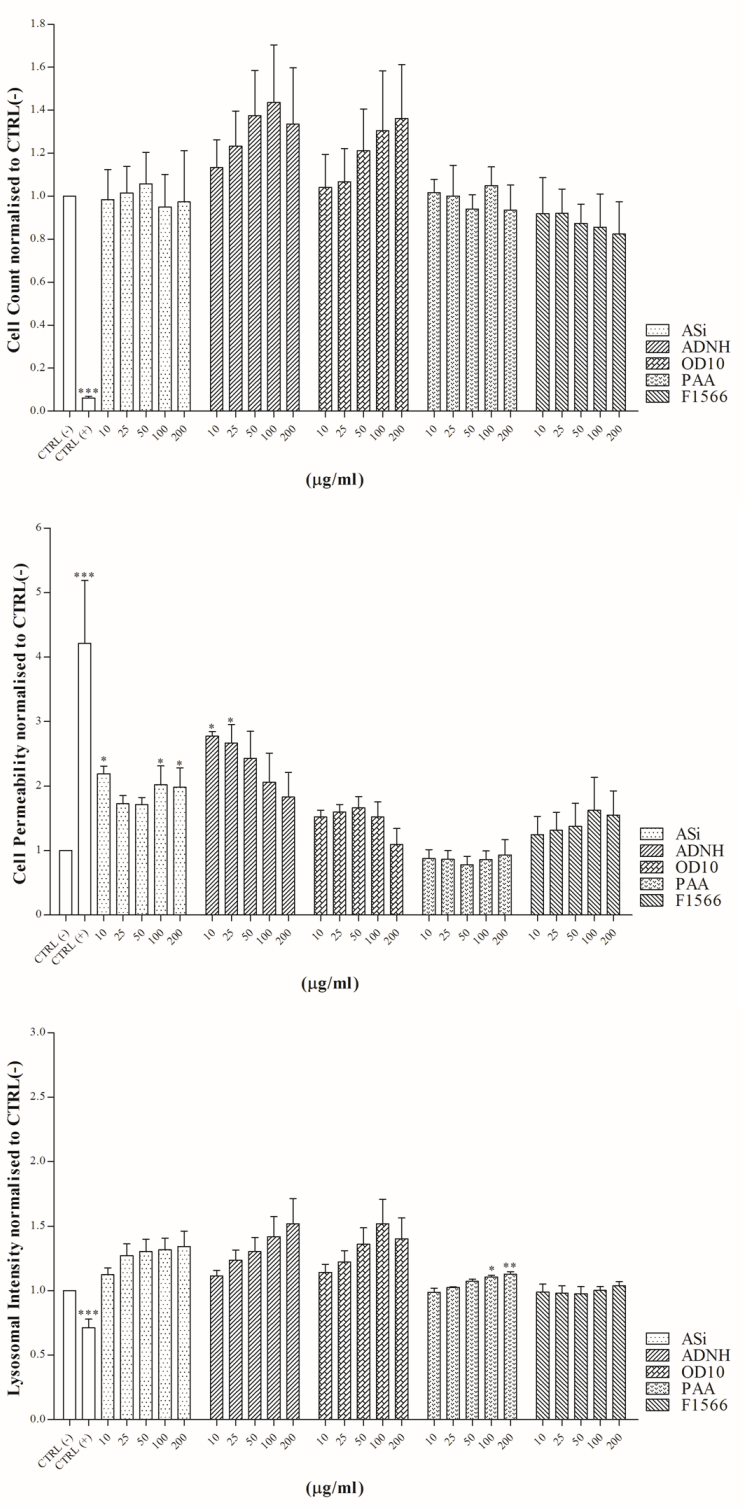

Figure S4: SK-BR-3 cell line exposed to basic MNP to determine cytotoxic potential.

SK-BR-3 breast-derived cell line was exposed to ASi, ADNH, OD10, PAA, F1566 MNP for 24 h. Cells were stained using the Cytotoxicity II HitKit™ and analysed using the InCell 1000 HCSA device. Variation in cell count, cell membrane permeability and lysosomal intensity were measured compared to untreated control (CTRL(-)) and 1µM CdSe positive control (CTRL(+)). Statistical significance was determined using the one way ANOVA with Tukey post-test for each column compared to untreated control (CTRL(-)). p value: *** = <0.001, **=<0.01, *=<0.05.

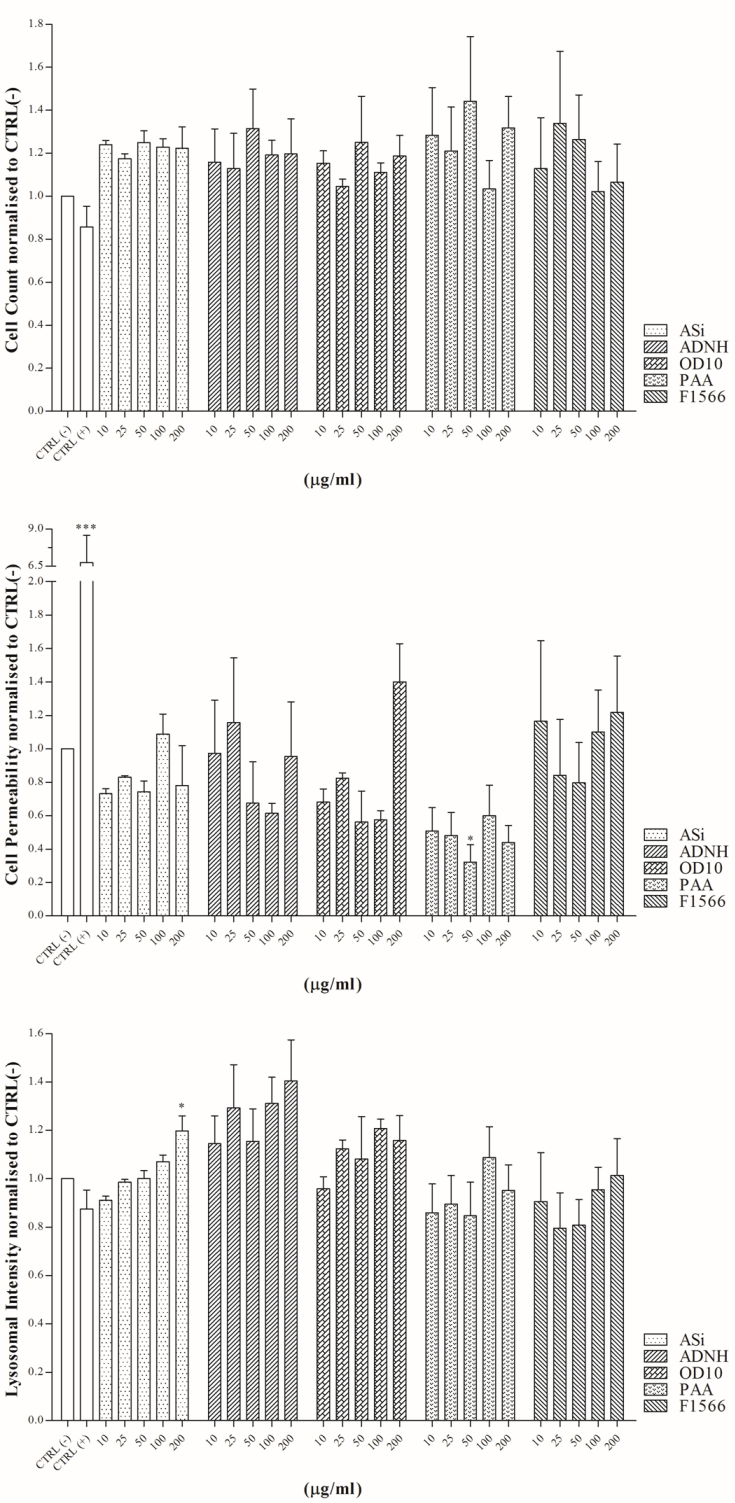

Figure S5: MCF-10A cell line exposed to basic MNP to determine cytotoxic potential.

MCF-10A breast-derived cell line was exposed to ASi, ADNH, OD10, PAA, F1566 MNP for 24 h. Cells were stained using the Cytotoxicity II HitKit™ and analysed using the InCell 1000 HCSA device. Variation in cell count, cell membrane permeability and lysosomal intensity were measured compared to untreated control (CTRL(-)) and 1µM CdSe positive control (CTRL(+)). Statistical significance was determined using the one way ANOVA with Tukey post-test for each column compared to untreated control (CTRL(-)). p value: *** = <0.001, **=<0.01, *=<0.05.

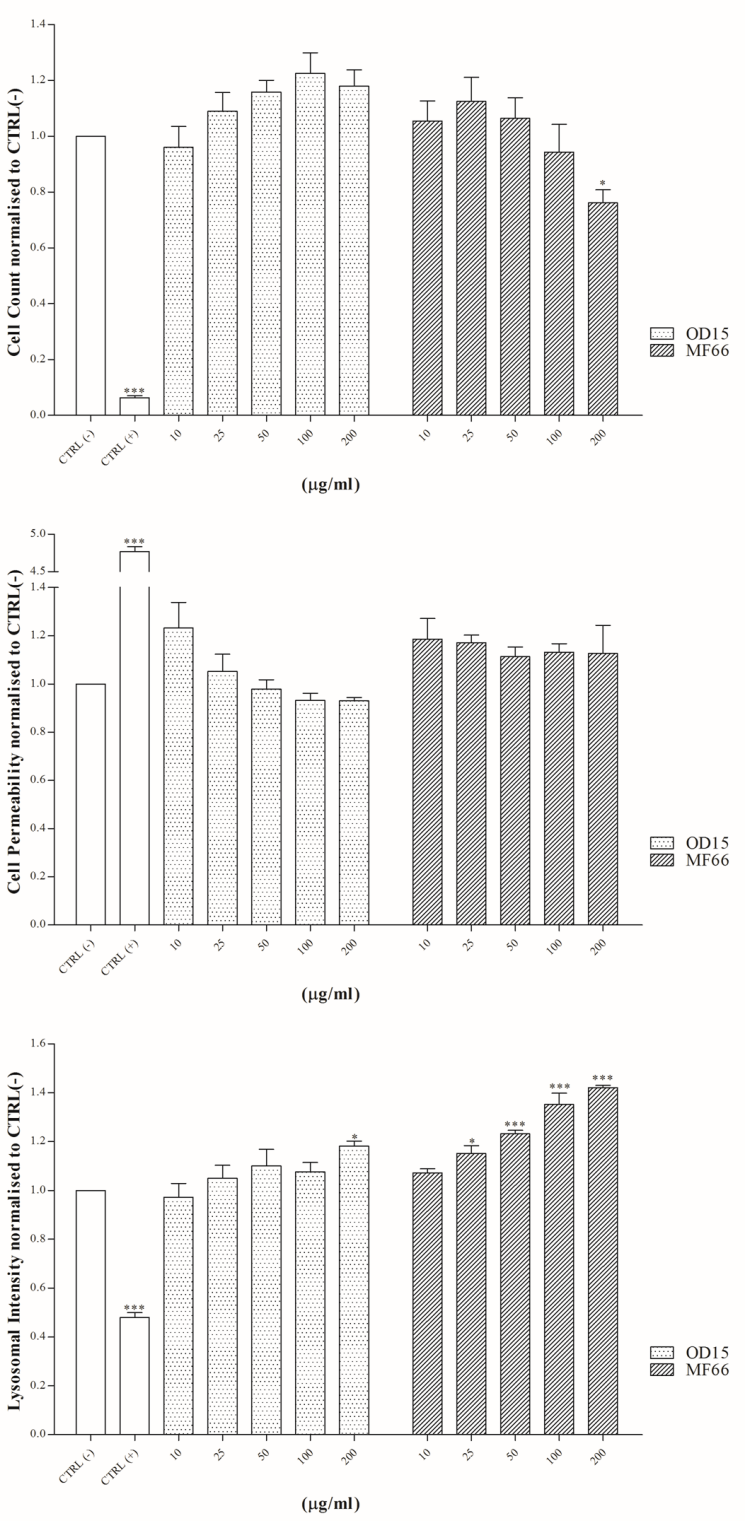

Figure S6: MCF-7 cell line exposed to basic MNP to determine cytotoxic potential.

MCF-7 breast-derived cell line was exposed to OD15 and MF66 MNP for 24 h. Cells were stained using the Cytotoxicity II HitKit™ and analysed using the InCell 1000 HCSA device. Variation in cell count, cell membrane permeability and lysosomal intensity were measured compared to untreated control (CTRL(-)) and 1µM CdSe positive control (CTRL(+)). Statistical significance was determined using the one way ANOVA with Tukey post-test for each column compared to untreated control (CTRL(-)). p value: *** = <0.001, **=<0.01, *=<0.05.

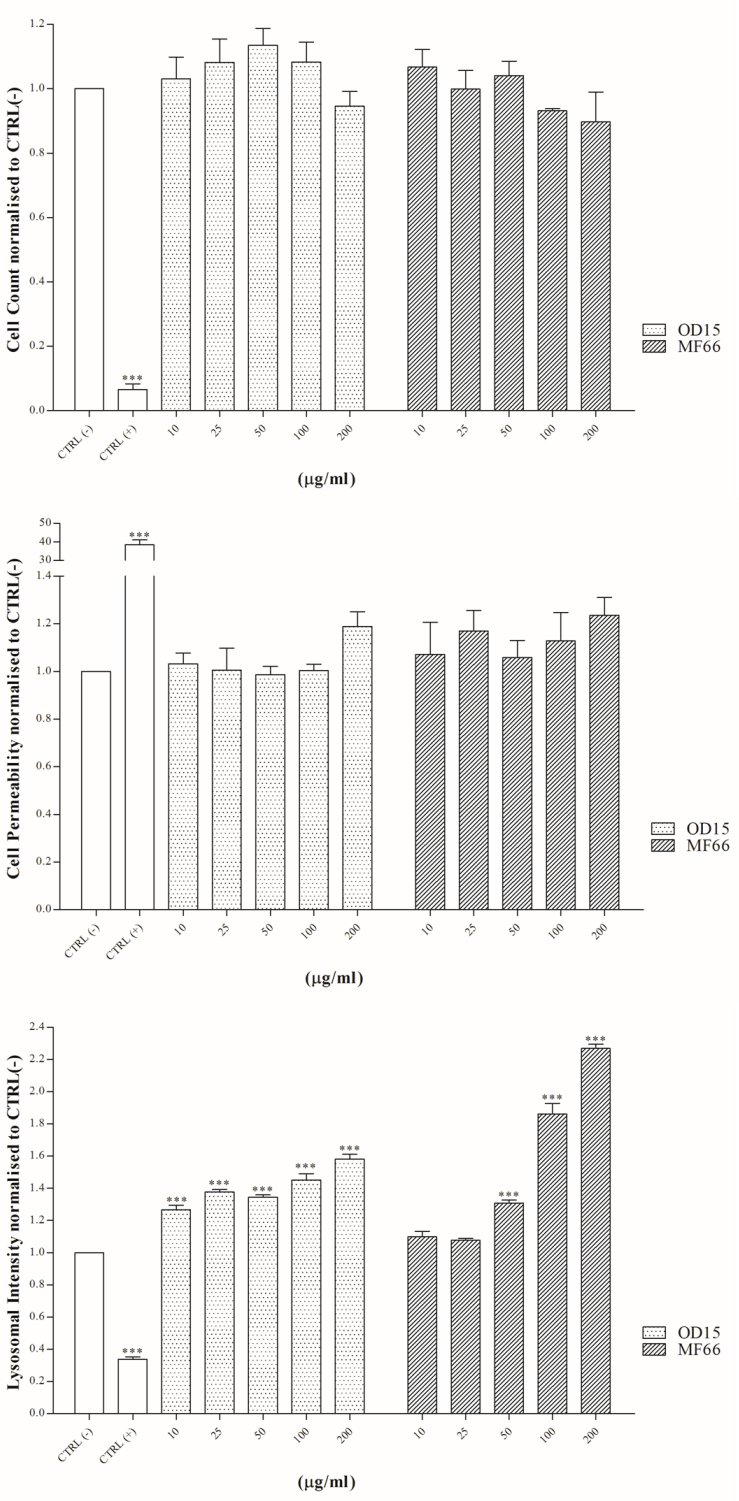

Figure S7: BT-474 cell line exposed to basic MNP to determine cytotoxic potential.

BT-474 breast-derived cell line was exposed to OD15 and MF66 MNP for 24 h. Cells were stained using the Cytotoxicity II HitKit™ and analysed using the InCell 1000 HCSA device. Variation in cell count, cell membrane permeability and lysosomal intensity were measured compared to untreated control (CTRL(-)) and 1µM CdSe positive control (CTRL(+)). Statistical significance was determined using the one way ANOVA with Tukey post-test for each column compared to untreated control (CTRL(-)). p value: *** = <0.001, **=<0.01, *=<0.05.

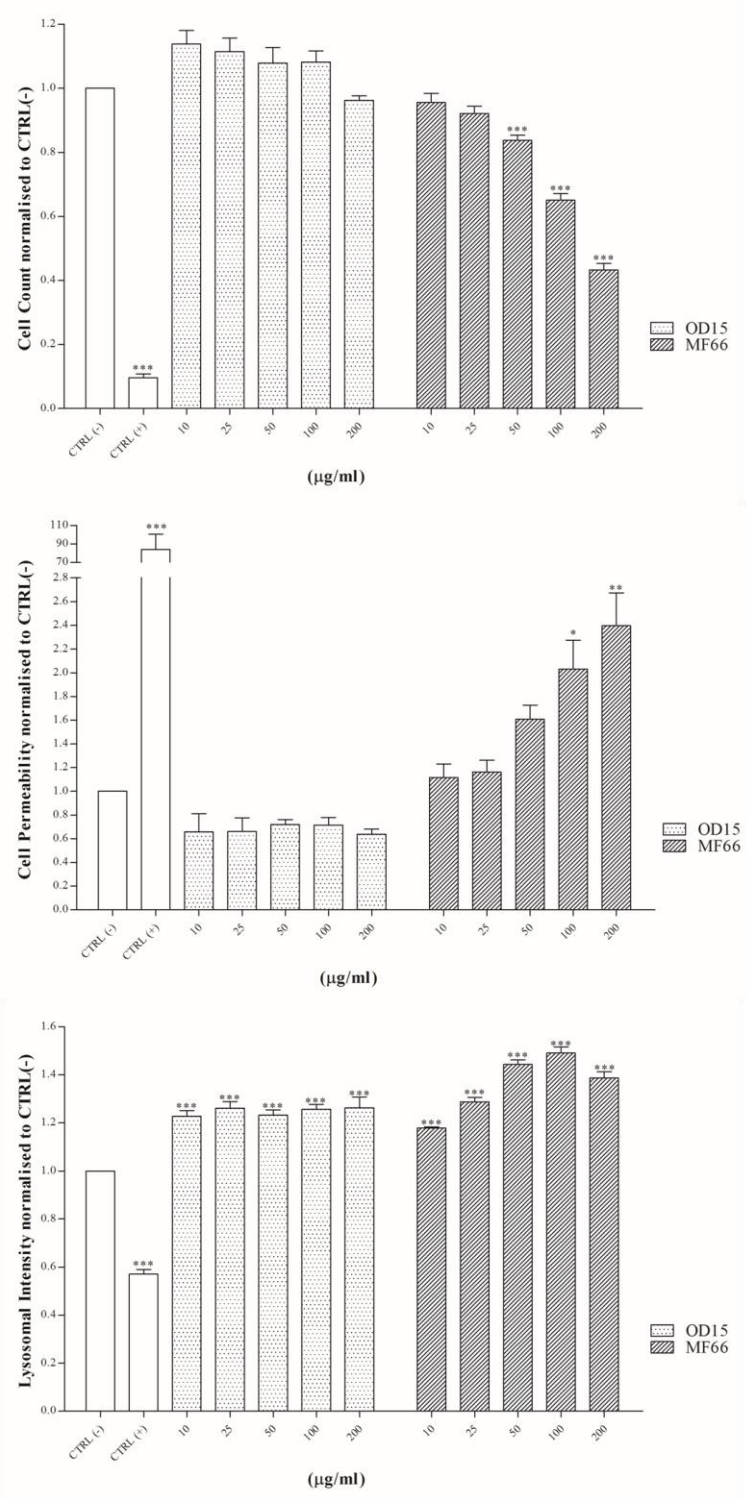

Figure S8: MDA-MB-231 cell line exposed to basic MNP to determine cytotoxic potential.

MDA-MB-231 breast-derived cell line was exposed to OD15 and MF66 MNP for 24 h. Cells were stained using the Cytotoxicity II HitKit™ and analysed using the InCell 1000 HCSA device. Variation in cell count, cell membrane permeability and lysosomal intensity were measured compared to untreated control (CTRL(-)) and 1µM CdSe positive control (CTRL(+)). Statistical significance was determined using the one way ANOVA with Tukey post-test for each column compared to untreated control (CTRL(-)). p value: *** = <0.001, **=<0.01, *=<0.05.

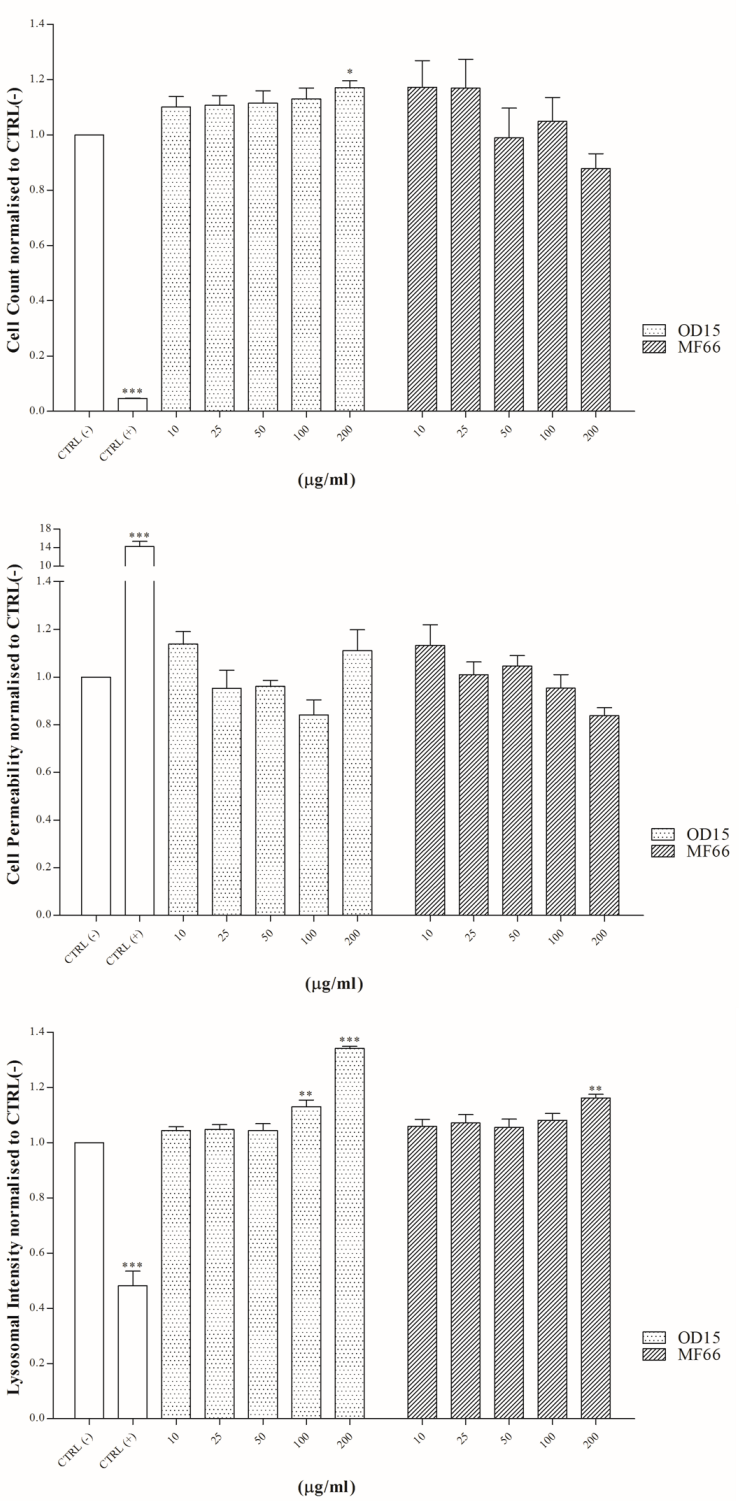

Figure S9: SK-BR-3 cell line exposed to basic MNP to determine cytotoxic potential.

SK-BR-3 breast-derived cell line was exposed to OD15 and MF66 MNP for 24 h. Cells were stained using the Cytotoxicity II HitKit™ and analysed using the InCell 1000 HCSA device. Variation in cell count, cell membrane permeability and lysosomal intensity were measured compared to untreated control (CTRL(-)) and 1µM CdSe positive control (CTRL(+)). Statistical significance was determined using the one way ANOVA with Tukey post-test for each column compared to untreated control (CTRL(-)). p value: *** = <0.001, **=<0.01, *=<0.05.

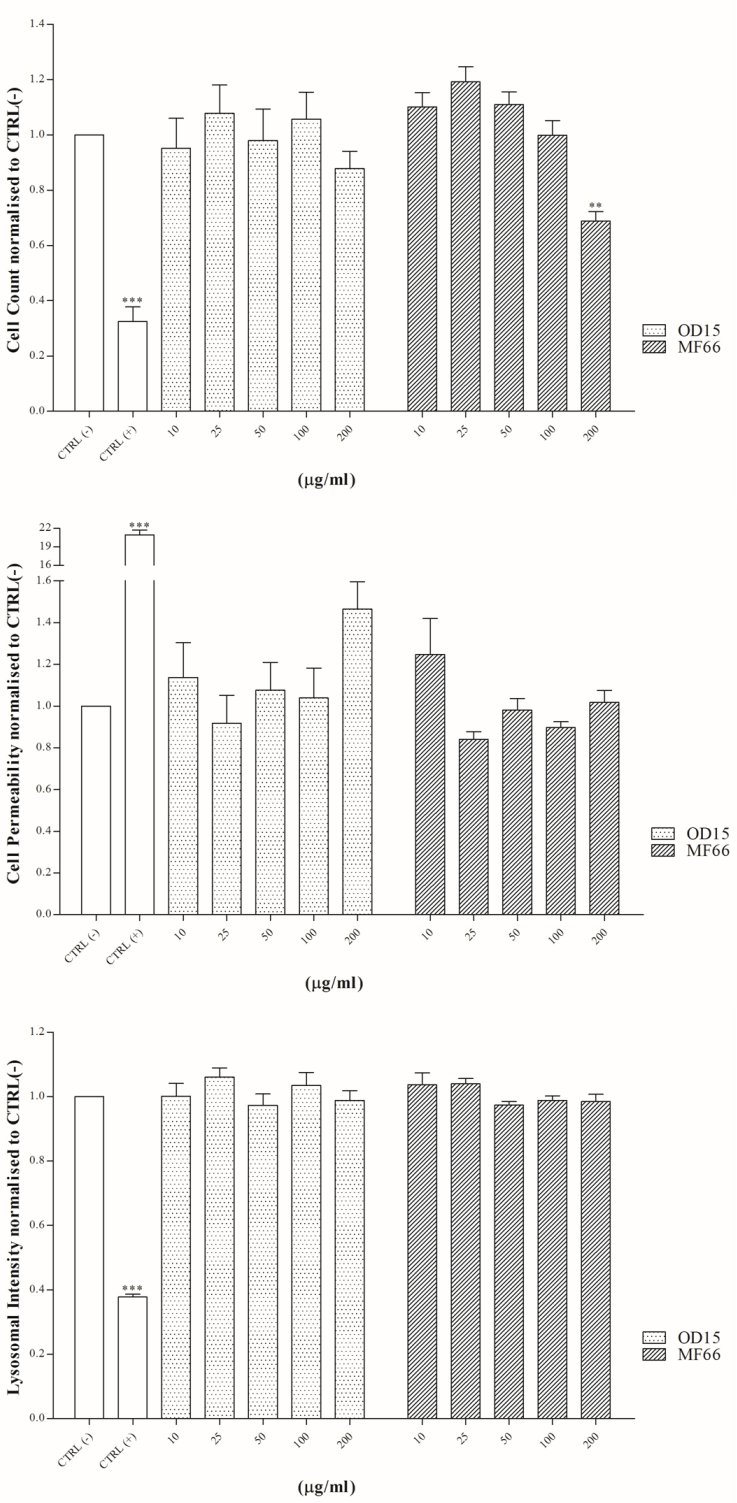

Figure S10: MCF-10A cell line exposed to basic MNP to determine cytotoxic potential.

MCF-10A breast-derived cell line was exposed to OD15 and MF66 MNP for 24 h. Cells were stained using the Cytotoxicity II HitKit™ and analysed using the InCell 1000 HCSA device. Variation in cell count, cell membrane permeability and lysosomal intensity were measured compared to untreated control (CTRL(-)) and 1µM CdSe positive control (CTRL(+)). Statistical significance was determined using the one way ANOVA with Tukey post-test for each column compared to untreated control (CTRL(-)). p value: *** = <0.001, **=<0.01, *=<0.05.

Appendix 2: Chapter 4 graphs

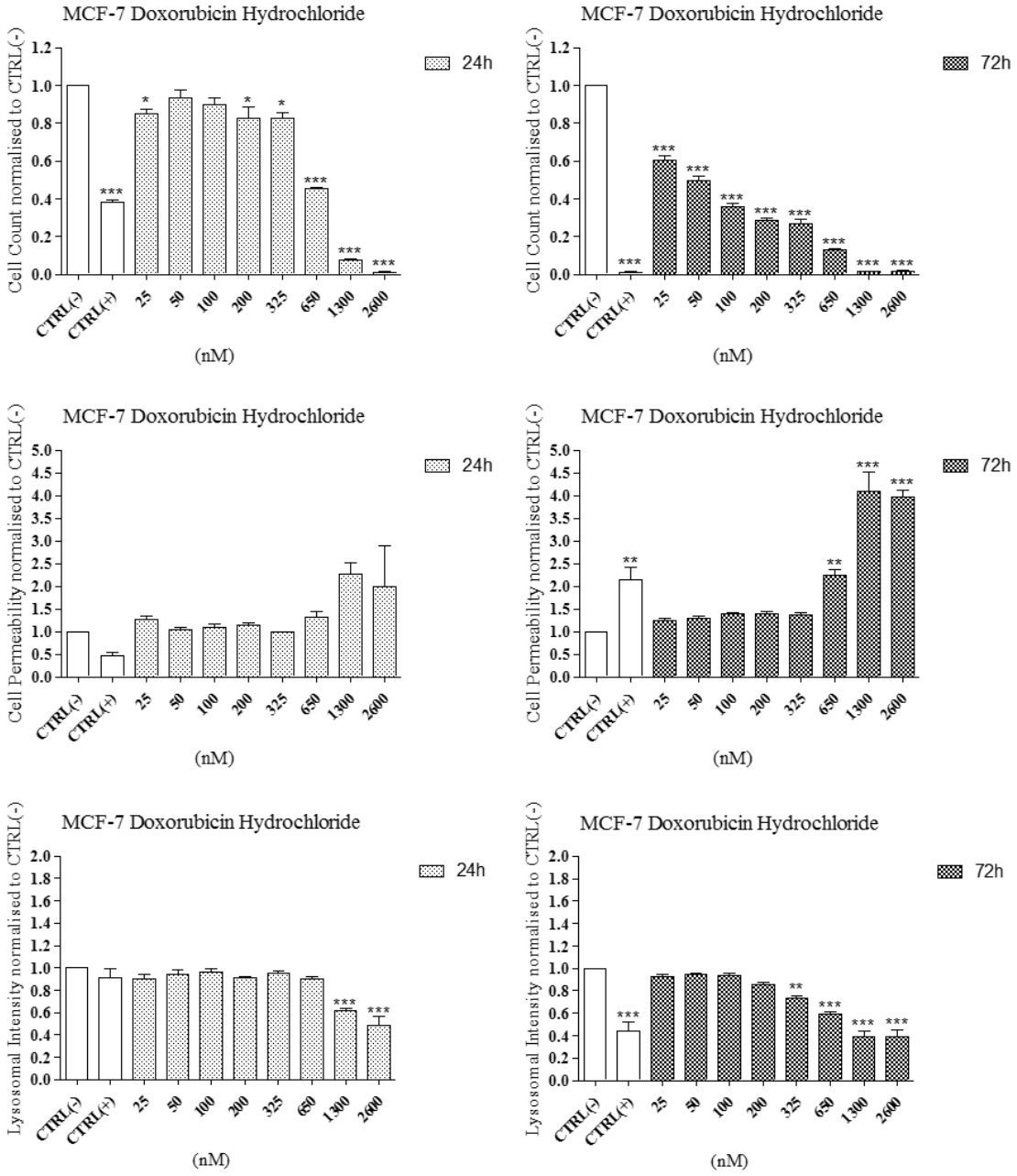

Figure S11: Effect of Doxorubicin hydrochloride on viability of MCF-7 cell line.

MCF-7 breast-derived cell line was exposed to free Doxorubicin hydrochloride for 24h and 72h. Cells were stained using the Cytotoxicity II HitKit™ and analysed using the InCell 1000 HCSA device. Variation in cell count, cell membrane permeability and lysosomal intensity were measured compared to untreated control (CTRL(-)) and 1µM CdSe positive control (CTRL(+)). Statistical significance was determined using the one way ANOVA with Tukey post-test for each column compared to untreated control (CTRL(-)). p value: *** = <0.001, **=<0.01, *=<0.05.

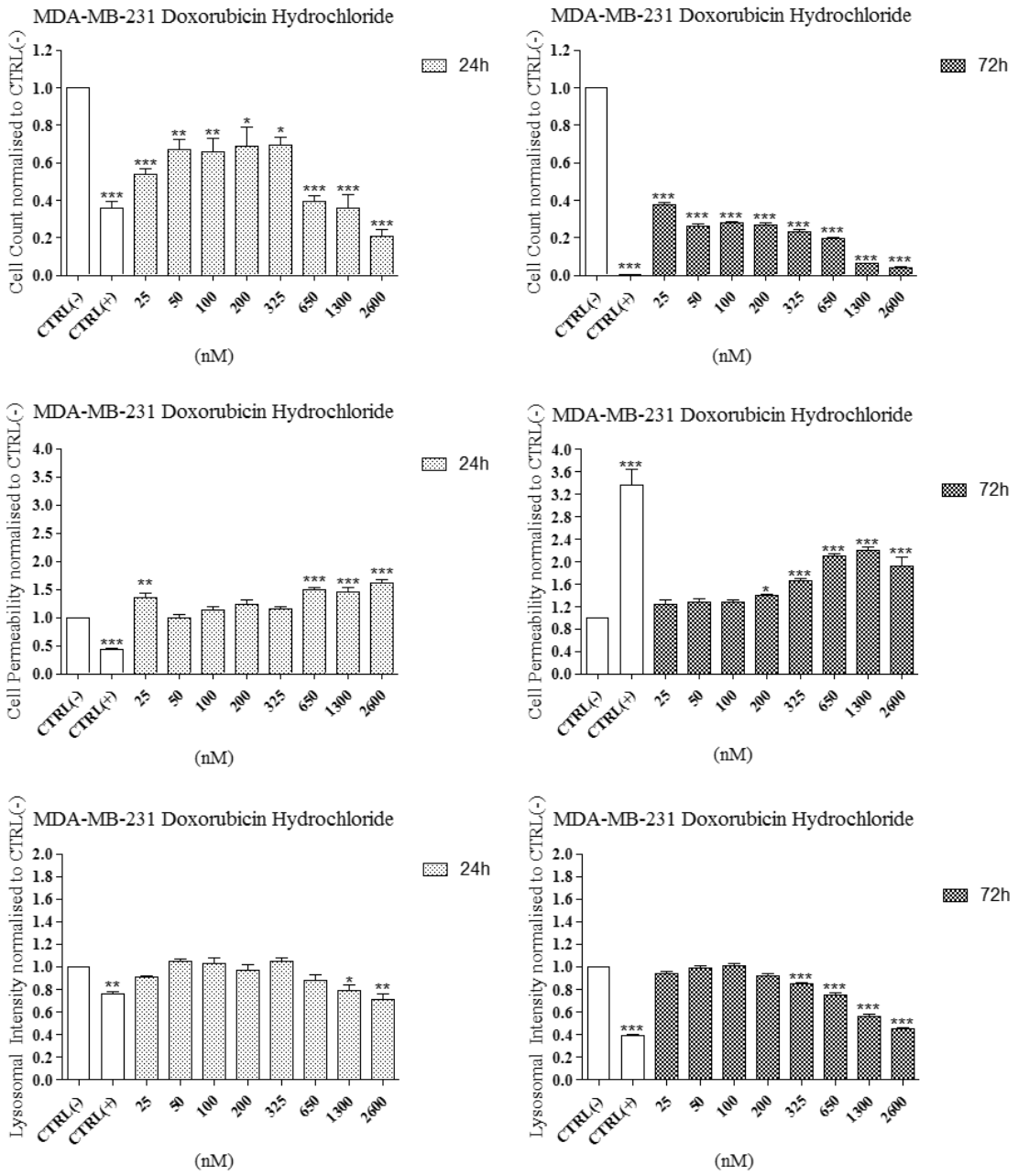

Figure S12: Effect of Doxorubicin hydrochloride on viability of MDA-MB-231 cell line.

MDA-MB-231 breast-derived cell line was exposed to free Doxorubicin hydrochloride for 24h and 72h. Cells were stained using the Cytotoxicity II HitKit™ and analysed using the InCell 1000 HCSA device. Variation in cell count, cell membrane permeability and lysosomal intensity were measured compared to untreated control (CTRL(-)) and 1µM CdSe positive control (CTRL(+)). Statistical significance was determined using the one way ANOVA with Tukey post-test for each column compared to untreated control (CTRL(-)). p value: *** = <0.001, **=<0.01, *=<0.05.

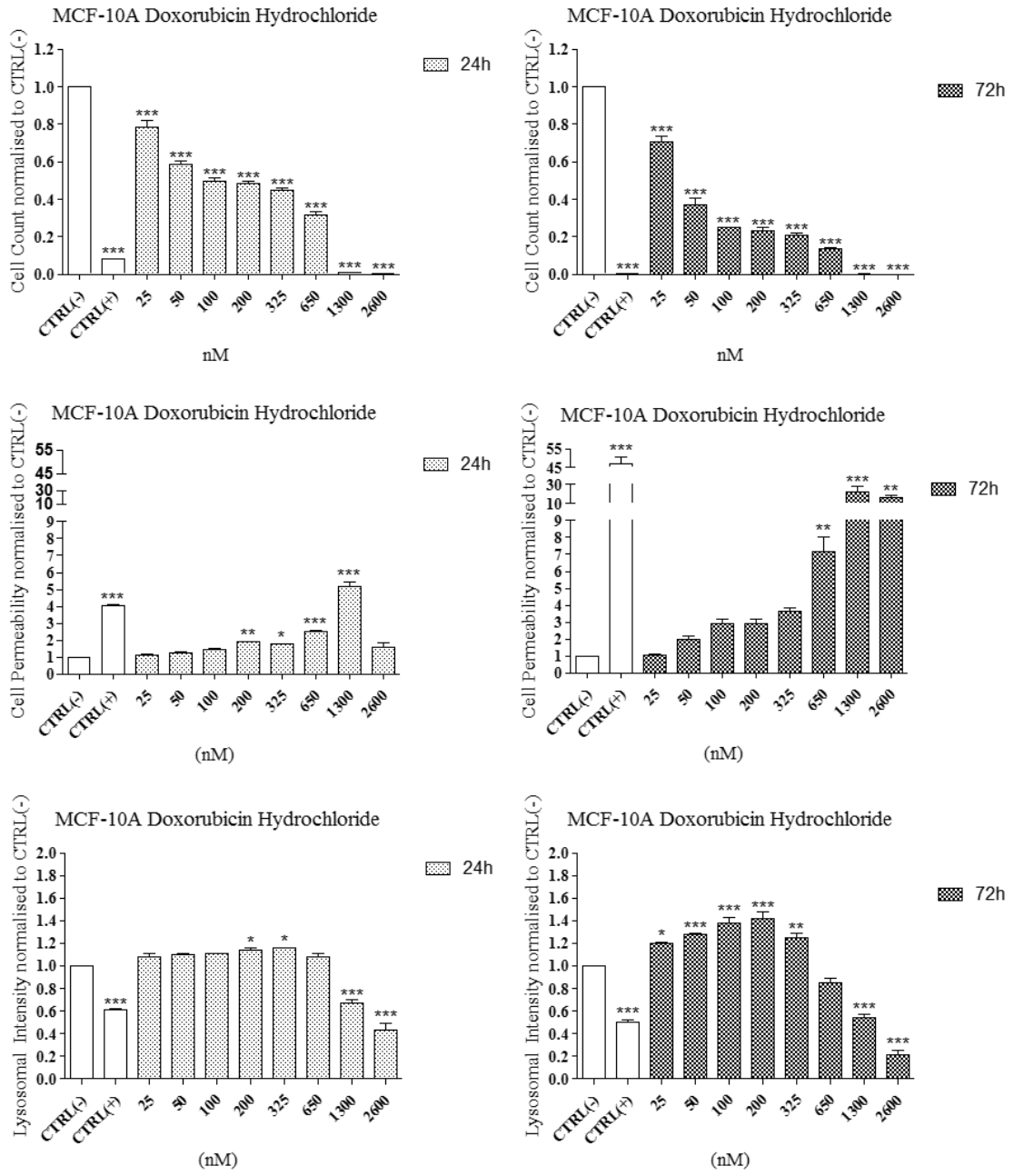

Figure S13: Effect of Doxorubicin hydrochloride on viability of MCF-10A cell line.

MCF-10A breast-derived cell line was exposed to free Doxorubicin hydrochloride for 24h and 72h. Cells were stained using the Cytotoxicity II HitKit™ and analysed using the InCell 1000 HCSA device. Variation in cell count, cell membrane permeability and lysosomal intensity were measured compared to untreated control (CTRL(-)) and 1µM CdSe positive control (CTRL(+)). Statistical significance was determined using the one way ANOVA with Tukey post-test for each column compared to untreated control (CTRL(-)). p value: *** = <0.001, **=<0.01, *=<0.05.

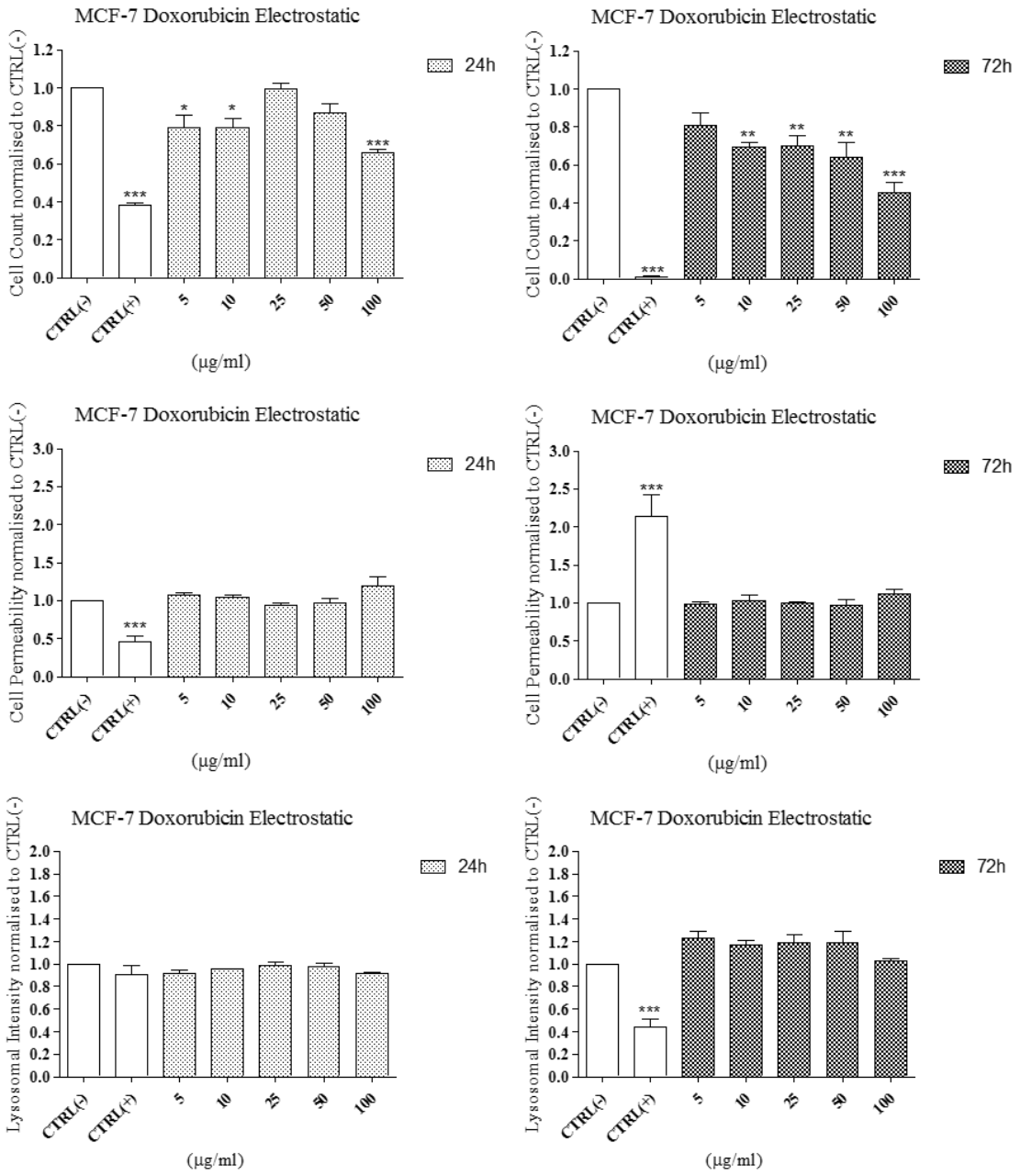

Figure S14: MCF-7 cell line exposed to MF66_Doxorubicin (electrostatic functionalisation).

MCF-7 breast-derived cell line was exposed to MF66 MNP electrostatically functionalised with Doxorubicin for 24h and 72h. Cells were stained using the Cytotoxicity II HitKit™ and analysed using the InCell 1000 HCSA device. Variation in cell count, cell membrane permeability and lysosomal intensity were measured compared to untreated control (CTRL(-)) and 1µM CdSe positive control (CTRL(+)). Statistical significance was determined using the one way ANOVA with Tukey post-test for each column compared to untreated control (CTRL(-)). p value: *** = <0.001, **=<0.01, *=<0.05.

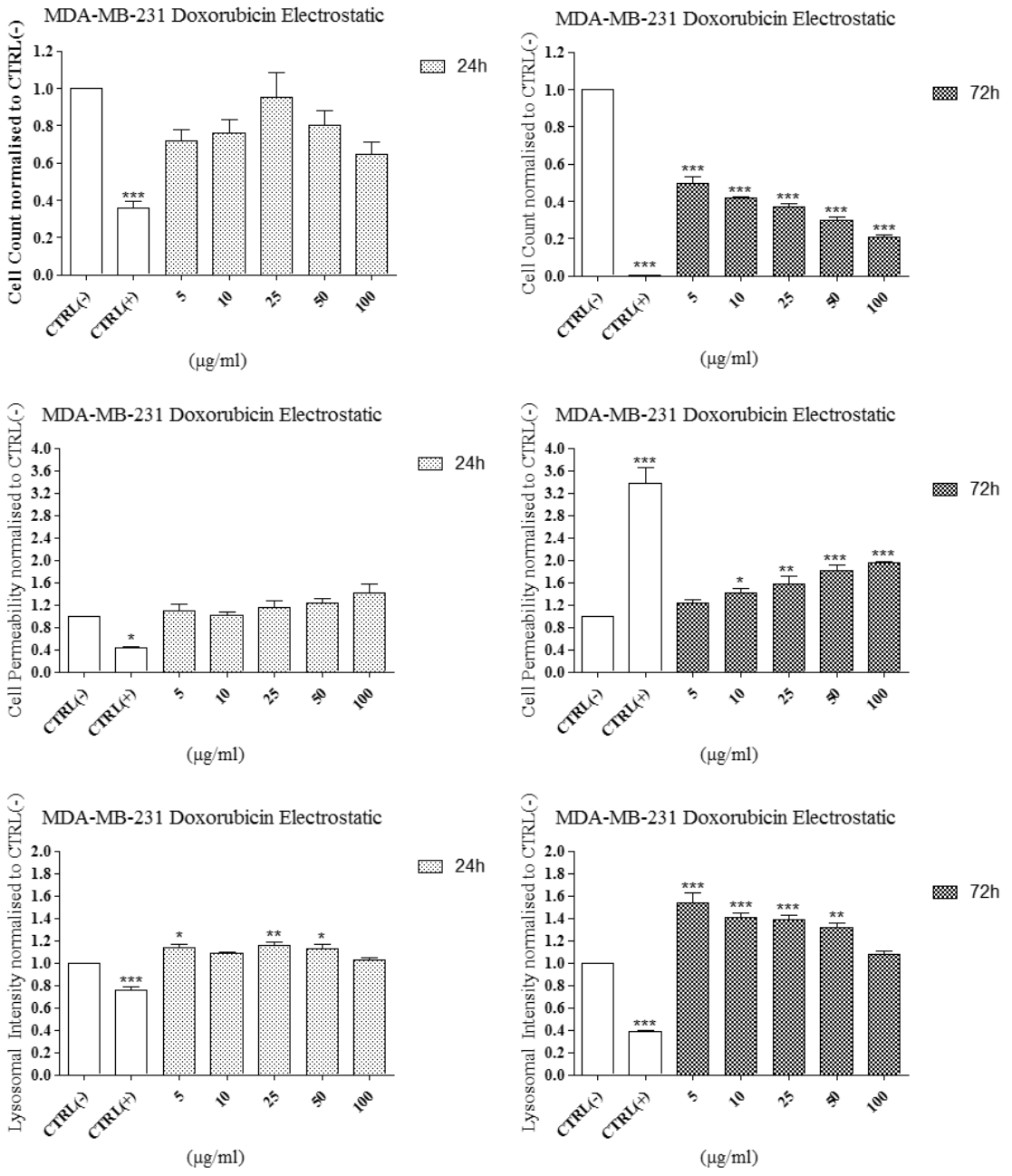

Figure S15: MDA-MB-231 cell line exposed to MF66_Doxorubicin (electrostatic functionalisation).

MDA-MB-231 breast-derived cell line was exposed to MF66 MNP electrostatically functionalised with Doxorubicin for 24h and 72h. Cells were stained using the Cytotoxicity II HitKit™ and analysed using the InCell 1000 HCSA device. Variation in cell count, cell membrane permeability and lysosomal intensity were measured compared to untreated control (CTRL(-)) and 1µM CdSe positive control (CTRL(+)). Statistical significance was determined using the one way ANOVA with Tukey post-test for each column compared to untreated control (CTRL(-)). p value: *** = <0.001, **=<0.01, *=<0.05.

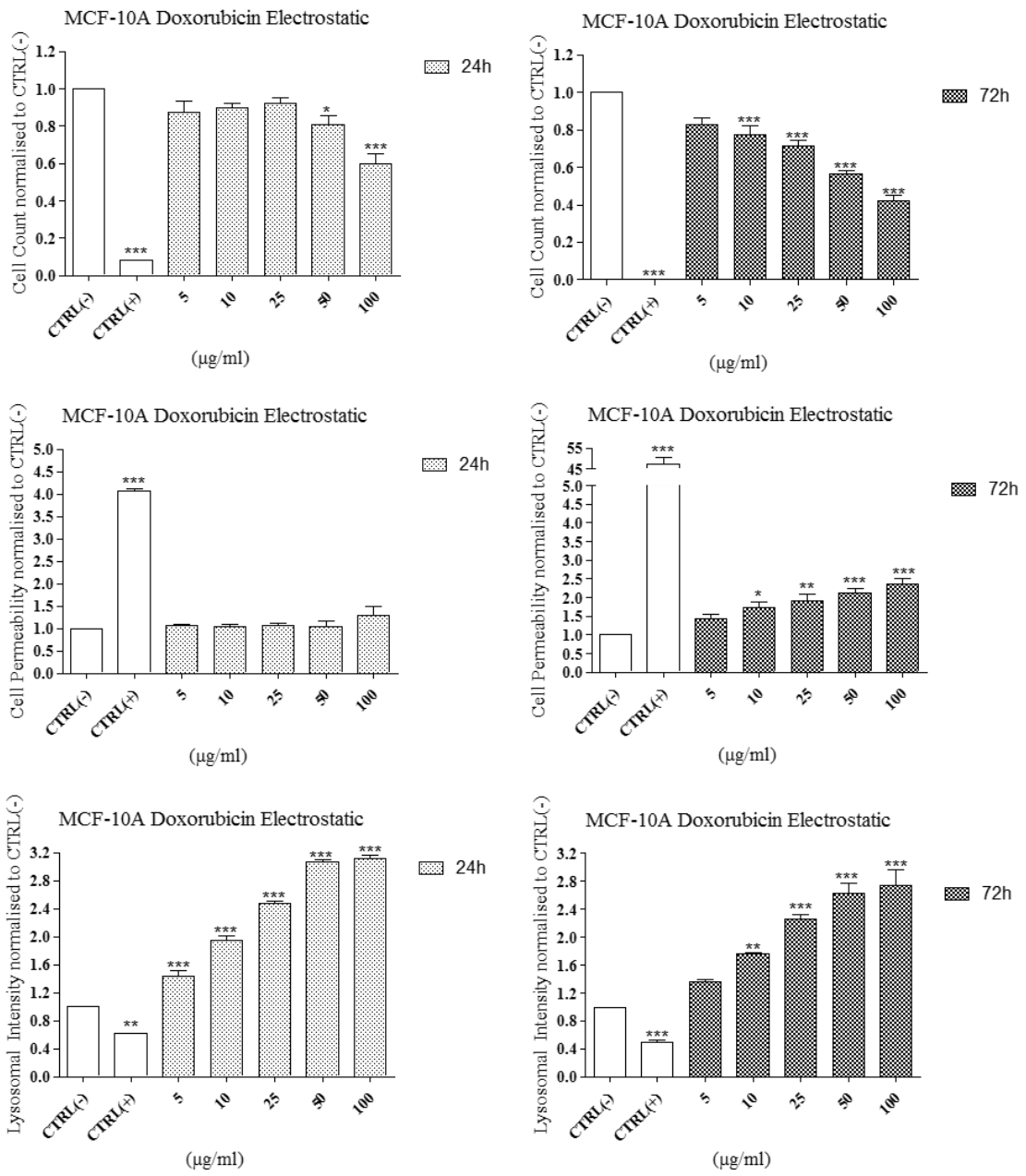

Figure S16: MCF-10A cell line exposed to MF66_Doxorubicin (electrostatic functionalisation).

MCF-10A breast-derived cell line was exposed to MF66 MNP electrostatically functionalised with Doxorubicin for 24h and 72h. Cells were stained using the Cytotoxicity II HitKit™ and analysed using the InCell 1000 HCSA device. Variation in cell count, cell membrane permeability and lysosomal intensity were measured compared to untreated control (CTRL(-)) and 1µM CdSe positive control (CTRL(+)). Statistical significance was determined using the one way ANOVA with Tukey post-test for each column compared to untreated control (CTRL(-)). p value: *** = <0.001, **=<0.01, *=<0.05.

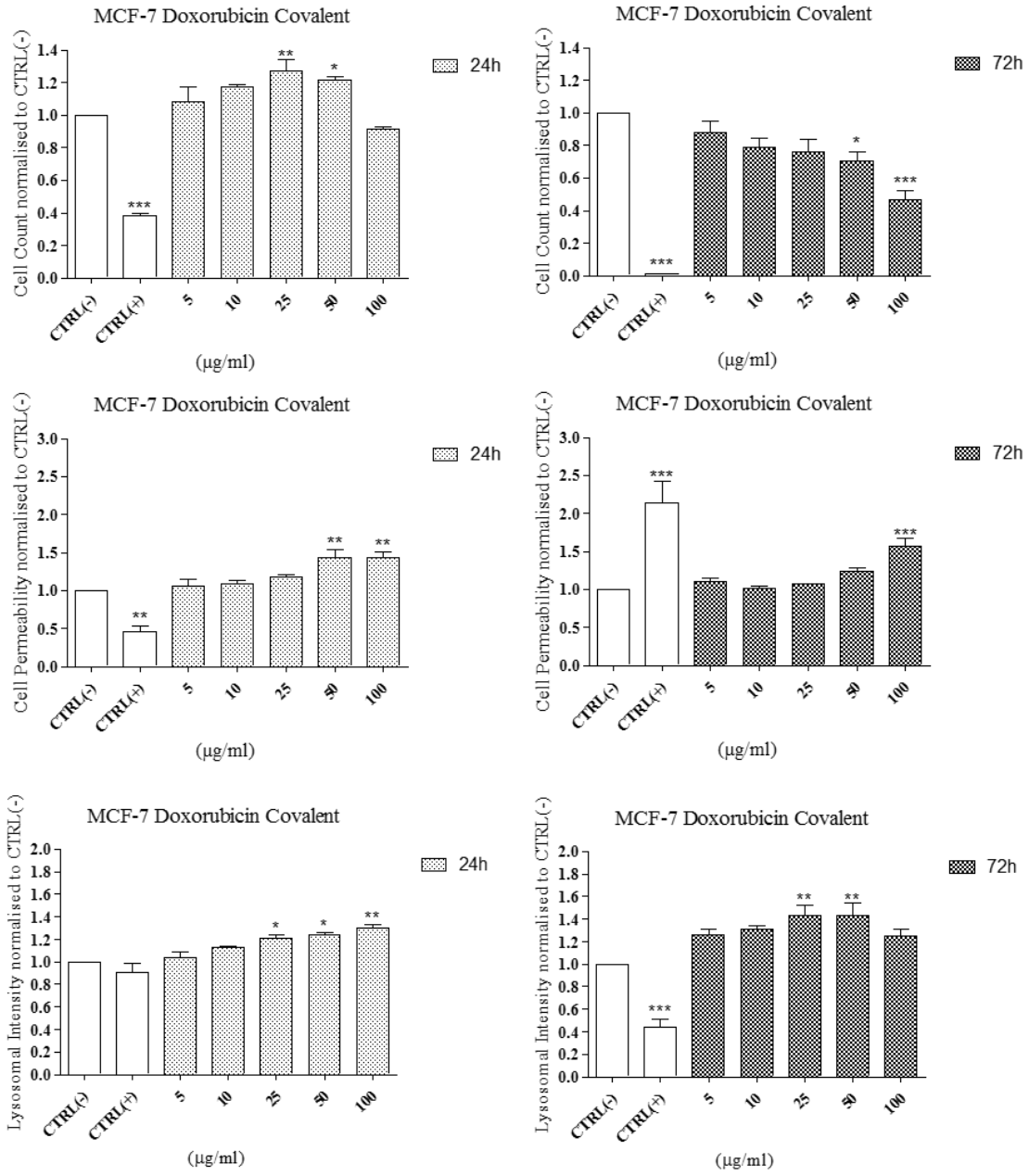

Figure S17: MCF-7 cell line exposed to MF66_Doxorubicin (covalent functionalisation).

MCF-7 breast-derived cell line was exposed to MF66 MNP covalently functionalised with Doxorubicin for 24h and 72h. Cells were stained using the Cytotoxicity II HitKit™ and analysed using the InCell 1000 HCSA device. Variation in cell count, cell membrane permeability and lysosomal intensity were measured compared to untreated control (CTRL(-)) and 1µM CdSe positive control (CTRL(+)). Statistical significance was determined using the one way ANOVA with Tukey post-test for each column compared to untreated control (CTRL(-)). p value: *** = <0.001, **=<0.01, *=<0.05.

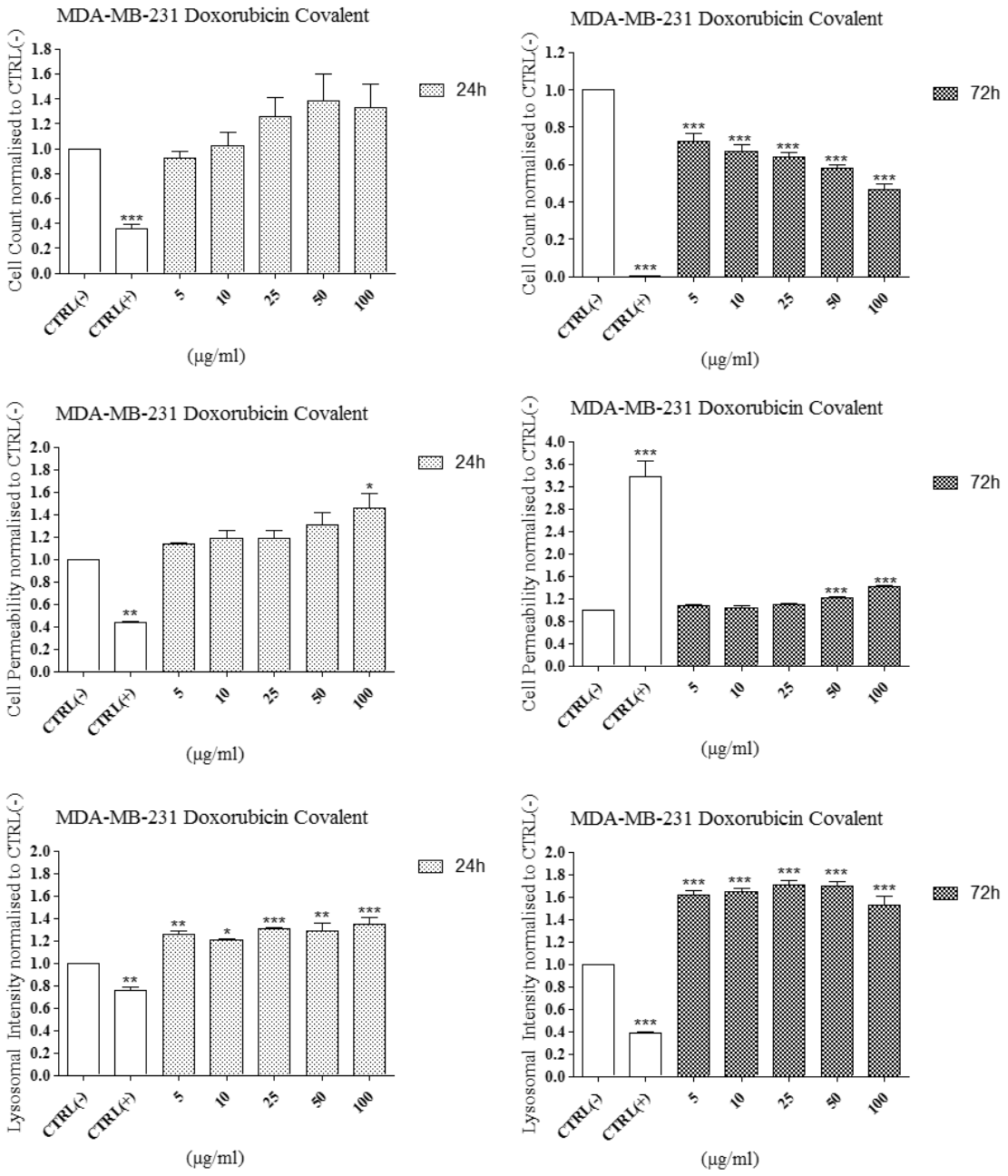

Figure S18: MDA-MB-231 cell line exposed to MF66_Doxorubicin (covalent functionalisation).

MDA-MB-231 breast-derived cell line was exposed to MF66 MNP covalently functionalised with Doxorubicin for 24h and 72h. Cells were stained using the Cytotoxicity II HitKit™ and analysed using the InCell 1000 HCSA device. Variation in cell count, cell membrane permeability and lysosomal intensity were measured compared to untreated control (CTRL(-)) and 1µM CdSe positive control (CTRL(+)). Statistical significance was determined using the one way ANOVA with Tukey post-test for each column compared to untreated control (CTRL(-)). p value: *** = <0.001, **=<0.01, *=<0.05.

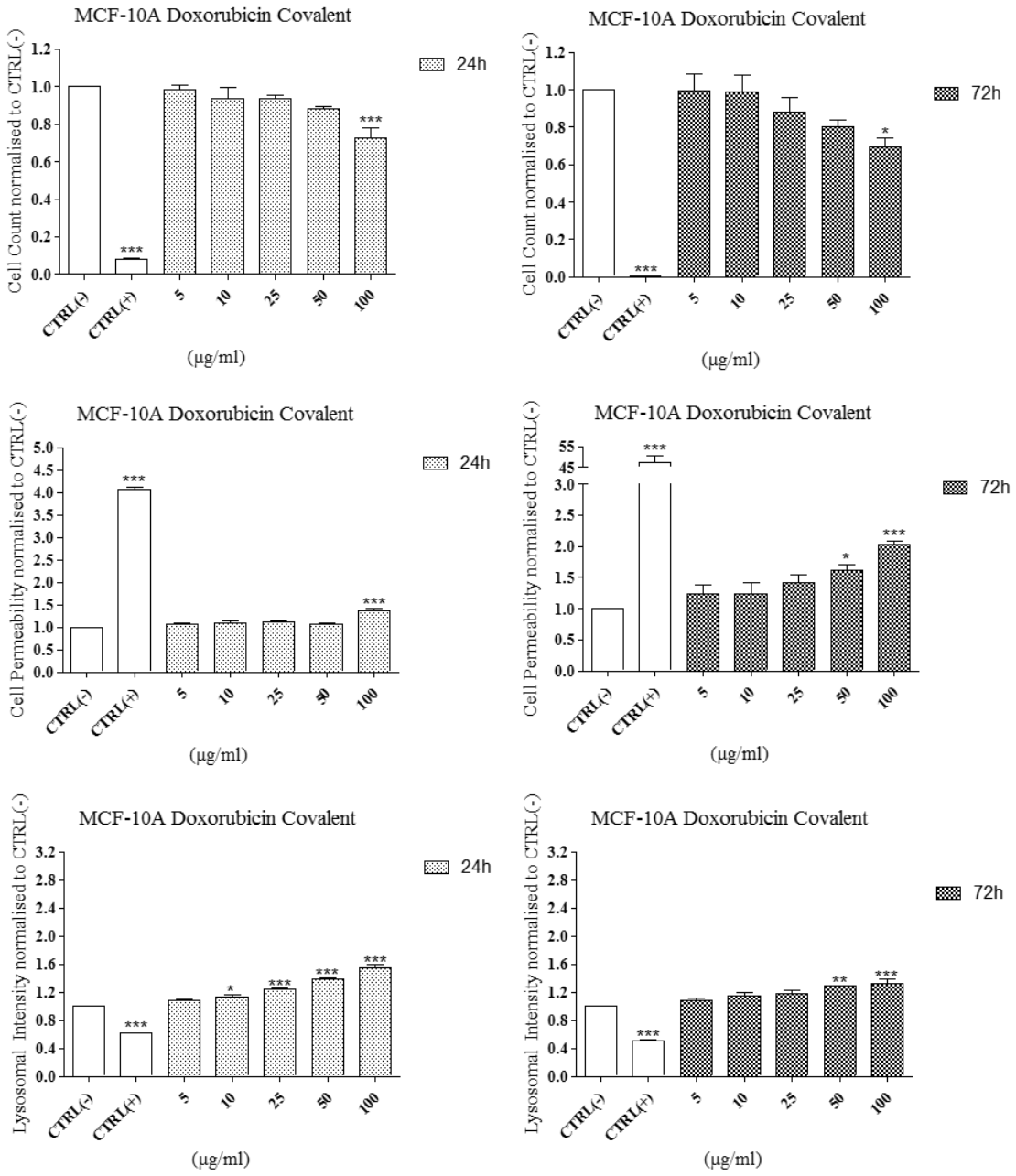

Figure S19: MCF-10A cell line exposed to MF66_Doxorubicin (covalent functionalisation).

MCF-10A breast-derived cell line was exposed to MF66 MNP covalently functionalised with Doxorubicin for 24h and 72h. Cells were stained using the Cytotoxicity II HitKit™ and analysed using the InCell 1000 HCSA device. Variation in cell count, cell membrane permeability and lysosomal intensity were measured compared to untreated control (CTRL(-)) and 1µM CdSe positive control (CTRL(+)). Statistical significance was determined using the one way ANOVA with Tukey post-test for each column compared to untreated control (CTRL(-)). p value: *** = <0.001, **=<0.01, *=<0.05.

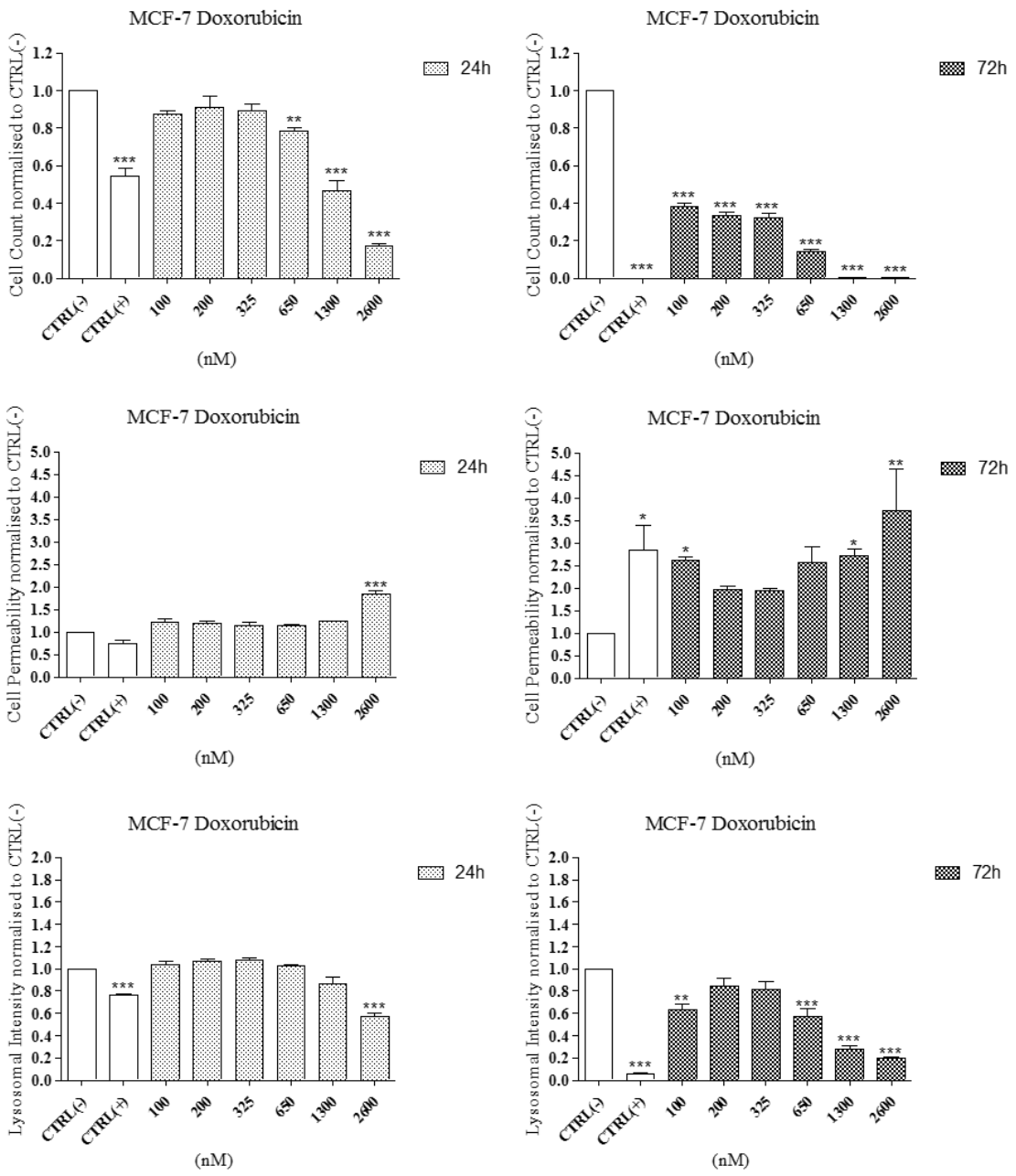

Figure S20: Effect of Doxorubicin hydrochloride on viability of MCF-7 cell line.

MCF-7 breast-derived cell line was exposed to free Doxorubicin hydrochloride for 24h and 72h. Cells were stained using the Cytotoxicity II HitKit™ and analysed using the InCell 1000 HCSA device. Variation in cell count, cell membrane permeability and lysosomal intensity were measured compared to untreated control (CTRL(-)) and 1µM CdSe positive control (CTRL(+)). Statistical significance was determined using the one way ANOVA with Tukey post-test for each column compared to untreated control (CTRL(-)). p value: *** = <0.001, **=<0.01, *=<0.05.

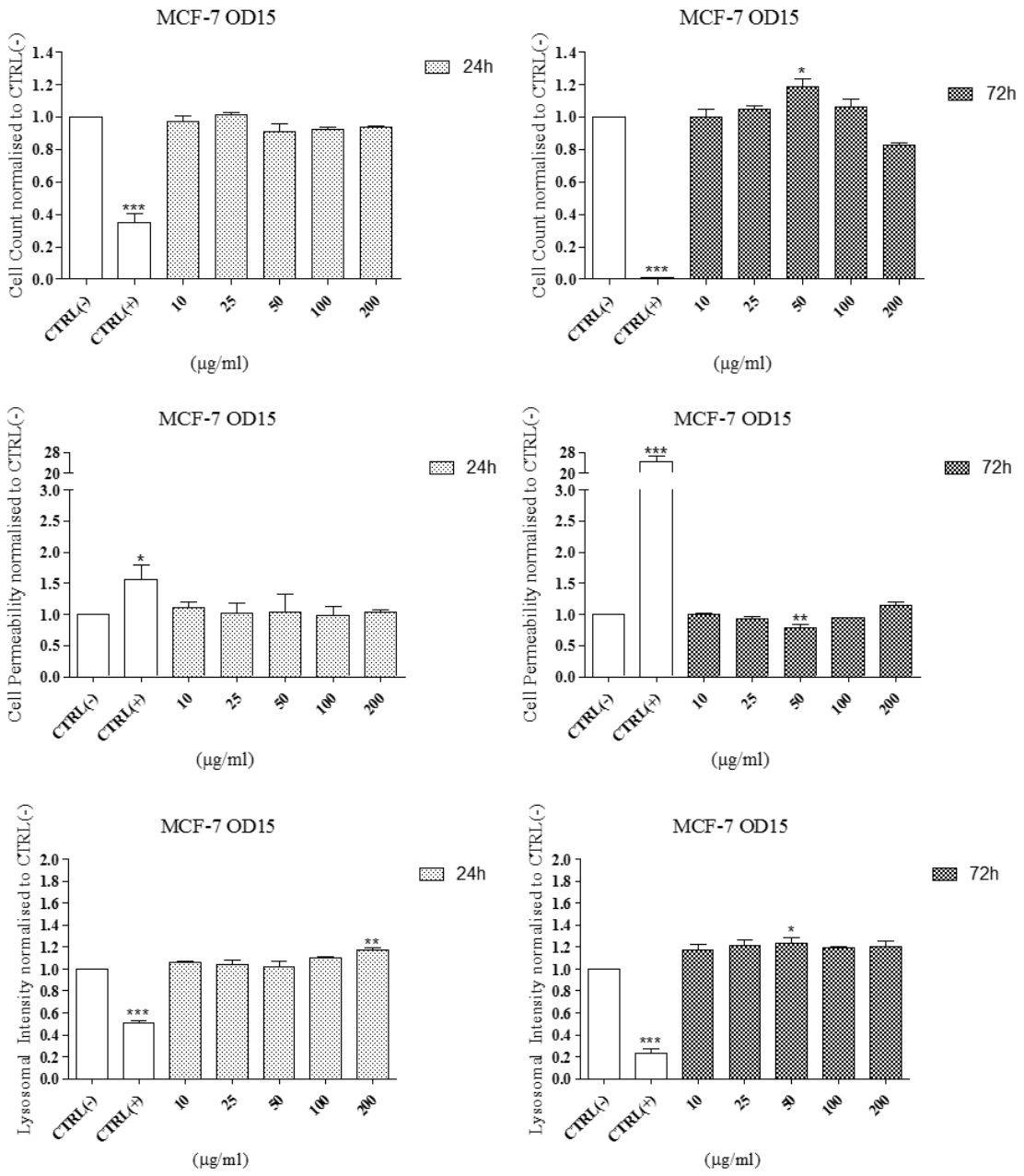

Figure S21: MCF-7 cell line exposed to OD15.

MCF-7 breast-derived cell line was exposed to OD15 MNP for 24h and 72h. Cells were stained using the Cytotoxicity II HitKit™ and analysed using the InCell 1000 HCSA device. Variation in cell count, cell membrane permeability and lysosomal intensity were measured compared to untreated control (CTRL(-)) and 1µM CdSe positive control (CTRL(+)). Statistical significance was determined using the one way ANOVA with Tukey post-test for each column compared to untreated control (CTRL(-)). p value: *** = <0.001, **=<0.01, *=<0.05.

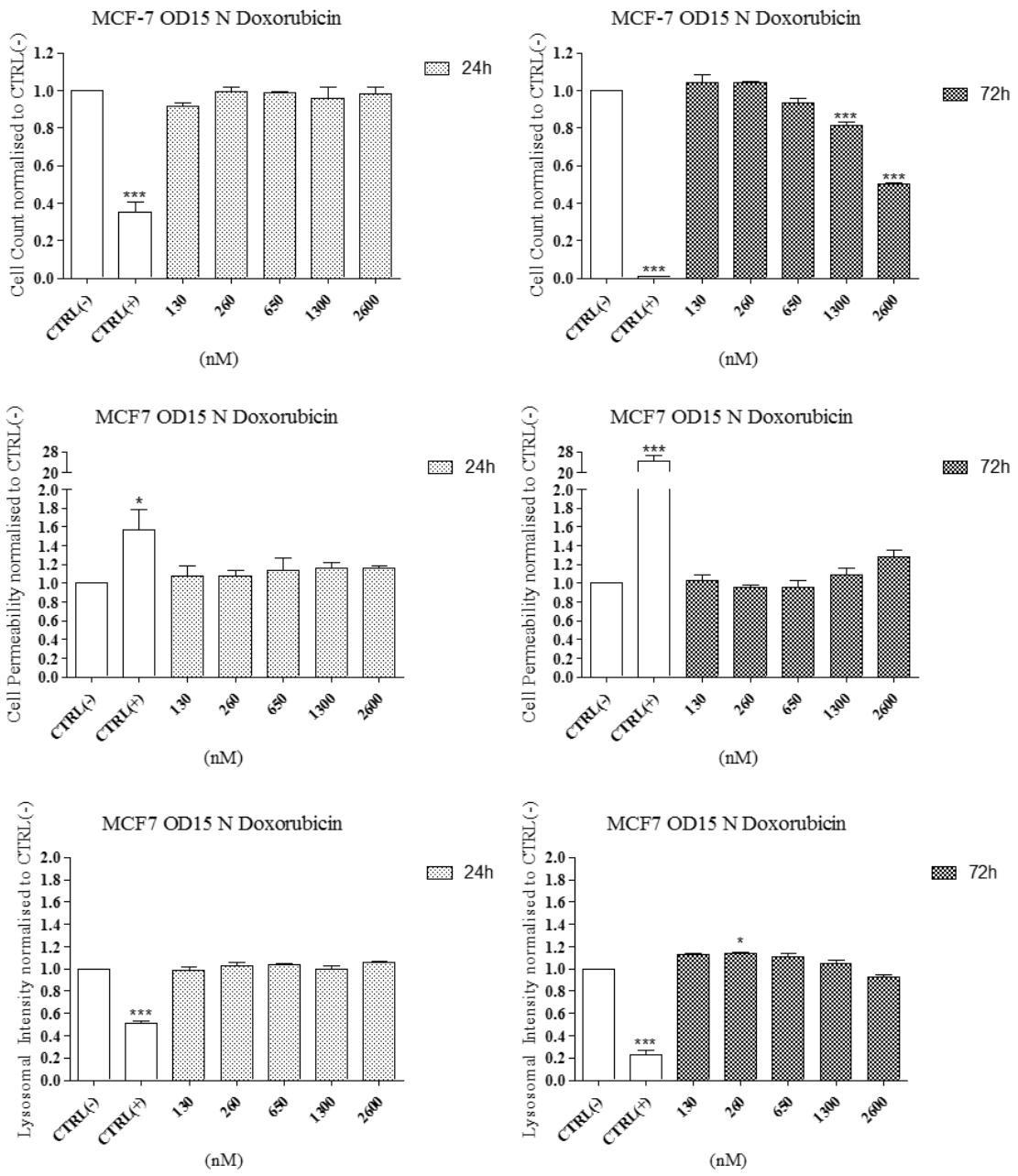

Figure S22: MCF-7 cell line exposed to OD15_N_Doxorubicin.

MCF-7 breast-derived cell line was exposed to OD15_N_Doxorubicin MNP for 24h and 72h. Cells were stained using the Cytotoxicity II HitKit™ and analysed using the InCell 1000 HCSA device. Variation in cell count, cell membrane permeability and lysosomal intensity were measured compared to untreated control (CTRL(-)) and 1µM CdSe positive control (CTRL(+)). Statistical significance was determined using the one way ANOVA with Tukey post-test for each column compared to untreated control (CTRL(-)). p value: *** = <0.001, **=<0.01, *=<0.05.

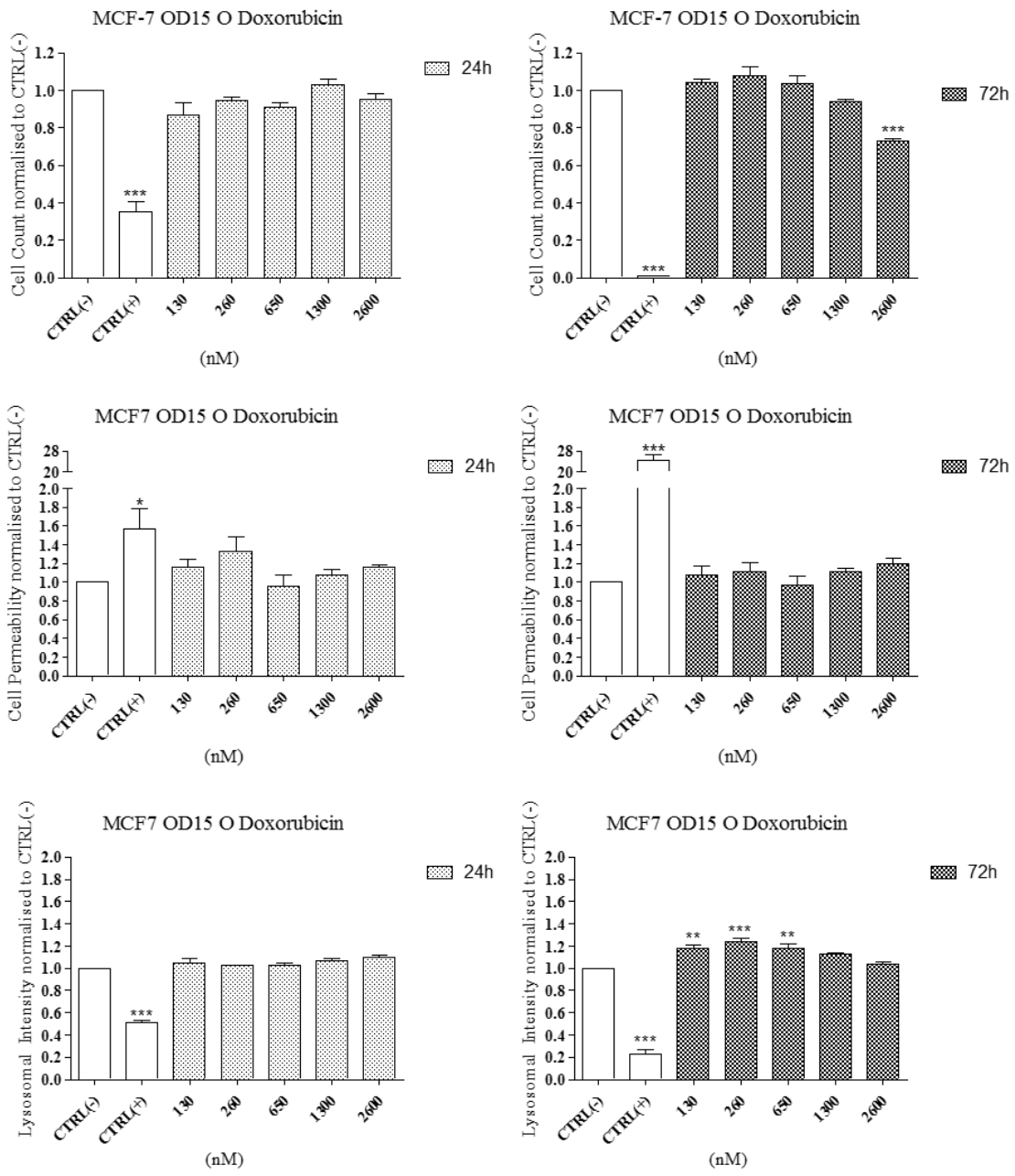

Figure S23: MCF-7 cell line exposed to OD15_O_Doxorubicin.

MCF-7 breast-derived cell line was exposed to OD15_O_Doxorubicin MNP for 24h and 72h. Cells were stained using the Cytotoxicity II HitKit™ and analysed using the InCell 1000 HCSA device. Variation in cell count, cell membrane permeability and lysosomal intensity were measured compared to untreated control (CTRL(-)) and 1µM CdSe positive control (CTRL(+)). Statistical significance was determined using the one way ANOVA with Tukey post-test for each column compared to untreated control (CTRL(-)). p value: *** = <0.001, **=<0.01, *=<0.05.

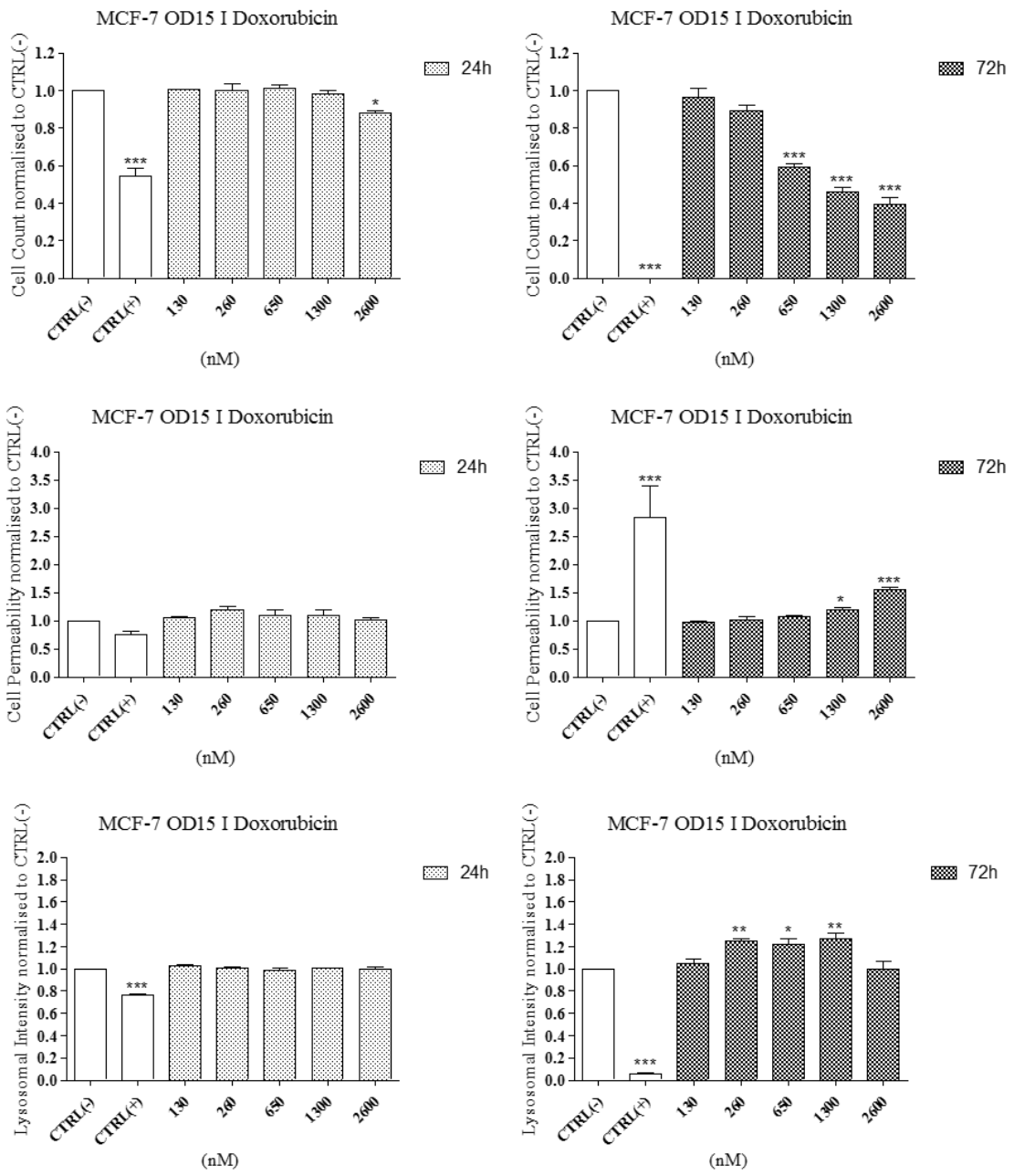

Figure S24: MCF-7 cell line exposed to OD15_I_Doxorubicin.

MCF-7 breast-derived cell line was exposed to OD15_I_Doxorubicin MNP for 24h and 72h. Cells were stained using the Cytotoxicity II HitKit™ and analysed using the InCell 1000 HCSA device. Variation in cell count, cell membrane permeability and lysosomal intensity were measured compared to untreated control (CTRL(-)) and 1µM CdSe positive control (CTRL(+)). Statistical significance was determined using the one way ANOVA with Tukey post-test for each column compared to untreated control (CTRL(-)). p value: *** = <0.001, **=<0.01, *=<0.05.

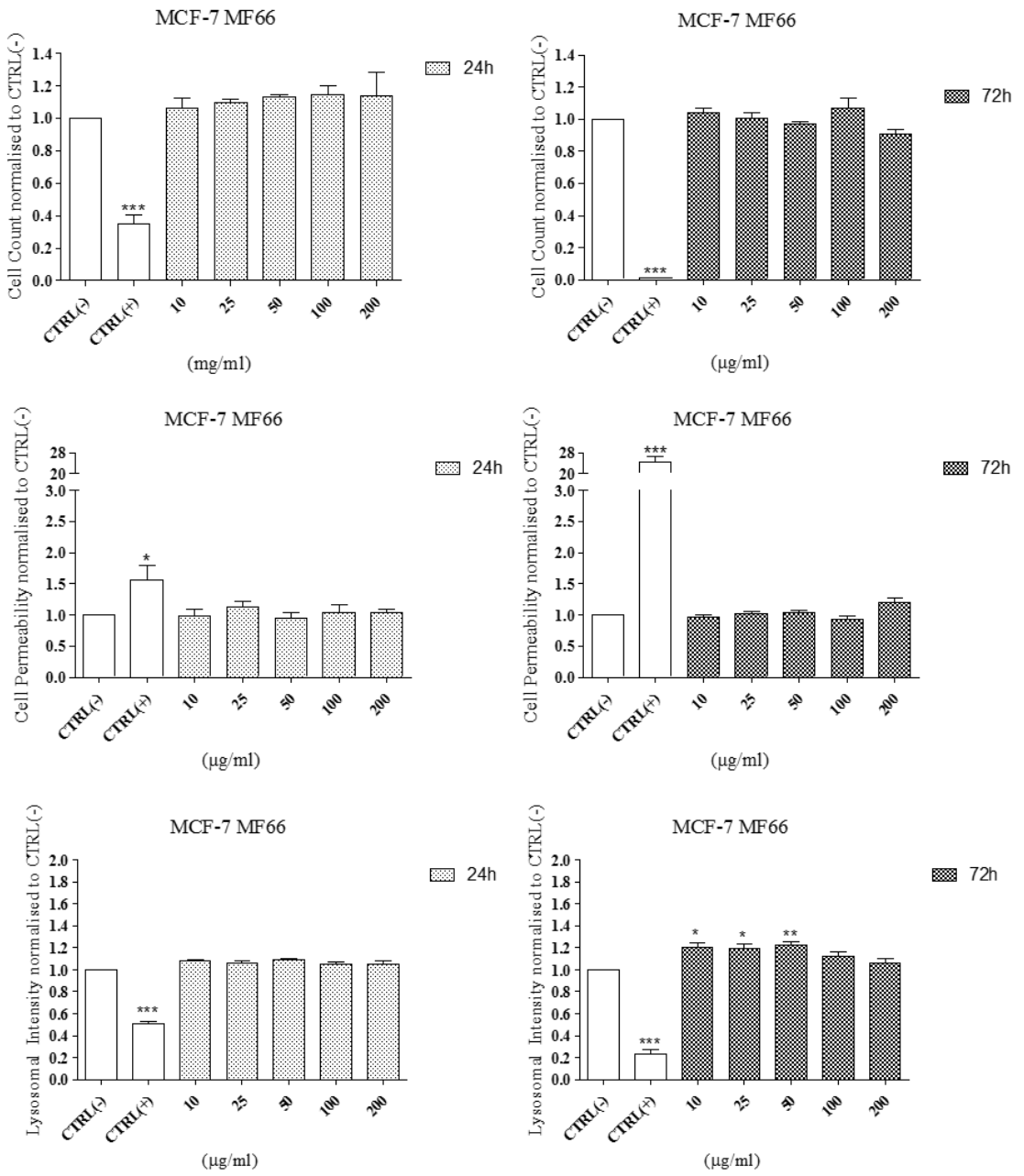

Figure S25: MCF-7 cell line exposed to MF66.

MCF-7 breast-derived cell line was exposed to MF66 MNP for 24h and 72h. Cells were stained using the Cytotoxicity II HitKit™ and analysed using the InCell 1000 HCSA device. Variation in cell count, cell membrane permeability and lysosomal intensity were measured compared to untreated control (CTRL(-)) and 1µM CdSe positive control (CTRL(+)). Statistical significance was determined using the one way ANOVA with Tukey post-test for each column compared to untreated control (CTRL(-)). p value: *** = <0.001, **=<0.01, *=<0.05.

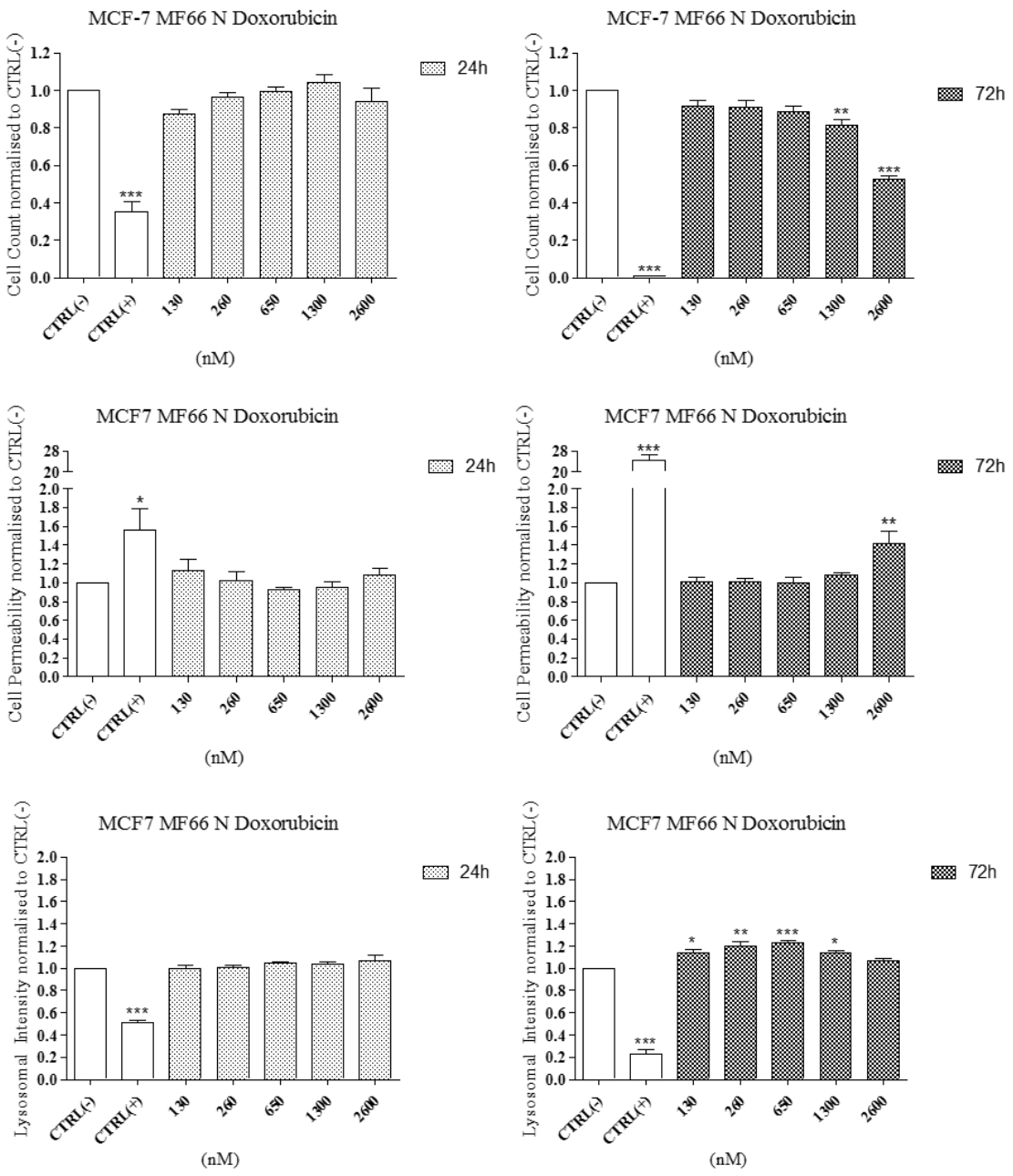

Figure S26: MCF-7 cell line exposed to MF66_N_Doxorubicin.

MCF-7 breast-derived cell line was exposed to MF66_N_Doxorubicin MNP for 24h and 72h. Cells were stained using the Cytotoxicity II HitKit™ and analysed using the InCell 1000 HCSA device. Variation in cell count, cell membrane permeability and lysosomal intensity were measured compared to untreated control (CTRL(-)) and 1µM CdSe positive control (CTRL(+)). Statistical significance was determined using the one way ANOVA with Tukey post-test for each column compared to untreated control (CTRL(-)). p value: *** = <0.001, **=<0.01, *=<0.05.

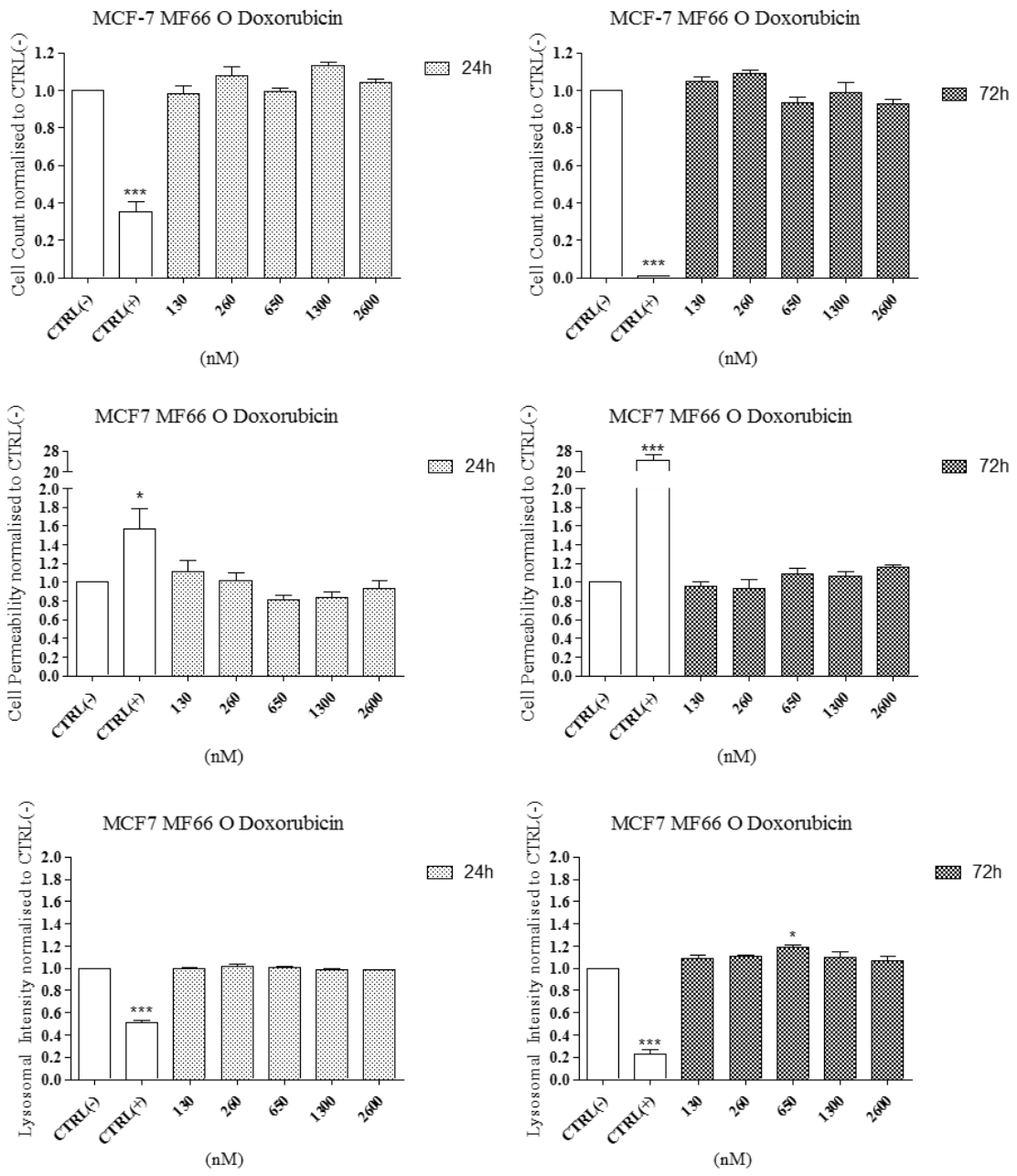

Figure S27: MCF-7 cell line exposed to MF66_O_Doxorubicin.

MCF-7 breast-derived cell line was exposed to MF66_O_Doxorubicin MNP for 24h and 72h. Cells were stained using the Cytotoxicity II HitKit™ and analysed using the InCell 1000 HCSA device. Variation in cell count, cell membrane permeability and lysosomal intensity were measured compared to untreated control (CTRL(-)) and 1µM CdSe positive control (CTRL(+)). Statistical significance was determined using the one way ANOVA with Tukey post-test for each column compared to untreated control (CTRL(-)). p value: *** = <0.001, **=<0.01, *=<0.05.

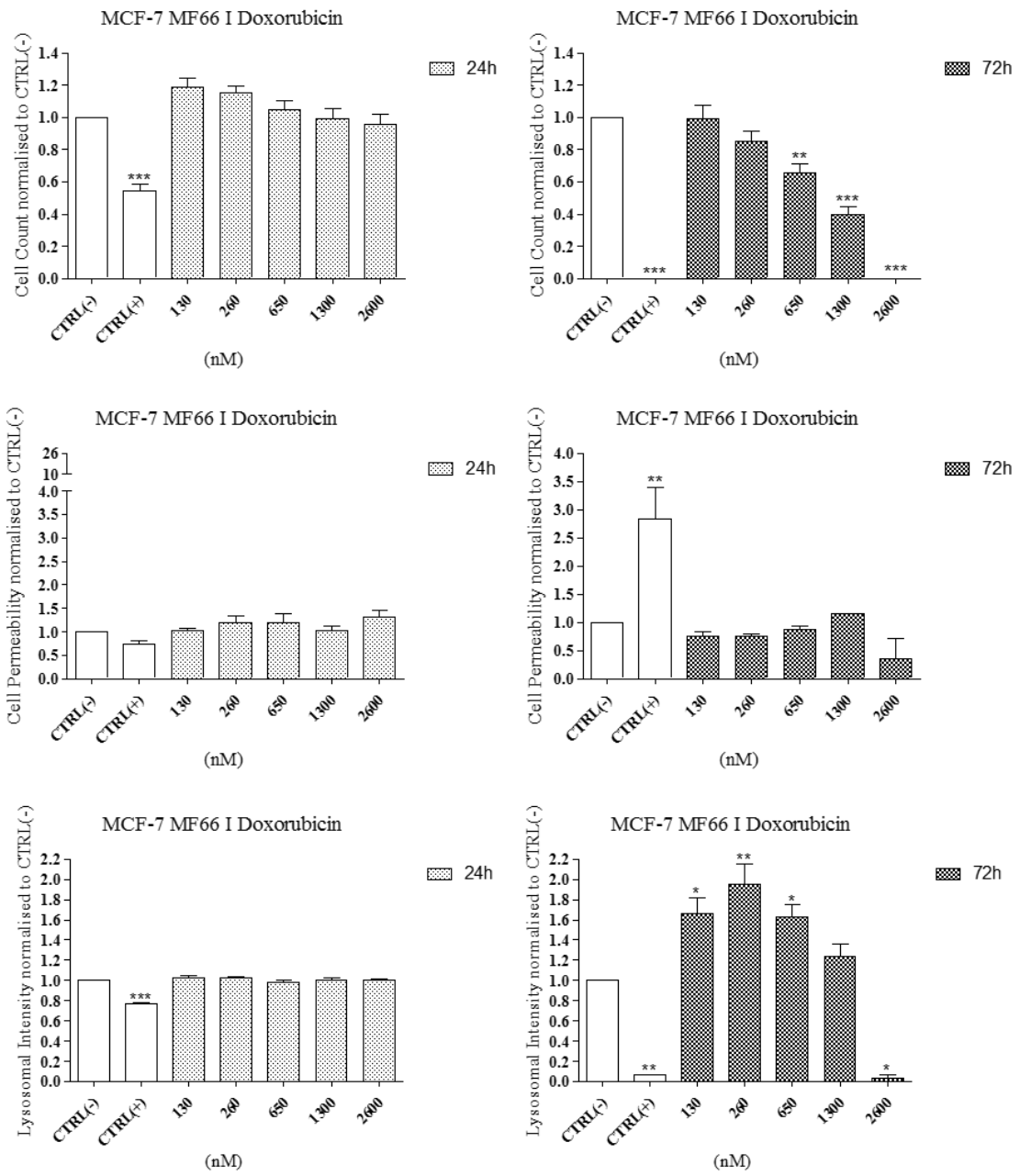

Figure S28: MCF-7 cell line exposed to MF66_I_Doxorubicin.

MCF-7 breast-derived cell line was exposed to MF66_I_Doxorubicin MNP for 24h and 72h. Cells were stained using the Cytotoxicity II HitKit™ and analysed using the InCell 1000 HCSA device. Variation in cell count, cell membrane permeability and lysosomal intensity were measured compared to untreated control (CTRL(-)) and 1µM CdSe positive control (CTRL(+)). Statistical significance was determined using the one way ANOVA with Tukey post-test for each column compared to untreated control (CTRL(-)). p value: *** = <0.001, **=<0.01, *=<0.05.

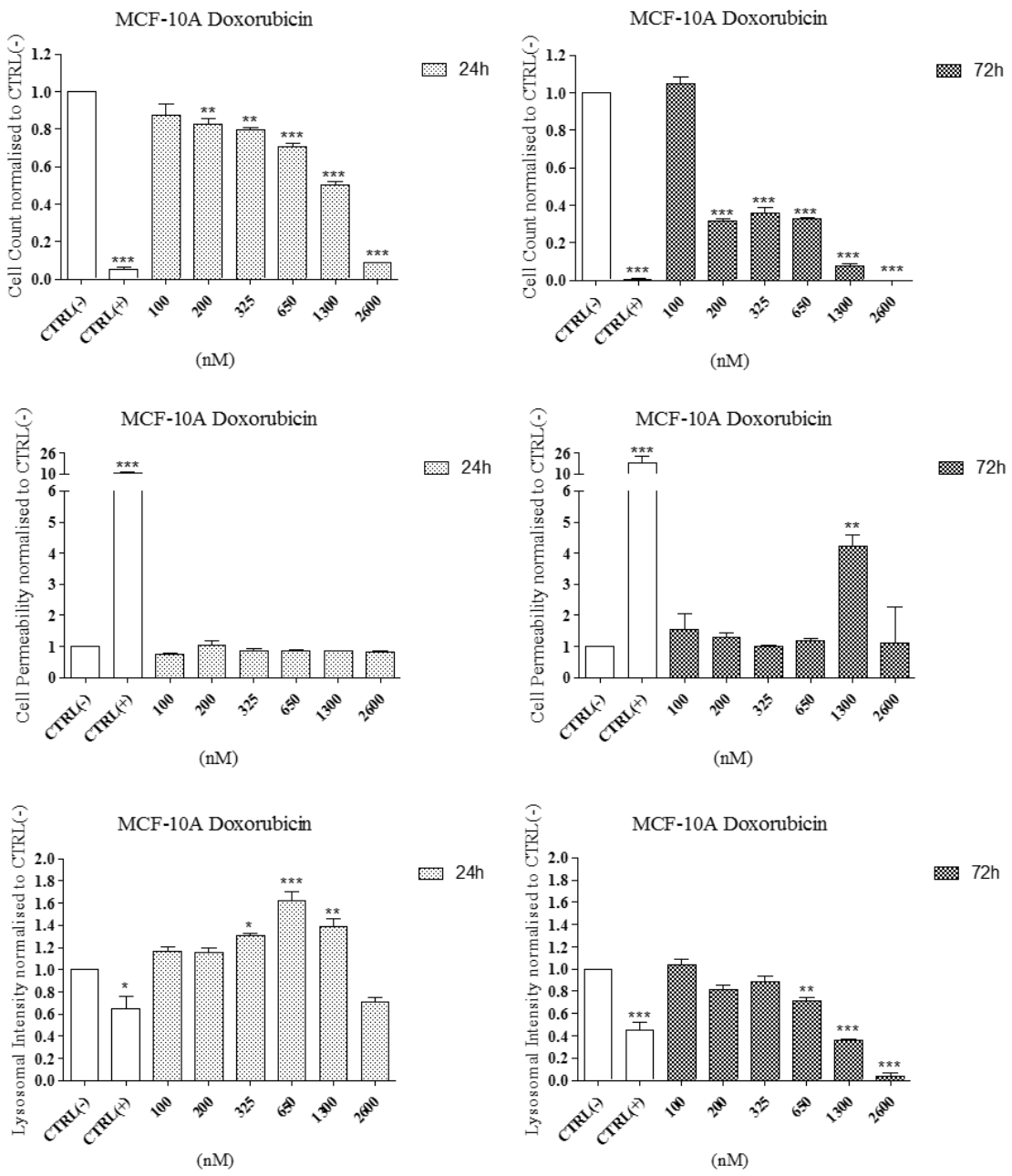

Figure S29: Effect of doxorubicin hydrochloride on viability of MCF-10A cell line.

MCF-10A breast-derived cell line was exposed to free doxorubicin hydrochloride for 24h and 72h. Cells were stained using the Cytotoxicity II HitKit™ and analysed using the InCell 1000 HCSA device. Variation in cell count, cell membrane permeability and lysosomal intensity were measured compared to untreated control (CTRL(-)) and 1µM CdSe positive control (CTRL(+)). Statistical significance was determined using the one way ANOVA with Tukey post-test for each column compared to untreated control (CTRL(-)). p value: *** = <0.001, **=<0.01, *=<0.05.

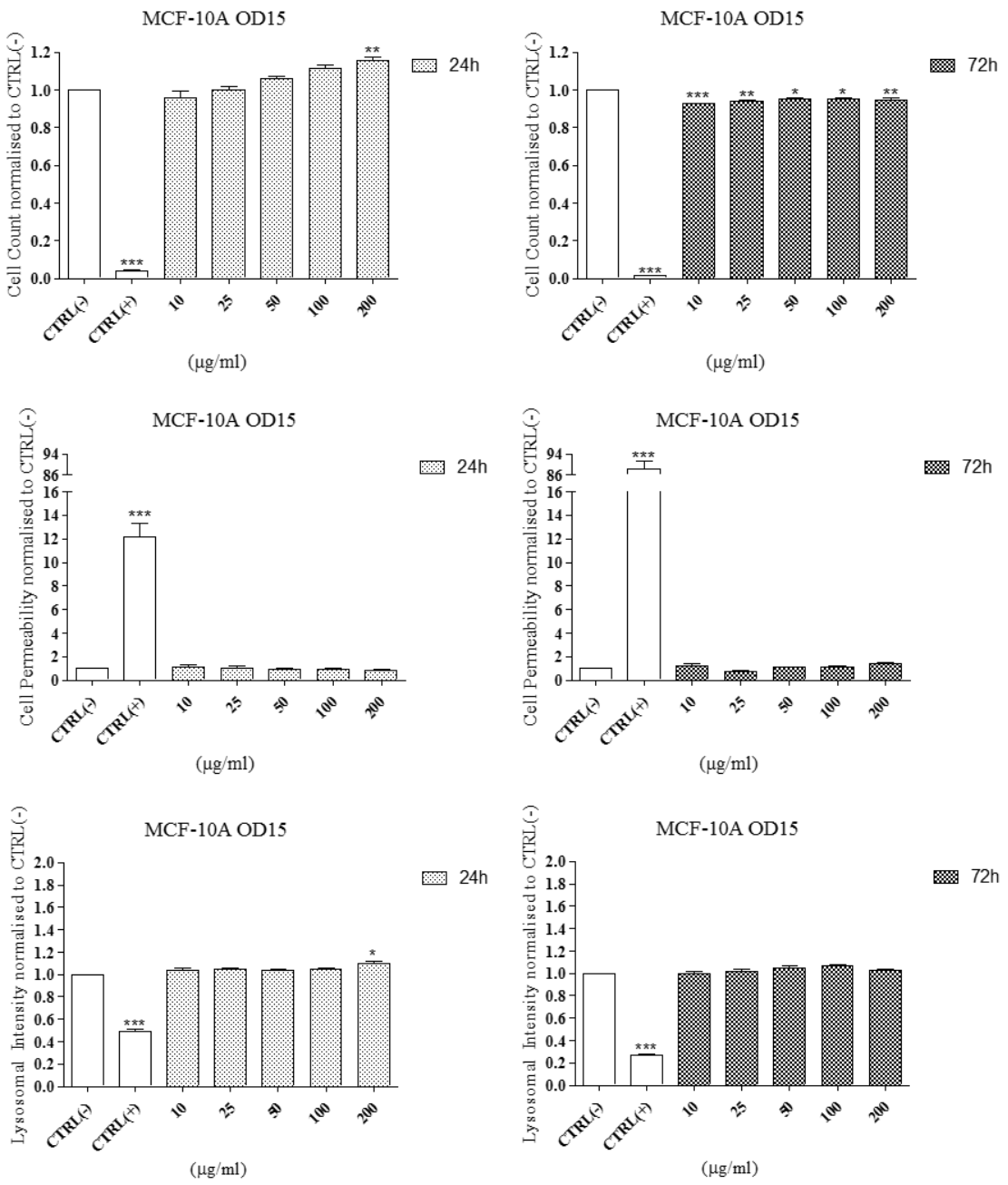

Figure S30: MCF-10A cell line exposed to OD15 MNP.

MCF-10A breast-derived cell line was exposed to OD15 MNP for 24h and 72h. Cells were stained using the Cytotoxicity II HitKit™ and analysed using the InCell 1000 HCSA device. Variation in cell count, cell membrane permeability and lysosomal intensity were measured compared to untreated control (CTRL(-)) and 1µM CdSe positive control (CTRL(+)). Statistical significance was determined using the one way ANOVA with Tukey post-test for each column compared to untreated control (CTRL(-)). p value: *** = <0.001, **=<0.01, *=<0.05.

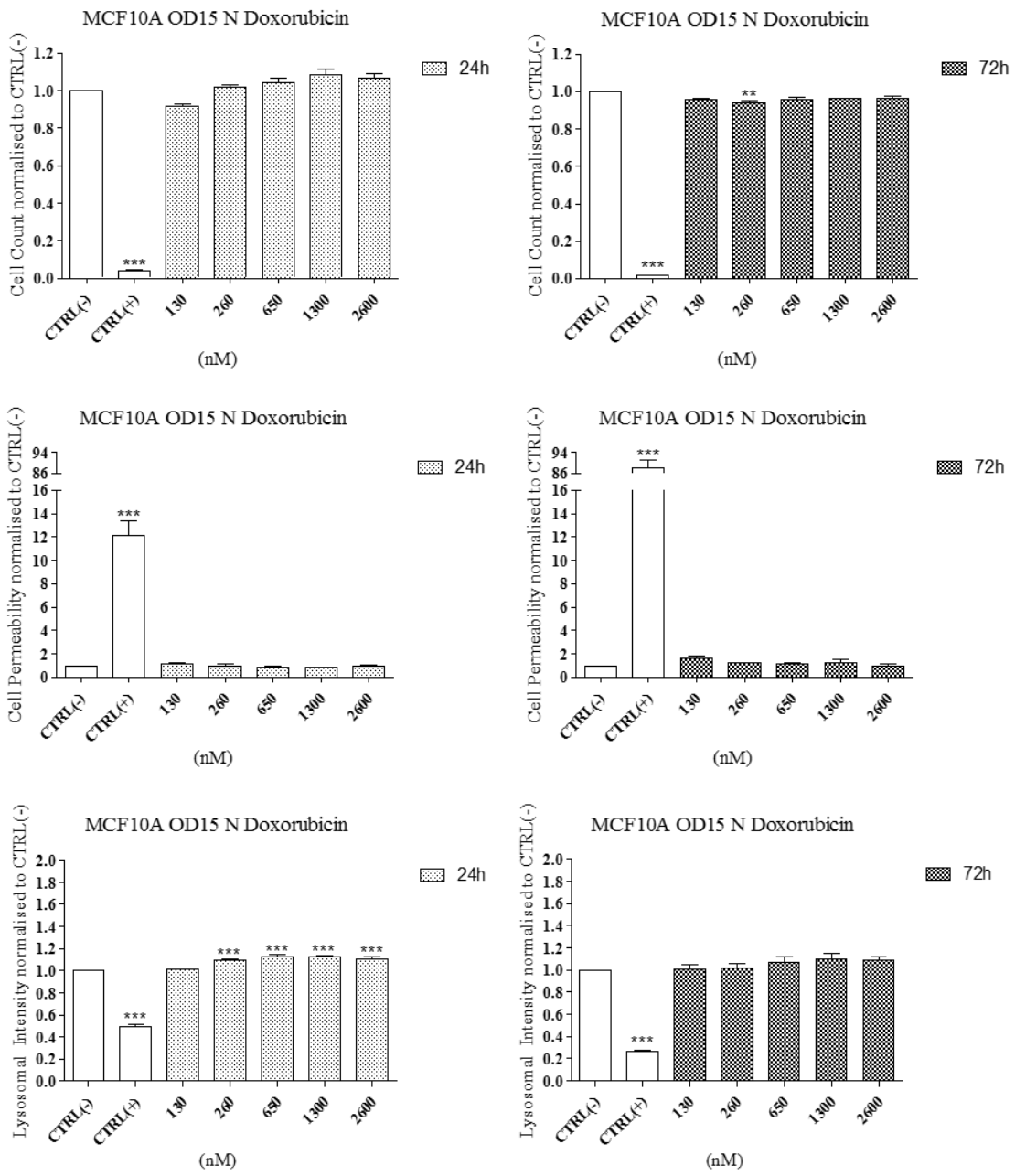

Figure S31: MCF-10A cell line exposed to OD15_N_Doxorubicin.

MCF-10A breast-derived cell line was exposed to OD15_N_Doxorubicin MNP for 24h and 72h. Cells were stained using the Cytotoxicity II HitKit™ and analysed using the InCell 1000 HCSA device. Variation in cell count, cell membrane permeability and lysosomal intensity were measured compared to untreated control (CTRL(-)) and 1µM CdSe positive control (CTRL(+)). Statistical significance was determined using the one way ANOVA with Tukey post-test for each column compared to untreated control (CTRL(-)). p value: *** = <0.001, **=<0.01, *=<0.05

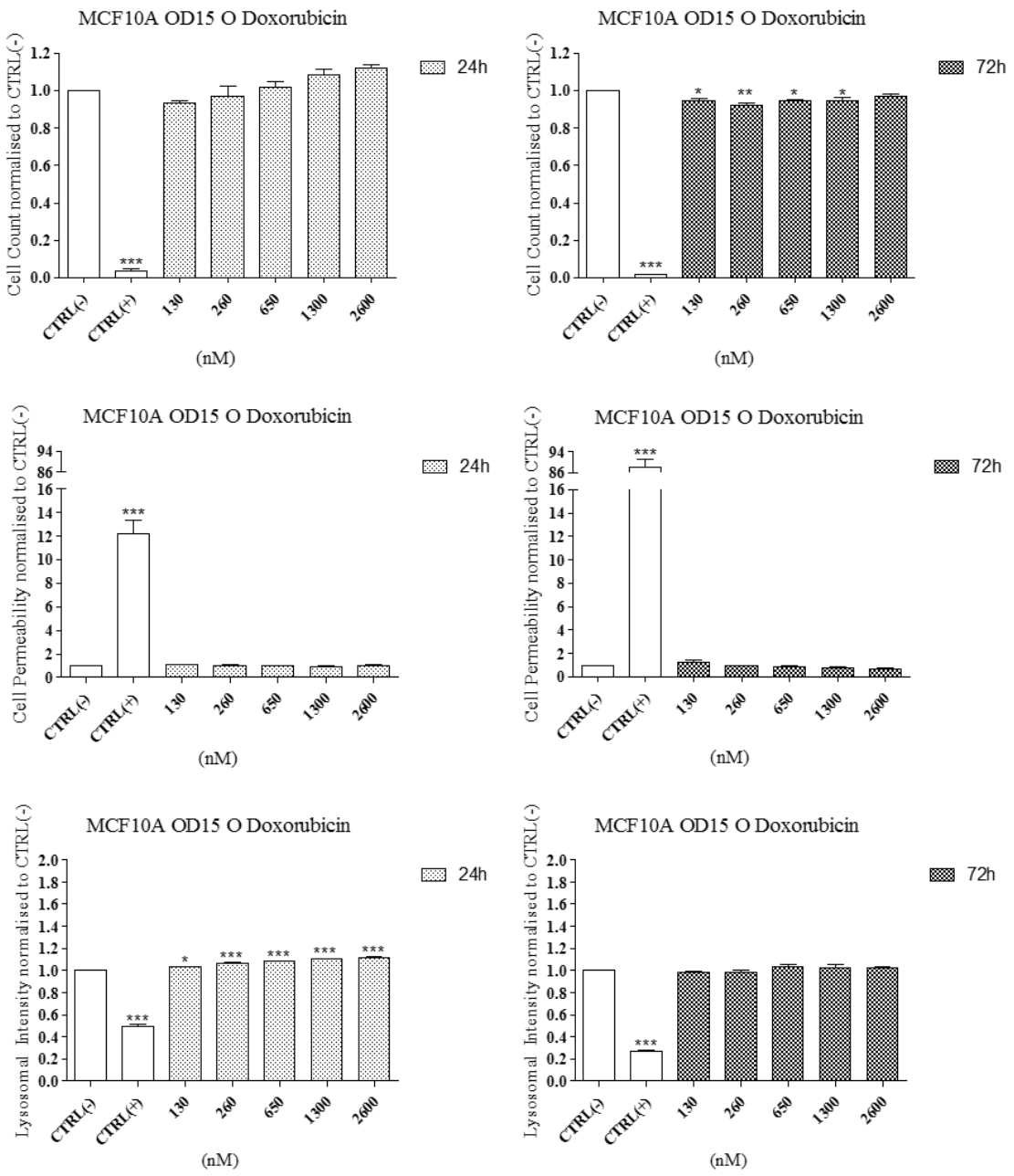

Figure S32: MCF-10A cell line exposed to OD15_O_Doxorubicin.

MCF-10A breast-derived cell line was exposed to OD15_O_Doxorubicin MNP for 24h and 72h. Cells were stained using the Cytotoxicity II HitKit™ and analysed using the InCell 1000 HCSA device. Variation in cell count, cell membrane permeability and lysosomal intensity were measured compared to untreated control (CTRL(-)) and 1µM CdSe positive control (CTRL(+)). Statistical significance was determined using the one way ANOVA with Tukey post-test for each column compared to untreated control (CTRL(-)). p value: *** = <0.001, **=<0.01, *=<0.05

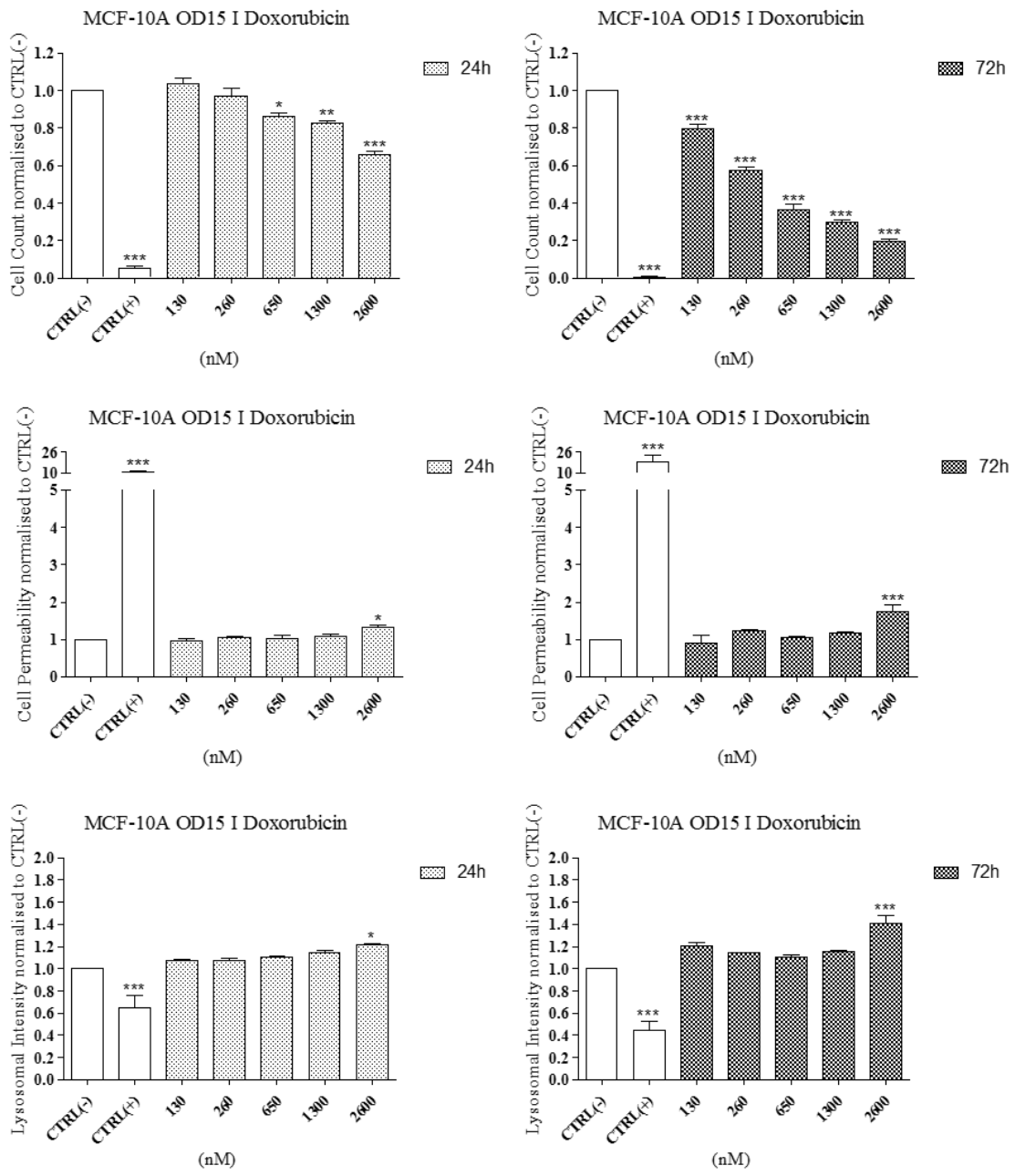

Figure S33: MCF-10A cell line exposed to OD15_I_Doxorubicin.

MCF-10A breast-derived cell line was exposed to OD15_I_Doxorubicin MNP for 24h and 72h. Cells were stained using the Cytotoxicity II HitKit™ and analysed using the InCell 1000 HCSA device. Variation in cell count, cell membrane permeability and lysosomal intensity were measured compared to untreated control (CTRL(-)) and 1µM CdSe positive control (CTRL(+)). Statistical significance was determined using the one way ANOVA with Tukey post-test for each column compared to untreated control (CTRL(-)). p value: *** = <0.001, **=<0.01, *=<0.05

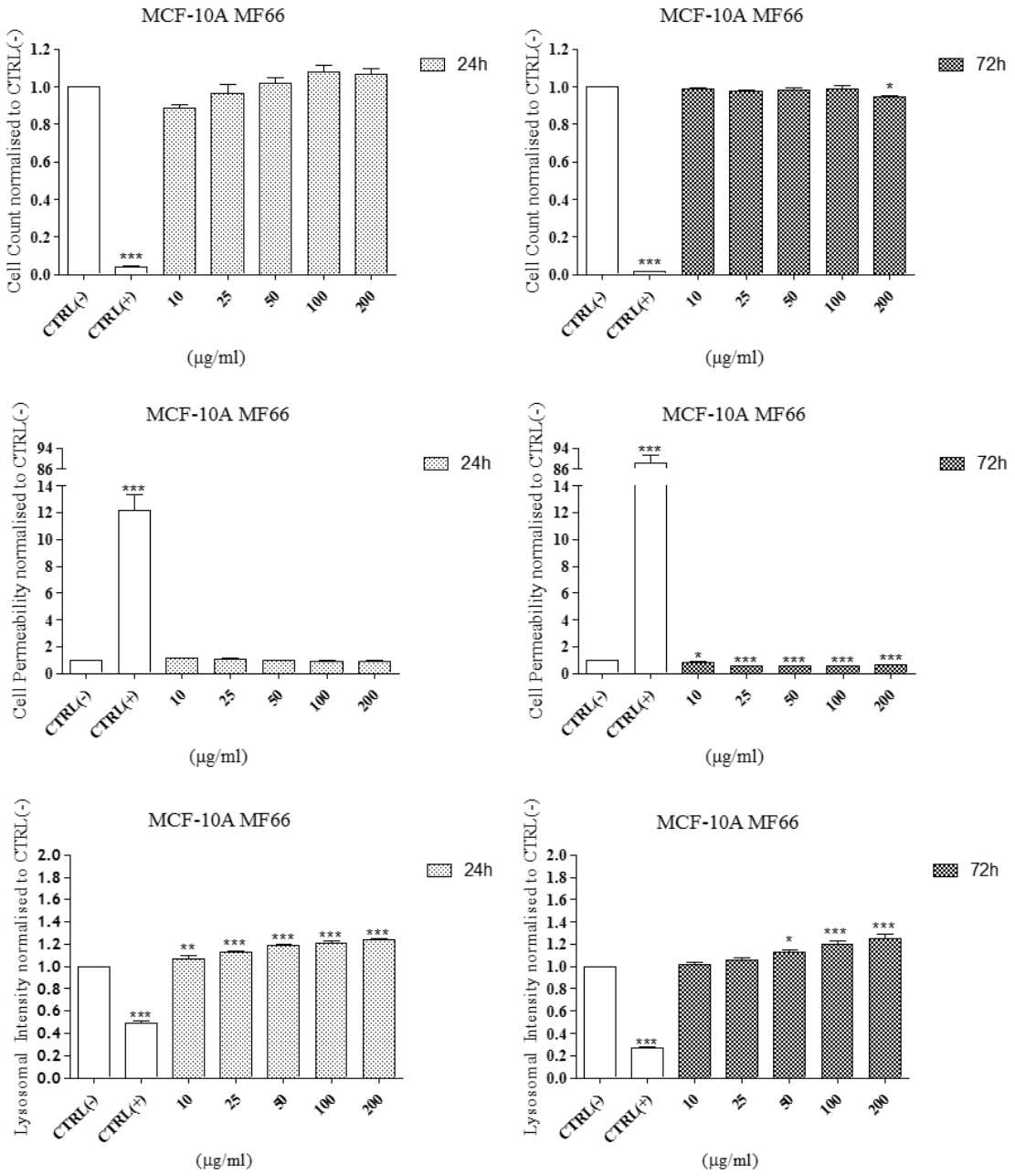

Figure S34: MCF-10A cell line exposed to MF66 MNP.

MCF-10A breast-derived cell line was exposed to MF66 MNP for 24h and 72h. Cells were stained using the Cytotoxicity II HitKit™ and analysed using the InCell 1000 HCSA device. Variation in cell count, cell membrane permeability and lysosomal intensity were measured compared to untreated control (CTRL(-)) and 1µM CdSe positive control (CTRL(+)). Statistical significance was determined using the one way ANOVA with Tukey post-test for each column compared to untreated control (CTRL(-)). p value: *** = <0.001, **=<0.01, *=<0.05

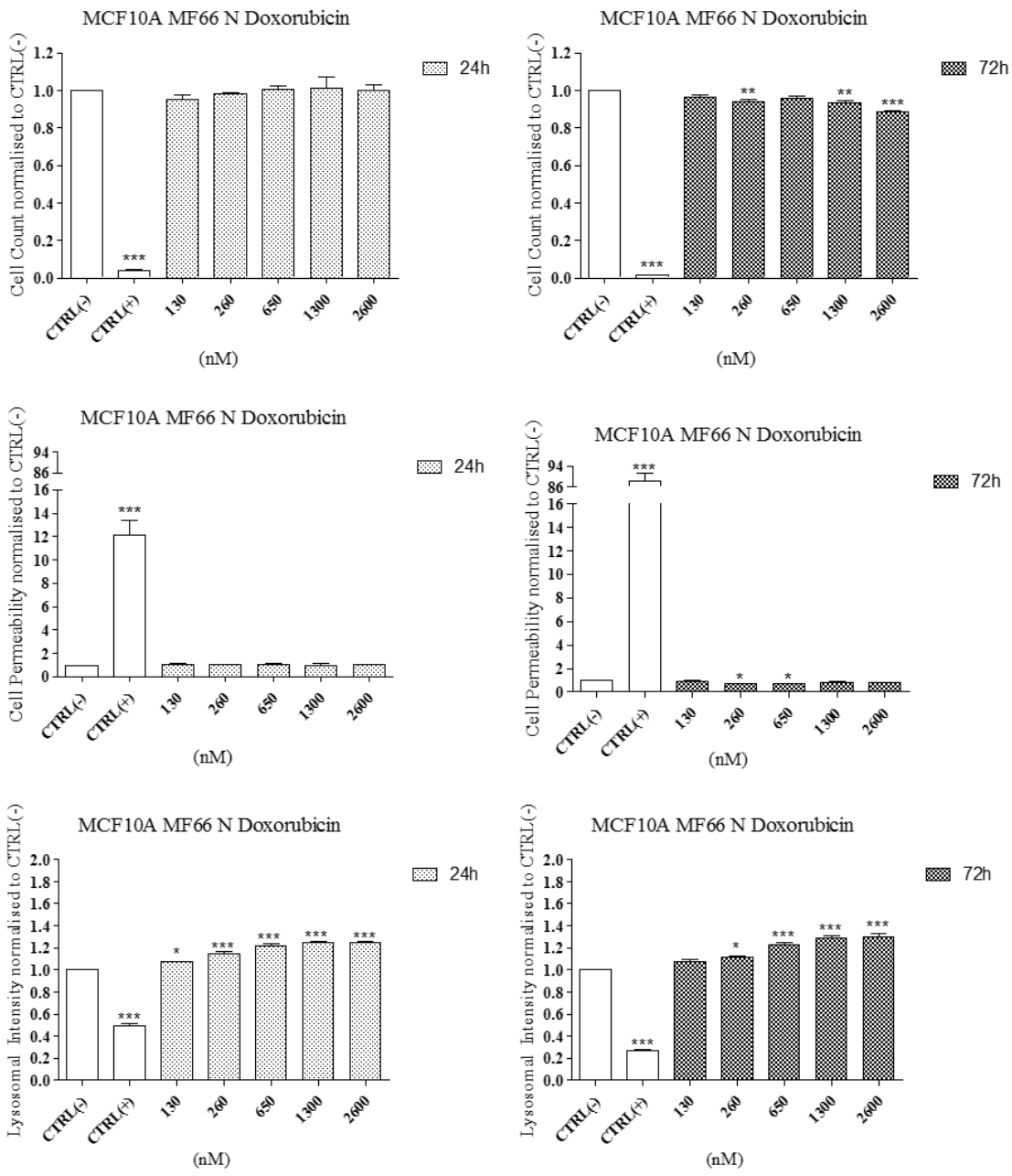

Figure S35: MCF-10A cell line exposed to MF66_N_Doxorubicin.

MCF-10A breast-derived cell line was exposed to MF66_N_Doxorubicin MNP for 24h and 72h. Cells were stained using the Cytotoxicity II HitKit™ and analysed using the InCell 1000 HCSA device. Variation in cell count, cell membrane permeability and lysosomal intensity were measured compared to untreated control (CTRL(-)) and 1µM CdSe positive control (CTRL(+)). Statistical significance was determined using the one way ANOVA with Tukey post-test for each column compared to untreated control (CTRL(-)). p value: *** = <0.001, **=<0.01, *=<0.05

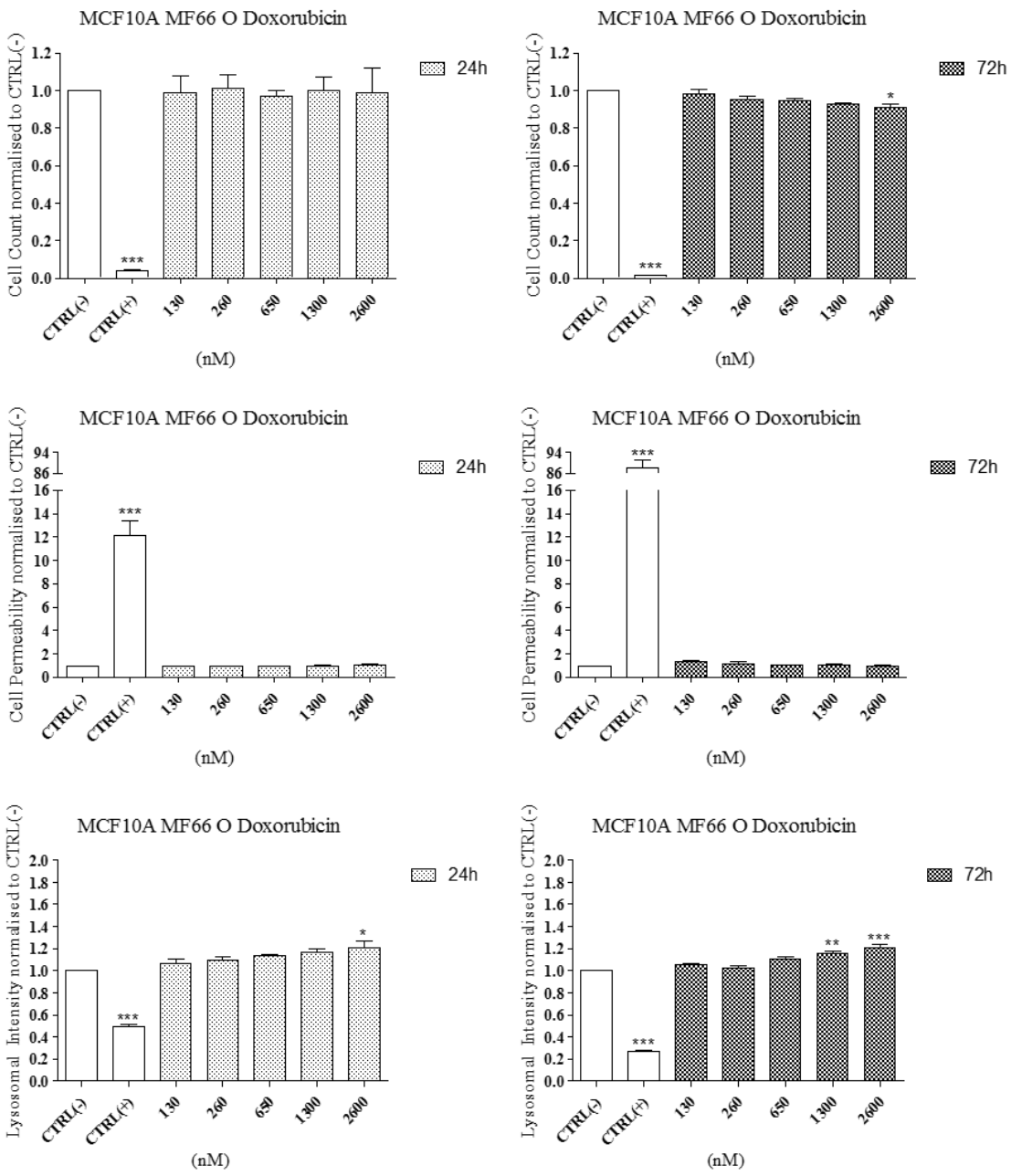

Figure S36: MCF-10A cell line exposed to MF66_O_Doxorubicin.

MCF-10A breast-derived cell line was exposed to MF66_O_Doxorubicin MNP for 24h and 72h. Cells were stained using the Cytotoxicity II HitKit™ and analysed using the InCell 1000 HCSA device. Variation in cell count, cell membrane permeability and lysosomal intensity were measured compared to untreated control (CTRL(-)) and 1µM CdSe positive control (CTRL(+)). Statistical significance was determined using the one way ANOVA with Tukey post-test for each column compared to untreated control (CTRL(-)). p value: *** = <0.001, **=<0.01, *=<0.05

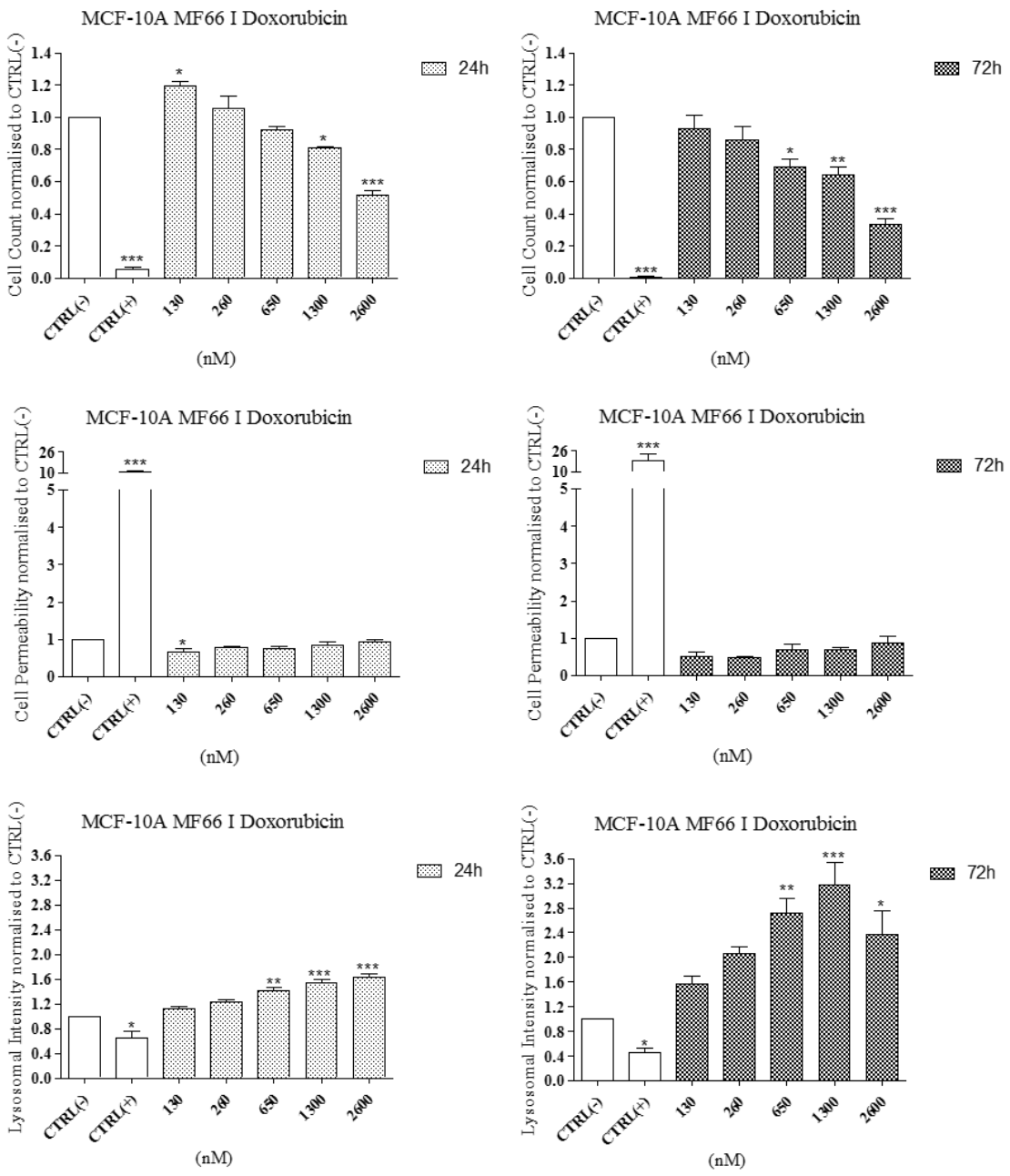

Figure S37: MCF-10A cell line exposed to MF66_I_Doxorubicin.

MCF-10A breast-derived cell line was exposed to MF66_I_Doxorubicin MNP for 24h and 72h. Cells were stained using the Cytotoxicity II HitKit™ and analysed using the InCell 1000 HCSA device. Variation in cell count, cell membrane permeability and lysosomal intensity were measured compared to untreated control (CTRL(-)) and 1µM CdSe positive control (CTRL(+)). Statistical significance was determined using the one way ANOVA with Tukey post-test for each column compared to untreated control (CTRL(-)). p value: *** = <0.001, **=<0.01, *=<0.05

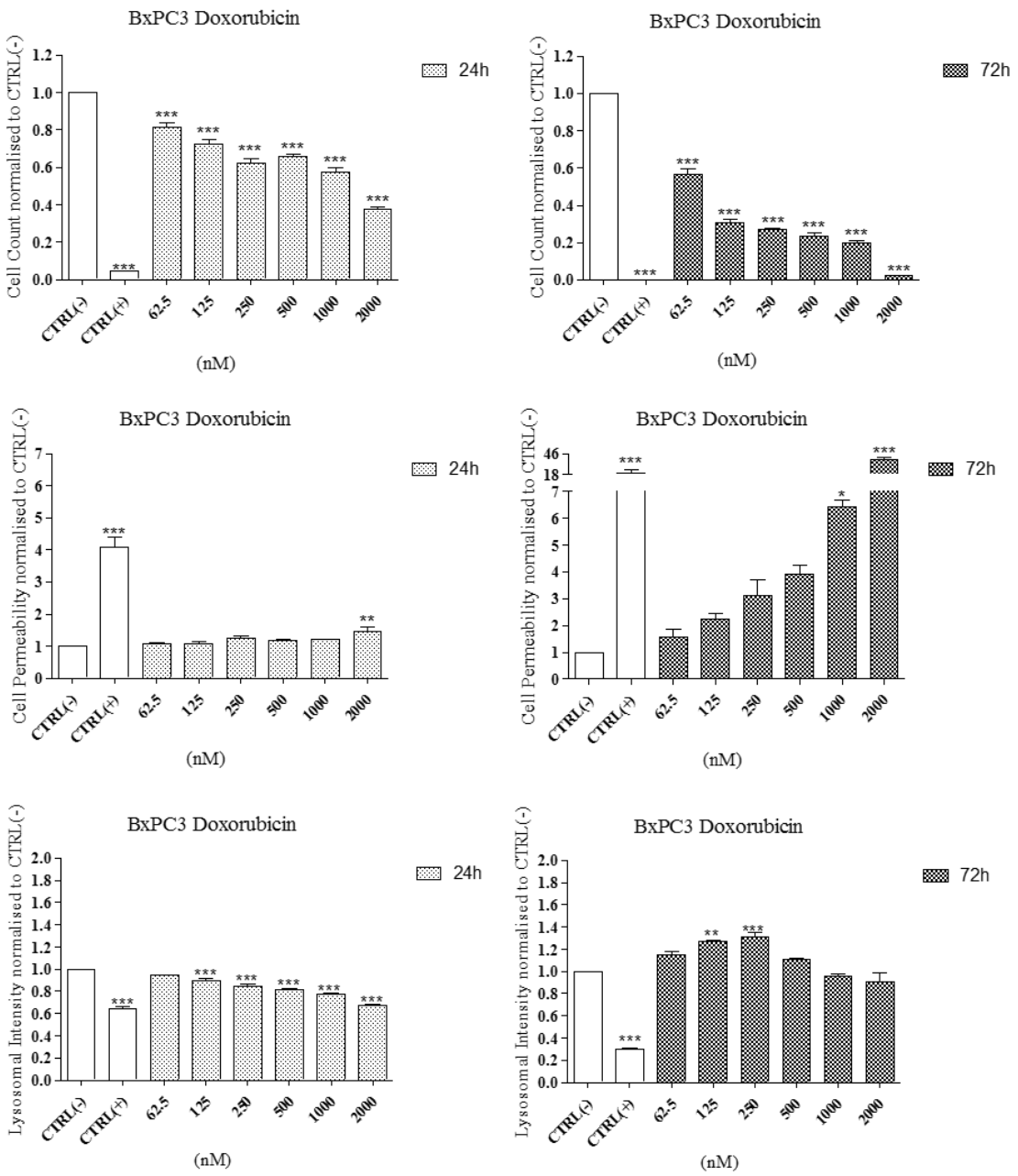

Figure S38: Effect of doxorubicin hydrochloride on viability of BxPC3 cell line.

BxPC3 pancreatic-derived cell line was exposed to free doxorubicin hydrochloride for 24h and 72h. Cells were stained using the Cytotoxicity II HitKit™ and analysed using the InCell 1000 HCSA device. Variation in cell count, cell membrane permeability and lysosomal intensity were measured compared to untreated control (CTRL(-)) and 1µM CdSe positive control (CTRL(+)). Statistical significance was determined using the one way ANOVA with Tukey post-test for each column compared to untreated control (CTRL(-)). p value: *** = <0.001, **=<0.01, *=<0.05.

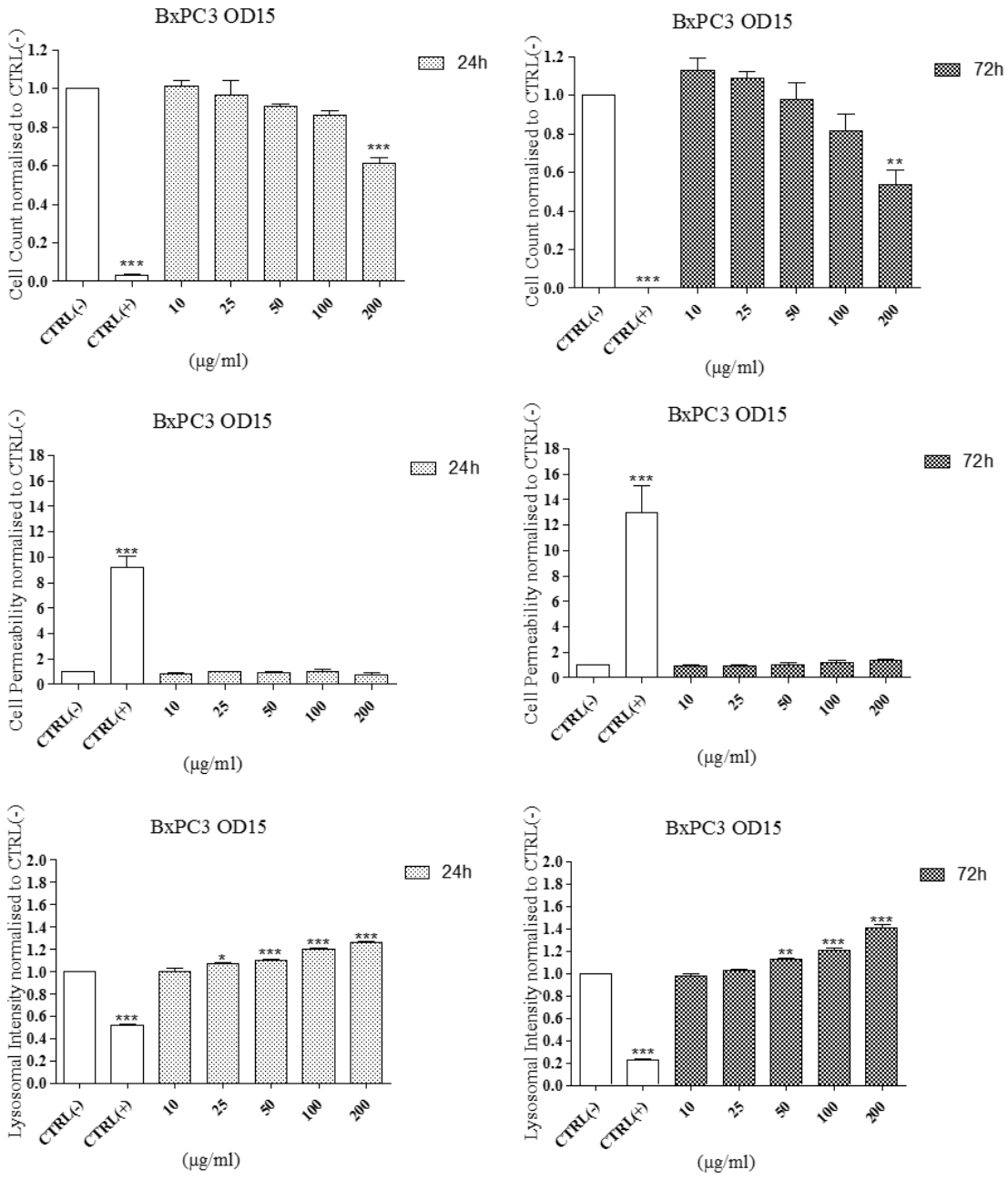

Figure S39: BxPC3 cell line exposed to OD15 MNP.

BxPC3 pancreatic-derived cell line was exposed to OD15 MNP for 24h and 72h. Cells were stained using the Cytotoxicity II HitKit™ and analysed using the InCell 1000 HCSA device. Variation in cell count, cell membrane permeability and lysosomal intensity were measured compared to untreated control (CTRL(-)) and 1µM CdSe positive control (CTRL(+)). Statistical significance was determined using the one way ANOVA with Tukey post-test for each column compared to untreated control (CTRL(-)). p value: *** = <0.001, **=<0.01, *=<0.05

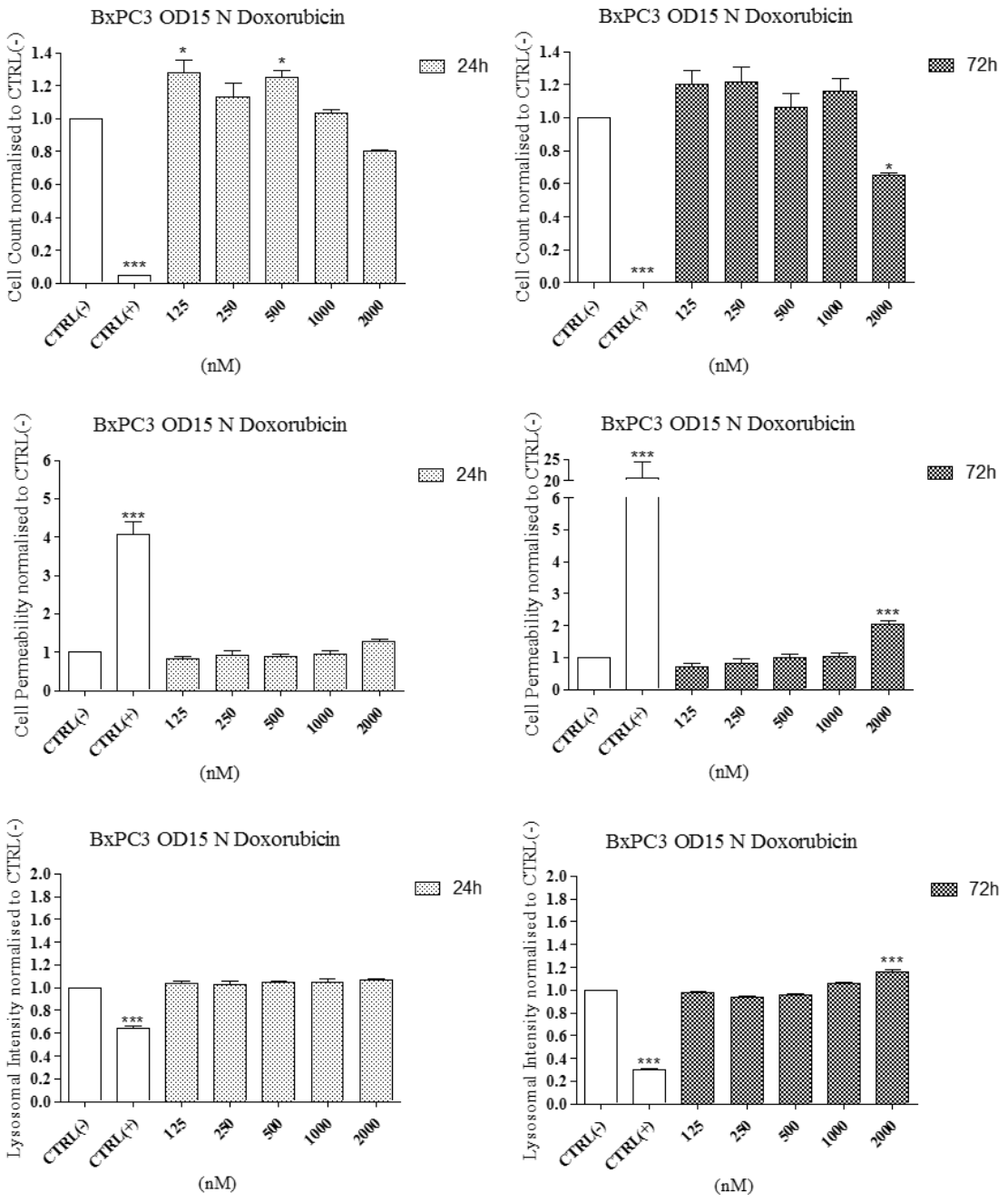

Figure S40: BxPC3 cell line exposed to OD15_N_Doxorubicin MNP.

BxPC3 pancreatic-derived cell line was exposed to OD15_N_Doxorubicin MNP for 24h and 72h. Cells were stained using the Cytotoxicity II HitKit™ and analysed using the InCell 1000 HCSA device. Variation in cell count, cell membrane permeability and lysosomal intensity were measured compared to untreated control (CTRL(-)) and 1µM CdSe positive control (CTRL(+)). Statistical significance was determined using the one way ANOVA with Tukey post-test for each column compared to untreated control (CTRL(-)). p value: *** = <0.001, **=<0.01, *=<0.05

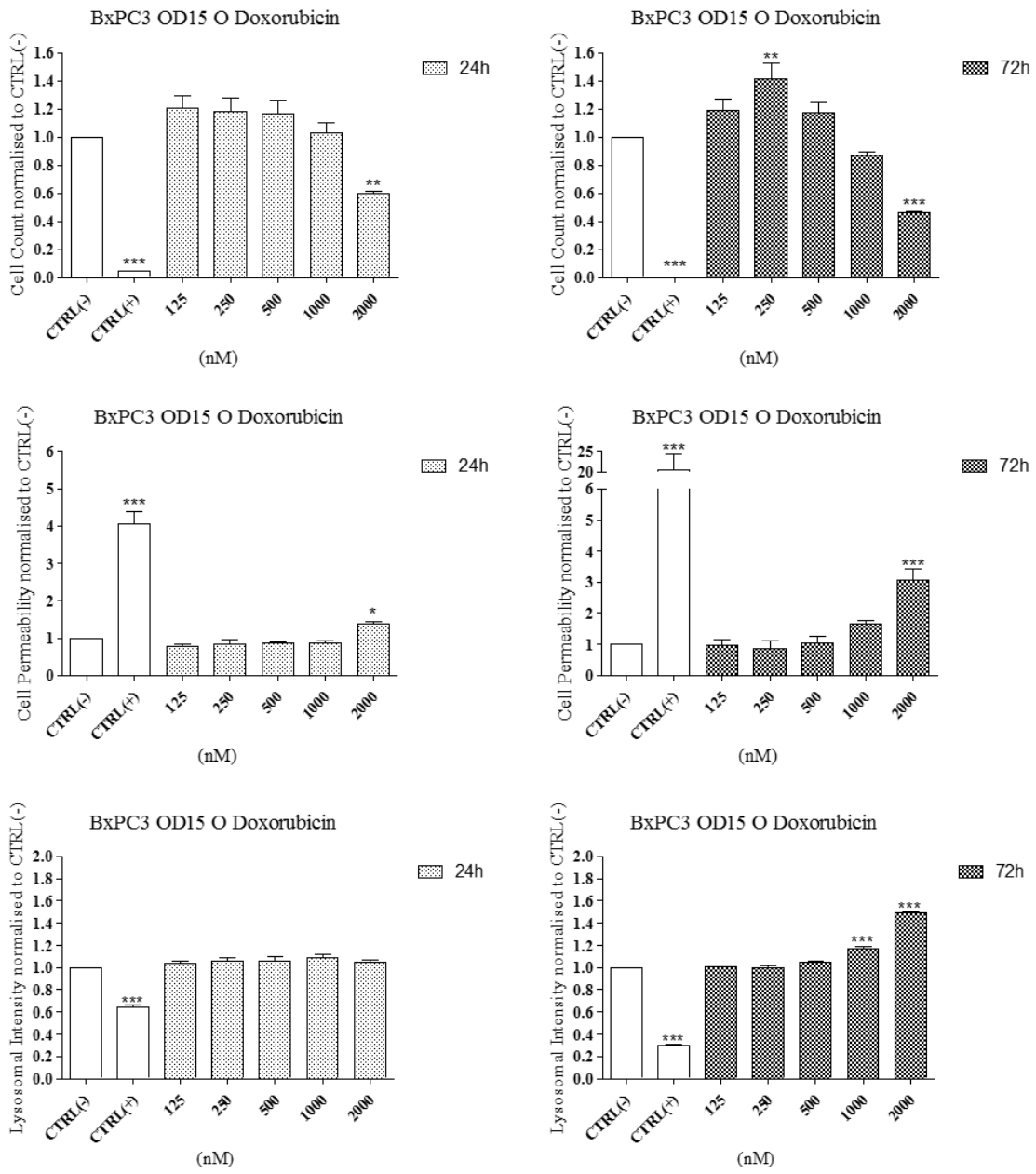

Figure S41: BxPC3 cell line exposed to OD15_O_Doxorubicin MNP.

BxPC3 pancreatic-derived cell line was exposed to OD15_O_Doxorubicin MNP for 24h and 72h. Cells were stained using the Cytotoxicity II HitKit™ and analysed using the InCell 1000 HCSA device. Variation in cell count, cell membrane permeability and lysosomal intensity were measured compared to untreated control (CTRL(-)) and 1µM CdSe positive control (CTRL(+)). Statistical significance was determined using the one way ANOVA with Tukey post-test for each column compared to untreated control (CTRL(-)). p value: *** = <0.001, **=<0.01, *=<0.05

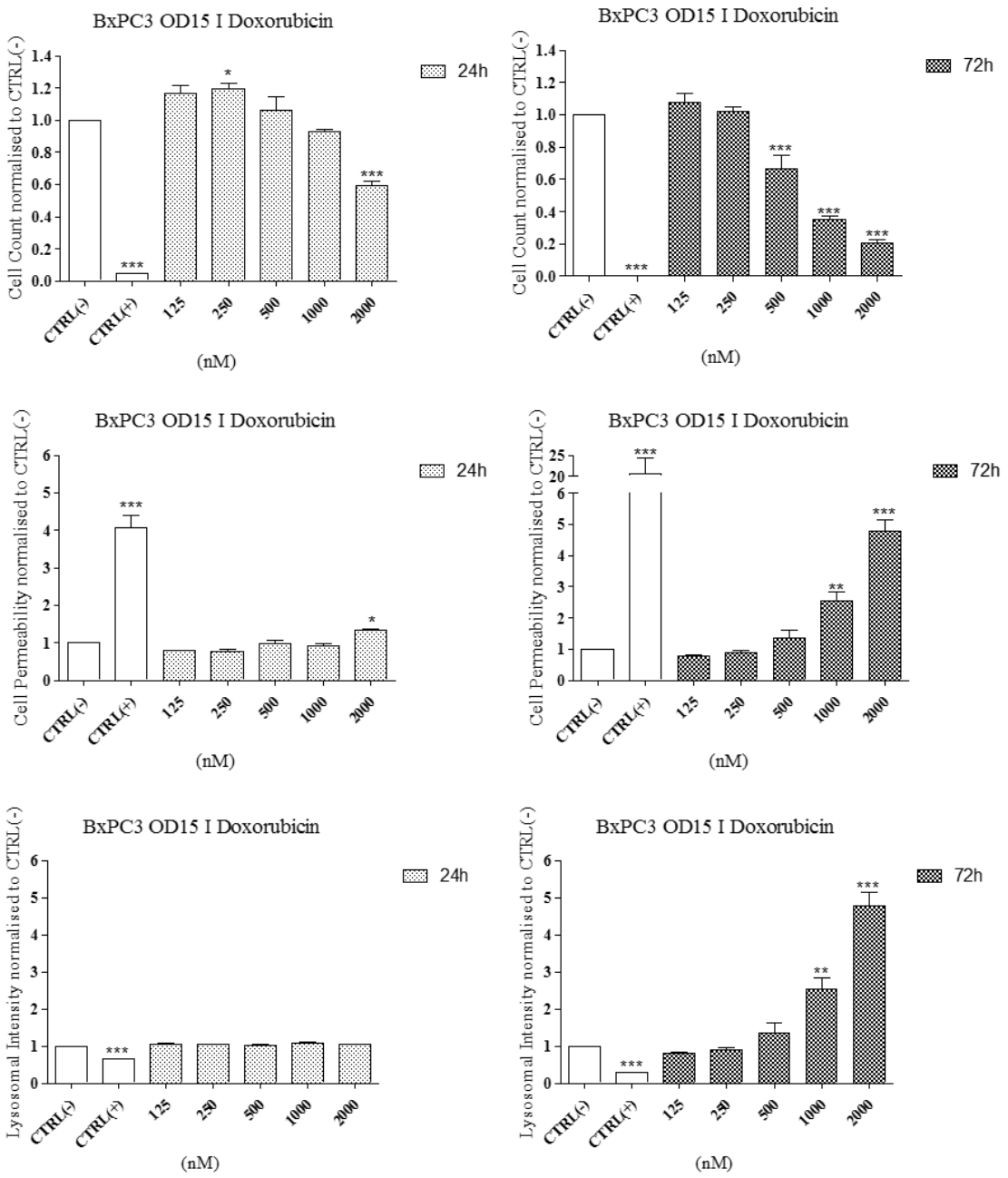

Figure S42: BxPC3 cell line exposed to OD15_I_Doxorubicin MNP.

BxPC3 pancreatic-derived cell line was exposed to OD15_I_Doxorubicin MNP for 24h and 72h. Cells were stained using the Cytotoxicity II HitKit™ and analysed using the InCell 1000 HCSA device. Variation in cell count, cell membrane permeability and lysosomal intensity were measured compared to untreated control (CTRL(-)) and 1µM CdSe positive control (CTRL(+)). Statistical significance was determined using the one way ANOVA with Tukey post-test for each column compared to untreated control (CTRL(-)). p value: *** = <0.001, **=<0.01, *=<0.05

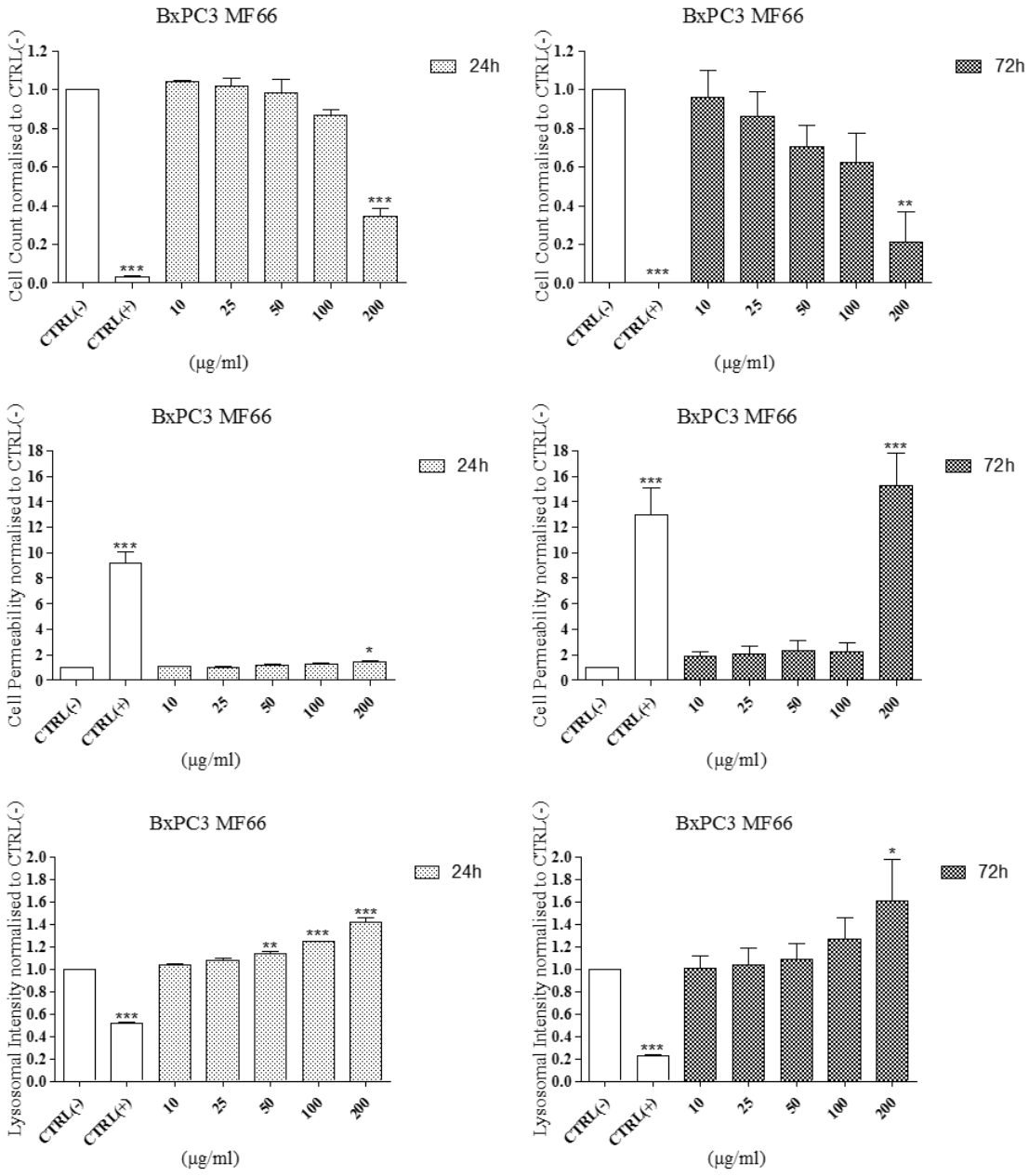

Figure S43: BxPC3 cell line exposed to MF66 MNP.

BxPC3 pancreatic-derived cell line was exposed to MF66 MNP for 24h and 72h. Cells were stained using the Cytotoxicity II HitKit™ and analysed using the InCell 1000 HCSA device. Variation in cell count, cell membrane permeability and lysosomal intensity were measured compared to untreated control (CTRL(-)) and 1µM CdSe positive control (CTRL(+)). Statistical significance was determined using the one way ANOVA with Tukey post-test for each column compared to untreated control (CTRL(-)). p value: *** = <0.001, **=<0.01, *=<0.05

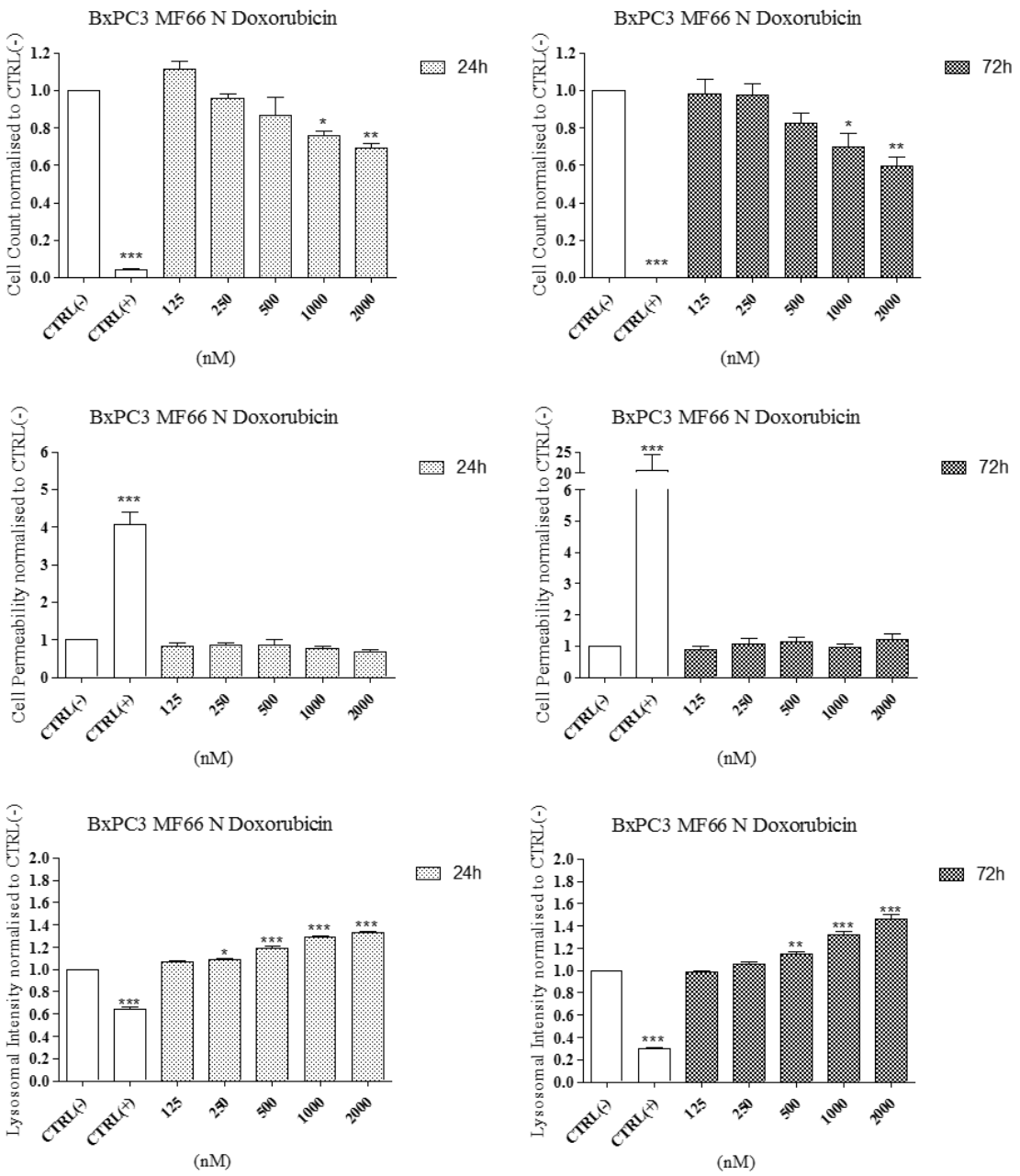

Figure S44: BxPC3 cell line exposed to MF66_N_Doxorubicin MNP.

BxPC3 pancreatic-derived cell line was exposed to MF66_N_Doxorubicin MNP for 24h and 72h. Cells were stained using the Cytotoxicity II HitKit™ and analysed using the InCell 1000 HCSA device. Variation in cell count, cell membrane permeability and lysosomal intensity were measured compared to untreated control (CTRL(-)) and 1µM CdSe positive control (CTRL(+)). Statistical significance was determined using the one way ANOVA with Tukey post-test for each column compared to untreated control (CTRL(-)). p value: *** = <0.001, **=<0.01, *=<0.05

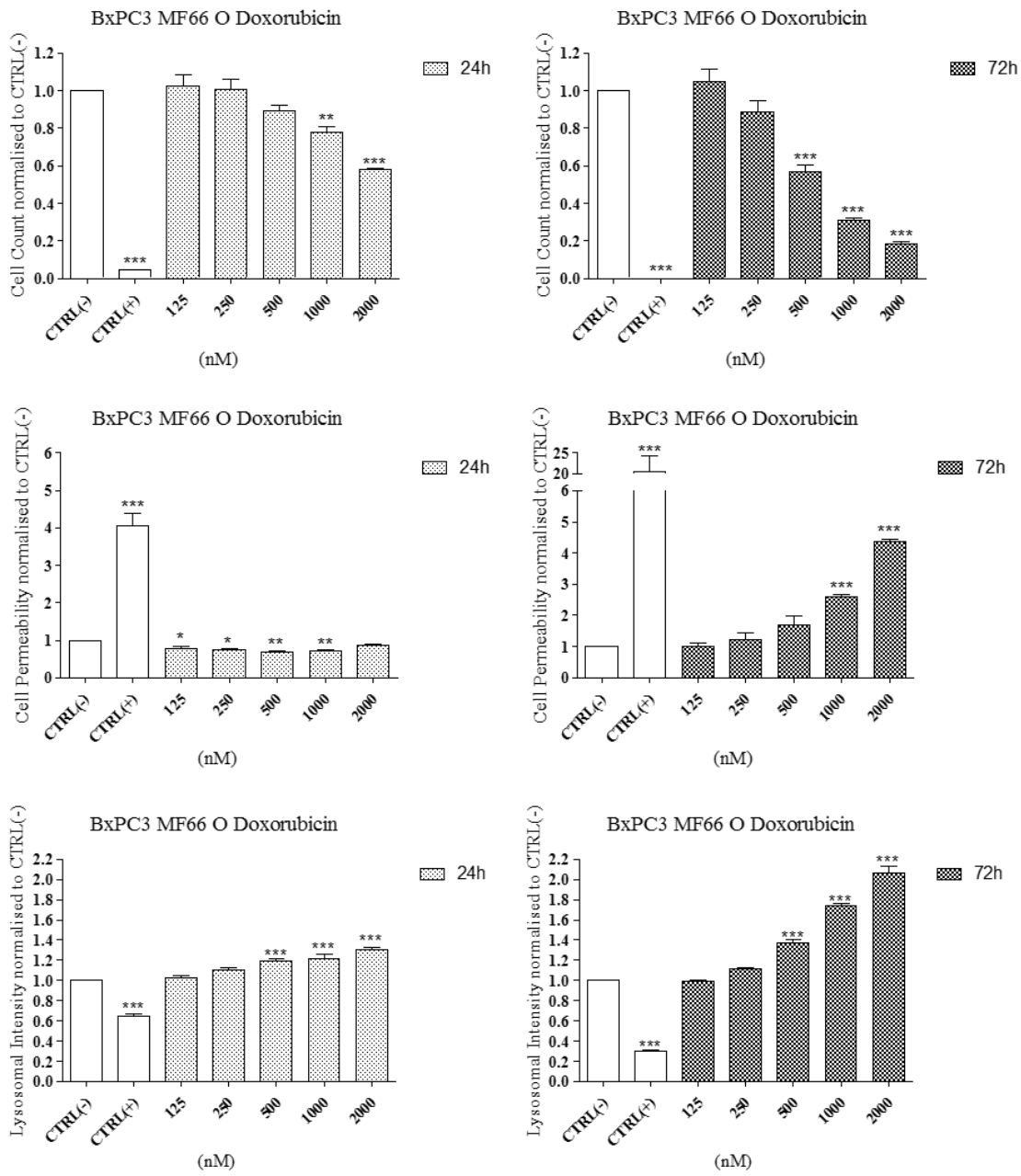

Figure S45: BxPC3 cell line exposed to MF66_O_Doxorubicin MNP.

BxPC3 pancreatic-derived cell line was exposed to MF66_O_Doxorubicin MNP for 24h and 72h. Cells were stained using the Cytotoxicity II HitKit™ and analysed using the InCell 1000 HCSA device. Variation in cell count, cell membrane permeability and lysosomal intensity were measured compared to untreated control (CTRL(-)) and 1µM CdSe positive control (CTRL(+)). Statistical significance was determined using the one way ANOVA with Tukey post-test for each column compared to untreated control (CTRL(-)). p value: *** = <0.001, **=<0.01, *=<0.05

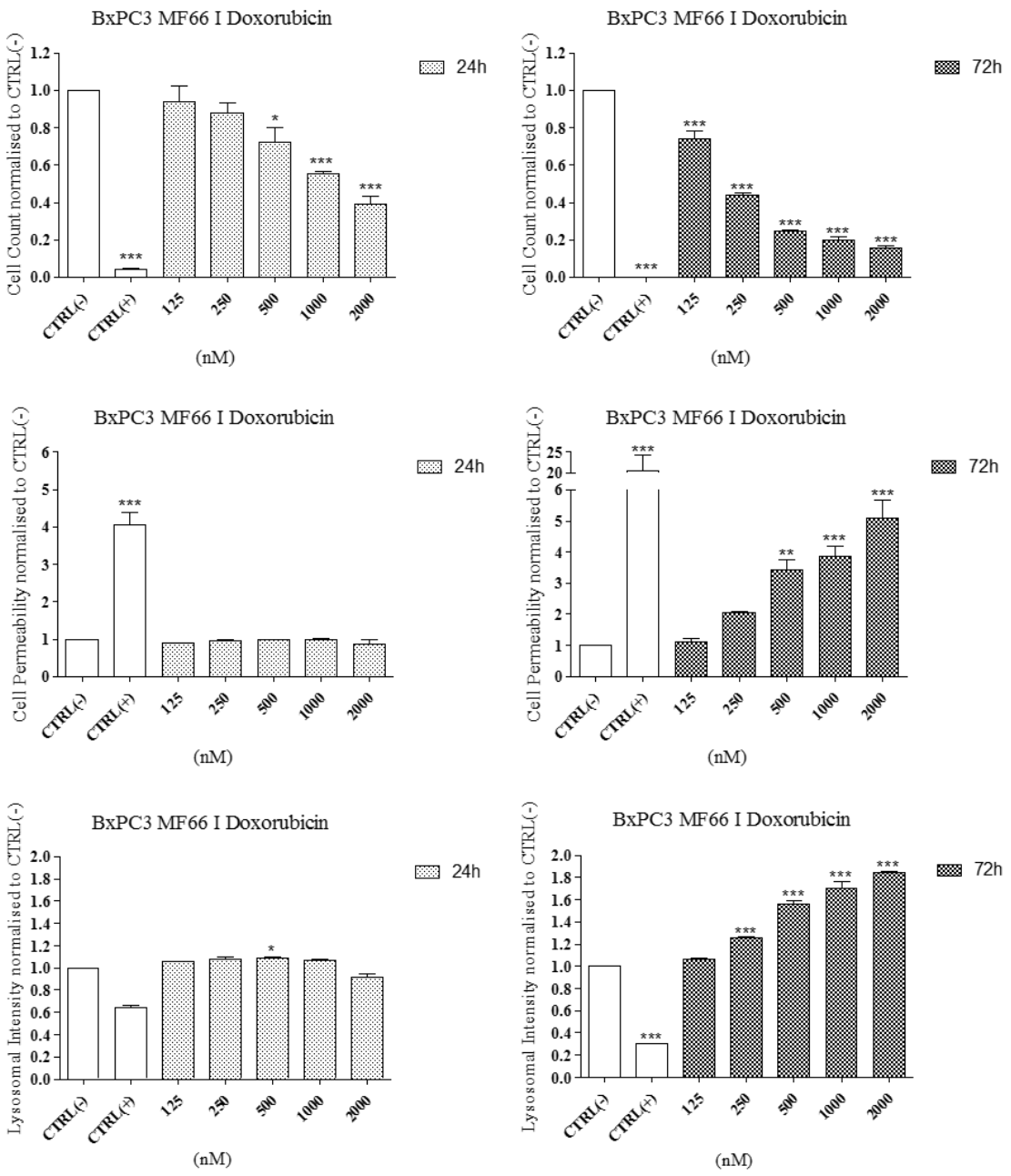

Figure S46: BxPC3 cell line exposed to MF66_I_Doxorubicin MNP.

BxPC3 pancreatic-derived cell line was exposed to MF66_I_Doxorubicin MNP for 24h and 72h. Cells were stained using the Cytotoxicity II HitKit™ and analysed using the InCell 1000 HCSA device. Variation in cell count, cell membrane permeability and lysosomal intensity were measured compared to untreated control (CTRL(-)) and 1µM CdSe positive control (CTRL(+)). Statistical significance was determined using the one way ANOVA with Tukey post-test for each column compared to untreated control (CTRL(-)). p value: *** = <0.001, **=<0.01, *=<0.05

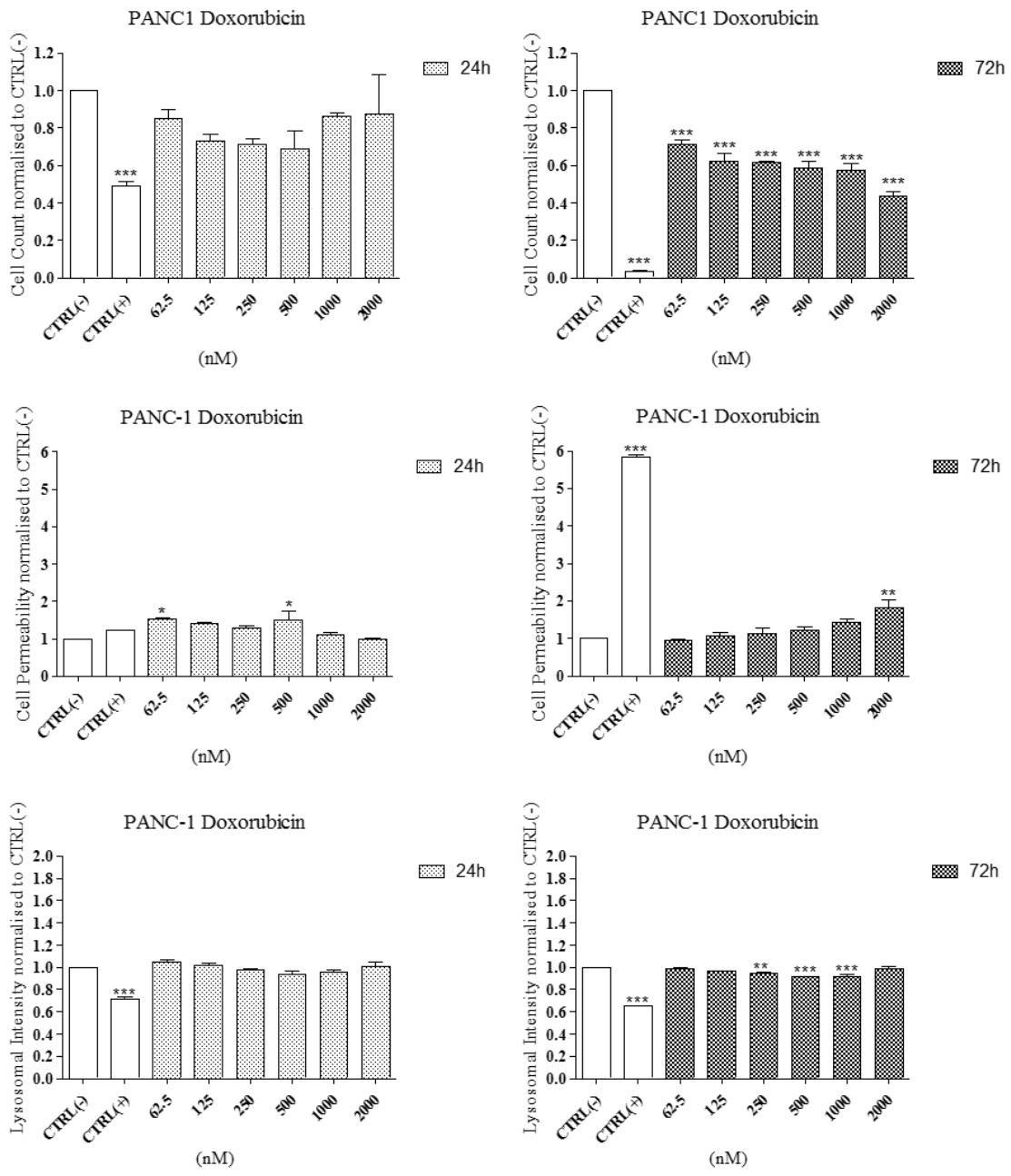

Figure S47: Effect of doxorubicin hydrochloride on viability of PANC1 cell line.

PANC1 pancreatic-derived cell line was exposed to free doxorubicin hydrochloride for 24h and 72h. Cells were stained using the Cytotoxicity II HitKit™ and analysed using the InCell 1000 HCSA device. Variation in cell count, cell membrane permeability and lysosomal intensity were measured compared to untreated control (CTRL(-)) and 1µM CdSe positive control (CTRL(+)). Statistical significance was determined using the one way ANOVA with Tukey post-test for each column compared to untreated control (CTRL(-)). p value: *** = <0.001, **=<0.01, *=<0.05.

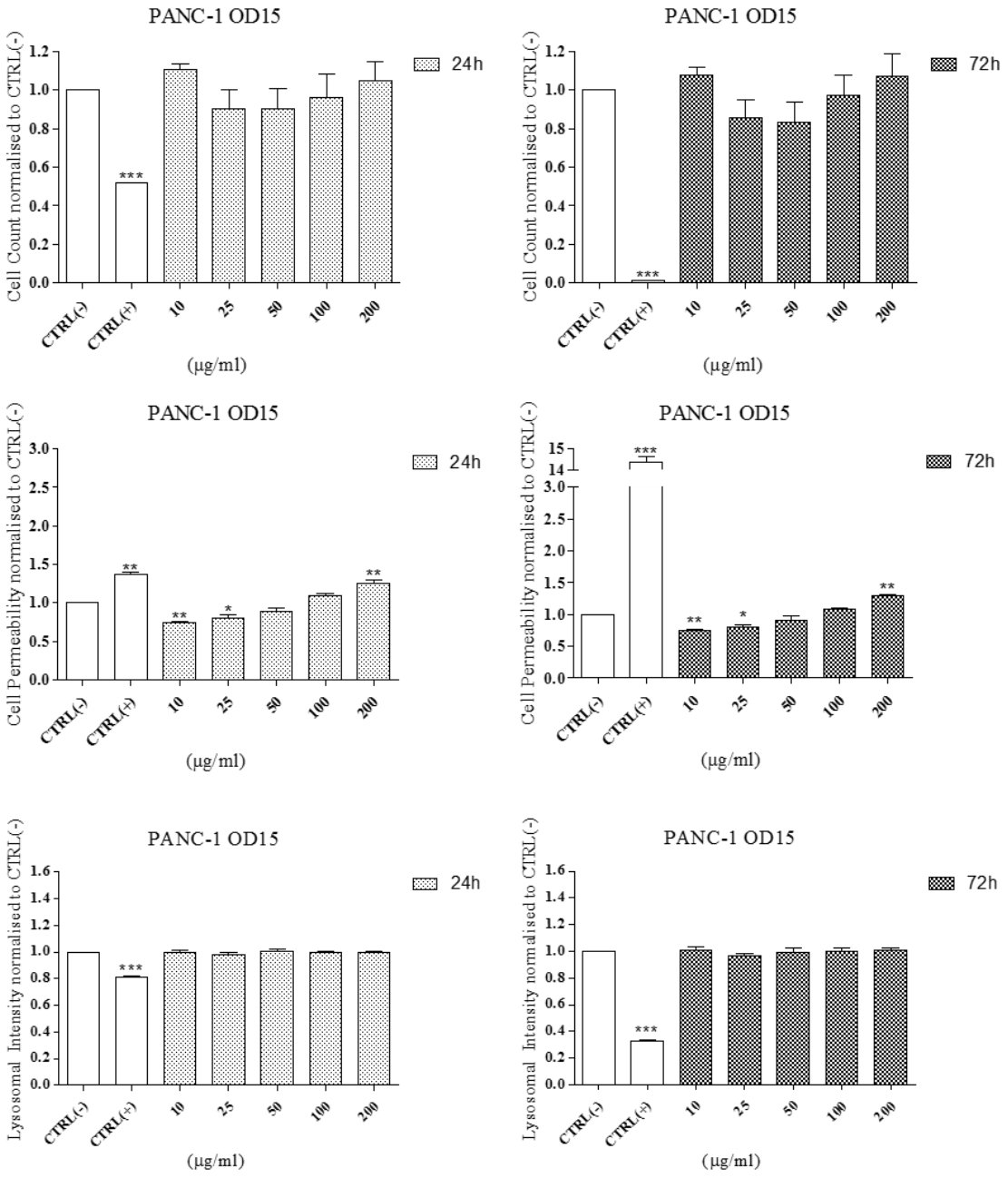

Figure S48: PANC1 cell line exposed to OD15 MNP.

PANC1 pancreatic-derived cell line was exposed to OD15 MNP for 24h and 72h. Cells were stained using the Cytotoxicity II HitKit™ and analysed using the InCell 1000 HCSA device. Variation in cell count, cell membrane permeability and lysosomal intensity were measured compared to untreated control (CTRL(-)) and 1µM CdSe positive control (CTRL(+)). Statistical significance was determined using the one way ANOVA with Tukey post-test for each column compared to untreated control (CTRL(-)). p value: *** = <0.001, **=<0.01, *=<0.05

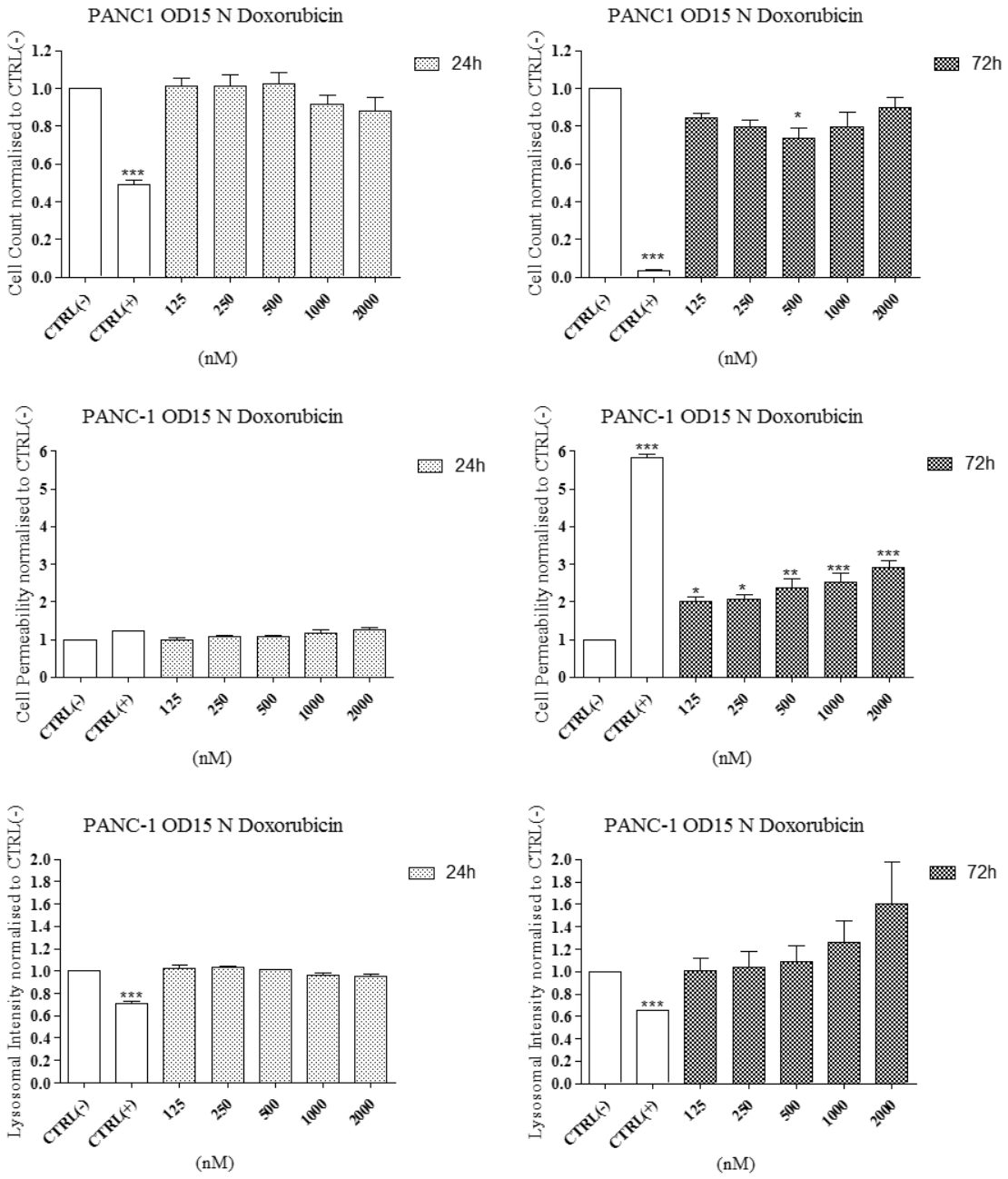

Figure S49: PANC1 cell line exposed to OD15_N_Doxorubicin MNP.

PANC1 pancreatic-derived cell line was exposed to OD15_N_Doxorubicin MNP for 24h and 72h. Cells were stained using the Cytotoxicity II HitKit™ and analysed using the InCell 1000 HCSA device. Variation in cell count, cell membrane permeability and lysosomal intensity were measured compared to untreated control (CTRL(-)) and 1µM CdSe positive control (CTRL(+)). Statistical significance was determined using the one way ANOVA with Tukey post-test for each column compared to untreated control (CTRL(-)). p value: *** = <0.001, **=<0.01, *=<0.05

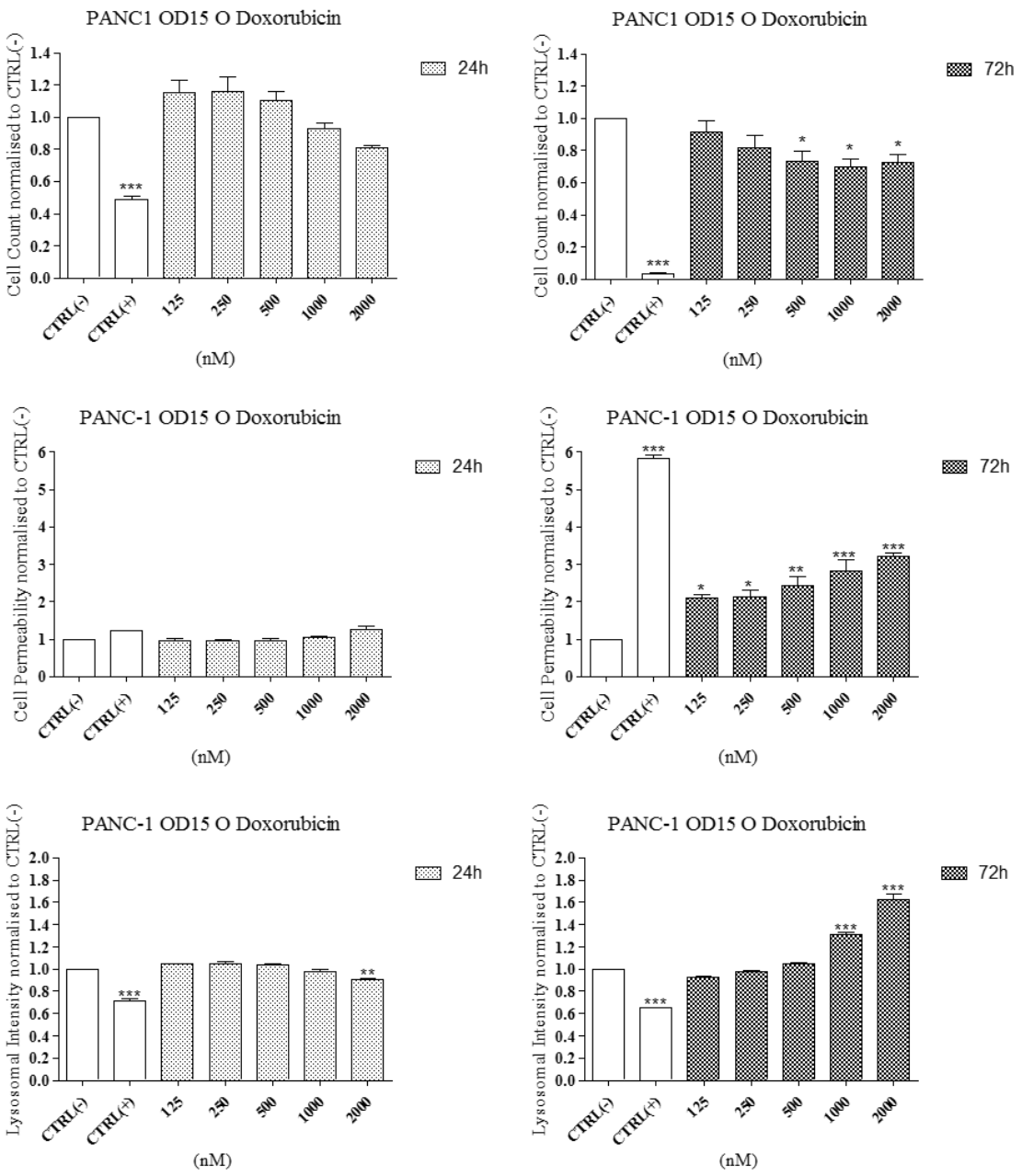

Figure S50: PANC1 cell line exposed to OD15_O_Doxorubicin MNP.

PANC1 pancreatic-derived cell line was exposed to OD15_O_Doxorubicin MNP for 24h and 72h. Cells were stained using the Cytotoxicity II HitKit™ and analysed using the InCell 1000 HCSA device. Variation in cell count, cell membrane permeability and lysosomal intensity were measured compared to untreated control (CTRL(-)) and 1µM CdSe positive control (CTRL(+)). Statistical significance was determined using the one way ANOVA with Tukey post-test for each column compared to untreated control (CTRL(-)). p value: *** = <0.001, **=<0.01, *=<0.05

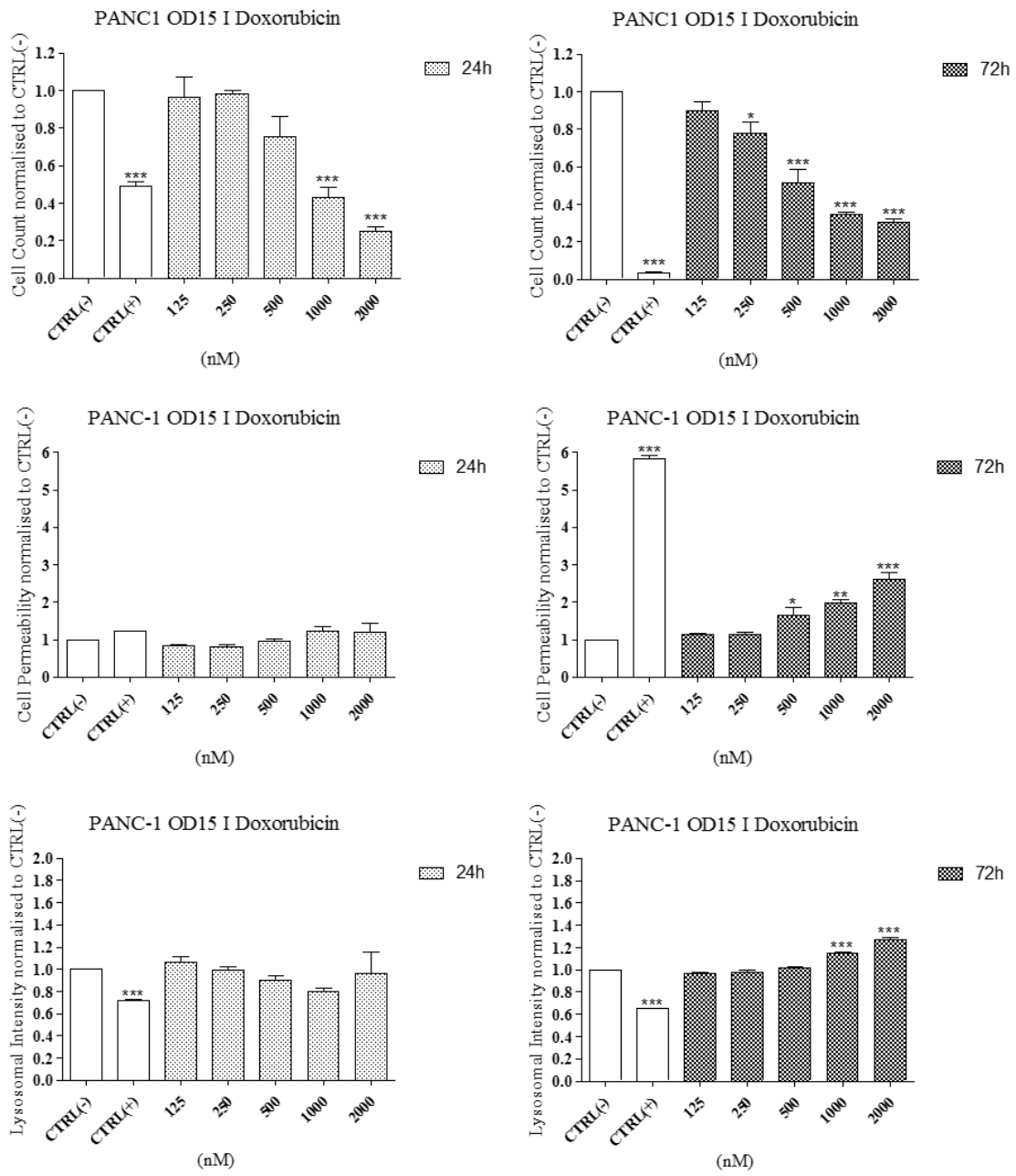

Figure S51: PANC1 cell line exposed to OD15_I_Doxorubicin MNP.

PANC1 pancreatic-derived cell line was exposed to OD15_I_Doxorubicin MNP for 24h and 72h. Cells were stained using the Cytotoxicity II HitKit™ and analysed using the InCell 1000 HCSA device. Variation in cell count, cell membrane permeability and lysosomal intensity were measured compared to untreated control (CTRL(-)) and 1µM CdSe positive control (CTRL(+)). Statistical significance was determined using the one way ANOVA with Tukey post-test for each column compared to untreated control (CTRL(-)). p value: *** = <0.001, **=<0.01, *=<0.05

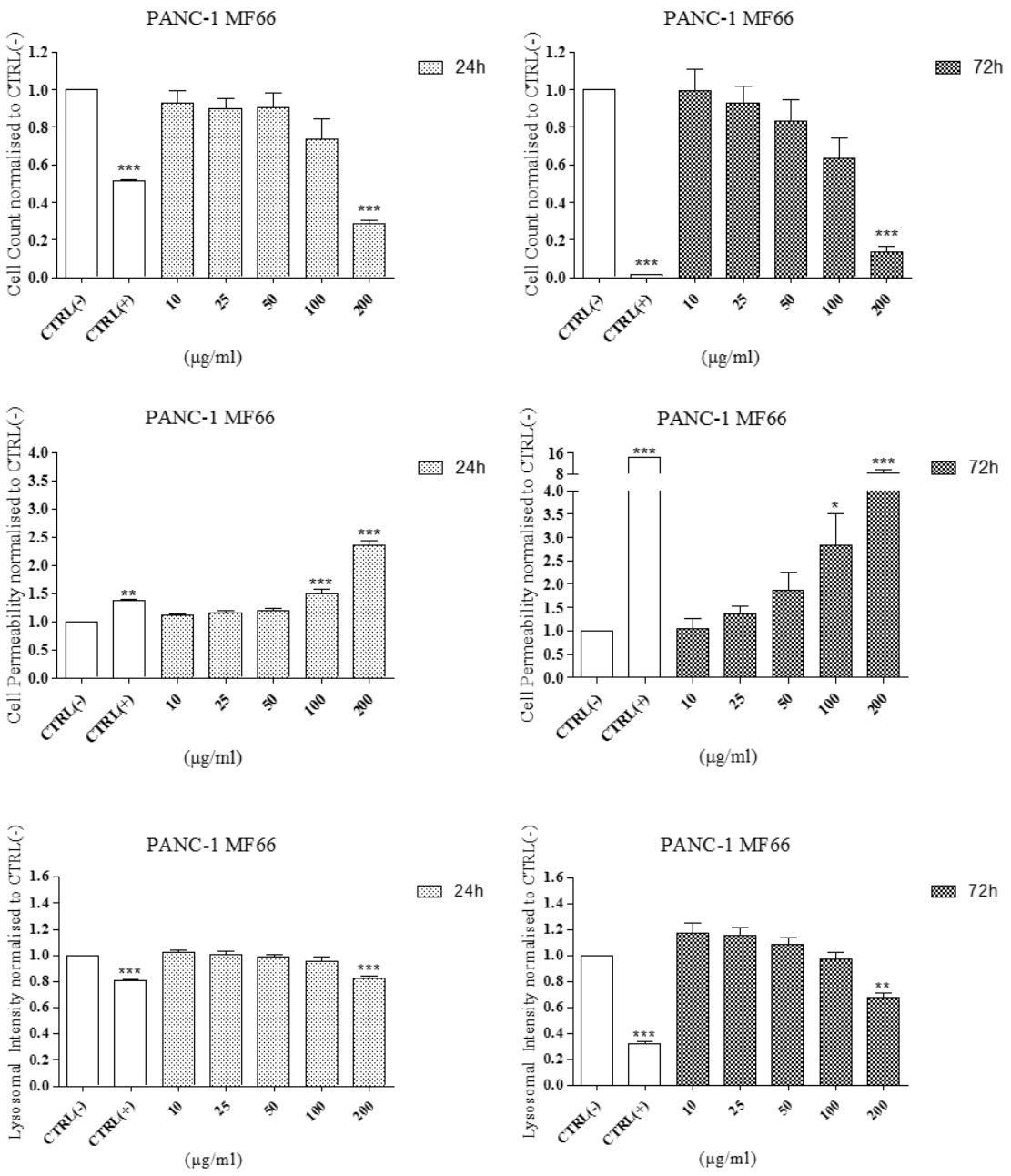

Figure S52: PANC1 cell line exposed to MF66 MNP.

PANC1 pancreatic-derived cell line was exposed to MF66 MNP for 24h and 72h. Cells were stained using the Cytotoxicity II HitKit™ and analysed using the InCell 1000 HCSA device. Variation in cell count, cell membrane permeability and lysosomal intensity were measured compared to untreated control (CTRL(-)) and 1µM CdSe positive control (CTRL(+)). Statistical significance was determined using the one way ANOVA with Tukey post-test for each column compared to untreated control (CTRL(-)). p value: *** = <0.001, **=<0.01, *=<0.05

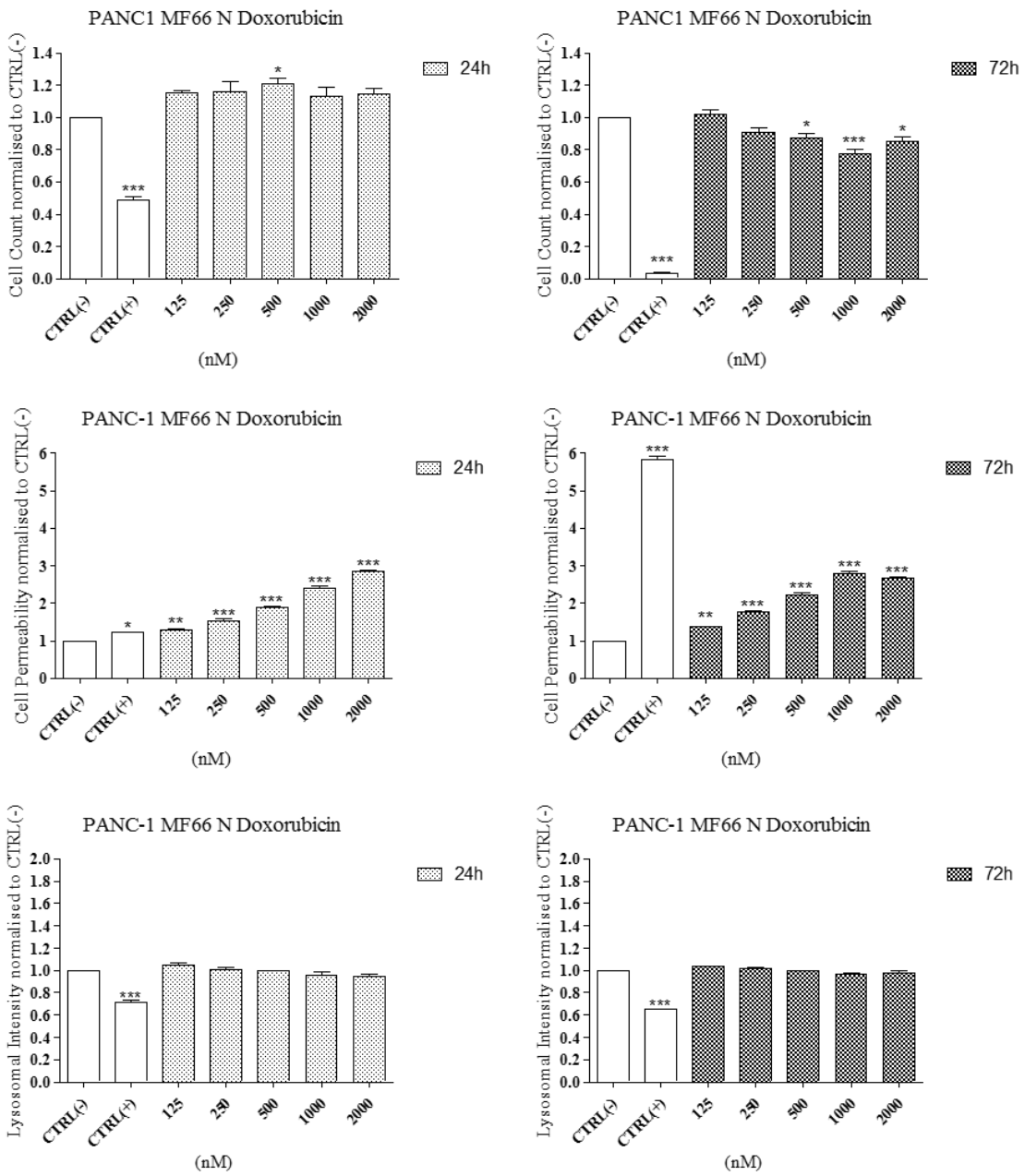

Figure S53: PANC1 cell line exposed to MF66_N_Doxorubicin MNP.

PANC1 pancreatic-derived cell line was exposed to MF66_N_Doxorubicin MNP for 24h and 72h. Cells were stained using the Cytotoxicity II HitKit™ and analysed using the InCell 1000 HCSA device. Variation in cell count, cell membrane permeability and lysosomal intensity were measured compared to untreated control (CTRL(-)) and 1µM CdSe positive control (CTRL(+)). Statistical significance was determined using the one way ANOVA with Tukey post-test for each column compared to untreated control (CTRL(-)). p value: *** = <0.001, **=<0.01, *=<0.05

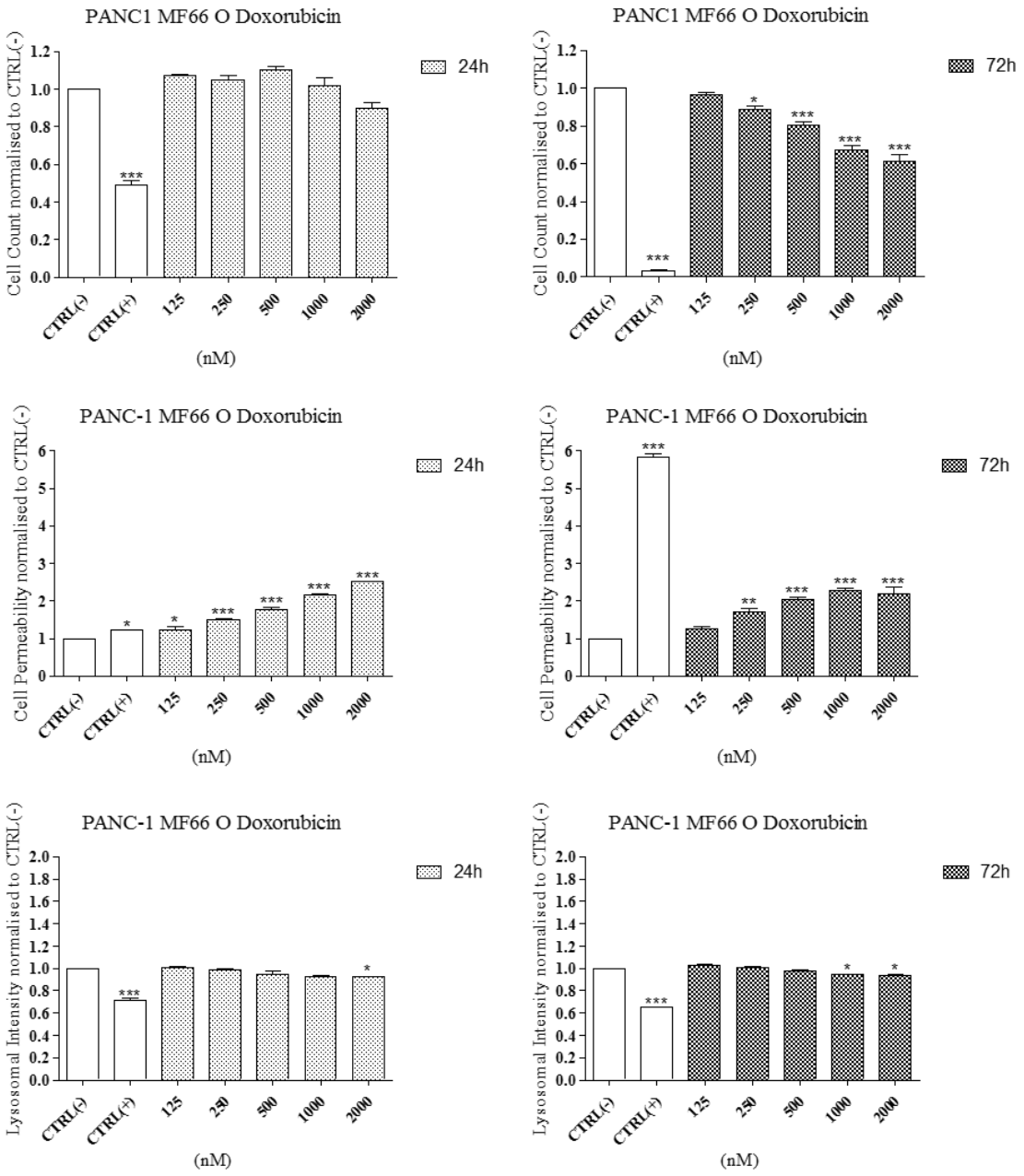

Figure S54: PANC1 cell line exposed to MF66_O_Doxorubicin MNP.

PANC1 pancreatic-derived cell line was exposed to MF66_O_Doxorubicin MNP for 24h and 72h. Cells were stained using the Cytotoxicity II HitKit™ and analysed using the InCell 1000 HCSA device. Variation in cell count, cell membrane permeability and lysosomal intensity were measured compared to untreated control (CTRL(-)) and 1µM CdSe positive control (CTRL(+)). Statistical significance was determined using the one way ANOVA with Tukey post-test for each column compared to untreated control (CTRL(-)). p value: *** = <0.001, **=<0.01, *=<0.05

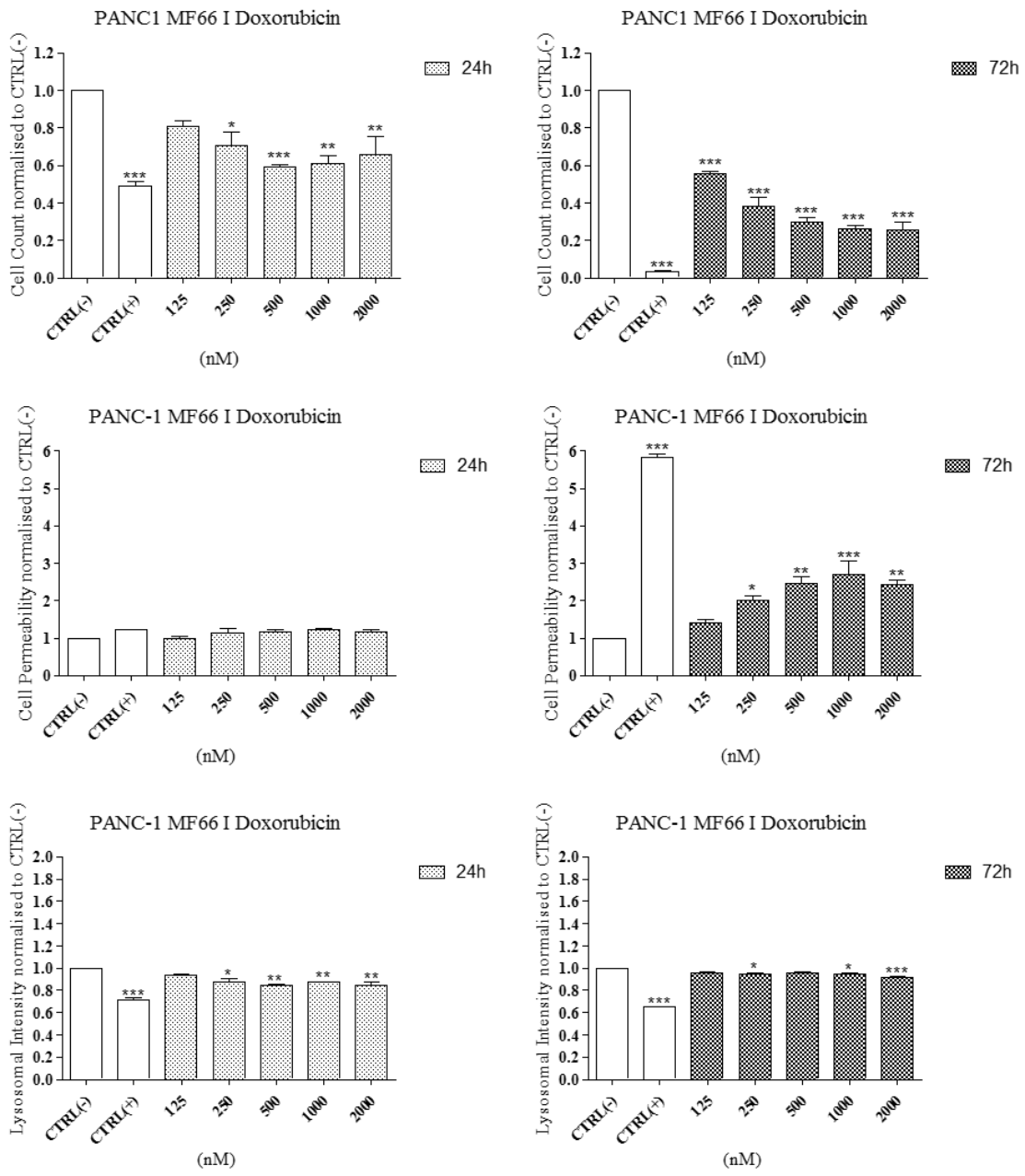

Figure S55: PANC1 cell line exposed to MF66_I_Doxorubicin MNP.

PANC1 pancreatic-derived cell line was exposed to MF66_O_Doxorubicin MNP for 24h and 72h. Cells were stained using the Cytotoxicity II HitKit™ and analysed using the InCell 1000 HCSA device. Variation in cell count, cell membrane permeability and lysosomal intensity were measured compared to untreated control (CTRL(-)) and 1µM CdSe positive control (CTRL(+)). Statistical significance was determined using the one way ANOVA with Tukey post-test for each column compared to untreated control (CTRL(-)). p value: *** = <0.001, **=<0.01, *=<0.05

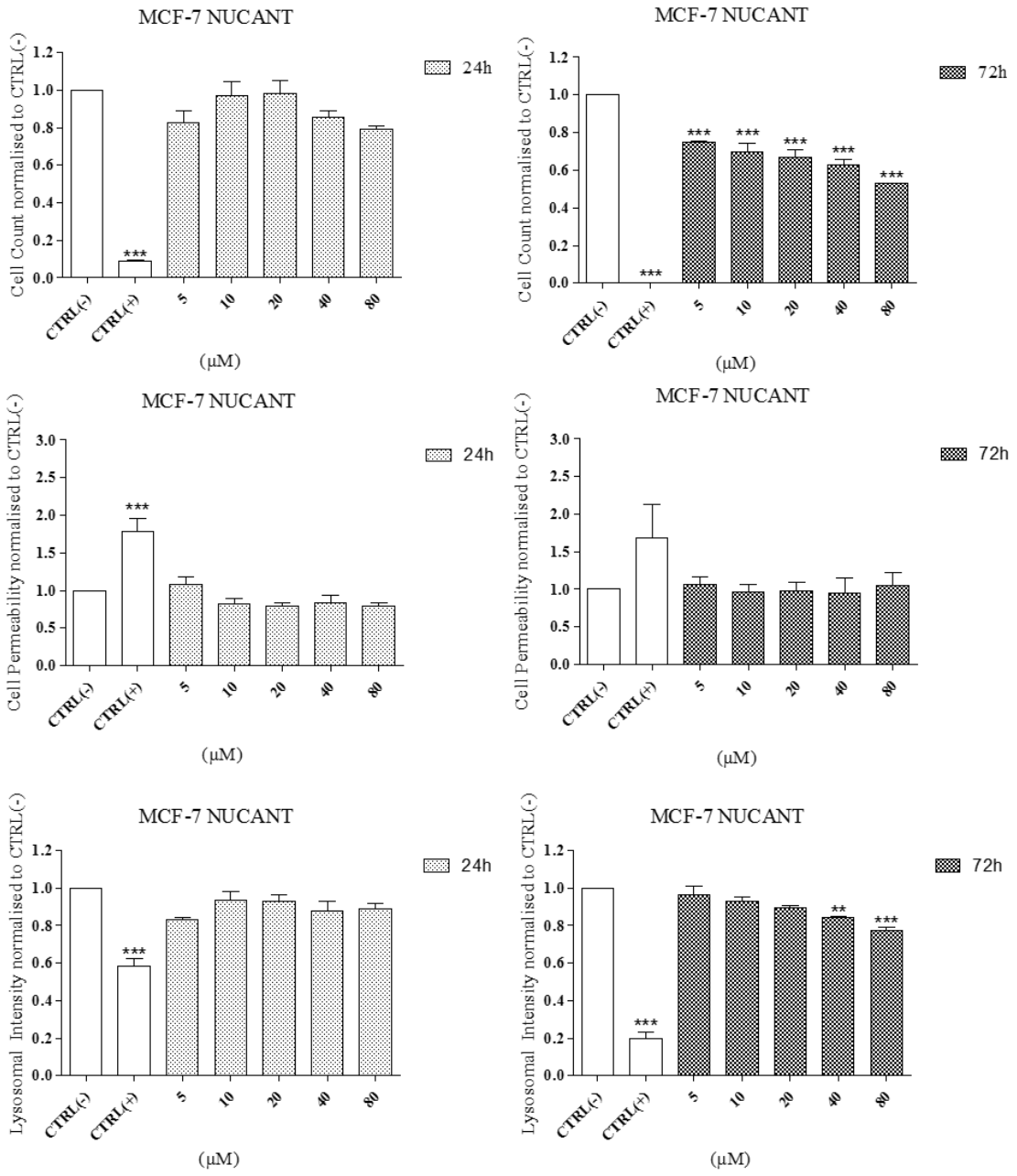

Figure S56: MCF-7 cell line exposed to NUCANT pseudopeptide.

MCF-7 breast-derived cell line was exposed to NUCANT pseudopeptide for 24h and 72h. Cells were stained using the Cytotoxicity II HitKit™ and analysed using the InCell 1000 HCSA device. Variation in cell count, cell membrane permeability and lysosomal intensity were measured compared to untreated control (CTRL(-)) and 1µM CdSe positive control (CTRL(+)). Statistical significance was determined using the one way ANOVA with Tukey post-test for each column compared to untreated control (CTRL(-)). p value: *** = <0.001, **=<0.01, *=<0.05

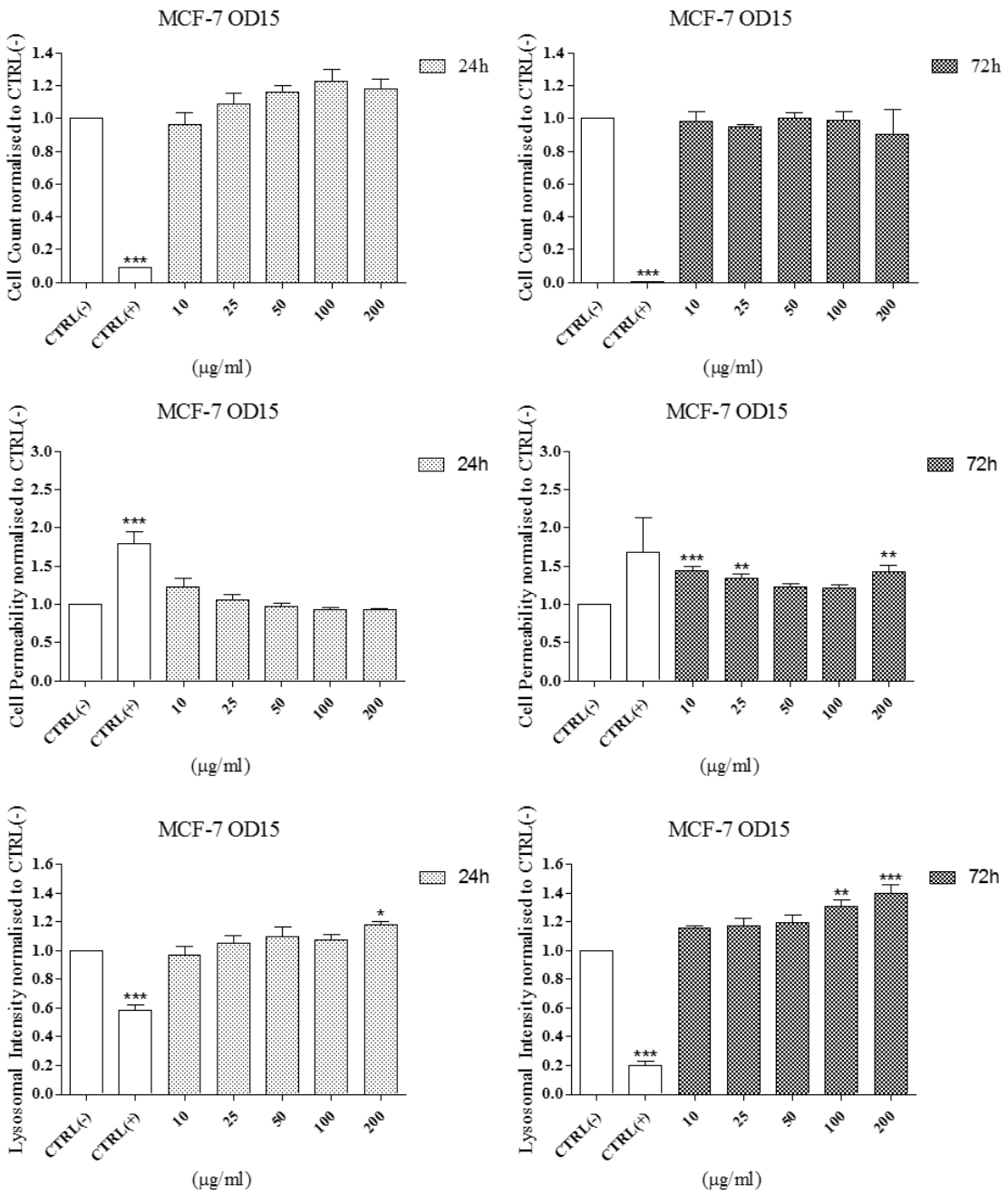

Figure S57: MCF-7 cell line exposed to OD15 MNP.

MCF-7 breast-derived cell line was exposed to OD15 MNP for 24h and 72h. Cells were stained using the Cytotoxicity II HitKit™ and analysed using the InCell 1000 HCSA device. Variation in cell count, cell membrane permeability and lysosomal intensity were measured compared to untreated control (CTRL(-)) and 1µM CdSe positive control (CTRL(+)). Statistical significance was determined using the one way ANOVA with Tukey post-test for each column compared to untreated control (CTRL(-)). p value: *** = <0.001, **=<0.01, *=<0.05

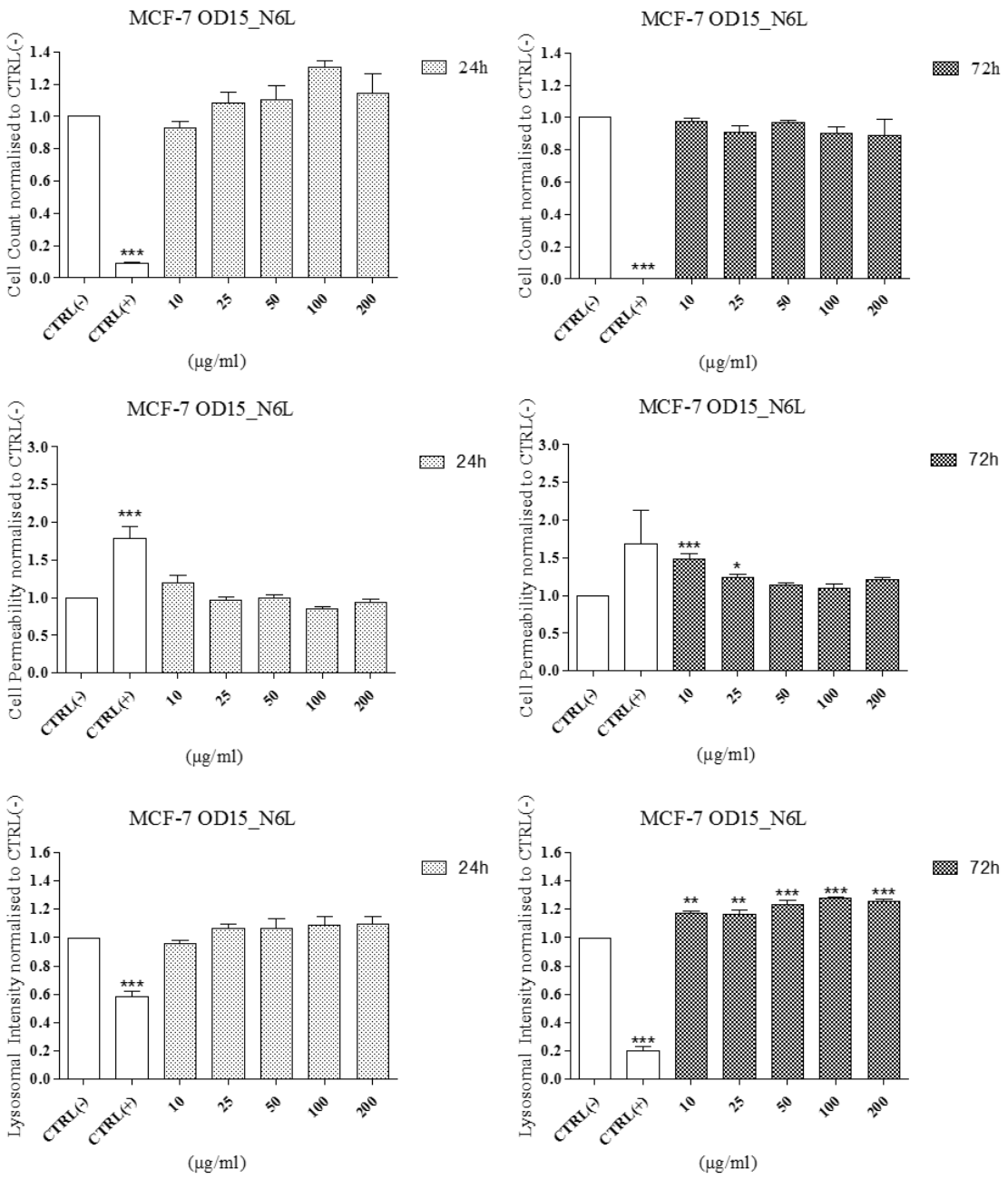

Figure S58: MCF-7 cell line exposed to OD15_N6L MNP.

MCF-7 breast-derived cell line was exposed to OD15_N6L MNP for 24h and 72h. Cells were stained using the Cytotoxicity II HitKit™ and analysed using the InCell 1000 HCSA device. Variation in cell count, cell membrane permeability and lysosomal intensity were measured compared to untreated control (CTRL(-)) and 1µM CdSe positive control (CTRL(+)). Statistical significance was determined using the one way ANOVA with Tukey post-test for each column compared to untreated control (CTRL(-)). p value: *** = <0.001, **=<0.01, *=<0.05

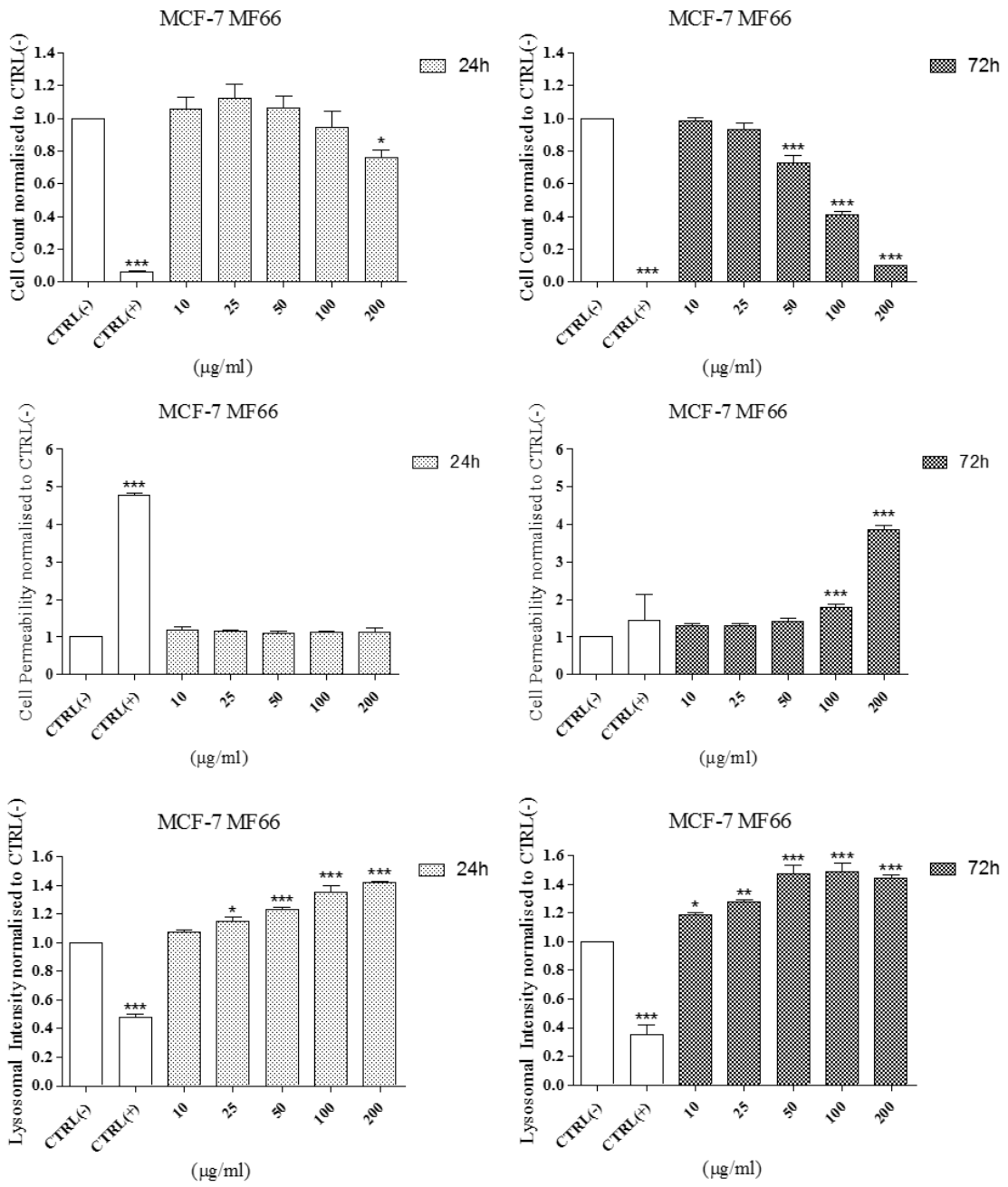

Figure S59: MCF-7 cell line exposed to MF66 MNP.

MCF-7 breast-derived cell line was exposed to MF66 MNP for 24h and 72h. Cells were stained using the Cytotoxicity II HitKit™ and analysed using the InCell 1000 HCSA device. Variation in cell count, cell membrane permeability and lysosomal intensity were measured compared to untreated control (CTRL(-)) and 1µM CdSe positive control (CTRL(+)). Statistical significance was determined using the one way ANOVA with Tukey post-test for each column compared to untreated control (CTRL(-)). p value: *** = <0.001, **=<0.01, *=<0.05

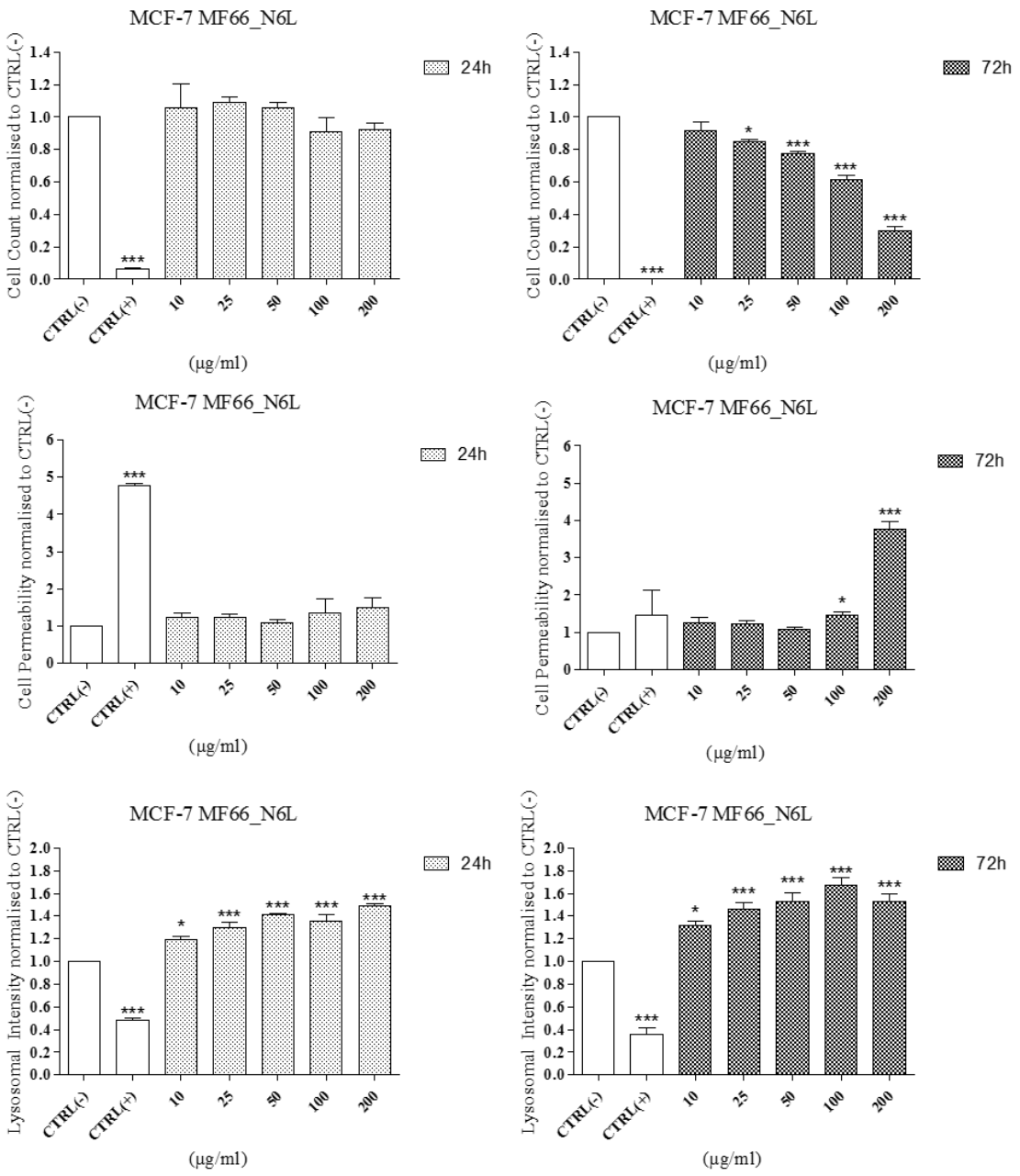

Figure S60: MCF-7 cell line exposed to MF66_N6L MNP.

MCF-7 breast-derived cell line was exposed to MF66_N6L MNP for 24h and 72h. Cells were stained using the Cytotoxicity II HitKit™ and analysed using the InCell 1000 HCSA device. Variation in cell count, cell membrane permeability and lysosomal intensity were measured compared to untreated control (CTRL(-)) and 1µM CdSe positive control (CTRL(+)). Statistical significance was determined using the one way ANOVA with Tukey post-test for each column compared to untreated control (CTRL(-)). p value: *** = <0.001, **=<0.01, *=<0.05

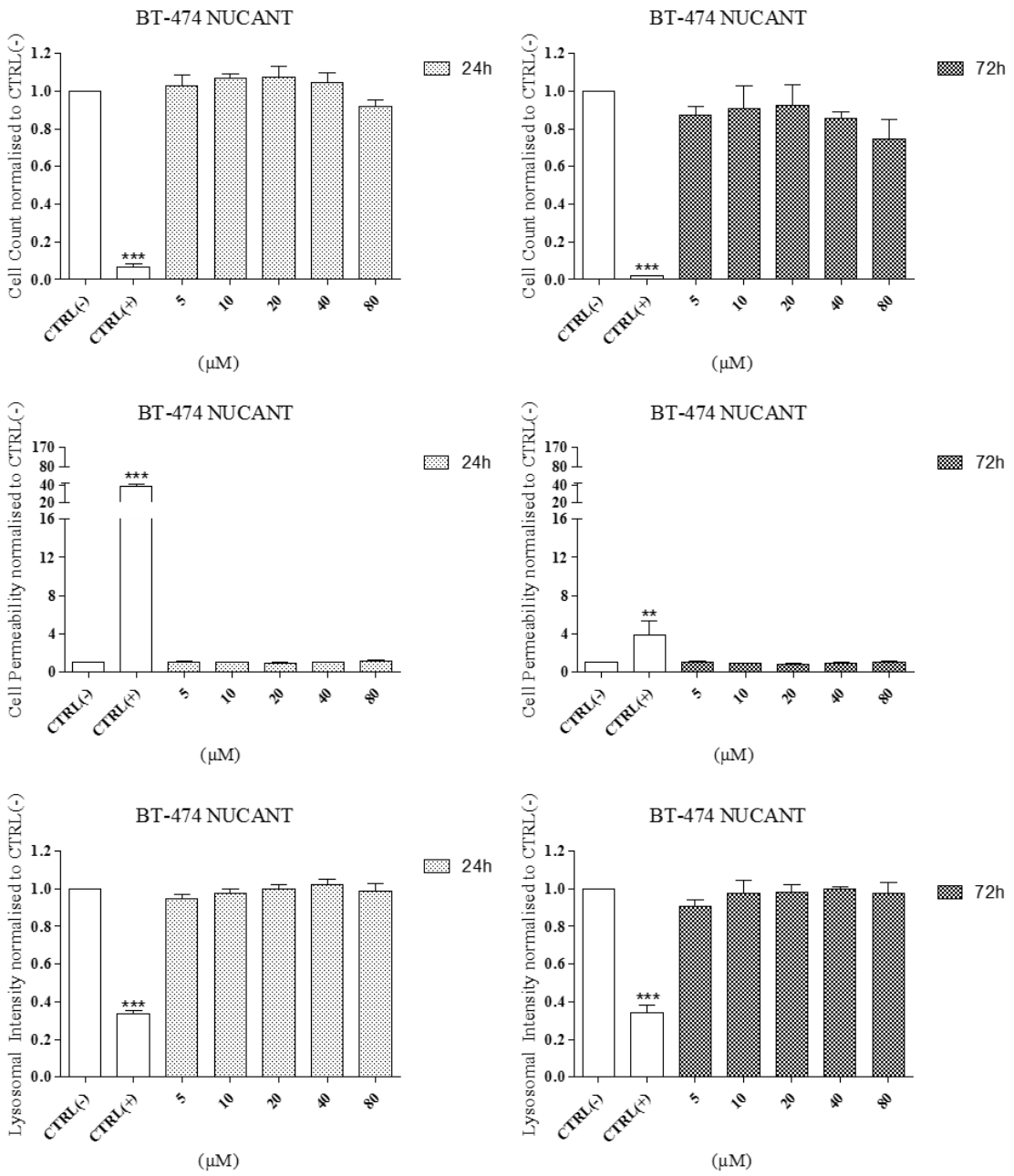

Figure S61: BT-474 cell line exposed to NUCANT pseudopeptide.

BT-474 breast-derived cell line was exposed to NUCANT pseudopeptide for 24h and 72h. Cells were stained using the Cytotoxicity II HitKit™ and analysed using the InCell 1000 HCSA device. Variation in cell count, cell membrane permeability and lysosomal intensity were measured compared to untreated control (CTRL(-)) and 1µM CdSe positive control (CTRL(+)). Statistical significance was determined using the one way ANOVA with Tukey post-test for each column compared to untreated control (CTRL(-)). p value: *** = <0.001, **=<0.01, *=<0.05

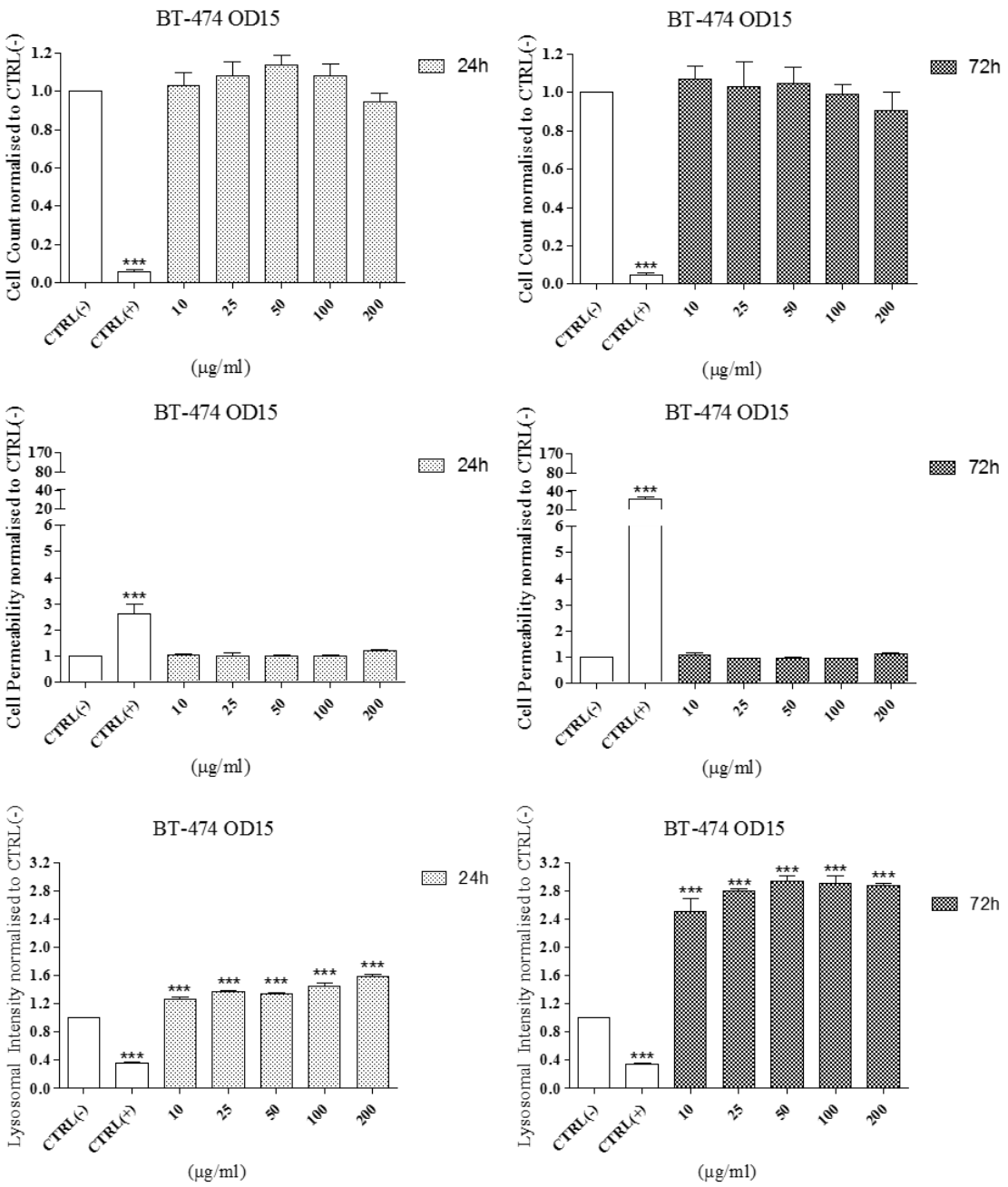

Figure S62: BT-474 cell line exposed to OD15 MNP.

BT-474 breast-derived cell line was exposed to OD15 MNP for 24h and 72h. Cells were stained using the Cytotoxicity II HitKit™ and analysed using the InCell 1000 HCSA device. Variation in cell count, cell membrane permeability and lysosomal intensity were measured compared to untreated control (CTRL(-)) and 1µM CdSe positive control (CTRL(+)). Statistical significance was determined using the one way ANOVA with Tukey post-test for each column compared to untreated control (CTRL(-)). p value: *** = <0.001, **=<0.01, *=<0.05

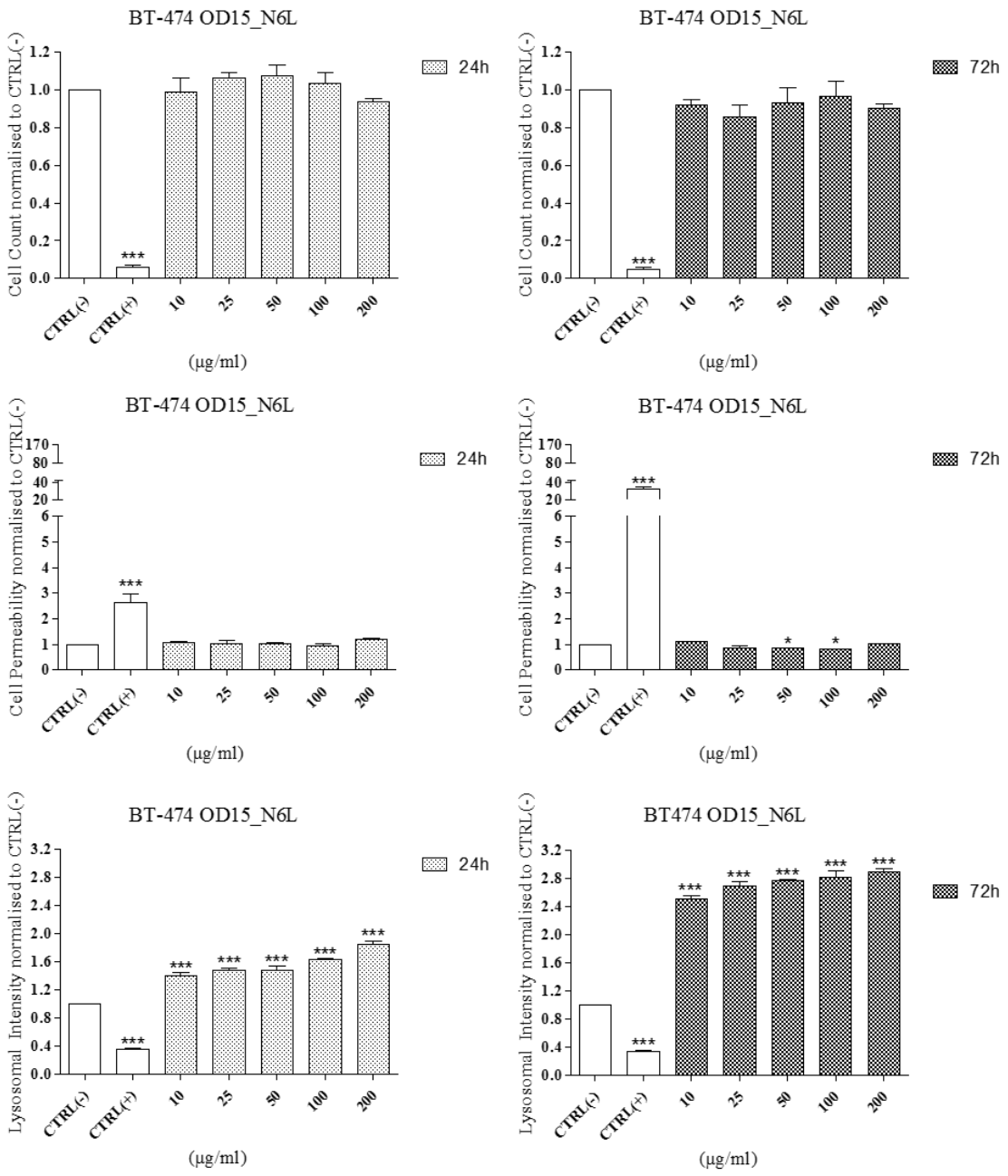

Figure S63: BT-474 cell line exposed to OD15_N6L MNP.

BT-474 breast-derived cell line was exposed to OD15_N6L MNP for 24h and 72h. Cells were stained using the Cytotoxicity II HitKit™ and analysed using the InCell 1000 HCSA device. Variation in cell count, cell membrane permeability and lysosomal intensity were measured compared to untreated control (CTRL(-)) and 1µM CdSe positive control (CTRL(+)). Statistical significance was determined using the one way ANOVA with Tukey post-test for each column compared to untreated control (CTRL(-)). p value: *** = <0.001, **=<0.01, *=<0.05

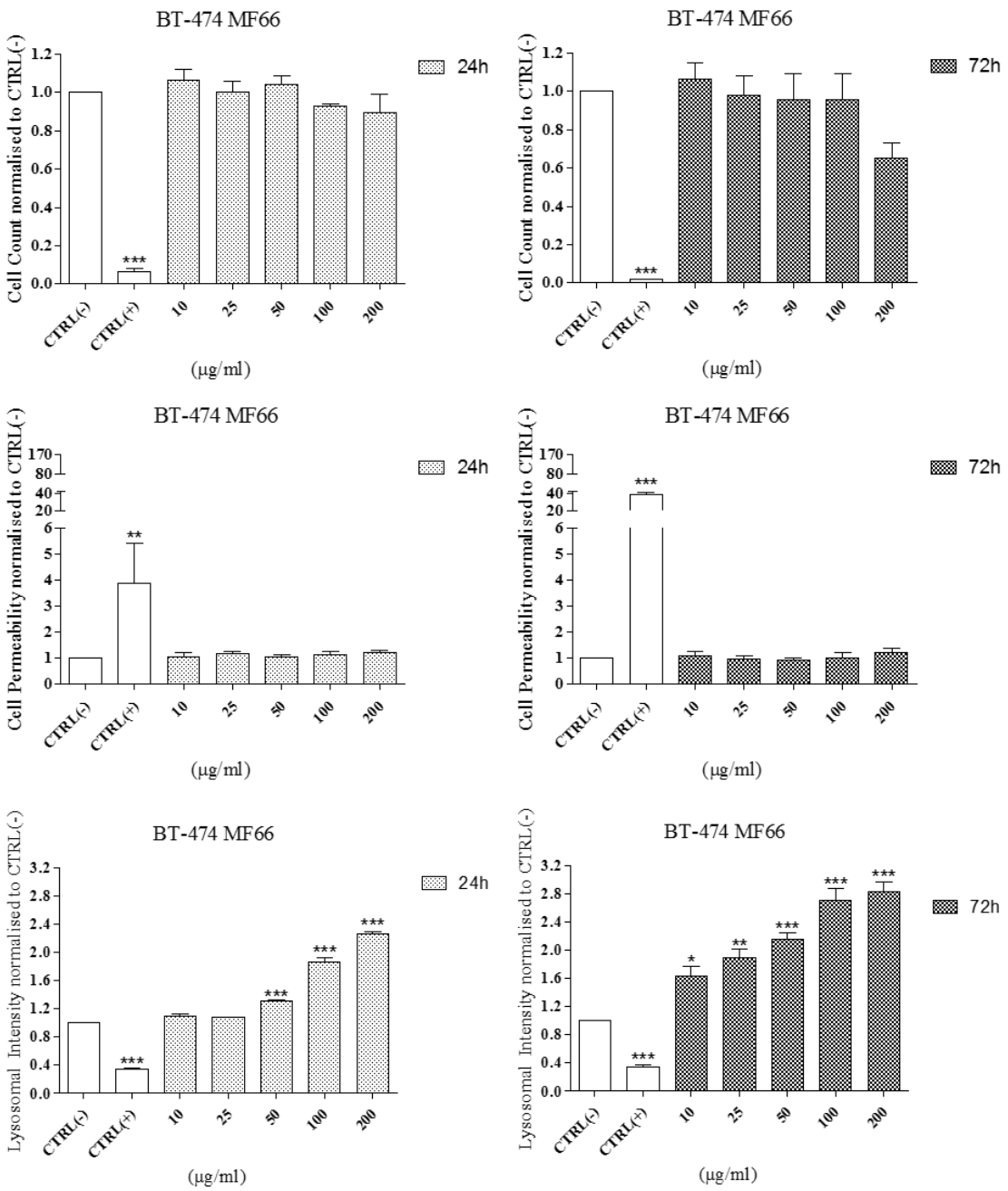

Figure S64: BT-474 cell line exposed to MF66 MNP.

BT-474 breast-derived cell line was exposed to MF66 MNP for 24h and 72h. Cells were stained using the Cytotoxicity II HitKit™ and analysed using the InCell 1000 HCSA device. Variation in cell count, cell membrane permeability and lysosomal intensity were measured compared to untreated control (CTRL(-)) and 1µM CdSe positive control (CTRL(+)). Statistical significance was determined using the one way ANOVA with Tukey post-test for each column compared to untreated control (CTRL(-)). p value: *** = <0.001, **=<0.01, *=<0.05

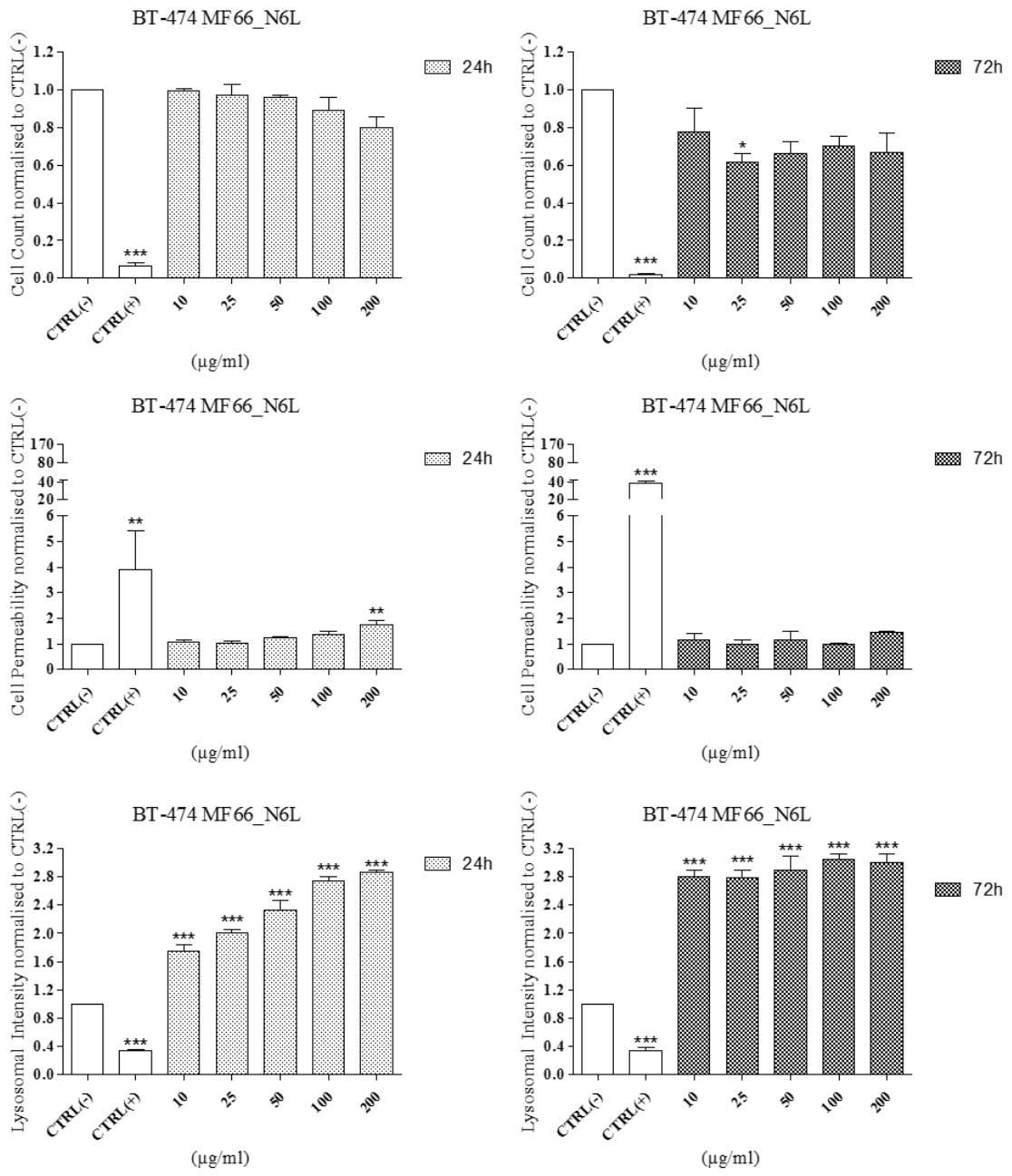

Figure S65: BT-474 cell line exposed to MF66_N6L MNP.

BT-474 breast-derived cell line was exposed to MF66_N6L MNP for 24h and 72h. Cells were stained using the Cytotoxicity II HitKit™ and analysed using the InCell 1000 HCSA device. Variation in cell count, cell membrane permeability and lysosomal intensity were measured compared to untreated control (CTRL(-)) and 1µM CdSe positive control (CTRL(+)). Statistical significance was determined using the one way ANOVA with Tukey post-test for each column compared to untreated control (CTRL(-)). p value: *** = <0.001, **=<0.01, *=<0.05

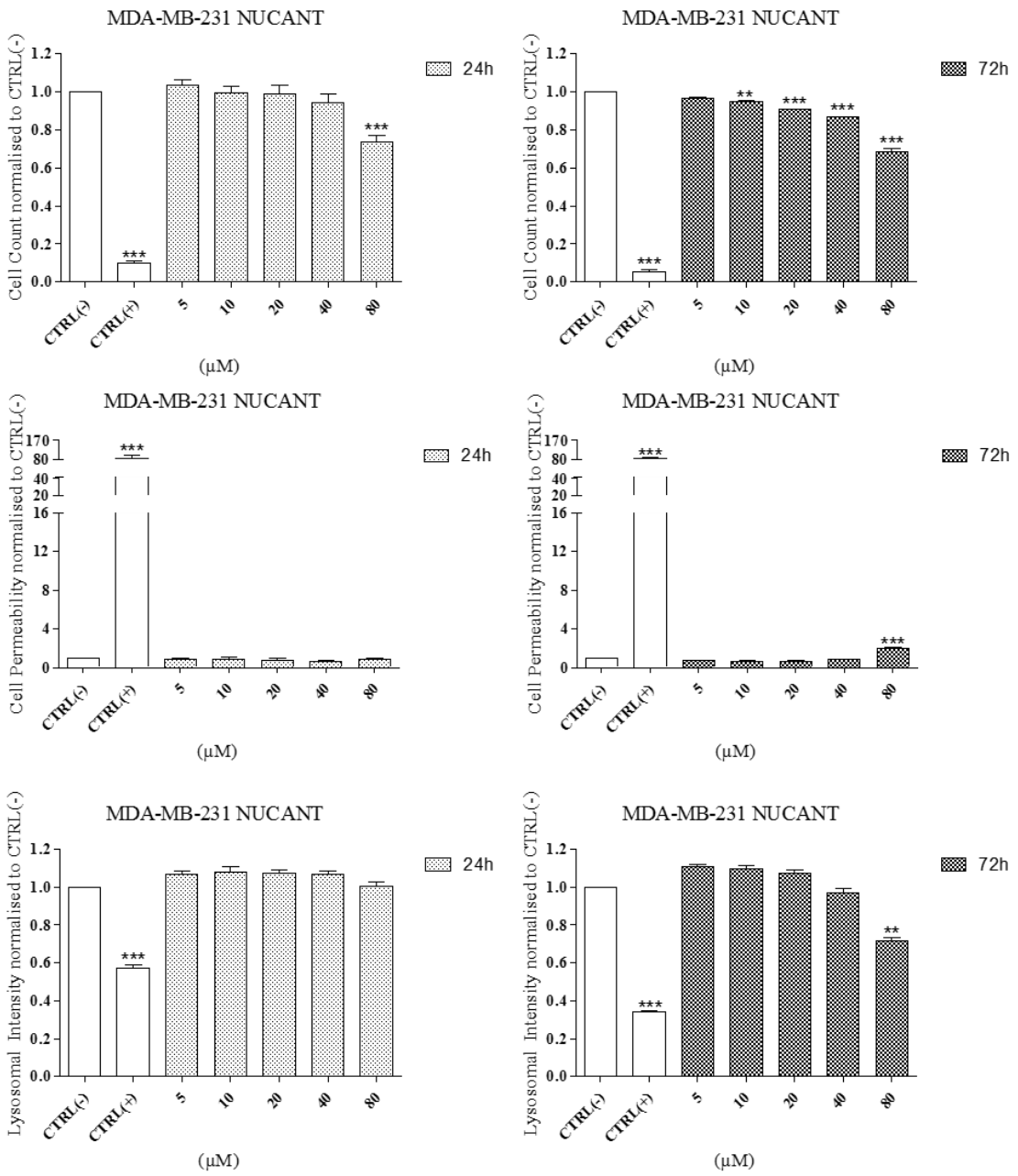

Figure S66: MDA-MB-231 cell line exposed to NUCANT pseudopeptide.

MDA-MB-231 breast-derived cell line was exposed to NUCANT pseudopeptide for 24h and 72h. Cells were stained using the Cytotoxicity II HitKit™ and analysed using the InCell 1000 HCSA device. Variation in cell count, cell membrane permeability and lysosomal intensity were measured compared to untreated control (CTRL(-)) and 1µM CdSe positive control (CTRL(+)). Statistical significance was determined using the one way ANOVA with Tukey post-test for each column compared to untreated control (CTRL(-)). p value: *** = <0.001, **=<0.01, *=<0.05

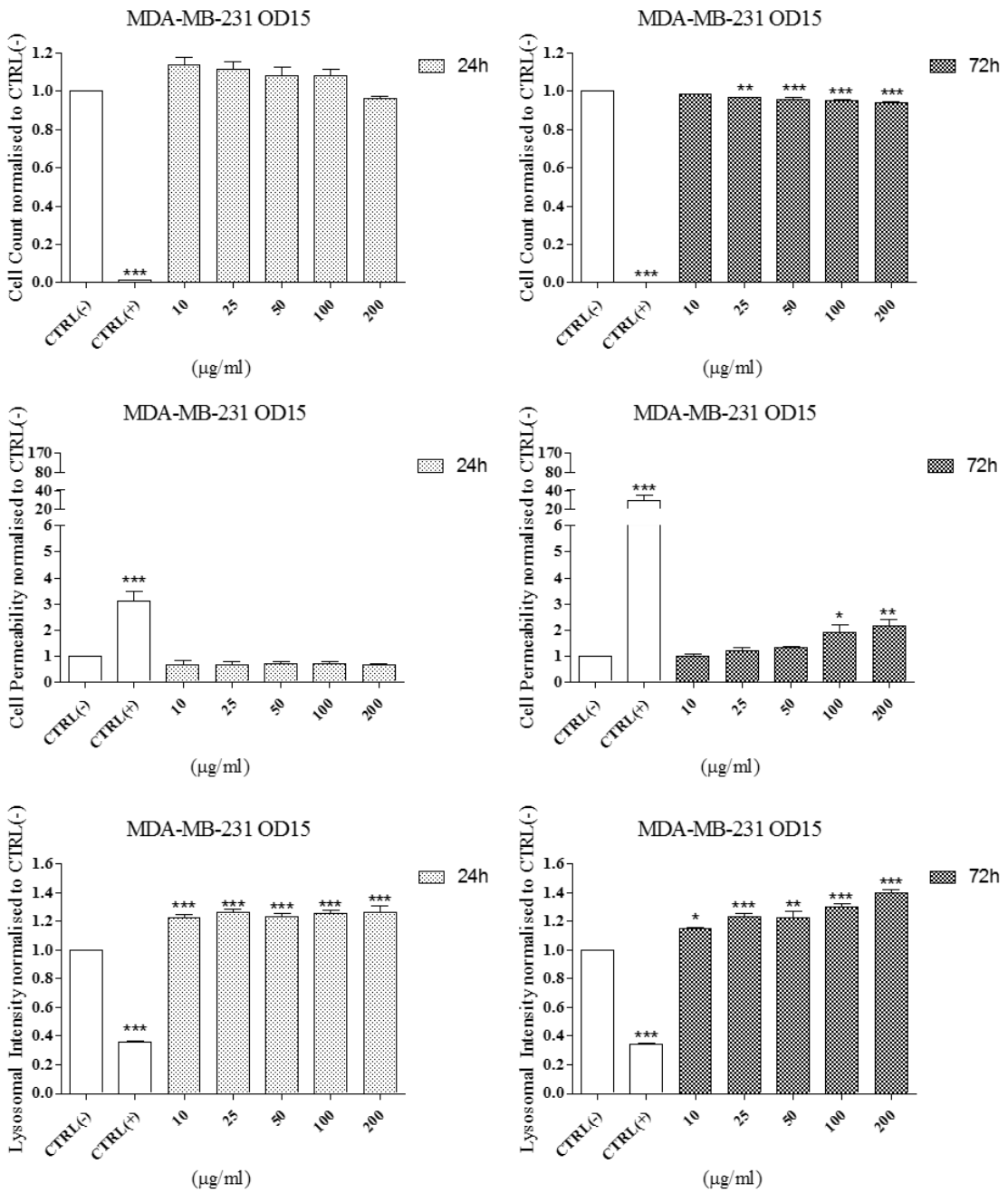

Figure S67: MDA-MB-231 cell line exposed to OD15 MNP.

MDA-MB-231 breast-derived cell line was exposed to OD15 MNP for 24h and 72h. Cells were stained using the Cytotoxicity II HitKit™ and analysed using the InCell 1000 HCSA device. Variation in cell count, cell membrane permeability and lysosomal intensity were measured compared to untreated control (CTRL(-)) and 1µM CdSe positive control (CTRL(+)). Statistical significance was determined using the one way ANOVA with Tukey post-test for each column compared to untreated control (CTRL(-)). p value: *** = <0.001, **=<0.01, *=<0.05

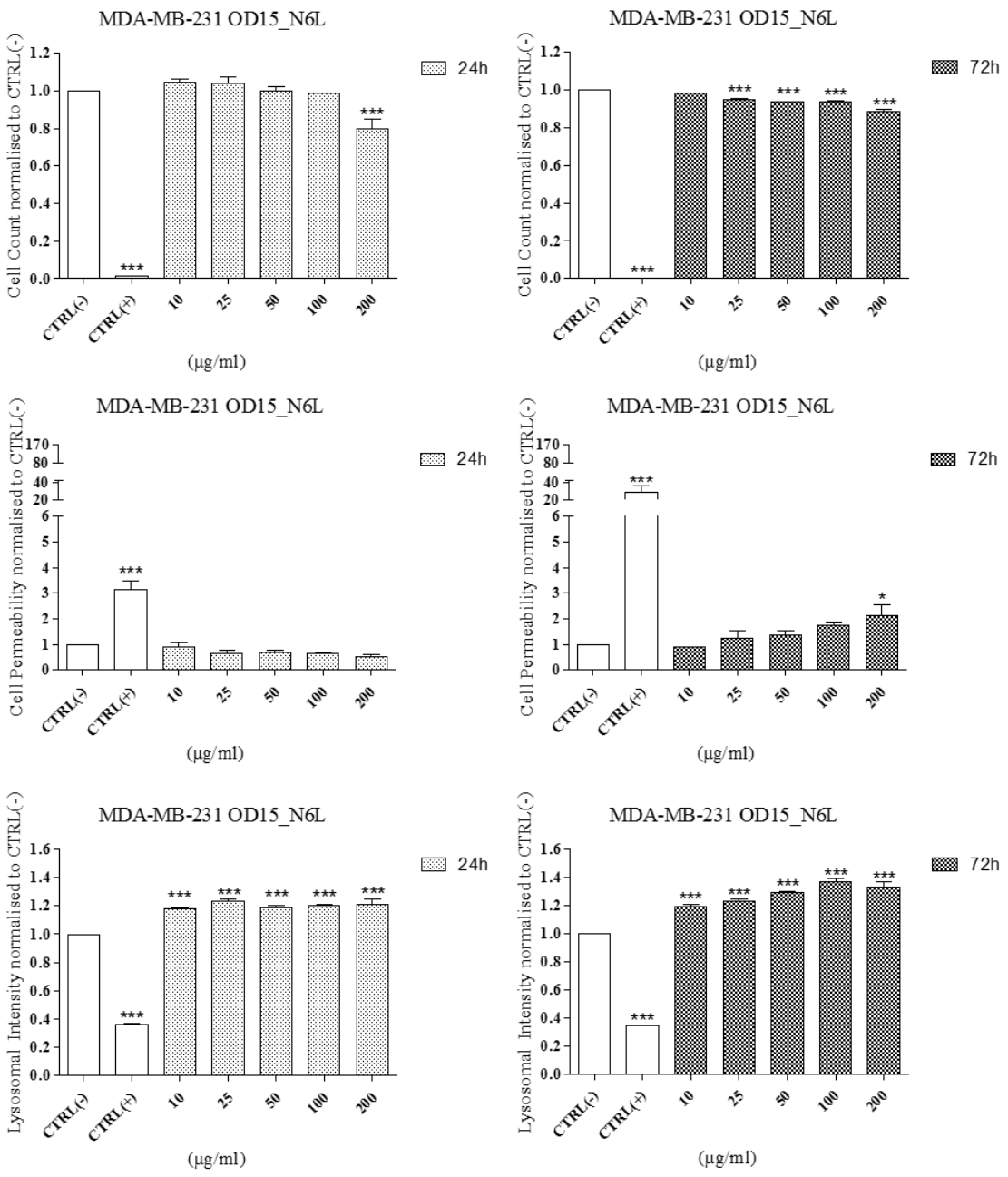

Figure S68: MDA-MB-231 cell line exposed to OD15_N6L MNP.

MDA-MB-231 breast-derived cell line was exposed to OD15_N6L MNP for 24h and 72h. Cells were stained using the Cytotoxicity II HitKit™ and analysed using the InCell 1000 HCSA device. Variation in cell count, cell membrane permeability and lysosomal intensity were measured compared to untreated control (CTRL(-)) and 1µM CdSe positive control (CTRL(+)). Statistical significance was determined using the one way ANOVA with Tukey post-test for each column compared to untreated control (CTRL(-)). p value: *** = <0.001, **=<0.01, *=<0.05

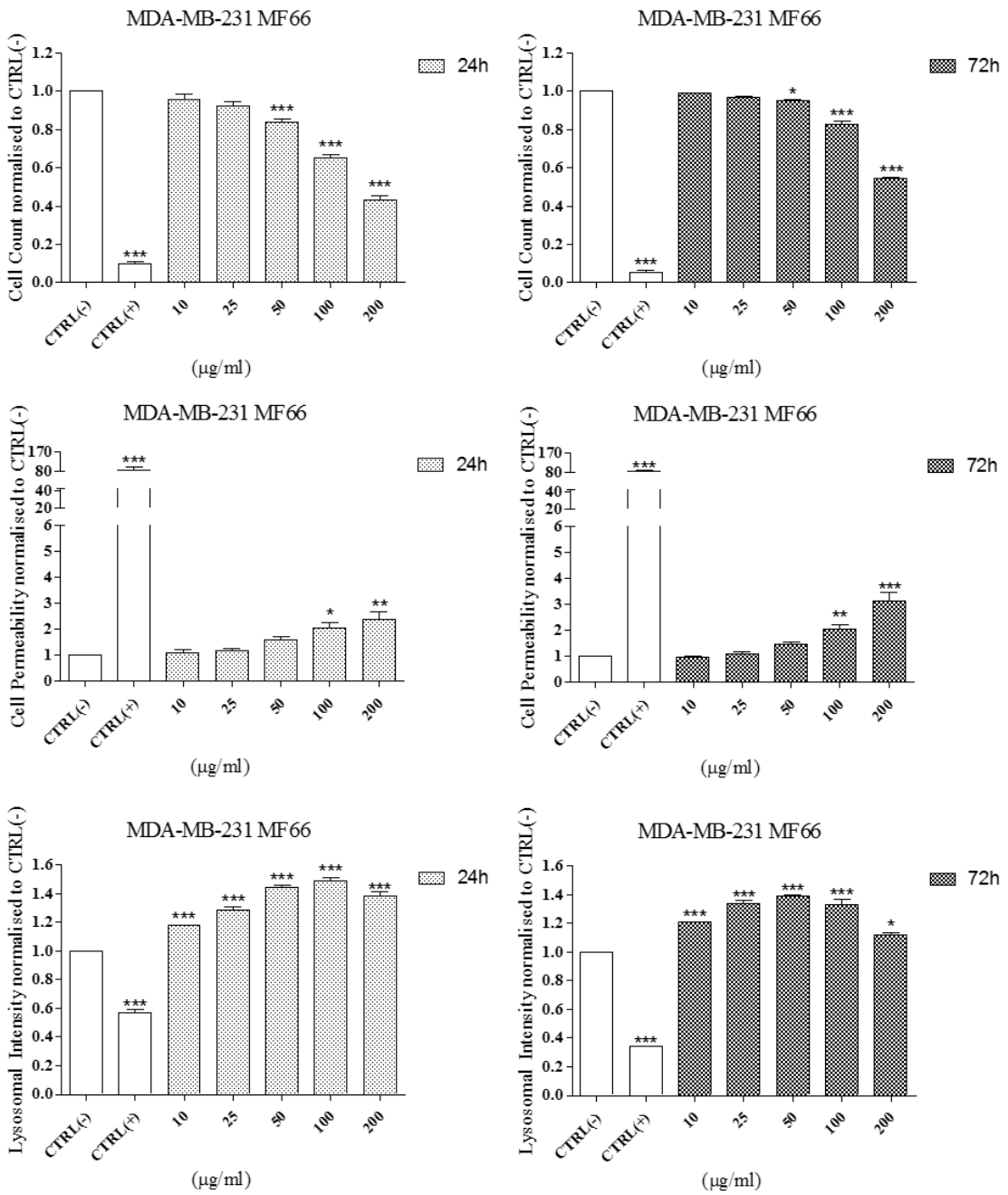

Figure S69: MDA-MB-231 cell line exposed to MF66 MNP.

MDA-MB-231 breast-derived cell line was exposed to MF66 MNP for 24h and 72h. Cells were stained using the Cytotoxicity II HitKit™ and analysed using the InCell 1000 HCSA device. Variation in cell count, cell membrane permeability and lysosomal intensity were measured compared to untreated control (CTRL(-)) and 1µM CdSe positive control (CTRL(+)). Statistical significance was determined using the one way ANOVA with Tukey post-test for each column compared to untreated control (CTRL(-)). p value: *** = <0.001, **=<0.01, *=<0.05

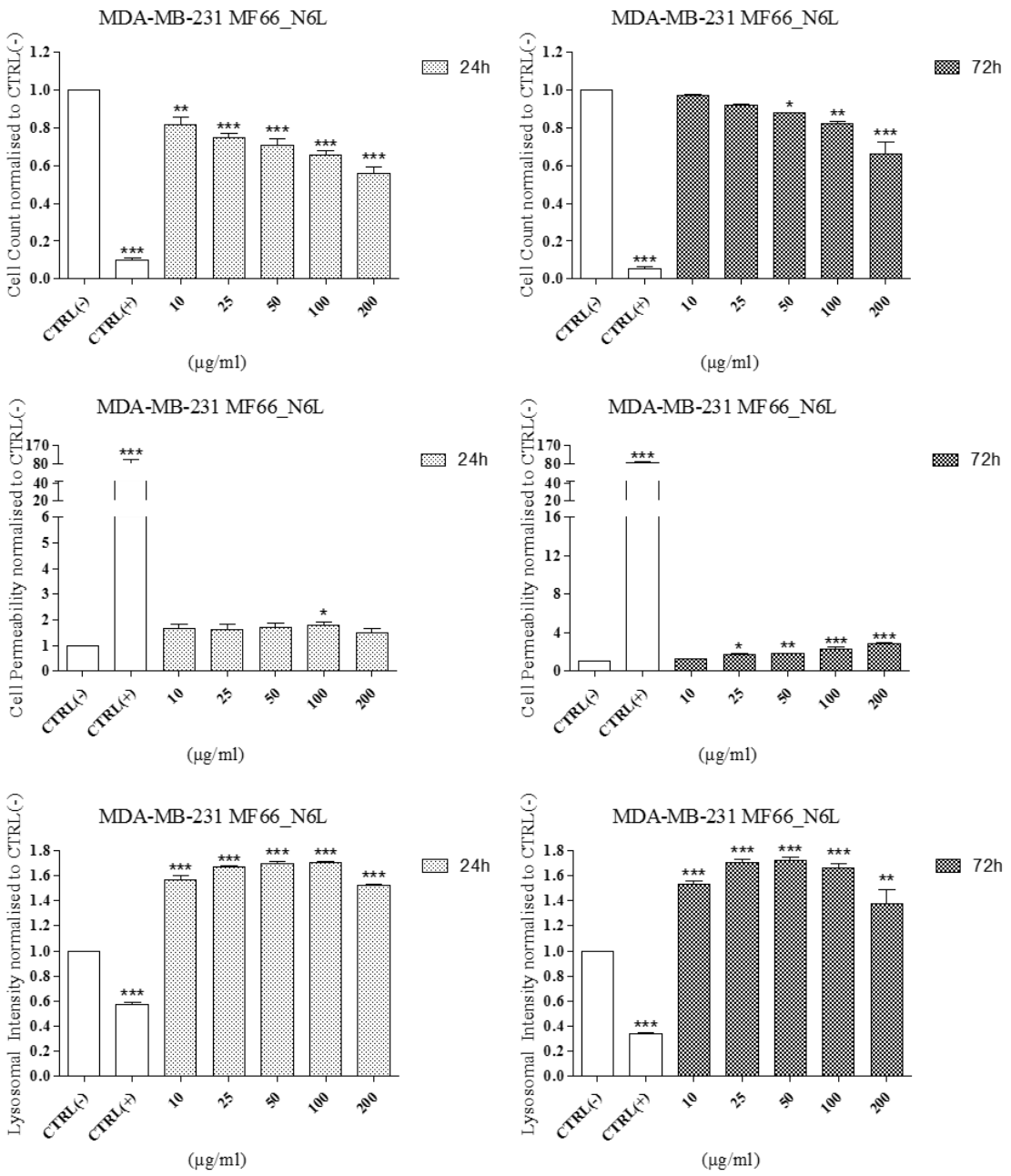

Figure S70: MDA-MB-231 cell line exposed to MF66_N6L MNP.

MDA-MB-231 breast-derived cell line was exposed to MF66_N6L MNP for 24h and 72h. Cells were stained using the Cytotoxicity II HitKit™ and analysed using the InCell 1000 HCSA device. Variation in cell count, cell membrane permeability and lysosomal intensity were measured compared to untreated control (CTRL(-)) and 1µM CdSe positive control (CTRL(+)). Statistical significance was determined using the one way ANOVA with Tukey post-test for each column compared to untreated control (CTRL(-)). p value: *** = <0.001, **=<0.01, *=<0.05

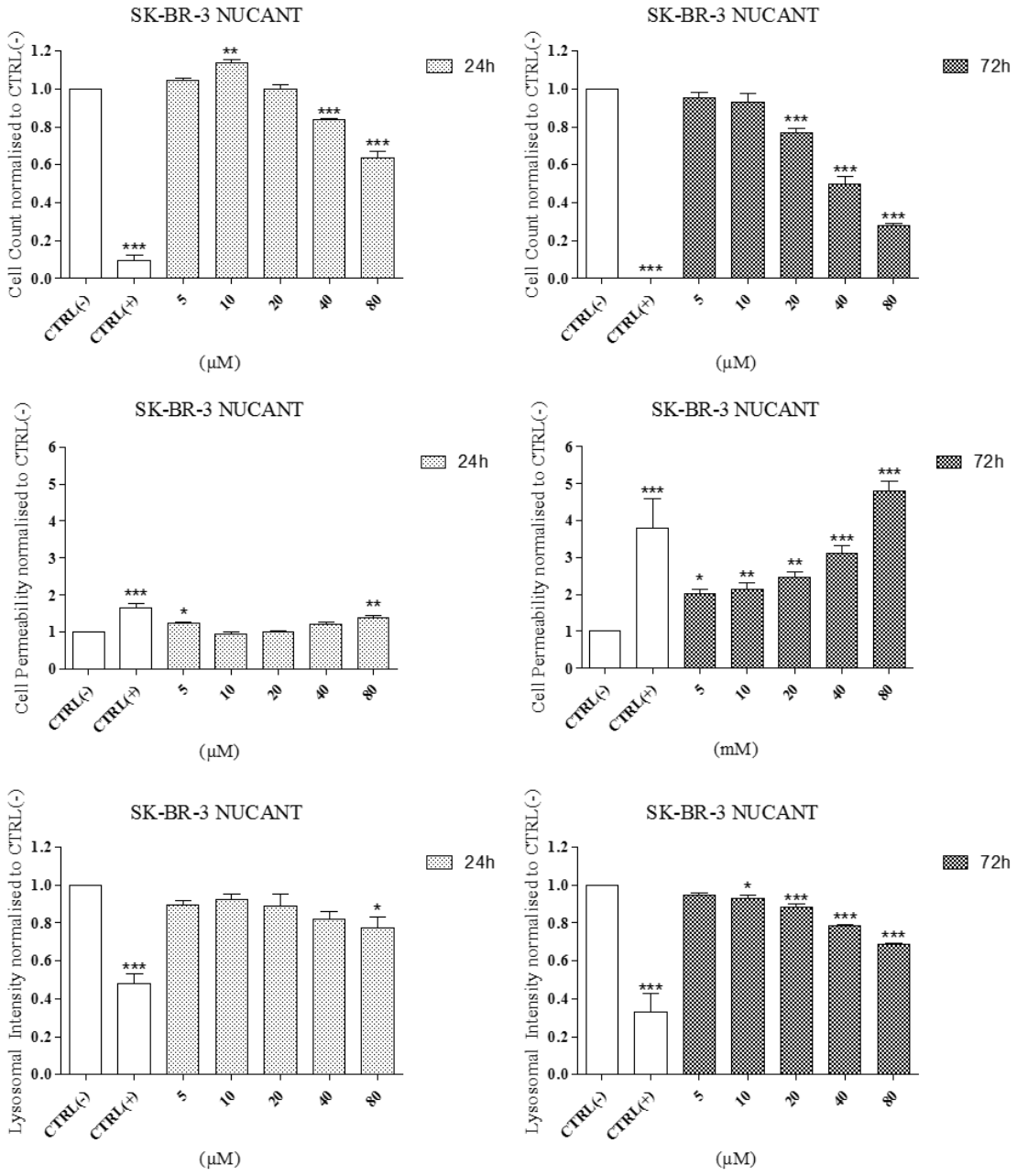

Figure S71: SK-BR-3 cell line exposed to NUCANT pseudopeptide.

SK-BR-3 breast-derived cell line was exposed to NUCANT pseudopeptide for 24h and 72h. Cells were stained using the Cytotoxicity II HitKit™ and analysed using the InCell 1000 HCSA device. Variation in cell count, cell membrane permeability and lysosomal intensity were measured compared to untreated control (CTRL(-)) and 1µM CdSe positive control (CTRL(+)). Statistical significance was determined using the one way ANOVA with Tukey post-test for each column compared to untreated control (CTRL(-)). p value: *** = <0.001, **=<0.01, *=<0.05

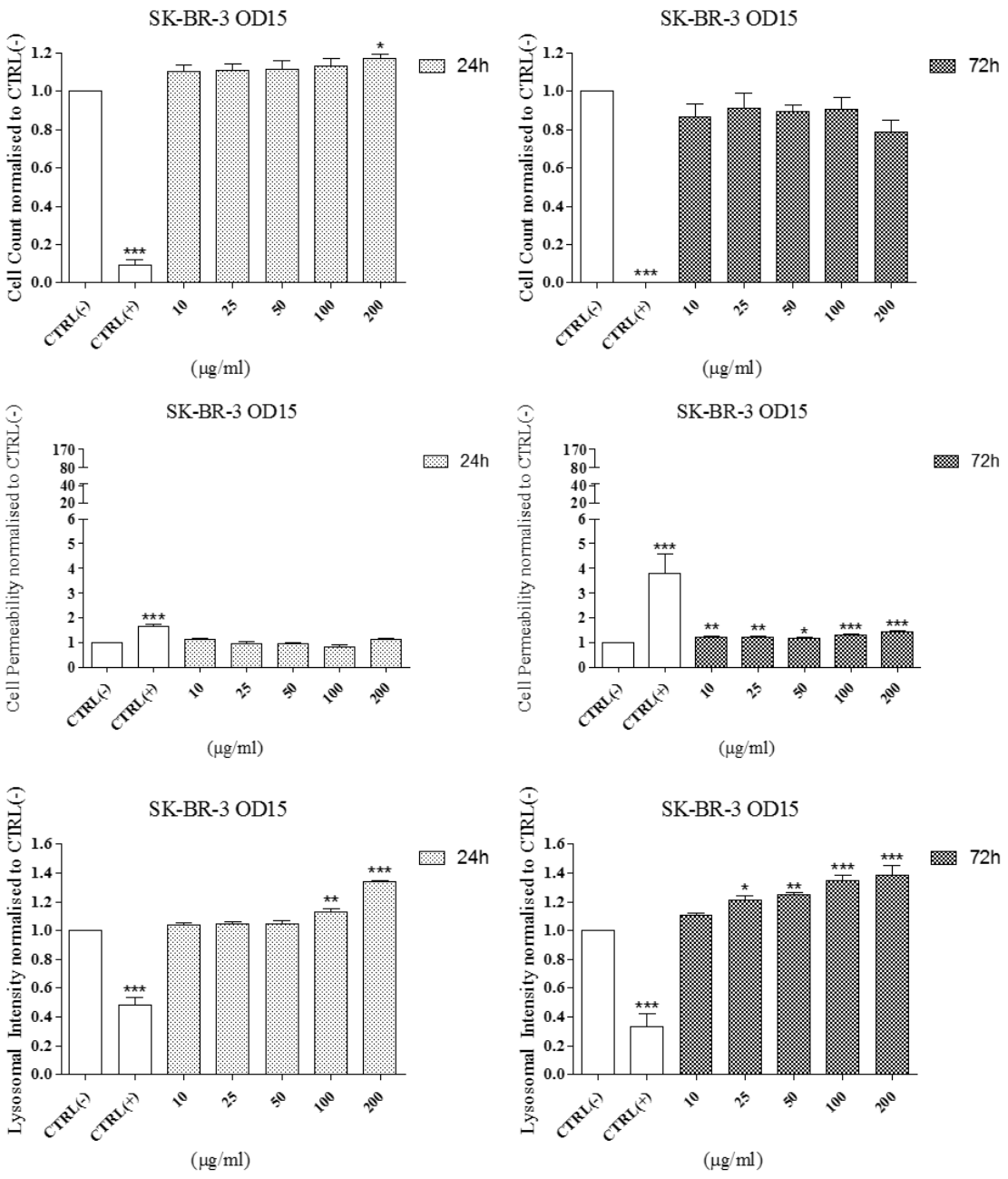

Figure S72: SK-BR-3 cell line exposed to OD15 MNP.

SK-BR-3 breast-derived cell line was exposed to OD15 MNP for 24h and 72h. Cells were stained using the Cytotoxicity II HitKit™ and analysed using the InCell 1000 HCSA device. Variation in cell count, cell membrane permeability and lysosomal intensity were measured compared to untreated control (CTRL(-)) and 1µM CdSe positive control (CTRL(+)). Statistical significance was determined using the one way ANOVA with Tukey post-test for each column compared to untreated control (CTRL(-)). p value: *** = <0.001, **=<0.01, *=<0.05

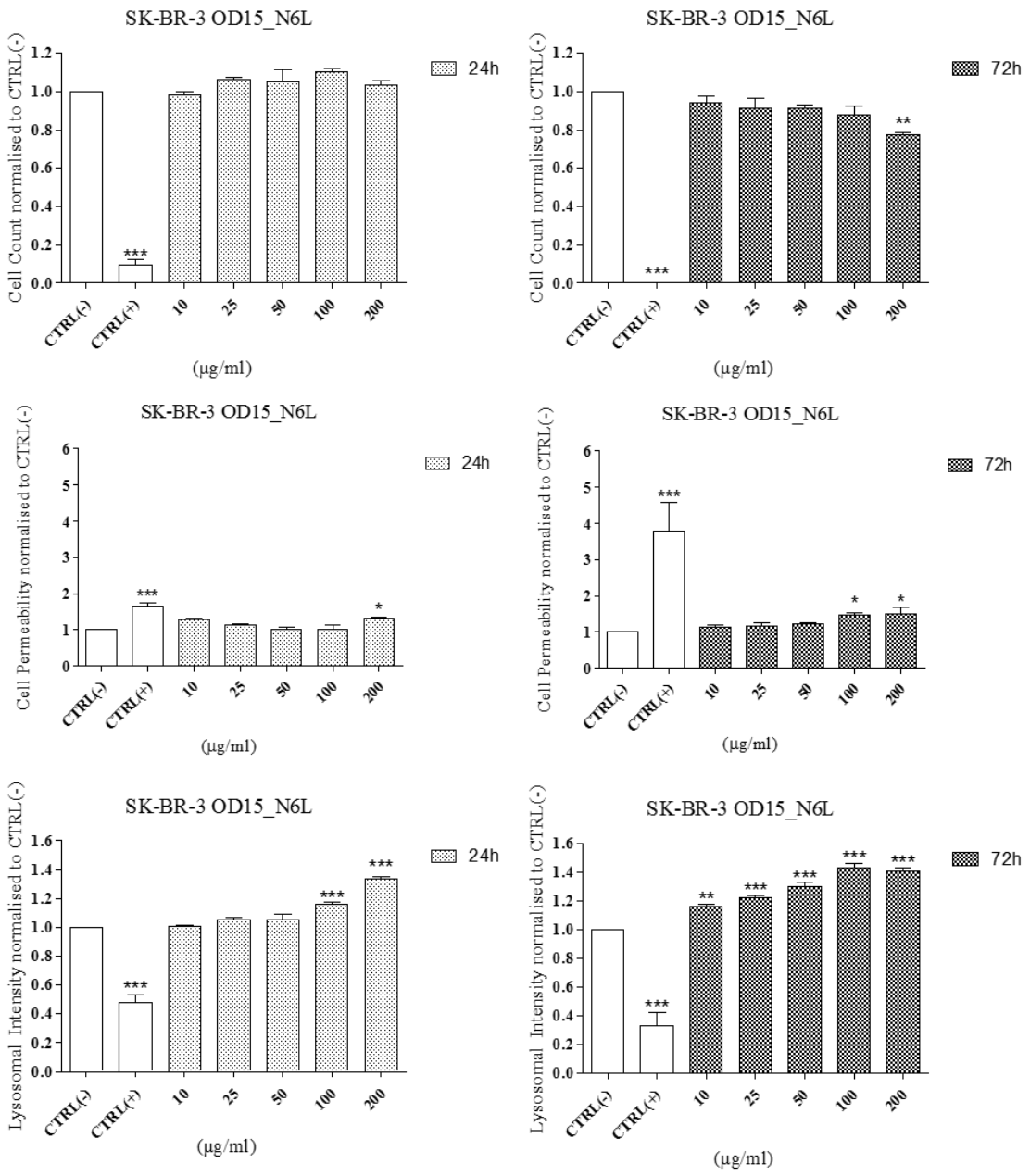

Figure S73: SK-BR-3 cell line exposed to OD15_N6L MNP.

SK-BR-3 breast-derived cell line was exposed to OD15_N6L MNP for 24h and 72h. Cells were stained using the Cytotoxicity II HitKit™ and analysed using the InCell 1000 HCSA device. Variation in cell count, cell membrane permeability and lysosomal intensity were measured compared to untreated control (CTRL(-)) and 1µM CdSe positive control (CTRL(+)). Statistical significance was determined using the one way ANOVA with Tukey post-test for each column compared to untreated control (CTRL(-)). p value: *** = <0.001, **=<0.01, *=<0.05

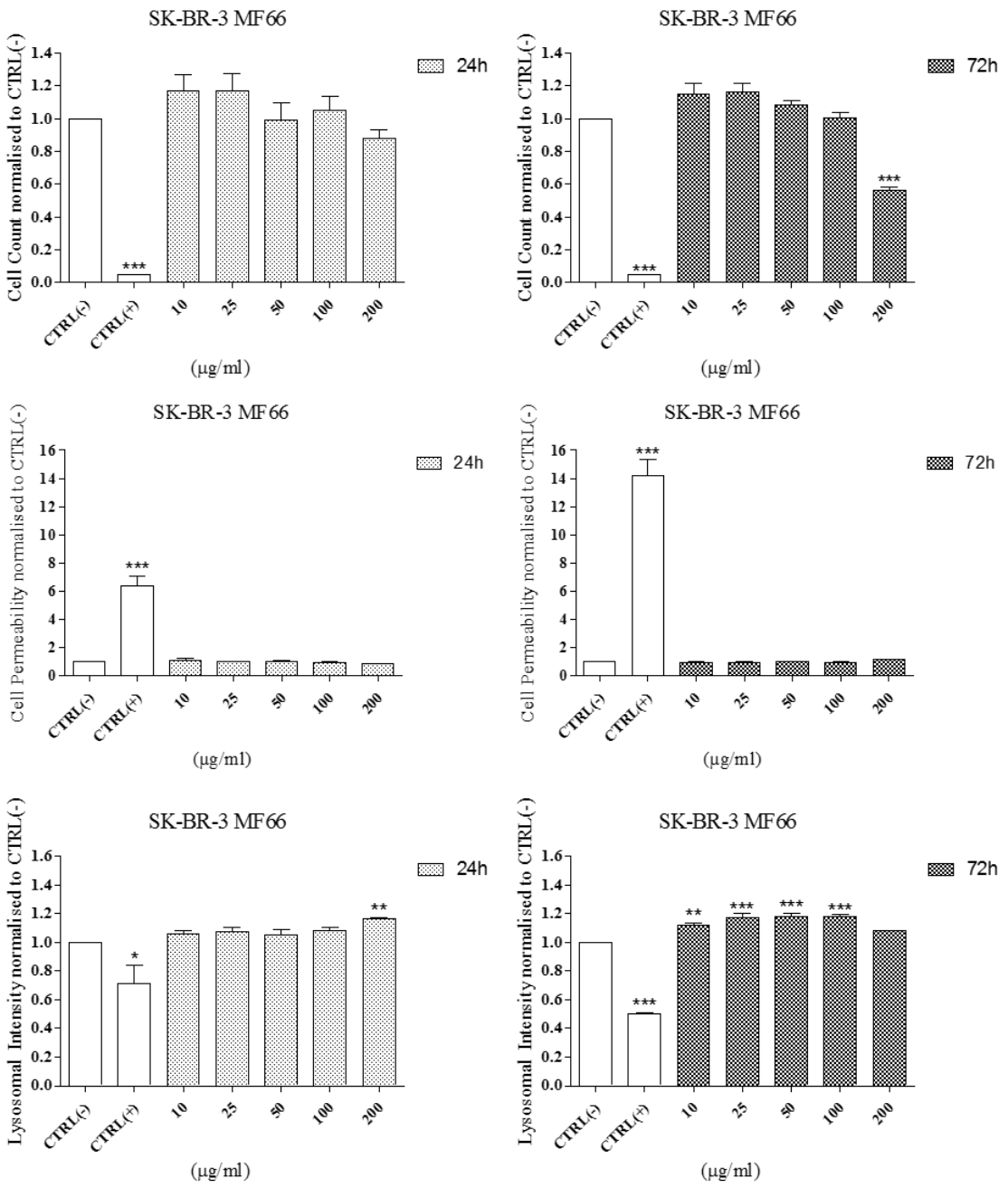

Figure S74: SK-BR-3 cell line exposed to MF66 MNP.

SK-BR-3 breast-derived cell line was exposed to MF66 MNP for 24h and 72h. Cells were stained using the Cytotoxicity II HitKit™ and analysed using the InCell 1000 HCSA device. Variation in cell count, cell membrane permeability and lysosomal intensity were measured compared to untreated control (CTRL(-)) and 1µM CdSe positive control (CTRL(+)). Statistical significance was determined using the one way ANOVA with Tukey post-test for each column compared to untreated control (CTRL(-)). p value: *** = <0.001, **=<0.01, *=<0.05

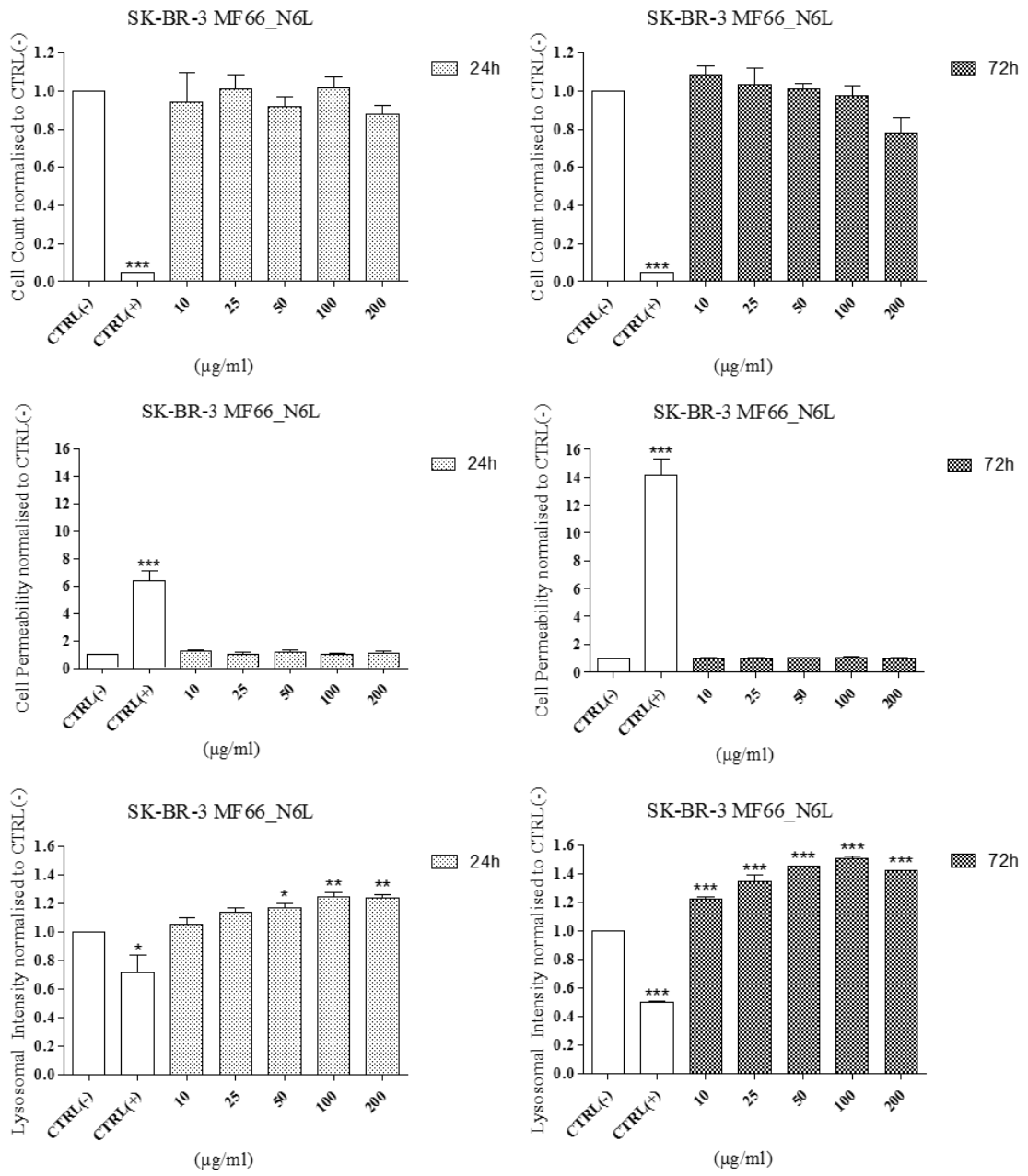

Figure S75: SK-BR-3 cell line exposed to MF66_N6L MNP.

SK-BR-3 breast-derived cell line was exposed to MF66_N6L MNP for 24h and 72h. Cells were stained using the Cytotoxicity II HitKit™ and analysed using the InCell 1000 HCSA device. Variation in cell count, cell membrane permeability and lysosomal intensity were measured compared to untreated control (CTRL(-)) and 1µM CdSe positive control (CTRL(+)). Statistical significance was determined using the one way ANOVA with Tukey post-test for each column compared to untreated control (CTRL(-)). p value: *** = <0.001, **=<0.01, *=<0.05

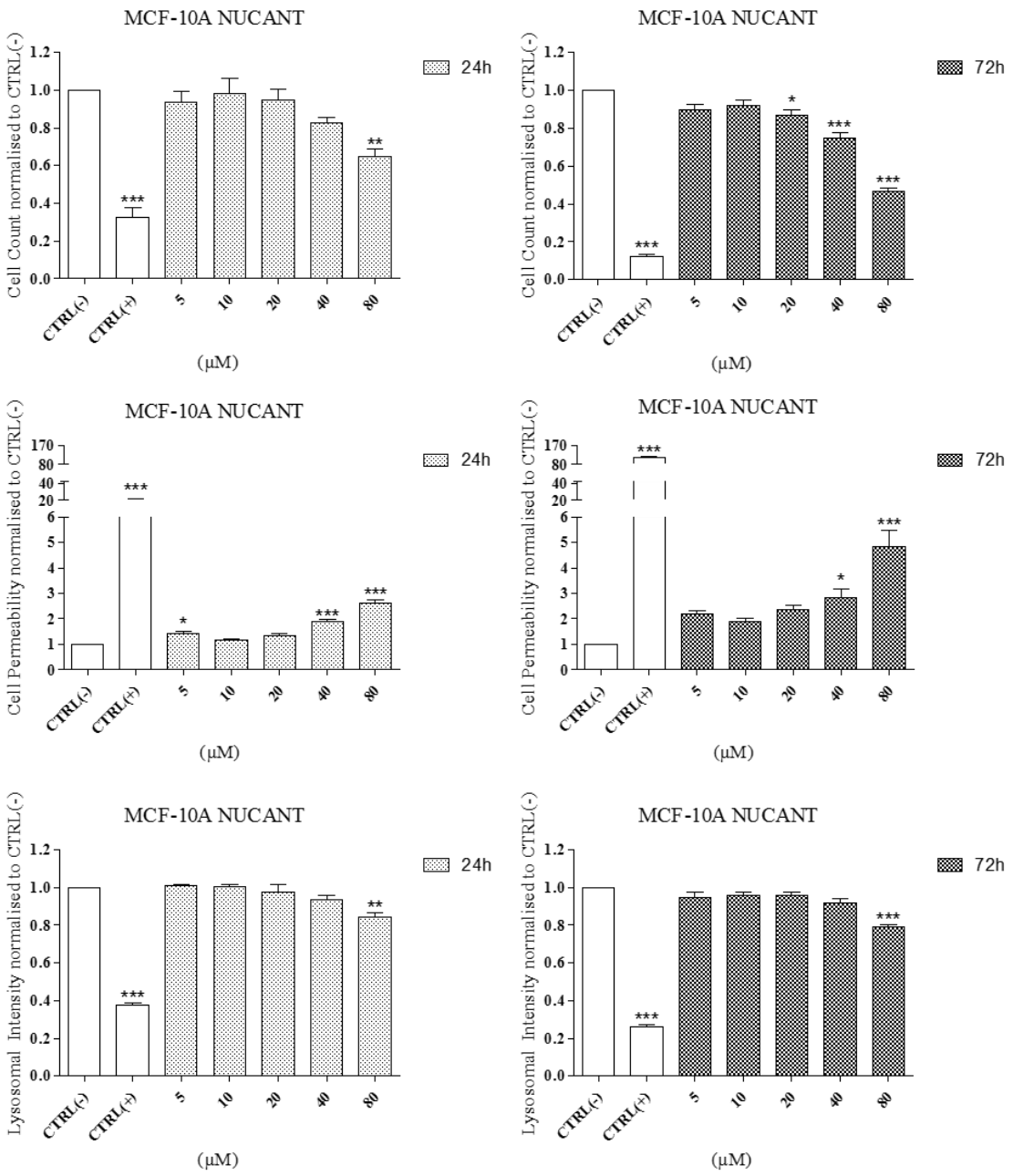

Figure S76: MCF-10A cell line exposed to NUCANT pseudopeptide.

MCF-10A breast-derived cell line was exposed to NUCANT pseudopeptide for 24h and 72h. Cells were stained using the Cytotoxicity II HitKit™ and analysed using the InCell 1000 HCSA device. Variation in cell count, cell membrane permeability and lysosomal intensity were measured compared to untreated control (CTRL(-)) and 1µM CdSe positive control (CTRL(+)). Statistical significance was determined using the one way ANOVA with Tukey post-test for each column compared to untreated control (CTRL(-)). p value: *** = <0.001, **=<0.01, *=<0.05

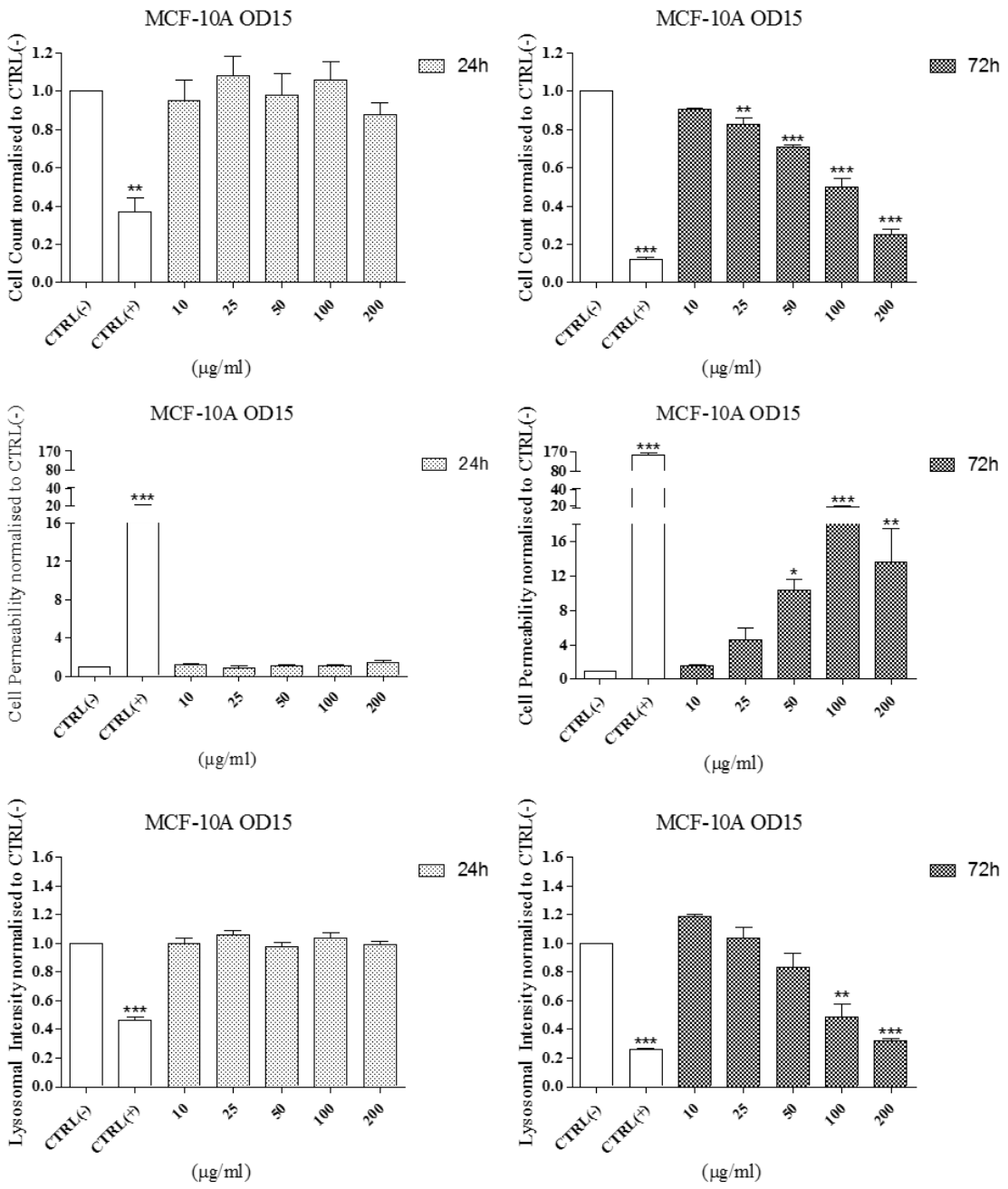

Figure S77: MCF-10A cell line exposed to OD15 MNP.

MCF-10A breast-derived cell line was exposed to OD15 MNP for 24h and 72h. Cells were stained using the Cytotoxicity II HitKit™ and analysed using the InCell 1000 HCSA device. Variation in cell count, cell membrane permeability and lysosomal intensity were measured compared to untreated control (CTRL(-)) and 1µM CdSe positive control (CTRL(+)). Statistical significance was determined using the one way ANOVA with Tukey post-test for each column compared to untreated control (CTRL(-)). p value: *** = <0.001, **=<0.01, *=<0.05

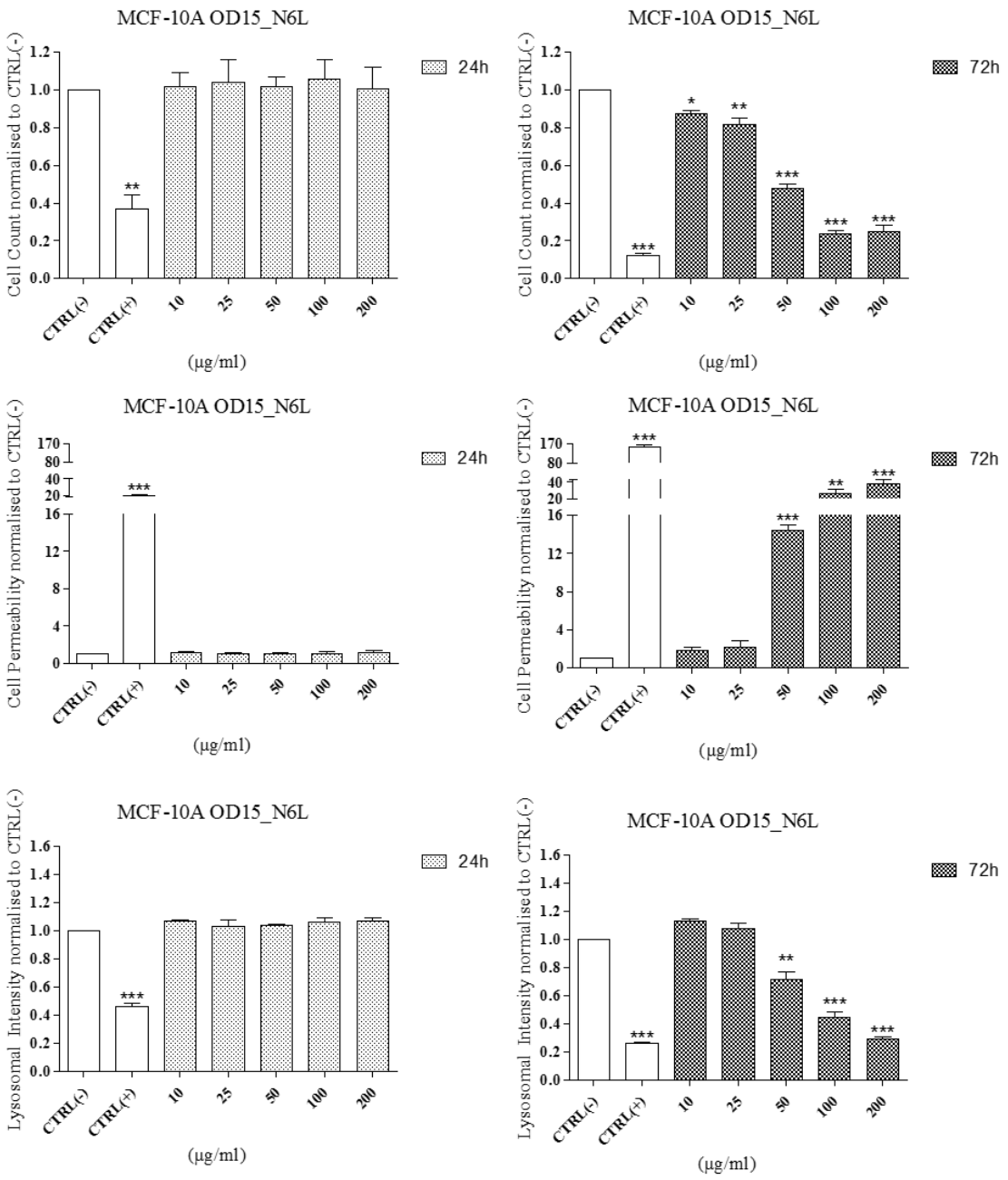

Figure S78: MCF-10A cell line exposed to OD15_N6L MNP.

MCF-10A breast-derived cell line was exposed to OD15_N6L MNP for 24h and 72h. Cells were stained using the Cytotoxicity II HitKit™ and analysed using the InCell 1000 HCSA device. Variation in cell count, cell membrane permeability and lysosomal intensity were measured compared to untreated control (CTRL(-)) and 1µM CdSe positive control (CTRL(+)). Statistical significance was determined using the one way ANOVA with Tukey post-test for each column compared to untreated control (CTRL(-)). p value: *** = <0.001, **=<0.01, *=<0.05

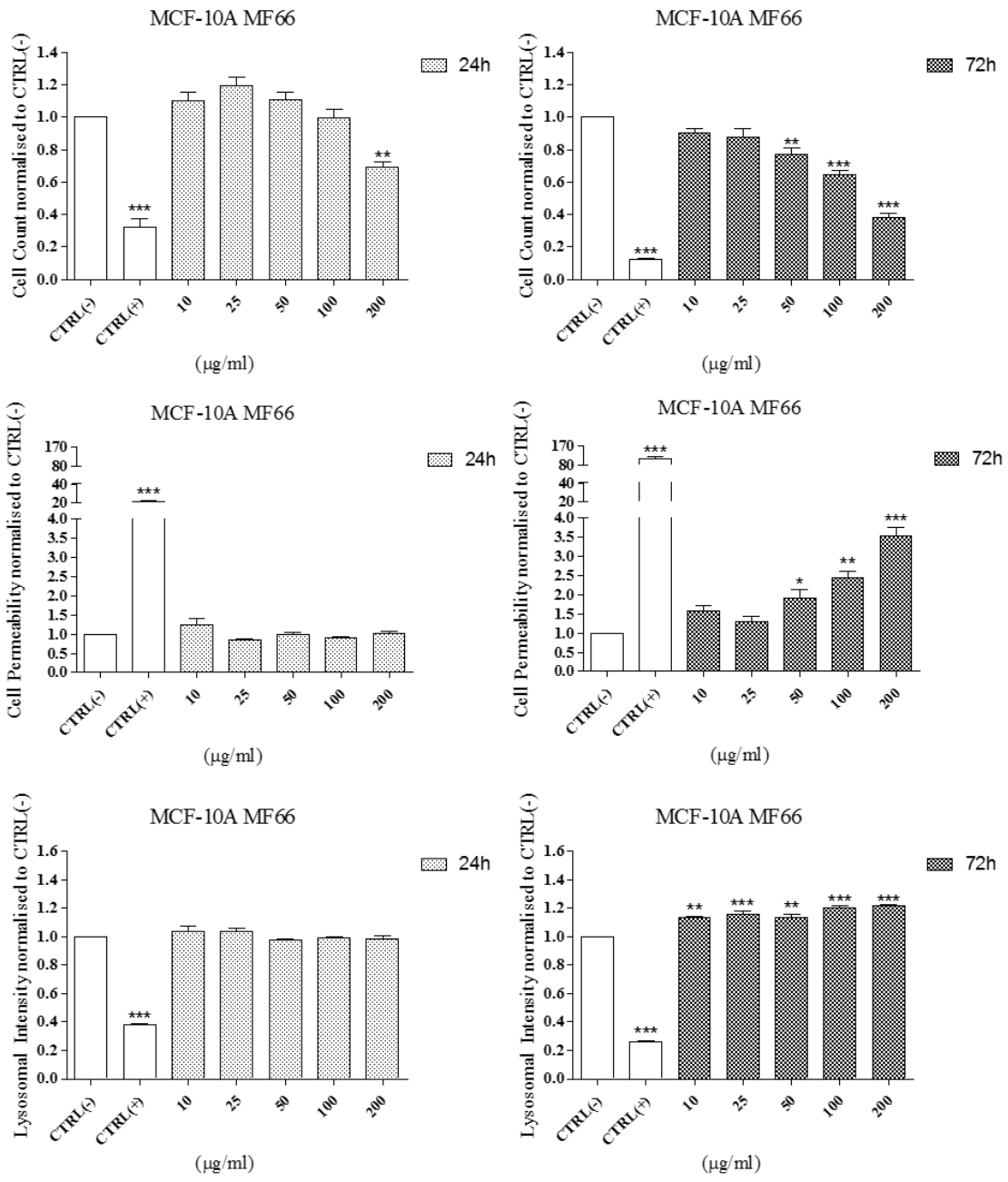

Figure S79: MCF-10A cell line exposed to MF66 MNP.

MCF-10A breast-derived cell line was exposed to MF66 MNP for 24h and 72h. Cells were stained using the Cytotoxicity II HitKit™ and analysed using the InCell 1000 HCSA device. Variation in cell count, cell membrane permeability and lysosomal intensity were measured compared to untreated control (CTRL(-)) and 1µM CdSe positive control (CTRL(+)). Statistical significance was determined using the one way ANOVA with Tukey post-test for each column compared to untreated control (CTRL(-)). p value: *** = <0.001, **=<0.01, *=<0.05

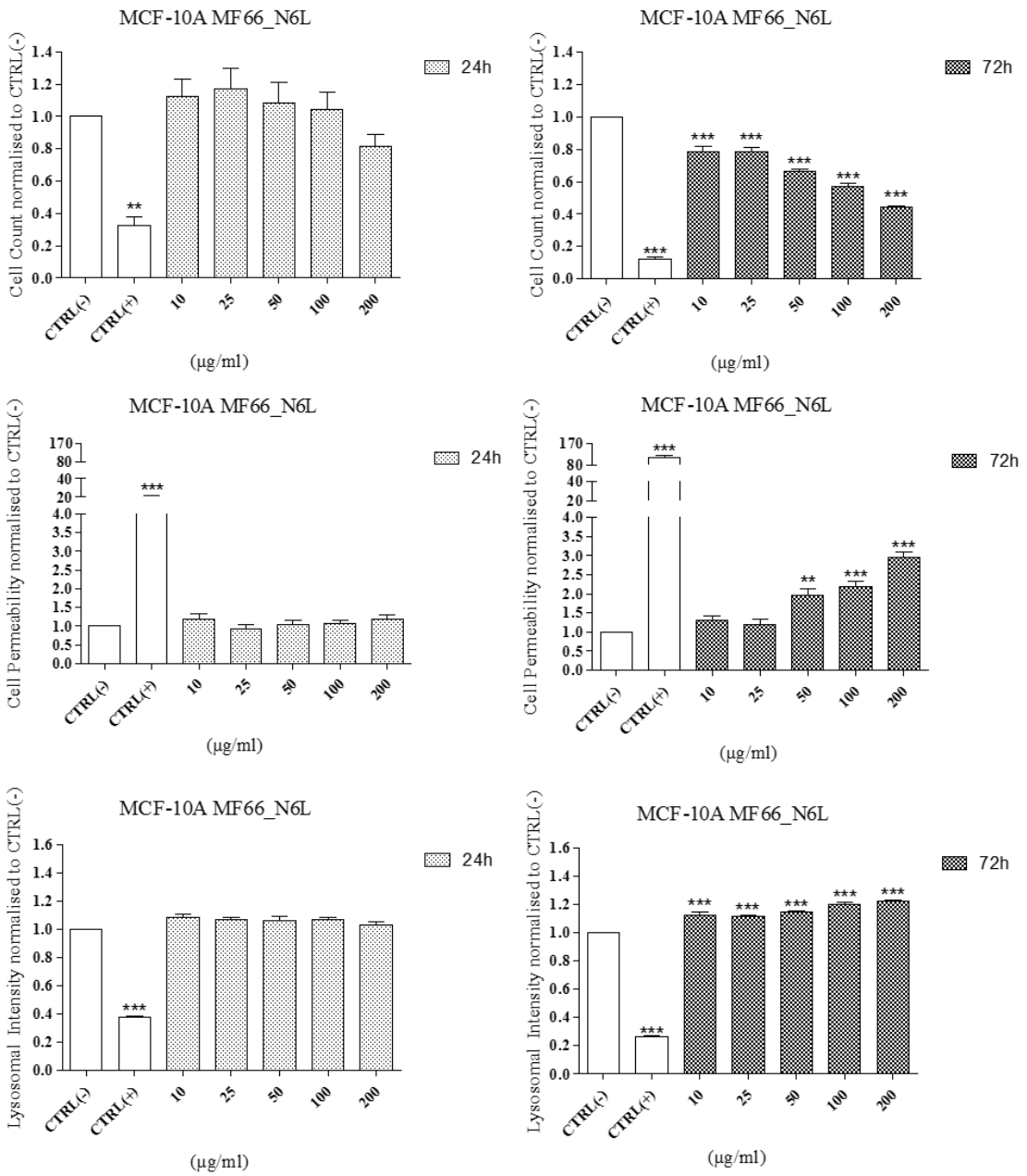

Figure S80: MCF-10A cell line exposed to MF66_N6L MNP.

MCF-10A breast-derived cell line was exposed to MF66_N6L MNP for 24h and 72h. Cells were stained using the Cytotoxicity II HitKit™ and analysed using the InCell 1000 HCSA device. Variation in cell count, cell membrane permeability and lysosomal intensity were measured compared to untreated control (CTRL(-)) and 1µM CdSe positive control (CTRL(+)). Statistical significance was determined using the one way ANOVA with Tukey post-test for each column compared to untreated control (CTRL(-)). p value: *** = <0.001, **=<0.01, *=<0.05

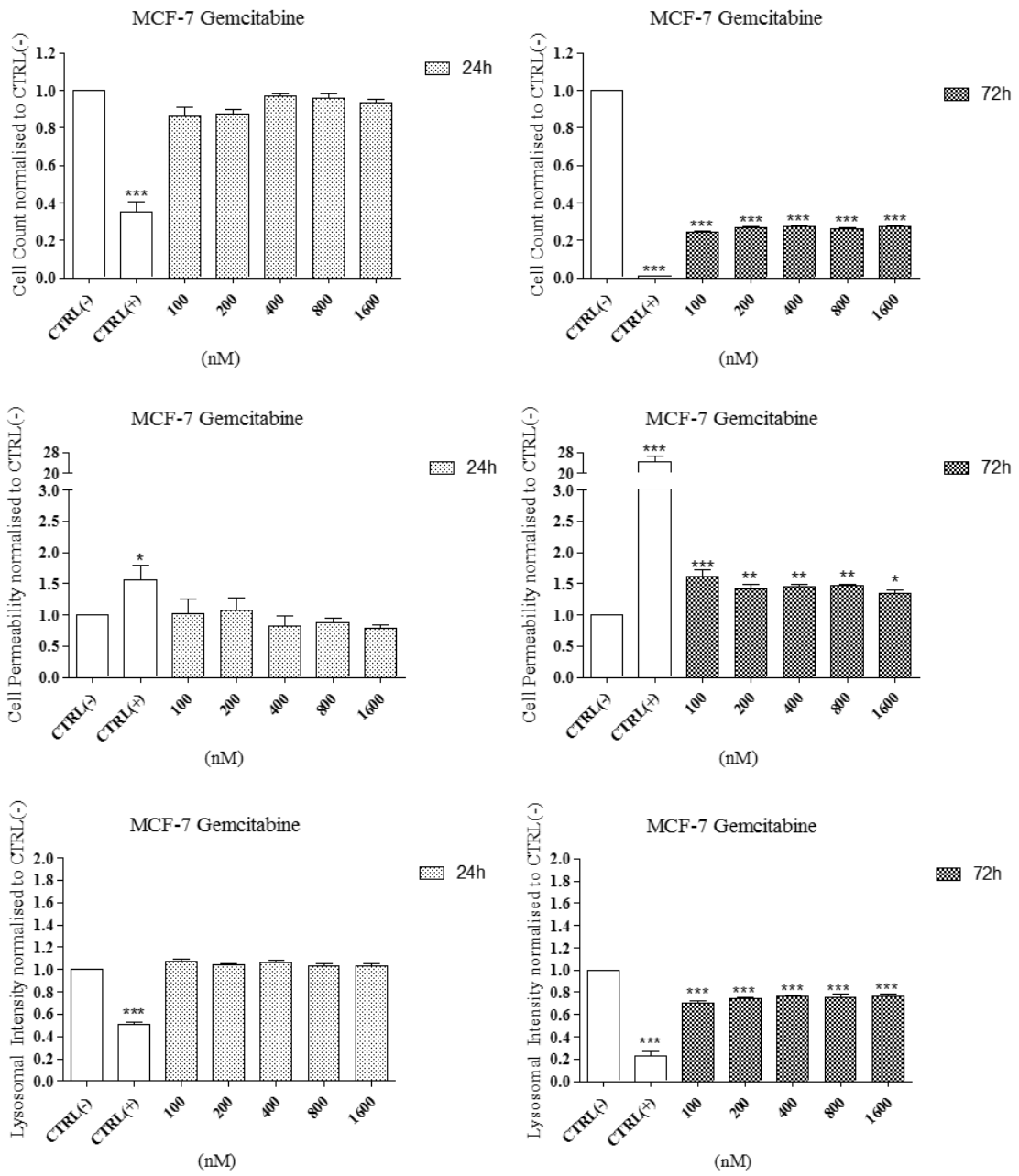

Figure S81: Effect of gemcitabine on viability of MCF-7 cell line.

MCF-7 breast-derived cell line was exposed to gemcitabine chemotherapeutic drug for 24h and 72h. Cells were stained using the Cytotoxicity II HitKit™ and analysed using the InCell 1000 HCSA device. Variation in cell count, cell membrane permeability and lysosomal intensity were measured compared to untreated control (CTRL(-)) and 1µM CdSe positive control (CTRL(+)). Statistical significance was determined using the one way ANOVA with Tukey post-test for each column compared to untreated control (CTRL(-)). p value: *** = <0.001, **=<0.01, *=<0.05

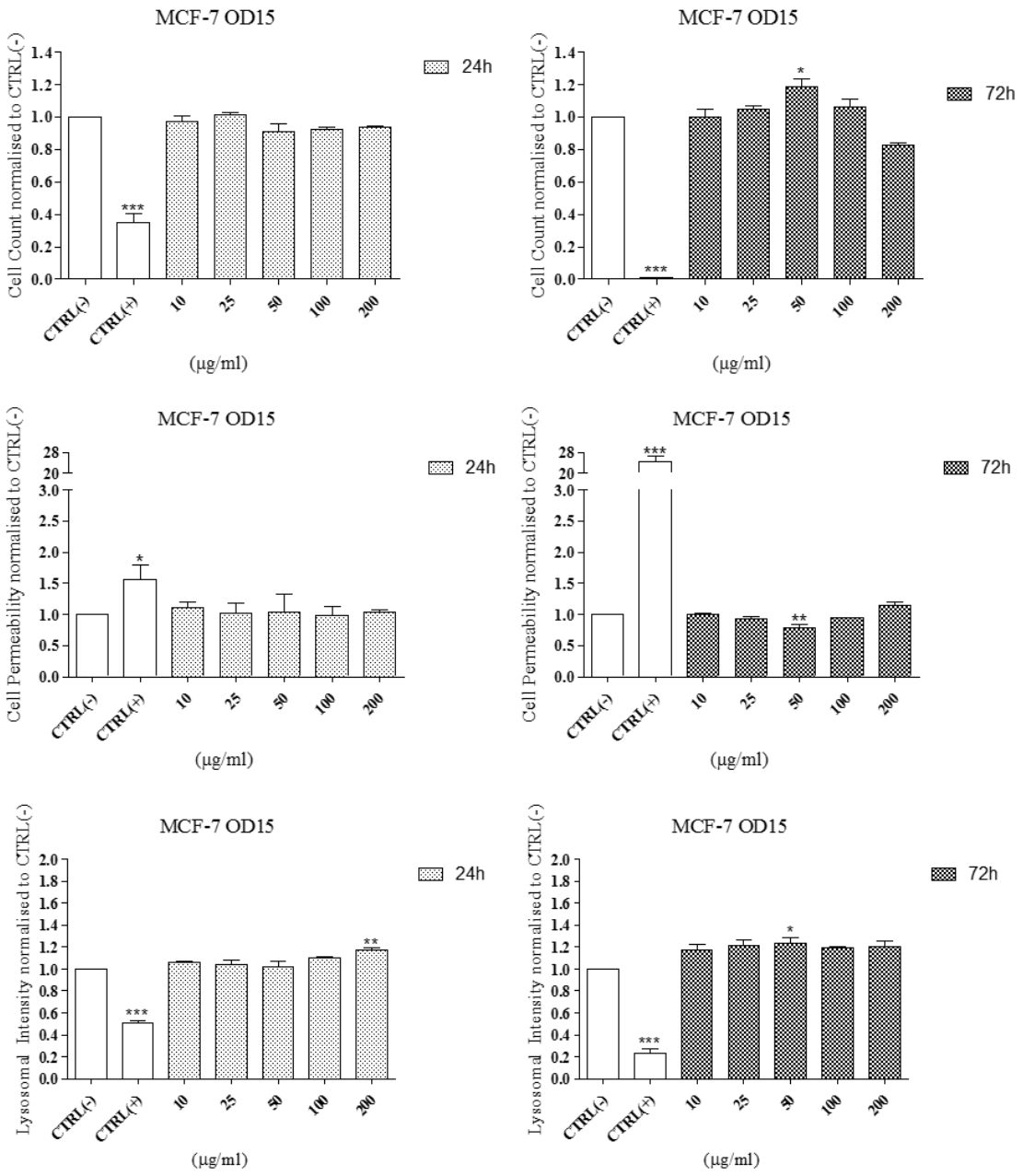

Figure S82: MCF-7 cell line exposed to OD15 MNP.

MCF-7 breast-derived cell line was exposed to OD15 MNP for 24h and 72h. Cells were stained using the Cytotoxicity II HitKit™ and analysed using the InCell 1000 HCSA device. Variation in cell count, cell membrane permeability and lysosomal intensity were measured compared to untreated control (CTRL(-)) and 1µM CdSe positive control (CTRL(+)). Statistical significance was determined using the one way ANOVA with Tukey post-test for each column compared to untreated control (CTRL(-)). p value: *** = <0.001, **=<0.01, *=<0.05

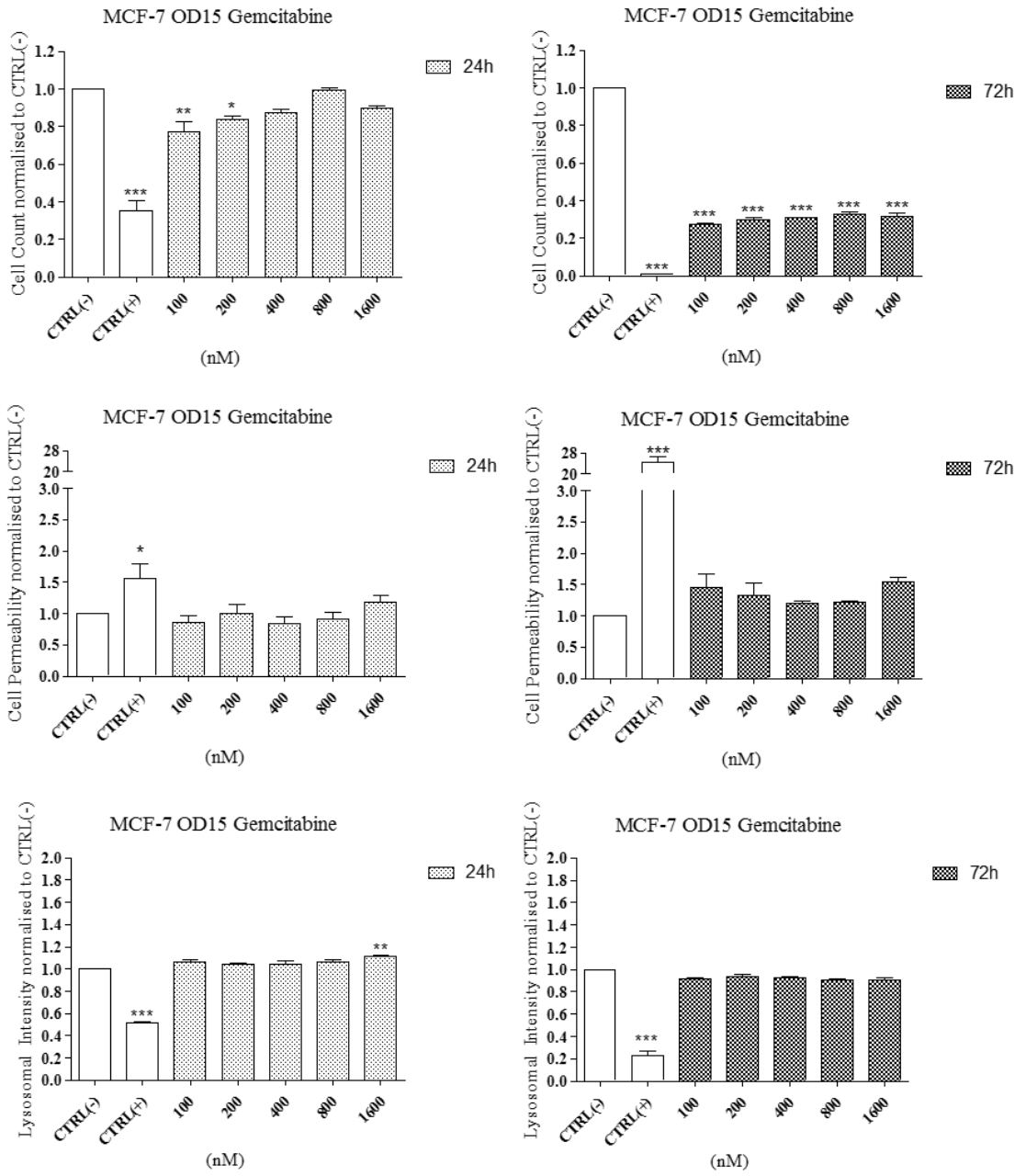

Figure S83: MCF-7 cell line exposed to OD15_Gemcitabine MNP.

MCF-7 breast-derived cell line was exposed to OD15_Gemcitabine MNP for 24h and 72h. Cells were stained using the Cytotoxicity II HitKit™ and analysed using the InCell 1000 HCSA device. Variation in cell count, cell membrane permeability and lysosomal intensity were measured compared to untreated control (CTRL(-)) and 1µM CdSe positive control (CTRL(+)). Statistical significance was determined using the one way ANOVA with Tukey post-test for each column compared to untreated control (CTRL(-)). p value: *** = <0.001, **=<0.01, *=<0.05

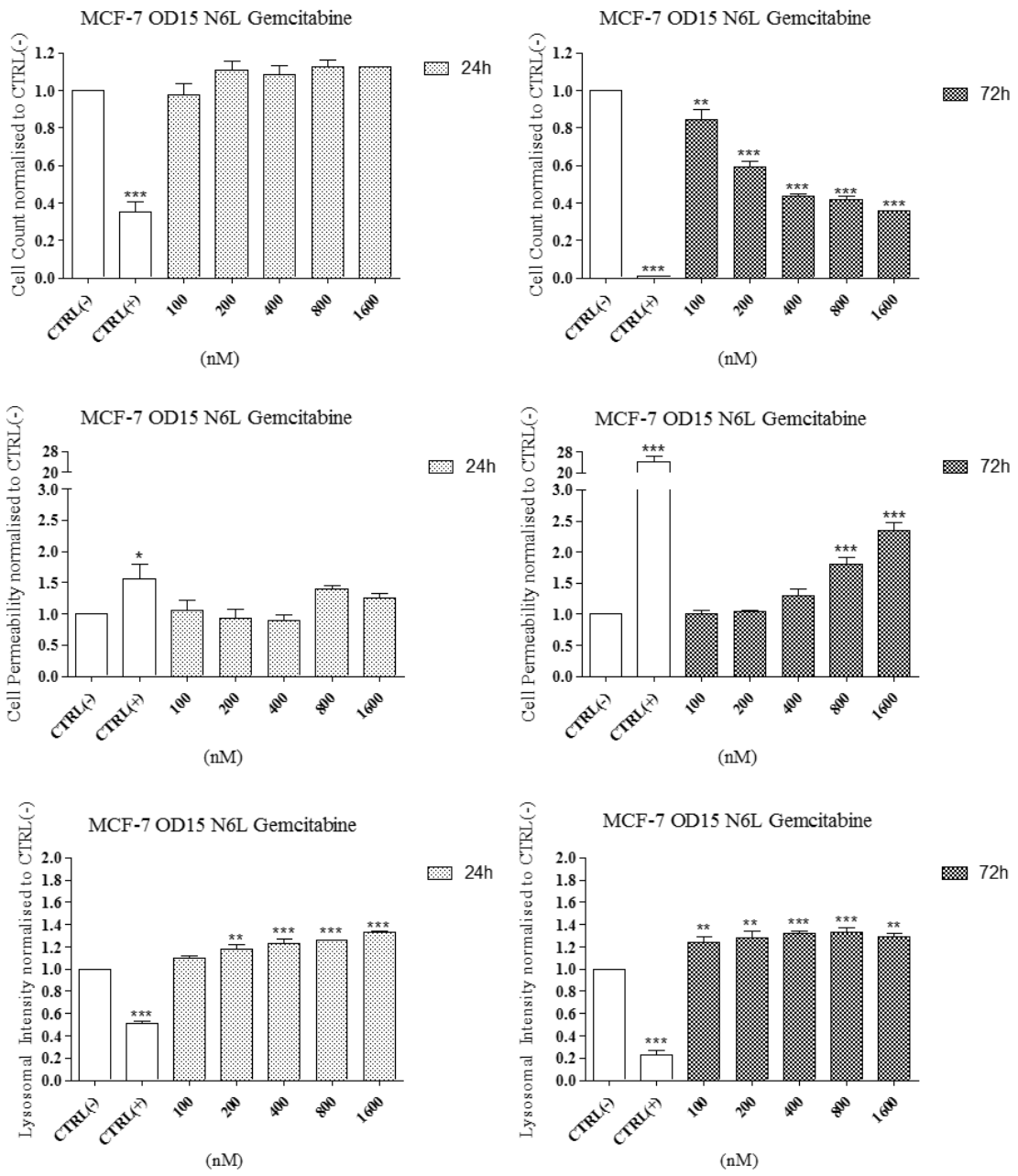

Figure S84: MCF-7 cell line exposed to OD15_N6L_Gemcitabine MNP.

MCF-7 breast-derived cell line was exposed to OD15_N6L_Gemcitabine MNP for 24h and 72h. Cells were stained using the Cytotoxicity II HitKit™ and analysed using the InCell 1000 HCSA device. Variation in cell count, cell membrane permeability and lysosomal intensity were measured compared to untreated control (CTRL(-)) and 1µM CdSe positive control (CTRL(+)). Statistical significance was determined using the one way ANOVA with Tukey post-test for each column compared to untreated control (CTRL(-)). p value: *** = <0.001, **=<0.01, *=<0.05

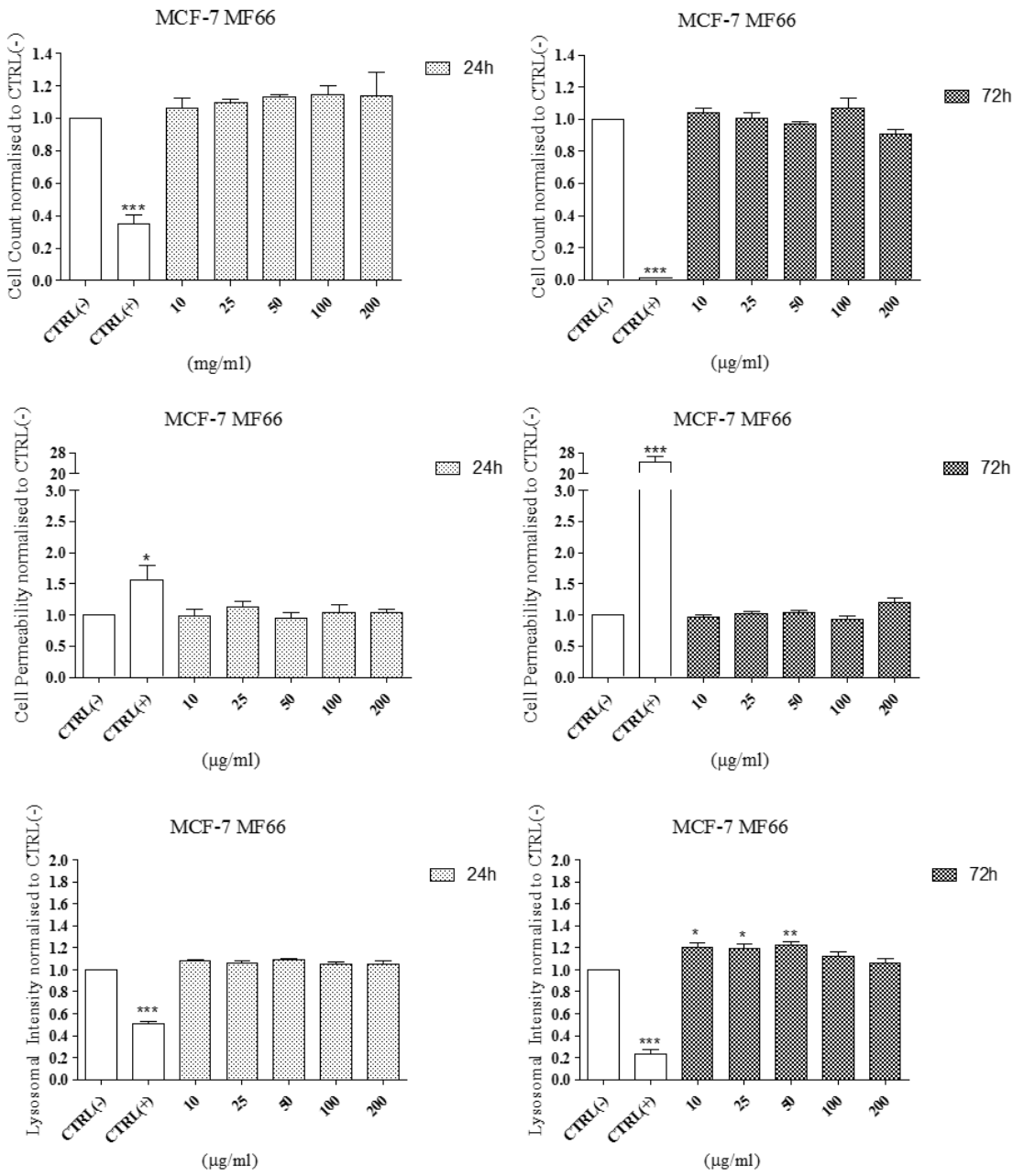

Figure S85: MCF-7 cell line exposed to MF66 MNP.

MCF-7 breast-derived cell line was exposed to MF66 MNP for 24h and 72h. Cells were stained using the Cytotoxicity II HitKit™ and analysed using the InCell 1000 HCSA device. Variation in cell count, cell membrane permeability and lysosomal intensity were measured compared to untreated control (CTRL(-)) and 1µM CdSe positive control (CTRL(+)). Statistical significance was determined using the one way ANOVA with Tukey post-test for each column compared to untreated control (CTRL(-)). p value: *** = <0.001, **=<0.01, *=<0.05

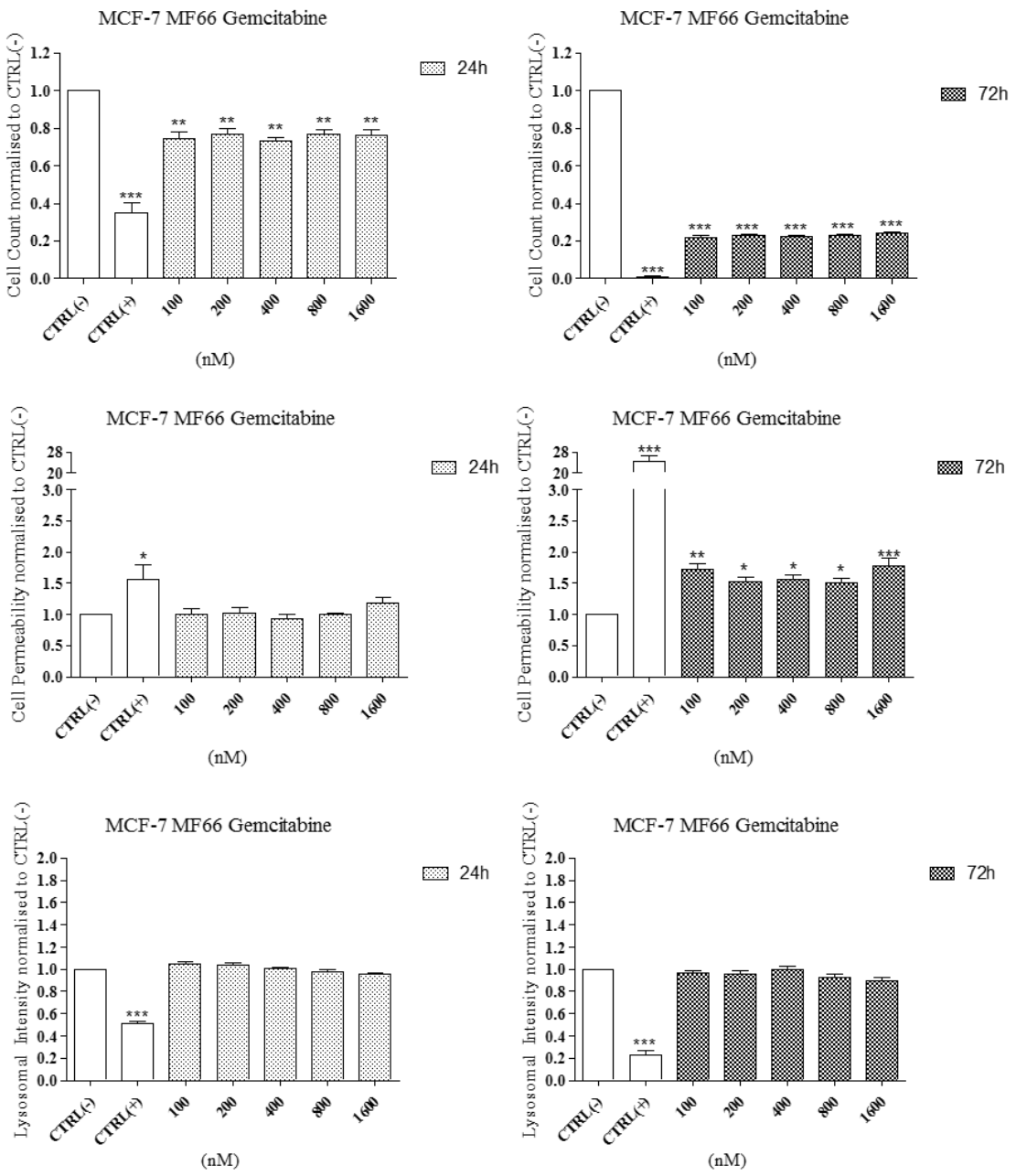

Figure S86: MCF-7 cell line exposed to MF66_Gemcitabine MNP.

MCF-7 breast-derived cell line was exposed to MF66_Gemcitabine MNP for 24h and 72h. Cells were stained using the Cytotoxicity II HitKit™ and analysed using the InCell 1000 HCSA device. Variation in cell count, cell membrane permeability and lysosomal intensity were measured compared to untreated control (CTRL(-)) and 1µM CdSe positive control (CTRL(+)). Statistical significance was determined using the one way ANOVA with Tukey post-test for each column compared to untreated control (CTRL(-)). p value: *** = <0.001, **=<0.01, *=<0.05

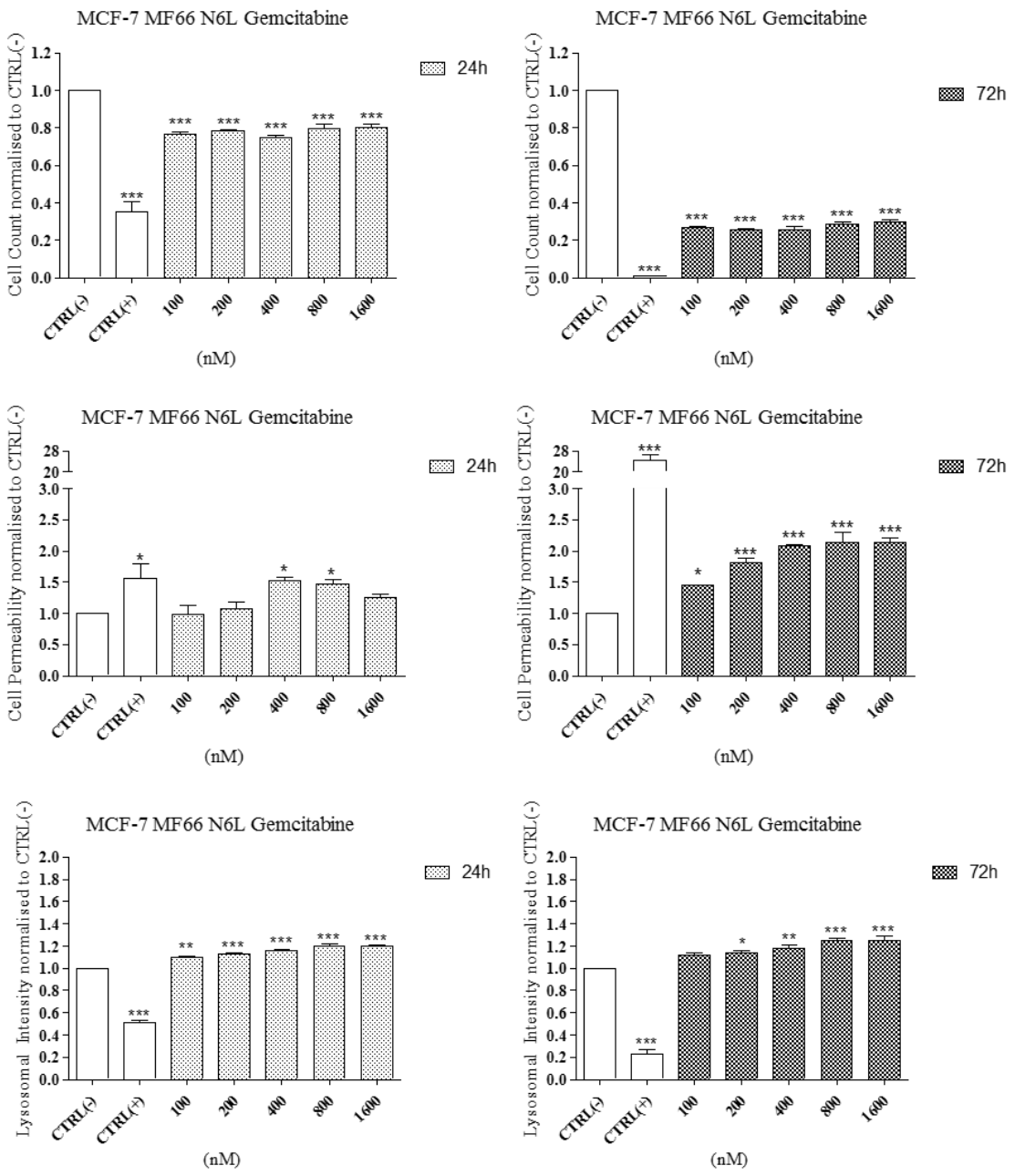

Figure S87: MCF-7 cell line exposed to MF66_N6L_Gemcitabine MNP.

MCF-7 breast-derived cell line was exposed to MF66_N6L_Gemcitabine MNP for 24h and 72h. Cells were stained using the Cytotoxicity II HitKit™ and analysed using the InCell 1000 HCSA device. Variation in cell count, cell membrane permeability and lysosomal intensity were measured compared to untreated control (CTRL(-)) and 1µM CdSe positive control (CTRL(+)). Statistical significance was determined using the one way ANOVA with Tukey post-test for each column compared to untreated control (CTRL(-)). p value: *** = <0.001, **=<0.01, *=<0.05

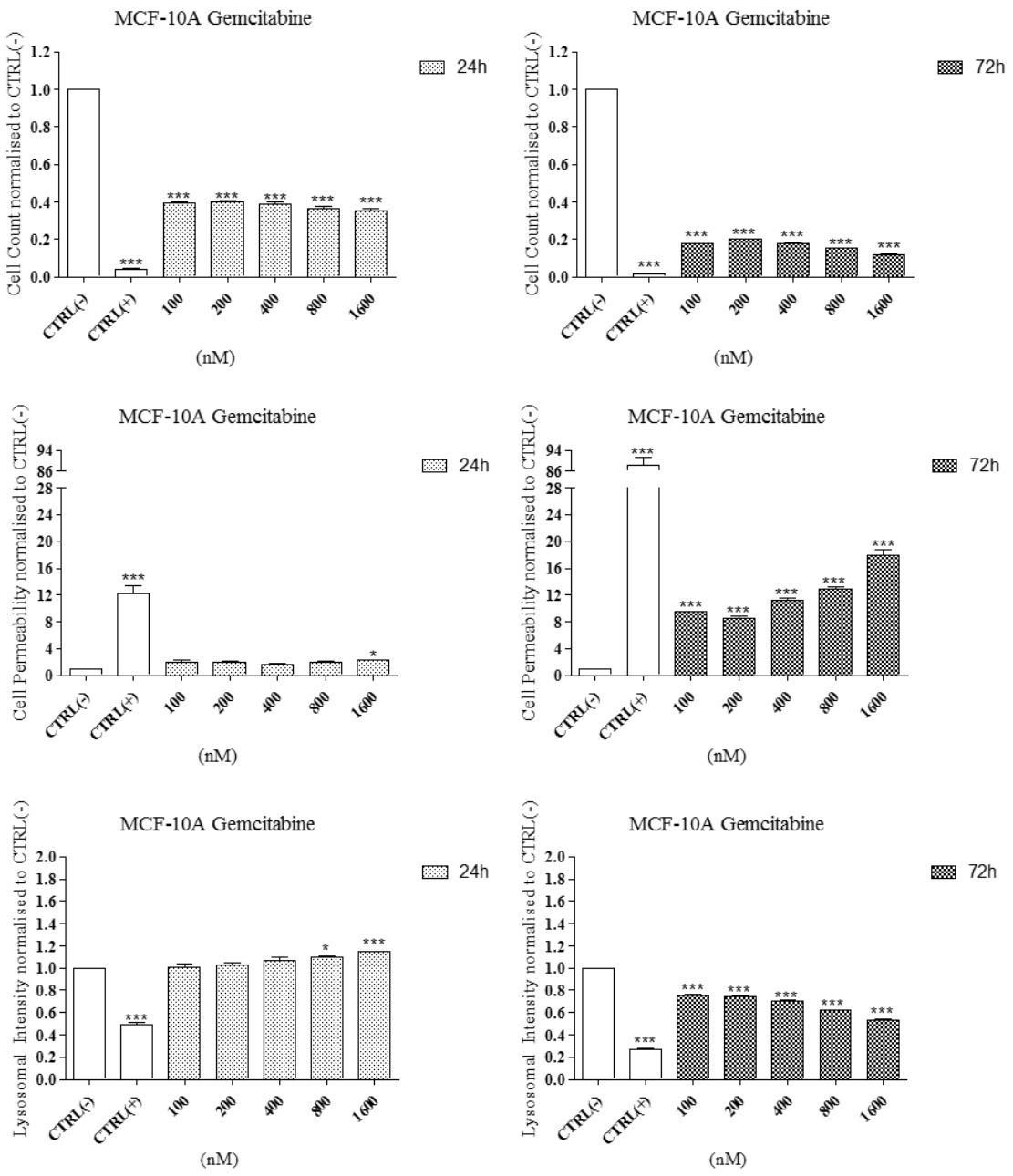

Figure S88: Effect of gemcitabine on viability of MCF-10A cell line.

MCF-10A breast-derived cell line was exposed to gemcitabine chemotherapeutic drug for 24h and 72h. Cells were stained using the Cytotoxicity II HitKit™ and analysed using the InCell 1000 HCSA device. Variation in cell count, cell membrane permeability and lysosomal intensity were measured compared to untreated control (CTRL(-)) and 1µM CdSe positive control (CTRL(+)). Statistical significance was determined using the one way ANOVA with Tukey post-test for each column compared to untreated control (CTRL(-)). p value: *** = <0.001, **=<0.01, *=<0.05

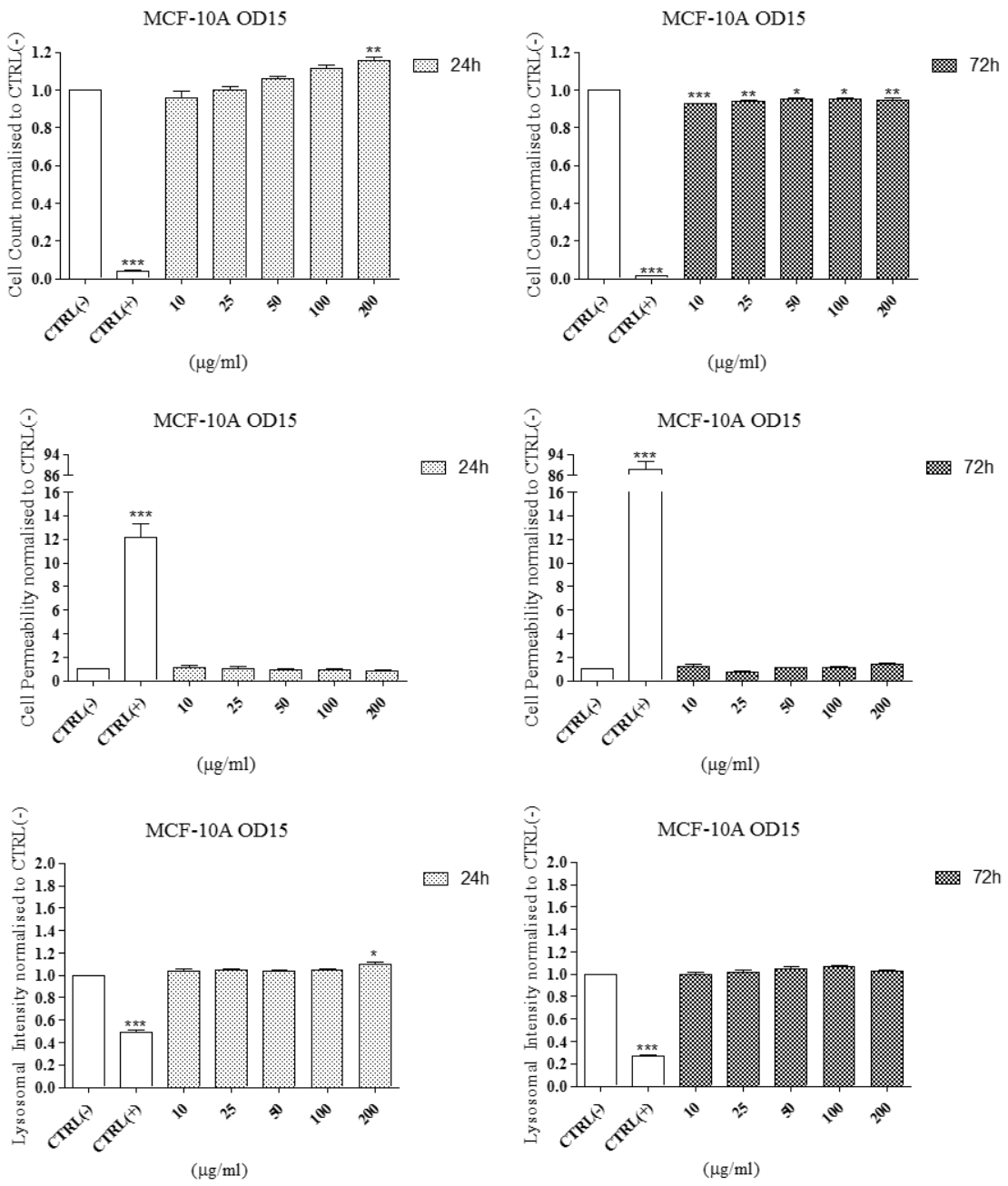

Figure S89: MCF-10A cell line exposed to OD15 MNP.

MCF-10A breast-derived cell line was exposed to OD15 MNP for 24h and 72h. Cells were stained using the Cytotoxicity II HitKit™ and analysed using the InCell 1000 HCSA device. Variation in cell count, cell membrane permeability and lysosomal intensity were measured compared to untreated control (CTRL(-)) and 1µM CdSe positive control (CTRL(+)). Statistical significance was determined using the one way ANOVA with Tukey post-test for each column compared to untreated control (CTRL(-)). p value: *** = <0.001, **=<0.01, *=<0.05

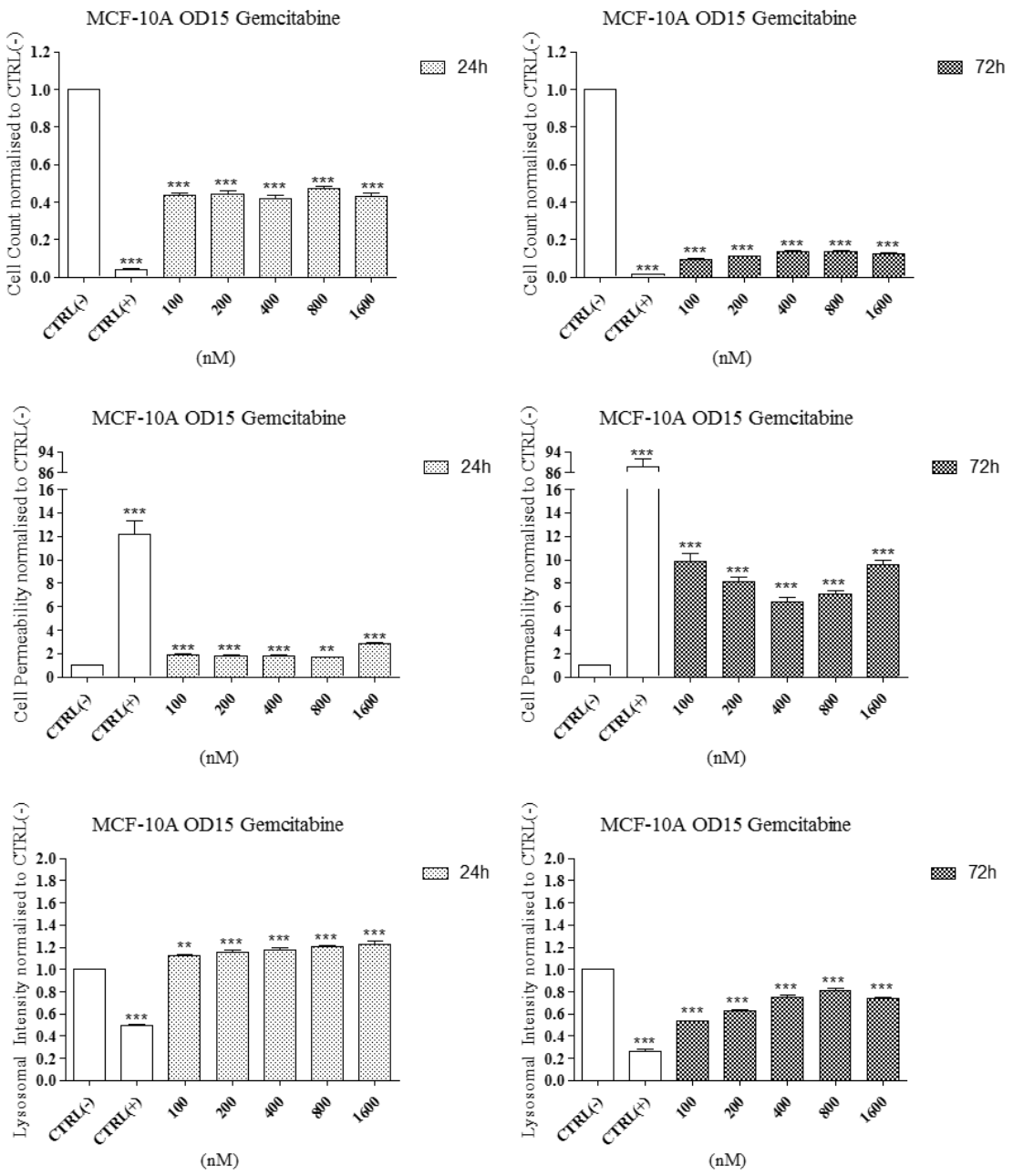

Figure S90: MCF-10A cell line exposed to OD15_Gemcitabine MNP.

MCF-10A breast-derived cell line was exposed to OD15_Gemcitabine MNP for 24h and 72h. Cells were stained using the Cytotoxicity II HitKit™ and analysed using the InCell 1000 HCSA device. Variation in cell count, cell membrane permeability and lysosomal intensity were measured compared to untreated control (CTRL(-)) and 1µM CdSe positive control (CTRL(+)). Statistical significance was determined using the one way ANOVA with Tukey post-test for each column compared to untreated control (CTRL(-)). p value: *** = <0.001, **=<0.01, *=<0.05

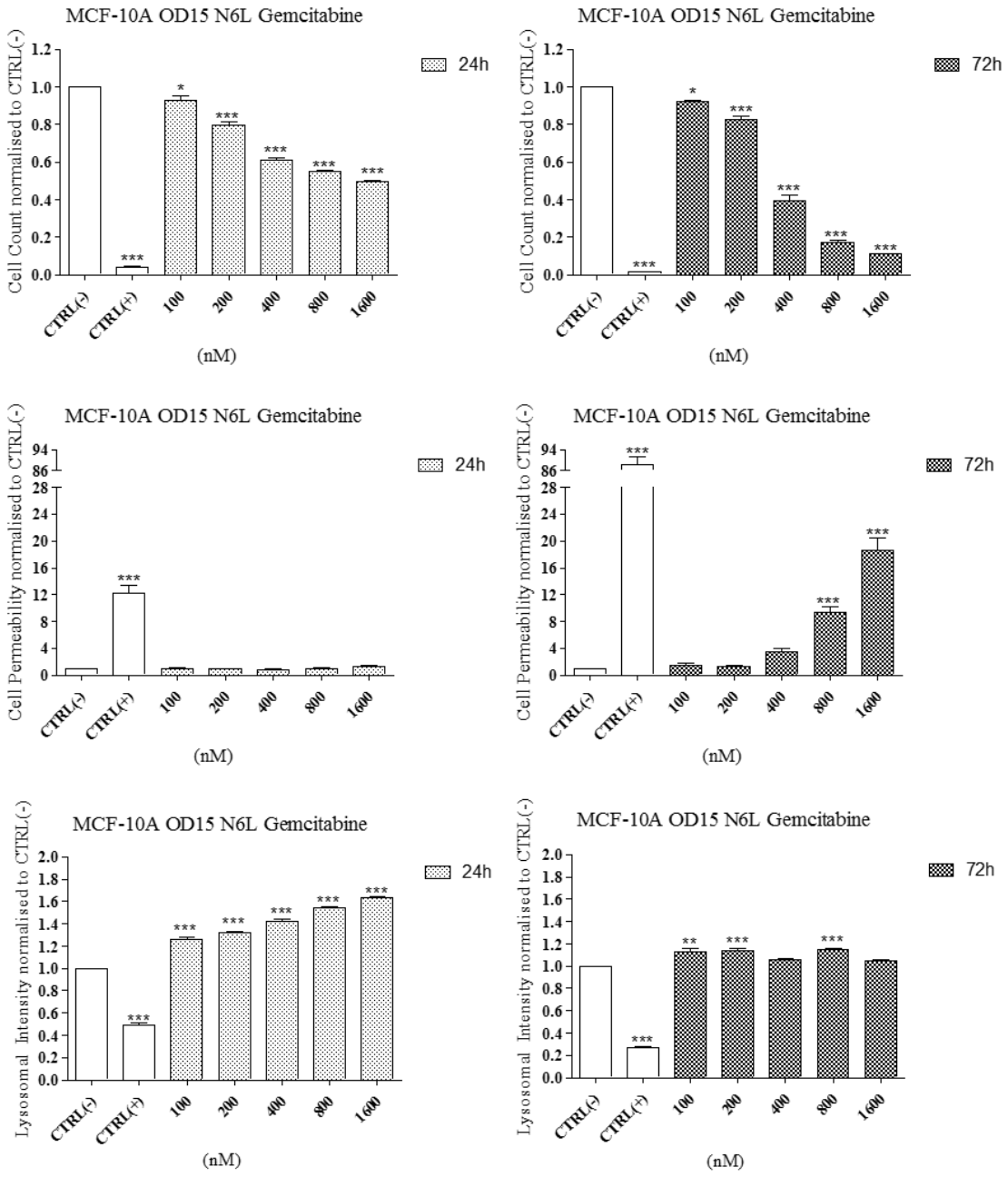

Figure S91: MCF-10A cell line exposed to OD15_N6L_Gemcitabine MNP.

MCF-10A breast-derived cell line was exposed to OD15_N6L_Gemcitabine MNP for 24h and 72h. Cells were stained using the Cytotoxicity II HitKit™ and analysed using the InCell 1000 HCSA device. Variation in cell count, cell membrane permeability and lysosomal intensity were measured compared to untreated control (CTRL(-)) and 1µM CdSe positive control (CTRL(+)). Statistical significance was determined using the one way ANOVA with Tukey post-test for each column compared to untreated control (CTRL(-)). p value: *** = <0.001, **=<0.01, *=<0.05

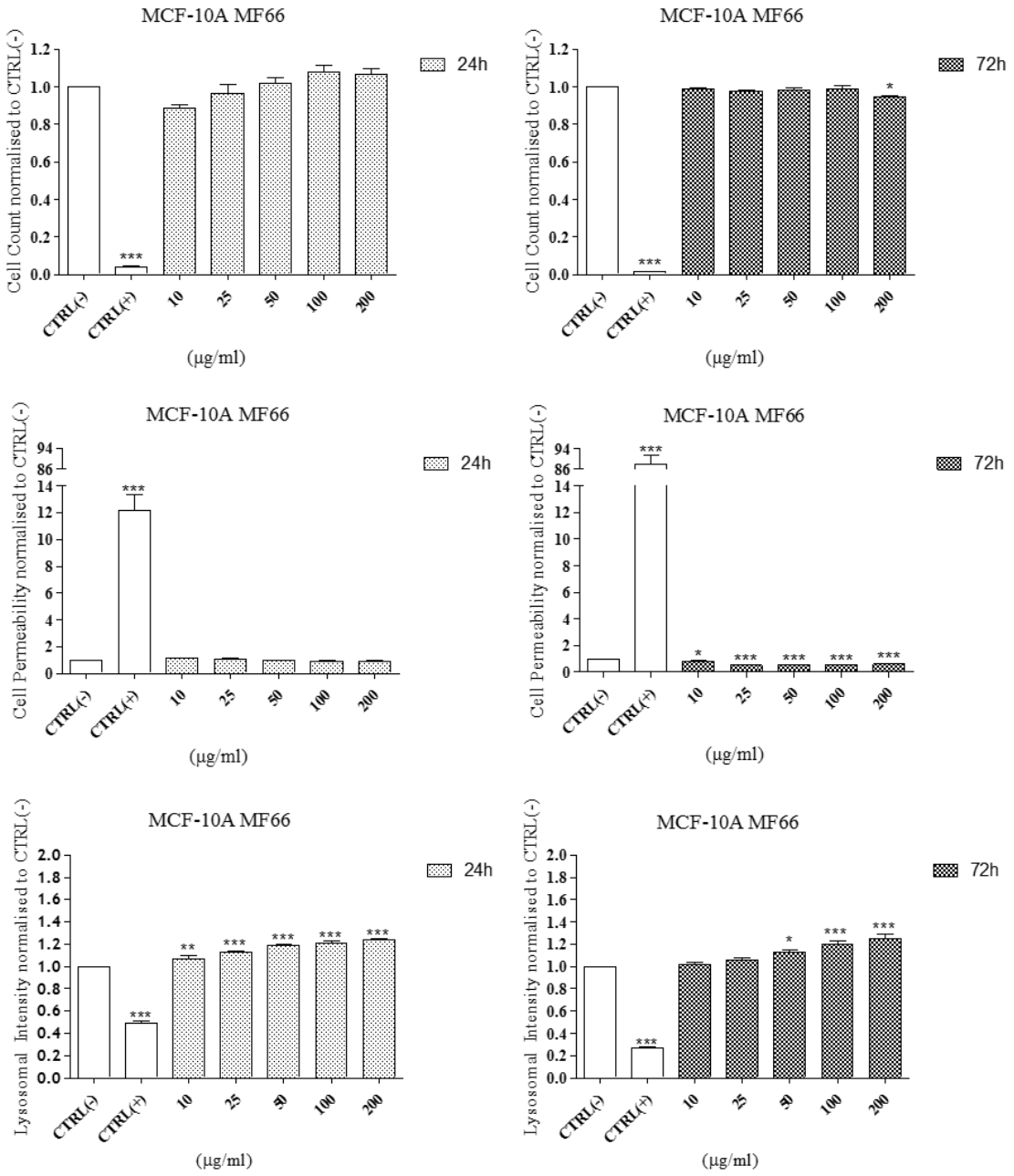

Figure S92: MCF-10A cell line exposed to MF66_N6L_Gemcitabine MNP.

MCF-10A breast-derived cell line was exposed to MF66 MNP for 24h and 72h. Cells were stained using the Cytotoxicity II HitKit™ and analysed using the InCell 1000 HCSA device. Variation in cell count, cell membrane permeability and lysosomal intensity were measured compared to untreated control (CTRL(-)) and 1µM CdSe positive control (CTRL(+)). Statistical significance was determined using the one way ANOVA with Tukey post-test for each column compared to untreated control (CTRL(-)). p value: *** = <0.001, **=<0.01, *=<0.05

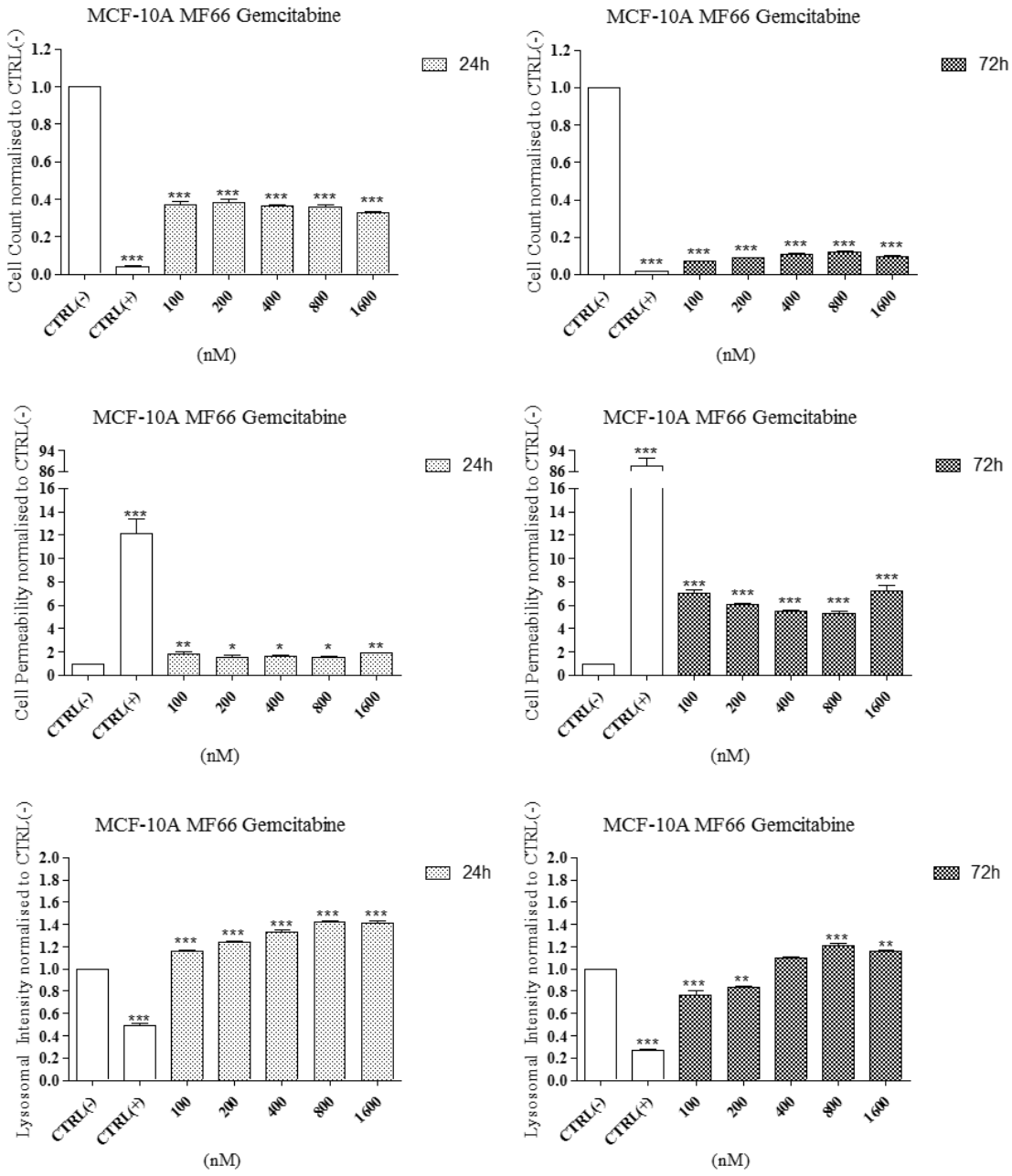

Figure S93: MCF-10A cell line exposed to MF66_Gemcitabine MNP.

MCF-10A breast-derived cell line was exposed to MF66_Gemcitabine MNP for 24h and 72h. Cells were stained using the Cytotoxicity II HitKit™ and analysed using the InCell 1000 HCSA device. Variation in cell count, cell membrane permeability and lysosomal intensity were measured compared to untreated control (CTRL(-)) and 1µM CdSe positive control (CTRL(+)). Statistical significance was determined using the one way ANOVA with Tukey post-test for each column compared to untreated control (CTRL(-)). p value: *** = <0.001, **=<0.01, *=<0.05

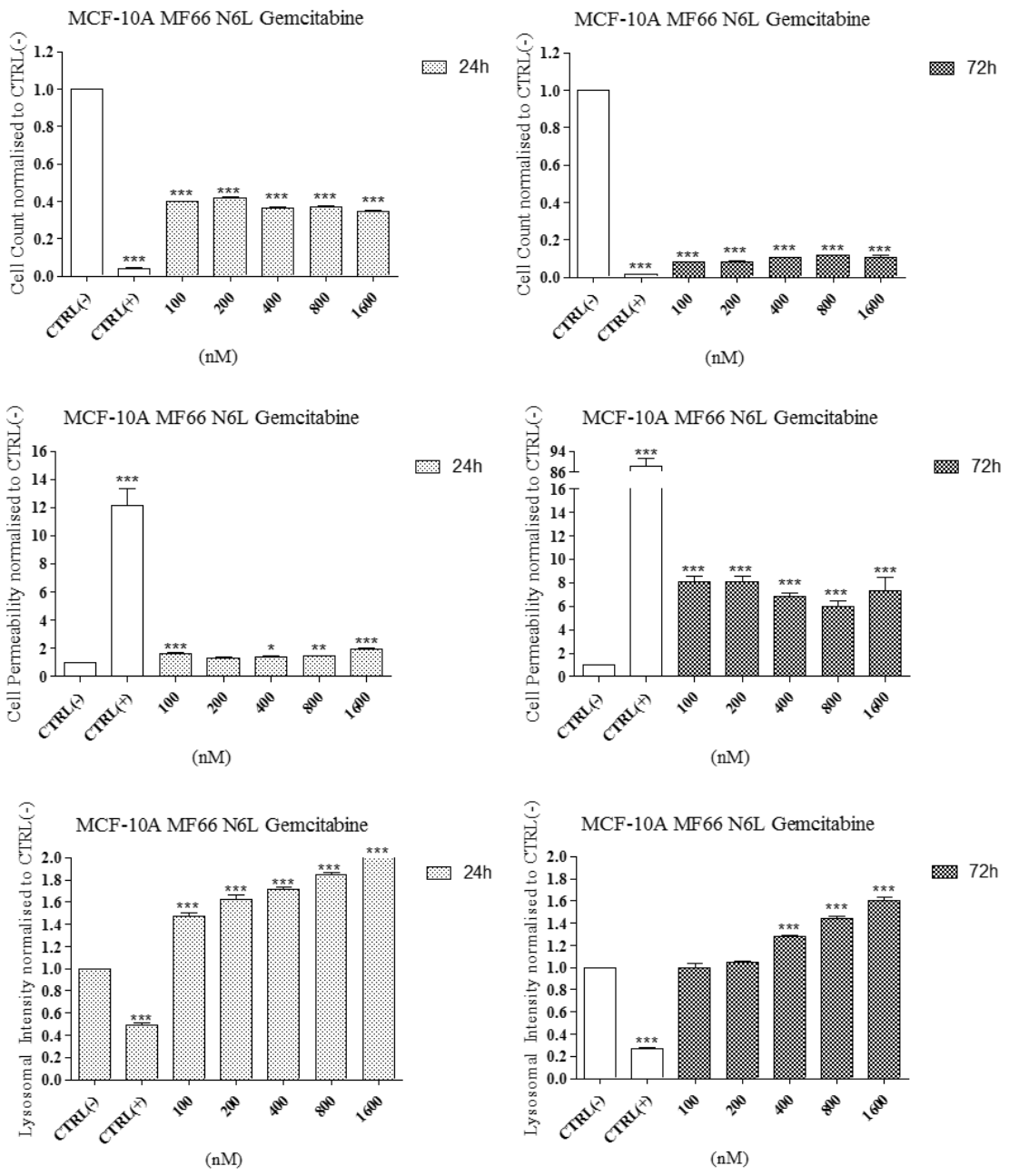

Figure S94: MCF-10A cell line exposed to MF66_N6L_Gemcitabine MNP.

MCF-10A breast-derived cell line was exposed to MF66_N6L_Gemcitabine MNP for 24h and 72h. Cells were stained using the Cytotoxicity II HitKit™ and analysed using the InCell 1000 HCSA device. Variation in cell count, cell membrane permeability and lysosomal intensity were measured compared to untreated control (CTRL(-)) and 1µM CdSe positive control (CTRL(+)). Statistical significance was determined using the one way ANOVA with Tukey post-test for each column compared to untreated control (CTRL(-)). p value: *** = <0.001, **=<0.01, *=<0.05

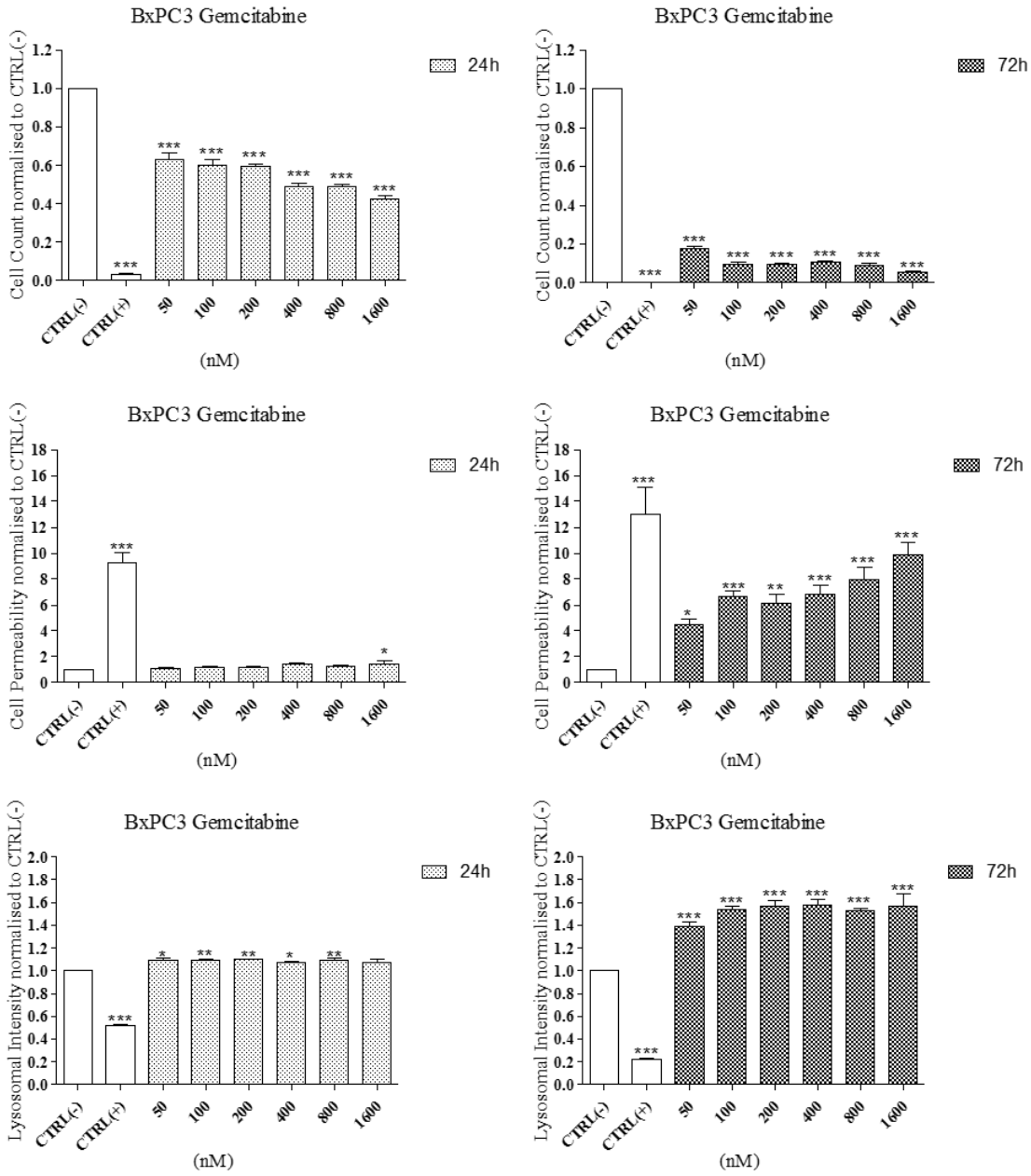

Figure S95: Effect of gemcitabine on viability of BxPC3 cell line.

BxPC3 pancreatic-derived cell line was exposed to gemcitabine chemotherapeutic drug for 24h and 72h. Cells were stained using the Cytotoxicity II HitKit™ and analysed using the InCell 1000 HCSA device. Variation in cell count, cell membrane permeability and lysosomal intensity were measured compared to untreated control (CTRL(-)) and 1µM CdSe positive control (CTRL(+)). Statistical significance was determined using the one way ANOVA with Tukey post-test for each column compared to untreated control (CTRL(-)). p value: *** = <0.001, **=<0.01, *=<0.05

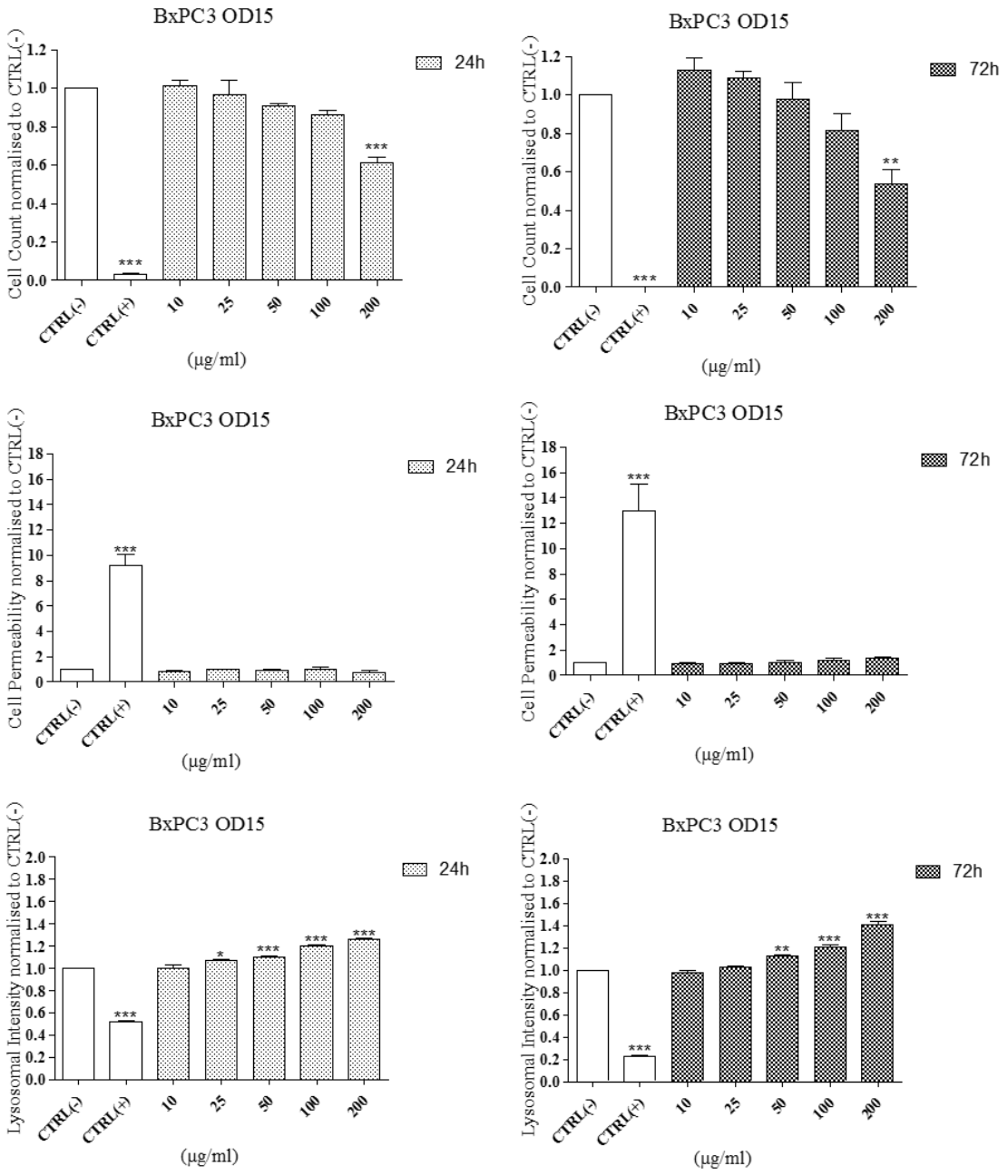

Figure S96: BxPC3 cell line exposed to OD15 MNP.

BxPC3 pancreatic-derived cell line was exposed to OD15 MNP for 24h and 72h. Cells were stained using the Cytotoxicity II HitKit™ and analysed using the InCell 1000 HCSA device. Variation in cell count, cell membrane permeability and lysosomal intensity were measured compared to untreated control (CTRL(-)) and 1µM CdSe positive control (CTRL(+)). Statistical significance was determined using the one way ANOVA with Tukey post-test for each column compared to untreated control (CTRL(-)). p value: *** = <0.001, **=<0.01, *=<0.05

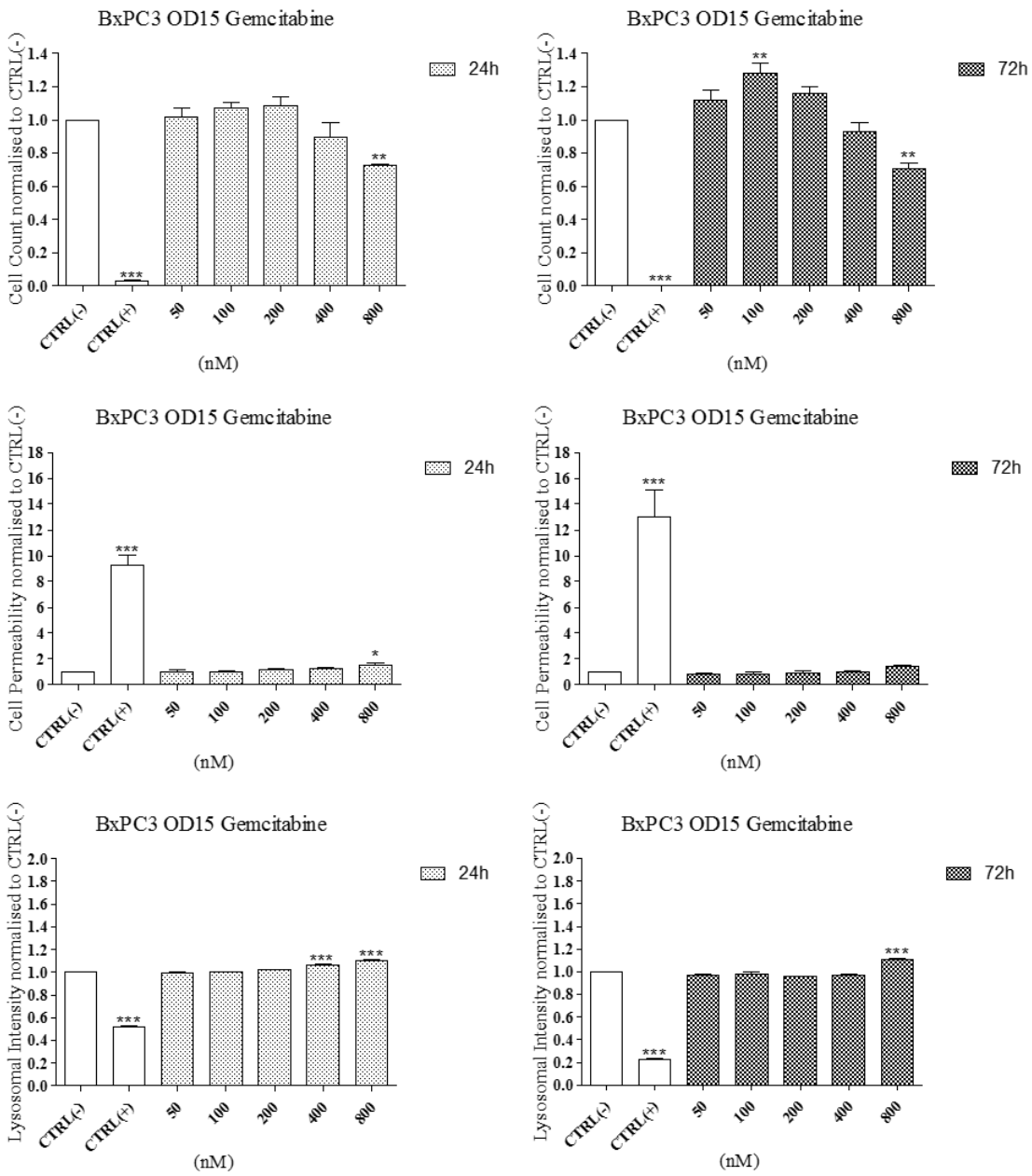

Figure S97: BxPC3 cell line exposed to OD15_Gemcitabine MNP.

BxPC3 pancreatic-derived cell line was exposed to OD15_Gemcitabine MNP for 24h and 72h. Cells were stained using the Cytotoxicity II HitKit™ and analysed using the InCell 1000 HCSA device. Variation in cell count, cell membrane permeability and lysosomal intensity were measured compared to untreated control (CTRL(-)) and 1µM CdSe positive control (CTRL(+)). Statistical significance was determined using the one way ANOVA with Tukey post-test for each column compared to untreated control (CTRL(-)). p value: *** = <0.001, **=<0.01, *=<0.05

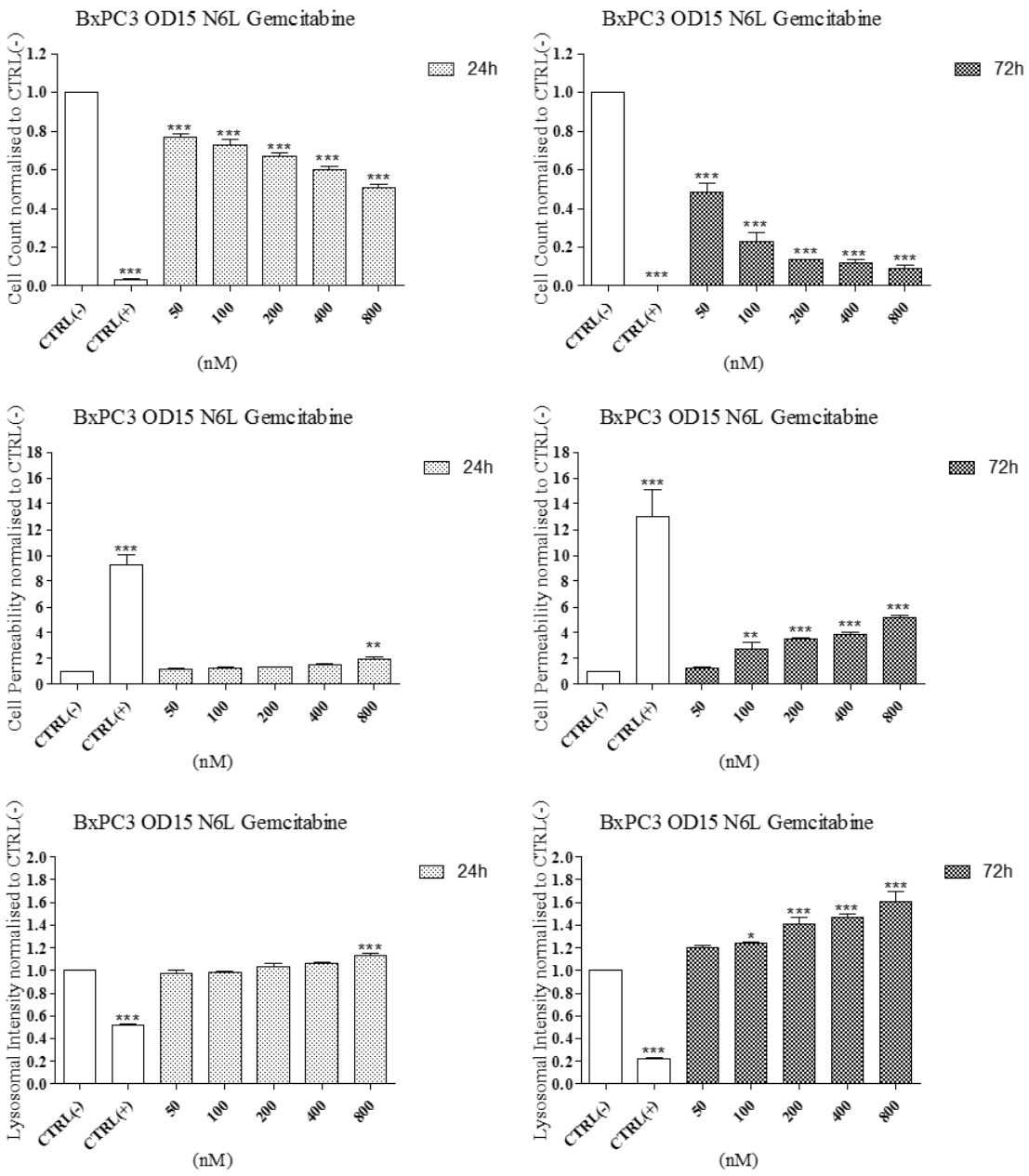

Figure S98: BxPC3 cell line exposed to OD15_N6L_Gemcitabine MNP.

BxPC3 pancreatic-derived cell line was exposed to OD15_N6L_Gemcitabine MNP for 24h and 72h. Cells were stained using the Cytotoxicity II HitKit™ and analysed using the InCell 1000 HCSA device. Variation in cell count, cell membrane permeability and lysosomal intensity were measured compared to untreated control (CTRL(-)) and 1µM CdSe positive control (CTRL(+)). Statistical significance was determined using the one way ANOVA with Tukey post-test for each column compared to untreated control (CTRL(-)). p value: *** = <0.001, **=<0.01, *=<0.05

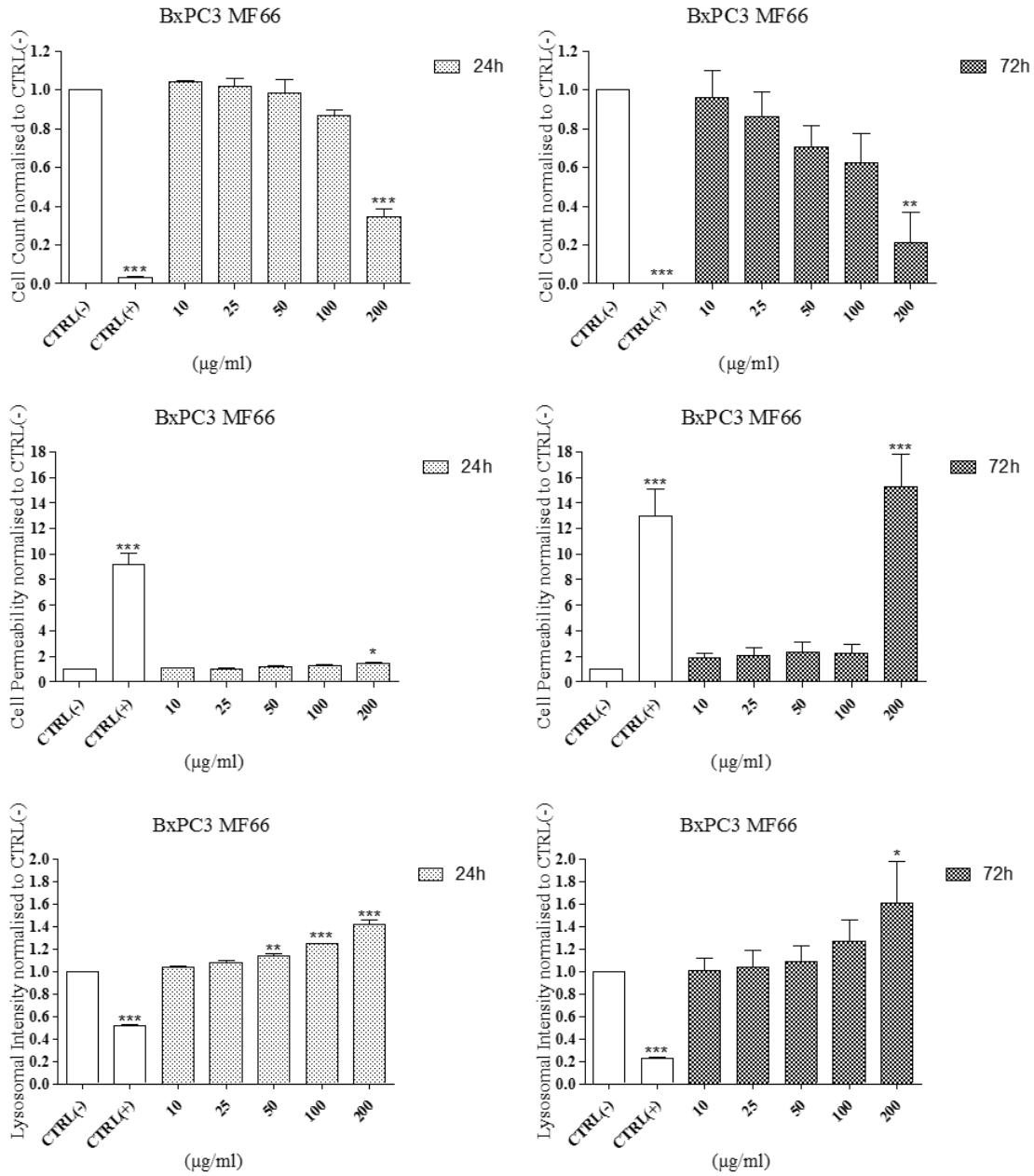

Figure S99: BxPC3 cell line exposed to MF66 MNP.

BxPC3 pancreatic-derived cell line was exposed to MF66 MNP for 24h and 72h. Cells were stained using the Cytotoxicity II HitKit™ and analysed using the InCell 1000 HCSA device. Variation in cell count, cell membrane permeability and lysosomal intensity were measured compared to untreated control (CTRL(-)) and 1µM CdSe positive control (CTRL(+)). Statistical significance was determined using the one way ANOVA with Tukey post-test for each column compared to untreated control (CTRL(-)). p value: *** = <0.001, **=<0.01, *=<0.05

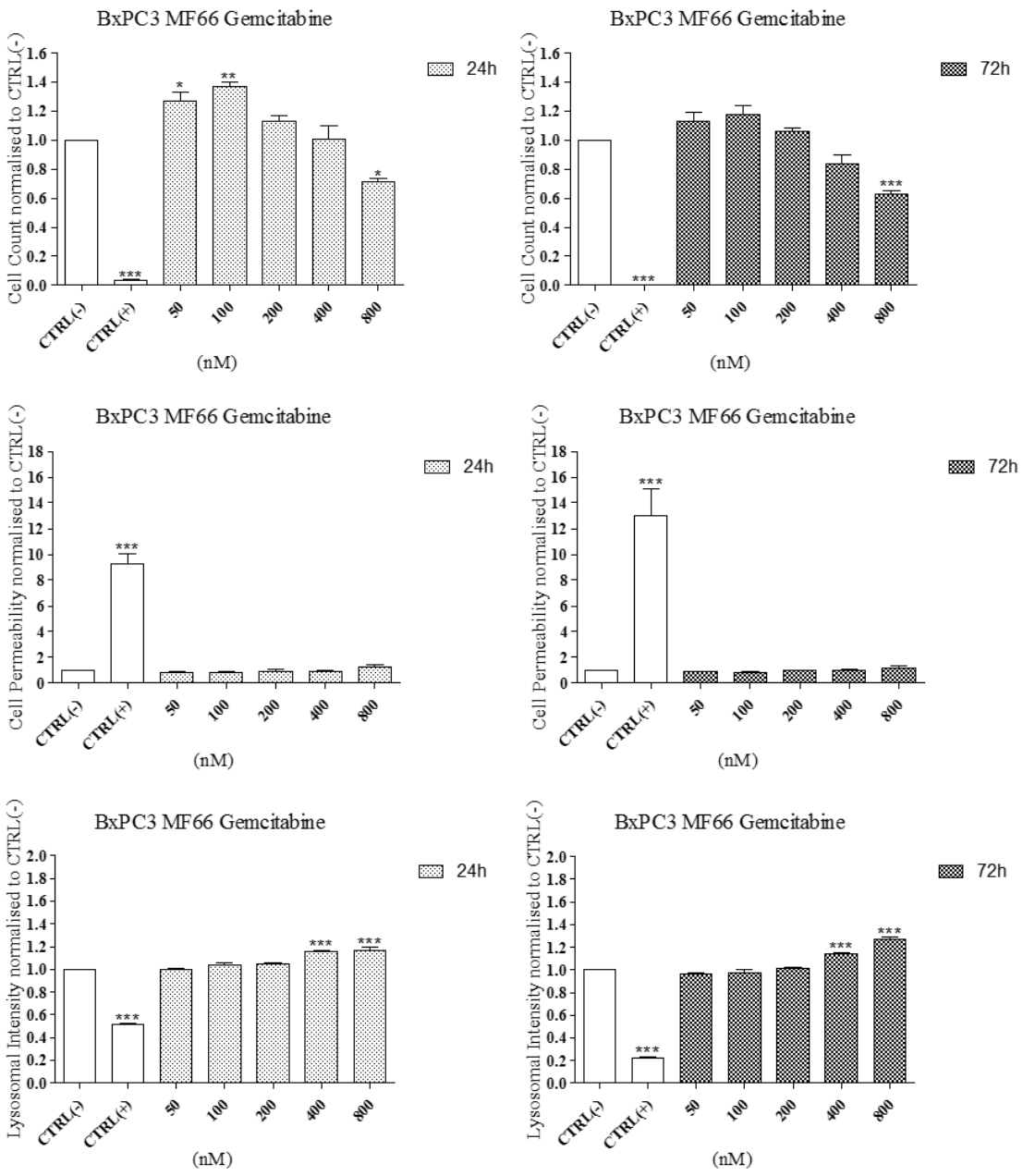

Figure S100: BxPC3 cell line exposed to MF66_Gemcitabine MNP.

BxPC3 pancreatic-derived cell line was exposed to MF66_Gemcitabine MNP for 24h and 72h. Cells were stained using the Cytotoxicity II HitKit™ and analysed using the InCell 1000 HCSA device. Variation in cell count, cell membrane permeability and lysosomal intensity were measured compared to untreated control (CTRL(-)) and 1µM CdSe positive control (CTRL(+)). Statistical significance was determined using the one way ANOVA with Tukey post-test for each column compared to untreated control (CTRL(-)). p value: *** = <0.001, **=<0.01, *=<0.05

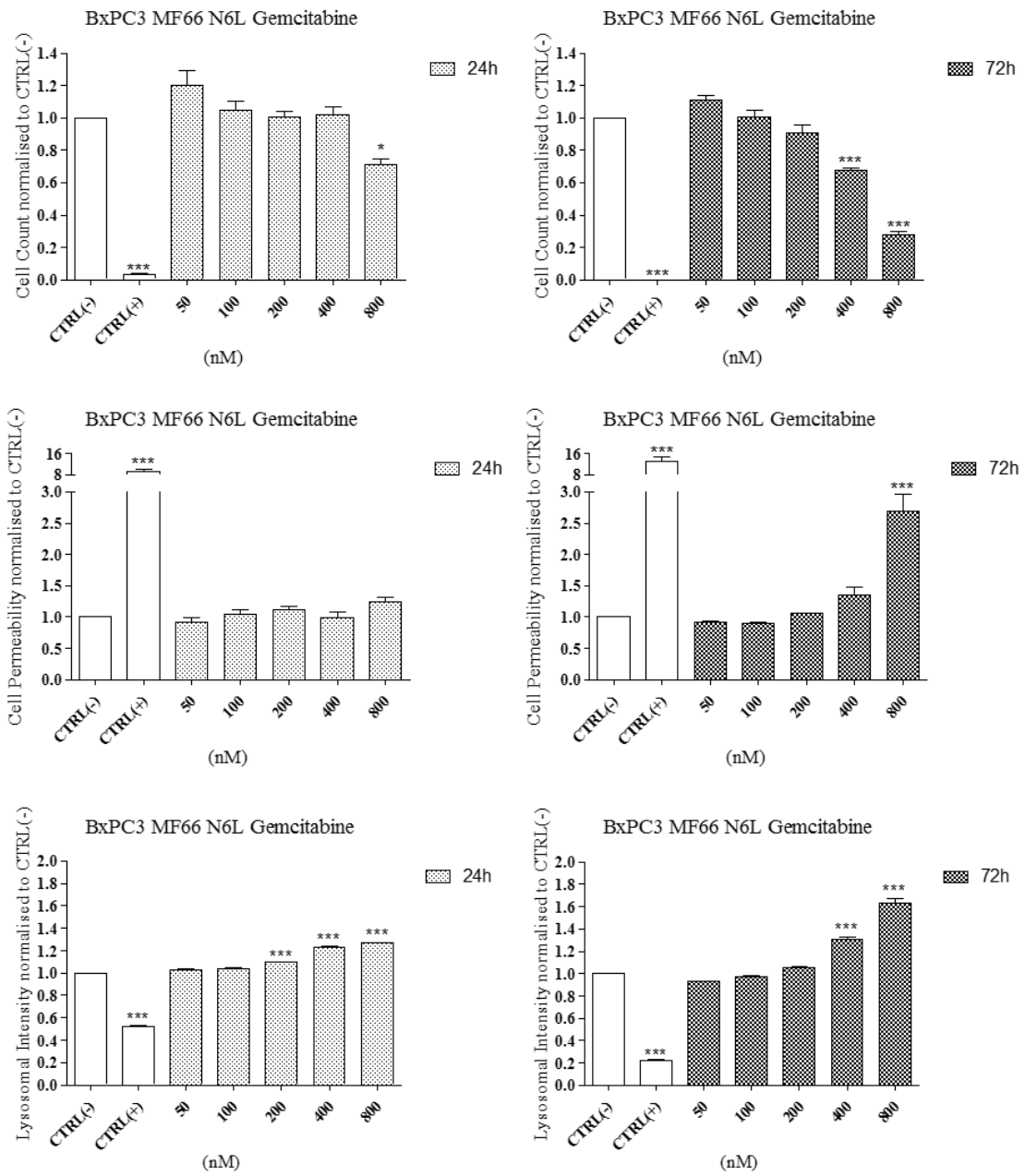

Figure S101: BxPC3 cell line exposed to MF66_N6L_Gemcitabine MNP.

BxPC3 pancreatic-derived cell line was exposed to MF66_N6L_Gemcitabine MNP for 24h and 72h. Cells were stained using the Cytotoxicity II HitKit™ and analysed using the InCell 1000 HCSA device. Variation in cell count, cell membrane permeability and lysosomal intensity were measured compared to untreated control (CTRL(-)) and 1µM CdSe positive control (CTRL(+)). Statistical significance was determined using the one way ANOVA with Tukey post-test for each column compared to untreated control (CTRL(-)). p value: *** = <0.001, **=<0.01, *=<0.05

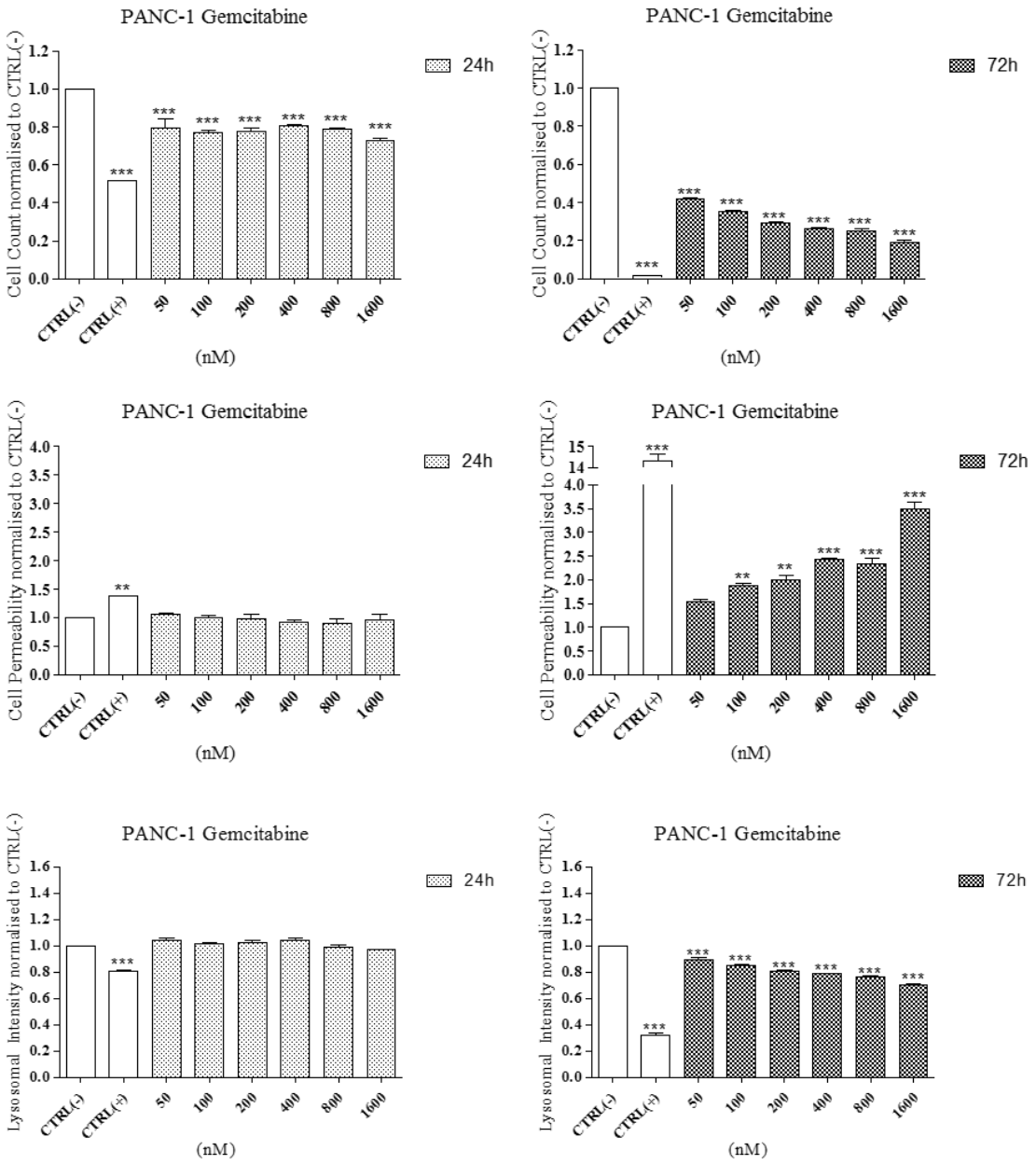

Figure S102: Effect of Gemcitabine on viability of PANC-1 cell line.

PANC-1 pancreatic-derived cell line was exposed to gemcitabine chemotherapeutic drug for 24h and 72h. Cells were stained using the Cytotoxicity II HitKit™ and analysed using the InCell 1000 HCSA device. Variation in cell count, cell membrane permeability and lysosomal intensity were measured compared to untreated control (CTRL(-)) and 1µM CdSe positive control (CTRL(+)). Statistical significance was determined using the one way ANOVA with Tukey post-test for each column compared to untreated control (CTRL(-)). p value: *** = <0.001, **=<0.01, *=<0.05

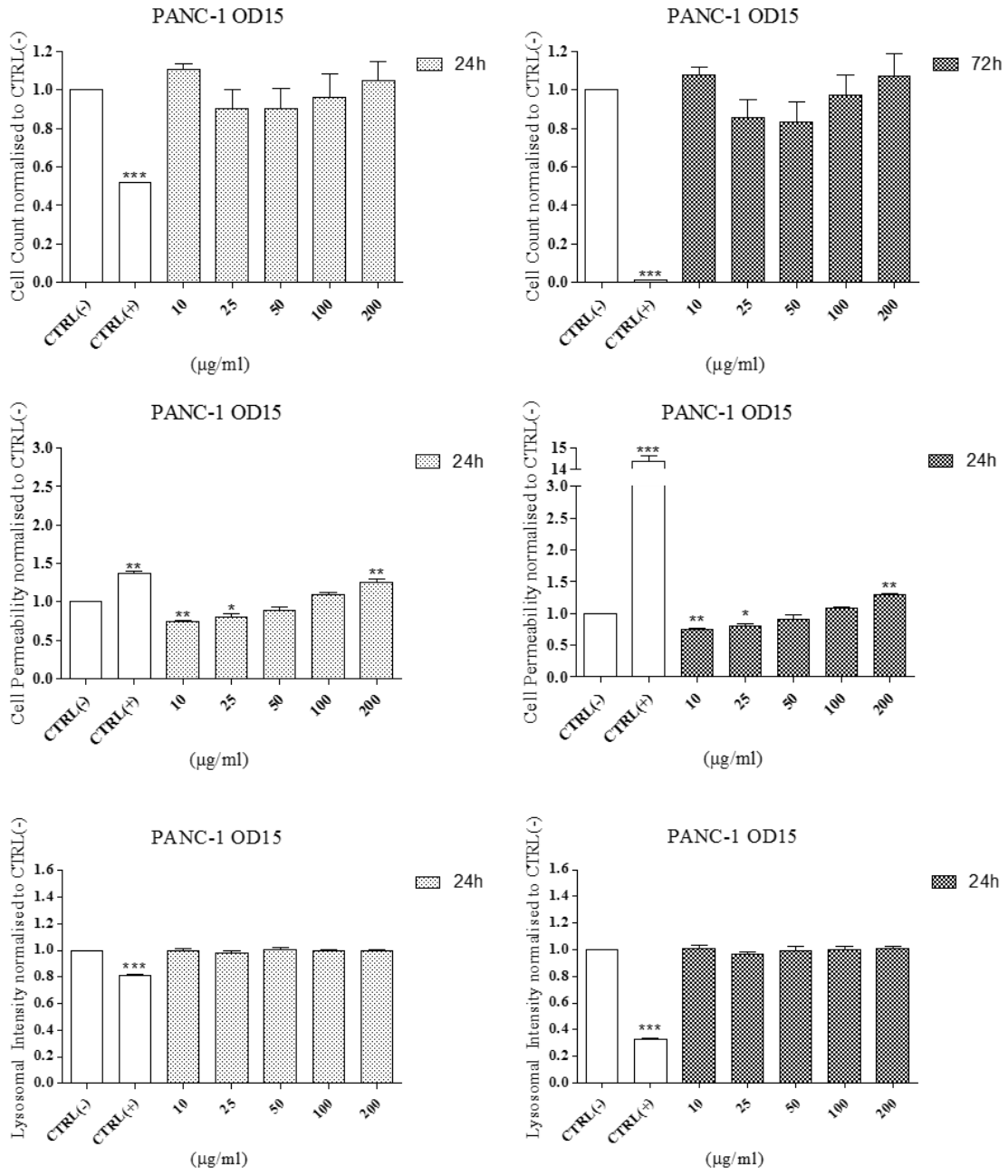

Figure S103: PANC-1 cell line exposed to OD15 MNP.

PANC-1 pancreatic-derived cell line was exposed to OD15 MNP for 24h and 72h. Cells were stained using the Cytotoxicity II HitKit™ and analysed using the InCell 1000 HCSA device. Variation in cell count, cell membrane permeability and lysosomal intensity were measured compared to untreated control (CTRL(-)) and 1µM CdSe positive control (CTRL(+)). Statistical significance was determined using the one way ANOVA with Tukey post-test for each column compared to untreated control (CTRL(-)). p value: *** = <0.001, **=<0.01, *=<0.05

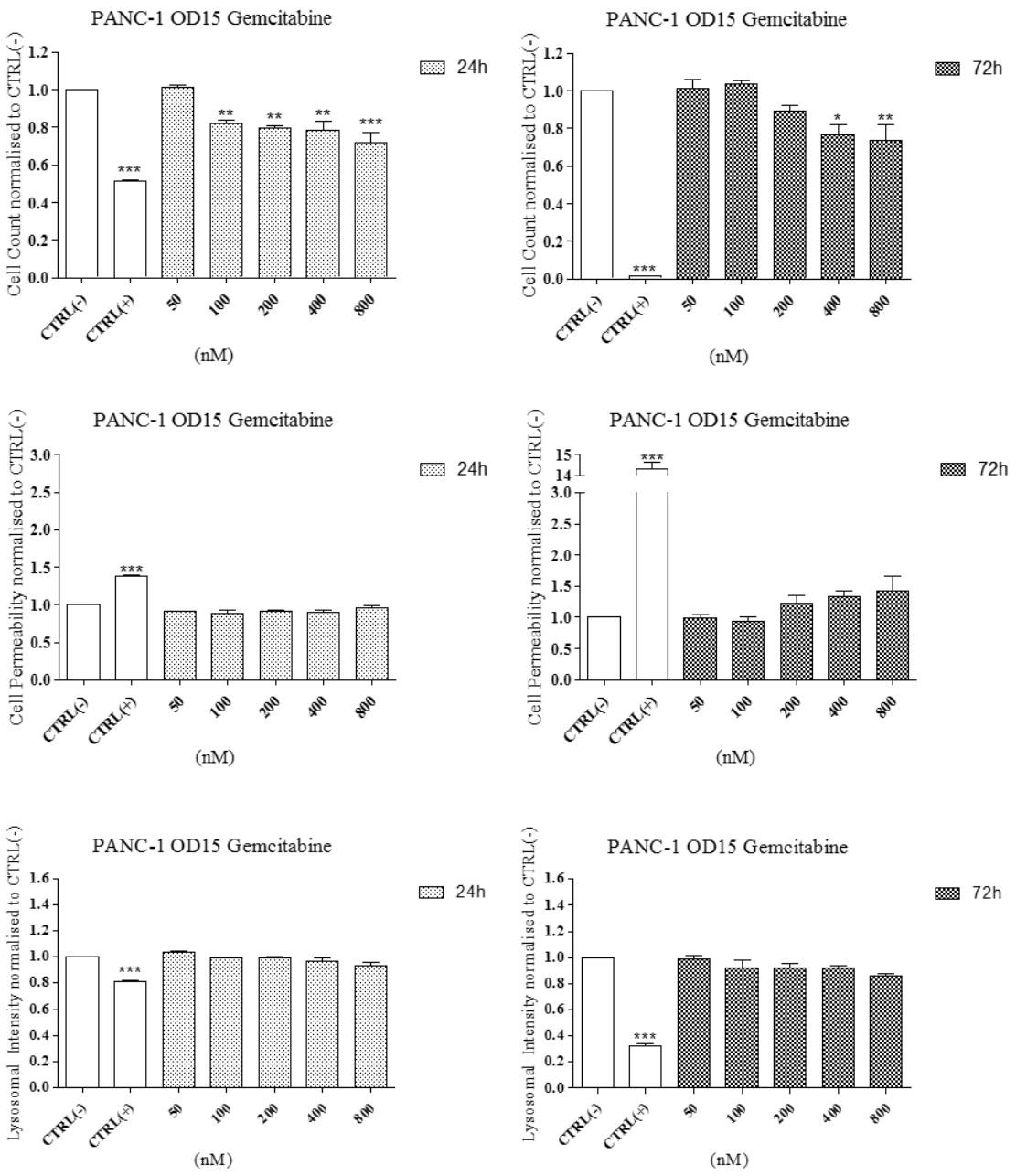

Figure S104: PANC-1 cell line exposed to OD15_Gemcitabine MNP.

PANC-1 pancreatic-derived cell line was exposed to OD15_Gemcitabine MNP for 24h and 72h. Cells were stained using the Cytotoxicity II HitKit™ and analysed using the InCell 1000 HCSA device. Variation in cell count, cell membrane permeability and lysosomal intensity were measured compared to untreated control (CTRL(-)) and 1µM CdSe positive control (CTRL(+)). Statistical significance was determined using the one way ANOVA with Tukey post-test for each column compared to untreated control (CTRL(-)). p value: *** = <0.001, **=<0.01, *=<0.05

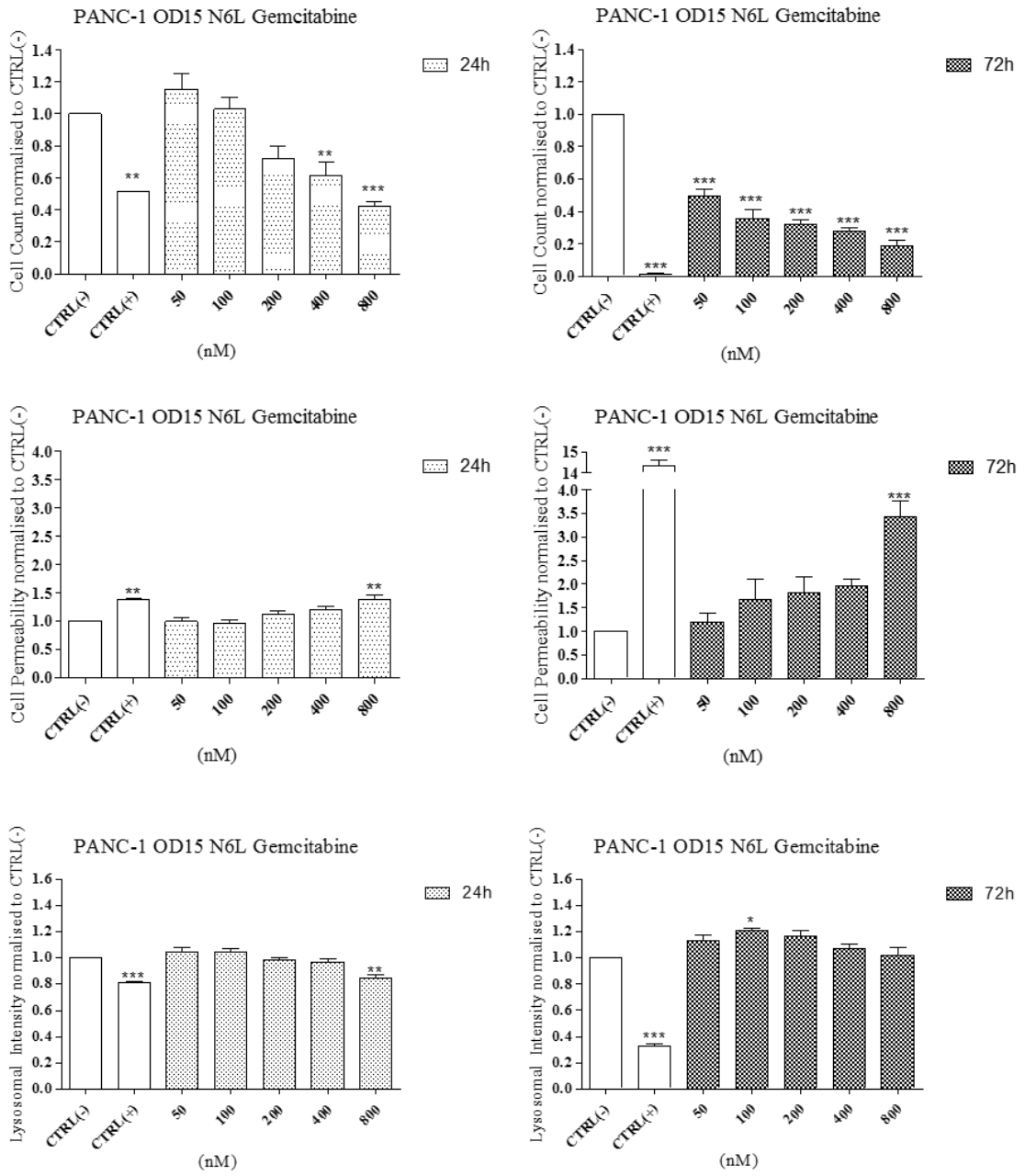

Figure S105: PANC-1 cell line exposed to OD15_N6L_Gemcitabine MNP.

PANC-1 pancreatic-derived cell line was exposed to OD15_N6L_Gemcitabine MNP for 24h and 72h. Cells were stained using the Cytotoxicity II HitKit™ and analysed using the InCell 1000 HCSA device. Variation in cell count, cell membrane permeability and lysosomal intensity were measured compared to untreated control (CTRL(-)) and 1µM CdSe positive control (CTRL(+)). Statistical significance was determined using the one way ANOVA with Tukey post-test for each column compared to untreated control (CTRL(-)). p value: *** = <0.001, **=<0.01, *=<0.05

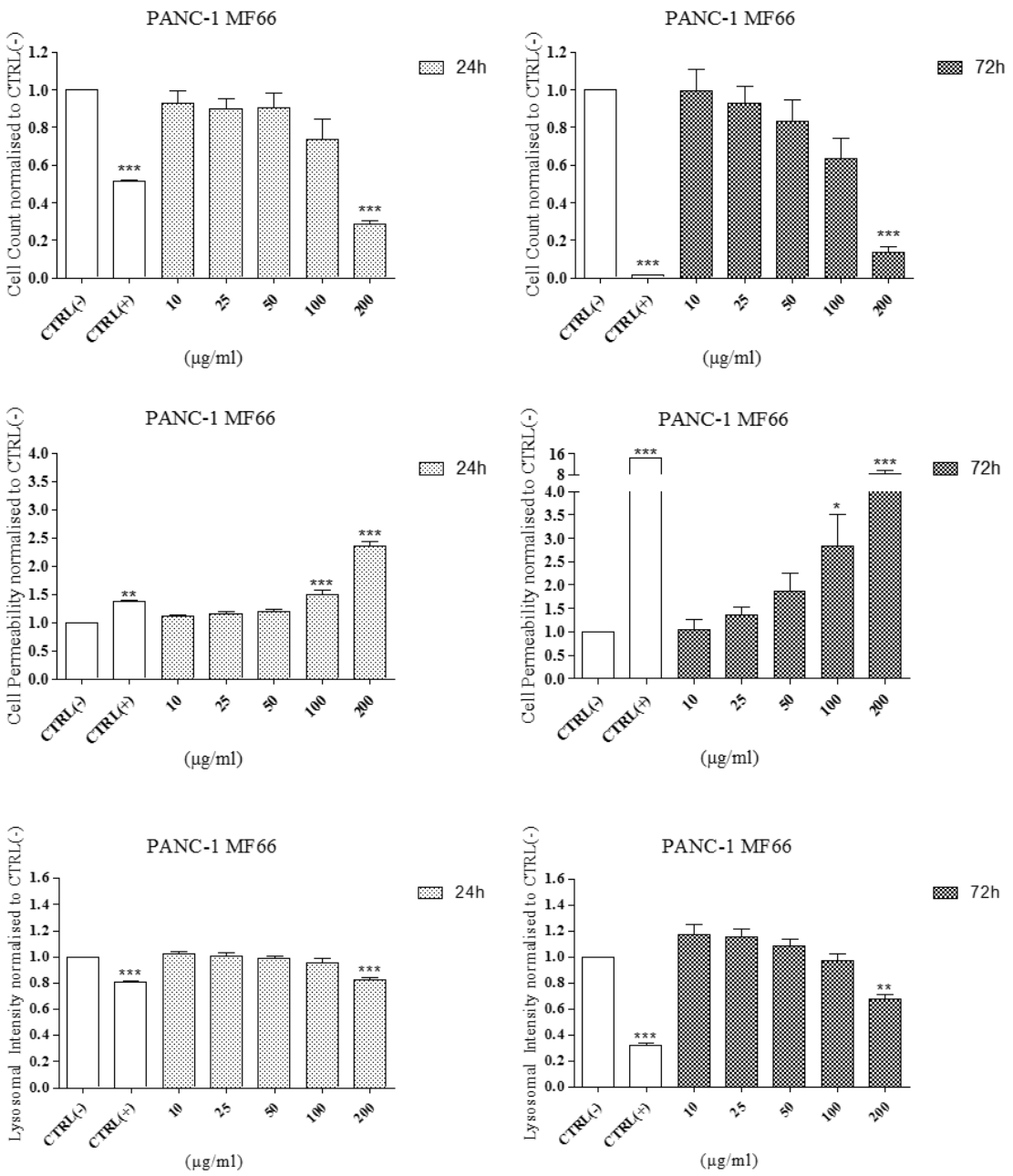

Figure S106: PANC-1 cell line exposed to MF66 MNP.

PANC-1 pancreatic-derived cell line was exposed to MF66 MNP for 24h and 72h. Cells were stained using the Cytotoxicity II HitKit™ and analysed using the InCell 1000 HCSA device. Variation in cell count, cell membrane permeability and lysosomal intensity were measured compared to untreated control (CTRL(-)) and 1µM CdSe positive control (CTRL(+)). Statistical significance was determined using the one way ANOVA with Tukey post-test for each column compared to untreated control (CTRL(-)). p value: *** = <0.001, **=<0.01, *=<0.05

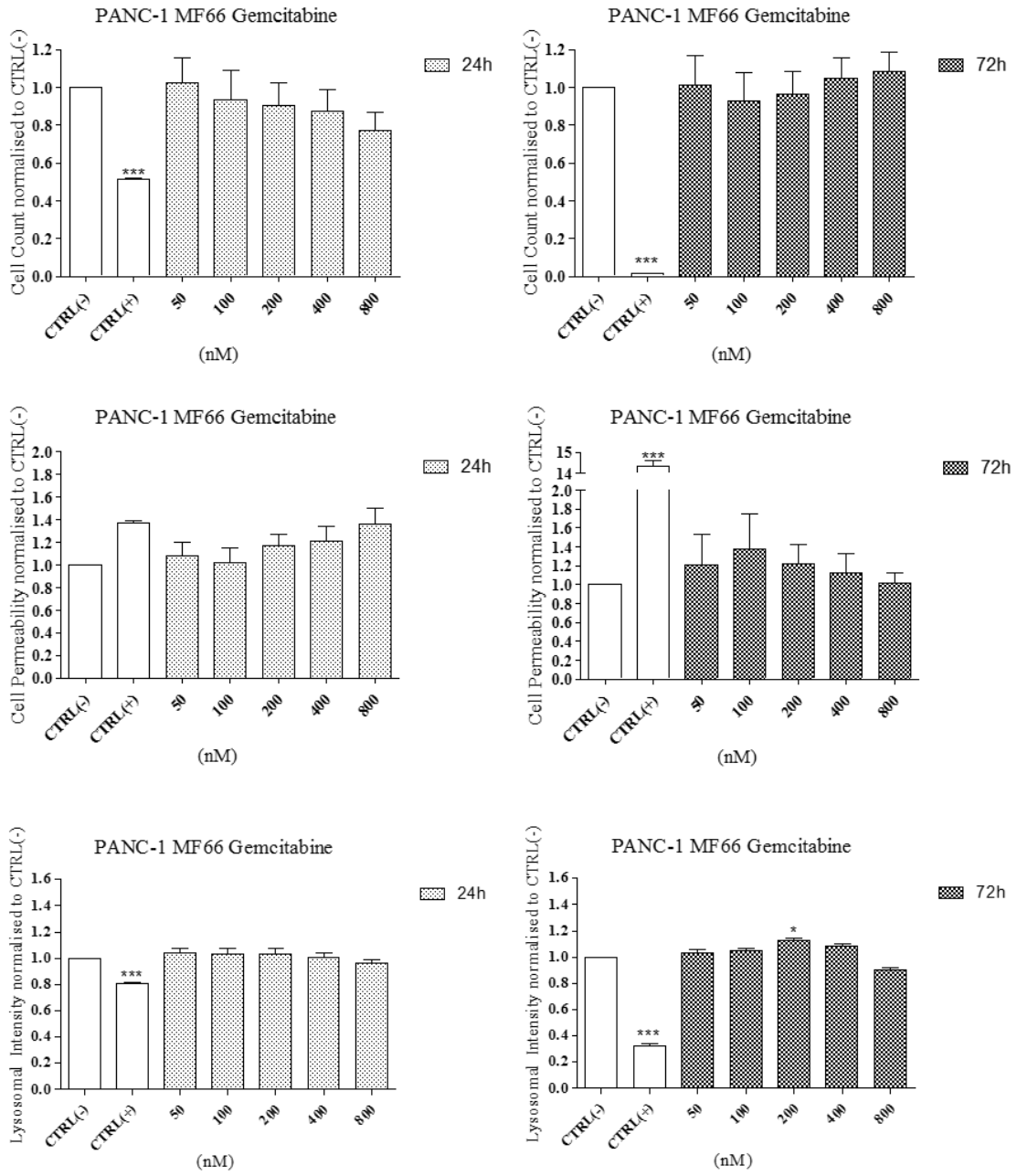

Figure S107: PANC-1 cell line exposed to MF66_Gemcitabine MNP.

PANC-1 pancreatic-derived cell line was exposed to MF66_Gemcitabine MNP for 24h and 72h. Cells were stained using the Cytotoxicity II HitKit™ and analysed using the InCell 1000 HCSA device. Variation in cell count, cell membrane permeability and lysosomal intensity were measured compared to untreated control (CTRL(-)) and 1µM CdSe positive control (CTRL(+)). Statistical significance was determined using the one way ANOVA with Tukey post-test for each column compared to untreated control (CTRL(-)). p value: *** = <0.001, **=<0.01, *=<0.05

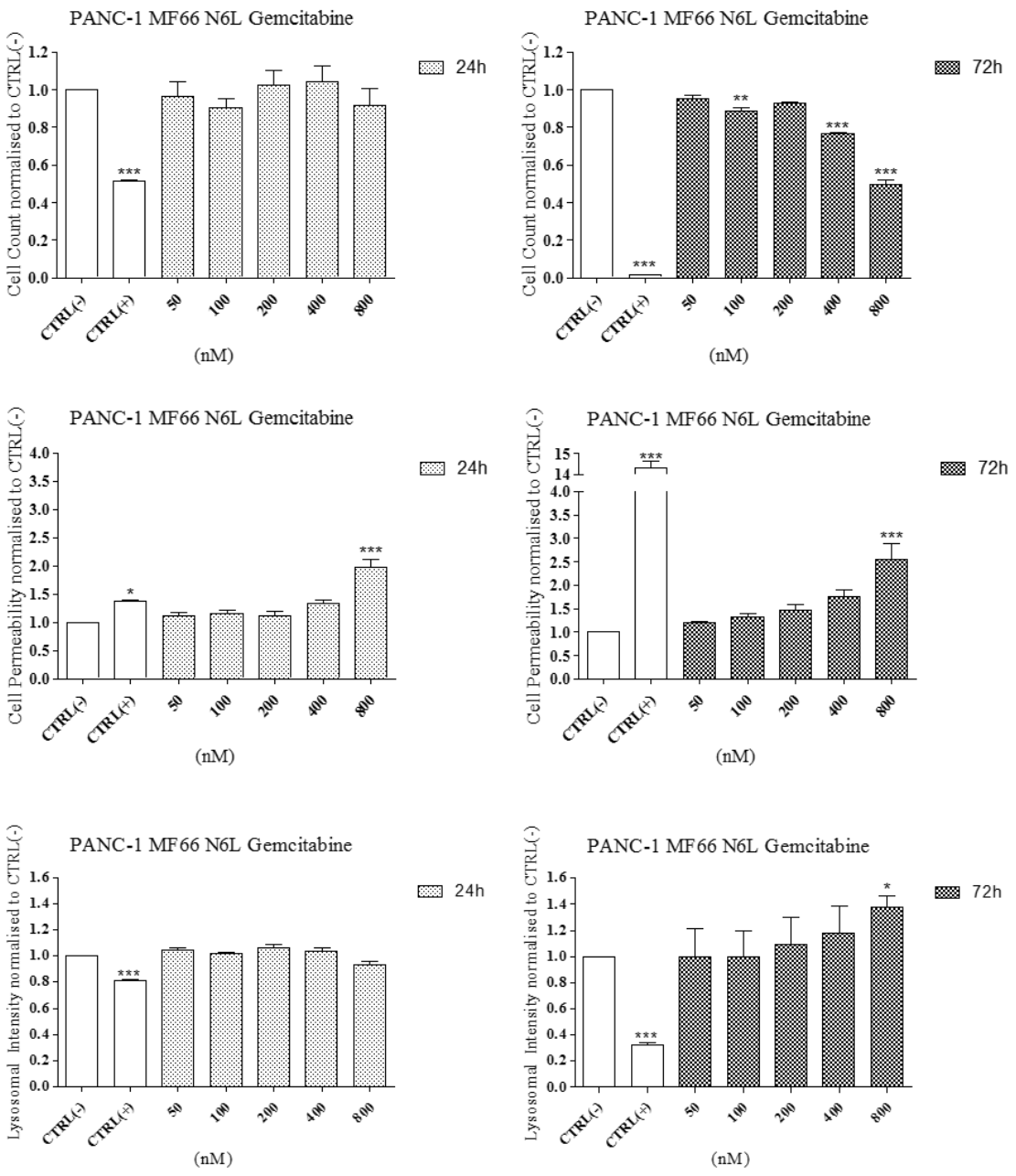

Figure S108: PANC-1 cell line exposed to MF66_N6L_Gemcitabine MNP.

PANC-1 pancreatic-derived cell line was exposed to MF66_N6L_Gemcitabine MNP for 24h and 72h. Cells were stained using the Cytotoxicity II HitKit™ and analysed using the InCell 1000 HCSA device. Variation in cell count, cell membrane permeability and lysosomal intensity were measured compared to untreated control (CTRL(-)) and 1µM CdSe positive control (CTRL(+)). Statistical significance was determined using the one way ANOVA with Tukey post-test for each column compared to untreated control (CTRL(-)). p value: *** = <0.001, **=<0.01, *=<0.05

Appendix 3: Chapter 5 graphs

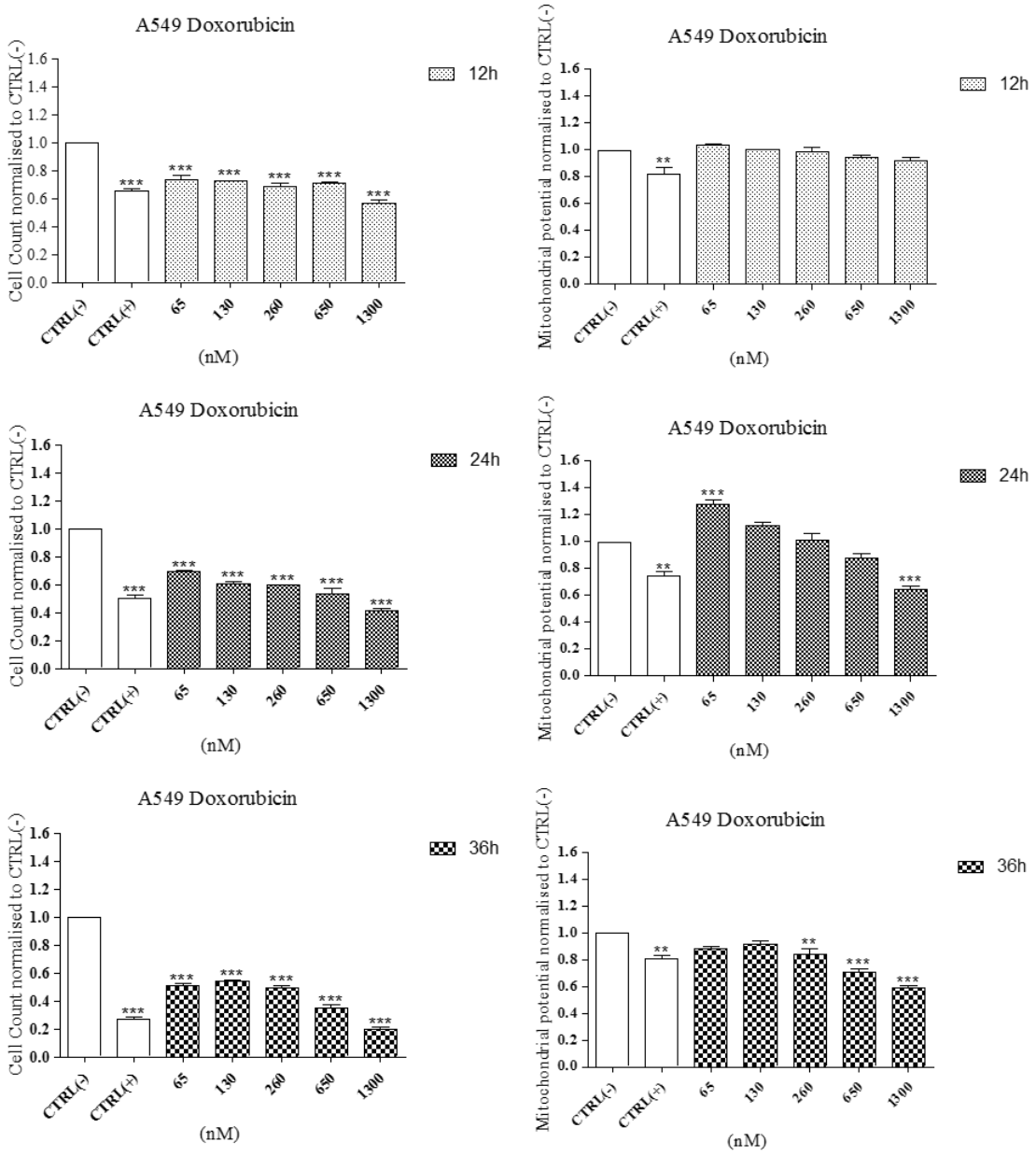

Figure S109: Effect of Doxorubicin on viability and mitochondrial potential of A549 cell line.

A549 lung epithelial-derived cell line was exposed to Doxorubicin for 12h, 24h and 36h. Cells were stained using the Cytotoxicity II HitKit™ and analysed using the InCell 1000 HCSA device. Variation in cell count and mitochondrial membrane potential were measured compared to untreated control (CTRL(-)) and 1µM CdSe positive control (CTRL(+)). Statistical significance was determined using the one way ANOVA with Tukey post-test for each column compared to untreated control (CTRL(-)). p value: *** = <0.001, **=<0.01, *=<0.05

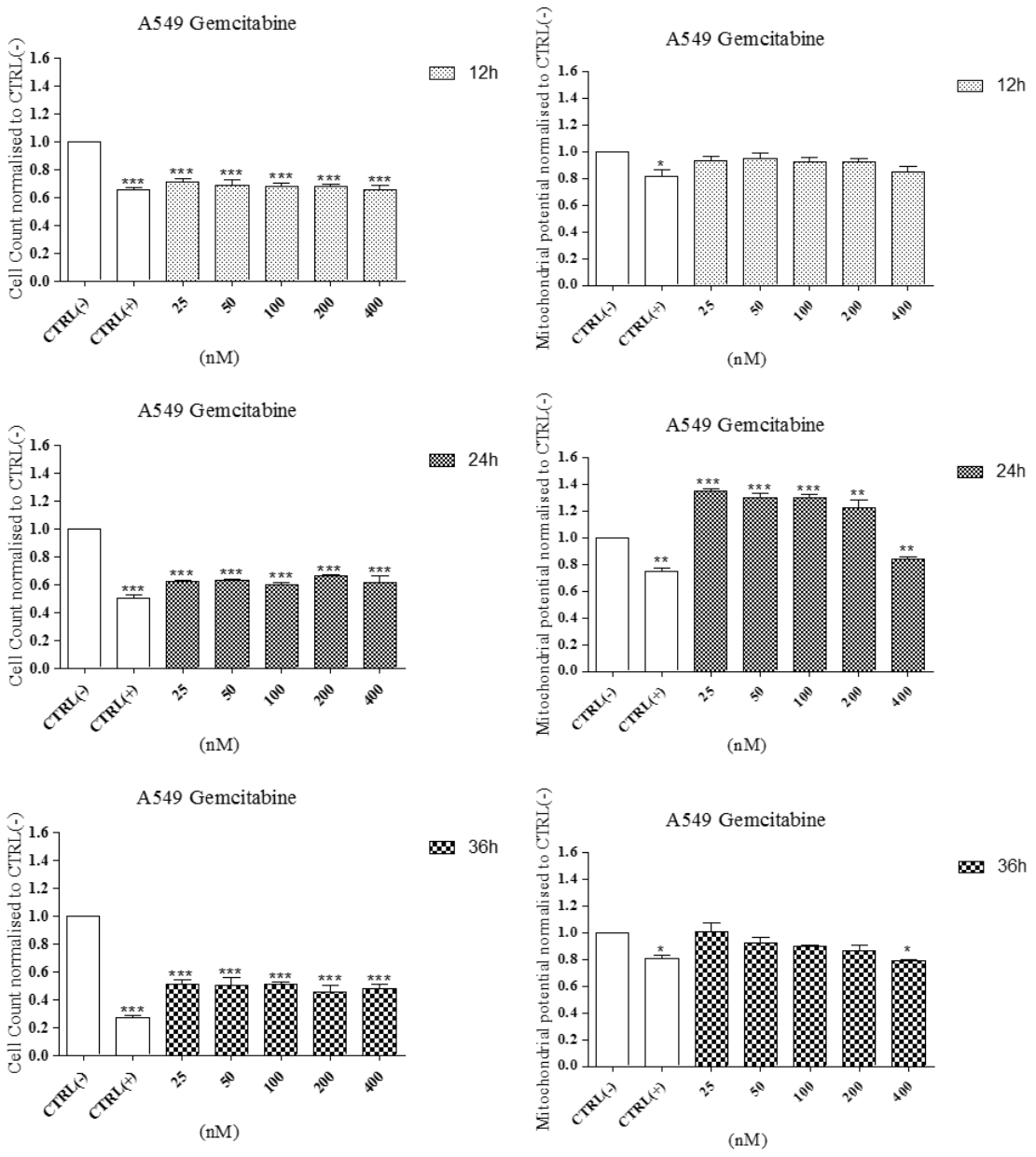

Figure S110: Effect of Gemcitabine on viability and mitochondrial potential of A549 cell line.

A549 lung epithelial-derived cell line was exposed to Gemcitabine for 12h, 24h and 36h. Cells were stained using the Cytotoxicity II HitKit™ and analysed using the InCell 1000 HCSA device. Variation in cell count and mitochondrial membrane potential were measured compared to untreated control (CTRL(-)) and 1µM CdSe positive control (CTRL(+)). Statistical significance was determined using the one way ANOVA with Tukey post-test for each column compared to untreated control (CTRL(-)). p value: *** = <0.001, **=<0.01, *=<0.05

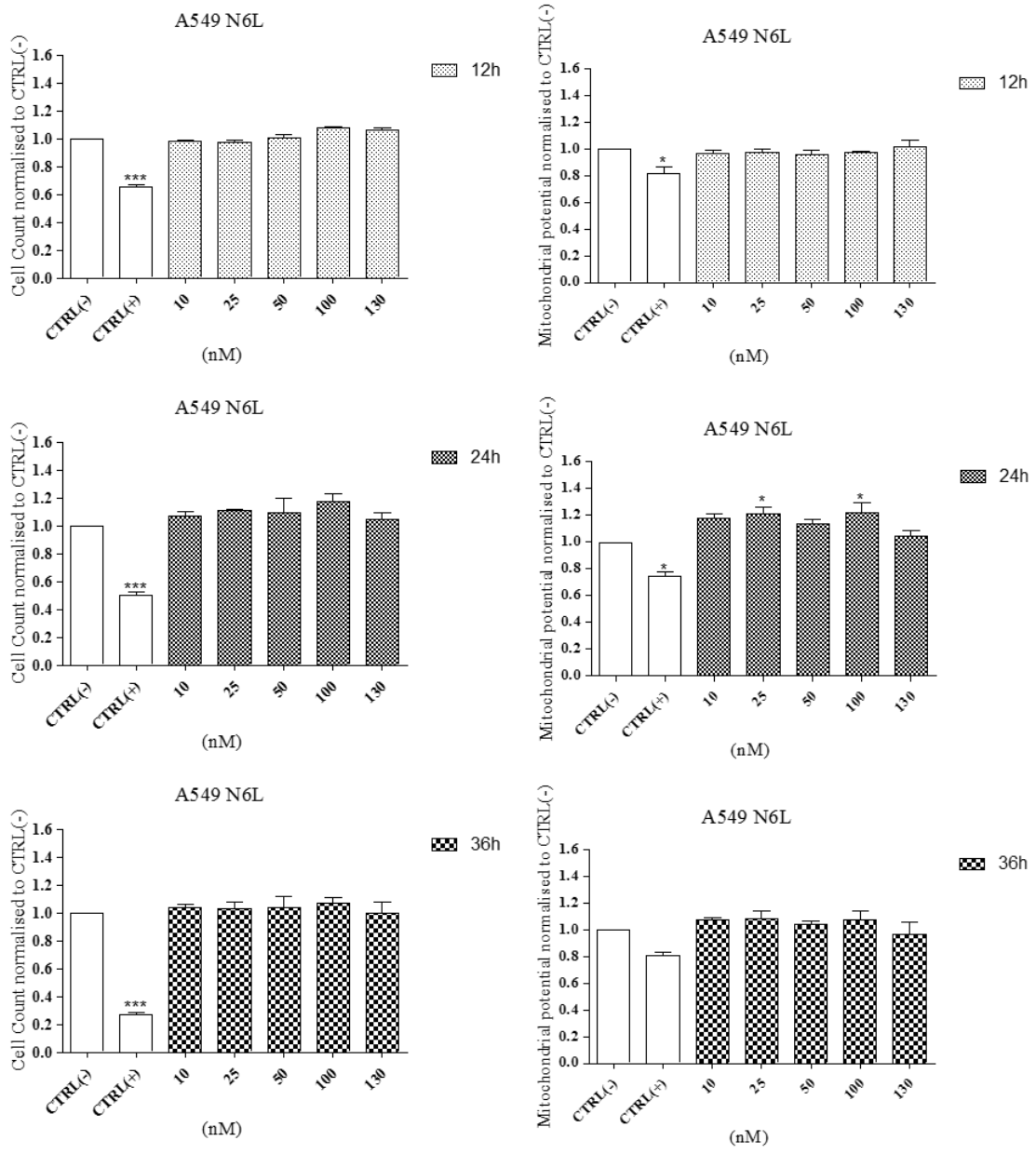

Figure S111: Effect of N6L on viability and mitochondrial potential of A549 cell line.

A549 lung epithelial-derived cell line was exposed to N6L for 12h, 24h and 36h. Cells were stained using the Cytotoxicity II HitKit™ and analysed using the InCell 1000 HCSA device. Variation in cell count and mitochondrial membrane potential were measured compared to untreated control (CTRL(-)) and 1µM CdSe positive control (CTRL(+)). Statistical significance was determined using the one way ANOVA with Tukey post-test for each column compared to untreated control (CTRL(-)). p value: *** = <0.001, **=<0.01, *=<0.05

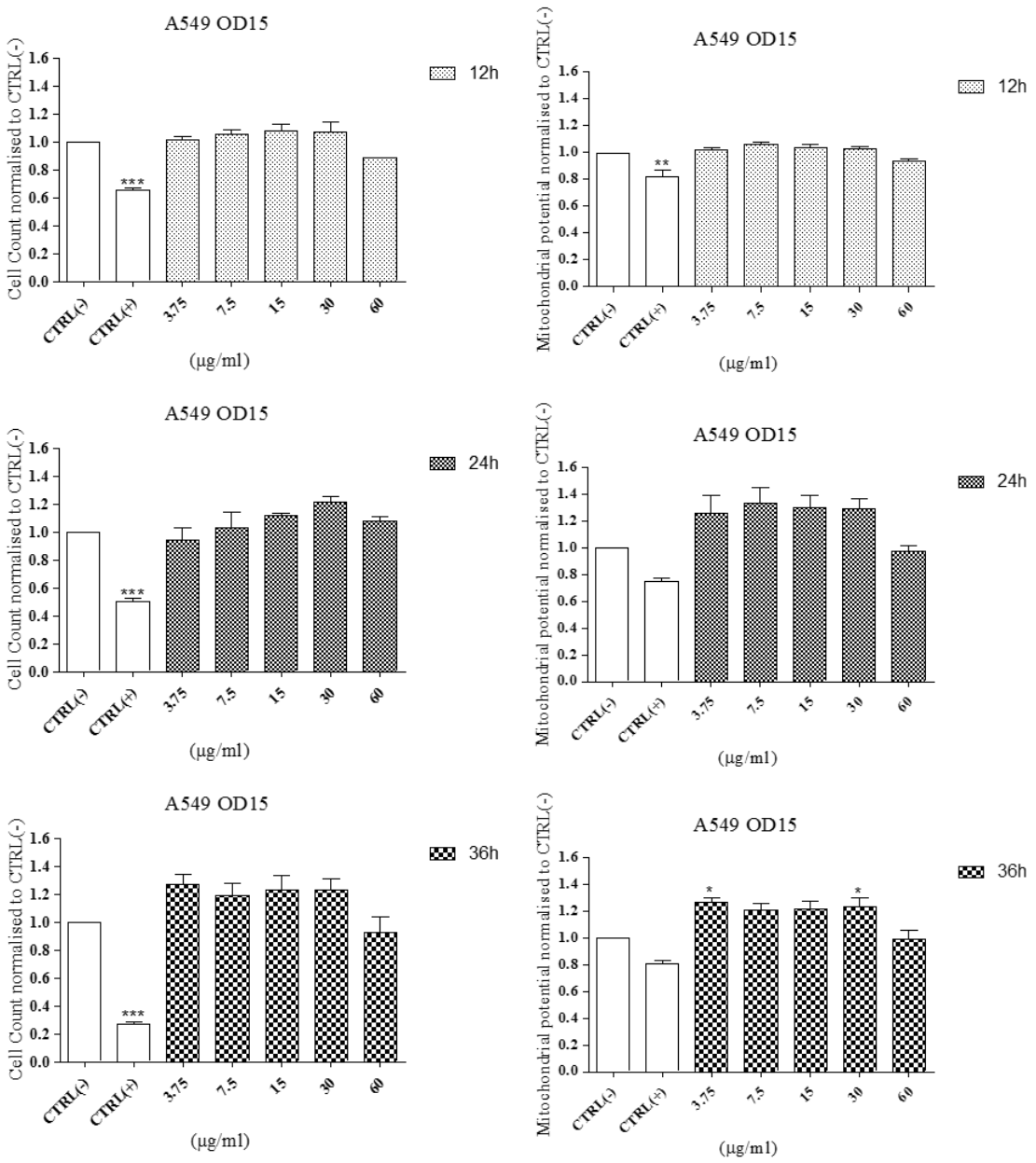

Figure S112: Effect of Doxorubicin on viability and mitochondrial potential of A549 cell line.

A549 lung epithelial-derived cell line was exposed to Doxorubicin for 12h, 24h and 36h. Cells were stained using the Cytotoxicity II HitKit™ and analysed using the InCell 1000 HCSA device. Variation in cell count and mitochondrial membrane potential were measured compared to untreated control (CTRL(-)) and 1µM CdSe positive control (CTRL(+)). Statistical significance was determined using the one way ANOVA with Tukey post-test for each column compared to untreated control (CTRL(-)). p value: *** = <0.001, **=<0.01, *=<0.05

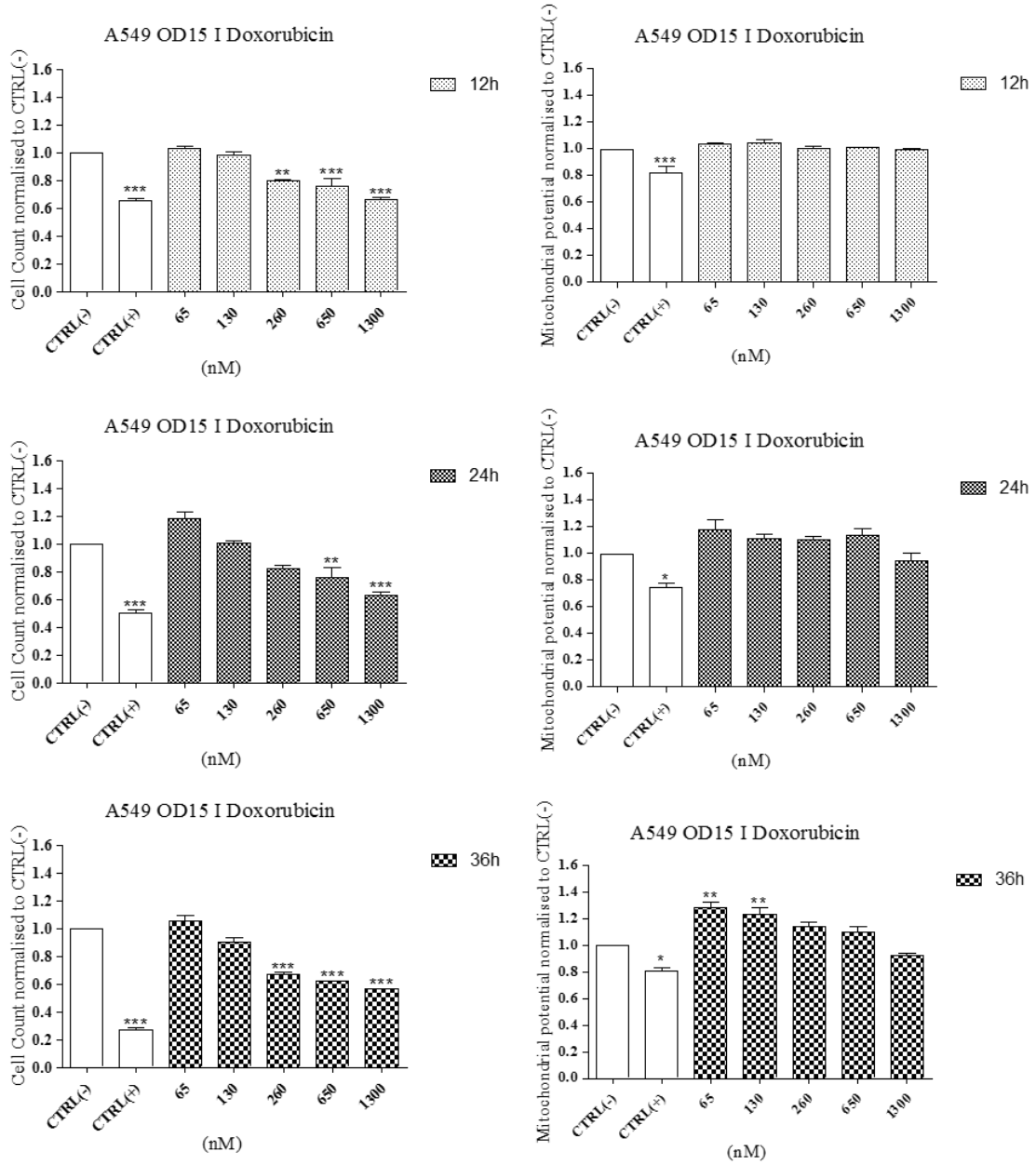

Figure S113: A549 cell line exposed to OD15_I_Doxorubicin MNP.

A549 lung epithelial-derived cell line was exposed to OD15_I_Doxorubicin MNP for 12h, 24h and 36h. Cells were stained using the Cytotoxicity II HitKit™ and analysed using the InCell 1000 HCSA device. Variation in cell count and mitochondrial membrane potential were measured compared to untreated control (CTRL(-)) and 1µM CdSe positive control (CTRL(+)). Statistical significance was determined using the one way ANOVA with Tukey post-test for each column compared to untreated control (CTRL(-)). p value: *** = <0.001, **=<0.01, *=<0.05

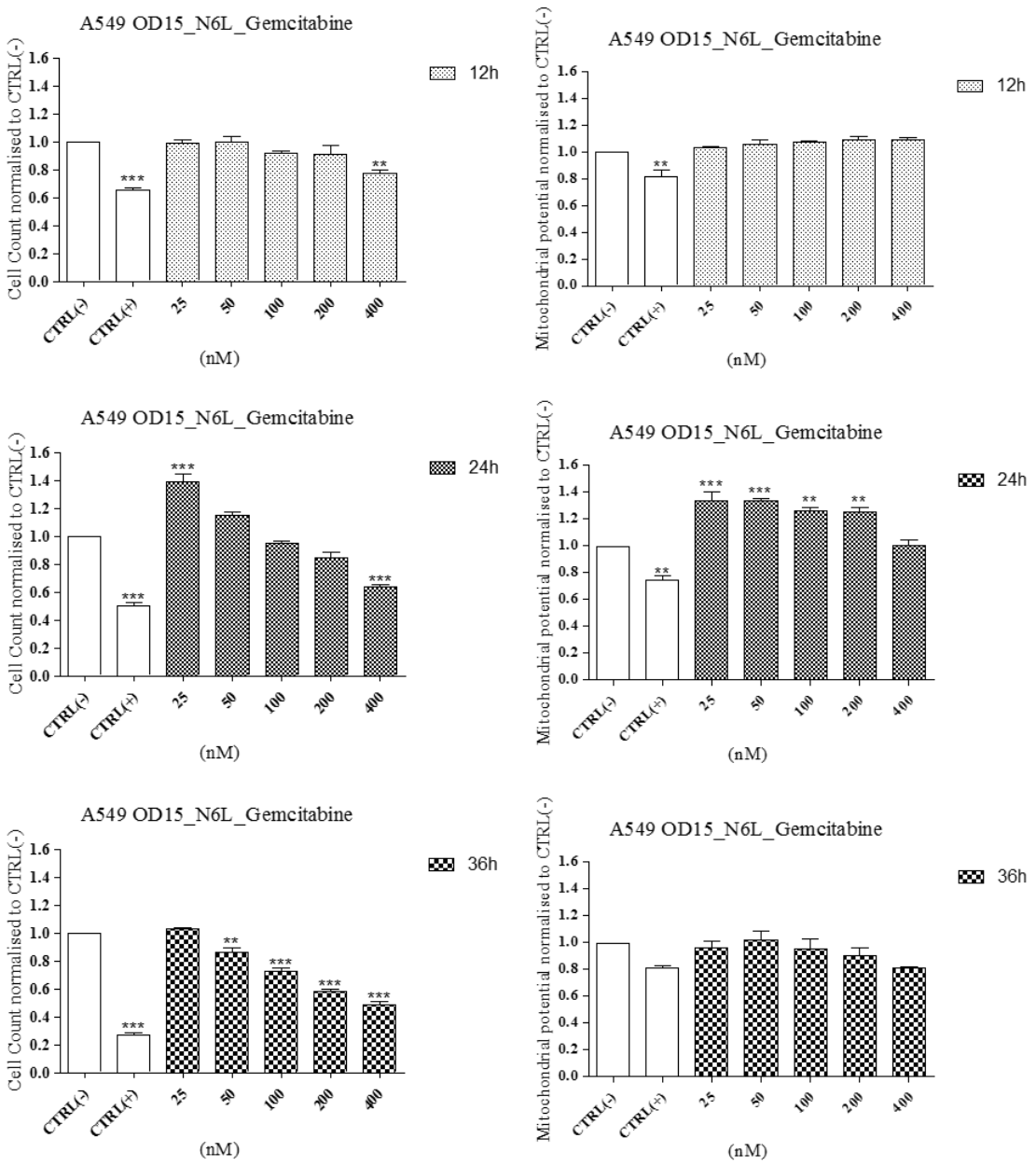

Figure S114: A549 cell line exposed to OD15_N6L_Gemcitabine MNP.

A549 lung epithelial-derived cell line was exposed to OD15_N6L_Gemcitabine MNP for 12h, 24h and 36h. Cells were stained using the Cytotoxicity II HitKit™ and analysed using the InCell 1000 HCSA device. Variation in cell count and mitochondrial membrane potential were measured compared to untreated control (CTRL(-)) and 1µM CdSe positive control (CTRL(+)). Statistical significance was determined using the one way ANOVA with Tukey post-test for each column compared to untreated control (CTRL(-)). p value: *** = <0.001, **=<0.01, *=<0.05

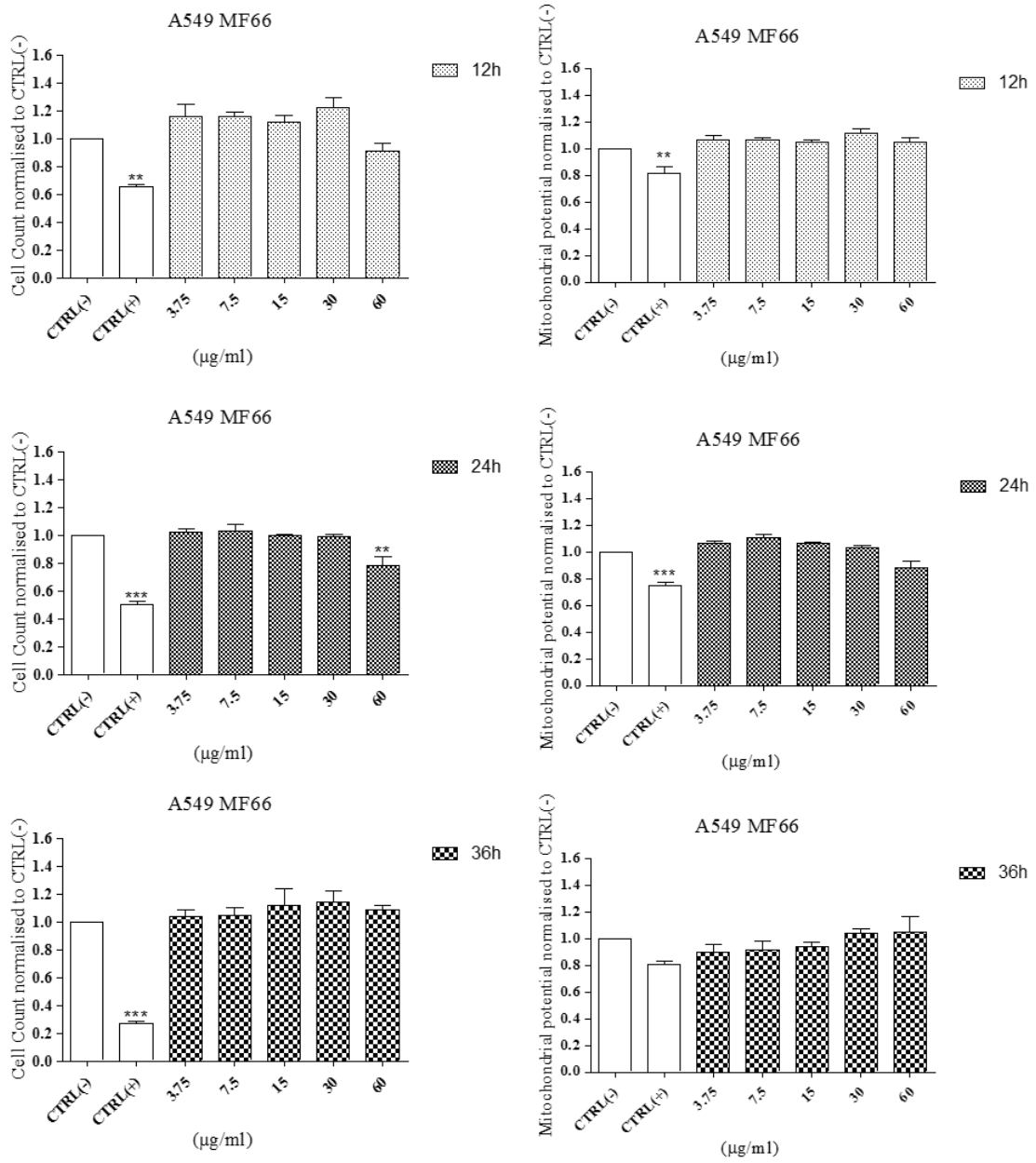

Figure S115: A549 cell line exposed to MF66 MNP.

A549 lung epithelial-derived cell line was exposed to MF66 MNP for 12h, 24h and 36h. Cells were stained using the Cytotoxicity II HitKit™ and analysed using the InCell 1000 HCSA device. Variation in cell count and mitochondrial membrane potential were measured compared to untreated control (CTRL(-)) and 1µM CdSe positive control (CTRL(+)). Statistical significance was determined using the one way ANOVA with Tukey post-test for each column compared to untreated control (CTRL(-)). p value: *** = <0.001, **=<0.01, *=<0.05

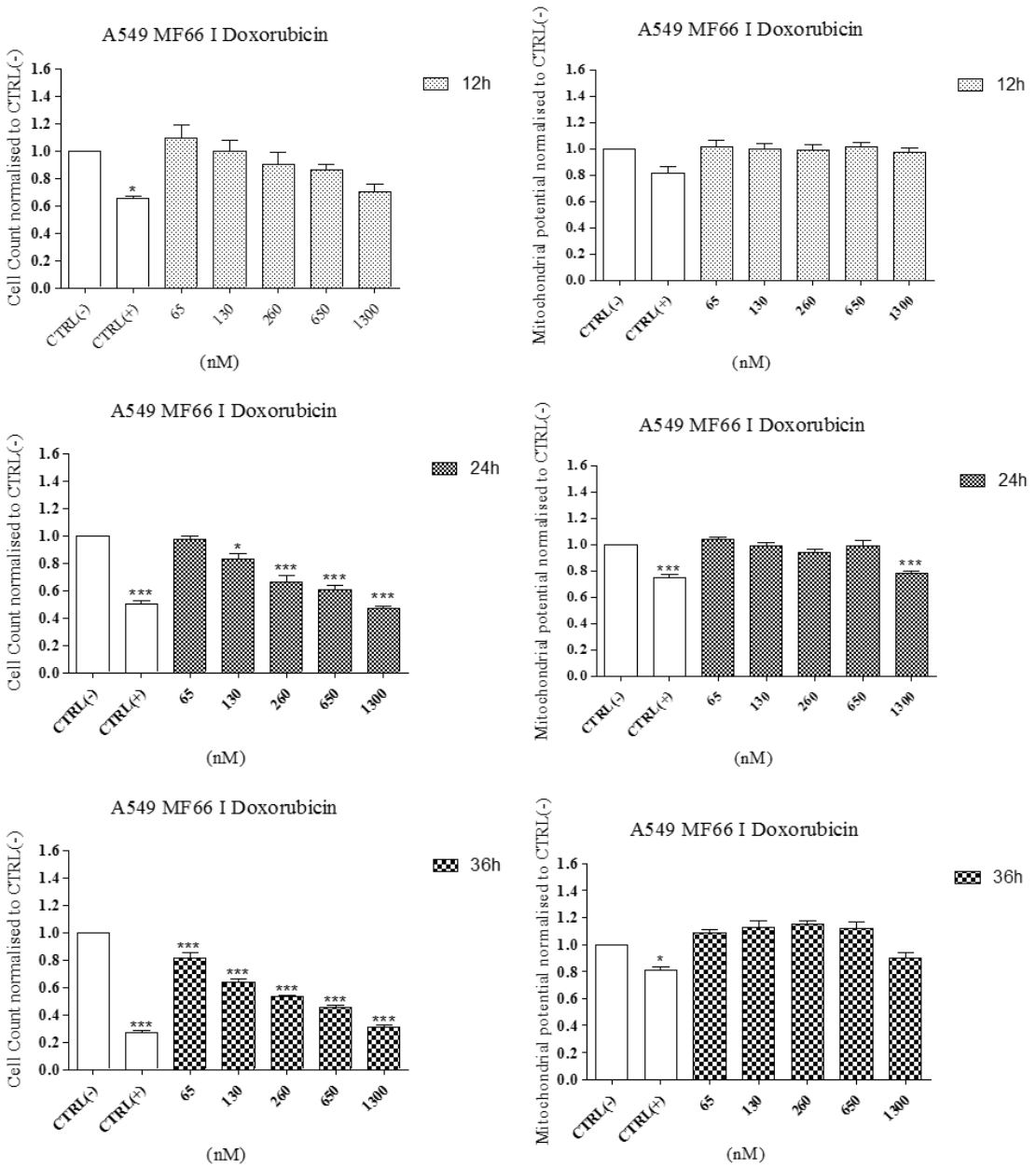

Figure S116: A549 cell line exposed to MF66_I_Doxorubicin MNP.

A549 lung epithelial-derived cell line was exposed to MF6_I_Doxorubicin MNP for 12h, 24h and 36h. Cells were stained using the Cytotoxicity II HitKit™ and analysed using the InCell 1000 HCSA device. Variation in cell count and mitochondrial membrane potential were measured compared to untreated control (CTRL(-)) and 1µM CdSe positive control (CTRL(+)). Statistical significance was determined using the one way ANOVA with Tukey post-test for each column compared to untreated control (CTRL(-)). p value: *** = <0.001, **=<0.01, *=<0.05

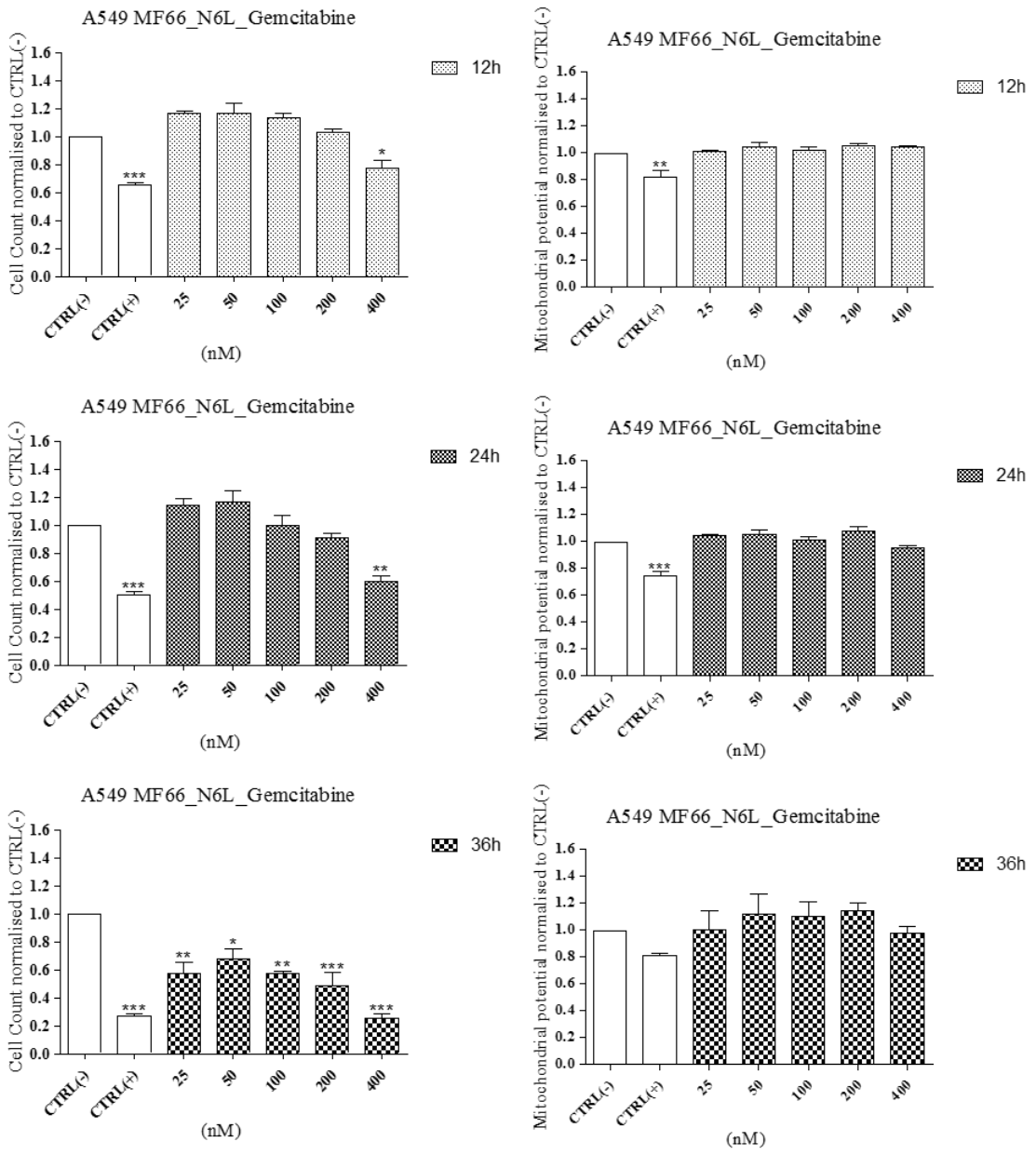

Figure S117: A549 cell line exposed to MF66_N6L_Gemcitabine MNP.

A549 lung epithelial-derived cell line was exposed to MF6_N6L_Gemcitabine MNP for 12h, 24h and 36h. Cells were stained using the Cytotoxicity II HitKit™ and analysed using the InCell 1000 HCSA device. Variation in cell count and mitochondrial membrane potential were measured compared to untreated control (CTRL(-)) and 1µM CdSe positive control (CTRL(+)). Statistical significance was determined using the one way ANOVA with Tukey post-test for each column compared to untreated control (CTRL(-)). p value: *** = <0.001, **=<0.01, *=<0.05

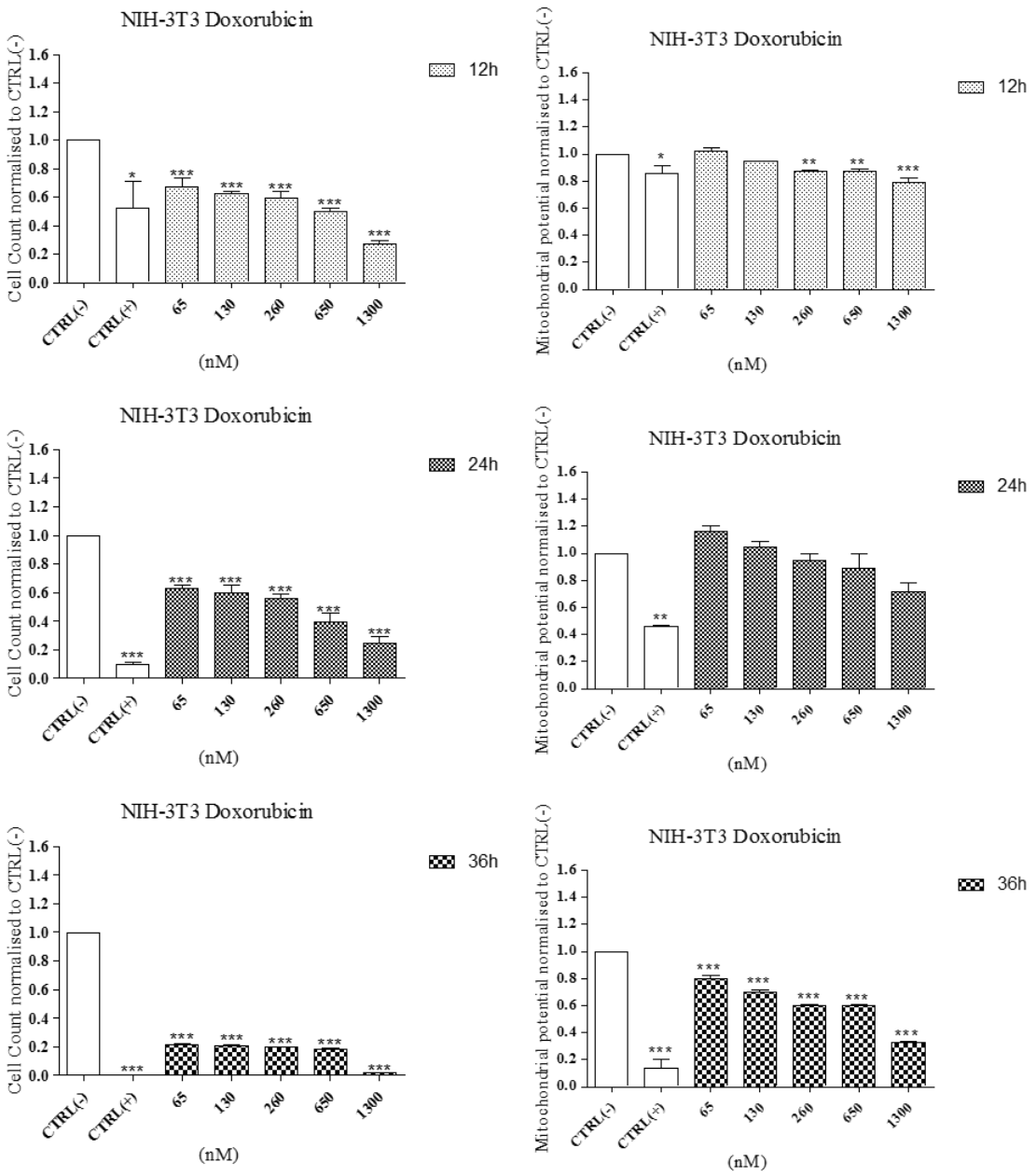

Figure S118: Effect of Doxorubicin on viability and mitochondrial potential of NIH-3T3 cell line.

NIH-3T3 mouse fibroblast-derived cell line was exposed to Doxorubicin for 12h, 24h and 36h. Cells were stained using the Cytotoxicity II HitKit™ and analysed using the InCell 1000 HCSA device. Variation in cell count and mitochondrial membrane potential were measured compared to untreated control (CTRL(-)) and 1µM CdSe positive control (CTRL(+)). Statistical significance was determined using the one way ANOVA with Tukey post-test for each column compared to untreated control (CTRL(-)). p value: *** = <0.001, **=<0.01, *=<0.05

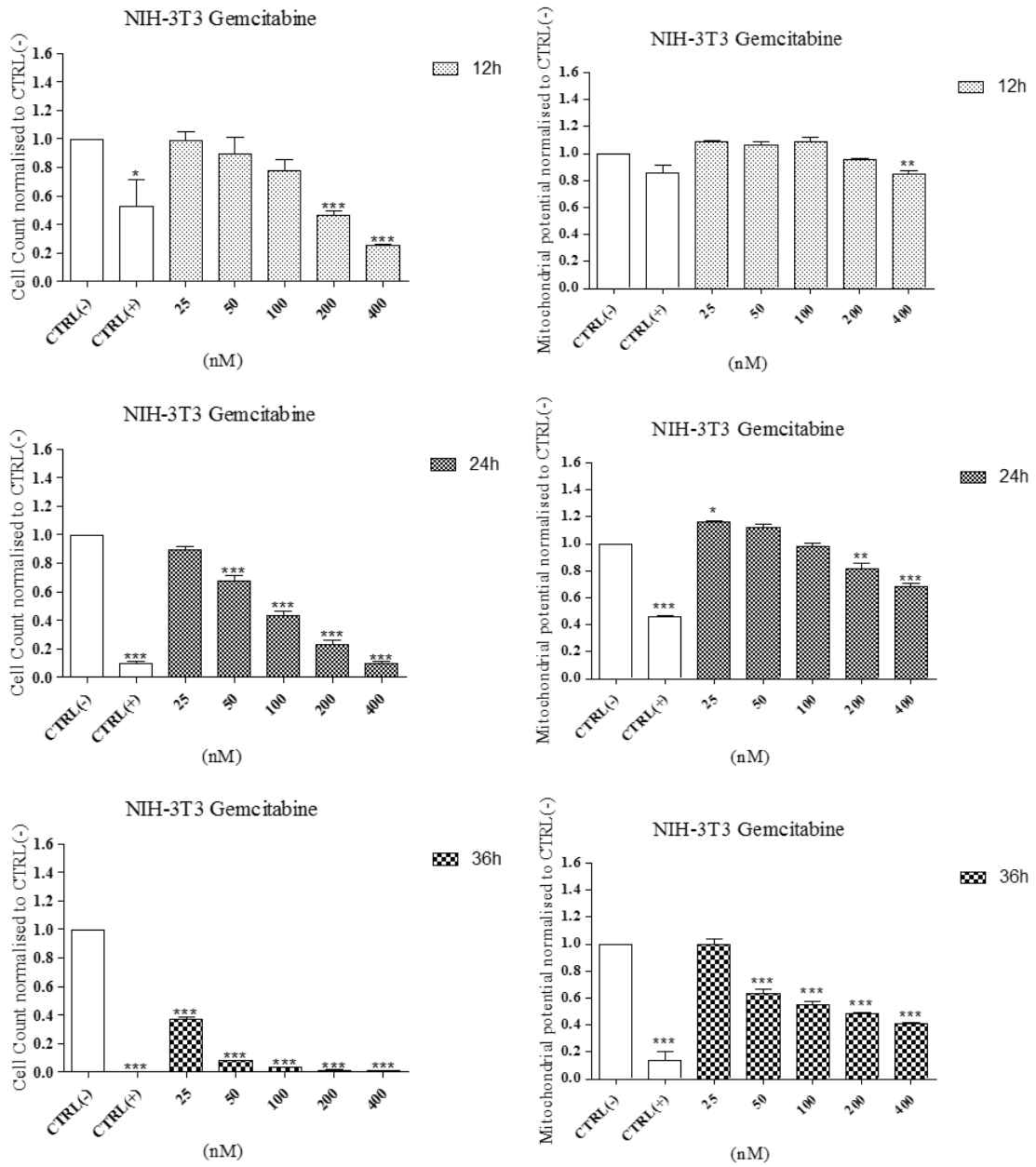

Figure S119: Effect of Gemcitabine on viability and mitochondrial potential of NIH-3T3 cell line.

NIH-3T3 mouse fibroblast-derived cell line was exposed to Gemcitabine for 12h, 24h and 36h. Cells were stained using the Cytotoxicity II HitKit™ and analysed using the InCell 1000 HCSA device. Variation in cell count and mitochondrial membrane potential were measured compared to untreated control (CTRL(-)) and 1µM CdSe positive control (CTRL(+)). Statistical significance was determined using the one way ANOVA with Tukey post-test for each column compared to untreated control (CTRL(-)). p value: *** = <0.001, **=<0.01, *=<0.05

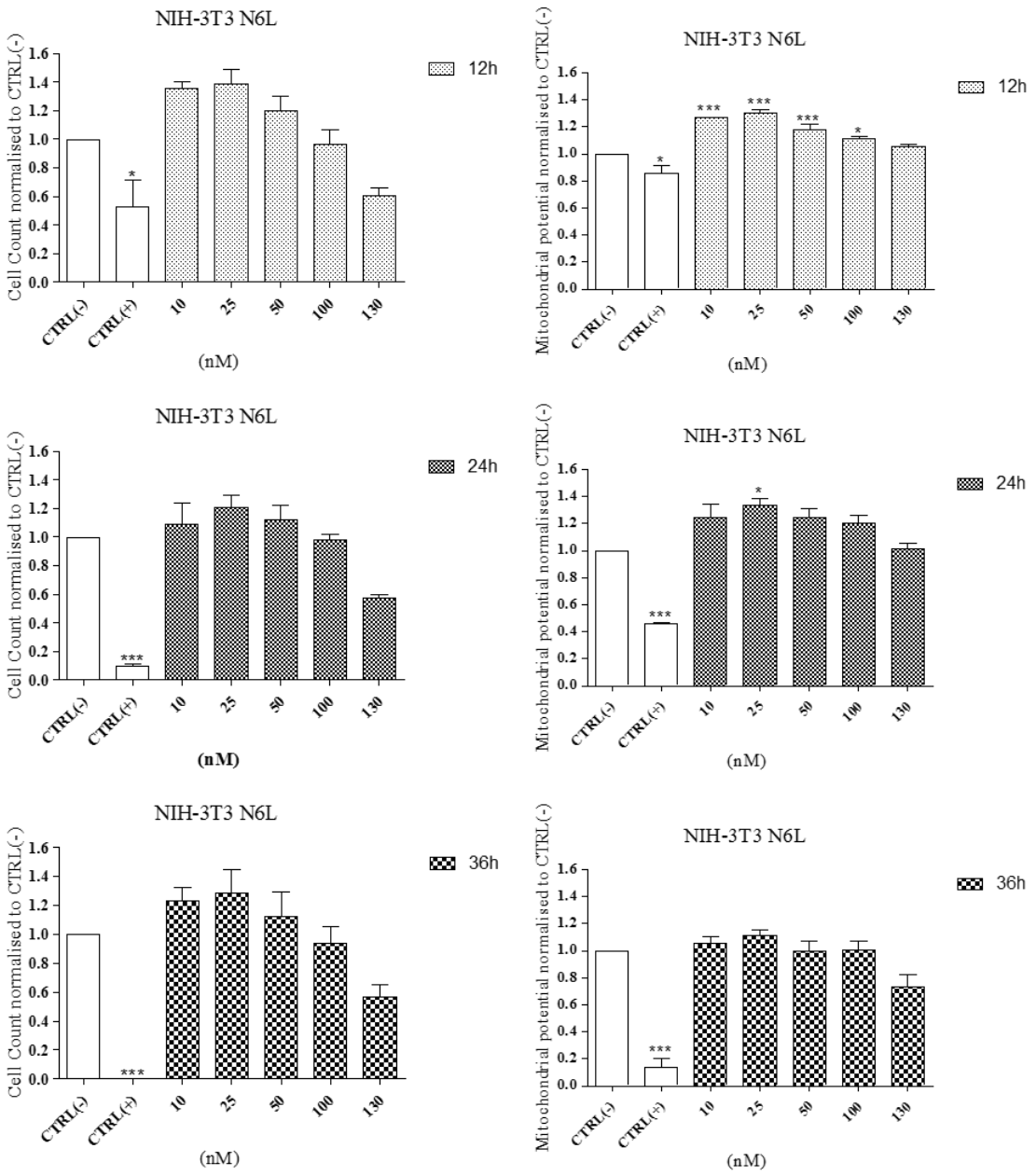

Figure S120: Effect of N6L on viability and mitochondrial potential of NIH-3T3 cell line.

NIH-3T3 mouse fibroblast-derived cell line was exposed to N6L for 12h, 24h and 36h. Cells were stained using the Cytotoxicity II HitKit™ and analysed using the InCell 1000 HCSA device. Variation in cell count and mitochondrial membrane potential were measured compared to untreated control (CTRL(-)) and 1µM CdSe positive control (CTRL(+)). Statistical significance was determined using the one way ANOVA with Tukey post-test for each column compared to untreated control (CTRL(-)). p value: *** = <0.001, **=<0.01, *=<0.05

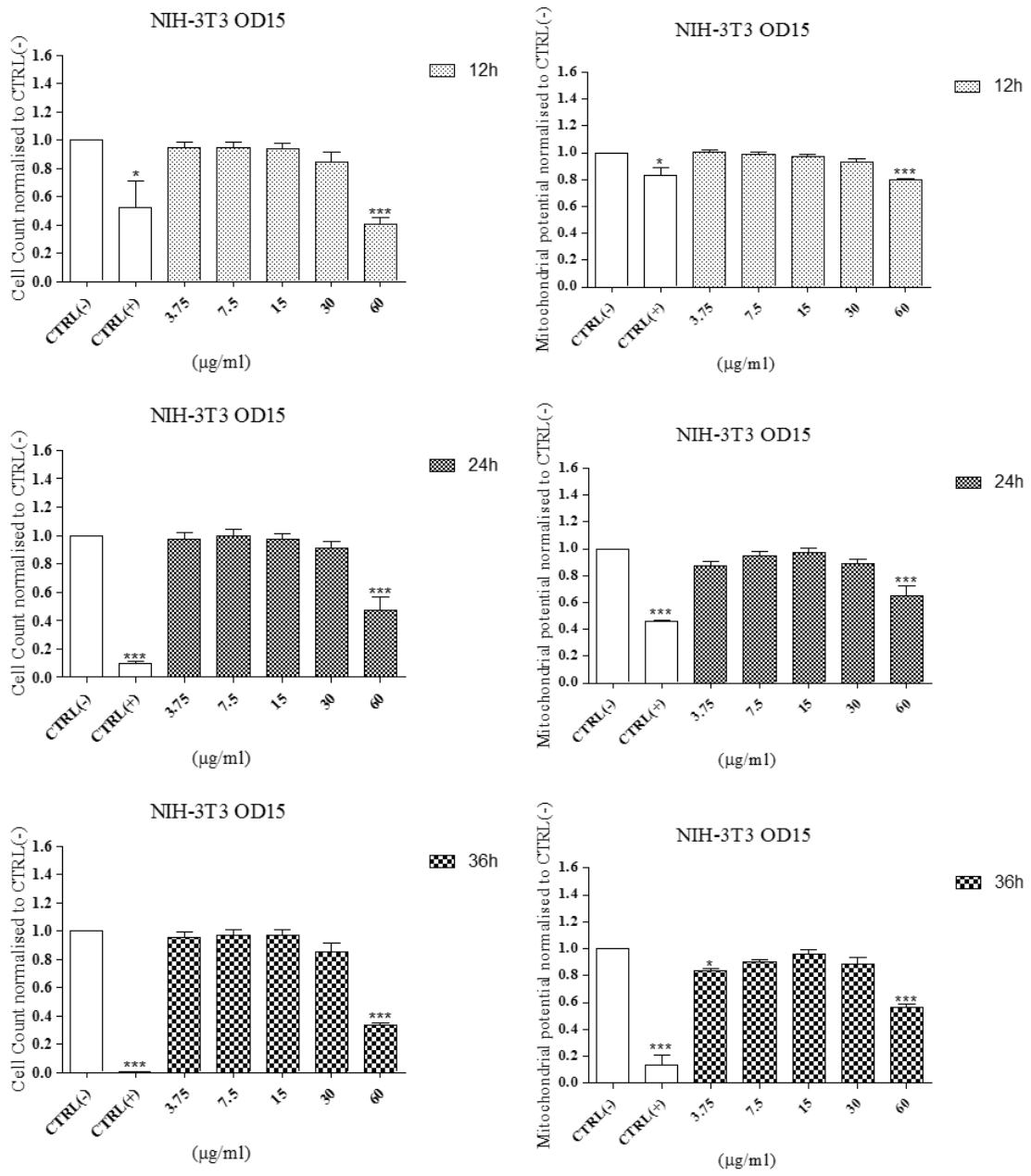

Figure S121: NIH-3T3 cell line exposed to OD15 MNP.

NIH-3T3 mouse fibroblast-derived cell line was exposed to OD15 MNP for 12h, 24h and 36h. Cells were stained using the Cytotoxicity II HitKit™ and analysed using the InCell 1000 HCSA device. Variation in cell count and mitochondrial membrane potential were measured compared to untreated control (CTRL(-)) and 1µM CdSe positive control (CTRL(+)). Statistical significance was determined using the one way ANOVA with Tukey post-test for each column compared to untreated control (CTRL(-)). p value: *** = <0.001, **=<0.01, *=<0.05

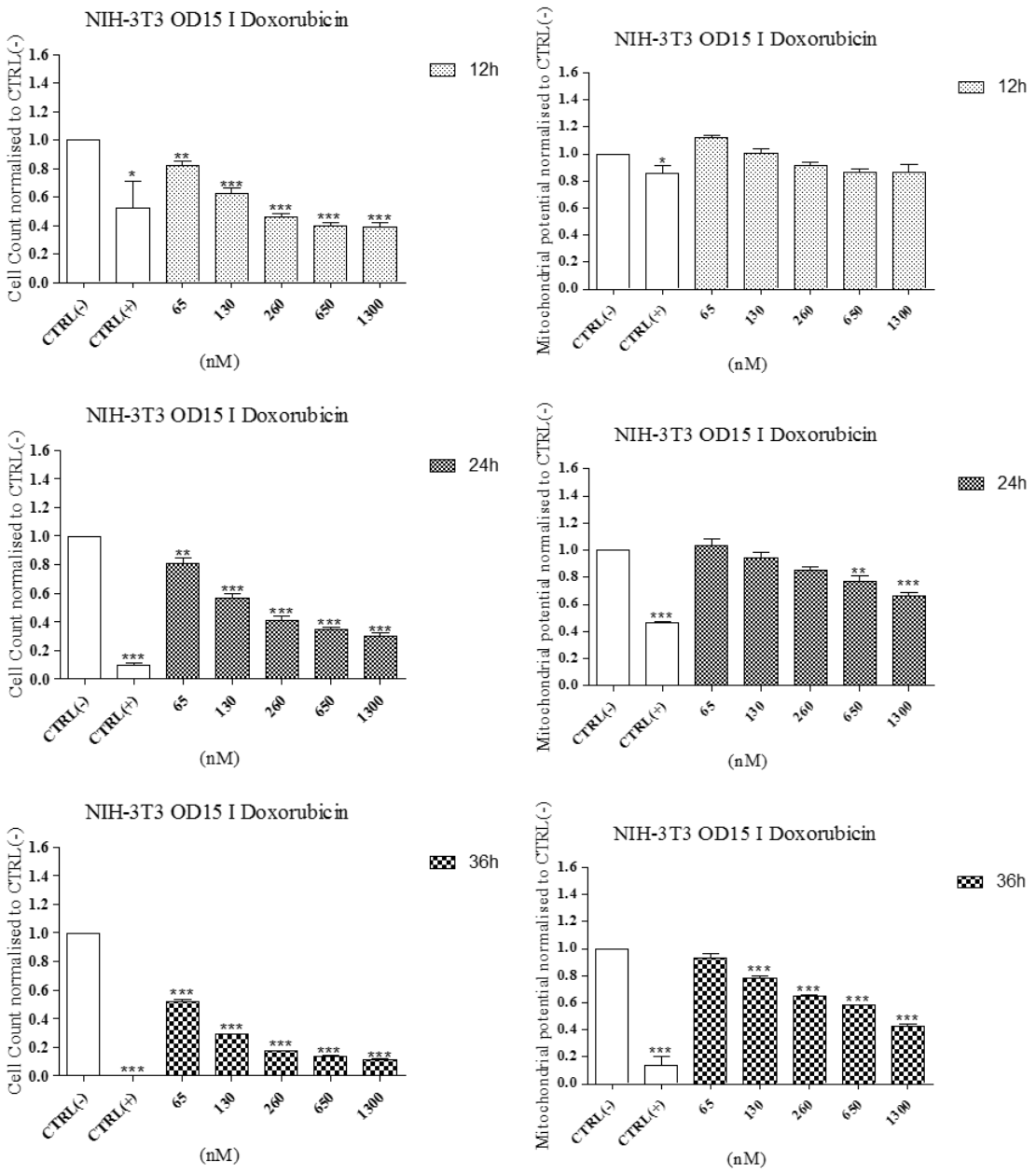

Figure S122: NIH-3T3 cell line exposed to OD15_I_Doxorubicin MNP.

NIH-3T3 mouse fibroblast-derived cell line was exposed to MF6_N6L_Gemcitabine MNP for 12h, 24h and 36h. Cells were stained using the Cytotoxicity II HitKit™ and analysed using the InCell 1000 HCSA device. Variation in cell count and mitochondrial membrane potential were measured compared to untreated control (CTRL(-)) and 1µM CdSe positive control (CTRL(+)). Statistical significance was determined using the one way ANOVA with Tukey post-test for each column compared to untreated control (CTRL(-)). p value: *** = <0.001, **=<0.01, *=<0.05

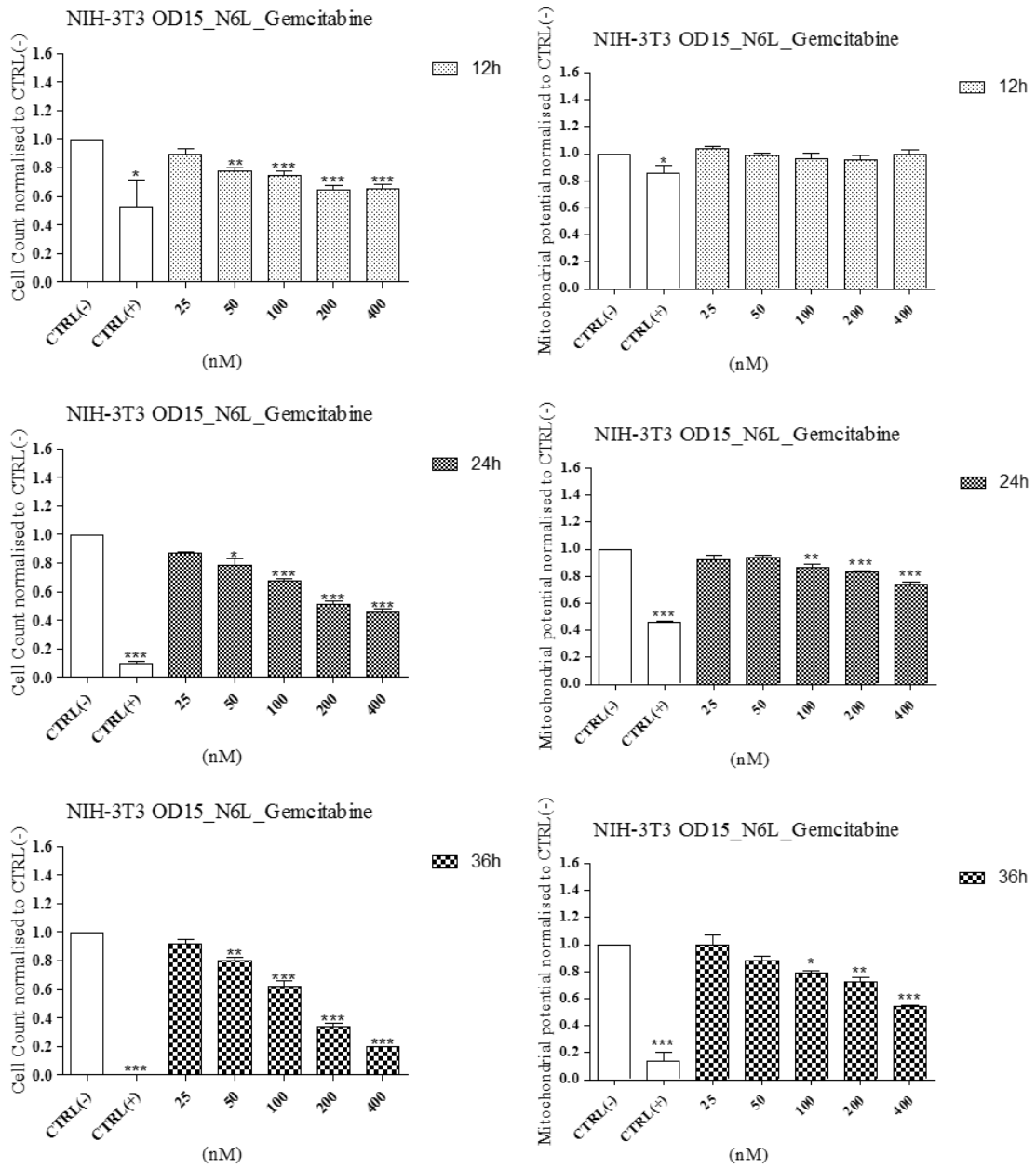

Figure S123: NIH-3T3 cell line exposed to OD15_N6L_Gemictabine MNP.

NIH-3T3 mouse fibroblast-derived cell line was exposed to MF6_N6L_Gemcitabine MNP for 12h, 24h and 36h. Cells were stained using the Cytotoxicity II HitKit™ and analysed using the InCell 1000 HCSA device. Variation in cell count and mitochondrial membrane potential were measured compared to untreated control (CTRL(-)) and 1µM CdSe positive control (CTRL(+)). Statistical significance was determined using the one way ANOVA with Tukey post-test for each column compared to untreated control (CTRL(-)). p value: *** = <0.001, **=<0.01, *=<0.05

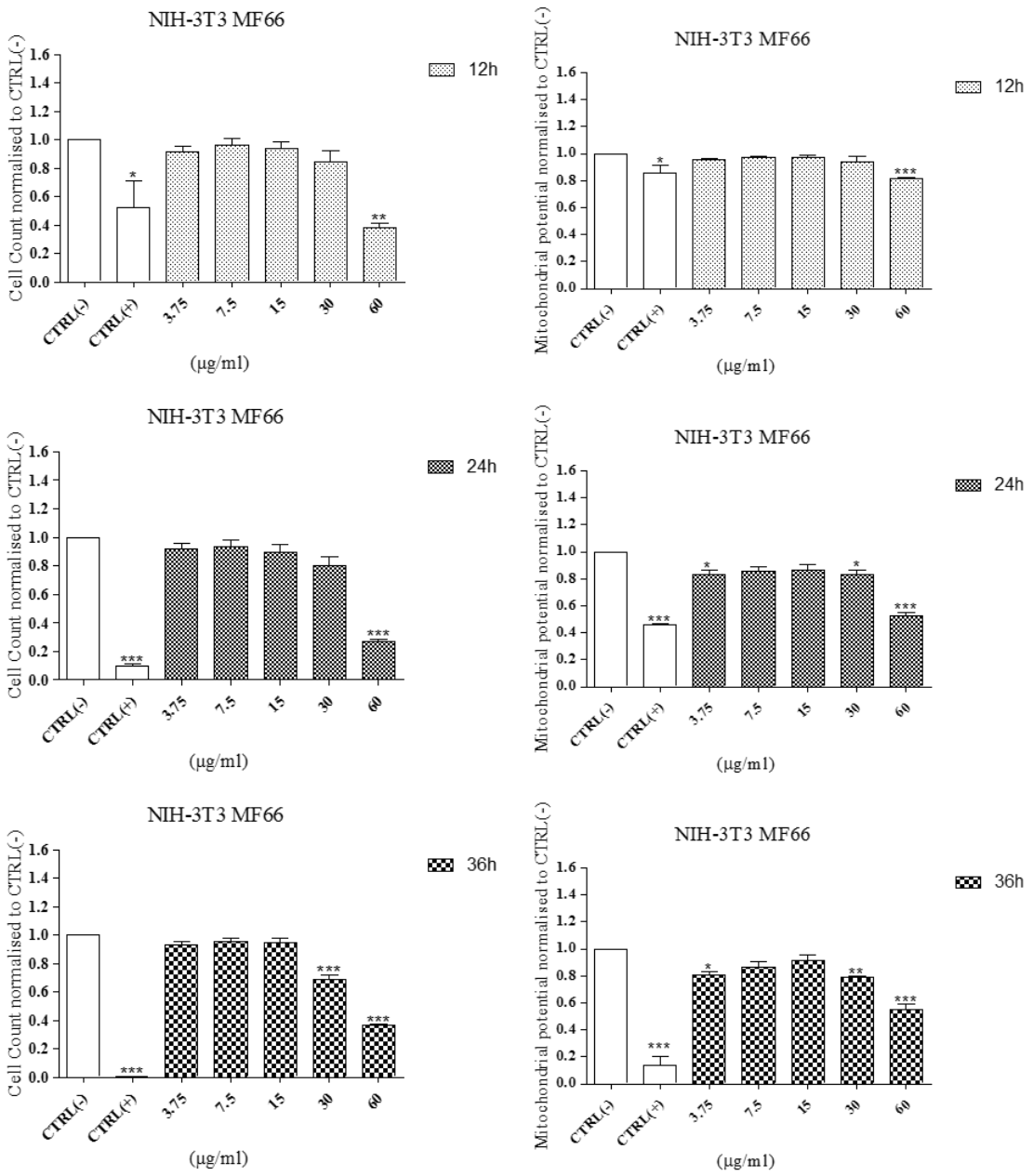

Figure S124: NIH-3T3 cell line exposed to MF66 MNP.

NIH-3T3 mouse fibroblast-derived cell line was exposed to MF66 MNP for 12h, 24h and 36h. Cells were stained using the Cytotoxicity II HitKit™ and analysed using the InCell 1000 HCSA device. Variation in cell count and mitochondrial membrane potential were measured compared to untreated control (CTRL(-)) and 1µM CdSe positive control (CTRL(+)). Statistical significance was determined using the one way ANOVA with Tukey post-test for each column compared to untreated control (CTRL(-)). p value: *** = <0.001, **=<0.01, *=<0.05

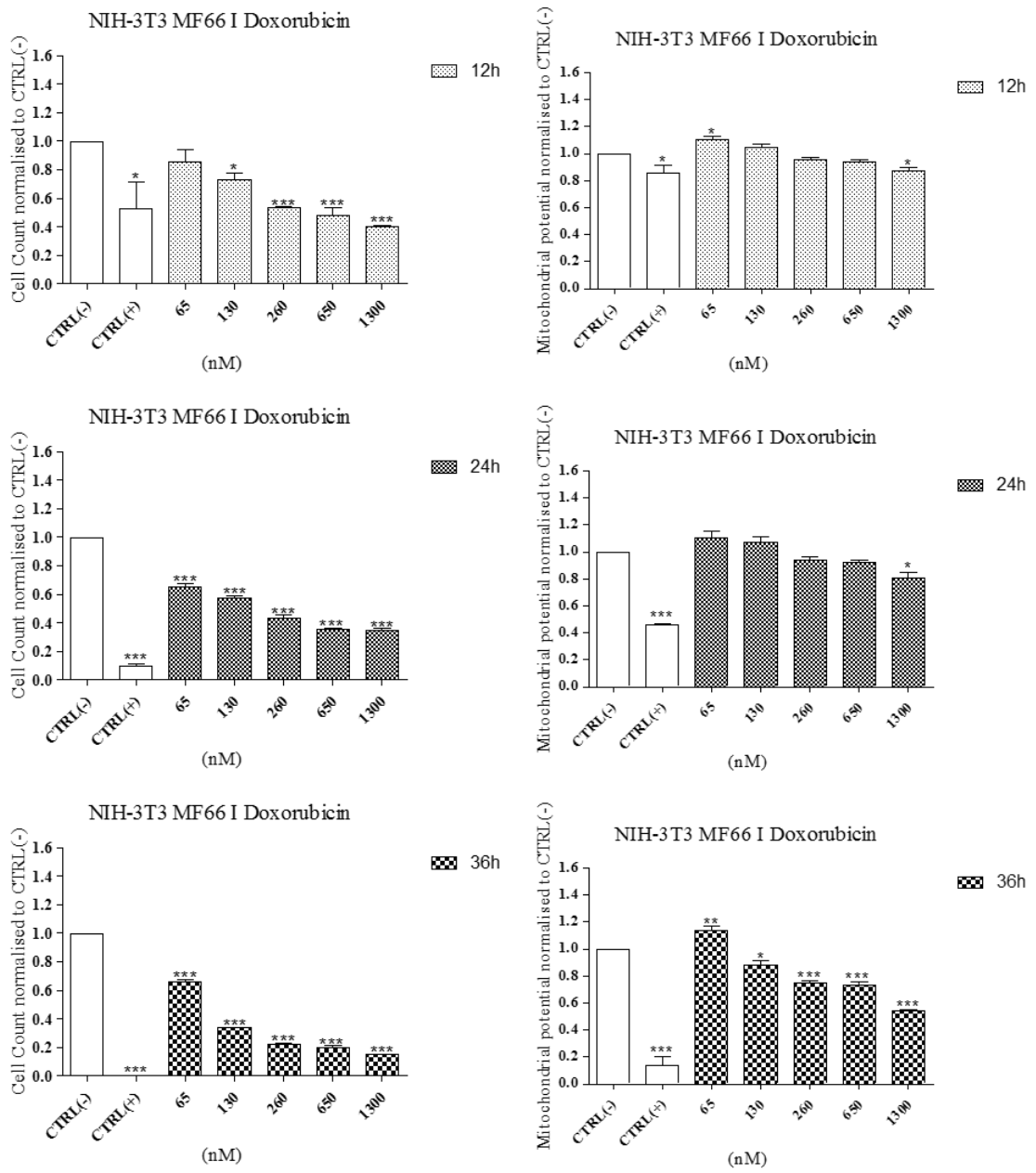

Figure S125: NIH-3T3 cell line exposed to MF66_I_Doxorubicin MNP.

NIH-3T3 mouse fibroblast-derived cell line was exposed to MF6_I_Doxorubicin MNP for 12h, 24h and 36h. Cells were stained using the Cytotoxicity II HitKit™ and analysed using the InCell 1000 HCSA device. Variation in cell count and mitochondrial membrane potential were measured compared to untreated control (CTRL(-)) and 1µM CdSe positive control (CTRL(+)). Statistical significance was determined using the one way ANOVA with Tukey post-test for each column compared to untreated control (CTRL(-)). p value: *** = <0.001, **=<0.01, *=<0.05

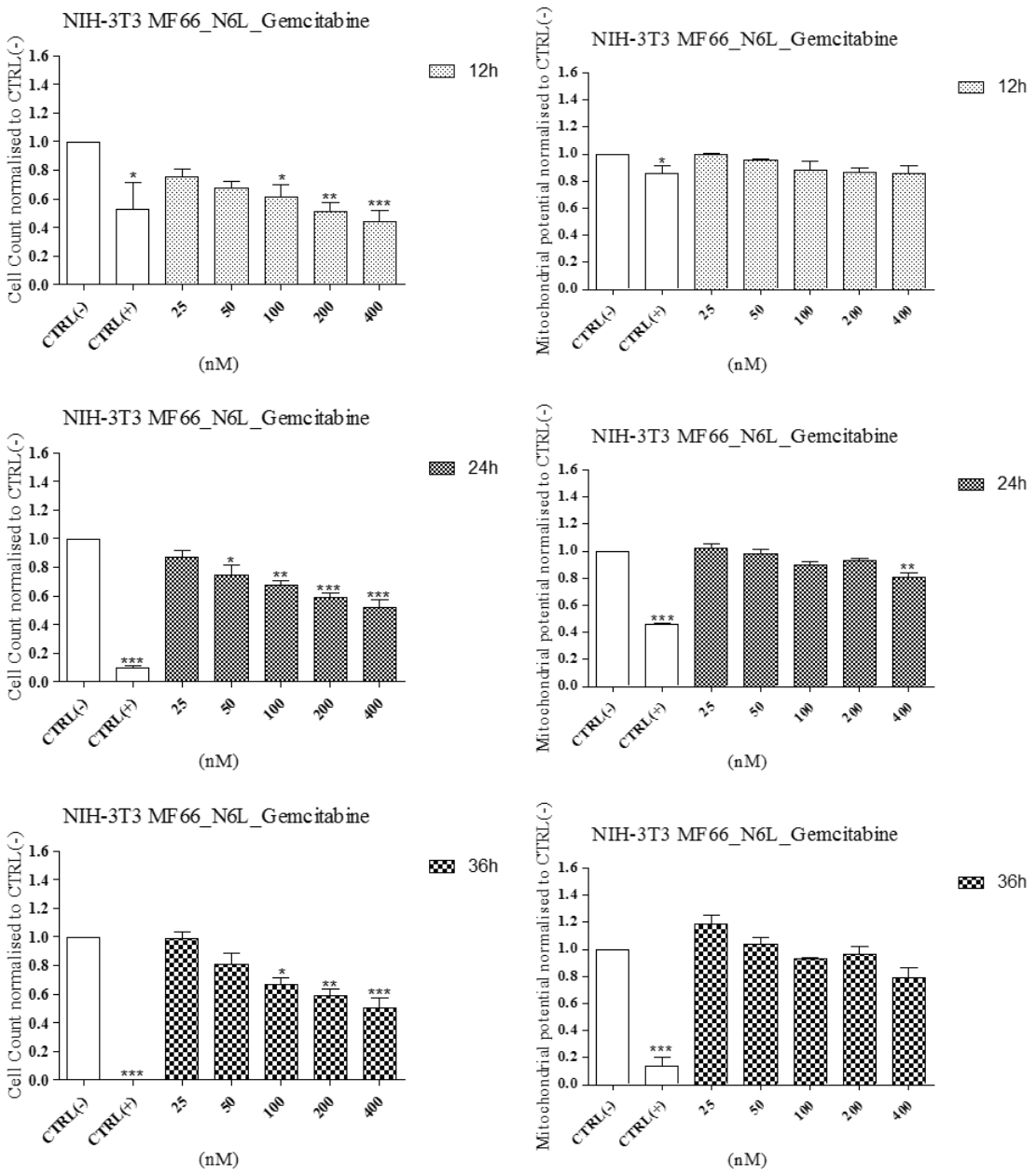

Figure S126: NIH-3T3 cell line exposed to MF66_N6L_Gemcitabine MNP.

NIH-3T3 mouse fibroblast-derived cell line was exposed to MF6_N6L_Gemcitabine MNP for 12h, 24h and 36h. Cells were stained using the Cytotoxicity II HitKit™ and analysed using the InCell 1000 HCSA device. Variation in cell count and mitochondrial membrane potential were measured compared to untreated control (CTRL(-)) and 1µM CdSe positive control (CTRL(+)). Statistical significance was determined using the one way ANOVA with Tukey post-test for each column compared to untreated control (CTRL(-)). p value: *** = <0.001, **=<0.01, *=<0.05

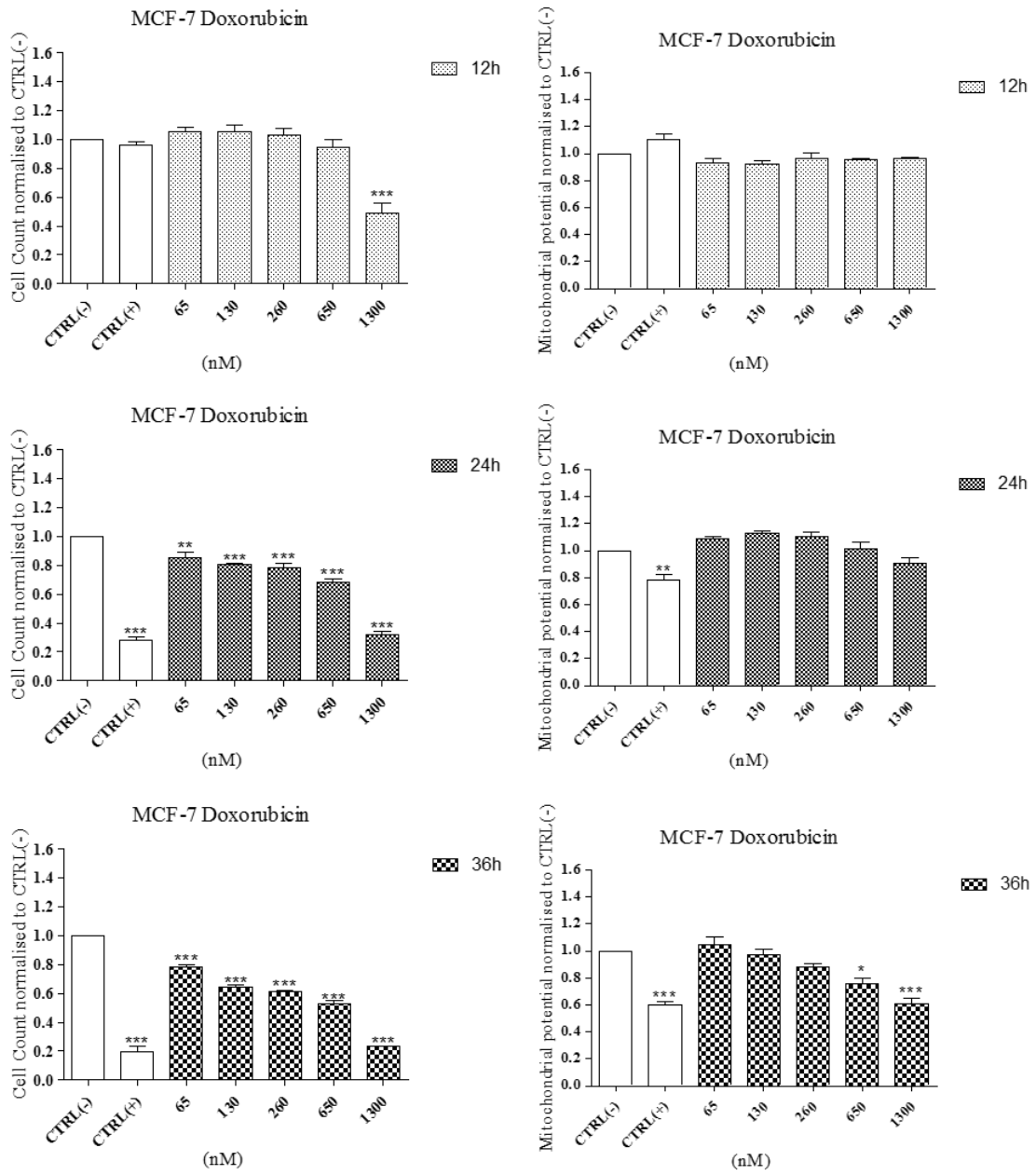

Figure S127: Effect of Doxorubicin on viability and mitochondrial potential of MCF-7 cell line.

MCF-7 breast-derived cell line was exposed to Doxorubicin for 12h, 24h and 36h. Cells were stained using the Cytotoxicity II HitKit™ and analysed using the InCell 1000 HCSA device. Variation in cell count and mitochondrial membrane potential were measured compared to untreated control (CTRL(-)) and 1µM CdSe positive control (CTRL(+)). Statistical significance was determined using the one way ANOVA with Tukey post-test for each column compared to untreated control (CTRL(-)). p value: *** = <0.001, **=<0.01, *=<0.05

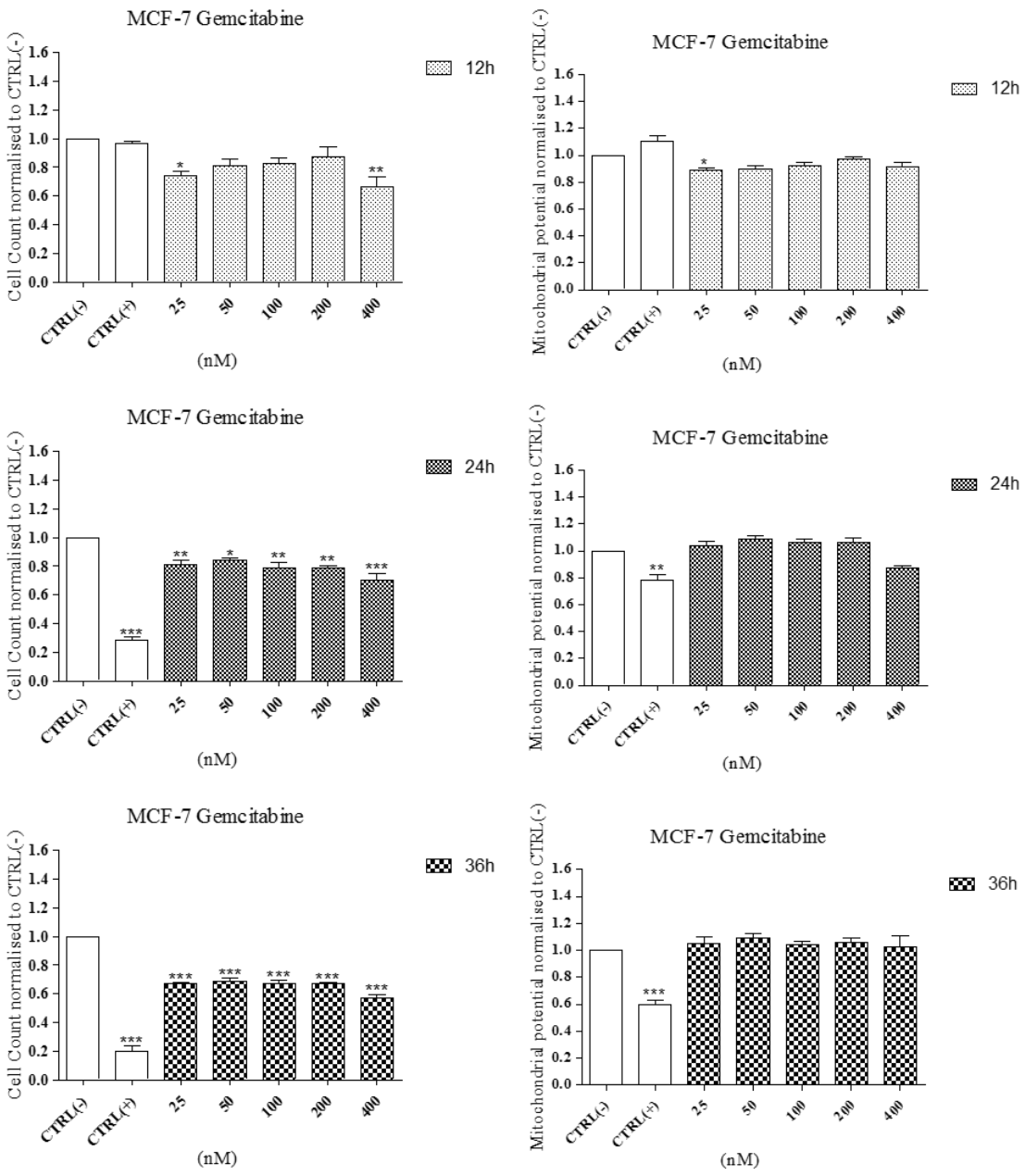

Figure S128: Effect of Gemcitabine on viability and mitochondrial potential of MCF-7 cell line.

MCF-7 breast-derived cell line was exposed to Gemcitabine for 12h, 24h and 36h. Cells were stained using the Cytotoxicity II HitKit™ and analysed using the InCell 1000 HCSA device. Variation in cell count and mitochondrial membrane potential were measured compared to untreated control (CTRL(-)) and 1µM CdSe positive control (CTRL(+)). Statistical significance was determined using the one way ANOVA with Tukey post-test for each column compared to untreated control (CTRL(-)). p value: *** = <0.001, **=<0.01, *=<0.05

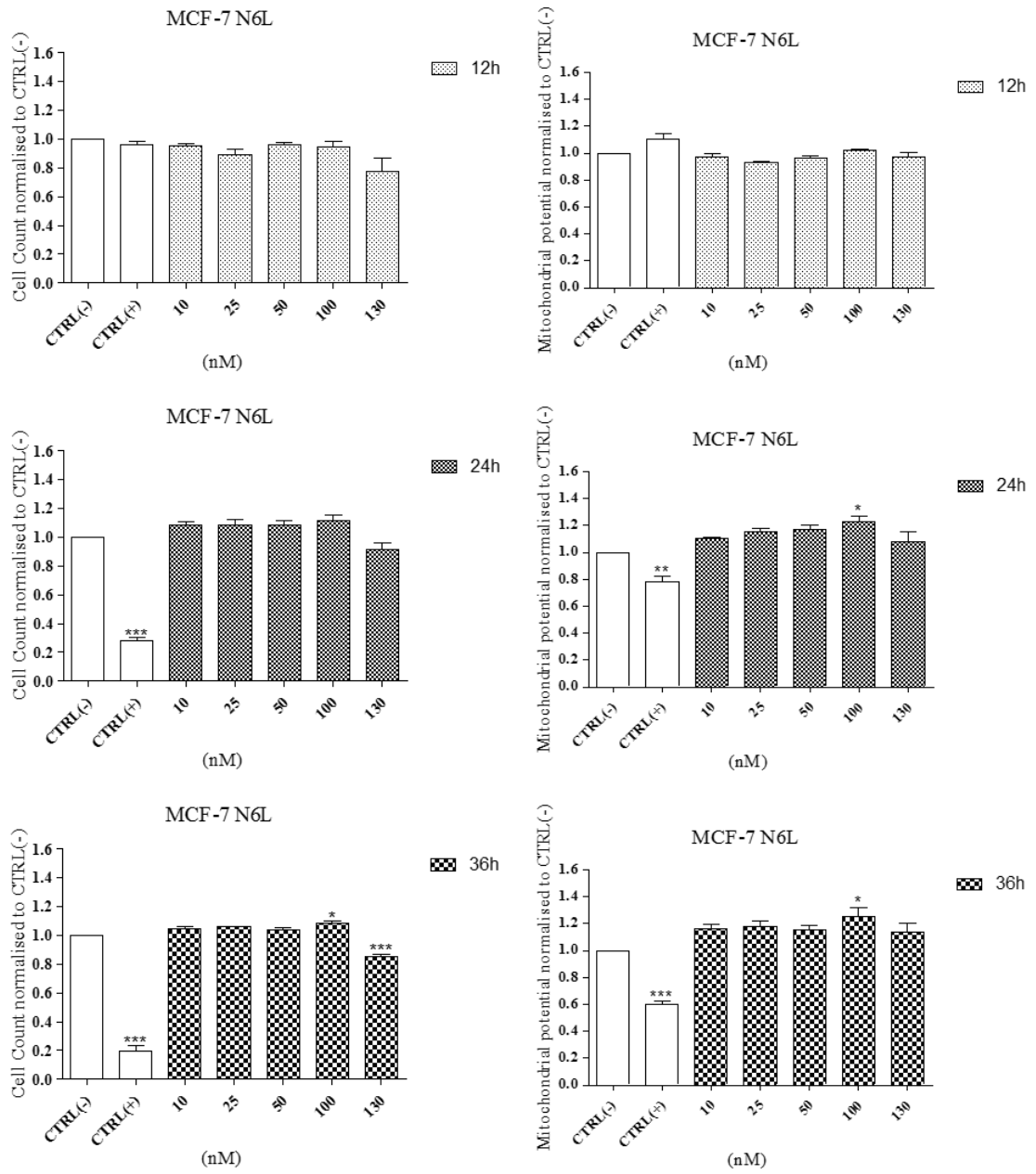

Figure S129: Effect of N6L on viability and mitochondrial potential of MCF-7 cell line.

MCF-7 breast-derived cell line was exposed to N6L for 12h, 24h and 36h. Cells were stained using the Cytotoxicity II HitKit™ and analysed using the InCell 1000 HCSA device. Variation in cell count and mitochondrial membrane potential were measured compared to untreated control (CTRL(-)) and 1µM CdSe positive control (CTRL(+)). Statistical significance was determined using the one way ANOVA with Tukey post-test for each column compared to untreated control (CTRL(-)). p value: *** = <0.001, **=<0.01, *=<0.05

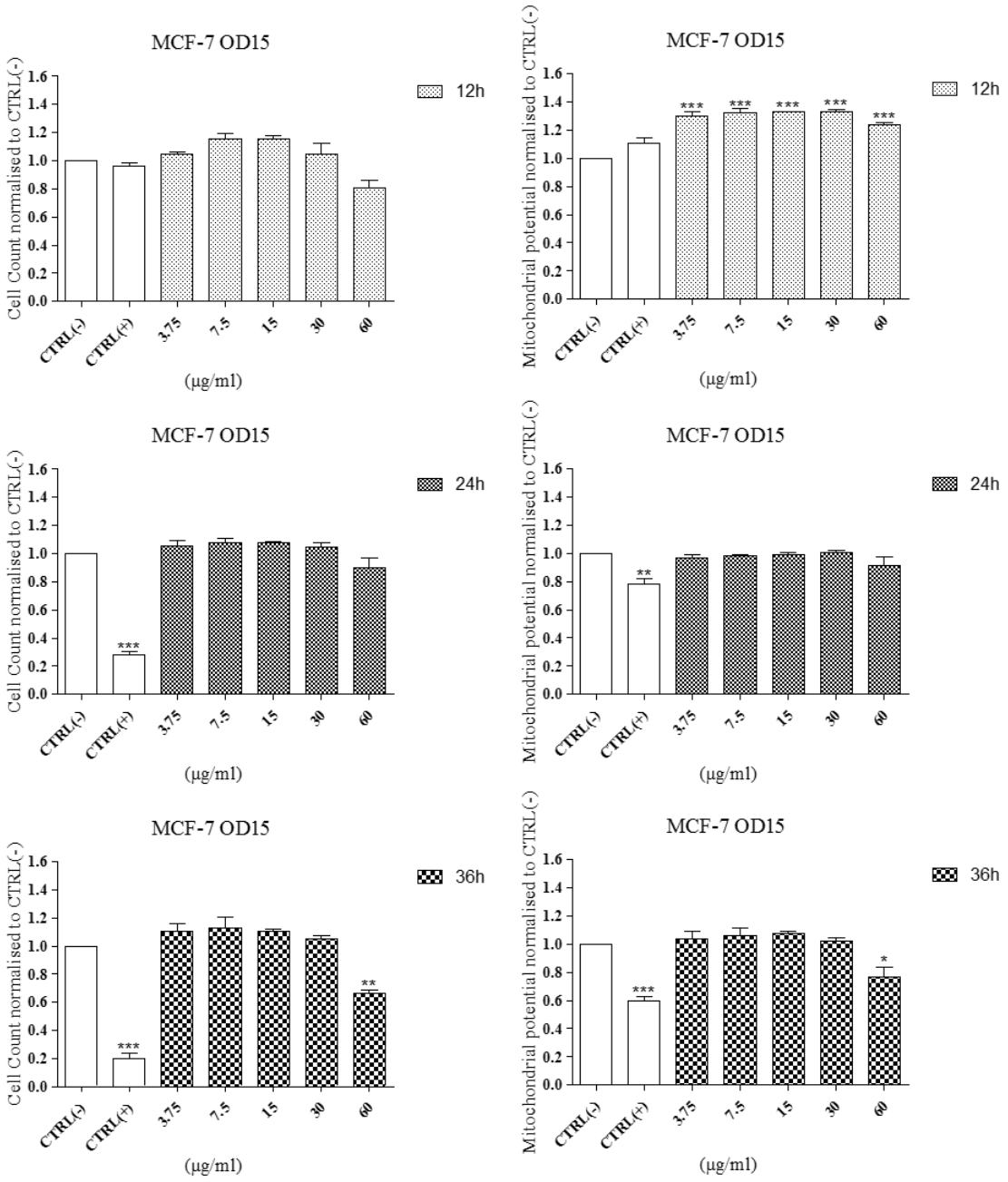

Figure S130: MCF-7 cell line exposed to OD15 MNP.

MCF-7 breast-derived cell line was exposed to OD15 MNP for 12h, 24h and 36h. Cells were stained using the Cytotoxicity II HitKit™ and analysed using the InCell 1000 HCSA device. Variation in cell count and mitochondrial membrane potential were measured compared to untreated control (CTRL(-)) and 1µM CdSe positive control (CTRL(+)). Statistical significance was determined using the one way ANOVA with Tukey post-test for each column compared to untreated control (CTRL(-)). p value: *** = <0.001, **=<0.01, *=<0.05

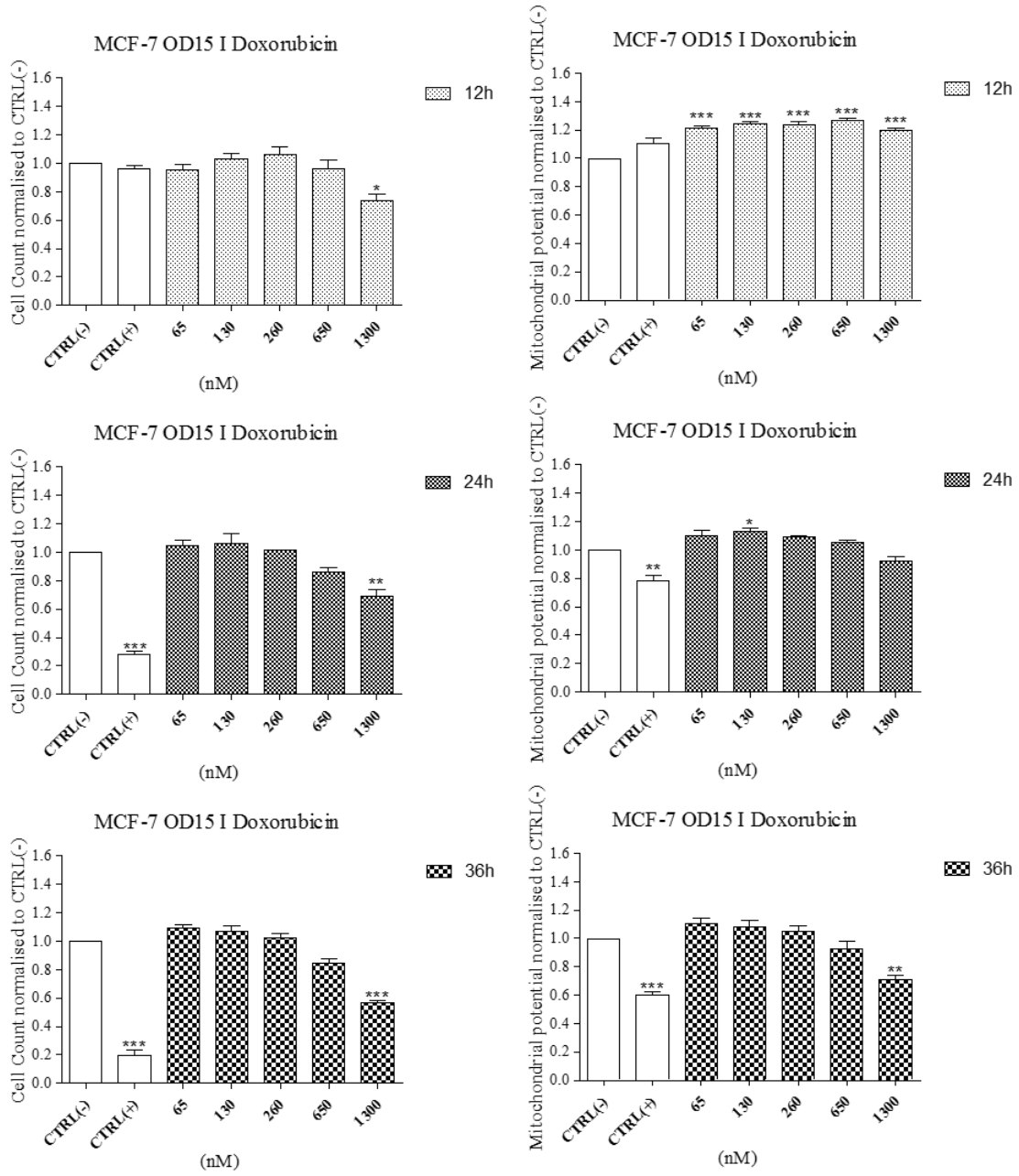

Figure S131: MCF-7 cell line exposed to OD15_I_Doxorubicin MNP.

MCF-7 breast-derived cell line was exposed to OD15_I_Doxorubicin MNP for 12h, 24h and 36h. Cells were stained using the Cytotoxicity II HitKit™ and analysed using the InCell 1000 HCSA device. Variation in cell count and mitochondrial membrane potential were measured compared to untreated control (CTRL(-)) and 1µM CdSe positive control (CTRL(+)). Statistical significance was determined using the one way ANOVA with Tukey post-test for each column compared to untreated control (CTRL(-)). p value: *** = <0.001, **=<0.01, *=<0.05

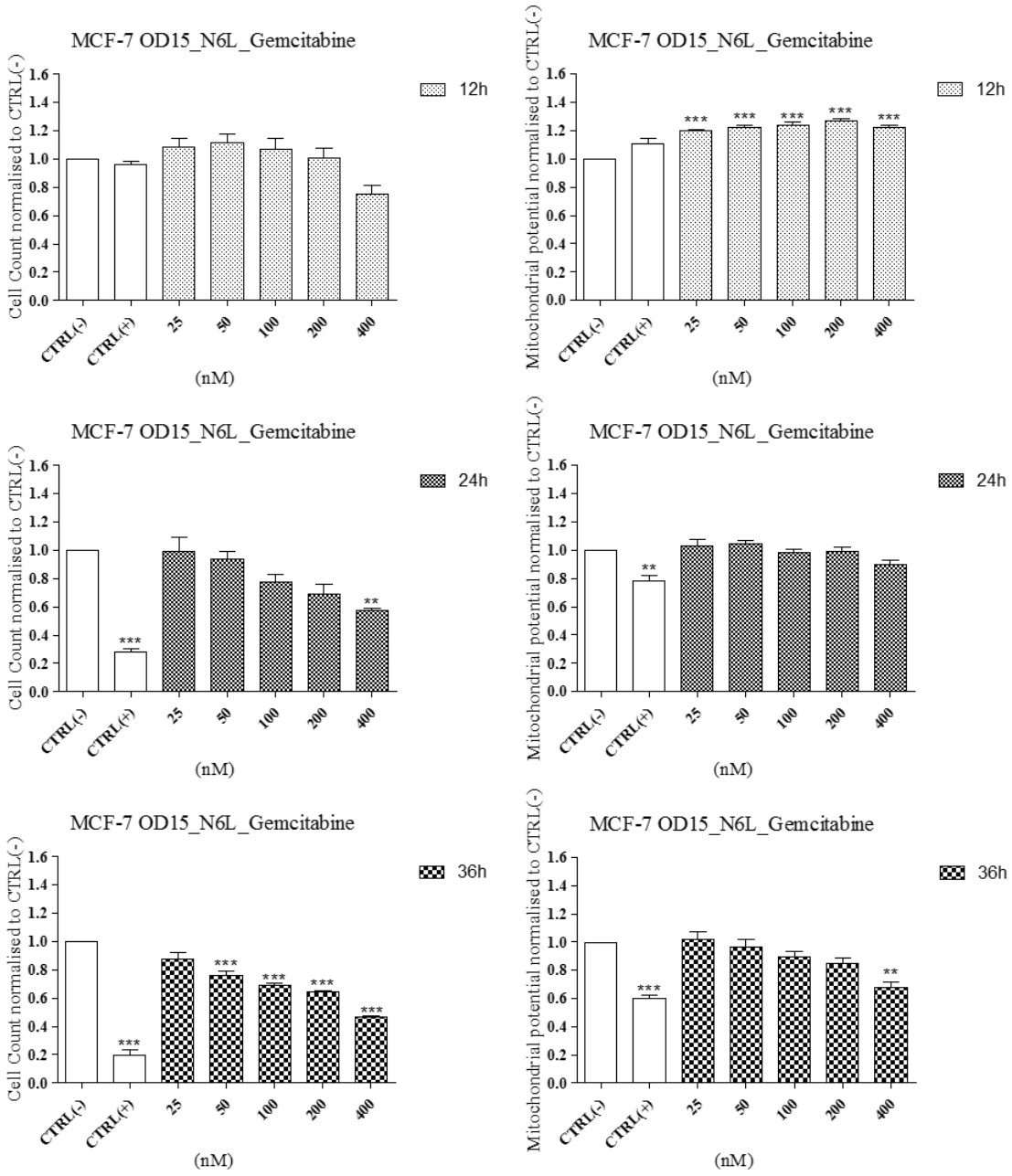

Figure S132: MCF-7 cell line exposed to OD15_N6L_Gemcitabine MNP.

MCF-7 breast-derived cell line was exposed to OD15_ N6L_Gemcitabine MNP for 12h, 24h and 36h. Cells were stained using the Cytotoxicity II HitKit™ and analysed using the InCell 1000 HCSA device. Variation in cell count and mitochondrial membrane potential were measured compared to untreated control (CTRL(-)) and 1µM CdSe positive control (CTRL(+)). Statistical significance was determined using the one way ANOVA with Tukey post-test for each column compared to untreated control (CTRL(-)). p value: *** = <0.001, **=<0.01, *=<0.05

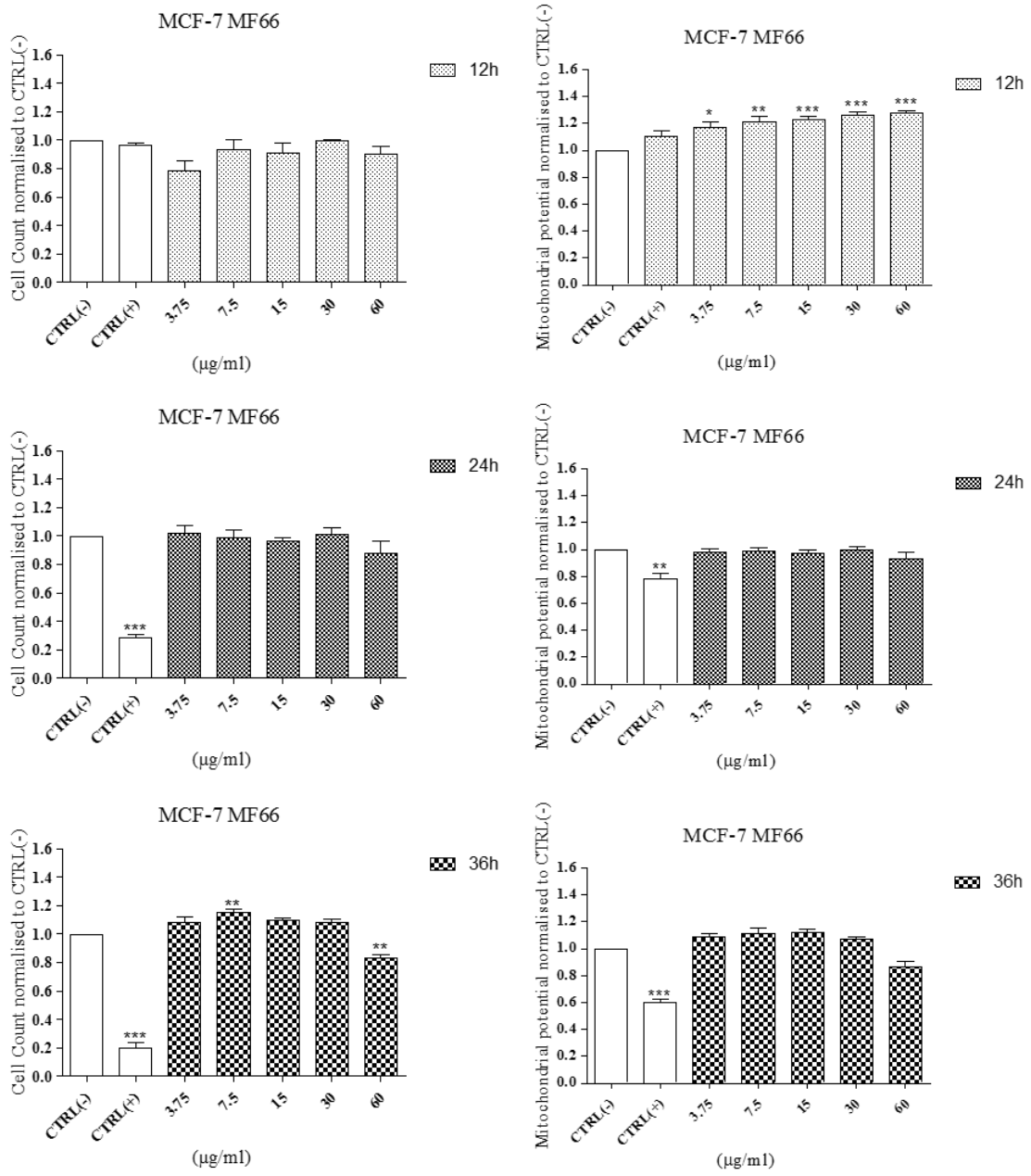

Figure S133: MCF-7 cell line exposed to MF66 MNP.

MCF-7 breast-derived cell line was exposed to MF66 MNP for 12h, 24h and 36h. Cells were stained using the Cytotoxicity II HitKit™ and analysed using the InCell 1000 HCSA device. Variation in cell count and mitochondrial membrane potential were measured compared to untreated control (CTRL(-)) and 1µM CdSe positive control (CTRL(+)). Statistical significance was determined using the one way ANOVA with Tukey post-test for each column compared to untreated control (CTRL(-)). p value: *** = <0.001, **=<0.01, *=<0.05

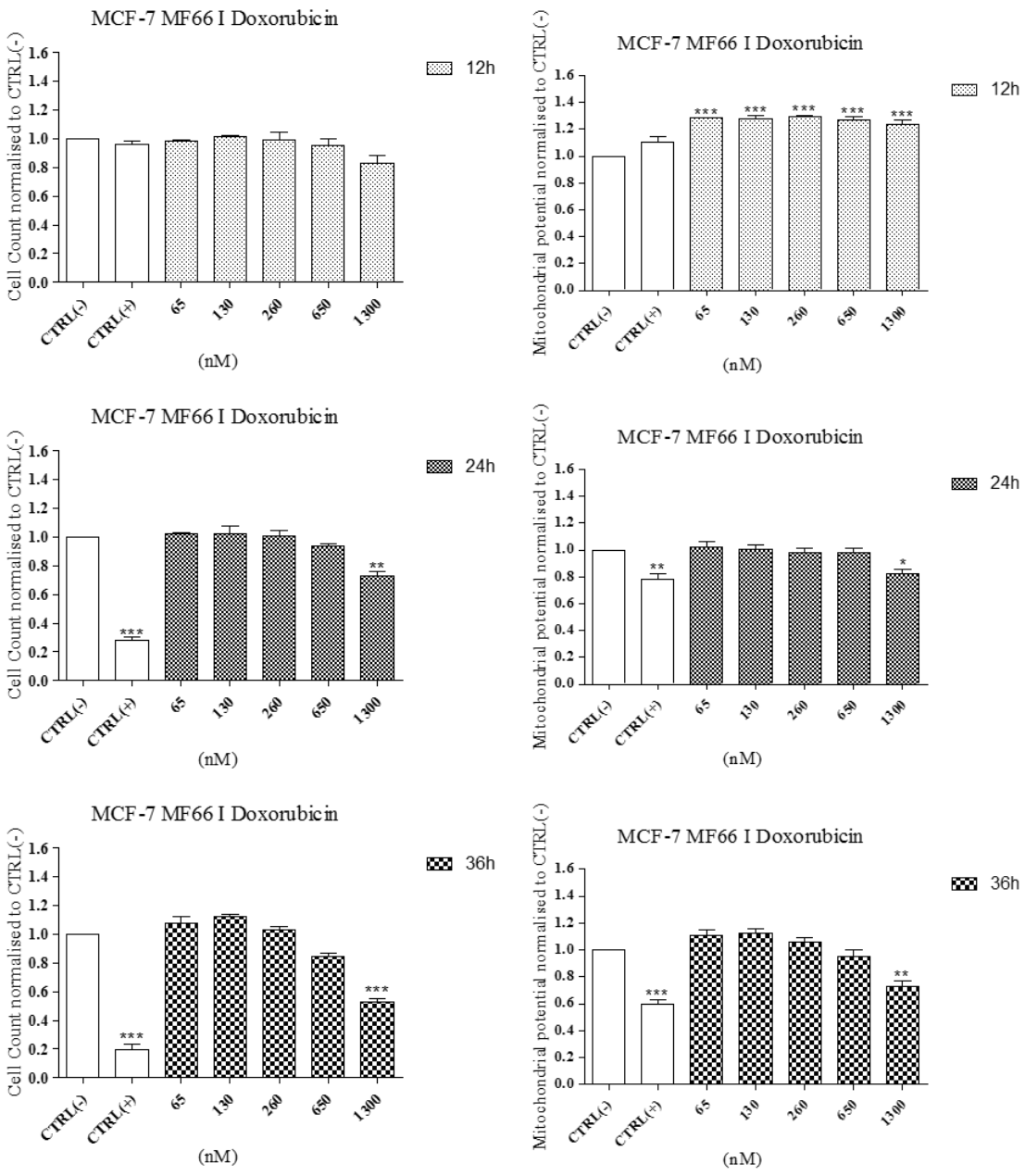

Figure S134: MCF-7 cell line exposed to MF66_I_Doxorubicin MNP.

MCF-7 breast-derived cell line was exposed to MF66_I_Doxorubicin MNP for 12h, 24h and 36h. Cells were stained using the Cytotoxicity II HitKit™ and analysed using the InCell 1000 HCSA device. Variation in cell count and mitochondrial membrane potential were measured compared to untreated control (CTRL(-)) and 1µM CdSe positive control (CTRL(+)). Statistical significance was determined using the one way ANOVA with Tukey post-test for each column compared to untreated control (CTRL(-)). p value: *** = <0.001, **=<0.01, *=<0.05

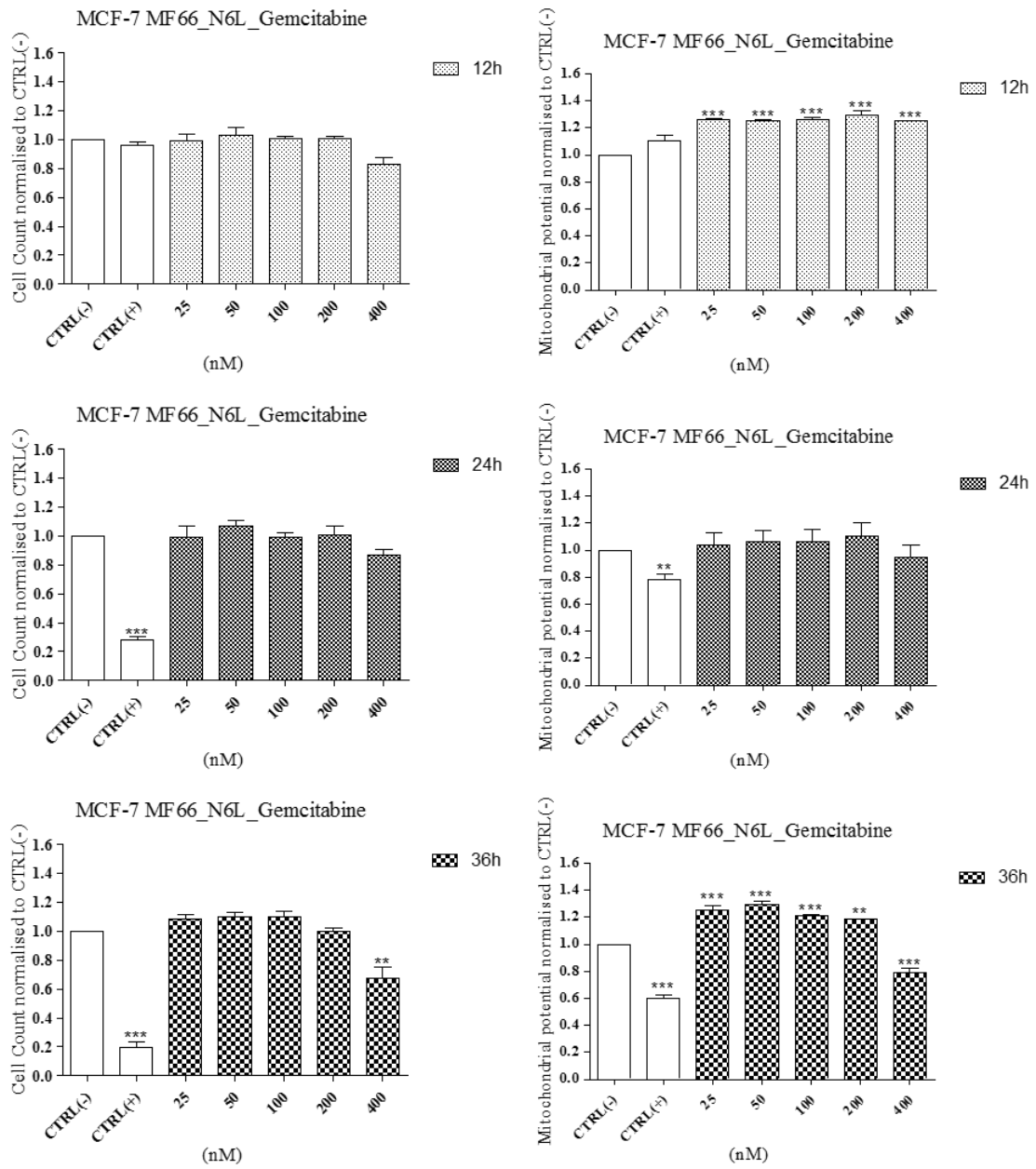

Figure S135: MCF-7 cell line exposed to MF66_N6L_Gemcitabine MNP.

MCF-7 breast-derived cell line was exposed to MF66_ N6L_Gemcitabine MNP for 12h, 24h and 36h. Cells were stained using the Cytotoxicity II HitKit™ and analysed using the InCell 1000 HCSA device. Variation in cell count and mitochondrial membrane potential were measured compared to untreated control (CTRL(-)) and 1µM CdSe positive control (CTRL(+)). Statistical significance was determined using the one way ANOVA with Tukey post-test for each column compared to untreated control (CTRL(-)). p value: *** = <0.001, **=<0.01, *=<0.05

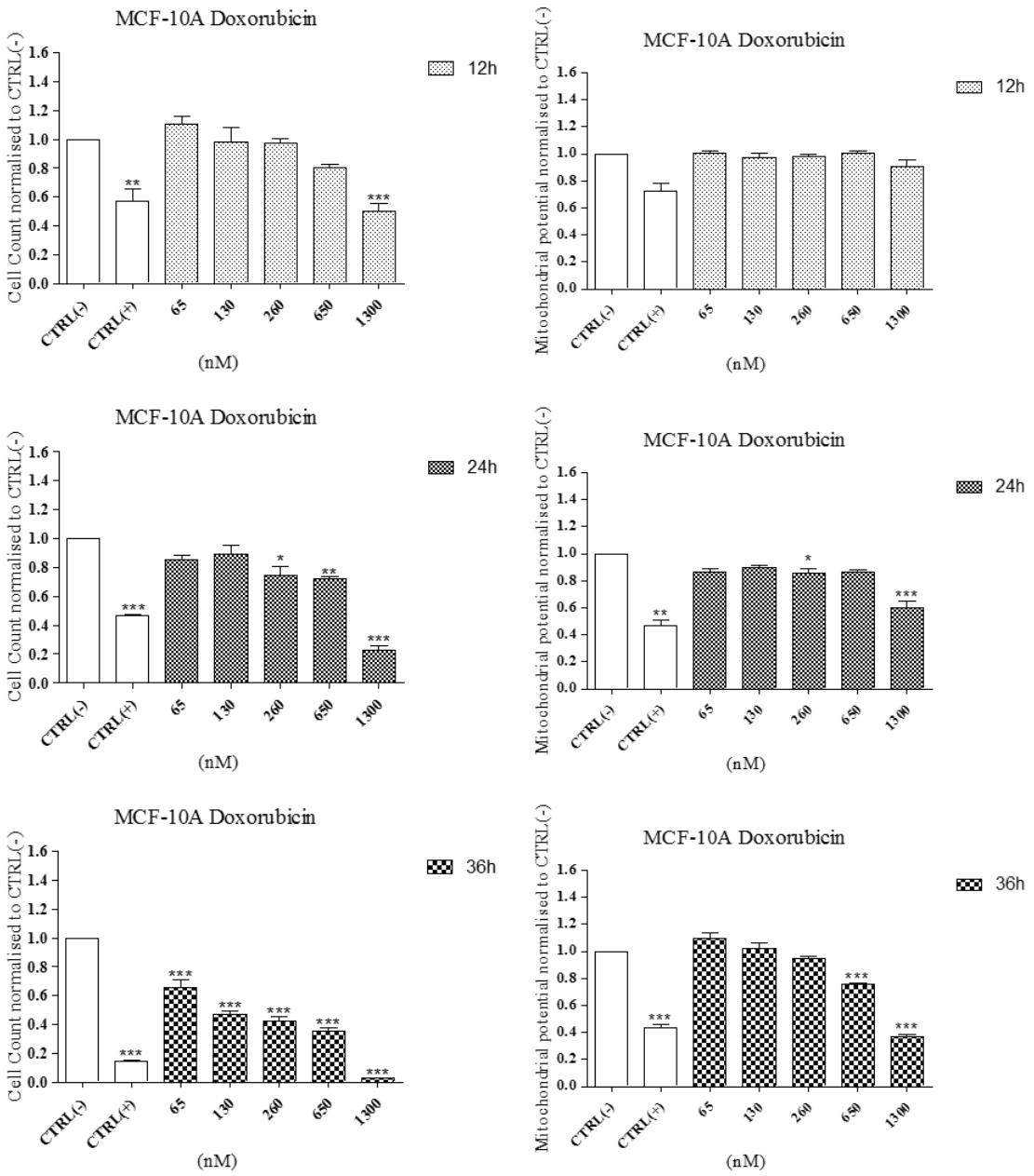

Figure S136: Effect of Doxorubicin on viability and mitochondrial potential of MCF-10A cell line.

MCF-10A breast-derived cell line was exposed to Doxorubicin for 12h, 24h and 36h. Cells were stained using the Cytotoxicity II HitKit™ and analysed using the InCell 1000 HCSA device. Variation in cell count and mitochondrial membrane potential were measured compared to untreated control (CTRL(-)) and 1µM CdSe positive control (CTRL(+)). Statistical significance was determined using the one way ANOVA with Tukey post-test for each column compared to untreated control (CTRL(-)). p value: *** = <0.001, **=<0.01, *=<0.05

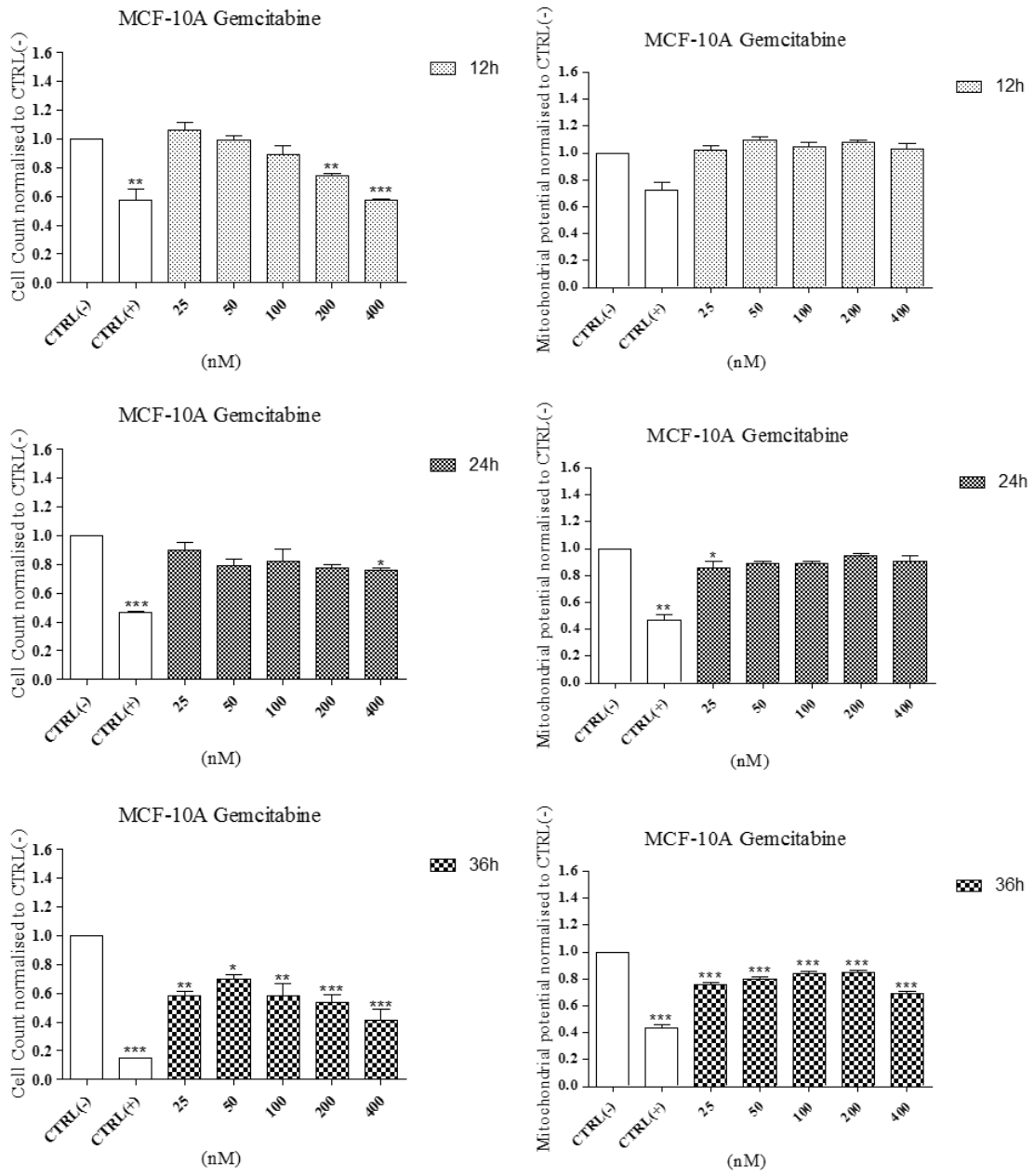

Figure S137: Effect of Gemcitabine on viability and mitochondrial potential of MCF-10A cell line

MCF-10A breast-derived cell line was exposed to Gemcitabine for 12h, 24h and 36h. Cells were stained using the Cytotoxicity II HitKit™ and analysed using the InCell 1000 HCSA device. Variation in cell count and mitochondrial membrane potential were measured compared to untreated control (CTRL(-)) and 1µM CdSe positive control (CTRL(+)). Statistical significance was determined using the one way ANOVA with Tukey post-test for each column compared to untreated control (CTRL(-)). p value: *** = <0.001, **=<0.01, *=<0.05

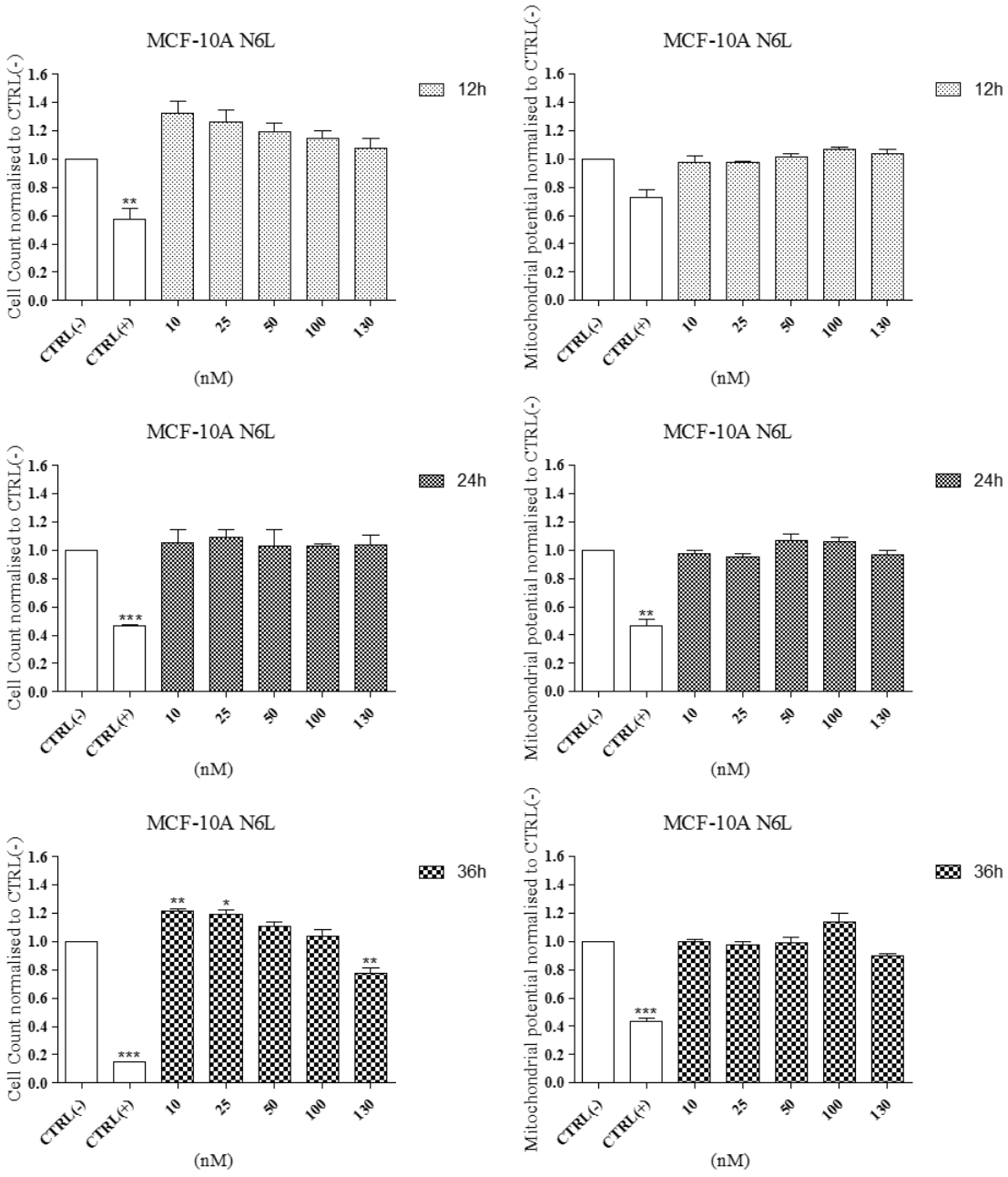

Figure S138: Effect of N6L on viability and mitochondrial potential of MCF-10A cell line.

MCF-10A breast-derived cell line was exposed to N6L for 12h, 24h and 36h. Cells were stained using the Cytotoxicity II HitKit™ and analysed using the InCell 1000 HCSA device. Variation in cell count and mitochondrial membrane potential were measured compared to untreated control (CTRL(-)) and 1µM CdSe positive control (CTRL(+)). Statistical significance was determined using the one way ANOVA with Tukey post-test for each column compared to untreated control (CTRL(-)). p value: *** = <0.001, **=<0.01, *=<0.05

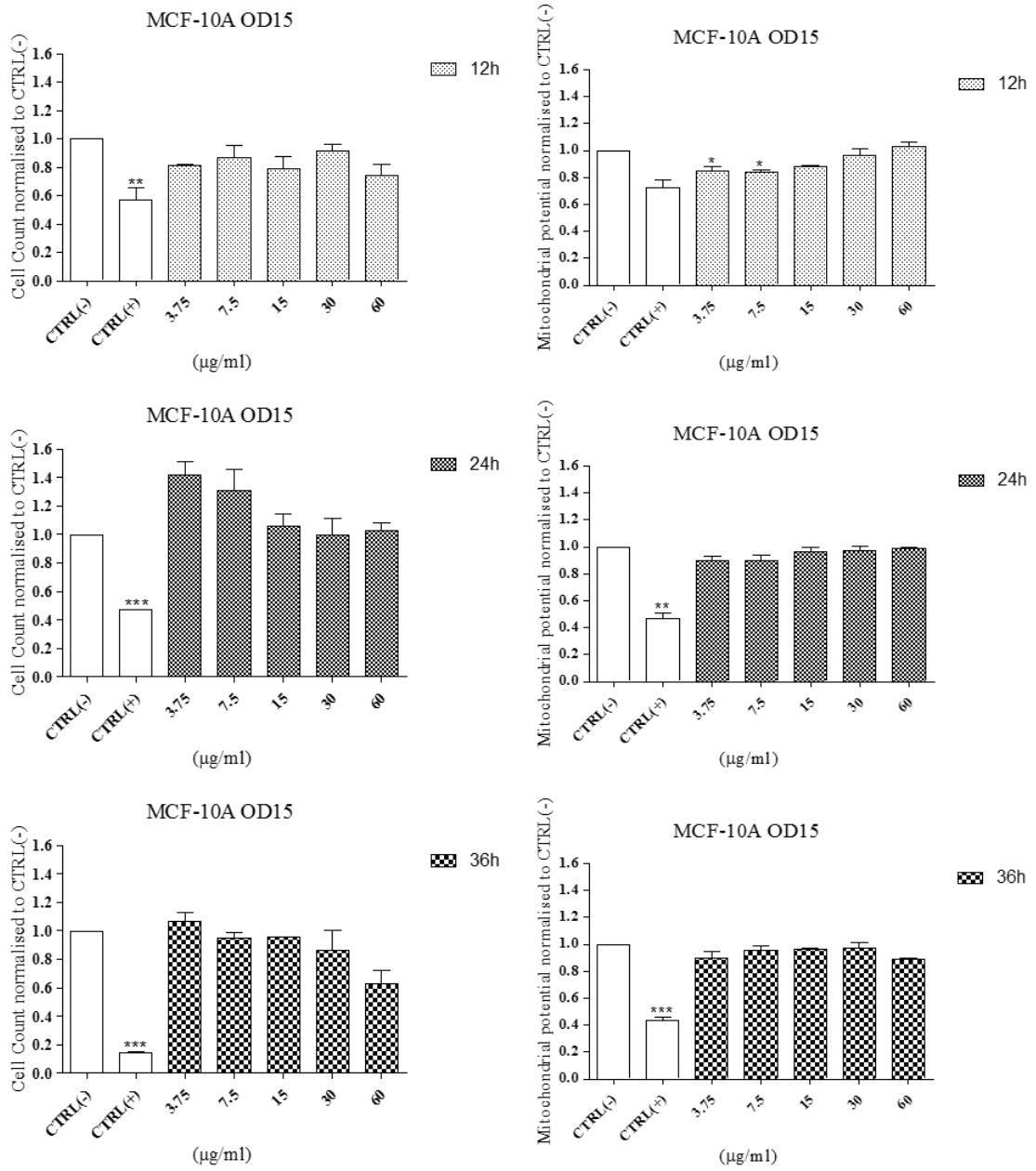

Figure S139: MCF-10A cell line exposed to OD15 MNP.

MCF-10A breast-derived cell line was exposed to OD15 MNP for 12h, 24h and 36h. Cells were stained using the Cytotoxicity II HitKit™ and analysed using the InCell 1000 HCSA device. Variation in cell count and mitochondrial membrane potential were measured compared to untreated control (CTRL(-)) and 1µM CdSe positive control (CTRL(+)). Statistical significance was determined using the one way ANOVA with Tukey post-test for each column compared to untreated control (CTRL(-)). p value: *** = <0.001, **=<0.01, *=<0.05

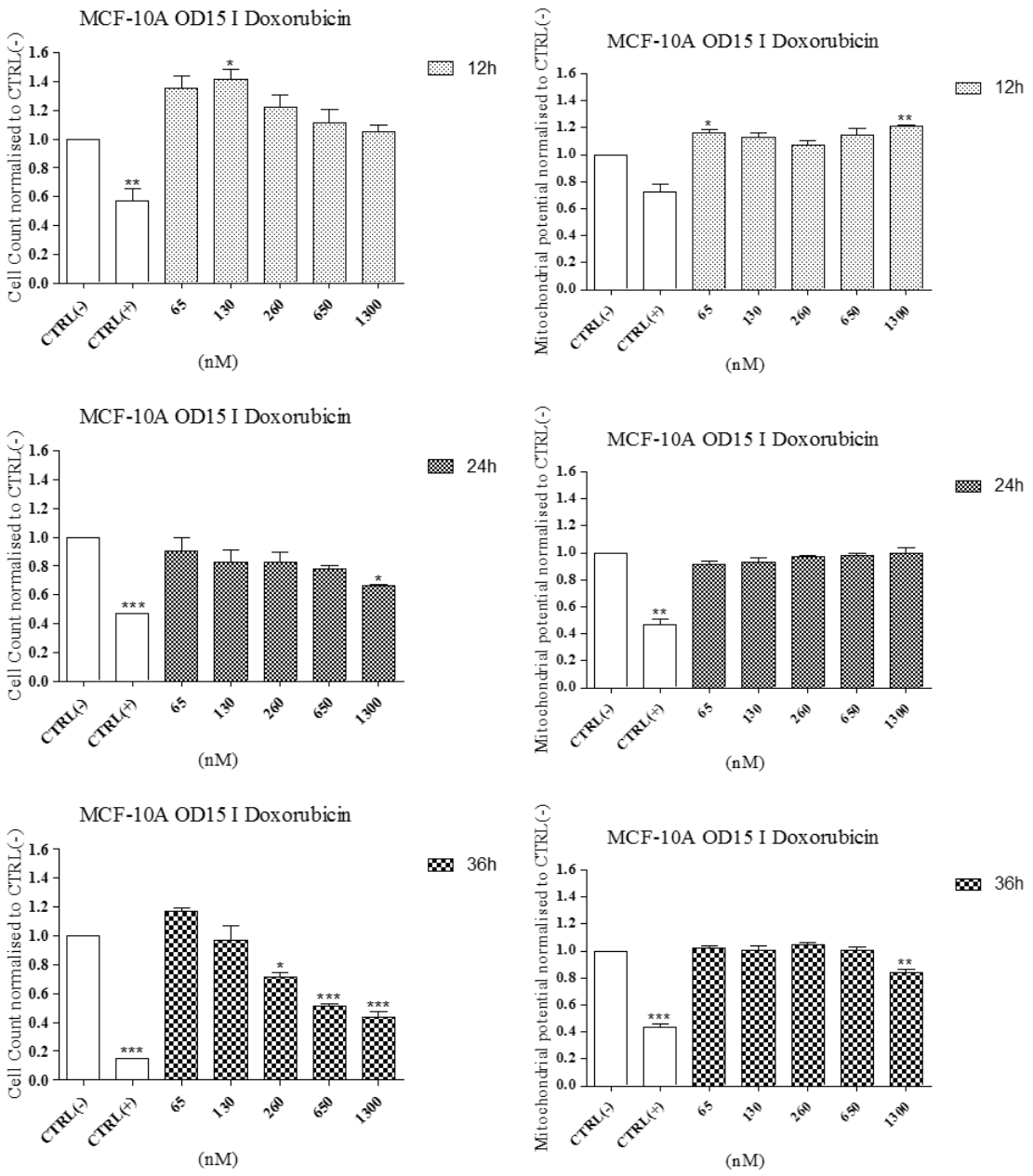

Figure S140: MCF-10A cell line exposed to OD15_I_Doxorubicin MNP.

MCF-10A breast-derived cell line was exposed to OD15_I_Doxorubicin MNP for 12h, 24h and 36h. Cells were stained using the Cytotoxicity II HitKit™ and analysed using the InCell 1000 HCSA device. Variation in cell count and mitochondrial membrane potential were measured compared to untreated control (CTRL(-)) and 1µM CdSe positive control (CTRL(+)). Statistical significance was determined using the one way ANOVA with Tukey post-test for each column compared to untreated control (CTRL(-)). p value: *** = <0.001, **=<0.01, *=<0.05

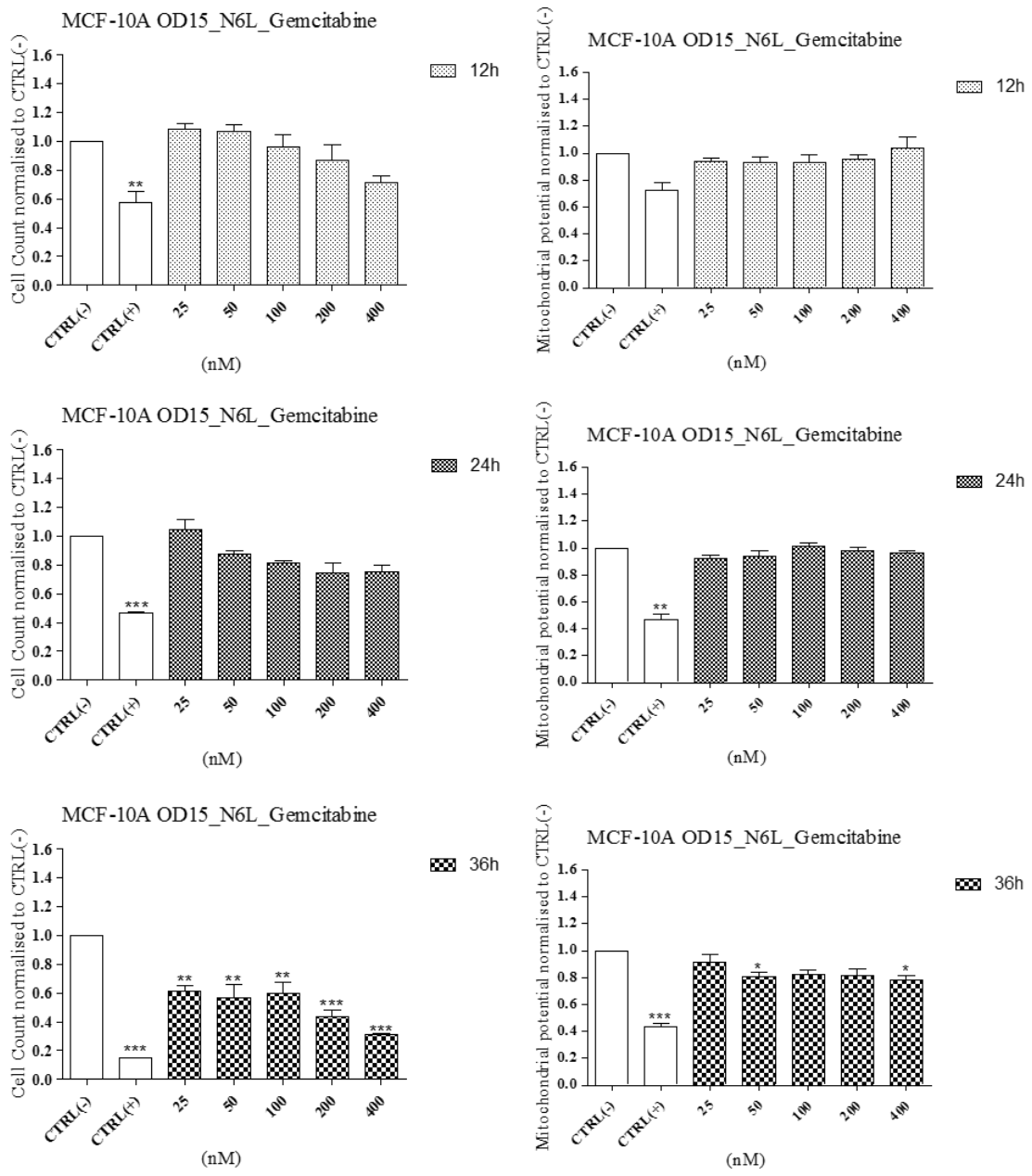

Figure S141: MCF-10A cell line exposed to OD15_N_Gemcitabine MNP.

MCF-10A breast-derived cell line was exposed to OD15_N_Gemcitabine MNP for 12h, 24h and 36h. Cells were stained using the Cytotoxicity II HitKit™ and analysed using the InCell 1000 HCSA device. Variation in cell count and mitochondrial membrane potential were measured compared to untreated control (CTRL(-)) and 1µM CdSe positive control (CTRL(+)). Statistical significance was determined using the one way ANOVA with Tukey post-test for each column compared to untreated control (CTRL(-)). p value: *** = <0.001, **=<0.01, *=<0.05

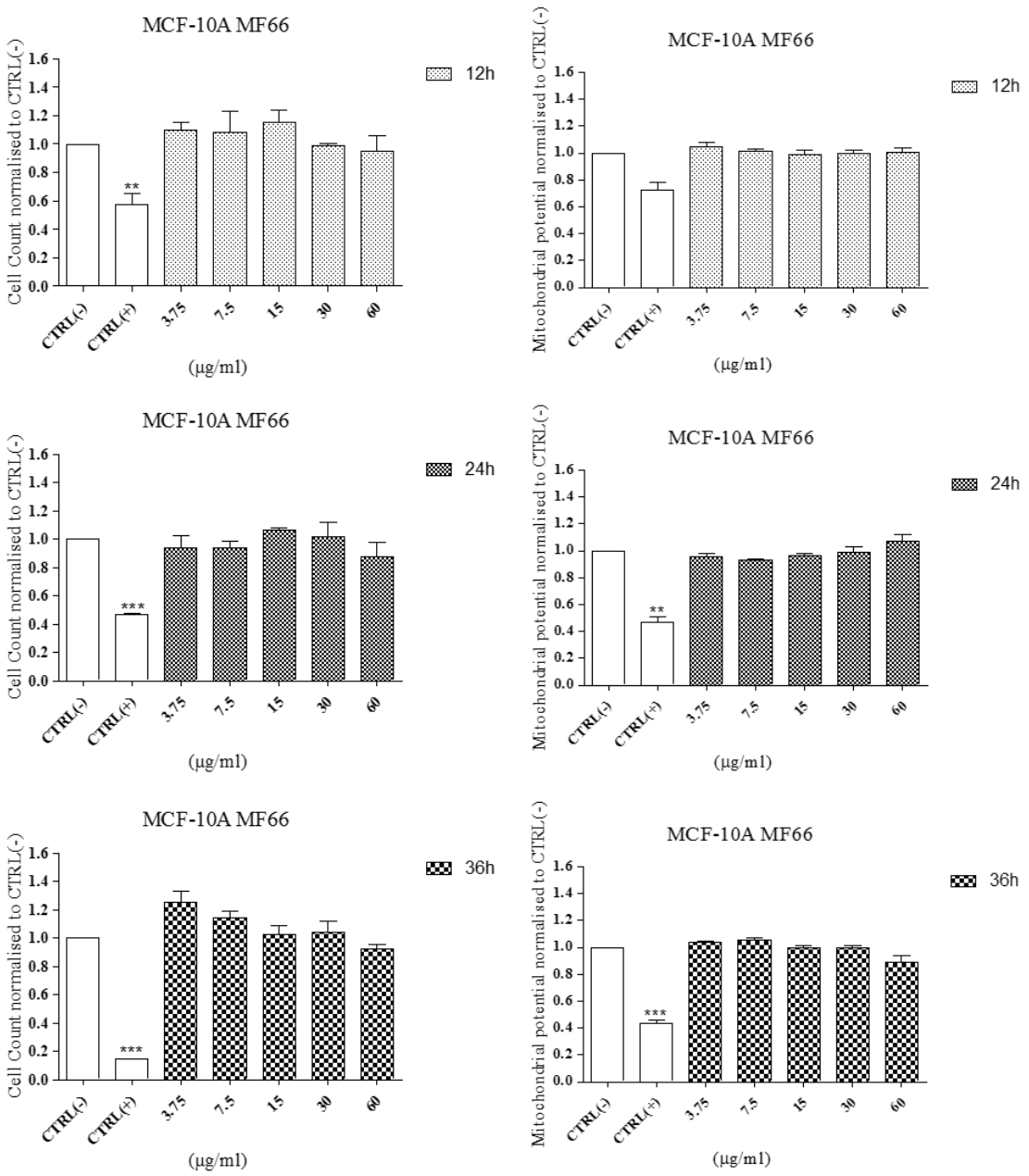

Figure S142: MCF-10A cell line exposed to MF66 MNP.

MCF-10A breast-derived cell line was exposed to MF66 MNP for 12h, 24h and 36h. Cells were stained using the Cytotoxicity II HitKit™ and analysed using the InCell 1000 HCSA device. Variation in cell count and mitochondrial membrane potential were measured compared to untreated control (CTRL(-)) and 1µM CdSe positive control (CTRL(+)). Statistical significance was determined using the one way ANOVA with Tukey post-test for each column compared to untreated control (CTRL(-)). p value: *** = <0.001, **=<0.01, *=<0.05

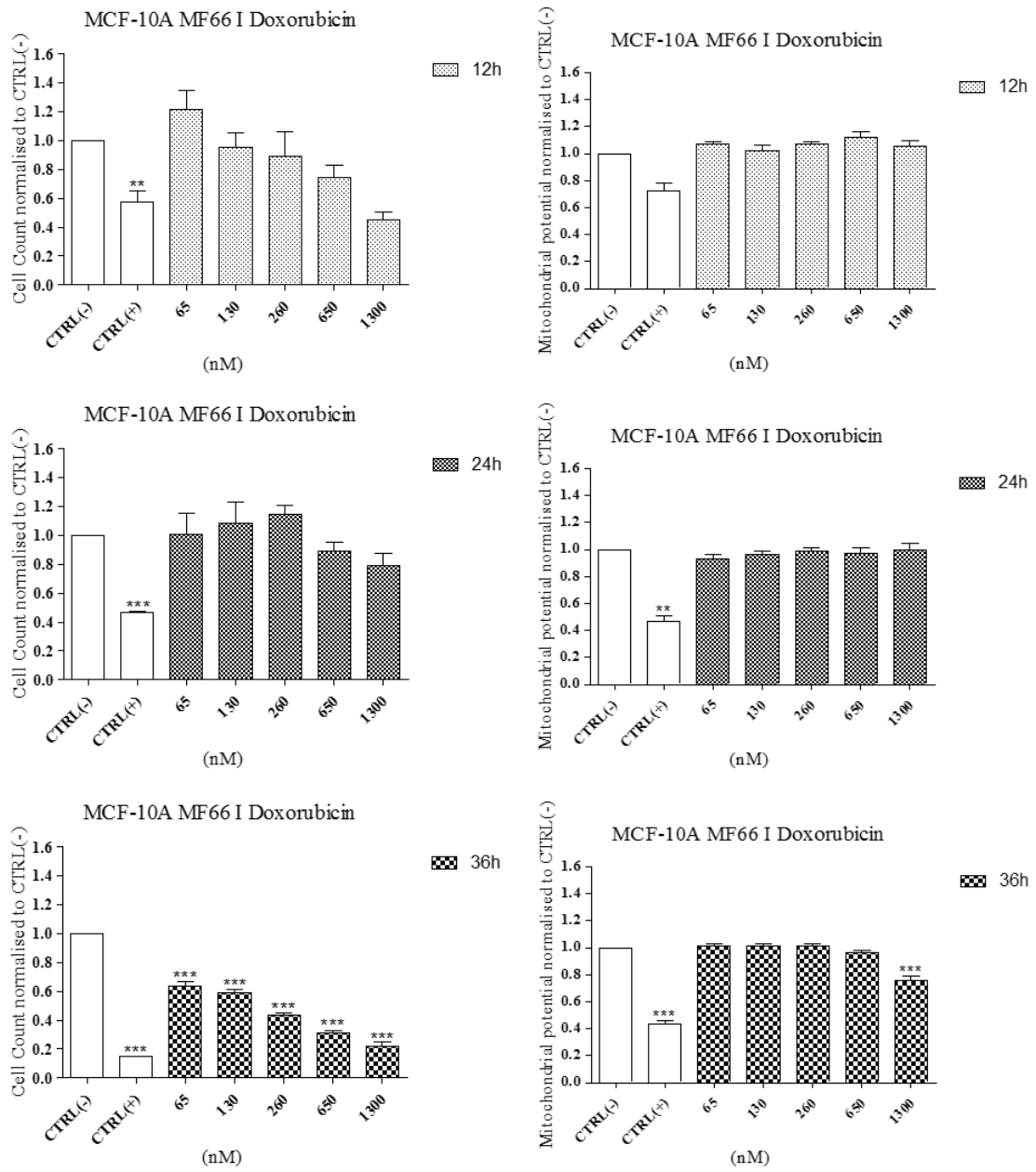

Figure S143: MCF-10A cell line exposed to MF66_I_Doxorubicin MNP.

MCF-10A breast-derived cell line was exposed to MF66_I_Doxorubicin MNP for 12h, 24h and 36h. Cells were stained using the Cytotoxicity II HitKit™ and analysed using the InCell 1000 HCSA device. Variation in cell count and mitochondrial membrane potential were measured compared to untreated control (CTRL(-)) and 1µM CdSe positive control (CTRL(+)). Statistical significance was determined using the one way ANOVA with Tukey post-test for each column compared to untreated control (CTRL(-)). p value: *** = <0.001, **=<0.01, *=<0.05

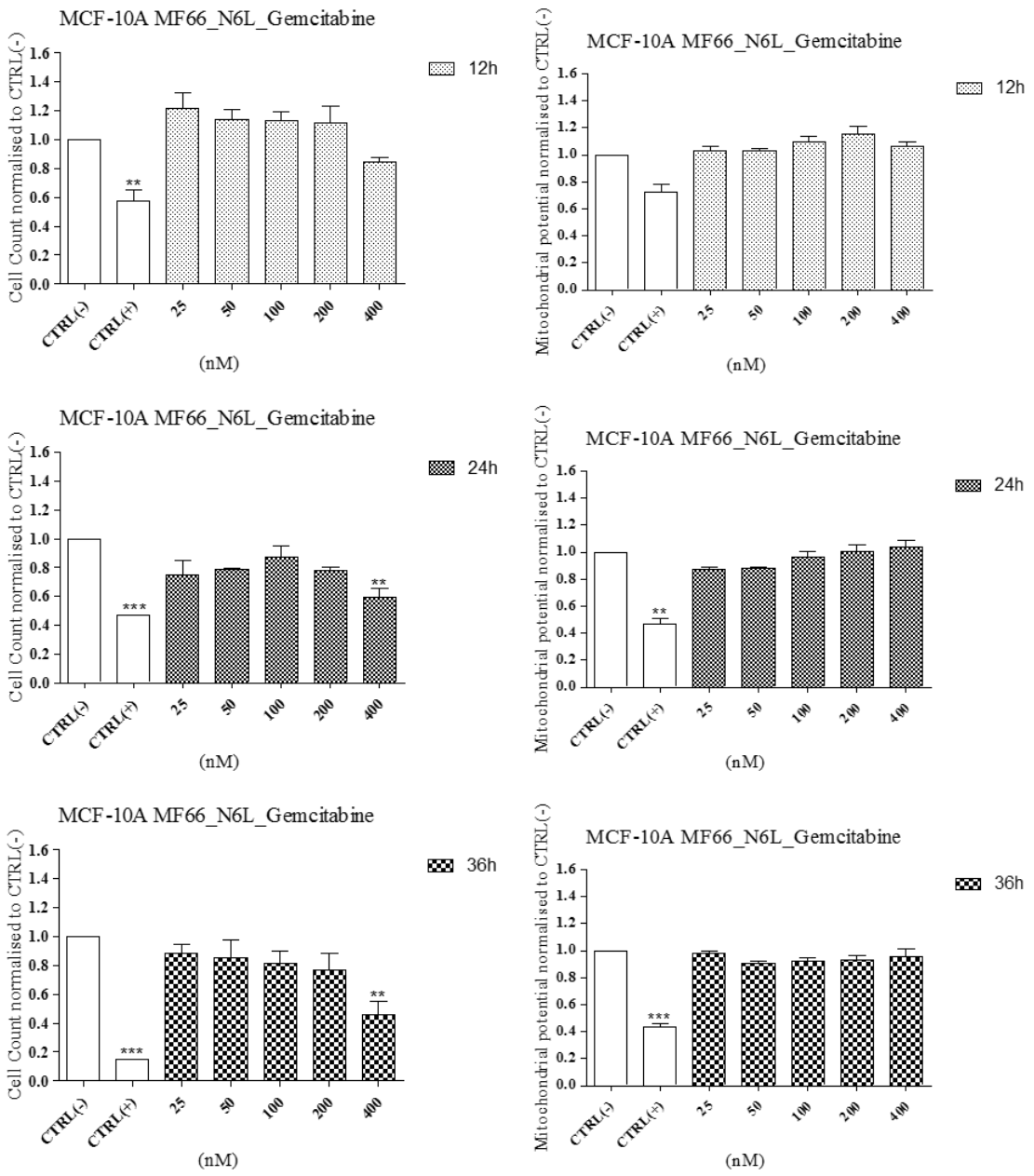

Figure S144: MCF-10A cell line exposed to MF66_N_Gemcitabine MNP.

MCF-10A breast-derived cell line was exposed to MF66_N_Gemcitabine MNP for 12h, 24h and 36h. Cells were stained using the Cytotoxicity II HitKit™ and analysed using the InCell 1000 HCSA device. Variation in cell count and mitochondrial membrane potential were measured compared to untreated control (CTRL(-)) and 1µM CdSe positive control (CTRL(+)). Statistical significance was determined using the one way ANOVA with Tukey post-test for each column compared to untreated control (CTRL(-)). p value: *** = <0.001, **=<0.01, *=<0.05

Appendix 4: Excitation and emission spectra

Fluorescent dye excitation and emission profiles with filter sets and light source used.

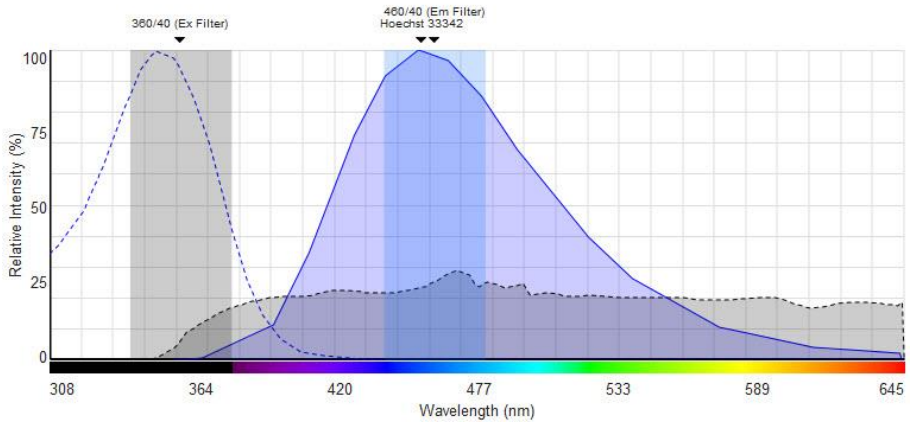

Figure S145: Hoechst 33342 spectrum.

Hoechst 33342 was excited with a xenon lamp (black dotted line) using the indicated D360/40X excitation filter and HQ460/40M emission filter.

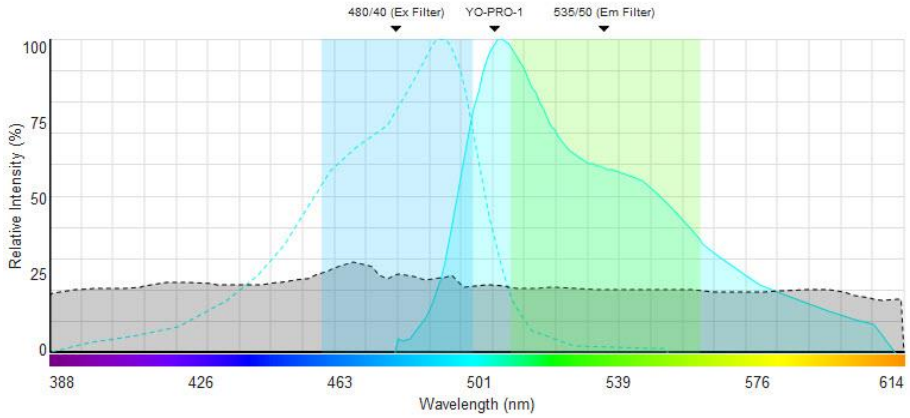

Figure S146: Cell membrane permeability (YO-PRO-1) spectrum.

YO-PRO-1 cell permeability dye was excited with a xenon lamp (black dotted line) using the indicated HQ480/40X excitation filter and HQ535/50M emission filter.

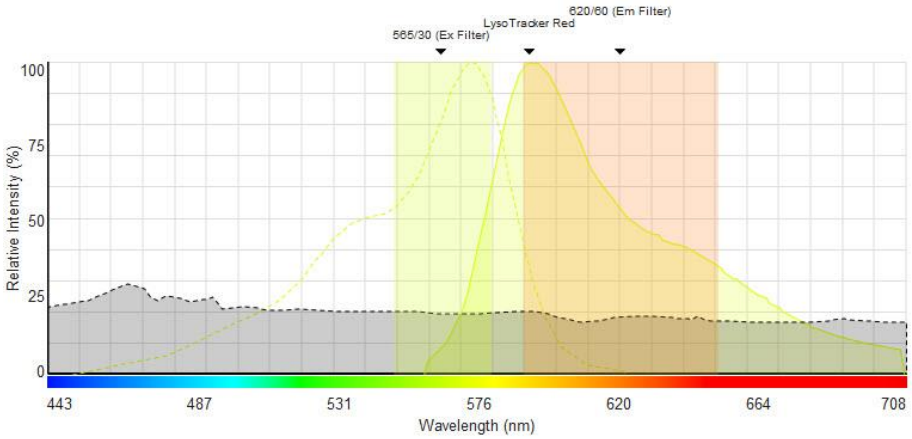

Figure S147: Lysotracker® Red spectrum.

Lysotracker® Red dye was excited with a xenon lamp (black dotted line) using the indicated HQ565/30X excitation filter and HQ620/60M emission filter.

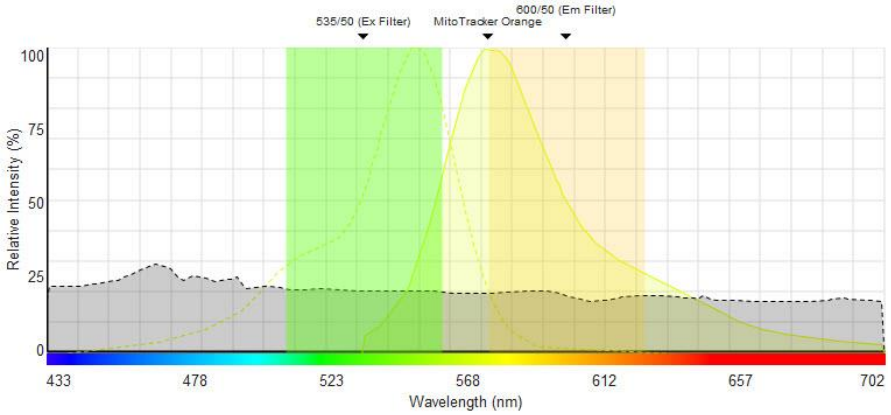

Figure S148: MitoTracker® Orange spectrum.

MitoTracker® dye was excited with a xenon lamp (black dotted line) using the indicated HQ535/50X excitation filter and HQ600/50M emission filter.

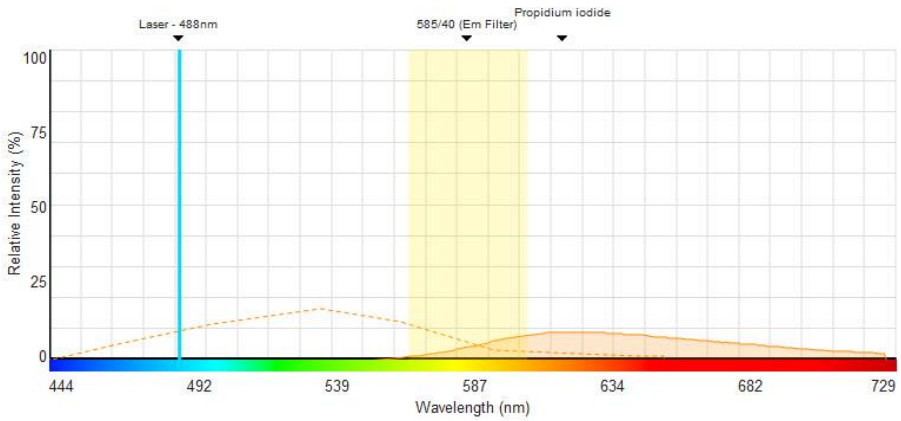

Figure S149: Propidium Iodide spectrum.

Propidium Iodide dye was excited with a 488 nm laser (vertical blue line) using a 585/40 emission filter

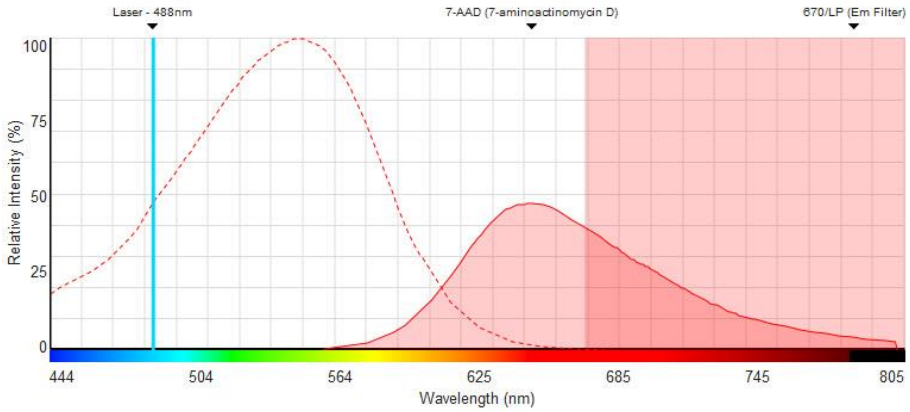

Figure S150: 7-AAD spectrum.

7-AAD dye was excited with a 488 nm laser (vertical blue line) and fluorescence detected using a 670/long pass emission filter

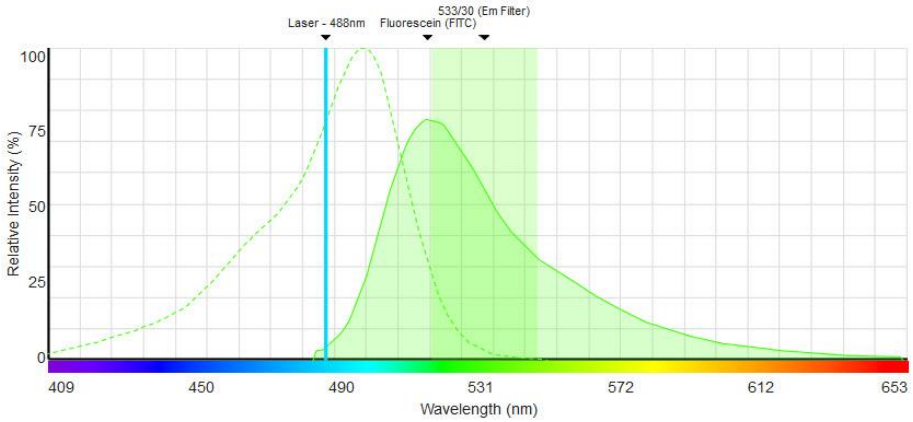

Figure S151: Annexin V FITC spectrum.

Annexin V-FITC dye was excited with a 488 nm laser (vertical blue line) and fluorescence detected using a 533/30 emission filter.